

Pertanika Journal of

SCIENCE &

TECHNOLOGY

JST

VOL. 32 (3) APR. 2024



PERTANIKA
JOURNALS

A scientific journal published by Universiti Putra Malaysia Press

PERTANIKA JOURNAL OF SCIENCE & TECHNOLOGY

About the Journal

Overview

Pertanika Journal of Science & Technology is an official journal of Universiti Putra Malaysia. It is an open-access online scientific journal. It publishes original scientific outputs. It neither accepts nor commissions third party content.

Recognised internationally as the leading peer-reviewed interdisciplinary journal devoted to the publication of original papers, it serves as a forum for practical approaches to improve quality on issues pertaining to science and engineering and its related fields.

Pertanika Journal of Science & Technology currently publishes 6 issues a year (*January, March, April, July, August, and October*). It is considered for publication of original articles as per its scope. The journal publishes in **English** and it is open for submission by authors from all over the world.

The journal is available world-wide.

Aims and scope

Pertanika Journal of Science & Technology aims to provide a forum for high quality research related to science and engineering research. Areas relevant to the scope of the journal include: bioinformatics, bioscience, biotechnology and bio-molecular sciences, chemistry, computer science, ecology, engineering, engineering design, environmental control and management, mathematics and statistics, medicine and health sciences, nanotechnology, physics, safety and emergency management, and related fields of study.

History

Pertanika Journal of Science & Technology was founded in 1993 and focuses on research in science and engineering and its related fields.

Vision

To publish a journal of international repute.

Mission

Our goal is to bring the highest quality research to the widest possible audience.

Quality

We aim for excellence, sustained by a responsible and professional approach to journal publishing. Submissions can expect to receive a decision within 90 days. The elapsed time from submission to publication for the articles averages 180 days. We are working towards decreasing the processing time with the help of our editors and the reviewers.

Abstracting and indexing of Pertanika

Pertanika Journal of Science & Technology is now over 27 years old; this accumulated knowledge and experience has resulted the journal being abstracted and indexed in SCOPUS (Elsevier), Clarivate Web of Science (ESCI), EBSCO, ASEAN CITATION INDEX, Microsoft Academic, Google Scholar, and MyCite.

Citing journal articles

The abbreviation for Pertanika Journal of Science & Technology is *Pertanika J. Sci. & Technol.*

Publication policy

Pertanika policy prohibits an author from submitting the same manuscript for concurrent consideration by two or more publications. It prohibits as well publication of any manuscript that has already been published either in whole or substantial part elsewhere. It also does not permit publication of manuscript that has been published in full in proceedings.

Code of Ethics

The *Pertanika* journals and Universiti Putra Malaysia take seriously the responsibility of all of its journal publications to reflect the highest in publication ethics. Thus, all journals and journal editors are expected to abide by the journal's codes of ethics. Refer to *Pertanika*'s **Code of Ethics** for full details, or visit the journal's web link at http://www.pertanika.upm.edu.my/code_of_ethics.php

Originality

The author must ensure that when a manuscript is submitted to *Pertanika*, the manuscript must be an original work. The author should check the manuscript for any possible plagiarism using any program such as Turn-It-In or any other software before submitting the manuscripts to the *Pertanika* Editorial Office, Journal Division.

All submitted manuscripts must be in the journal's acceptable similarity index range:
≤ 20% – PASS; > 20% – REJECT.

International Standard Serial Number (ISSN)

An ISSN is an 8-digit code used to identify periodicals such as journals of all kinds and on all media—print and electronic.

Pertanika Journal of Science & Technology: e-ISSN 2231-8526 (Online).

Lag time

A decision on acceptance or rejection of a manuscript is reached in 90 days (average). The elapsed time from submission to publication for the articles averages 180 days.

Authorship

Authors are not permitted to add or remove any names from the authorship provided at the time of initial submission without the consent of the journal's Chief Executive Editor.

Manuscript preparation

For manuscript preparation, authors may refer to *Pertanika*'s **INSTRUCTION TO AUTHORS**, available on the official website of *Pertanika*.

Editorial process

Authors who complete any submission are notified with an acknowledgement containing a manuscript ID on receipt of a manuscript, and upon the editorial decision regarding publication.

Pertanika follows a **double-blind peer-review** process. Manuscripts deemed suitable for publication are sent to reviewers. Authors are encouraged to suggest names of at least 3 potential reviewers at the time of submission of their manuscripts to *Pertanika*, but the editors will make the final selection and are not, however, bound by these suggestions.

Notification of the editorial decision is usually provided within 90 days from the receipt of manuscript. Publication of solicited manuscripts is not guaranteed. In most cases, manuscripts are accepted conditionally, pending an author's revision of the material.

The journal's peer review

In the peer-review process, 2 to 3 referees independently evaluate the scientific quality of the submitted manuscripts. At least 2 referee reports are required to help make a decision.

Peer reviewers are experts chosen by journal editors to provide written assessment of the **strengths** and **weaknesses** of written research, with the aim of improving the reporting of research and identifying the most appropriate and highest quality material for the journal.

Operating and review process

What happens to a manuscript once it is submitted to *Pertanika*? Typically, there are 7 steps to the editorial review process:

1. The journal's Chief Executive Editor and the Editor-in-Chief examine the paper to determine whether it is relevance to journal needs in terms of novelty, impact, design, procedure, language as well as presentation and allow it to proceed to the reviewing process. If not appropriate, the manuscript is rejected outright and the author is informed.
2. The Chief Executive Editor sends the article-identifying information having been removed, to 2 to 3 reviewers. They are specialists in the subject matter of the article. The Chief Executive Editor requests that they complete the review within 3 weeks.

Comments to authors are about the appropriateness and adequacy of the theoretical or conceptual framework, literature review, method, results and discussion, and conclusions. Reviewers often include suggestions for strengthening of the manuscript. Comments to the editor are in the nature of the significance of the work and its potential contribution to the research field.

3. The Editor-in-Chief examines the review reports and decides whether to accept or reject the manuscript, invite the authors to revise and resubmit the manuscript, or seek additional review reports. In rare instances, the manuscript is accepted with almost no revision. Almost without exception, reviewers' comments (to the authors) are forwarded to the authors. If a revision is indicated, the editor provides guidelines for attending to the reviewers' suggestions and perhaps additional advice about revising the manuscript.
4. The authors decide whether and how to address the reviewers' comments and criticisms and the editor's concerns. The authors return a revised version of the paper to the Chief Executive Editor along with specific information describing how they have addressed the concerns of the reviewers and the editor, usually in a tabular form. The authors may also submit a rebuttal if there is a need especially when the authors disagree with certain comments provided by reviewers.
5. The Chief Executive Editor sends the revised manuscript out for re-review. Typically, at least 1 of the original reviewers will be asked to examine the article.
6. When the reviewers have completed their work, the Editor-in-Chief examines their comments and decides whether the manuscript is ready to be published, needs another round of revisions, or should be rejected. If the decision is to accept, the Chief Executive Editor is notified.
7. The Chief Executive Editor reserves the final right to accept or reject any material for publication, if the processing of a particular manuscript is deemed not to be in compliance with the S.O.P. of *Pertanika*. An acceptance letter is sent to all the authors.

The editorial office ensures that the manuscript adheres to the correct style (in-text citations, the reference list, and tables are typical areas of concern, clarity, and grammar). The authors are asked to respond to any minor queries by the editorial office. Following these corrections, page proofs are mailed to the corresponding authors for their final approval. At this point, **only essential changes are accepted**. Finally, the manuscript appears in the pages of the journal and is posted on-line.

Pertanika Journal of
**SCIENCE
& TECHNOLOGY**

Vol. 32 (3) Apr. 2024



A scientific journal published by Universiti Putra Malaysia Press

EDITOR-IN-CHIEF

Luqman Chuah Abdullah
Chemical Engineering

CHIEF EXECUTIVE EDITOR

Mohd Sapuan Salit

UNIVERSITY PUBLICATIONS COMMITTEE

CHAIRMAN

Zamberi Sekawi

EDITORIAL STAFF

Journal Officers:

Ellyianur Puteri Zainal
Kanagamalar Silvarajoo
Siti Zuhaila Abd Wahid
Tee Syin Ying

Editorial Assistants:

Ku Ida Mastura Ku Baharom
Siti Juridah Mat Arip
Zulinaardawati Kamarudin

English Editor:

Norhanizah Ismail

PRODUCTION STAFF

Pre-press Officers:

Nur Farrah Dila Ismail
Wong Lih Jiun

WEBMASTER

IT Officer:

Illi Najwa Mohamad Sakri

EDITORIAL OFFICE

JOURNAL DIVISION

Putra Science Park
1st Floor, IDEA Tower II
UPM-IMTDC Technology Centre
Universiti Putra Malaysia
43400 Serdang, Selangor Malaysia.

General Enquiry

Tel. No: +603 9769 1622 | 1616

E-mail:

executive_editor.pertanika@upm.edu.my

URL: www.journals-jd.upm.edu.my

PUBLISHER

UPM Press

Universiti Putra Malaysia
43400 UPM, Serdang, Selangor, Malaysia.
Tel: +603 9769 8851
E-mail: penerbit@putra.upm.edu.my
URL: <http://penerbit.upm.edu.my>



ASSOCIATE EDITOR

2023-2024

Adem Kilicman

Mathematical Sciences
Universiti Putra Malaysia, Malaysia

Miss Laiha Mat Kiah

Security Services Sn: Digital Forensic,
Steganography, Network Security,
Information Security, Communication
Protocols, Security Protocols
Universiti Malaya, Malaysia

Saidur Rahman

Renewable Energy, Nanofluids, Energy
Efficiency, Heat Transfer, Energy Policy
Sunway University, Malaysia

EDITORIAL BOARD

2022-2024

Abdul Latif Ahmad

Chemical Engineering
Universiti Sains Malaysia, Malaysia

Ho Yuh-Shan

Water research, Chemical Engineering
and Environmental Studies
Asia University, Taiwan

Mohd Zulkifly Abdullah

Fluid Mechanics, Heat Transfer,
Computational Fluid Dynamics (CFD)
Universiti Sains Malaysia, Malaysia

Ahmad Zaharin Aris

Hydrochemistry, Environmental
Chemistry, Environmental Forensics,
Heavy Metals
Universiti Putra Malaysia, Malaysia

Hsiu-Po Kuo

Chemical Engineering
National Taiwan University, Taiwan

Mohd. Ali Hassan

Bioprocess Engineering, Environmental
Biotechnology
Universiti Putra Malaysia, Malaysia

Azlina Harun@Kamaruddin

Enzyme Technology, Fermentation
Technology
Universiti Sains Malaysia, Malaysia

Ivan D. Rukhlenko

Nonlinear Optics, Silicon Photonics,
Plasmonics and Nanotechnology
The University of Sydney, Australia

Nor Azah Yusof

Biosensors, Chemical Sensor, Functional
Material
Universiti Putra Malaysia, Malaysia

Bassim H. Hameed

Chemical Engineering: Reaction
Engineering, Environmental Catalysis &
Adsorption
Qatar University, Qatar

Lee Keat Teong

Energy Environment, Reaction
Engineering, Waste Utilization,
Renewable Energy
Universiti Sains Malaysia, Malaysia

Norbahiah Misran

Communication Engineering
Universiti Kebangsaan Malaysia,
Malaysia

Biswajeet Pradhan

Digital image processing, Geographical
Information System (GIS), Remote
Sensing
University of Technology Sydney,
Australia

Mohamed Othman

Communication Technology and
Network, Scientific Computing
Universiti Putra Malaysia, Malaysia

Roslan Abd-Shukur

Physics & Materials Physics,
Superconducting Materials
Universiti Kebangsaan Malaysia,
Malaysia

Daud Ahmad Israf Ali

Cell Biology, Biochemical, Pharmacology
Universiti Putra Malaysia, Malaysia

Mohd Shukry Abdul Majid

Polymer Composites, Composite
Pipes, Natural Fibre Composites,
Biodegradable Composites, Bio-
Composites
Universiti Malaysia Perlis, Malaysia

Wing Keong Ng

Aquaculture, Aquatic Animal Nutrition,
Aqua Feed Technology
Universiti Sains Malaysia, Malaysia

INTERNATIONAL ADVISORY BOARD

2021-2024

CHUNG, Neal Tai-Shung

Polymer Science, Composite and
Materials Science
National University of Singapore,
Singapore

Mohamed Pourkashanian

Mechanical Engineering, Energy, CFD
and Combustion Processes
Sheffield University, United Kingdom

Yulong Ding

Particle Science & Thermal Engineering
University of Birmingham, United
Kingdom

Hiroshi Uyama

Polymer Chemistry, Organic
Compounds, Coating, Chemical
Engineering
Osaka University, Japan

Mohini Sain

Material Science, Biocomposites,
Biomaterials
University of Toronto, Canada

ABSTRACTING AND INDEXING OF PERTANIKA JOURNALS

The journal is indexed in SCOPUS (Elsevier), Clarivate-Emerging Sources Citation Index (ESCI), BIOSIS, National Agricultural Science (NAL), Google Scholar, MyCite, ISC. In addition, Pertanika JSSH is recipient of "CREAM" Award conferred by Ministry of Higher Education (MoHE), Malaysia.

The publisher of Pertanika will not be responsible for the statements made by the authors in any articles published in the journal. Under no circumstances will the publisher of this publication be liable for any loss or damage caused by your reliance on the advice, opinion or information obtained either explicitly or implied through the contents of this publication.

All rights of reproduction are reserved in respect of all papers, articles, illustrations, etc., published in Pertanika. Pertanika provides free access to the full text of research articles for anyone, web-wide. It does not charge either its authors or author-institution for refereeing/publishing outgoing articles or user-institution for accessing incoming articles.

No material published in Pertanika may be reproduced or stored on microfilm or in electronic, optical or magnetic form without the written authorization of the Publisher.

Copyright © 2021 Universiti Putra Malaysia Press. All Rights Reserved.

Pertanika Journal of Science & Technology
Vol. 32 (3) Apr. 2024

Contents

Foreword	i
<i>Mohd Sapuan Salit</i>	
 <i>Review Article</i>	
A Review of Non-wood Lignocellulose Waste Material Reinforced Concrete for Light-weight Construction Applications	979
<i>Hossam Saleh Salem Saeed, Agusril Syamsir, Mohd Supian Abu Bakar, Muhammad Imran Najeeb, Abdulrahman Alhayek, Zarina Itam, Muhammad Rizal Muhammad Asyraf and Mohd Radzi Ali</i>	
Development of Small-scale Integrated Hydroponics—Animal Waste Bioreactor (AWB) for Romaine Lettuce (<i>Lactuca sativa</i> L. var. longifolia) Production	1003
<i>Elman Cantero Torres, Theody Bernardo Sayco, Marvin Mateo Cinense, Jonathan Viernes Fabula, Wendy Mateo and Carolyn Grace Galo Somera</i>	
Anti-friction and Wear Resistance Performance of Palm Olein Grease with Molybdenum Disulfide Additive	1023
<i>Nadiyah Aqilahwati Abdullah, Nurul Farhana Mohd Yusof and Zaidi Mohd Ripin</i>	
 <i>Review Article</i>	
Supercritical Carbon Dioxide Extraction of Citronella Oil Review: Process Optimization, Product Quality, and Applications	1043
<i>Nicky Rahmana Putra, Ahmad Hazim Abdul Aziz, Dwila Nur Rizkiyah, Mohd Azizi Che Yunus, Ratna Surya Alwi, Reny Tri Anggraini, Siti Khodijah, Irianto Irianto and Lailatul Qomariyah</i>	
An Empirical Evaluation of Adapting Hybrid Parameters for CNN-based Sentiment Analysis	1071
<i>Mohammed Maree, Mujahed Eleyat and Shatha Rabayah</i>	
Mathematical Modelling of Scission Electrospun Polystyrene Fibre by Ultrasonication Scission	1087
<i>Cheryl Rinai Raja, Marini Sawawi, Shirley Johnathan Tanjong and Nurliyana Truna</i>	

An Accident Prediction Model Based on ARIMA in Kuala Lumpur, Malaysia, Using Time Series of Actual Accidents and Related Data <i>Boon Chong Choo, Musab Abdul Razak, Mohd Zahirasri Mohd Tohir, Dayang Radiah Awang Biak and Syafie Syam</i>	1103
Effects of NaOH Concentration and Plate Surface Texture on the Performance of the HHO Generator <i>Asmawi Marullah Ridwan, Muhd Ridzuan Mansor, Noreffendy Tamaldin, Fahamsyah Hamdan Latief and Viktor Vekky Ronald Repi</i>	1123
Effect of Bimetallic Co-Cu/Dolomite Catalyst on Glycerol Conversion to 1,2-Propanediol <i>Norsahida Azri, Ramli Irmawati, Usman Idris Nda-Umar, Mohd Izham Saiman, Yun Hin Taufiq-Yap and Ghassan Abdulkareem-Alsultan</i>	1141
Evaluation of Microalgae <i>Chlorella vulgaris</i> and <i>Tetradesmus bernardii</i> for Cultivation and Nutrient Removal in Palm Oil Mill Effluent <i>Mohammad Navid Wais, Shahrizim Zulkifly, Mohd Hafiz Ibrahim, Afiqah Mohamed and Zana Ruhaizat Zana Rudin</i>	1161
Study of LED Retrofit Lamps in HSPV Luminaires Based on Photometric Method for Road Lighting <i>Mohd Hanif Jamaludin, Wan Zakiah Wan Ismail, Elina Mohd Husini and Nor Ain Mohd Bahrar</i>	1187
Application of Membrane-less Microbial Fuel Cell in Reducing Human Hazards from Dewatered Sludge <i>Fatin Nur Izzati Mohd Fadzil, Chen Sep Ngee, Mohammed Zharif Asyrani Mohammed Alias, Muhammad Adib Fadhlullah Muhammad Lukman, Amira Suriaty Yaakop, Muaz Mohd Zaini Makhtar and Ana Masara Ahmad Mokhtar</i>	1203
<i>Review Article</i>	
Weed Management Using UAV and Remote Sensing in Malaysia Paddy Field: A Review <i>Zaid Ramli, Abdul Shukor Juraimi, Mst. Motmainna, Nik Norasma Che'Ya, Muhammad Huzairah Mohd Roslim, Nisfariza Mohd Noor and Anuar Ahmad</i>	1219
SPICE Modeling and Performance Analysis of Enhancement- Mode GaN HEMTs for Augmented Hard-Switching Energy Conversion Efficiency <i>Xinzhong Liu, Suhaidi Shafie, Mohd Amran Mohd Radzi, Norhafiz Azis, Nurbahirah Norddin, Ismail Lawal, Normaziah Zulkifli and Abdul Hafiz Abdul Karim</i>	1243

- Optimisation of the Distribution System Reliability with Shielding and Grounding Design Under Various Soil Resistivities 1263
Jia-Wen Tang, Chin-Leong Wooi, Wen-Shan Tan, Hadi Nabipour Afrouzi, Hana Abdull Halim and Syahrin Nizam Md Arshad@Hashim
- Identifying Communities with Modularity Metric Using Louvain and Leiden Algorithms 1285
Siti Haryanti Hairol Anuar, Zuraida Abal Abas, Norhazwani Md Yunos, Mohd Fariduddin Mukhtar, Tedy Setiadi and Abdul Samad Shibghatullah
- Elicitation of Cryptic Secondary Metabolites and Antibacterial Activities from Mangrove and Cave Soil Actinomycetes 1301
Intan Azzween Natasha Ahmad Razi, Nurunajah Ab Ghani, Siti Hajar Sadiran, Suhaidi Ariffin, Sharifah Aminah Syed Mohamad and Anis Low Muhammad Low
- Review Article*
- Detection of Sedge Weeds Infestation in Wetland Rice Cultivation Using Hyperspectral Images and Artificial Intelligence: A Review 1317
Muhamad Noor Hazwan Abd Manaf, Abdul Shukor Juraimi, Mst. Motmainna, Nik Norasma Che'Ya, Ahmad Suhaizi Mat Su, Muhammad Huzairah Mohd Roslim, Anuar Ahmad and Nisfariza Mohd Noor
- An Improved Ensemble Machine Learning Approach for Diabetes Diagnosis 1335
Mohanad Mohammed Rashid, Omar Mahmood Yaseen, Rana Riyadh Saeed and Maher Talal Alasaady
- Integrating Green Infrastructure Distribution and Green Corridor Mapping with Proposed Green Trail Area and Wildlife-Human Conflict Using Remote Sensing-GIS Approach 1351
Syarifuddin Misbari, Jacqueline Isabella Anak Gisen, Nur Arissa Farhanis Mohd Rosli, Amir Asyraf Mohd Fauzi and Aishah Abu Bakar
- Model-driven Approach to Improve Sago Drying with a Fluidized Bed Dryer 1363
Nur Tantiyani Ali Othman and Nurfadilah Izaty Senu
- Evaluation of Field Performance and Energy Consumption of a Medium-sized Combine Harvester for Harvesting Glutinous Rice in Malaysia 1385
Nazmi Mat Nawi, Bomo Muhammad Isa, Samsuzana Abd Aziz and Mohamad Saufi Mohd Kassim

Effect of Maturity Stages on Physical Properties of Cocoa (*Theobroma cacao* L.) Pods 1401

Babatunde Oluwamayokun Soyoye, Nazmi Mat Nawi, Mohamad Ariffin Zulkifli, Guangnan Chen, Nurfadzilah Madian, Ahmad Faiz Mokhtar, Siti Nooradzah Adam and Dimas Firmanda Al Riza

Selected papers from the 5th International Conference on Innovation in Science and Technology

Guest Editors: Eri Sato-Shimokawara, Muslihah Wook and Kurnianingsih

C-Slot Circular Polarized Antenna for Hybrid Energy Harvesting and Wireless Sensing 1413

Irfan Mujahidin, Sidiq Syamsul Hidayat, Muhamad Cahyo Ardi Prabowo and Akio Kitagawa

Modeling of Light Lifting Robotic Arm 1427

Norfarahana Adibah Raffie, Noor Hafizah Amer, Syed Mohd Fairuz Syed Mohd Dardin, Khisbullah Hudha and Saiddi Ali Firdaus Mohamed Ishak

Foreword

Welcome to the third issue of 2024 for the *Pertanika Journal of Science and Technology (PJST)*!

PJST is an open-access journal for studies in Science and Technology published by Universiti Putra Malaysia Press. It is independently owned and managed by the university for the benefit of the world-wide science community.

This issue contains 25 articles; four review articles and the rest are regular articles. The authors of these articles come from different countries namely Afghanistan, Indonesia, Iraq, Japan, Kingdom of Saudi Arabia, Malaysia, Nigeria, Palestine, Philippines and United Arab Emirates.

A regular article titled “Development of Small-Scale Integrated Hydroponics—Animal Waste Bioreactor (AWB) for Romaine Lettuce (*Lactuca sativa* L. var. longifolia) Production” written by Elman Cantero Torres and co-researchers from Philippines. In their research, three integrated hydroponics-AWB systems, with varying concentrations of CMT at 1,000 ppm, 1,200 ppm, and 1,400 ppm total dissolved solids (maintained within an upper and lower bound of 50 ppm), were constructed, tested, and compared to conventional hydroponics that used a nutrient solution maintained at 1,000 ppm TDS. The test result suggests that the ideal concentration of CMT in the system is 1,000 ppm. Within the optimum manure tea concentration, the small-scale integrated hydroponics-AWB produced romaine lettuce with growth parameters comparable to conventional hydroponics. In addition, increasing the CMT concentration to 1,400 ppm negatively impacts the plant growth parameters of romaine lettuce. Detailed information on this study can be found on page 1003.

Xinzhi Liu et al. from Universiti Putra Malaysia and Universiti Malaysia Perlis evaluated the enhanced semiconducting characteristics of Gallium Nitride (GaN) high-electron-mobility transistors (HEMT) over conventional silicon power devices by analyzing spontaneous and piezoelectric polarizations of wurtzite GaN crystalline structure and the formation of two-dimensional electron gas (2DEG). The lateral device structure of enhancement-mode GaN HEMT and normally switched-on depletion mode GaN HEMT are compared. A device-under-test (DUT) equivalent model incorporating parasitic components is proposed, adopting the EPC2204 Level 3 SPICE model. The model is simulated in a novel Double Pulse Test (DPT) topology with clamping and snubber subcircuits using LTSPICE software. The performance of GaN HEMT is compared to a MOSFET with similar parameters, and the impact of parasitic inductances and stray capacitances is evaluated through switching analysis. The findings underscore the potential of E-GaN HEMTs to enhance the efficiency of DC-DC converters, particularly for photovoltaic energy delivery. Further details of the article are available on page 1243.

Another article that we wish to highlight is “Identifying Communities with Modularity Metric Using Louvain and Leiden Algorithms” by Siti Haryanti Hairol Anuar, Zuraida Abal Abas, Norhazwani Md Yunos, Mohd Fariduddin Mukhtar, Tedy Setiadi and Abdul Samad Shibghatullah. Their research focuses on two community detection algorithms, the Louvain and Leiden methods, which are based on agglomerative techniques using modularity. Both Louvain and Leiden have an optimal value of the result, but there is an improvement from Leiden. The Leiden method was found to perform better in terms of execution time and the modularity metric. Detailed information on this study is presented on page 1285.

We anticipate that you will find the evidence presented in this issue to be intriguing, thought-provoking and useful in reaching new milestones in your own research. Please recommend the journal to your colleagues and students to make this endeavour meaningful.

All the papers published in this edition underwent Pertanika’s stringent peer-review process involving a minimum of two reviewers comprising internal as well as external referees. This was to ensure that the quality of the papers justified the high ranking of the journal, which is renowned as a heavily-cited journal not only by authors and researchers in Malaysia but by those in other countries around the world as well.

We would also like to express our gratitude to all the contributors, namely the authors, reviewers, Editor-in-Chief and Editorial Board Members of PJST, who have made this issue possible.

PJST is currently accepting manuscripts for upcoming issues based on original qualitative or quantitative research that opens new areas of inquiry and investigation.

Chief Executive Editor

Mohd Sapuan Salit

executive_editor.pertanika@upm.edu.my

Review Article

A Review of Non-wood Lignocellulose Waste Material Reinforced Concrete for Light-weight Construction Applications

Hossam Saleh Salem Saeed¹, Agusril Syamsir^{1,2*}, Mohd Supian Abu Bakar², Muhammad Imran Najeeb², Abdulrahman Alhayek¹, Zarina Itam^{1,2}, Muhammad Rizal Muhammad Asyraf³ and Mohd Radzi Ali⁴

¹*Civil Engineering Department, College of Engineering, Universiti Tenaga Nasional, Jalan IKRAM - UNITEN, 43000 Kajang, Selangor, Malaysia*

²*Institute of Energy Infrastructure, College of Engineering, Universiti Tenaga Nasional, Jalan IKRAM - UNITEN, 43000 Kajang, Selangor, Malaysia*

³*Centre for Advanced Composite Materials (CACM), Universiti Teknologi Malaysia (UTM), Johor Bahru 81310, Johor, Malaysia*

⁴*Institute of Tropical Forestry and Forest Products, Universiti Putra Malaysia, 43400 UPM, Serdang, Selangor, Malaysia*

ABSTRACT

In recent decades, non-wood lignocellulosic materials have gained significant attention, particularly in concrete applications for construction purposes. This study delves into utilising non-wood lignocellulosic materials for reinforcing concrete in construction applications. Lignocellulosic material emerges as a promising option for formulating new fibre cement compositions, thereby enhancing the sustainability, affordability, and performance of construction materials. Moreover, this research broadens the horizons of

recycling agricultural waste by facilitating rational disposal and optimal utilisation. Through a comprehensive review, the study reveals that flax fibres, coir pith, prickly pear fibres, and rice husk ash waste exhibit superior workability compared to their counterparts. Furthermore, the strength of non-wood lignocellulosic reinforced concrete, incorporating bagasse ash, rice husk ash, and nutshell ash, peaked when fine aggregate replacement reached 15%, surpassing other types of non-wood

ARTICLE INFO

Article history:

Received: 07 March 2023

Accepted: 09 October 2023

Published: 01 April 2024

DOI: <https://doi.org/10.47836/pjst.32.3.01>

E-mail addresses:

Hussam7us@gmail.com (Hossam Saleh Salem Saeed)

Agusril@uniten.edu.my (Agusril Syamsir)

mohd.supian@uniten.edu.my (Mohd Supian Abu Bakar)

imran.najeeb@uniten.edu.my (Muhammad Imran Najeeb)

rahman.hayek@gmail.com (Abdulrahman Alhayek)

iZarina@uniten.edu.my (Zarina Itam)

muhammadasyraf.mr@utm.my (Muhammad Rizal

Muhammad Asyraf)

mohd.radzi@utm.my (Mohd Radzi Ali)

* Corresponding author

lignocellulosic reinforced concrete. Adding a small quantity of prickly pear fibre to cement enhances the thermal conductivity of concrete, consequently improving compressive strength, flexural strength, tensile strength, and elastic modulus. This research is relevant to international research as it advances sustainable construction materials with desirable properties, benefiting society and various industries.

Keywords: Impact, light-weight construction, mechanical properties, non-wood lignocellulose waste, reinforced-concrete

INTRODUCTION

Lignocellulosic materials, derived from crop residues, are vital resources comprising lignin, cellulose, and hemicellulose. They fall into two categories: wood and non-wood. Wood includes hardwood and softwood (Feen et al., 2017; Radzi et al., 2019), while non-wood encompasses materials like sugarcane bagasse (Monteiro et al., 2019), rice husks (Yang et al., 2006), and pineapple leaves (Najeeb et al., 2021). Non-wood resources are gaining prominence due to tree scarcity and global fibre demand. They offer advantages like easier processing and shorter growth cycles. Non-wood lignocellulosic materials find applications across diverse fields, from pulp and paper to bioenergy and construction materials. Increasing demand for construction materials, the depletion of fossil fuels, and environmental concerns pose challenges (Gregorova et al., 2011; Supian et al., 2018; Thiruganasambanthan et al., 2022).

Several factors affect the demand for lignocellulosic materials. The depletion of fossil fuel resources, raw material shortages, increased demand for building materials, and emerging environmental issues such as pollution and global warming pose significant challenges to the construction industry. In the context of concrete, lignocellulosic materials are utilised as substitutes for cement, aiming to address the environmental impact of the cement industry, which accounts for a substantial portion of worldwide CO² emissions (Ali et al., 2020, 2021; Syamsir et al., 2023; Zeidabadi et al., 2018). The use of agricultural waste materials as concrete aggregates has been identified as a viable approach to reducing raw material consumption. Developing nations generate approximately 400 million metric tonnes of agricultural waste annually, and the adoption of waste materials in concrete production could contribute to a more sustainable building sector (Bakar & Chin, 2021; Kadier et al., 2021; Omran et al., 2021; Pil et al., 2016). The manufacturing process of Portland cement, as well as the energy, water, aggregate, and fillers required for concrete production and the subsequent disposal of concrete waste, raise concerns regarding the ecological criteria of the contemporary sustainable building sector.

Over the past four decades, extensive research has focused on non-wood lignocellulosic-reinforced concrete composites, aiming to create cost-effective innovations (Hamid et al., 2022; Lima et al., 2013; Momoh & Osofero, 2019; Singh et al., 2021). These studies

consistently show that when lignocellulosic materials are added to cement, it boosts tensile strength and lowers density, enabling applications like fire resistance, thermal insulation, and acoustics. They can replace asbestos-cement and reconstituted wood products such as plywood and particleboard. A significant study by Momoh and Osofero (2019) specifically investigated using oil palm fibres in reinforced concrete. This study highlighted the growing global concerns about carbon emissions in the construction industry. As construction activities contribute significantly to yearly CO₂ emissions and resource use, it is essential to explore sustainable alternatives. With the world's population expected to increase by a third by 2050, agricultural operations and the generation of agricultural waste will rise, especially in emerging nations. It emphasises the need for sustainable construction practices.

Therefore, this study review has been conducted with a comprehensive review of academic literature to provide an overview of how agricultural waste can be used in the concrete industry. Specifically, this study investigates how different agricultural waste materials can replace some of the cement or aggregate in concrete, affecting its properties in various ways. After analysing existing research, this paper identifies the most suitable types of agricultural waste for concrete applications and discusses their broader implications. It includes their positive environmental impact and how they can efficiently utilise agricultural waste. Therefore, this review highlights the importance of agricultural waste research for the concrete industry, contributing valuable insights to the global research community.

AGRICULTURE WASTE

Recent developments in the management and utilisation of agricultural waste signify a paradigm shift in the perception of these materials, which were once considered mere by-products or residues. This critical review assesses these recent advancements and highlights their potential benefits and applications across various sectors. Agricultural waste encompasses a wide array of materials, including crop residues, weeds, leaf litter, sawdust, forest waste, and livestock waste. These materials are generated while cultivating and utilising various agricultural products, such as maize, nutmeg, sugar cane, wood, and palm oil. Recognising and categorising these waste streams is a crucial step in harnessing their potential (Alhazmi & Loy, 2021; Athira et al., 2019; Drück et al., 2020; Hulle et al., 2015; Jain et al., 2015; Lee et al., 2009; Li et al., 2014; Manickam et al., 2015; Pinto et al., 2012; Reddy & Santhosha, 2018).

Recent research has transformed our vision of agricultural waste. These materials are no longer mere by-products but valuable resources that can be harnessed for various purposes. The shift in perception has led to re-evaluating their potential across diverse applications. It includes bioenergy production, composting to enhance soil health, and the development of sustainable construction materials and value-added products (Jha et al., 2021; Kumar et al., 2016; Momoh & Osofero, 2020; Shafiqh et al., 2014). Several factors drive the growing

interest in agricultural waste management and utilisation. First, it aligns with sustainability goals by reducing waste and environmental impact. Second, it offers economic benefits by creating opportunities for generating income from waste streams. Additionally, it addresses pressing challenges, such as the need for alternative energy sources and sustainable construction materials in an era of environmental concerns and resource scarcity.

While recent developments are promising, challenges persist. These include logistical issues related to waste collection and processing, technological constraints in converting waste to valuable products, and the need for regulatory frameworks to govern waste utilisation. Future research should focus on optimising waste utilisation methods, exploring innovative applications, and addressing the environmental and social implications of these practices. Therefore, recent advancements in agricultural waste management and utilisation mark a significant shift towards recognising the value of these materials. Their multifaceted applications, ranging from energy production to sustainable construction, promise a more sustainable and resource-efficient future. However, addressing existing challenges and fostering interdisciplinary collaboration will be crucial to fully realising the potential of agricultural waste across various sectors.

Types of Crop Agricultural Waste

Numerous improvements have been made lately in agricultural waste, showing a wide range of options and advantages in numerous industries (Figure 1). The utilisation of various crop waste products is examined in depth in this critical assessment, which also discusses their economic and environmental significance. The landscape of agricultural waste is incredibly diverse, encompassing a wide range of materials. It includes rice paws, rice husk ash, bagasse ash, sugar cane fibres, flax fibres, ash waste, palm oil, nutshell ash, bamboo leaves, apricots, and numerous other agricultural residues (Asyraf et al., 2021; Kadier et al., 2021). These materials are generated globally in millions of metric tonnes each year, primarily consisting of plant stems, leaves, and mesocarp that remain after the main plant products are harvested (Jaafar et al., 2018; Kengkhetkit & Amornsakchai, 2012; Khan et al., 2010; Norrahim et al., 2019; Saba et al., 2015; Sreekala et al., 1997).

The realisation of value-added opportunities linked with agricultural waste, particularly in rural regions, is a significant development in economic opportunities. These waste materials, often considered burdensome, can become valuable resources when properly harnessed. This shift can have substantial economic implications for industrial activities in rural regions (Azman et al., 2021; Nurazzi et al., 2021; Chavan et al., 2020). Figures 1 to 4 in this review visually represent some of the most prevalent types of agricultural waste discussed. This visual representation underscores these materials' sheer diversity and potential (Al-shayaa et al., 2021; Alhazmi & Loy, 2021; Heniegal et al., 2020). As this critical analysis emphasises, the optimal use of agricultural waste goes well beyond waste reduction, moving towards

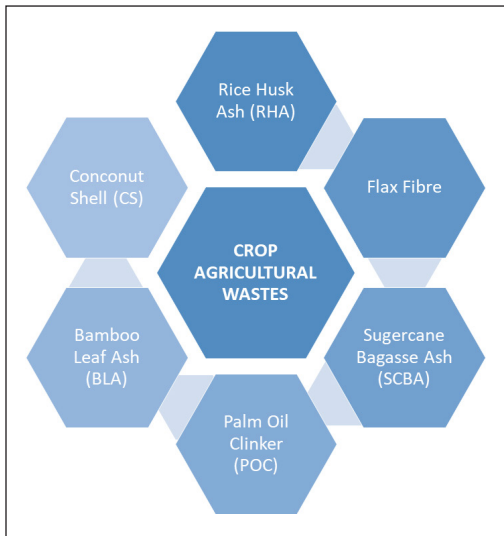


Figure 1. Classification of lignocellulose material from crop agricultural wastes used in the industry of concrete from other studies (Foo & Hameed, 2009; Susilawati et al., 2020)

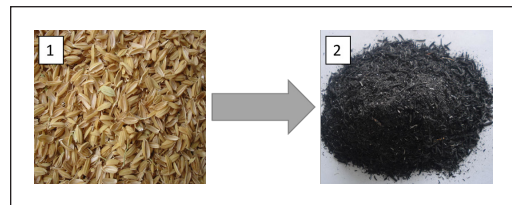


Figure 2. Examples of agro-waste: (1) Rice husk. (2) Rice husk ash (Mohamad et al., 2019)

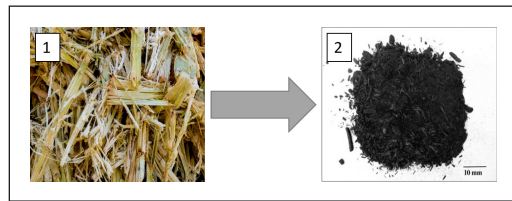


Figure 3. Examples of agro-waste: (1) Sugarcane bagasse. (2) Sugarcane bagasse ash (Mohamad et al., 2019)

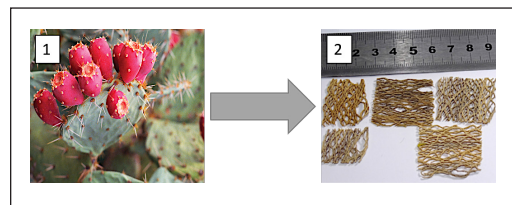


Figure 4. Examples of agro-waste: (1) Prickly pear. (2) Prickly pear fibres (Kammoun & Trabelsi, 2019)

sustainability and economic practices. It offers a pathway to sustainable and economically sound practices. Converting these waste materials into valuable products, such as bioenergy, construction, and value-added products, reduces environmental burdens and contributes to economic growth.

While the potential is evident, challenges remain. These include technological and logistical hurdles in converting waste to valuable products, as well as the need for supportive policies and practices. Future developments should focus on optimising utilisation methods, exploring innovative applications, and addressing sustainability concerns. Thus, recent developments in agricultural waste utilisation emphasise the vast potential of these materials. From waste reduction to economic growth and sustainability, the proper management and utilisation of agricultural waste can revolutionise various industries. As research and practices evolve, the world is poised to unlock new possibilities for harnessing these resources, fostering economic and environmental prosperity.

The Importance of Using Agricultural Waste in Concrete

Recent developments in the utilisation of agricultural waste in concrete construction have sparked significant advancements in the housing and infrastructure sectors, offering

promising long-term benefits, cost-effectiveness, and environmental sustainability compared to conventional Portland cement (El-Messiry et al., 2017; Libre et al., 2011). The increasing interest among researchers and builders in utilising agro-residuals in concrete is driven by their potential to revolutionise the construction industry and improve nationwide infrastructure. This approach aligns with expanding socio-economic conditions and engineering innovations (Alsubari et al., 2021; Sizirici et al., 2021). Crop wastes, which make up a substantial portion of global agricultural biomass, have gained prominence due to their abundance and cost-effectiveness, making them a viable choice for sustainable construction practices. Agricultural waste products contain fibres with valuable characteristics, including stiffness, high efficacy, thermal insulation, and tensile properties. These fibres contribute to the overall performance of agro-cement composites, enhancing their suitability for various construction applications. Agro-cement composites demonstrate exceptional heat insulation capabilities. This feature addresses the challenge of agricultural waste disposal and contributes to mitigating the urban heat island effect. It aligns with sustainable urban development goals by creating more comfortable and energy-efficient living environments.

Using agricultural waste in concrete reduces waste and disposal issues and the carbon footprint associated with traditional cement production. This eco-friendly approach supports environmental conservation and sustainability goals. Additionally, it offers economic benefits through cost savings and potentially opens up new revenue streams for farmers and agricultural industries. Furthermore, recent developments in integrating agricultural waste into concrete have unveiled a sustainable and efficient approach with multiple advantages. These include waste reduction, cost-effectiveness, enhanced material properties, and environmental friendliness. This innovation holds the potential to transform the construction industry and improve the quality of infrastructure while promoting environmental responsibility. However, challenges remain, including optimising processing methods, ensuring product consistency, and addressing regulatory considerations. Future research and development efforts should focus on overcoming these challenges to fully harness the potential of agro-cement composites.

FRESH CONCRETE PROPERTIES

Workability

The workability of such compositions, essential for their practical application in construction, is vital information gained from carefully examining recent developments in using agro-waste materials in concrete mixtures. Workability is a key consideration when incorporating agro-waste materials into concrete, and researchers have extensively investigated this aspect. Slump tests have been widely conducted to evaluate the workability of various concrete mixtures (Givi et al., 2010; Oorkalan & Chithra, 2020). Researchers

have found that the choice of agro-waste material significantly influences workability. For instance, rice husk ash has been associated with a high slump value, indicating good workability. On the other hand, when used as a partial substitute for fine aggregate, coconut coir pith resulted in a lower slump value, suggesting reduced workability. Several factors contribute to variations in workability. The inclusion of certain agro-waste materials, such as oil palm broom fibre (OPBF), red mud (RM), and fine palm oil clinker (POC) aggregate, can decrease workability. The reduction in workability with fine POC is attributed to fewer voids compared to aggregate size, reducing the need for additional lubrication (Abutaha et al., 2016). Similarly, RM's weight and fine particle size lead to increased water absorption and reduced flow.

The impact of agro-waste fibres on workability varies. For instance, prickly pear fibres have minimal effects on workability, with only a slight decrease in slump value observed for longer fibres. Longer fibres can sometimes cause segregation during concrete mixing (Kammoun & Trabelsi, 2019). Moreover, the presence of specific agro-waste materials can influence the water-to-binder ratio. Rice husk ash allows for a lower water-to-binder ratio while maintaining the required workability. In contrast, samples containing processed waste tea ash (PWTA) require an increased water-to-binder ratio due to its porous nature and high specific surface area, leading to water absorption during mixing (Djamaluddin et al., 2020). Different agro-waste materials exhibit unique characteristics that impact workability. For example, concrete mixes containing blast furnace slag (BLA) require more water than powdered clay brick mixes to achieve a comparable slump (Kolawole et al., 2021).

The increased workability of the coir pith (CP) can be attributed to its substantial water absorption capacity (Oorkalan & Chithra, 2020). Even short-length fibres in materials like prickly pear fibres (PPF) and flax fibres (FF) can significantly affect workability. Figure 5 illustrates the influence of various agro-waste materials on concrete workability. It provides

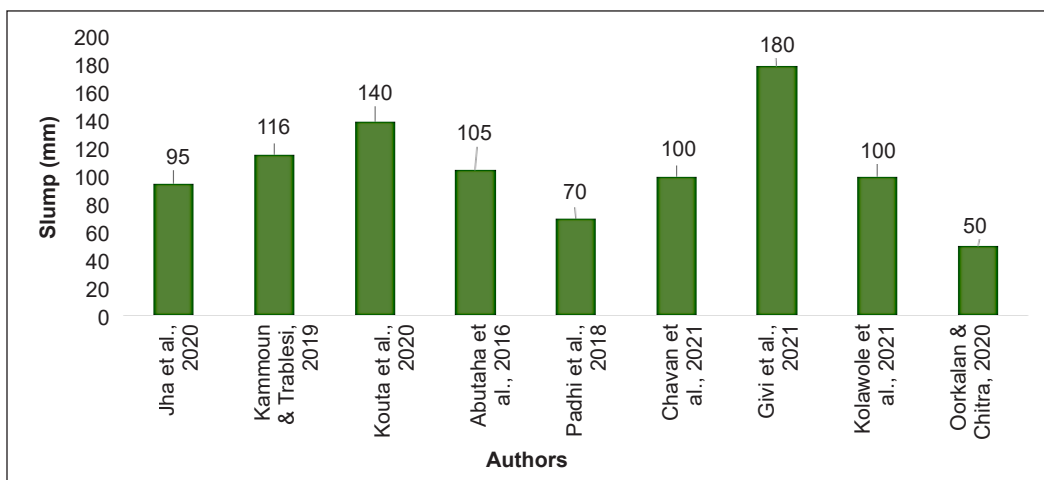


Figure 5. Maximum slump result from different studies

valuable insights into their effects on the water-to-binder ratio, water absorption, and slump values. These findings contribute to optimising concrete mixtures and effectively utilising agro-waste materials in construction applications. In outcome, successful agro-waste integration into construction practice depends on understanding how various agro-waste elements affect the workability of concrete mixtures. To create sustainable and successful concrete formulations, researchers have discovered critical elements and traits that affect workability.

Bulk Density

A thorough analysis of recent advancements in the field reveals a variety of findings regarding the bulk density of concrete containing various types of agro-waste materials (Ogundipe et al., 2021; Wu et al., 2018). Figure 6 compares the maximum bulk density values reported in various studies. Ogundipe et al. (2021) recorded the highest value of 2500 kg/m³ when using Periwinkle (PWS) and Palm Kernel Shells (PKS) as agricultural waste in their study. On the other hand, Wu et al. (2018) reported the lowest value of 575 kg/m³ when utilising carbonised apricot shell (CAS) as a substitute for coarse aggregate in the concrete mix. Figure 6 also presents the bulk density values of other agro-waste materials, such as Corn Cob Ash (CCA), Palm Oil Clinker (POC), Periwinkle (PWS), Palm Kernel Shells (PKS), Processed Waste Tea Ash (PWTA), Rice Husk Ash (RHA), and Bagasse Ash (BA). The use of carbonised materials resulted in reduced concrete density and specific density. The concrete density of peach shell (PS) was lower than that of apricot shell (AS) due to the lighter nature of peach shells.

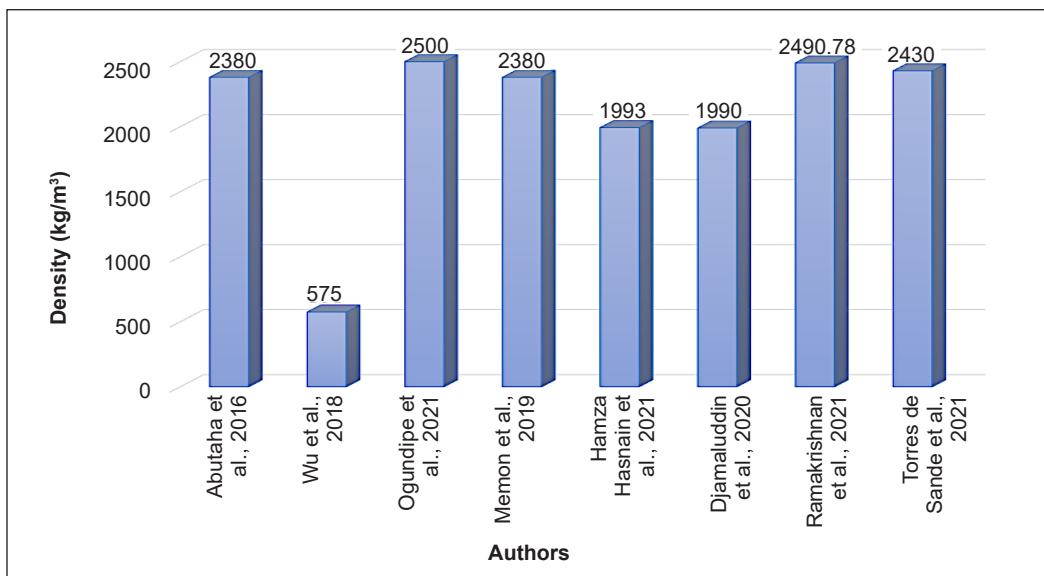


Figure 6. Maximum bulk density results from different studies

The reduction in bulk density observed in the Memon et al. (2019) study with corncob ash (CCA) was attributed to its lower density compared to fine aggregates (Memon et al., 2019). Similarly, the reduction in density with PwTA was due to its lower density, which also affected the overall density of paving block concrete (Djamaluddin et al., 2020; de Sande et al., 2021). Furthermore, the study by de Sande et al. (2021) has indicated that when sugarcane bagasse ash (ScBA) was used as a substitute, the density values initially increased to an optimum replacement level of 15%. However, concentrations of ScBA exceeding 15% delayed the hydration process, leading to a decline in density. The finer particles of ScBA filled the voids in the concrete mass, resulting in an increased density of up to 15% replacement. Therefore, the thorough research emphasises how different agro-waste elements affect the bulk density of concrete. The results show how diverse waste kinds, including carbonised materials, the effect of ash content on hydration, and the connection between agro-ashes and overall concrete porosity affect density. These observations help us better understand how to optimise concrete mixtures for use in construction applications employing agro-waste components.

Shrinkage

The data presented in Figure 7 illustrates the range of shrinkage values obtained from various studies, where most agro-waste materials contribute to a decrease in shrinkage (Kouta et al., 2020; Shaaban, 2021). The study by Kouta et al. (2020) reported a maximum shrinkage value of 3,520 microstrain when utilising flax fibre. Conversely, Shaaban (2021) discovered that the combination of rice husk ash and calcined dolomite powder resulted in the lowest shrinkage value of 60 microstrains. Otherwise, the presence of specific additives such as alum sludge (AS), flax fibre (FF), carpet fibre (CF), and rice husk ash (RHA) leads to a reduction in shrinkage. For instance, increasing the content of alum sludge by 5% to 10% decreases shrinkage during drying and heating processes (Kaish et al., 2021). It can

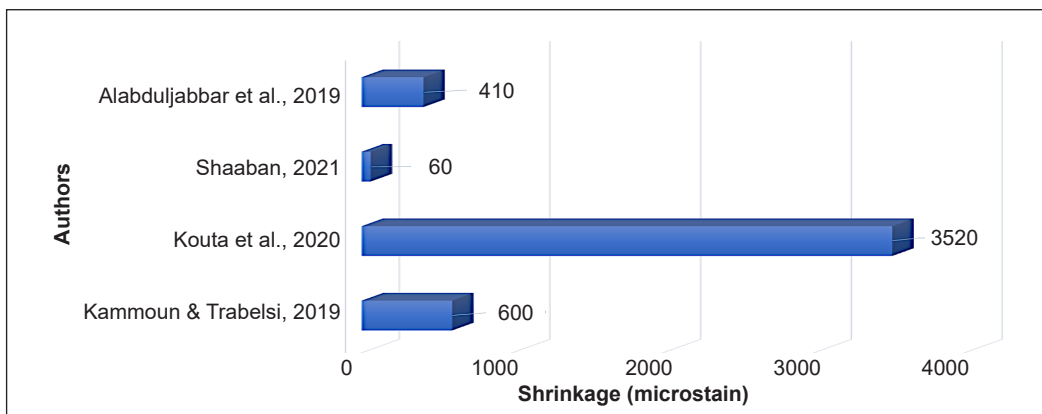


Figure 7. Maximum shrinkage results from different studies

be attributed to small granules of alum sludge within the concrete, which effectively fills capillary gaps and reduces water loss within the concrete structure.

Furthermore, Kouta et al. (2020) indicated that adding 0.3% and 0.6% flax fibres demonstrates a significant decrease in plastic shrinkage compared to the control sample. The length of the flax fibres plays a crucial role, with longer fibres exhibiting a greater impact on reducing the rate and magnitude of plastic shrinkage. This behaviour can be attributed to the increased surface area coverage of longer fibres, which enhances the bonding between concrete particles and mitigates shrinkage (Kaish et al., 2021; Kouta et al., 2020). The presence of additives like alum sludge and flax fibres demonstrates promising results in mitigating plastic and drying shrinkage. Further research and experimentation are warranted to optimise the proportions and combinations of agro-waste materials to achieve the desired reduction in shrinkage while maintaining the overall mechanical properties of the concrete. Overall, the studies reviewed indicate that incorporating certain agro-waste materials can effectively reduce shrinkage in concrete.

HARDENED CONCRETE PROPERTIES

Compressive Strength

Recent developments in using agro-waste materials in concrete have shed light on their impact on compressive strength. Figure 8 provides a comparative analysis of maximum compressive strength values reported in various studies, revealing valuable insights. The data indicates a wide range of compressive strength values achieved through different agro-waste materials. The highest compressive strength, reaching 50.67 MPa, was observed in a

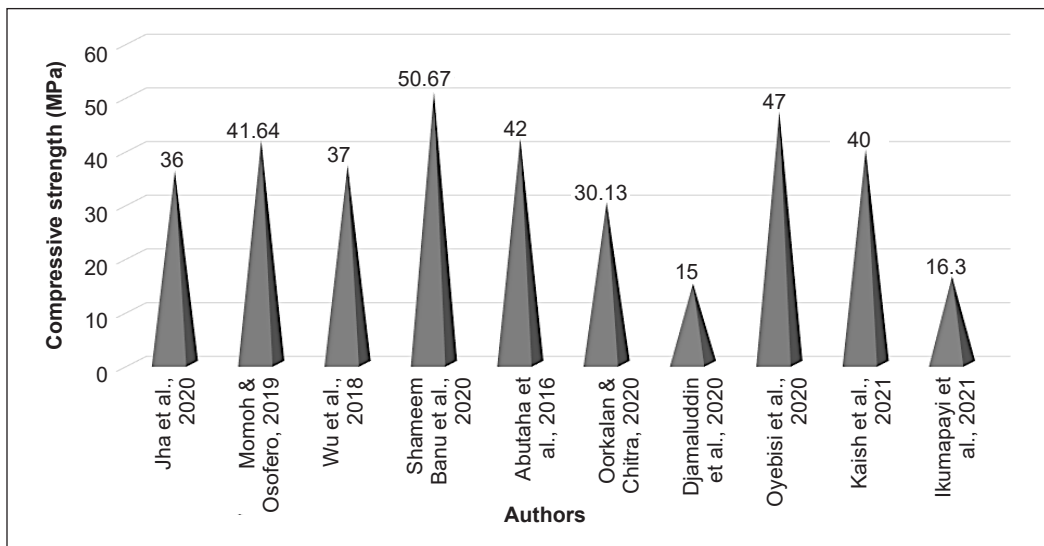


Figure 8. Maximum compressive strength results after 28 days from different studies

study using rice husk ash (RHA) conducted by Banu et al. (2020). Conversely, the lowest compressive strength, 15 MPa, was reported in a study utilising processed waste tea ash (PWTA) by Djameluddin et al. (2020). It is noteworthy that the inclusion of PWTA and oil palm broom fibres (OPBF) has been found to decrease compressive strength, as reported in studies by Djameluddin et al. (2020) and Momoh and Dahunsi (2017). In contrast, the compressive strength was observed to increase with the addition of alum sludge (AS), rice husk ash (RHA), and carbonised apricot shell (CAS) (Djameluddin et al., 2020; Momoh & Dahunsi, 2017; Banu et al., 2020).

Some agro-waste replacements reached their maximum compressive strength at relatively low substitution percentages. For instance, groundnut shell ash (GSA), coconut coir pith (CCP), sugarcane bagasse ash (ScBA), and *Anacardium occidentale* nutshell ash (AONSA) achieved their peak compressive strengths at modest substitution levels (Djameluddin et al., 2020; Ikumapayi et al., 2021; Jha et al., 2021; Momoh & Dahunsi, 2017; Oorkalan & Chithra, 2020; Oyebisi et al., 2020; Banu et al., 2020). Otherwise, the study by Ikumapayi et al. (2021) revealed that the highest compressive strength with groundnut shell ash (GSA) was achieved at an 8% ordinary Portland cement (OPC) substitution, with a subsequent decline in strength at higher substitution percentages. Its decrease in strength is attributed to the higher hydration response of 8% GSA.

The water absorption characteristics of agro-waste materials, such as coir pith, also affect compressive strength. The study by Oorkalan and Chithra (2020) demonstrated a steady loss of strength when the coir pith was replaced by more than 5% in the concrete mix due to the absorbed water content of the coir pith. Agro-waste materials like sugarcane bagasse ash (ScBA) exhibited increased compressive strength due to their pozzolanic characteristics and unique physical and chemical properties. Furthermore, carbonised apricot shell (CAS) showed improved compressive strength, attributed to enhanced bonding between mortar and raw aggregates. The carbonisation process results in a rougher surface and improved interlocking of concrete particles (Kaish et al., 2021; Wu et al., 2018). The variations in compressive strength observed with different agro-waste materials highlight the importance of considering the type and proportion of agro-waste, as well as curing conditions. Achieving desired compressive strength levels while maintaining concrete quality and durability requires further research and the establishment of standardised guidelines for agro-waste incorporation in concrete.

Therefore, recent developments emphasise the potential for agro-waste materials to impact concrete compressive strength positively (Abutaha et al., 2016; Djameluddin et al., 2020; Momoh & Osofero, 2019; Banu et al., 2020). However, the influence of specific agro-waste types, proportions, and curing conditions must be carefully considered to optimise concrete formulations effectively. Further research is essential to refine practices and ensure consistent results while utilising these sustainable materials in construction.

Flexural Strength

A comprehensive analysis of recent developments in flexural strength, considering various materials as additives in concrete, reveals intriguing findings. Thus, numerous studies indicate that the inclusion of certain materials in concrete can either enhance or weaken its flexural strength. For instance, carpet fibre (CF), prickly pear fibre (PPF), and rice husk ash (RHA) have been found to boost flexural strength. Conversely, when sugar cane bagasse ash (ScBA) and processed waste tea ash (PWTA) are incorporated, flexural strength tends to weaken (Alabduljabbar et al., 2021; Djamaluddin et al., 2020; Kaish et al., 2021; Oorkalan & Chithra, 2020; Gar et al., 2017; Shaaban, 2021). Figure 9 showcases the highest flexural strength value of 7.4 MPa reported in Shaaban's (2021) study using rice husk ash (RHA). In contrast, the lowest flexural strength of 1.53 MPa was observed in a Gar et al. (2017) study using sugarcane bagasse ash (ScBA).

Otherwise, the alum sludge (AS) demonstrated a slight increase in flexural strength, up to 10% fine aggregate replacement, as reported by Kaish et al. (2021). However, flexural strength declined with a 15% AS replacement. Meanwhile, the flexural strength of concrete mixes with 5% coir pith (CP), according to Oorkalan and Chithra's (2020) study, remained relatively consistent initially but decreased after 28 days of curing.

Furthermore, Momoh and Osofero's (2019) study found that flexural strength initially increased with adding oil palm broom fibres (OPBF) by up to 3%; however, it decreased when the percentage of OPBF exceeded 3%. The weak radial strength of OPBF and insufficient fibre-to-concrete matrix bonding may explain the lack of significant gains in flexural strength.

Meanwhile, Alabduljabbar et al. (2021) proposed that the improved flexural performance of concrete, especially with carpet fibres, may result from the bridging

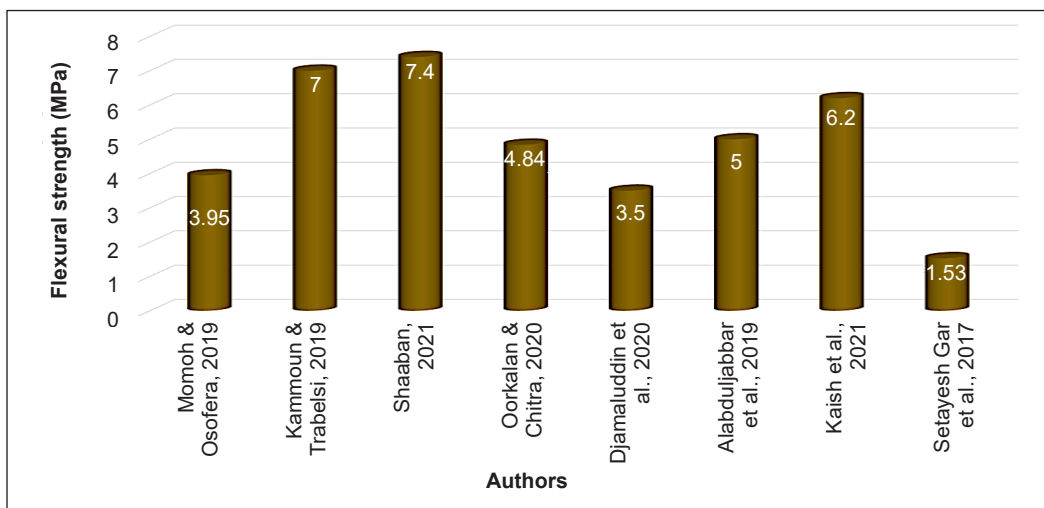


Figure 9. Maximum flexural strength results after 28 days from different studies

effect of these fibres. This effect enables fibres to transmit stress across cracks, enhancing flexural strength. Gar et al. (2017) observed that concrete compositions containing 5% coir pith (CP) exhibited better flexural strength, regardless of curing methods. However, when the temperature exceeded 300°C, samples containing sugarcane bagasse ash (ScBA) experienced a noticeable decrease in residual flexural strength. Shaaban (2021) explained that the increase in flexural strength with RHA can be attributed to a growth in possible flexural failure modes with increasing fault density. Excess unreacted RHA after CaO-MgO depletion contributes to this rise in flexural strength.

Therefore, these results highlight the complex link between different additives and how they affect the flexural strength of concrete. Understanding the mechanisms underlying these effects is crucial to optimise concrete compositions and achieve the required flexural strength while considering parameters such as material kind, proportion, and curing conditions. More study is required to establish standard practices and recommendations for these materials to be used efficiently in construction applications.

Modulus of Elasticity

Insights of note can be obtained from a thorough examination of recent advancements in the context of the modulus of elasticity in concrete, taking into consideration a variety of additives (Ahsan & Hossain, 2018; Islam et al., 2016; Kammoun & Trabelsi, 2019; Wu et al., 2018). Various studies have explored the effects of different additives on concrete's modulus of elasticity. Figure 10 illustrates the highest modulus of elasticity value, reaching 33.8 GPa, as reported by Kammoun and Trabelsi (2019), who utilised prickly pear fibre (PPF). Conversely, the lowest modulus of elasticity, 14 GPa, was observed in the study by Islam et al. (2016) when incorporating palm oil fuel ash (POFA).

Meanwhile, Kammoun and Trabelsi (2019) proposed that the addition of carbonised apricot shell (CAS) and rice husk ash (RHA) tends to increase the modulus of elasticity,

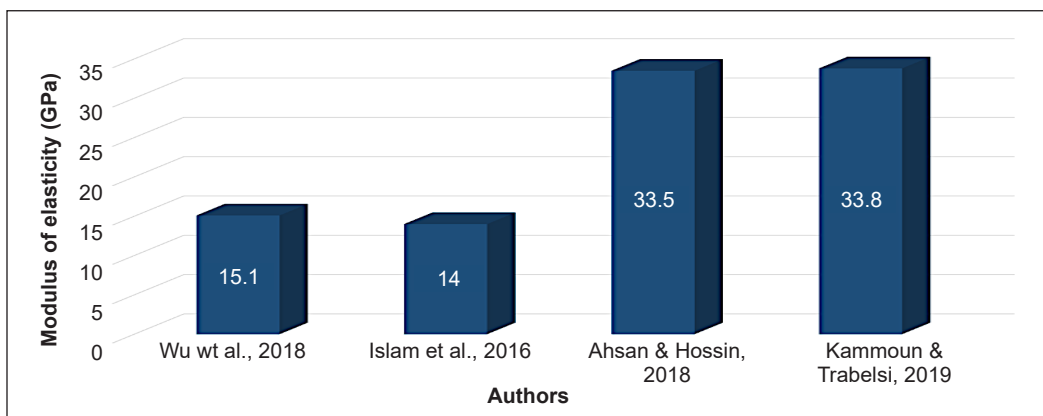


Figure 10. Maximum modulus of elasticity result from different studies

while it decreases with the addition of palm oil fuel ash (POFA) and prickly pear fibre (PPF). Furthermore, the inclusion of prickly pear fibres in concrete, particularly at a content of 15 kg/m^3 , led to a substantial 40% reduction in the modulus of elasticity. Wu et al.'s (2018) study indicates that the modulus of elasticity increases by approximately 42.5% using a carbonised apricot shell (CAS). This improvement is attributed to enhanced binding capabilities at the aggregate-mortar interface when employing carbonised aggregates (Kammoun & Trabelsi, 2019; Wu et al., 2018). Meanwhile, the decrease in modulus of elasticity observed with rice husk ash (RHA) suggests lower concrete quality and reduced particle density. Additionally, using finer RHA reduced Poisson's ratio, indicating changes in lateral strain response to axial stress (Ahsan & Hossain, 2018). Interestingly, the length of prickly pear fibre (PPF) was not found to have any significant effect on the modulus of elasticity. Thus, this discussion provides valuable insights into how different additives impact the modulus of elasticity in concrete. It highlights the importance of understanding these additive effects on the elastic properties of concrete, which is crucial for optimising concrete mixtures and ensuring the desired performance characteristics. Further research is needed to explore these relationships in greater detail and develop guidelines for effectively incorporating additives in concrete mixtures.

Splitting Tensile Strength

A thorough investigation of recent improvements in splitting tensile strength (STS) in concrete, considering various additives, yields significant insights. Figure 11 illustrates the reported splitting tensile strength values from various studies, shedding light on concrete performance (Jha et al., 2021; Ramakrishnan et al., 2021; Selvasofia et al., 2021). Ramakrishnan et al. (2021) achieved a notably high splitting tensile strength of 6.74 MPa

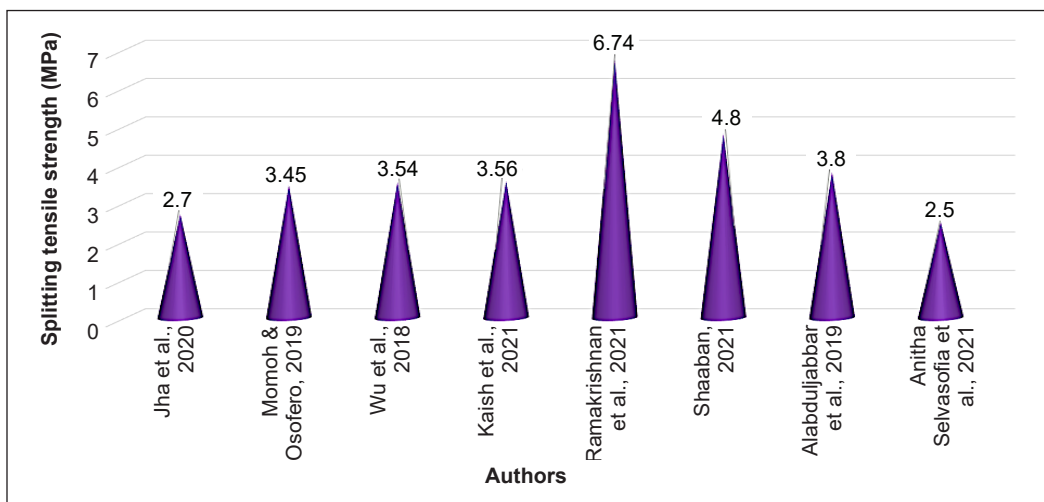


Figure 11. Maximum splitting tensile strength results after 28 days from different studies

using sugarcane bagasse ash. Conversely, Anitha et al. (2020) reported a lower value of 2.5 MPa when waste marble powder (WMP) was incorporated. The incorporation of WMP resulted in a 10% increase in splitting tensile strength, attributed to the finer size and angular shape of WMP particles. This characteristic enhances the concrete's performance. The study by Jha et al. (2021) observed an increase in splitting tensile strength with the addition of alum sludge (AS), carbonised apricot shell (CAS), and carpet fibre (CF), which has positively influenced STS.

However, incorporating oil palm broom fibres (OPBF) decreased splitting tensile strength. This reduction can be attributed to the agglomeration of OPBF at the top of the samples during the splitting tensile test, resulting in biaxial compression zones beneath the packing strips (Momoh & Osofero, 2019; Wu et al., 2018). Furthermore, Wu et al. (2018) reported improved STS with CAS. This enhancement is attributed to the rough concave surface of CAS particles, which are free of biological materials.

The evaluated research provides insightful information about the variables affecting concrete's splitting tensile strength. Besides, the additives, including carpet fibre (CF), waste marble powder (WMP), alum sludge (AS), carbonised apricot shell (CAS), and sugarcane bagasse ash can have a good effect on STS. However, due to agglomeration effects, adding oil palm broom fibres (OPBF) may cause a reduction in tensile strength (Wu et al., 2018). These results emphasise the importance of choosing the right additives to enhance concrete performance and guarantee optimum tensile strength characteristics.

THERMAL CONCRETE PROPERTIES

An in-depth analysis and critical examination of current advancements in the context of thermal conductivity in concrete, taking into consideration a variety of additives, provides significant insights, including the subsequent discussion (Kammoun & Trabelsi, 2019; Katare & Madurwar, 2021). Figure 12 presents a comparison of thermal conductivity results from various studies, offering valuable insights into the thermal properties of concrete. Kammoun and Trabelsi (2019) reported a relatively high thermal conductivity of 1.59 watts/mK when using prickly pear fibre (PPF). Conversely, Katare and Madurwar (2021) found a lower thermal conductivity value of 1.38 Watt/mK when incorporating sugarcane bagasse ash (ScBA).

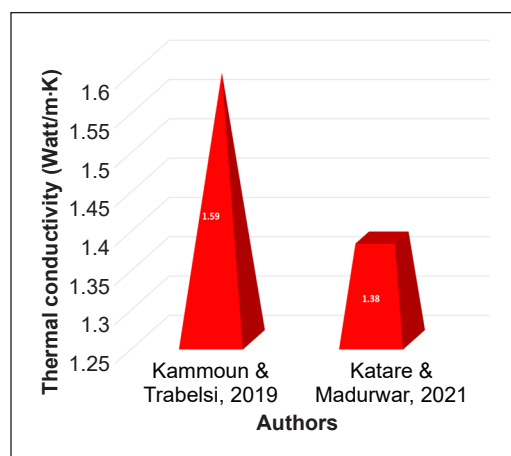


Figure 12. Maximum thermal conductivity results from different studies

Furthermore, the increase in the amount of sugarcane bagasse ash (ScBA) and prickly pear fibre (PPF) led to a decrease in the thermal conductivity of concrete. Katare and Madurwar's study demonstrated that higher percentages of ScBA resulted in lower densities and reduced thermal conductivity (2021). This reduction in density can be attributed to increased porosity and air-filled voids in the concrete, which lower the gas thermal capacity compared to the solid thermal conductivity of typical concrete. Otherwise, the study by Kammoun and Trabelsi (2019) indicated that the inclusion of longer fibres in composites often reduces heat conductivity. It suggests that longer fibres, such as PPF, can act as thermal insulators and reduce heat transfer within the concrete.

As a result of their effects on density and porosity, additives like sugarcane bagasse ash (ScBA) and prickly pear fibre (PPF) can reduce thermal conductivity in concrete. Longer fibres may also improve the thermal insulation capabilities of concrete, making this a promising method for raising its thermal performance. These results highlight the possibility of modifying concrete compositions to get the desired thermal conductivity properties for a range of applications.

CONCLUSION

In conclusion, this study primarily focused on assessing the workability of agro-waste concrete, and several key implications have arisen from our findings. As the proportion of agricultural waste increases, concrete strength and workability tend to decrease, indicating a potential trade-off when using such materials as partial replacements for conventional aggregates or cementitious substances. Prickly pear fibre inclusion in concrete results in heightened shrinkage, accelerating the ageing and drying processes and potentially leading to cracking. Conversely, carbonised apricot shells and rice husk ash have showcased promising performance as alternatives for both coarse and fine aggregates, offering opportunities to enhance concrete strength, resilience, and sustainability. Additionally, significantly incorporating sugarcane bagasse ash, carpet fibres, and alum sludge bolsters concrete's tensile strength, enabling it to withstand greater tensile forces and resist cracking.

Therefore, this study review emphasises the importance of judiciously selecting and proportioning agricultural waste in concrete formulations to optimise performance while advancing sustainable construction practices. Moreover, these findings have significant implications for future research and practice in the construction industry, highlighting the need for precise selection and proportioning of agricultural waste materials to optimise concrete performance while minimising environmental impact and paving the way for more sustainable and resilient construction practices.

ACKNOWLEDGEMENTS

The authors express their gratitude to Universiti Tenaga Nasional (UNITEN), Malaysia, for supporting this research under the Higher Education Centre of Excellence (HiCoE) grant, project number J510050002/HICOE05, and the Dato' Low Tuck Kwong (DLTK) International Research Grant through project number: 20238002DLTK—special thanks to those who have contributed to this project, directly or indirectly.

REFERENCES

- Abutaha, F., Razak, H. A., & Kanadasan, J. (2016). Effect of palm oil clinker (POC) aggregates on fresh and hardened properties of concrete. *Construction and Building Materials*, *112*, 416–423. <https://doi.org/10.1016/j.conbuildmat.2016.02.172>
- Ahsan, M. B., & Hossain, Z. (2018). Supplemental use of rice husk ash (RHA) as a cementitious material in concrete industry. *Construction and Building Materials*, *178*, 1–9. <https://doi.org/10.1016/j.conbuildmat.2018.05.101>
- Al-shayaa, M. S., Al-wabel, M., Herab, A. H., Sallam, A., Barjees, M., & Usman, A. R. A. (2021). Environmental issues in relation to agricultural practices and attitudes of farmers: A case study from Saudi Arabia. *Saudi Journal of Biological Sciences*, *28*(1), 1080–1087. <https://doi.org/10.1016/j.sjbs.2020.11.026>
- Alabduljabbar, H., Mohammadhosseini, H., Tahir, M. M., & Alyousef, R. (2021). Green and sustainable concrete production using carpet fibers waste and palm oil fuel ash. *Materials Today: Proceedings*, *39*(2), 929–934. <https://doi.org/10.1016/j.matpr.2020.04.047>
- Alhazmi, H., & Loy, A. C. M. (2021). Bioresource technology reports a review on environmental assessment of conversion of agriculture waste to bio-energy via different thermochemical routes: Current and future trends. *Bioresource Technology Reports*, *14*, Article 100682. <https://doi.org/10.1016/j.biteb.2021.100682>
- Ali, S. S. S., Razman, M. R., & Awang, A. (2020). The estimation and relationship of domestic electricity consumption and appliances ownership in Malaysia's intermediate city. *International Journal of Energy Economics and Policy*, *10*(6), 116–122. <https://doi.org/10.32479/ijeep.8358>
- Ali, S. S. S., Razman, M. R., Awang, A., Asyraf, M. R. M., Ishak, M. R., Ilyas, R. A., & Lawrence, R. J. (2021). Critical determinants of household electricity consumption in a rapidly growing city. *Sustainability*, *13*(8), Article 4441. <https://doi.org/10.3390/su1308444>
- Alsubari, S., Zuhri, M. Y. M., Sapuan, S. M., Ishak, M. R., Ilyas, R. A., & Asyraf, M. R. M. (2021). Potential of natural fiber reinforced polymer composites in sandwich structures: A review on its mechanical properties. *Polymers*, *13*(3), Article 423. <https://doi.org/10.3390/polym13030423>
- Anitha, S. D. S., Dinesh, A., & Babu, V. S. (2020). Investigation of waste marble powder in the development of sustainable concrete. *Materials Today: Proceedings*, *44*, 4223–4226. <https://doi.org/10.1016/j.matpr.2020.10.536>
- Asyraf, M. R. M., Ishak, M. R., Norraahim, M. N. F., Nurazzi, N. M., Shazleen, S. S., Ilyas, R. A., Rafidah, M., & Razman, M. R. (2021). Recent advances of thermal properties of sugar palm lignocellulosic fibre

- reinforced polymer composites. *International Journal of Biological Macromolecules*, 193, 1587–1599. <https://doi.org/10.1016/j.ijbiomac.2021.10.221>
- Athira, G., Bahurudeen, A., & Appari, S. (2019). Sustainable alternatives to carbon intensive paddy field burning in India: A framework for cleaner production in agriculture, energy, and construction industries. *Journal of Cleaner Production*, 236, Article 117598. <https://doi.org/10.1016/j.jclepro.2019.07.073>
- Azman, M. A., Asyraf, M. R. M., Khalina, A., Petrú, M., Ruzaidi, C. M., Sapuan, S. M., Wan Nik, W. B., Ishak, M. R., Ilyas, R. A., & Suriani, M. J. (2021). Natural fiber reinforced composite material for product design: A short review. *Polymers*, 13(12), Article 1917. <https://doi.org/10.3390/polym13121917>
- Bakar, N., & Chin, S. C. (2021). Performance of bamboo fiber reinforced composites: Mechanical properties. *Key Engineering Materials*, 879, 284–293. <https://doi.org/10.4028/www.scientific.net/KEM.879.284>
- Banu, S. S., Karthikeyan, J., & Jayabalan, P. (2020). Effect of agro-waste on strength and durability properties of concrete. *Construction and Building Materials*, 258, Article 120322. <https://doi.org/10.1016/j.conbuildmat.2020.120322>
- Chavan, S. P., Salokhe, S. A., Nadagauda, P. A., Patil, S. T., & Mane, K. M. (2020). An investigational study on properties of concrete produced with industrial waste red mud. *Materials Today: Proceedings*, 42, 733–738. <https://doi.org/10.1016/j.matpr.2020.11.156>
- de Sande, V. T., Sadique, M., Pineda, P., Bras, A., Atherton, W., & Riley, M. (2021). Potential use of sugar cane bagasse ash as sand replacement for durable concrete. *Journal of Building Engineering*, 39, Article 102277. <https://doi.org/10.1016/j.jobbe.2021.102277>
- Djamaluddin, A. R., Caronge, M. A., Tjaronge, M. W., Lando, A. T., & Irmawaty, R. (2020). Evaluation of sustainable concrete paving blocks incorporating processed waste tea ash. *Case Studies in Construction Materials*, 12, Article e00325. <https://doi.org/10.1016/j.cscm.2019.e00325>
- Drück, H., Mathur, J., Panthalookaran, V., & Sreekumar, V. M. (2020). *Green buildings and sustainable engineering*. Springer.
- El-Messiry, M., El-Tarfawy, S., & El-Deeb, R. (2017). Enhanced impact properties of cementitious composites reinforced with pultruded flax/polymeric matrix fabric. *Alexandria Engineering Journal*, 56(3), 297–307. <https://doi.org/10.1016/j.aej.2017.03.032>
- Foo, K. Y., & Hameed, B. H. (2009). Utilization of rice husk ash as novel adsorbent: A judicious recycling of the colloidal agricultural waste. *Advances in Colloid and Interface Science*, 152(1–2), 39–47. <https://doi.org/10.1016/j.cis.2009.09.005>
- Feen, O. S., Mohamed, R. N., Mohamed, A., & A. Khalid, N. H. A. (2017). Effects of coarse palm oil clinker on properties of self-compacting lightweight concrete. *Jurnal Teknologi*, 79(6), 111–120. <https://doi.org/10.11113/jt.v79.10593>
- Gar, P. S., Suresh, N., & Bindiganavile, V. (2017). Sugar cane bagasse ash as a pozzolanic admixture in concrete for resistance to sustained elevated temperatures. *Construction and Building Materials*, 153, 929–936. <https://doi.org/10.1016/j.conbuildmat.2017.07.107>

- Givi, A. N., Rashid, S. A., Aziz, F. N. A., & Salleh, M. A. M. (2010). Assessment of the effects of rice husk ash particle size on strength, water permeability and workability of binary blended concrete. *Construction and Building Materials*, 24(11), 2145–2150. <https://doi.org/10.1016/j.conbuildmat.2010.04.045>
- Gregorova, A., Hrabalova, M., Kovalcik, R., & Wimmer, R. (2011). Surface modification of spruce wood flour and effects on the dynamic fragility of PLA/wood composites. *Polymer Engineering & Science*, 51(1), 143-150. <https://doi.org/10.1002/pen.21799>
- Hamid, N. H., Bakar, M. S. A., Ludin, N. A., Abdullah, U. H., & Najm, A. S. (2022). The processing and treatment of other types of oil palm biomass. In S. M. Sapuan, M. T. Paridah, S. O. A. SaifulAzry & S. H. Lee (Eds.), *Oil Palm Biomass for Composite Panels* (pp. 191-213). Elsevier Inc. <https://doi.org/10.1016/b978-0-12-823852-3.00020-9>
- Heniegal, A. M., Ramadan, M. A., Naguib, A., & Agwa, I. S. (2020). Case studies in construction materials study on properties of clay brick incorporating sludge of water treatment plant and agriculture waste. *Case Studies in Construction Materials*, 13, Article e00397. <https://doi.org/10.1016/j.cscm.2020.e00397>
- Hulle, A., Kadole, P., & Katkar, P. (2015). Agave Americana leaf fibers. *Fibers*, 3(1), 64–75. <https://doi.org/10.3390/fib3010064>
- Ikumapayi, C. M., Arum, C., & Alaneme, K. K. (2021). Reactivity and hydration behavior in groundnut shell ash based pozzolanic concrete. *Materials Today: Proceedings*, 38(2), 508–513. <https://doi.org/10.1016/j.matpr.2020.02.385>
- Islam, M. M. U., Mo, K. H., Alengaram, U. J., & Jumaat, M. Z. (2016). Mechanical and fresh properties of sustainable oil palm shell lightweight concrete incorporating palm oil fuel ash. *Journal of Cleaner Production*, 115, 307–314. <https://doi.org/10.1016/j.jclepro.2015.12.051>
- Jaafar, C. N. A., Rizal, M. A. M., & Zainol, I. (2018). Effect of kenaf alkalization treatment on morphological and mechanical properties of epoxy / silica / kenaf composite. *International Journal of Engineering and Technology*, 7, 258–263. <https://doi.org/10.14419/ijet.v7i4.35.22743>
- Jain, S., Sharma, A., Ash, F., Ash, R., Ash, W. S., & Ash, F. (2015). Application of industrial and agricultural waste in cement concrete. *International Journal for Scientific Research & Development* 3(7), 176–178.
- Jha, P., Sachan, A. K., & Singh, R. P. (2021). Agro-waste sugarcane bagasse ash (ScBA) as partial replacement of binder material in concrete. *Materials Today: Proceedings*, 44(1), 419–427. <https://doi.org/10.1016/j.matpr.2020.09.751>
- Kadier, A., Ilyas, R. A., Huzaifah, M. R. M., Hariastuti, N., Sapuan, S. M., Harussani, M. M., Azlin, M. N. M., Yuliasni, R., Ibrahim, R., Atikah, M. S. N., Wang, J., Chandrasekhar, K., Islam, M. A., Sharma, S., Punia, S., Rajasekar, A., Asyraf, M. R. M., & Ishak, M. R. (2021). Use of industrial wastes as sustainable nutrient sources for bacterial cellulose (BC) production: Mechanism, advances, and future perspectives. *Polymers*, 13(19), Article 3365. <https://doi.org/10.3390/polym13193365>
- Kaish, A. B. M. A., Odimegwu, T. C., Zakaria, I., Abood, M. M., & Nahar, L. (2021). Properties of concrete incorporating alum sludge in different conditions as partial replacement of fine aggregate. *Construction and Building Materials*, 284, Article 122669. <https://doi.org/10.1016/j.conbuildmat.2021.122669>
- Kammoun, Z., & Trabelsi, A. (2019). Development of lightweight concrete using prickly pear fibres. *Construction and Building Materials*, 210, 269–277. <https://doi.org/10.1016/j.conbuildmat.2019.03.167>

- Katare, V. D., & Madurwar, M. V. (2021). Process standardization of sugarcane bagasse ash to develop durable high-volume ash concrete. *Journal of Building Engineering*, 39, Article 102151. <https://doi.org/10.1016/j.job.2021.102151>
- Kengkhetkit, N., & Amornsakchai, T. (2012). Utilisation of pineapple leaf waste for plastic reinforcement: 1. A novel extraction method for short pineapple leaf fiber. *Industrial Crops and Products*, 40, 55–61. <https://doi.org/10.1016/j.indcrop.2012.02.037>
- Khan, G. M. A., Razzaque, S. M. A., Hossain, M. M., Rahman, M. M., Paul, D. K., & Alam, M. S. (2010). Effect of chemical treatment on the properties of PALF / BSF reinforced polypropylene composites effect of chemical treatment on the properties of PALF / BSF reinforced polypropylene composites. *Journal of Applied Science and Technology*, 7(2), 101–105.
- Kolawole, J. T., Olusola, K. O., Babafemi, A. J., Olalusi, O. B., & Fanijo, E. (2021). Blended cement binders containing bamboo leaf ash and ground clay brick waste for sustainable concrete. *Materialia*, 15, Article 101045. <https://doi.org/10.1016/j.mtla.2021.101045>
- Kouta, N., Saliba, J., & Saiyouri, N. (2020). Effect of flax fibers on early age shrinkage and cracking of earth concrete. *Construction and Building Materials*, 254, Article 119315. <https://doi.org/10.1016/j.conbuildmat.2020.119315>
- Kumar, J., Kumar, S., & Basarkar, S. S. (2016). Gulf Organisation for Research and Development Concrete using agro-waste as fine aggregate for sustainable built environment – A review. *International Journal of Sustainable Built Environment*, 5(2), 312–333. <https://doi.org/10.1016/j.ijbsbe.2016.06.003>
- Lee, B. H., Kim, H. S., Lee, S., Kim, H. J., & Dorgan, J. R. (2009). Bio-composites of kenaf fibers in polylactide: Role of improved interfacial adhesion in the carding process. *Composites Science and Technology*, 69(15–16), 2573–2579. <https://doi.org/10.1016/j.compscitech.2009.07.015>
- Li, J., Agarwal, A., Iveson, S. M., Kiani, A., Dickinson, J., Zhou, J., & Galvin, K. P. (2014). Recovery and concentration of buoyant cenospheres using an Inverted Reflux Classifier. *Fuel Processing Technology*, 123, 127–139. <https://doi.org/10.1016/j.fuproc.2014.01.043>
- Libre, N. A., Shekarchi, M., Mahoutian, M., & Soroushian, P. (2011). Mechanical properties of hybrid fiber reinforced lightweight aggregate concrete made with natural pumice. *Construction and Building Materials*, 25(5), 2458–2464. <https://doi.org/10.1016/j.conbuildmat.2010.11.058>
- Lima, C., Caggiano, A., Faella, C., Martinelli, E., Pepe, M., & Realfonzo, R. (2013). Physical properties and mechanical behaviour of concrete made with recycled aggregates and fly ash. *Construction and Building Materials*, 47, 547–559. <https://doi.org/10.1016/j.conbuildmat.2013.04.051>
- Manickam, T., Cornelissen, G., Bachmann, R. T., Ibrahim, I. Z., Mulder, J., & Hale, S. E. (2015). Biochar application in Malaysian sandy and acid sulfate soils: Soil amelioration effects and improved crop production over two cropping seasons. *Sustainability*, 7(12), 16756–16770. <https://doi.org/10.3390/su71215842>
- Memon, S. A., Javed, U., & Khushnood, R. A. (2019). Eco-friendly utilization of corncob ash as partial replacement of sand in concrete. *Construction and Building Materials*, 195, 165–177. <https://doi.org/10.1016/j.conbuildmat.2018.11.063>

- Mohamad, N., Lakhiar, M. T., Samad, A. A. A., Mydin, M. A. O., Jhatial, A. A., Sofia, A. A., Goh, W. I., & Ali, N. (2019). Innovative and sustainable green concrete – A potential review on utilization of agricultural waste. *IOP Conference Series: Materials Science and Engineering*, 601(1), Article 012026. <https://doi.org/10.1088/1757-899X/601/1/012026>
- Momoh, E. O., & Dahunsi, B. I. O. (2017). Suitability of oil-palm-broom-fibres as reinforcement for laterite-based roof tiles. *International Journal of Software & Hardware Research in Engineering*, 5(4), 27–35.
- Momoh, E. O., & Osofero, A. I. (2019). Behaviour of oil palm broom fibres (OPBF) reinforced concrete. *Construction and Building Materials*, 221, 745–761. <https://doi.org/10.1016/j.conbuildmat.2019.06.118>
- Momoh, E. O., & Osofero, A. I. (2020). Recent developments in the application of oil palm fibers in cement composites. *Frontiers of Structural and Civil Engineering*, 14(1), 94–108. <https://doi.org/10.1007/s11709-019-0576-9>
- Monteiro, S. N., Drellich, J. W., Lopera, H. A. C., Nascimento, L. F. C., da Luz, F. S., da Silva, L. C., dos Santos, J. L., da Costa Garcia Filho, F., de Assis, F. S., Lima, É. P., Pereira, A. C., Simonassi, N. T., Oliveira, M. S., da Cruz Demosthenes, L. C., Costa, U. O., Reis, R. H. M., & Bezerra, W. B. A. (2019). Natural fibers reinforced polymer composites applied in ballistic multilayered armor for personal protection - An overview. In S. Ikhmayies, J. Li, C. M. F. Vieira, J. I. Margem & F. D. O. Braga (Eds.), *Green Materials Engineering* (pp. 33-47). Springer. https://doi.org/10.1007/978-3-030-10383-5_4
- Najeeb, M. I., Sultan, M. T. H., Andou, Y., Shah, A. U. ., Eksiler, K., Jawaid, M., & Ariffin, A. H. (2021). Characterization of lignocellulosic biomass from Malaysian's Yankee pineapple AC6 toward composite application. *Journal of Natural Fibers*, 18(12), 2006–2018. <https://doi.org/10.1080/15440478.2019.1710655>
- Nurazzi, N. M., Shazleen, S. S., Aisyah, H. A., Asyraf, M. R. M., Sabaruddin, F. A., Mohidem, N. A., Norraahim, M. N. F., Kamarudin, S. H., Ilyas, R. A., & Ishak, M. R. (2021). Effect of silane treatments on mechanical performance of kenaf fibre reinforced polymer composites: A review. *Functional Composites and Structures*, 3(4), Article 045003. <https://doi.org/10.1088/2631-6331/ac351b>
- Norraahim, M. N. F., Ariffin, H., Hassan, M. A., Ibrahim, N. A., Wan Yunus, W. M. Z., & Nishida, H. (2019). Utilisation of superheated steam in oil palm biomass pretreatment process for reduced chemical use and enhanced cellulose nanofibre production. *International Journal of Nanotechnology*, 16(11/12), 668–679. <https://doi.org/10.1504/IJNT.2019.107360>
- Ogundipe, K. E., Ogunbayo, B. F., Olofinnade, O. M., Amusan, L. M., & Aigbavboa, C. O. (2021). Affordable housing issue: Experimental investigation on properties of eco-friendly lightweight concrete produced from incorporating periwinkle and palm kernel shells. *Results in Engineering*, 9, Article 100193. <https://doi.org/10.1016/j.rineng.2020.100193>
- Omran, A. A. B., Mohammed, A. A. B. A., Sapuan, S. M., Ilyas, R. A., Asyraf, M. R. M., Koloor, S. S. R., & Petru, M. (2021). Micro- and nanocellulose in polymer composite materials: A review. *Polymers*, 13(2), Article 231. <https://doi.org/10.3390/polym13020231>
- Oorkalan, A., & Chithra, S. (2020). Effect of coconut coir pith as partial substitute for river sand in eco-friendly concrete. *Materials Today: Proceedings*, 21(1), 488–491. <https://doi.org/10.1016/j.matpr.2019.06.639>

- Oyebisi, S., Igba, T., Raheem, A., & Olutoge, F. (2020). Predicting the splitting tensile strength of concrete incorporating anacardium occidentale nut shell ash using reactivity index concepts and mix design proportions. *Case Studies in Construction Materials*, 13, Article e00393. <https://doi.org/10.1016/j.cscm.2020.e00393>
- Pil, L., Bensadoun, F., Pariset, J., & Verpoest, I. (2016). Why are designers fascinated by flax and hemp fibre composites? *Composites Part A: Applied Science and Manufacturing*, 83, 193–205. <https://doi.org/10.1016/j.compositesa.2015.11.004>
- Pinto, J., Vieira, B., Pereira, H., Jacinto, C., Vilela, P., Paiva, A., Pereira, S., Cunha, V. M. C. F., & Varum, H. (2012). Corn cob lightweight concrete for non-structural applications. *Construction and Building Materials*, 34, 346–351. <https://doi.org/10.1016/j.conbuildmat.2012.02.043>
- Radzi, A. M., Sapuan, S. M., Jawaid, M., & Mansor, M. R. (2019). Effect of alkaline treatment on mechanical, physical and thermal properties of roselle/sugar palm fiber reinforced thermoplastic polyurethane hybrid composites. *Fibers and Polymers*, 20(4), 847–855. <https://doi.org/10.1007/s12221-019-1061-8>
- Ramakrishnan, K., Ganesh, V., Vignesh, G., Vignesh, M., Shriram, V., & Suryaprakash, R. (2021). Mechanical and durability properties of concrete with partial replacement of fine aggregate by sugarcane bagasse ash (SCBA). *Materials Today: Proceedings*, 42(2), 1070-1076. <https://doi.org/10.1016/j.matpr.2020.12.172>
- Reddy, S. V. B., & Santhosha, V. (2018). Experimental study on fibre reinforced polymer concrete. *International Journal of Applied Engineering Research*, 13(15), 11844–11856.
- Saba, N., Paridah, M. T., Jawaid, M., Abdan, K., & Ibrahim, N. A. (2015). Manufacturing and processing of kenaf fibre-reinforced epoxy composites via different methods. In S. M. Sapuan, M. Jawaid, N. Yusof & M. E. Hoque (Eds.), *Manufacturing of Natural Fibre Reinforced Polymer Composites* (pp. 101–124). Springer. https://doi.org/10.1007/978-3-319-07944-8_5
- Selvasofia, S. D. A., Dinesh, A., & Sarath Babu, V. (2021). Investigation of waste marble powder in the development of sustainable concrete. *Materials Today: Proceedings*, 44(6), 4223–4226. <https://doi.org/10.1016/j.matpr.2020.10.536>
- Shaaban, M. (2021). Heliyon properties of concrete with binary binder system of calcined dolomite powder and rice husk ash. *Heliyon*, 7, Article e06311. <https://doi.org/10.1016/j.heliyon.2021.e06311>
- Shafiqh, P., Bin, H., Zamin, M., & Zargar, M. (2014). Agricultural wastes as aggregate in concrete mixtures – A review. *Construction and Building Materials*, 53, 110–117. <https://doi.org/10.1016/j.conbuildmat.2013.11.074>
- Singh, S. P., Jawaid, M., Yadav, B., & Supian, A. B. M. (2021). Mathematical modelling of infra-red evaporation characteristics of wheat straw black liquor. *Pertanika Journal of Science and Technology*, 29(4), 2845–2862. <https://doi.org/10.47836/pjst.29.4.33>
- Sizirci, B., Fseha, Y., Cho, C. S., Yildiz, I., & Byon, Y. J. (2021). A review of carbon footprint reduction in construction industry, from design to operation. *Materials*, 14(20), Article 6094. <https://doi.org/10.3390/ma14206094>
- Sreekala, M. S., Kumaran, M. G., & Thomas, S. (1997). Oil palm fibers: Morphology, chemical composition, surface modification, and mechanical properties. *Journal of Applied Polymer Science*, 66(5), 821–835. [https://doi.org/10.1002/\(SICI\)1097-4628\(19971031\)66:5<821::AID-APP2>3.0.CO;2-X](https://doi.org/10.1002/(SICI)1097-4628(19971031)66:5<821::AID-APP2>3.0.CO;2-X)

- Supian, A. B. M., Sapuan, S. M., Zuhri, M. Y. M., Zainudin, E. S., & Ya, H. H. (2018). Hybrid reinforced thermoset polymer composite in energy absorption tube application: A review. *Defence Technology*, 14(4), 291–305. <https://doi.org/10.1016/j.dt.2018.04.004>
- Susilawati, A., Maftuah, E., & Fahmi, A. (2020). The utilization of agricultural waste as biochar for optimizing swampland: A review. *IOP Conference Series: Materials Science and Engineering*, 980(1), Article 012065. <https://doi.org/10.1088/1757-899X/980/1/012065>
- Syamsir, A., Ean, L. W., Asyraf, M. R. M., Supian, A. B. M., Madenci, E., Özkılıç, Y. O., & Aksoylu, C. (2023). Recent advances of GFRP composite cross arms in energy transmission tower: A short review on design improvements and mechanical properties. *Materials*, 16(7), Article 2778. <https://doi.org/10.3390/ma16072778>
- Thiruganasambanthan, T., Ilyas, R. A., Norraahim, M. N. F., Kumar, T. S. M., Siengchin, S., Misenan, M. S. M., Farid, M. A. A., Nurazzi, N. M., Asyraf, M. R. M., Zakaria, S. Z. S., & Razman, M. R. (2022). Emerging developments on nanocellulose as liquid crystals: A biomimetic approach. *Polymers*, 14(8), 1 Article 546. <https://doi.org/10.3390/polym14081546>
- Wu, F., Liu, C., Zhang, L., Lu, Y., & Ma, Y. (2018). Comparative study of carbonized peach shell and carbonized apricot shell to improve the performance of lightweight concrete. *Construction and Building Materials*, 188, 758–771. <https://doi.org/10.1016/j.conbuildmat.2018.08.094>
- Yang, H. S., Kim, H. J., Park, H. J., Lee, B. J., & Hwang, T. S. (2006). Water absorption behavior and mechanical properties of lignocellulosic filler-polyolefin bio-composites. *Composite Structures*, 72(4), 429–437. <https://doi.org/10.1016/j.compstruct.2005.01.013>
- Zeidabadi, Z. A., Bakhtiari, S., Abbaslou, H., & Ghanizadeh, A. R. (2018). Synthesis, characterization and evaluation of biochar from agricultural waste biomass for use in building materials. *Construction and Building Materials*, 181, 301–308. <https://doi.org/10.1016/j.conbuildmat.2018.05.271>

Development of Small-scale Integrated Hydroponics—Animal Waste Bioreactor (AWB) for Romaine Lettuce (*Lactuca sativa* L. var. *longifolia*) Production

Elman Cantero Torres^{1*}, Theody Bernardo Sayco², Marvin Mateo Cinense², Jonathan Viernes Fabula², Wendy Mateo² and Carolyn Grace Galo Somera²

¹College of Agriculture, University of Rizal System – Main campus, Tanay, 1980 Rizal, Philippines

²Department of Agricultural and Biosystems Engineering, College of Engineering, Central Luzon State University, Science City of Muñoz, 3120 Nueva Ecija, Philippines

ABSTRACT

As improper processing and disposal of animal waste cause negative impacts on the environment, the animal industry sector must shift to more sustainable practices to lessen these effects. Recently, the application of the circular economy concept in agriculture, using animal waste as part of nutrient cycling, has emerged as a sustainable approach. The study aims to develop and test the small-scale integrated hydroponics-animal waste bioreactor (AWB) for romaine lettuce production using chicken manure tea (CMT) derived from dried chicken manure as a primary nutrient source. Three integrated hydroponics-AWB systems, with varying concentrations of CMT at 1,000 ppm, 1,200 ppm, and 1,400 ppm total dissolved solids (maintained within an upper and lower bound of 50 ppm), were constructed, tested, and compared to conventional hydroponics that used a nutrient solution maintained at 1,000 ppm TDS. The test result suggests that the ideal concentration of CMT in the system is 1,000 ppm. Within the optimum manure tea concentration, the small-scale

integrated hydroponics-AWB produced romaine lettuce with growth parameters comparable to conventional hydroponics. In addition, increasing the CMT concentration to 1,400 ppm negatively impacts the plant growth parameters of romaine lettuce. The developed small-scale integrated hydroponics-AWB system provides a viable approach for growing lettuce using animal waste as the major source of nutrients. The developed production system could help

ARTICLE INFO

Article history:

Received: 12 March 2023

Accepted: 02 November 2023

Published: 01 April 2024

DOI: <https://doi.org/10.47836/pjst.32.3.02>

E-mail addresses:

elman.torres@urs.edu.ph (Elman Cantero Torres)

tbsayco@clsu.edu.ph (Theody Bernardo Sayco)

marvin_cinense@clsu.edu.ph (Marvin Mateo Cinense)

jonathan.fabula@clsu2.edu.ph (Jonathan Viernes Fabula)

wcmateo@clsu.edu.ph (Wendy Mateo)

cggssomera@clsu.edu.ph (Carolyn Grace Galo Somera)

* Corresponding author

mitigate the negative environmental effects of improper handling and disposal of animal waste and dependence on chemical-based nutrient solutions in hydroponic crop production.

Keywords: Bioponics, chicken manure tea, mineralization, nutrient cycling, soilless culture, sustainable crop production

INTRODUCTION

The continuous increase of agricultural waste globally can be attributed to several factors. Due to the continuous increase in population worldwide, the demand for food from agriculture is also increasing (Valin et al., 2014). To meet this demand, farmers are growing more crops and raising more animals, which leads to increased agricultural waste (Borlaug, 2019; Bradford, 1999; Spiertz & Ewert, 2009). Moreover, the increase in agricultural waste could be attributed to industrialization, which uses artificially synthesized fertilizers, insecticides, and other chemical substances that augment crop productivity (Horrihan et al., 2002). Furthermore, problems with animal waste from the poultry and livestock sector resulted in nutrient pollution problems in land and water (Hu et al., 2019; Khoshnevisan et al., 2021).

Problems in agricultural waste could be solved by implementing sustainable crop production using farming technologies to improve crop yield and quality, as well as by reducing synthetic input. Hydroponics is deemed to be a sustainable method of crop production due to various environmental and economic benefits such as low water use, reduced pesticide applications, precise nutrient supply, space efficiency, and higher yield per area compared to conventional farming methods (De Clercq et al., 2018). However, the excessive use of chemical fertilizers as plant nutrient sources still contributes to soil, water, and air pollution, causing environmental and health problems (Savci, 2012). Moreover, manufacturing and transporting chemical fertilizers use fossil fuel-derived energy, contributing to net greenhouse gas emissions (Koga, 2008).

Due to its environmental benefits, there is a growing interest in using agricultural waste-derived fertilizer as an alternative plant nutrient source in a hydroponics system. Animal manure is one example of agricultural waste containing significant nutrients that could support crop growth. Although animal manure is a valuable soil amendment for crop production, improper management, processing, and utilization could negatively impact the environment and plants (Khoshnevisan et al., 2021; Ren et al., 2022). Due to the limited management of agricultural waste, there is an urgent need to implement a solution for the utilization and valorization of agricultural waste for sustainability, food security, and health security (Koul et al., 2022).

Several studies were conducted to utilize animal waste as a nutrient source in hydroponics as an alternative to the chemical-based nutrient solution. Bioprocessed animal

waste using a biogas digester (digestate) was utilized as a substitute nutrient source in hydroponics. However, crop growth using different digestate and nutrient solution ratios was negatively impacted compared with conventional hydroponics (Mupambwa et al., 2019). In addition, with the use of aerated chicken and cow manure extract as a plant nutrient source in the ebb and flow hydroponics, the recorded aboveground wet and dry weights were lower compared to conventional hydroponics (Tikasz et al., 2019). Both studies suggested that low plant growth performance could be attributed to ammonia toxicity, which is the least preferable form of nitrogen compared to nitrate.

Chicken manure is a widely used organic fertilizer in agriculture due to its high nutrient content, such as nitrogen (N), phosphorus (P), and potassium (K) essential for plant growth (Waldrup et al., 2020). The typical nutrient analysis for chicken manure can vary depending on several factors, such as the bird's diet, age, and moisture content. A typical chicken manure on a dry basis (i.e., broiler and layer chicken manure as excreted) can contain around 5.0 and 5.4 % total Kjeldahl nitrogen, 1.29 and 1.32 % total ammonia nitrogen, 3.08 and 4.20 % total phosphorus, and 2.31 and 2.40 % total potassium (Ashworth et al., 2020; Collins et al., 1999). It also contains secondary and micronutrients like calcium, magnesium, sulfur, zinc, and copper. These nutrients fulfill specific roles in plant metabolic processes, whether soil-based or hydroponic. Chicken manure requires proper treatment and management to maximize its utility as a plant nutrient source. Fresh chicken manure contains high levels of ammonia, which can be phytotoxic.

In our recent study, we successfully designed an animal waste bioreactor (AWB) capable of producing significant amounts of nitrate within a 7 to 14-day bioprocessing period (Torres et al., 2023). Integrating our designed animal waste bioreactor into hydroponics could be a viable solution for using animal waste as a nutrient source. Thus, the present study aims to achieve the following objectives: to develop a small-scale integrated system of hydroponic system and animal waste bioreactor (AWB) for romaine lettuce production and to investigate the effect of varying concentrations of manure tea on the growth parameters of romaine lettuce compared to convention hydroponics system utilizing the commercial nutrient solution.

Integrating hydroponics systems and AWB can provide a more sustainable alternative plant nutrient source while reducing the negative impact of improper animal waste management on the environment. The results of this study not only offer valuable data for farmers and scientists but highlight the potential of circular economy principles to create more sustainable and efficient systems in the agricultural sector through nutrient cycling. Furthermore, the results of this study may have implications for other crops and different scale systems, providing valuable information in utilizing animal waste as a plant nutrient source.

METHODS

Location of the Study

The development and performance evaluation of an integrated hydroponics-AWB were conducted at the Land and Water Laboratory of the College of Engineering at Central Luzon State University in the province of Nueva Ecija, Philippines, from November 2022 to January 2023. The bioreactor system was assembled in a dome-type greenhouse, covered with a layer of polyethylene film and a 50% shade net to create an optimal growing environment. The greenhouse was $12 \times 6 \times 6$ m (length \times width \times height) and lacked roof vents but was equipped with side screens to allow for proper airflow. The greenhouse also had a 40-cm masonry bottom, which served as the foundation for the system. Temperature and humidity inside the greenhouse were monitored using a humidity-temperature data logger (Benetech, GM1365) during the production phase of the study.

Design Concept of the Small-scale Integrated Hydroponics-AWB

The design concept for developing a technology for romaine lettuce production utilizing dried chicken manure (DCM) as a main source of nutrients consists of two major components: the hydroponics system and the AWB. Each component is composed of different parts to work as an integrated system, as shown in Figure 1.

The hydroponics system is composed of nutrient film technique (NFT) grow bed channels, a water delivery channel, a water discharge channel, and a support frame. The NFT grow bed channels are the primary component of the hydroponic system and are responsible for providing a space for the plants to grow. These channels are made of PVC

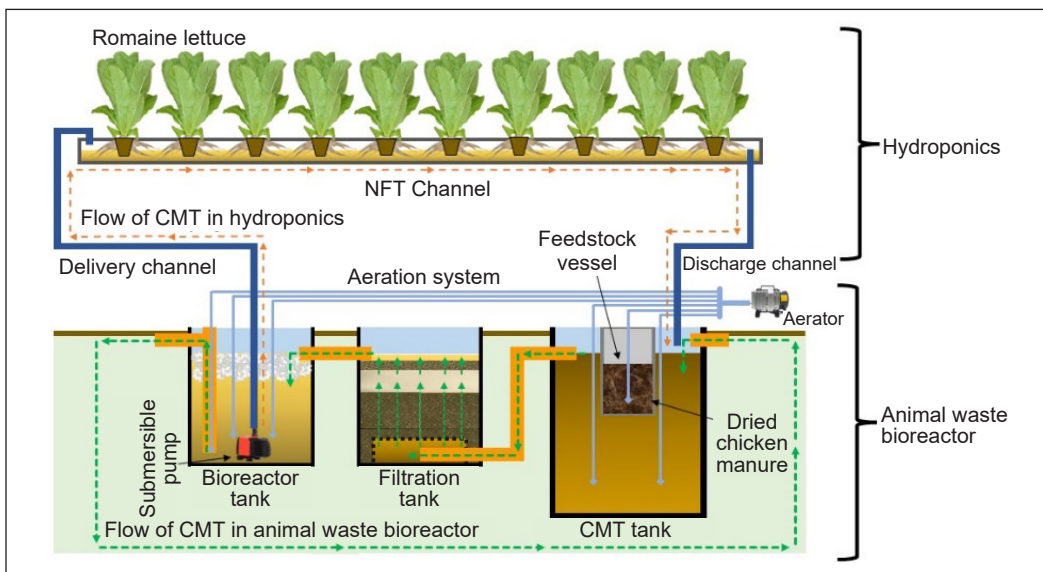


Figure 1. Schematic layout of the integrated hydroponics—animal waste bioreactor

pipe with a diameter of 5.08 cm and a length of 152 cm, providing an area for the plants to grow. The channels are designed with 10 evenly spaced holes, each measuring 5.08 cm in diameter and 15 cm apart, to ensure that the plants receive optimal water, nutrients, and sunlight.

The water delivery and discharge channel consists of a pipe, fittings, pump, and valve responsible for the flow of CMT from the AWB on the NFT grow bed channel. The water delivery channel consists of a PVC pipe with a diameter of 1.90 cm that connects the submersible pump (20 L/min), a gate valve to control the flow of water, and a 2 mm diameter flexible hose to distribute the flow of liquid fertilizer in each NFT grow bed channel. The water discharge channel is responsible for removing any excess water and debris. The support frame is made of slotted angle bars to hold the channels in place and provide structural stability to the system.

The AWB is composed of a bioreactor tank, CMT tank, filtration tank, water circulation channels, and aeration system. The CMT tank, made of a plastic container (50 L capacity, 40 cm diameter, 55 cm height), holds the DCM in a filter-lined vessel (200 microns) to slowly release nutrients into the water during the bioprocessing period. The filtration tank, made of a plastic container (35 L capacity, 36 cm diameter, 40 cm height), separates solid particulates in the CMT using perforated plastic, fishnet (1 m × 2.5 m with 1 mm grid size), fiber wool (160 g), and aquarium foam (30 PPI, 2.5 cm thickness) to filter the CMT.

The bioreactor tank processed CMT with nitrifying bacteria using K1 biofilm media (500g) suspended by diffused air from the aeration system. K1 biofilm media is a cylindrical polyethylene plastic (10 mm diameter, 0.5–0.8 mm thickness, 0.123 g/L density, 500 m²/m³ specific surface area) which serves as a carrier for nitrifying bacteria to convert ammonia present in CMT into nitrate. The aeration system supports a constant supply of dissolved oxygen in the CMT tank and bioreactor tank by using an air pump (35 Watts, rated airflow of 65 L/min at 0.027 MPa) to maintain a dissolved oxygen level of at least 2 mg/L or above. It also serves as a CMT tank and bioreactor unit mixing mechanism. The circulation of CMT in the system is facilitated using PVC pipes and fittings and an airlift pump, which recirculates the CMT without the need for an additional water pump.

Experimental Setup of the Study

The experiment was designed to test and compare the effect of varying concentrations (in terms of total dissolved solids in ppm) of CMT on the growth and yield of romaine using the developed integrated hydroponics-AWB system and a hydroponics system utilizing a commercial nutrient solution. The experimental setup consisted of four closed-loop hydroponics systems, which included three integrated hydroponics-AWB with CMT total

dissolved solids (TDS) levels controlled to fall within the ranges of 1000 ± 50 ppm (CMT1), 1200 ± 50 ppm (CMT2), and 1400 ± 50 ppm (CMT3). In addition, one hydroponics system was maintained using a commercial nutrient solution as a control (CNS), with TDS levels maintained within the range of 1000 ± 50 ppm based on the recommended range between 800 and 1,200 ppm (Sace & Jr Natividad, 2015). Each setup consists of five NFT channels with ten plants, each with 50 plants per treatment.

Operation of the Small-Scale Integrated Hydroponics-AWB

The operations of the integrated hydroponics-AWB were divided into three phases. Phases 1 and 2 were based on recently conducted methods to produce CMT using AWB (Torres et al., 2023). Phase 3 involves the production stage using the developed system. In Phase 1, the AWB was inoculated with beneficial bacteria from vermicompost tea. The vermicompost tea was prepared using a 1:10 ratio of vermicompost to water and brewed for 24 hours at room temperature using the bucket bubbler method. Five (5) liters of the produced vermicompost tea were added to the AWB containing 105 liters of water. The system was operated for 15 days without additional DCM or water to establish microorganisms in the biofilm.

Phase 2 of the operation involved bioprocessing DCM to produce a nutrient-rich CMT as a source of nutrients for romaine lettuce. It was accomplished using AWB, loaded with varying amounts of DCM to achieve specific total dissolved solids (TDS) ranges for each treatment. Initially, CMT1, CMT2, and CMT3 were loaded with 1.0 kg, 1.5 kg, and 2.0 kg of DCM, respectively. The bioreactors were operated for 7 days to complete the bioprocessing process.

Phase 3 of the operation involved the utilization of a nutrient-rich CMT for romaine lettuce production. Initially, each system was supplemented with 10 g per 100 L chelated iron ethylenediamine-N, N'-di[(ortho-hydroxyphenyl) acetic] (EDDHA 6%). The prepared seedlings were transplanted to the NFT grow bed channel. The plant growing period set for this study is 30 days after transplanting. The plants were harvested for plant growth and development measurement at the end of the growing period.

Quality Monitoring and Management of CMT

CMT samples were collected from each system between 8:00 and 10:00 a.m. and were analyzed for various water quality parameters, including dissolved oxygen (DO), pH, total dissolved solids (TDS), and nitrate. These measurements were used to monitor and maintain the CMT quality required in the study. DO was determined using a pen-type auto-calibration DO meter (Lutron, PDO 519). pH level was measured using a pocket-sized pH meter (Hanna, HI98107). TDS was measured using a digital water tester (HM Digital, AP-1). Nitrate levels were estimated using the acid reduction method (API, nitrate test kit). The pH of the water in each system was adjusted using a 33% sulfuric acid solution

to maintain an optimal range of 6.5–7.0 (Blanchard et al., 2020). DCM and water were added to the system every five days from the start of the growing period to maintain the required TDS at each treatment. The water level in each treatment was regularly monitored, and any additions were recorded to maintain consistent conditions.

Evaluation of Plant Growth Parameters

Upon harvest, the perforated cup on each plant sample was gently removed, and the roots were lightly rinsed with water to remove the attached cocopeat and then drained. The fresh weight of each plant sample was quantitatively determined by separating the shoot and root portions and measuring their respective weight. Both portions of each plant sample were dried in an oven set at 80°C within a 24-hour time frame, and subsequently, the weight of dried samples for plant biomass determination.

For the measurement of the brix level of leaves from each plant sample, first, the leaves were carefully separated from the stem using a clean knife. The separated leaves were then cut horizontally into small pieces and mixed thoroughly to ensure homogeneity. The cut leaves were grated using a grater with a mesh size of at least 1mm, placed in a fine mesh strainer (200 microns), and manually pressed to collect the plant juice. The collected juice sample was then placed in a handheld brix meter (Soonda, 0–32% model) to measure the Brix value of collected juice from romaine lettuce according to the manufacturer's instructions.

Physiochemical Analysis of Samples

The nutrient content of DCM and the produced liquid fertilizer were analyzed by an accredited laboratory (Regional Soils Laboratory of Department of Agriculture, Regional Field Office III, San Fernando City, Pampanga, Philippines). The moisture content was measured using the gravimetric method. The total nitrogen was determined using the Kjeldahl method. Total phosphorus and total potassium were determined using acid digestion, vanadomolybdate method, and flame atomic emission spectroscopy, respectively. Organic carbon and organic matter were measured using the Walkley-Black method (titrimetric).

Data Analysis

Data from plant growth parameters were displayed as mean \pm standard error (SE) of the number of samples gathered at each treatment. Data analyses were performed with the α set at 0.05 (significantly different at a p-value less than 0.05) and were subjected to one-way ANOVA for comparison between treatments. Tukey's post hoc test determined the significant difference among treatments.

RESULTS AND DISCUSSION

Description of the Developed Small-scale Integrated Hydroponics-AWB

The small-scale integrated hydroponics-AWB was designed to combine two different technologies to create a sustainable and efficient method of producing food and managing animal waste (Figure 2). The system's operation involves converting animal waste into a valuable resource that can be used to sustainably produce crops. The system is a closed-loop cycle that benefits both the environment and the farmer by reducing waste and producing high-value crops.

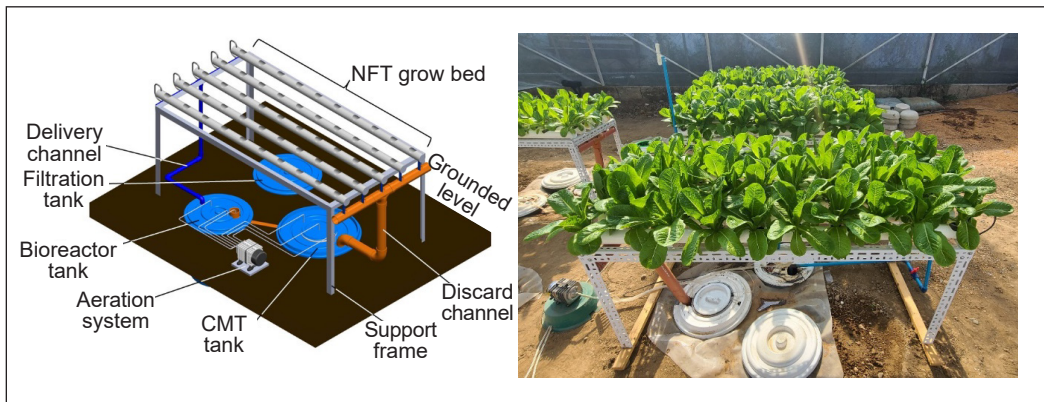


Figure 2. The design (left) and the experimental setup (right) of the small-scale integrated hydroponics-animal waste bioreactor for romaine lettuce production

The system has two main components: a hydroponics system and an AWB. The AWB operates on the principle of aerobic decomposition, where microorganisms use oxygen to break down organic matter in the DCM. The AWB is filled with a medium that provides a surface area for beneficial bacteria to grow. The bacteria feed on the organic matter present in the manure. These bacteria are essential for nitrification, which involves the conversion of ammonia present in DCM to produce a nitrate-rich CMT as a byproduct.

The CMT produced by the AWB is utilized in a hydroponic system, which provides plants with essential nutrients and water without using soil. The CMT is circulated throughout the hydroponic system, facilitating plant growth and development while allowing plants to absorb nutrients from the DCM. Table 1 shows the specification of the developed small-scale integrated hydroponics-AWB.

Environmental Conditions During the Production Period

Lettuce growth could be affected by temperature and relative humidity (RH). The temperature influences various aspects of plant development, such as photosynthesis, respiration, transpiration, and nutrient uptake (Hatfield & Prueger, 2015). The optimum

Table 1

Specification of the developed small-scale integrated hydroponics-AWB for romaine lettuce production

Specifications	Values
CMT capacity	105 Liters
Feedstock capacity	Up to 4 kg
Hydraulic retention period	7 to 14 days
Media-specific surface area (SSA)	500g of K1 media (with SSA of 500m ² /m ³)
Grow bed capacity	50 plants
Plant spacing	15 cm × 15 cm
Aeration System	Airflow rate: 65 Liters per minute
Power rating	65 watts (pump + aerator)

temperature for lettuce production ranges between 15°C to 25°C under greenhouse conditions (Ferrarezi & Testezlaf, 2016). In addition, relative humidity can affect the rate of transpiration, which is crucial for water and nutrient uptake, as well as plant growth and development (Chia & Lim, 2022). A study for lettuce growth and development under controlled humidity levels suggests that plants grown under 85% RH significantly have a faster growth rate compared to plants grown under 50% RH (Tibbitts & Bottenberg, 1976). The temperature and humidity in the greenhouse widely varied between 20.8°C (night) and 42.8°C (day) and 37.5% (day) to 96.2% (night), respectively, during the production period of the study (Figure 3). The values of temperature and RH were favorable during the nighttime compared to the daytime, which exceeded the recommended level.

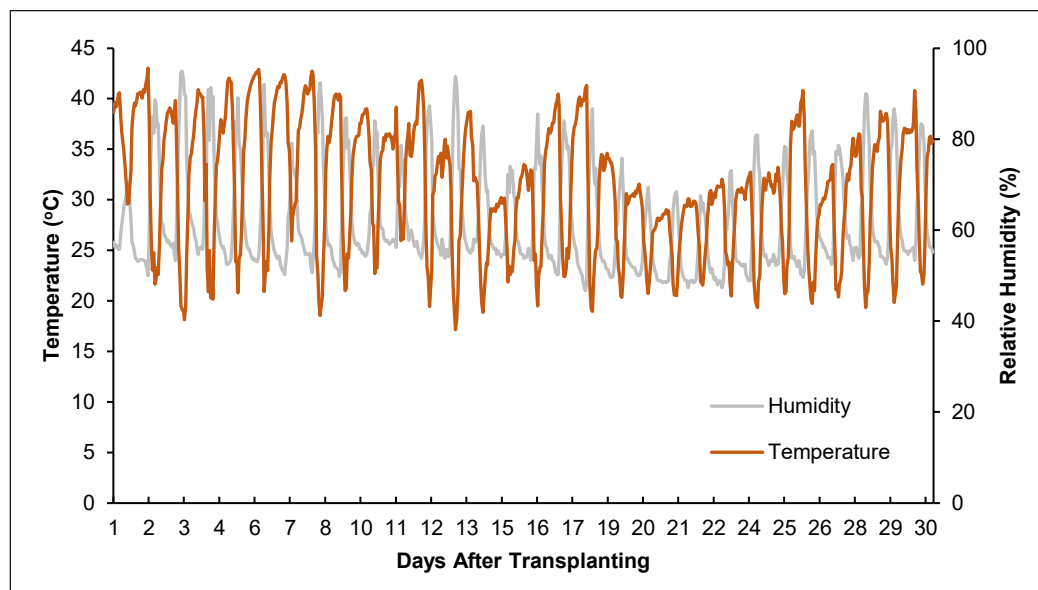


Figure 3. Temperature and relative humidity inside the greenhouse during the production period of romaine lettuce using the developed small-scale integrated hydroponics-AWB for romaine lettuce production

CMT Quality Parameters

Figure 4 shows the trend of dissolved oxygen levels in four different treatments of romaine lettuce over a growing period of 30 days using the developed small-scale integrated hydroponics-AWB. The DO levels observed in this study are critical for the success of the developed system. DO levels can impact the growth and survival of plants and microorganisms in the water (EPA, 2015). Overall, the mean DO level for each treatment remained within a relatively narrow range throughout the study period. Figure 4 shows that CNS had the highest DO levels, with an average of 6.92 mg/L over the 30 days compared to other treatment average DO levels (CMT1 = 6.64 mg/L, CMT2 = 6.19 mg/L and CMT3 = 5.83 mg/L). It suggests that the CNS had a better oxygen supply, possibly due to a lack of animal waste and associated microbial growth that could have consumed the oxygen in the system.

Applying organic fertilizers in hydroponic solutions has been reported to cause the decline of dissolved oxygen in a hydroponic system (Atkin & Nichols, 2004). In comparison with other studies on the utilization of waste as a nutrient source in hydroponic lettuce and cucumber production, the recorded DO level of liquid fertilizer derived from food waste ranges between 8.4 to 9.2 mg/L (Siddiqui et al., 2022). Lower dissolved oxygen levels in treatment with CMT compared to the CNS could be attributed to the higher organic loading rate in this treatment, which may have led to an increased demand for oxygen for the decomposition of organic matter in the DCM.

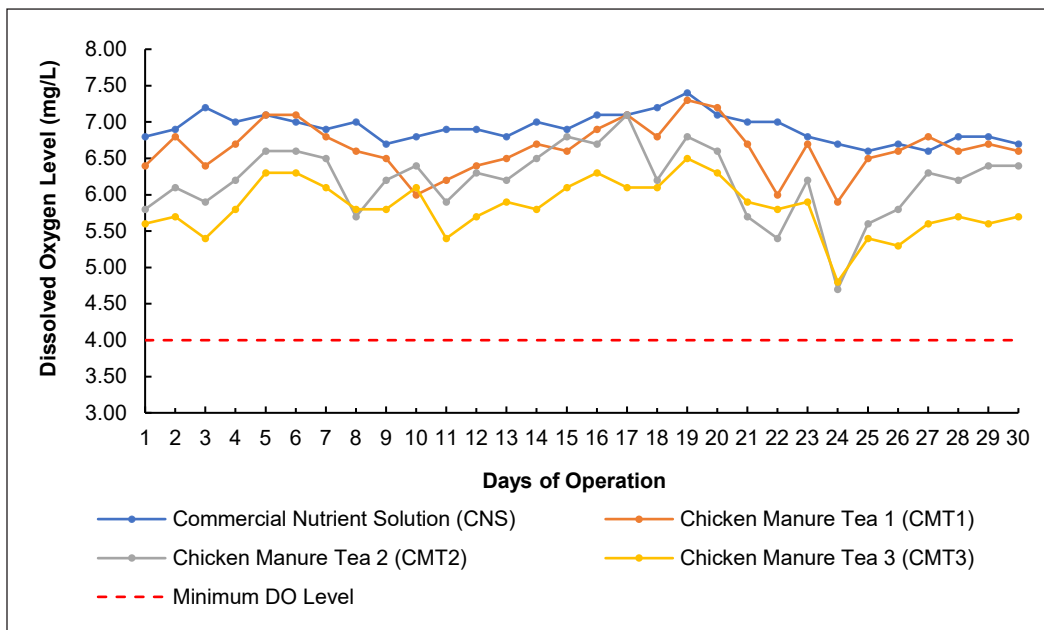


Figure 4. The dissolved oxygen level of chicken manure tea during the production period of romaine lettuce using the developed small-scale integrated hydroponics-AWB for romaine lettuce production

The DO levels in all treatment groups were generally within an optimal level for nitrifying bacteria to oxidize ammonia present in the water at 4 mg/mL and above (Stenstrom & Poduska, 1980). The minimum dissolved oxygen level observed during the study was 4.70 mg/L, considered the minimum acceptable level. Therefore, the dissolved oxygen levels observed in this study suggest that the integrated hydroponics-AWB system could support the growth of both plants and microorganisms without any significant negative impact on DO levels.

However, with the concern of food safety in lettuce production using the developed system, animal waste is regarded as a carrier of pathogenic microorganisms (Zhang et al., 2020). There could be similarities in diseases, such as those found in aquaponics and hydroponics systems; hydrophilic fungi or fungus-like protists are responsible for root or collar diseases (Stouvenakers et al., 2019). Maintaining an optimum level of dissolved oxygen could be a way to reduce the pathogens in the system. The study on biological aerobic treatment of wastewater from piggery suggests that pathogenic bacteria are lower in the products from this kind of treatment than in conventional systems (Béline et al., 2008). Furthermore, the oxidation of biosolids through aerobic digestion at specific durations and temperatures could potentially reduce pathogens (Al-Gheethi et al., 2018). Further studies are needed to ensure that the pathogenic bacteria in this system will be reduced or even eliminated during the bioprocessing period.

Table 2 presents the major nutrient content of CNS, CMT1, CMT2, and CMT3 under varying total dissolved solids using the developed small-scale integrated hydroponics-animal waste bioreactor for romaine lettuce production before and after the production period. There is an observed increase in the total NPK percentage in treatments 1, 2, and 3, while a decrease in NPK percentage is observed in the control. Although the study maintained the specific range of TDS levels on each treatment and control by adding DCM, nutrient solution, and water, there is an observable difference in the total NPK % before and after the production period.

Table 2

Nutrient content of the nutrient solution and chicken manure tea under varying total dissolved solids using a small-scale integrated hydroponics-animal waste bioreactor for romaine lettuce production

Nutrients	Treatments							
	CNS		CMT1		CMT2		CMT3	
	Before	After	Before	After	Before	After	Before	After
Total N, %	0.01	0.01	0.02	0.02	0.05	0.02	0.02	0.03
Total P, %	0.05	0.02	0.03	0.03	0.02	0.03	0.04	0.02
Total K, %	0.01	0.01	0.04	0.07	0.04	0.07	0.07	0.06
Total NPK, %	0.07	0.04	0.09	0.11	0.011	0.12	0.13	0.11

Note. CNS (Commercial Nutrient Solution), CMT 1 (Chicken Manure Tea 1), CMT 2 (Chicken Manure Tea 2), CMT 3 (Chicken Manure Tea 3), Total N (Total Nitrogen), Total P (Total Phosphorus), Total K (Total Potassium) and Total NPK (Total Nitrogen-Phosphorus-Potassium).

Compared with the previously conducted research on the optimum hydraulic retention period of CMT using AWB, there is an observed increasing trend of total NPK content during the production period of CMT (Torres et al., 2023). The slight increase of NPK content after the production period could be attributed to the continuous biodegradation of DCM recently added inside the AWB to maintain a specific range of TDS at each treatment. Based on the most recent research examining different chicken manure loadings on a lettuce-based bioponic system, residual nitrogen and phosphorus present in the system's liquid fertilizer after the production period was attributed to the process's incomplete microbial degradation and could also be utilized by the plant after the extended growing period (Wongkiew et al., 2021).

In the study, the developed integrated hydroponics-AWB could mineralize the organic nitrogen in the DCM into nitrate. The presence of nitrate was determined and monitored using the test kits. Throughout the growth period, the nitrate concentration of CNS was consistently high, ranging between 80 and 160 ppm. During the bioprocessing phase, the nitrate levels in CMT1 and CMT2 increased by up to 80 ppm. However, in CMT3, the nitrate level was below that of the other treatments, which ranged between 5 ppm and 10 ppm. The changes in nitrate levels of different concentrations of CMT could be attributed to the mineralization of organic forms of nitrogen present in DCM using the AWB during the bioprocessing and growth period of the study and absorption of plants with nutrients. Research on using organic fertilizers in hydroponics has found that cultured soil microorganisms could mineralize the organic nitrogen present in organic fertilizer through ammonification and nitrification into nitrates (Shinohara et al., 2011). Furthermore, the study found that excessive amounts of organic fertilizer could inhibit nitrification, which explains the nitrate production level in CMT3 (Shinohara et al., 2011).

During the growing period, both the nitrate levels of CMT1 and CMT2 decline to as low as 40 ppm after 10 days of the growing period. It was observed that after adding DCM to maintain the required TDS level of CMT in the integrated hydroponics-AWB, nitrate levels on both treatments increased by up to 80 ppm. It could be attributed to plant uptake and nitrate utilization for growth and development (Morgan & Connolly, 2013). In addition, microbial denitrification, a process by which bacteria convert nitrate to nitrogen gas (N₂) and release it to the atmosphere, could be another reason for the decrease in nitrate level present in CMT (Albina et al., 2019).

Effect of Varying Concentration of CMT on the Growth Parameters of Romaine Lettuce

There is a significant difference in the growth parameters of romaine lettuce produced using conventional hydroponics and integrated hydroponics-AWB with varying CMT concentrations at $p < 0.05$, as shown in Table 3. The highest fresh lettuce weight produced

Table 3

Plant growth parameters of romaine lettuce produced using the nutrient solution and chicken manure tea under varying concentrations using a small-scale integrated hydroponics-animal waste bioreactor for romaine lettuce production

Growth Parameters	Treatment			
	CNS	CMT1	CMT2	CMT3
Plant fresh weight	153.7 ± 9.54a	136.3 ± 13.49ab	100.3 ± 8.98b	43.3 ± 3.45c
Plant dry weight	7.12 ± 0.32a	6.85 ± 0.77ab	4.90 ± 0.63b	2.34 ± 0.18c
Shoot fresh weight	132.3 ± 6.67a	112.7 ± 10.85a	79.8 ± 7.10b	34.7 ± 2.43c
Shoot dry weight	6.00 ± 0.26a	5.78 ± 0.66a	3.98 ± 0.52b	1.84 ± 0.14c
Root fresh weight	21.17 ± 2.65a	23.67 ± 2.33a	20.50 ± 1.33a	8.67 ± 3.20b
Root dry weight	1.115 ± 0.071a	1.042 ± 0.097a	0.930 ± 0.118a	0.502 ± 0.049b

Note. Values within the same row followed by different letters are significantly different at $p < 0.05$. Note: CNS (Commercial Nutrient Solution), CMT 1 (Chicken Manure Tea 1), CMT 2 (Chicken Manure Tea 2), CMT 3 (Chicken Manure Tea 3)

was observed in the CNS (153.7 ± 9.54 g), which is highly significant compared to CMT2 and CMT3. No significant difference was observed between CNS and CMT1 in terms of the fresh weight of romaine lettuce (Figure 5). CMT3 produced the lowest fresh lettuce weight (43.3 ± 3.45 g), significantly different among the treatments. The plant dry weight showed a similar tendency as the plant fresh weight, with the CNS having the highest plant dry weight (7.12 ± 0.32 g) and CMT3 having the lowest dry weight (2.34 ± 0.18 g). No significant difference was observed between the CNS and CMT1 in terms of plant dry weight.

The same result could be observed in both root and shoot growth. The shoot fresh weight and dry weight of romaine lettuce produced in CNS were highly significant in comparison to the shoot fresh weight and dry weight of romaine lettuce produced in CMT2 and CMT3 ($P < 0.01$). On the other hand, there is no significant difference between the CNS and CMT1 ($P > 0.05$). The

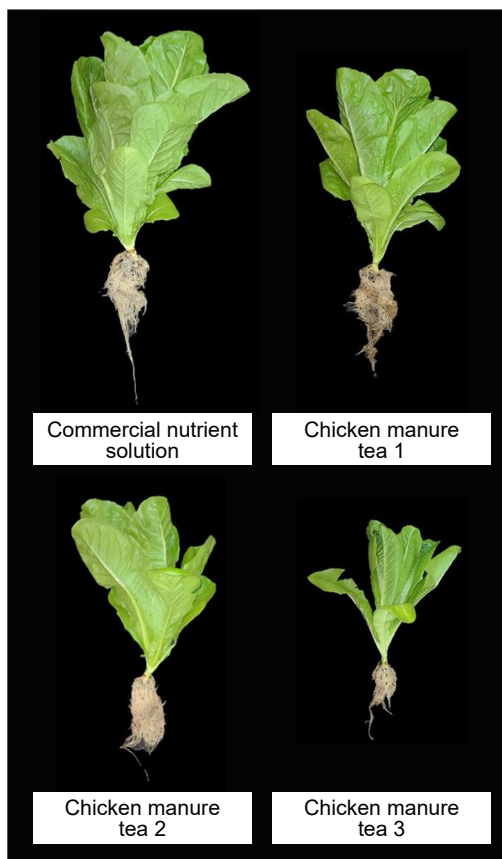


Figure 5. Romaine lettuce is produced using conventional hydroponics and small-scale integrated hydroponics-AWB

root fresh and dry weight of romaine lettuce produced in CNS were highly significant in comparison with CMT3 ($P < 0.01$). No significant difference was observed among CNS, CMT1, and CMT2 ($P > 0.05$).

There is a significant difference in the weight and mean of the number of romaine lettuce leaves produced using conventional hydroponics and integrated hydroponics-AWB with varying CMT concentrations at $p > 0.05$ (Figure 6). The mean number of leaves of romaine lettuce produced using the control, Treatments 1 and 2, was significantly higher than the mean number of leaves of romaine lettuce produced using Treatment 3. The leaf fresh weight was observed in the control, and this value decreased significantly with increasing concentrations of CMT. Treatment 3 showed the lowest fresh leaf weight, significantly different from the control.

In comparison between the CNS and CMT1, the result suggests that CMT1 could be a potential replacement for the CNS for romaine lettuce production using the developed integrated hydroponics-AWB. On the other hand, the result of the experiment also implies that using CMT at a high ppm level had a negative impact on the growth parameters of lettuce. The experiment's findings were in line with other research that showed a reduction in plant weight above ground when aerated chicken manure extract concentration was raised from 10 to 25 g/L and a permanent wilting of the plant at 50 g/L (Tikasz et al., 2019). In contrast, in a study of different chicken manure loadings (200 g, 300 g, and 400 g) on bioponic lettuce production, raising the manure loading rate increased plant yield (Wongkiew et al., 2021).

The observed decrease in values of growth parameters of romaine lettuce with higher ppm levels of CMT could be attributed to the toxic effects of organic nutrients in CMT

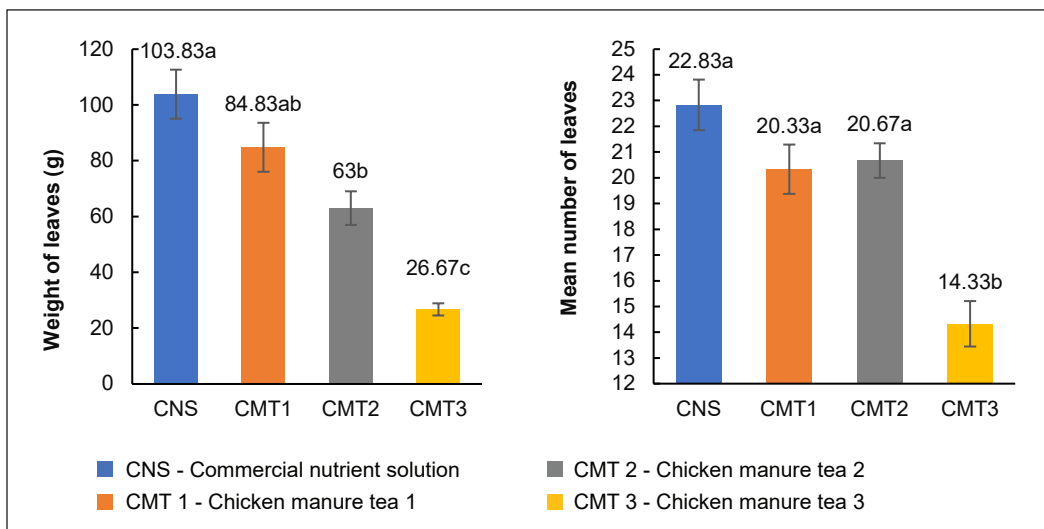


Figure 6. Influence of varying concentrations of chicken manure tea on the leaf weight (left) and number of leaves (right) of romaine lettuce produced using small-scale integrated hydroponics-AWB

on the plant. The quality of organic-based inputs for the growth of plants depends on mineralization rates that can be highly variable due to the quality of organic inputs and environmental conditions (Zandvakili et al., 2019). Unlike inorganic fertilizers, organic nutrients from animal waste are not readily available to the plant and must be converted to plant-available forms by microbes present in the system (Bi et al., 2010). Likely, higher ammonia levels in CMT3 and other organic nutrients could have resulted in stunted lettuce growth in weight and number of leaves. On the other hand, the values of growth parameters of romaine lettuce produced at lower concentration (CMT1) using the developed was comparable to the romaine lettuce produced in conventional hydroponics (CNS). It implies that the use of CMT at lower concentrations could be used for lettuce production using the developed system.

There was no significant difference in the moisture content and brix value of lettuce produced among each treatment using the integrated hydroponics-AWB at $p > 0.05$ (Figure 7). The moisture content of romaine lettuce plants is an important quality parameter as it affects the nutrient concentration present in the plant (Mou, 2012). The findings of the research on the comparison of the growth characteristics between hydroponically grown and soil-grown lettuce resulted in a lettuce moisture content of 94.23% and 92.94%, respectively (Lei & Engeseth, 2021). The dry matter of lettuce cultivated using typical hydroponics and decoupled aquaponics was 4.9% (95.1% MC) and 4.7% (95.3%), respectively (Monsees et al., 2019). The moisture content of the romaine lettuce produced using integrated hydroponics-AWB is comparable to that of the other studies conducted. The findings may indicate that the developed small-scale integrated hydroponics-animal waste bioreactor did not significantly impact the moisture content of the romaine lettuce plants.

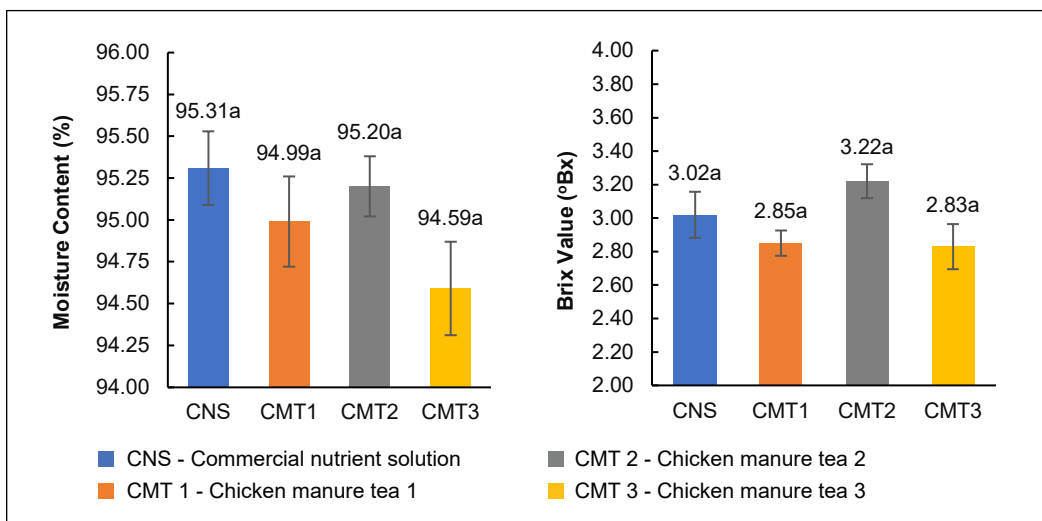


Figure 7. Influence of varying concentrations of chicken manure tea on the plant moisture content (left) and brix value (right) of romaine lettuce produced using small-scale integrated hydroponics-AWB

In terms of the brix value of the romaine lettuce produced using conventional hydroponics and integrated hydroponics-AWB with varying CMT concentrations, data suggests no significant differences in the Brix levels among the treatments. Brix value is used to express the level of soluble solids (sugars, pectin, organic acids, and amino acids) in a liquid, representing estimates of sugar content in fruits and vegetables (Kleinhenz & Bumgarner, 2012). In studying the effect of varying nutrient solutions on the brix value of lettuce produced in an NFT system, the results on romaine lettuce vary between 4.5 and 5.4 (Thakulla et al., 2021). Research on the use of biofertilizer from microalgae (*Chlorella vulgaris*) in hydroponic lettuce production resulted in a brix value ranging between 3.7 and 4.5.

The brix value of romaine lettuce produced using integrated hydroponics-AWB was slightly lower than in the other literature. However, it is important to take into consideration that it could have been influenced by other factors, such as the specific cultivar of lettuce used in the experiment and the type of nutritional support for plants. The lack of significant differences in the brix value of romaine lettuce produced at conventional hydroponics and integrated hydroponics-AWB with varying CMT concentrations implies that the use of DCM as a nutrient source for hydroponically grown lettuce could not affect the quality of the produced lettuce.

CONCLUSION

The small-scale integrated hydroponics animal waste bioreactor was designed, fabricated, and tested to determine the ideal concentration of chicken manure tea as a source of nutrients for romaine lettuce in comparison with conventional hydroponics. The result of the study implies that the optimum concentration of chicken manure tea in the system should be between $1,000 \pm 50$ ppm. Within the optimum concentration of chicken manure tea in the system, the small-scale integrated hydroponics animal waste bioreactor produced romaine lettuce with growth parameters comparable to those produced on conventional hydroponics. Increasing the chicken manure tea concentration to $1,400 \pm 50$ ppm using the developed system negatively impacted the plant growth parameters of romaine lettuce in comparison to conventional hydroponics. The result of the study provides an alternative and sustainable method for hydroponic romaine lettuce production using the developed small-scale integrated hydroponics-animal waste bioreactor to bioprocess the chicken manure into nutrient-rich chicken manure tea as a plant nutrient source. Further studies are recommended to determine the scalability and techno-economic feasibility of the developed system for larger-scale hydroponic farming operations. In addition, it is also recommended to observe the secondary nutrient and micronutrient level of the chicken manure tea further to assess its impact on plant growth and development.

ACKNOWLEDGEMENT

The authors thank the Department of Agricultural and Biosystems Engineering, College of Engineering, Central Luzon State University, Philippines, and Engineering Research and Development for Technology of the Department of Science and Technology.

REFERENCES

- Albina, P., Durban, N., Bertron, A., Albrecht, A., Robinet, J. C., & Erable, B. (2019). Influence of hydrogen electron donor, alkaline pH, and high nitrate concentrations on microbial denitrification: A review. *International Journal of Molecular Sciences*, *20*(20), Article 5163. <https://doi.org/10.3390/ijms20205163>
- Al-Gheethi, A. A., Efaq, A. N., Bala, J. D., Norli, I., Abdel-Monem, M. O., & Ab. Kadir, M. O. (2018). Removal of pathogenic bacteria from sewage-treated effluent and biosolids for agricultural purposes. *Applied Water Science*, *8*(2), Article 74. <https://doi.org/10.1007/s13201-018-0698-6>
- Ashworth, A. J., Chastain, J. P., & Moore Jr, P. A. (2020). Nutrient characteristics of poultry manure and litter. In H. M. Waldrip, P. H. Pagliari & Z. He (Eds.), *Animal Manure: Production, Characteristics, Environmental Concerns, and Management* (pp. 15-26). John Wiley & Sons. <https://doi.org/10.2134/adaspecpub67.c5>
- Atkin, K., & Nichols, M. A. (2004). Organic hydroponics. *Acta Horticulturae*, *648*, 121–127. <https://doi.org/10.17660/ActaHortic.2004.648.14>
- Béline, F., Daumer, M. L., Loyon, L., Pourcher, A. M., Dabert, P., Guiziou, F., & Peu, P. (2008). The efficiency of biological aerobic treatment of piggery wastewater to control nitrogen, phosphorus, pathogen and gas emissions. *Water Science and Technology*, *57*(12), 1909–1914. <https://doi.org/10.2166/wst.2008.316>
- Bi, G., Evans, W. B., Spiers, J. M., & Witcher, A. L. (2010). Effects of organic and inorganic fertilizers on marigold growth and flowering. *HortScience*, *45*(9), 1373–1377.
- Blanchard, C., Wells, D. E., Pickens, J. M., & Blersch, D. M. (2020). Effect of pH on cucumber growth and nutrient availability in a decoupled aquaponic system with minimal solids removal. *Horticulturae*, *6*(1), Article 10. <https://doi.org/10.3390/horticulturae6010010>
- Borlaug, N. E. (2019). Using plants to meet world food needs. In R. G. Woods (Ed.), *Future Dimensions of World Food and Population* (pp. 101–182). CRC Press.
- Bradford, G. E. (1999). Contributions of animal agriculture to meeting global human food demand. *Livestock Production Science*, *59*(2), 95–112. [https://doi.org/10.1016/S0301-6226\(99\)00019-6](https://doi.org/10.1016/S0301-6226(99)00019-6)
- Chia, S. Y., & Lim, M. W. (2022). A critical review on the influence of humidity for plant growth forecasting. *IOP Conference Series: Materials Science and Engineering*, *1257*(1), Article 012001. <https://doi.org/10.1088/1757-899X/1257/1/012001>
- Collins, E., Barker, J. C., Carr, L. E., Brodie, H. L., & Martin, J. H. (1999). *Poultry waste management handbook*. Natural Resource, Agriculture, and Engineering Service.
- De Clercq, M., Vats, A., & Biel, A. (2018). *Agriculture 4.0: The future of farming technology*. Oliver Wyman.
- EPA. (2015). *Dissolved Oxygen*. United States Environmental Protection Agency. <https://www.epa.gov/caddis-vol2/dissolved-oxygen>

- Ferrarezi, R. S., & Testezlaf, R. (2016). Performance of wick irrigation system using self-compensating troughs with substrates for lettuce production. *Journal of Plant Nutrition*, 39(1), 147–161. <https://doi.org/10.1080/01904167.2014.983127>
- Hatfield, J. L., & Prueger, J. H. (2015). Temperature extremes: Effect on plant growth and development. *Weather and Climate Extremes*, 10(Part A), 4–10. <https://doi.org/10.1016/j.wace.2015.08.001>
- Horrigan, L., Lawrence, R. S., & Walker, P. (2002). How sustainable agriculture can address the environmental and human health harms of industrial agriculture. *Environmental Health Perspectives*, 110(5), 445–456. <https://doi.org/10.1289/ehp.02110445>
- Hu, Y., Sampat, A. M., Ruiz-Mercado, G. J., & Zavala, V. M. (2019). Logistics network management of livestock waste for *Spatiotemporal* control of nutrient pollution in water bodies. *ACS Sustainable Chemistry & Engineering*, 7(22), 18359–18374. <https://doi.org/10.1021/acssuschemeng.9b03920>
- Khoshnevisan, B., Duan, N., Tsapekos, P., Awasthi, M. K., Liu, Z., Mohammadi, A., Angelidaki, I., Tsang, D. C.W., Zhang, Z., Pan, J., Ma, L., Aghbashlo, M., Tabatabaei, M., & Liu, H. (2021). A critical review on livestock manure biorefinery technologies: Sustainability, challenges, and future perspectives. *Renewable and Sustainable Energy Reviews*, 135, Article 110033. <https://doi.org/10.1016/j.rser.2020.110033>
- Kleinhenz, M. D., & Bumgarner, N. R. (2012). *Using Brix as an Indicator of Vegetable Quality: Fact Sheet Agriculture and Natural Resources*. The Ohio State University. chrome-extension://efaidnbmninnkpcjpcglclefindmkaj/https://u.osu.edu/vegprolab/files/2015/10/HYG_1650_12_0-1evpds.pdf
- Koga, N. (2008). An energy balance under a conventional crop rotation system in northern Japan: Perspectives on fuel ethanol production from sugar beet. *Agriculture, Ecosystems & Environment*, 125(1), 101–110. <https://doi.org/10.1016/j.agee.2007.12.002>
- Koul, B., Yakoob, M., & Shah, M. P. (2022). Agricultural waste management strategies for environmental sustainability. *Environmental Research*, 206, Article 112285. <https://doi.org/10.1016/j.envres.2021.112285>
- Lei, C., & Engeseth, N. J. (2021). Comparison of growth characteristics, functional qualities, and texture of hydroponically grown and soil-grown lettuce. *Lwt-Food Science and Technology*, 150, Article 111931. <https://doi.org/10.1016/j.lwt.2021.111931>
- Monsees, H., Suhl, J., Paul, M., Kloas, W., Dannehl, D., & Würtz, S. (2019). Lettuce (*Lactuca sativa*, variety Salanova) production in decoupled aquaponic systems: Same yield and similar quality as in conventional hydroponic systems but drastically reduced greenhouse gas emissions by saving inorganic fertilizer. *PLoS One*, 14(6), Article e0218368. <https://doi.org/10.1371/journal.pone.0218368>
- Morgan, J. B., & Connolly, E. L. (2013). Plant-soil interactions: Nutrient uptake. *Nature Education Knowledge*, 4(8), Article 2.
- Mou, B. (2012). Nutritional quality of lettuce. *Current Nutrition & Food Science*, 8(3), 177–187. <https://doi.org/10.2174/157340112802651121>
- Mupambwa, H. A., Namwoonde, A. S., Liswaniso, G. M., Hausiku, M. K., & Ravindran, B. (2019). Biogas digestates are not an effective nutrient solution for hydroponic tomato (*Lycopersicon esculentum* L.) production under a deep water culture system. *Heliyon*, 5(10), Article e02736. <https://doi.org/10.1016/j.heliyon.2019.e02736>

- Ren, F., Sun, N., Misselbrook, T., Wu, L., Xu, M., Zhang, F., & Xu, W. (2022). Responses of crop productivity and reactive nitrogen losses to the application of animal manure to China's main crops: A meta-analysis. *Science of The Total Environment*, 850, Article 158064. <https://doi.org/10.1016/j.scitotenv.2022.158064>
- Sace, C. F., & Jr Natividad, E. P. (2015). Economic analysis of an urban vertical garden for hydroponic production of lettuce (*Lactuca sativa*). *International Journal of Contemporary Applied Sciences*, 2(7), 42–56.
- Savci, S. (2012). Investigation of effect of chemical fertilizers on environment. *Apctee Procedia*, 1, 287–292. <https://doi.org/10.1016/j.apctee.2012.03.047>
- Shinohara, M., Aoyama, C., Fujiwara, K., Watanabe, A., Ohmori, H., Uehara, Y., & Takano, M. (2011). Microbial mineralization of organic nitrogen into nitrate to allow the use of organic fertilizer in hydroponics. *Soil Science and Plant Nutrition*, 57(2), 190–203. <https://doi.org/10.1080/00380768.2011.554223>
- Siddiqui, Z., Hagare, D., Chen, Z. H., Jayasena, V., Shahriar, A. A., Panatta, O., Liang, W., & Boyle, N. (2022). Growing lettuce and cucumber in a hydroponic system using food waste derived organic liquid fertiliser. *Environmental Sustainability*, 5(3), 325–334. <https://doi.org/10.1007/s42398-022-00234-9>
- Spiertz, J. H. J., & Ewert, F. (2009). Crop production and resource use to meet the growing demand for food, feed and fuel: Opportunities and constraints. *NJAS: Wageningen Journal of Life Sciences*, 56(4), 281–300. [https://doi.org/10.1016/S1573-5214\(09\)80001-8](https://doi.org/10.1016/S1573-5214(09)80001-8)
- Stenstrom, M. K., & Poduska, R. A. (1980). The effect of dissolved oxygen concentration on nitrification. *Water Research*, 14(6), 643–649. [https://doi.org/10.1016/0043-1354\(80\)90122-0](https://doi.org/10.1016/0043-1354(80)90122-0)
- Stouvenakers, G., Dapprich, P., Massart, S., & Jijakli, M. H. (2019). Plant pathogens and control strategies in aquaponics. In S. Goddek, A. Joyce, B. Kotzen & G. M. Burnell (Eds.), *Aquaponics Food Production Systems* (pp. 353–378). Springer.
- Thakulla, D., Dunn, B., Hu, B., Goad, C., & Maness, N. (2021). Nutrient solution temperature affects growth and °brix parameters of seventeen lettuce cultivars grown in an NFT hydroponic system. *Horticulturae*, 7(9), Article 321. <https://doi.org/10.3390/horticulturae7090321>
- Tibbitts, T. W., & Bottenberg, G. (1976). Growth of lettuce under controlled humidity levels 1. *Journal of the American Society for Horticultural Science*, 101(1), 70–73. <https://doi.org/10.21273/JASHS.101.1.70>
- Tikasz, P., MacPherson, S., Adamchuk, V., & Lefsrud, M. (2019). Aerated chicken, cow, and turkey manure extracts differentially affect lettuce and kale yield in hydroponics. *International Journal of Recycling of Organic Waste in Agriculture*, 8(3), 241–252. <https://doi.org/10.1007/s40093-019-0261-y>
- Torres, E., Sayco, T., Cinense, M., Fabula, J., Mateo, W., & Somera, C. G. (2023). Development of an organic fertilizer bioreactor for the bioconversion of dried chicken manure into organic liquid solution. *International Journal of Agricultural Technology*, 19(3), 1359–1378.
- Valin, H., Sands, R. D., van der Mensbrugge, D., Nelson, G. C., Ahammad, H., Blanc, E., Bodirsky, B., Fujimori, S., Hasegawa, T., Havlik, P., Heyhoe, E., Kyle, P., Mason-D'Croz, D., Paltsev, S., Rolinski, S., Tabeau, A., van Meijl, H., von Lampe, M., & Willenbockel, D. (2014). The future of food demand: Understanding differences in global economic models. *Agricultural Economics*, 45(1), 51–67. <https://doi.org/10.1111/agec.12089>

- Waldrip, H. M., Pagliari, P. H., & He, Z. (2020). *Animal manure: Production, characteristics, environmental concerns, and management*. John Wiley & Sons. <https://doi.org/10.2134/aspectpub67>
- Wongkiew, S., Koottatep, T., Polprasert, C., Prombutara, P., Jinsart, W., & Khanal, S. K. (2021). Bioponic system for nitrogen and phosphorus recovery from chicken manure: Evaluation of manure loading and microbial communities. *Waste Management, 125*, 67–76. <https://doi.org/10.1016/j.wasman.2021.02.014>
- Zandvakili, O. R., Barker, A. V., Hashemi, M., & Etemadi, F. (2019). Biomass and nutrient concentration of lettuce grown with organic fertilizers. *Journal of Plant Nutrition, 42*(5), 444-457. <https://doi.org/10.1080/01904167.2019.1567778>
- Zhang, H., Vocasek, F., Antonangelo, J., & Gillespie, C. (2020). Temporal changes of manure chemical compositions and environmental awareness in the Southern Great Plains. In H. M. Waldrip, P. H. Pagliari & Z. He (Eds.), *Animal Manure: Production, Characteristics, Environmental Concerns, and Management* (pp. 15-26). John Wiley & Sons.

Anti-friction and Wear Resistance Performance of Palm Olein Grease with Molybdenum Disulfide Additive

Nadiah Aqilahwati Abdullah, Nurul Farhana Mohd Yusof* and Zaidi Mohd Ripin

School of Mechanical Engineering, Engineering Campus, Universiti Sains Malaysia, 14300 Nibong Tebal, Penang, Malaysia

ABSTRACT

In this study, palm olein-based grease with a micro-molybdenum disulfide (MoS_2) additive has been developed. The grease was prepared using various MoS_2 concentrations to investigate the role of additives in improving grease performance. A four-ball tribological test was conducted to investigate the surface morphology, wear depth, and volume loss of the steel ball. The results indicated that the MoS_2 additive reduced the coefficient of friction and wear scar diameter compared to pure palm olein grease. The value of 0.5 wt.% was considered the optimum value, reflecting the best grease performance indicated by low friction coefficient, wear diameter, wear depth, and volume loss. Elemental analysis revealed that the MoS_2 additive was deposited onto the wear tracks, improving the surface protection. Thus, this additive was found to have a good potential for improving palm olein-based grease.

Keywords: Four-ball, friction, MoS_2 , palm olein grease, wear

INTRODUCTION

Lubricants are essential in various industrial applications to minimize friction and wear between the interacting surfaces. In addition, it helps protect metal surfaces from corrosion, operates as a heat transfer fluid, flushes out impurities, absorbs stress, and acts as a seal against dirt, dust, and water. Most commercial greases are based on mineral oil that generally is not environmentally friendly. Mineral oil is not readily biodegradable and is known to pose

ARTICLE INFO

Article history:

Received: 14 May 2023

Accepted: 27 November 2023

Published: 01 April 2024

DOI: <https://doi.org/10.47836/pjst.32.3.03>

E-mail addresses:

nadiahaqilah@student.usm.my (Nadiah Aqilahwati Abdullah)

mefarhana@usm.my (Nurul Farhana Mohd Yusof)

mezaidi@usm.my (Zaidi Mohd Ripin)

* Corresponding author

hazards due to its accumulation in plants, animals, and groundwater (Nowak et al., 2019). It has led the effort to produce a bio-based lubricant with a less toxic base oil. Synthetic oil and vegetable-based oil are the most reliable alternatives to mineral oil as they have desired lubrication properties (Heikal et al., 2017; Hou et al., 2020; Koshy et al., 2015; Quinchia et al., 2014). Synthetic oils offer a wide range of temperature applications and oxidation stability; however, the price is higher than mineral oil.

As a vegetable oil, palm oil possesses excellent properties such as high lubricity, high viscosity index, and low volatility (Yahaya et al., 2018). In addition, palm olein has long fatty acid chains and polar groups that are naturally attracted to metal and provide strong interactions with the lubricated surfaces (Borda et al., 2018; Reeves et al., 2015), which makes it good at boundary lubrication regime (Fox & Stachowiak, 2007; Wang et al., 2022). Palm oil fatty acids consist of unsaturated double bonds, which results in less oxidation stability. Due to this, studies have been conducted by modifying the chemical structure of palm oils. Palm trimethylolpropane ester (TMP) (Gulzar et al., 2017) and double-fractionated palm olein (Zulhanafi & Syahrullail, 2019) are among the modified palm oil derivatives that have been evaluated for their lubrication abilities in the form of lubricating oil. However, major chemical modifications are expensive and tend to reduce the natural tribological properties of vegetable oils.

Palm oil can be further refined as palm olein, which is the liquid fraction of the palm oil after a fractionation process and is in liquid form at room temperature (Pande et al., 2012). The unsaturated fatty acids in the palm olein comprise mono-unsaturated and poly-unsaturated (Yahaya et al., 2018). Despite the unsaturation properties, mono-unsaturated fatty acids have a greater oxidation stability than poly-unsaturated (Fox & Stachowiak, 2007). Palm olein has only 11.0% poly-unsaturated fatty acids, whereas the rest of the compositions come from 50% saturated and 39% mono-unsaturated. In addition, a study proved that palm olein has better oxidation stability at high temperatures than olive oil and rapeseed oil (Tabee et al., 2008). It shows that palm olein can be a good candidate as a lubricant. Palm olein outperformed engine oil without chemical modification in friction reduction properties and exhibited only slightly higher wear scar diameter (Jabal et al., 2014).

In certain applications, grease lubrication is preferable as it requires relatively simple retention devices and is suitable for application under extreme conditions. A thickener must be dispersed in the base oil to develop a grease. It was found that thickeners affect grease's mechanical and thermal stability and play roles in reducing friction and wear (Fan et al., 2018). Despite the existing mineral greases, biological greases derived from vegetable oils have been actively developed as an alternative (Kozdrach & Skowroński, 2018).

A palm bio-grease using calcium soap thickener added with additives (calcium carbonate (CaCO_3) and hydroxyapatite (HA)) was produced and investigated for its wear-

preventive and extreme pressure properties (Razak & Ahmad, 2021). The study proved that the tribological properties of the formulated bio-based grease are comparable to synthetic-based grease, with great improvement in the load-carrying capacity of the additive-added formulations. In addition, a previous study (Sukirno et al., 2009) produced and evaluated the performance of palm grease using modified refined, bleached, and deodorized (RBD) palm oil and lithium soap thickener. The wear of the palm grease-lubricated specimens was lower than that of the mineral grease-lubricated specimens, indicating good surface protection and anti-wear properties. Thus, adding a thickener can improve the performance of the vegetable oils.

Furthermore, additives are usually added to improve the desired tribological properties of a lubricant. In vegetable grease, copper (Cu) (Borda et al., 2018), molybdenum disulfide (MoS_2) (Bagi & Aswath, 2015), and zinc dialkyldithiophosphate (ZDDP) (Nagendramma & Kumar, 2015) are some additives that have been proven to reduce friction and wear. MoS_2 particles are among the most common additives due to their layered two-dimensional structure and weak van der Waals force between molecular bonds (Holinski & Gänzheimer, 1972). The effectiveness of MoS_2 in enhancing the tribological properties of a lubricant was demonstrated in many studies (Bagi & Aswath, 2015; Gulzar et al., 2015; Koshy et al., 2015). Specifically for vegetable-based oil lubricant, it was reported that 1.0 wt.% MoS_2 exhibited good wear protection and high weld load when added to a chemically modified RBD palm oil (Gulzar et al., 2015). In coconut oil, MoS_2 nanoparticles produced less friction and wear rate than pure base oil and were accomplished better by adding surfactants (Koshy et al., 2015). Furthermore, the addition of 0.25 wt.% MoS_2 nanosheets to white oil demonstrated excellent friction reduction and wear protection compared with the addition of 1.0 wt.% of ZDDP under high load conditions (Wu et al., 2018).

To date, reports on the tribological properties of grease produced from RBD palm oil are very limited (Sukirno et al., 2009, 2010), and the tribological performance of palm grease with RBD palm olein as the base oil has never been reported. Thus, the roles of additives in the RBD palm olein grease remain to be investigated. RBD palm oil is semi-solid at room temperature, consisting of RBD palm olein (liquid fraction) and palm stearin (solid fraction). This study investigates the tribological performance of palm olein-based grease without chemical structure modification of the RBD palm olein base oil to evaluate the effectiveness of thickener and additive (MoS_2) on its performance. The micro-scale MoS_2 was selected to be used in the study. The selection of the particle sizes was based on a few kinds of literature showing that the effect of MoS_2 on the tribological properties is different in different base oils and greases under different testing conditions. For example, (Xu et al., 2013) reported that the micro MoS_2 exhibited better lubricating performance than the nano MoS_2 when rapeseed oil was used as the base oil. In addition, (Gulzar et al., 2017) tested two sizes of MoS_2 in polyalphaolefin (PAO) oil for two different applications. Small-size

(20 nm to 150 nm) particles performed better under the four-ball extreme pressure test, whereas large-size (50 nm to 2000 nm) MoS₂ was excellent for cylinder liner application.

In this study, exploring the MoS₂ effect on palm grease was initiated using a micro size before going into the nano size in the next stage of the study. A standard four-ball tribometer was utilized to evaluate the tribological properties of the developed greases. Further analysis of the steel ball wear scar is conducted by measuring the wear volume based on the volume of the material loss at the wear scar.

METHODOLOGY

Materials

Four samples were prepared in this study: palm oil grease without additive as a reference and another three with different percentages of MoS₂ additive. RBD palm olein was purchased from a local distributor, and its properties are presented in Table 1. A lithium 12-hydroxystearate powder was selected as a thickener for the grease formulation. MoS₂ with a particle size of 1- 3 μm was used as an additive for this study, as presented in Figure 1. The properties of the MoS₂ are listed in Table 1.

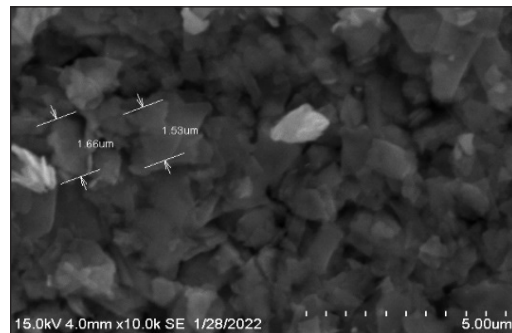


Figure 1. Scanning electron microscopy (SEM) image of the MoS₂ additive

Preparation of the Greases

For grease preparation, 87 wt.% of base oil and 13 wt.% of thickener were added into a glass cylinder on a hot plate and mixed at a temperature of 90°C. Next, the temperature was increased to 160°C while stirring the mixture for 30 min. The temperature was further increased to 210°C while stirring for 5 min and immediately cooled to 120°C to dissolve the lithium. The grease was then separated into four portions for the addition of the additive at different concentrations.

Dispersion of Additive

The concentration of MoS₂ was apportioned into three, specifically 0.25, 0.50, and 0.75

Table 1
Properties of the base oil and additive

Materials	Properties	
Base Oil	Density (kg/m ³)	898.2
	Viscosity at 40°C (mm ² /s)	46.76
	Viscosity at 100°C (mm ² /s)	8.91
	Viscosity Index	174
Thickener	Melting point	220°C
	Color	White
Additive	Morphology	Hexagonal with sharp edges
	Size	1-3 μm
	Color	Grey
	Purity	98.5%

wt.%. The grease temperature was maintained at 120°C while the additive was added to disperse the additive into the grease. An overhead stirrer was used for stirring, and the speed was set to 800 rpm while slowly adding the additive. Once the additive was fully added, the stirrer was sped up to 2200 rpm, and stirring was performed for around 60 min for homogenization.

Physical Properties of the Grease

The synthesized grease's physical characteristics were assessed using cone penetration and dropping point tests. The cone penetration test followed ASTM D217 guidelines, while the dropping point test adhered to ASTM D556 standards. The resulting measurements for the pure grease indicated a dropping point of 208.7°C and a penetration depth of 276.4 (mm/10), indicating an NLGI 2 grade.

Friction and Wear Performance

A four-ball tribometer (Ducom TR-30L-IAS, Netherlands) was used to evaluate the friction and wear performance of the greases. The test method was performed in accordance with the Standard Test Method for Wear Preventive Characteristics of Lubricating Grease (ASTM D2266). Figure 2 presents the illustration of the test setup. The experiment was run under a nominal load of 392 N, a rotating speed of 1200 rpm (0.46 m/s), and an operating temperature of 75°C for 60 min. The test used a GCr15 (AISI 52100) steel ball with a 12.7 mm diameter and hardness of 62 to 64 HRC. The initial average surface roughness (Ra) of the ball was measured as 0.1613 μm using Alicona IFM G4. The balls, ball pot set, and chuck were thoroughly cleansed prior to each test using acetone. The wear scar diameter of the balls was measured after each run. Frictional torque obtained from the four-ball torque reading was transformed into the coefficient of friction (COF), and its average value was reported for each sample. New sets of balls were used prior to each test.

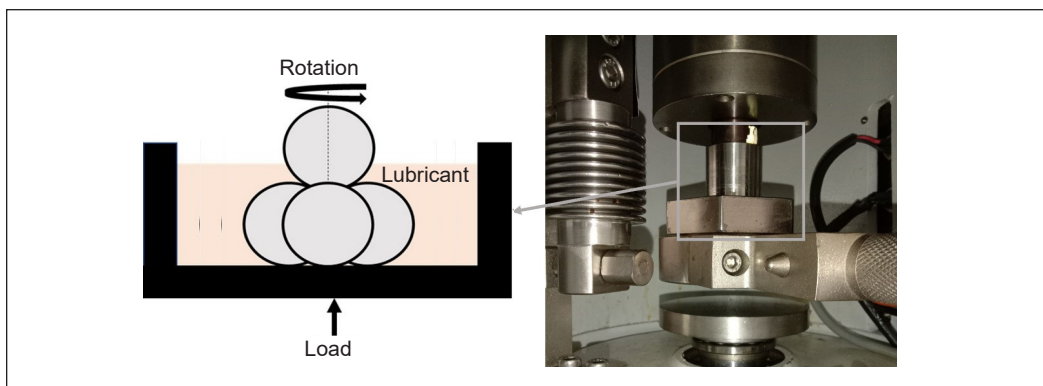


Figure 2. Schematic illustration of the DUCOM four-ball test mechanism. The upper ball is rotated at a specified speed while the three lower balls are filled with lubricant

Analysis of the Worn Surface

A tabletop scanning electron microscopy (Hitachi TM-1000, Japan) with 15 kV accelerating voltage EDX spectroscopy (Oxford Instruments, UK) was adopted to evaluate the characteristics of wear scar surfaces. Each wear scar surface was analyzed at magnifications of 200× and 1200×. Elemental scanning using EDX was made at 1200× magnification. The wear depth profile and volume loss were measured *via* a 3D profilometry (Alicona InfiniteFocus Microscope (IFM) G4, Bruker, USA). Surface scanning was performed on the surface of the steel ball, and the wear depth measurement was performed by obtaining the surface profile perpendicular to the wear grooves. The edge of the wear scar was taken as the reference for the wear depth measurement, as presented in Figure 3(a). The wear volume was obtained by measuring the volume of the material loss at the wear scar area, as presented in Figures 3(b) and 3(c), using the volume measurement feature in the Alicona IFM software. The average roughness (Ra) was measured using the same profilometer for each ball from edge to edge of the wear scar (perpendicular to the wear scratches) with a cutoff length of 0.8 mm.

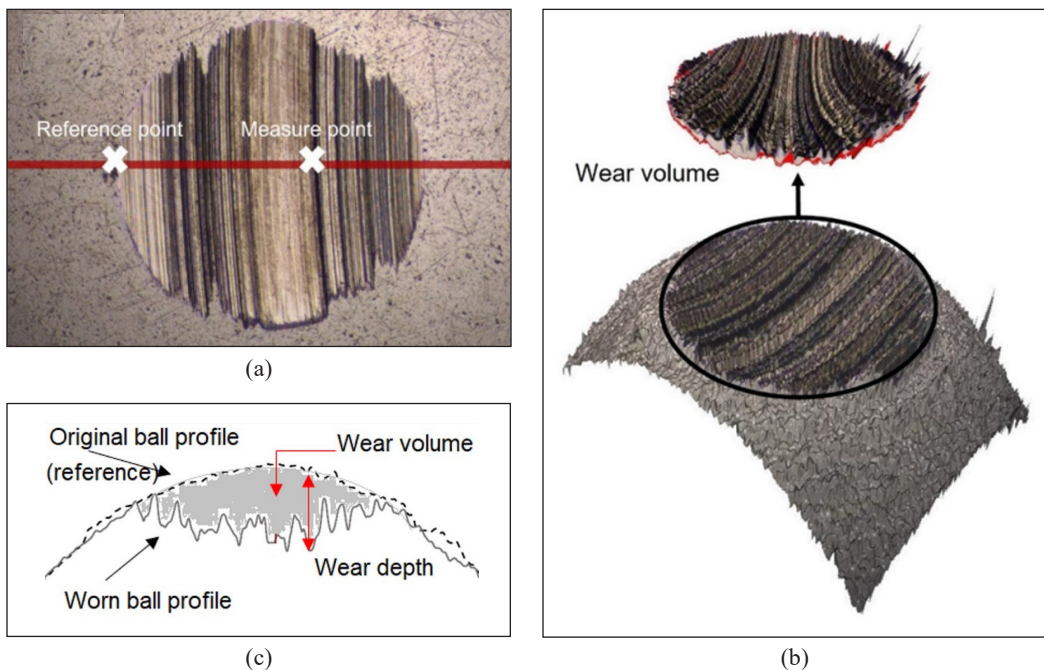


Figure 3. Description of the wear depth (a) and wear volume measurement (b and c)

RESULTS AND DISCUSSION

COF and Wear Scar Diameter

Figure 4 presents the trend of COF as a function of time for the palm grease with and without additives. The COF values were calculated based on the procedure described in

ASTM D2266. From the graph, the trend is almost identical, where at the first 80 s, the COF exhibits an increasing trend due to a high wear rate where more asperities of the rubbing areas came in contact, leading to plastic deformations of the tips of asperities or known as running-in period (Blau, 2005). Furthermore, the fluctuations of the COF amplitude, especially upon the addition of 0.25 and 0.75 wt.% of MoS₂, might be due to the accumulation of wear debris and agglomeration of the additive particles (Nabhan et al., 2021). The COF generally starts to stabilize after 1200 s, where less fluctuation in the amplitude can be observed (Abdollah et al., 2020).

The COF value and wear scar diameter of the greases are presented in Figure 5. It is apparent that the COF value and wear scar diameter decreased with the addition of MoS₂. The grease with 0.50 wt.% MoS₂ had the lowest COF value of 0.0411 ± 0.0039 , followed by 0.25 wt.% MoS₂ with a COF value of 0.0421 ± 0.0040 , 0.75 wt.% MoS₂ with a COF value of 0.0435 ± 0.0045 and pure grease (without additive) with a COF value of 0.0444 ± 0.0043 . Under the same tribological test condition (ASTM D2266), the developed pure palm grease had a considerably good friction performance when compared with the friction performance of a mineral grease (COF: 0.089) from a previous study under similar test conditions by He et al. (He et al., 2018), in accordance with the findings from (Abdollah et al., 2020), where palm oil exhibited better friction performance (COF: 0.08) than commercial SAE 15W40 engine oil (COF: 0.12). The excellent performance of the palm oil-

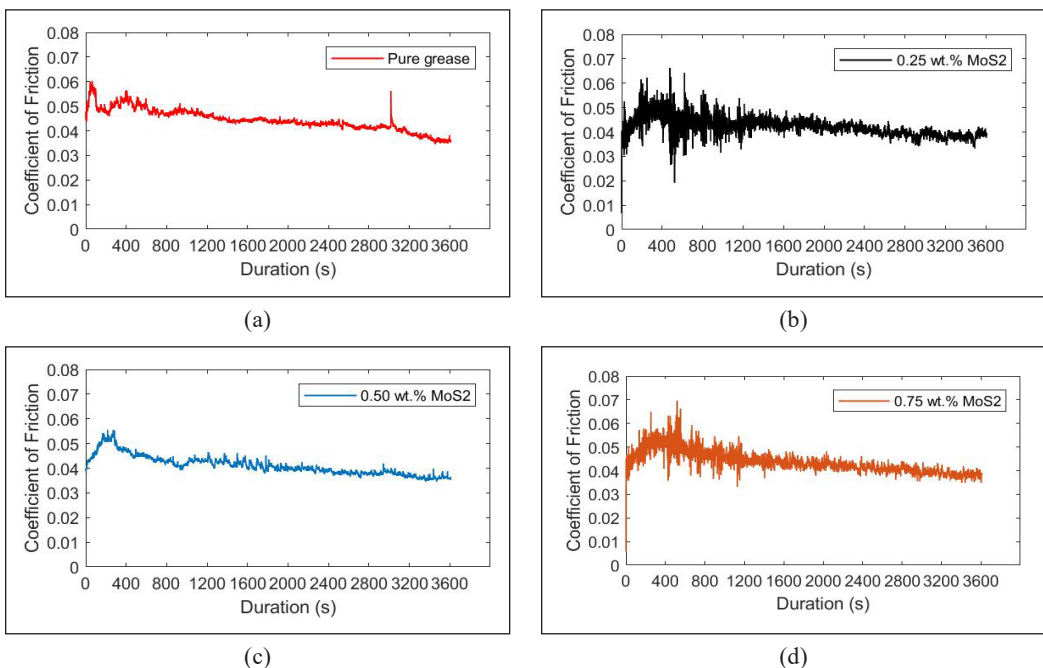


Figure 4. Dynamic coefficient of friction: (a) pure palm grease; (b) palm grease + 0.25 wt.% MoS₂; (c) palm grease + 0.50 wt.% MoS₂; and (d) palm grease + 0.75 wt.% MoS₂

based lubricant was due to the base oil polar molecule attraction to the surface material, which reduced the friction (Mannekote & Kailas, 2012; Yahaya et al., 2018).

The relatively good performance of palm olein grease can also be attributed to the synergistic effect between the base oil and the thickener (Fan et al., 2018). In this case, the polarity of the base oil and the thickener can play an important role in their synergistic effect. In the form of oil, the polar heads of the palm fatty acid chains are attached to the metal surface and form a monolayer film with the non-polar end tail of fatty acids facing away from the metal

surface (Abdulbari & Zuhan, 2018). In grease, the thickener particles having the same polarity as the palm olein fatty acids will bind together during the grease formulation, allowing the thickener to hold the oil. In addition, palm olein has active sites (unsaturated chains), enabling it to bind with other elements from the thickener and additive while maintaining attraction to the metal surface.

In addition, the physical structure of the palm grease may also contribute to its performance. Palm olein grease can be classified as a viscoelastic material that possesses both elastic and viscous behavior. The elastic part can recoil to its original shape after the stress is removed, whereas the viscous material starts to flow if stress is applied. The elasticity is essential for preventing grease leakage from the lubricated surface. In contrast, fluidity is essential for the grease's lubricating efficiency and to be well dispersed on the rubbing pair.

Furthermore, it was demonstrated that the additive improves the tribological properties of palm-based grease. It was also suggested that the optimum concentration of the MoS₂ additive is 0.50 wt.%, which offers the best tribological performance from the wear scar diameter and friction coefficient perspective. Compared with pure grease, the COF was reduced by 7.50%, 5.18%, and 1.92% at the concentrations of 0.50, 0.25, and 0.75 wt.%, respectively. The reduction can be attributed to the additive intrinsic factor, which is a weak van der Waals bond between the molecular layers, where it takes relatively weak shear forces to displace the layers (Holinski & Gänsheimer, 1972). However, the reduction of the COF value was not that significant, which can be explained by the insufficient shearing of MoS₂ due to the low load applied (Winer, 1967). In a previous study, Bagi and Aswath (2015) evaluated the performance of MoS₂ in lithium grease under different spectrum

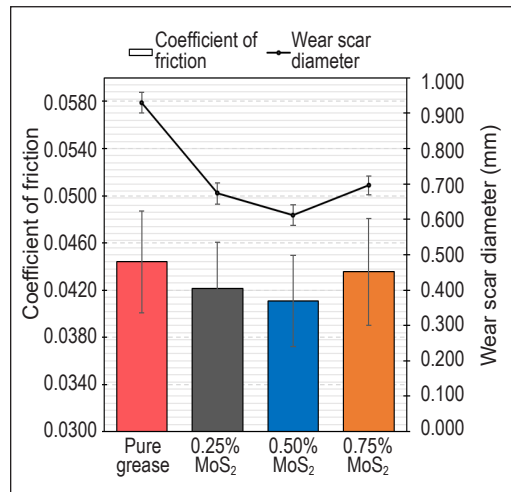


Figure 5. Trend of the COF and WSD of the greases

loading conditions from 40 to 80 kg. They found that higher loads could shear the van der Waals forces between Mo and S better than the lower load, consequently leading to a lower COF value.

In addition, the MoS₂ particles in the palm grease might not be able to enter the contact region entirely due to their size. From a previous study by (Hu et al., 2017), micro MoS₂ exhibited a lower friction and wear reduction performance compared to nano sizes MoS₂, where a nano size is easier to enter the contact region and protect the friction pair. Furthermore, the X-ray photoelectron spectroscopy (XPS) spectra results from the same study showed the occurrence of MoS₂ oxidation during the friction process, which leads to the lower particles remaining within the contact region. Therefore, the oxidation of MoS₂ might be present, which resulted in the insignificant friction improvement of the palm grease with the addition of micro MoS₂.

In the case of different MoS₂ concentrations, 0.50 wt.% has better friction performance than 0.25 and 0.75 wt.%. At a concentration of 0.25%, the large wear scar diameter can be attributed to the insufficient amount of MoS, which could not exert a good friction reduction effect compared with the optimum concentration. At MoS₂ concentration of 0.75%, the condition can be explained by the possible agglomeration of particles in the palm grease structure. Agglomeration promotes friction due to the increase in shear force required for maintaining the movement between the interacting surfaces whenever the agglomerate particles come into contact (Abdollah et al., 2020; Gong et al., 2021). In other words, agglomeration creates new asperities between the surfaces in contact, which induces high friction and wear to overcome them. Furthermore, agglomeration is closely related to dispersion stability, where a surfactant or dispersant can be introduced into the grease and additive formulation to improve the dispersibility of the additive (Gulzar et al., 2015). However, no surfactant was introduced into the formulation to avoid any influences from the surfactant on the tribological properties of the grease.

The efficiency of a lubricant is determined not only by its ability to provide a low COF but also by its ability to protect a surface from wear. Observation of the wear scar diameter revealed that the grease with 0.50 wt.% MoS₂ improved the wear protection with the highest reduction of 31.19% of the scar diameter compared with pure grease, from 0.930 ± 0.029 to 0.612 ± 0.030 mm. MoS₂ tends to exhibit a mending effect as one of the lubrication mechanisms where particles are deposited on the wear surface and fill the grooves, which helps reduce the wear (Kumar et al., 2020; Mushtaq & Hanief, 2021). Meanwhile, the diameters of the 0.25 and 0.75 wt.% MoS₂ greases have been reduced by 27.63% (to 0.673 ± 0.030 mm) and 25.16% (to 0.696 ± 0.027 mm), respectively. It was observed that 0.25 and 0.75 wt.% MoS₂ produced a larger scar diameter than the 0.50 wt.% MoS₂. An insufficient amount of additive is expected to result in a slightly larger scar diameter of 0.25 wt.% MoS₂ grease. As for the 0.75 wt.% MoS₂, a larger scar diameter can

be attributed to dispersion stability and particle aggregation along with the sharp edges of the additive, which cause metal rollout and abrasive wear (Chaurasia et al., 2020).

Worn Surfaces Morphology

Wear morphology is important in evaluating the wear-protective performance of a lubricant. Scanning electron microscopy (SEM) was employed to characterize the worn surfaces of the steel balls. Figure 6 presents the micrograph image of the wear scar areas on the steel ball after the four-ball test at magnification of 200 \times and 1200 \times . A circular scar with deep and shallow parallel grooves was found to form on all worn surfaces. Figure 6(a) presents a worn surface of the ball lubricated with pure grease. The appearance of grooves was more prominent on the pure grease-lubricated surface than on those with additives at 0.25 wt.% MoS₂-lubricated surface, noticeable abrasion marks with shallow grooves were observed with a pattern almost similar to pure grease, as presented in Figure 6(b). Figure 6(c) shows that for the 0.50 wt.% MoS₂ grease, shallower grooves were formed as a result of the lubrication effect coming from the sufficient additive to fill in the grooves and avoid more severe wear. In addition, the 0.75 wt.% MoS₂ produced a wear surface with shallow and deep grooves and visible metal pullout primarily on the focused region, as presented in Figure 6(d). Moreover, sediments were also observed on each surface, deposited onto the surface and filled into scratches.

The sharp edges of MoS₂ can cause scratch marks and deep grooves when agglomerate particles are present in the lubricant film. It can be observed at a 1200 \times magnification scar

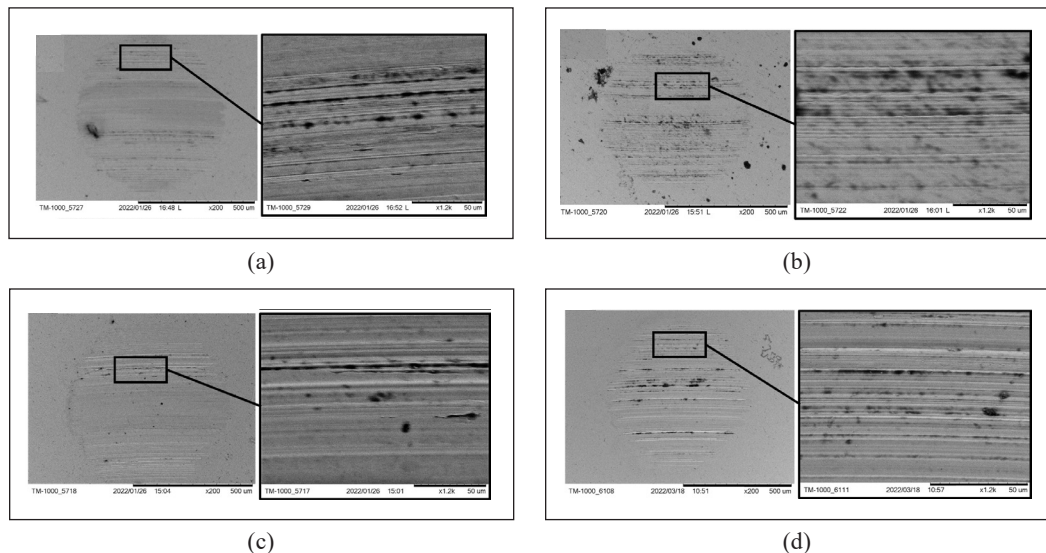


Figure 6. SEM images of WSD after the ASTM D2266 tests conducted on (a) pure grease, (b) grease + 0.25 wt.% MoS₂, (c) grease + 0.50 wt.% MoS₂ and (d) 0.75 wt.% MoS₂ at magnifications of 200 \times (left) and 1200 \times (right)

image, 0.75 wt.% MoS₂ produced ragged edges and deeper grooves than the 0.50 wt.% grease. Abrasive wear was also apparent in the selected region. The additive elements on the worn surface were further validated *via* EDX, measured at a magnification of 1200 \times .

Average Roughness of the Wear Region

After the friction and wear test, the average surface roughness (Ra) of the worn steel balls under the grease lubrication was measured *via* 3D profilometry. As can be seen from Figure 8, the average roughness (Ra: 0.7836 \pm 0.0900 μ m) of the pure grease-lubricated surface [Figure 7 (a)] is lower than those of the other greases. The optimum concentration of MoS₂ produced the lowest roughness (Ra: 0.8765 \pm 0.0740 μ m) among all concentrations, followed by 0.75 wt.% (Ra: 0.8814 \pm 0.0431 μ m) and 0.25 wt.% (Ra: 1.1063 \pm 0.0036 μ m). It can be seen that the greases with additives produced higher roughness than the pure grease, which can be attributed to factors such as the shape of the additive particles (Hu, 2005) and the direction of the MoS₂ interlayer sliding (Winer, 1967). The orientation of the MoS₂ needs to be in the direction of the sliding during the experiment for the interlayer bonded by a weak van der Waals force to be smeared and provide effective film protection (Bagi & Aswath, 2015). As mentioned before, the MoS₂ employed in this study has sharp

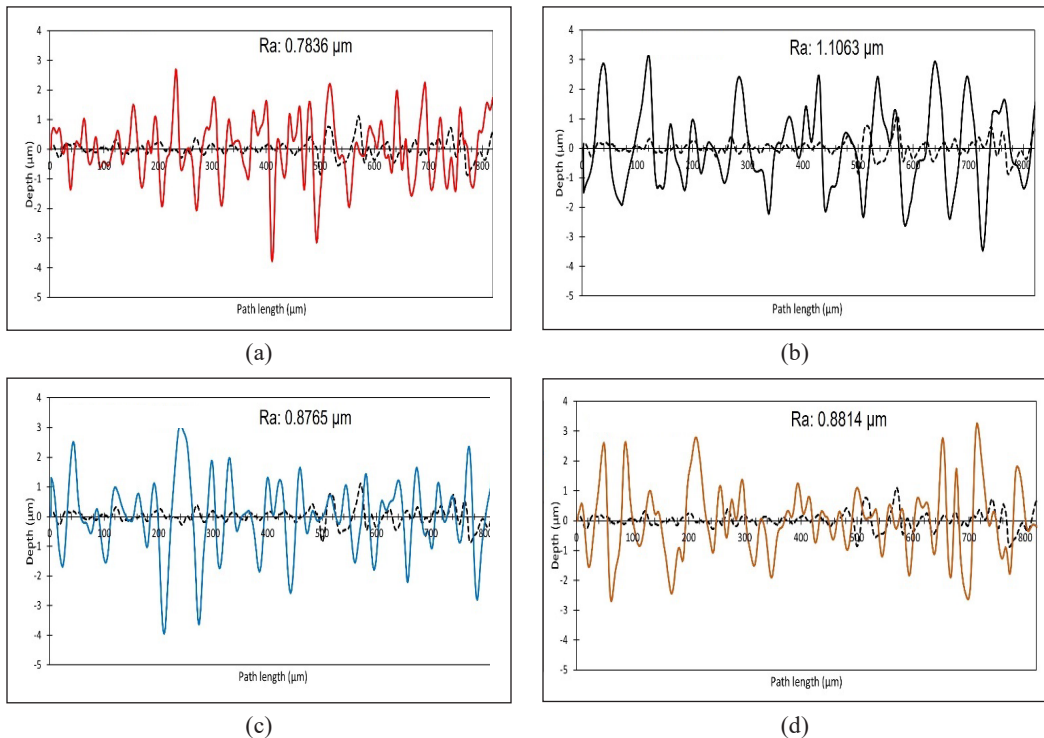


Figure 7. Roughness plot: (a) pure grease; (b) 0.25 wt.% MoS₂; (c) 0.50 wt.% MoS₂; and (d) 0.75 wt.% MoS₂. The dotted line plot on every graph indicates the roughness of the ball prior to the test (Ra: 0.1613 μ m)

edges, which can cause abrasive wear, especially when the MoS_2 is not oriented toward the direction of sliding and particles accumulate during contact (Yu et al., 2019). It is important to note that even though the surface roughness of the grease with MoS_2 additive is slightly higher than that of the pure grease, the surface protection in terms of friction and wear is excellent compared with the pure grease.

Wear Depth Profile and Wear Volume

Further investigation of the wear morphology was performed to quantify the wear depth and volume losses on the steel ball using Alicona IFM—the wear profile of each ball after the experiment is illustrated in Figure 8. The profile shows a significant difference in the scar width between the pure grease and the grease with the MoS_2 additive. With the MoS_2 additive, the scar diameter becomes smaller with apparent roughness. Figure 9 presents the wear surface topography and wear profile, where the dotted line represents the original shape of the steel ball measured before the experiment. The maximum wear depth for pure grease is high, with a measured value of $35.57 \pm 1.12 \mu\text{m}$, as presented in Figure 9(a). The presence of MoS_2 was found to reduce the wear depth, as presented in Figure 9(b & c); the 0.25 and 0.50 wt.% concentrations reduced the wear depth to 17.92 ± 0.48 and $18.15 \pm 0.74 \mu\text{m}$, respectively. Figure 9(d) shows that the wear profile becomes rougher, and the wear depth is slightly higher at $19.05 \pm 0.81 \mu\text{m}$. The finding indicates that the wear depth can be reduced by 48.97% with the optimum additive concentration. The wear depth reduction denotes improved surface protection caused by the deposition of additives on the wear tracks or grooves, which further avoids more severe wear between the contacting surfaces (Qiang et al., 2017).

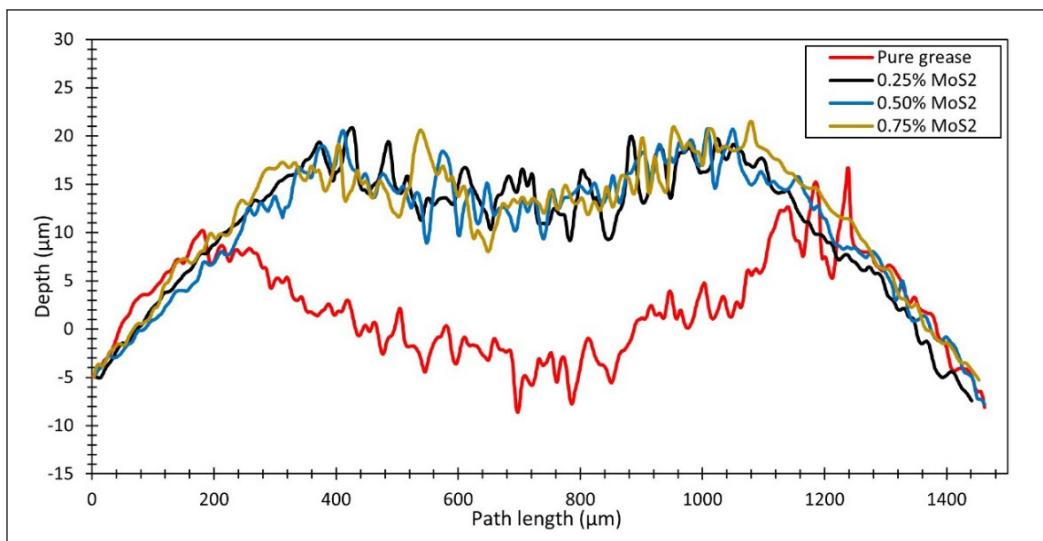


Figure 8. The profile of the worn steel balls lubricated with different greases

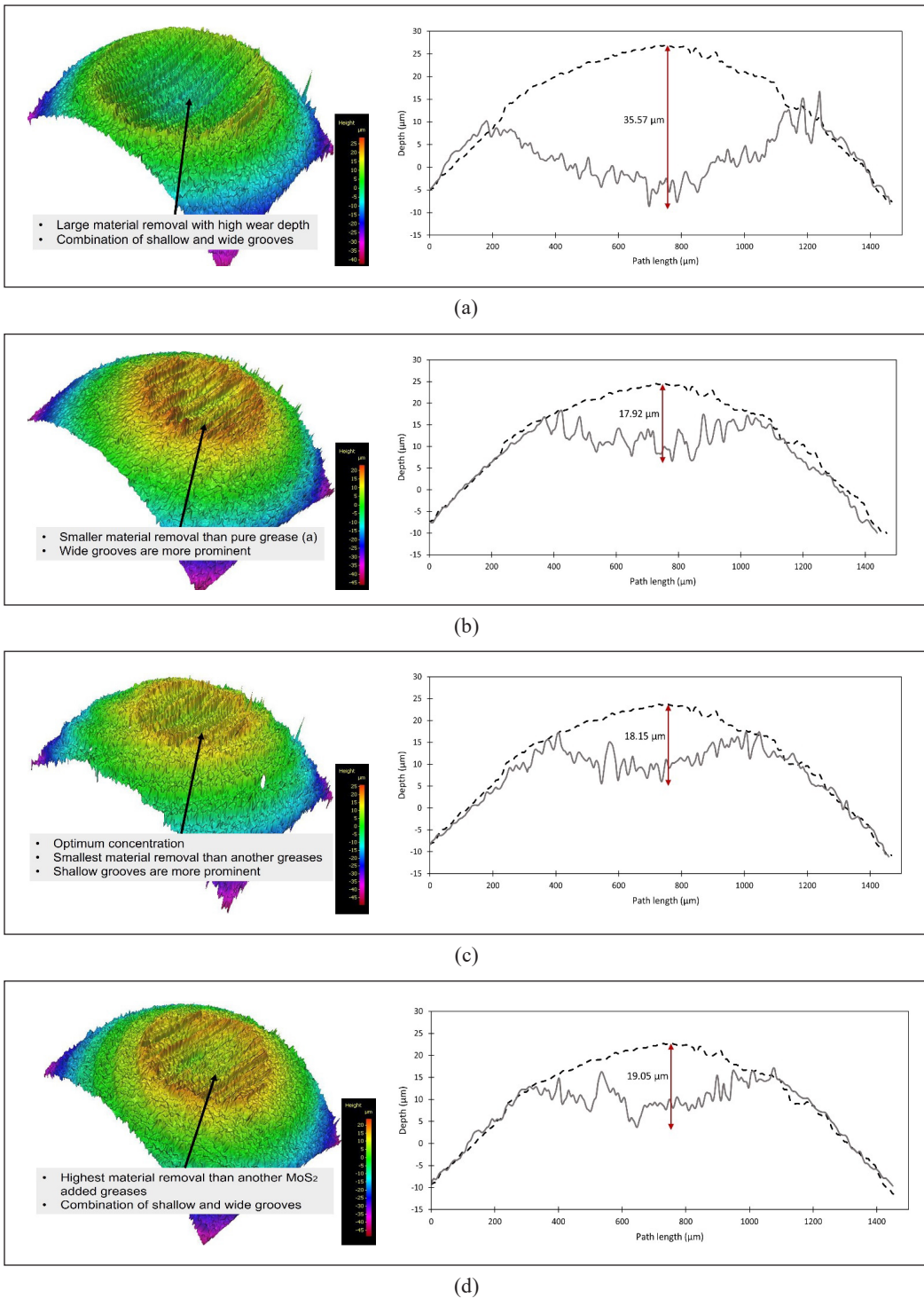


Figure 9. Wear scar morphology and depth of wear of the steel ball lubricated with pure grease (a), grease with 0.25 wt.% MoS_2 (b), grease with 0.50 wt.% MoS_2 (c), and grease with 0.75 wt.% MoS_2 (d)

The wear volume was quantified by measuring the volume of the material removed from the steel ball surface at the wear scar, and the results are presented in Figure 10. Pure grease has a wear volume of around $5.3618 \pm 0.1594 \times 10^6 \mu\text{m}^3$. In contrast, the additive significantly reduced the wear volume, where 0.75 wt.% MoS₂ produced a wear volume of $1.4385 \pm 0.0343 \times 10^6 \mu\text{m}^3$, followed by 0.25 wt.% MoS₂ ($1.2208 \pm 0.1438 \times 10^6 \mu\text{m}^3$), and the lowest, being 0.50 wt.% MoS₂ ($1.1361 \pm 0.0640 \times 10^6 \mu\text{m}^3$). The greases with additives performed better than the pure grease, with 0.50 wt.% MoS₂ provides the best wear protection and has the smallest volume of material removed—the 0.25 wt.% MoS₂ grease had apparent abrasion marks with larger wear diameter and wear volume compared with the optimum MoS₂ grease.

Moreover, despite having an almost similar wear depth, the 0.75 wt.% MoS₂-lubricated surface had a higher wear volume than the 0.50 wt.% MoS₂-lubricated surface. From the peak and valley graph of the worn surfaces, it can be seen that the deepest valley of the 0.75 wt.% MoS₂-lubricated surface had a width of approximately 60 μm , which can be due to particle agglomeration. Another study has reported the same hypothesis, i.e., agglomerate particles cause deeper abrasive wear and enhanced friction and wear than the optimum additive concentration (Chaurasia et al., 2020).

Elemental Analysis of the Worn Surfaces

Elemental composition analysis of the wear scar surface was conducted *via* energy-dispersive X-ray spectroscopy (EDX). The related element details of the selected wear scar regions are presented in Figure 11 and Table 2. The Fe, Cr, and C on the worn surface were identified as the main elements of the test steel ball. The deposition of the additive on the wear scar surface can be observed where a molybdenum (Mo) element was detected on the surfaces lubricated with the greases containing an additive, showing that the additive was transferred and accumulated on the surface. Furthermore, Mo existed due to the interlayer shearing of MoS₂ and the mending effect where Mo filled the valleys of the wear scratches (Srinivas et al., 2017; Waqas et al., 2021). The 0.75 wt.% MoS₂ grease had a higher deposition than the 0.50 wt.% MoS₂ grease, indicating that a higher additive concentration induced more deposition on the worn surface. The deposition percentage was similar to

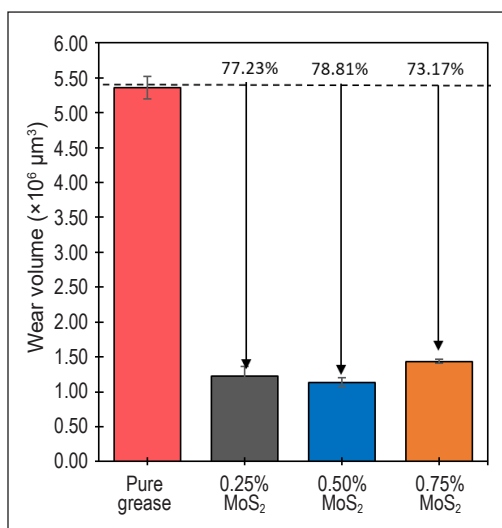
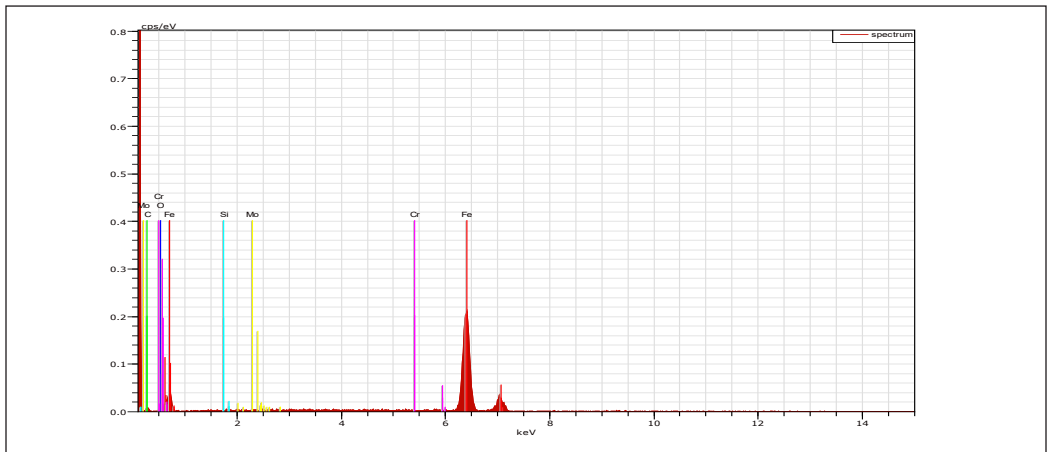
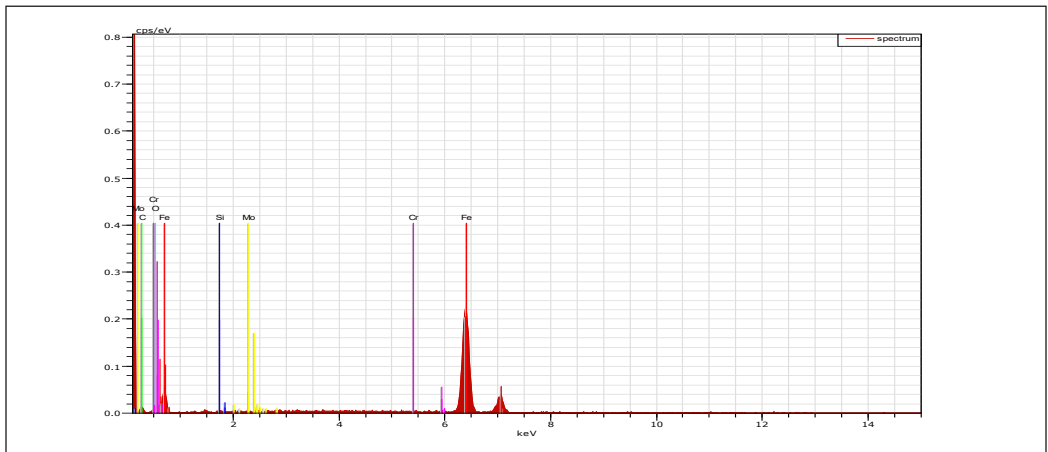


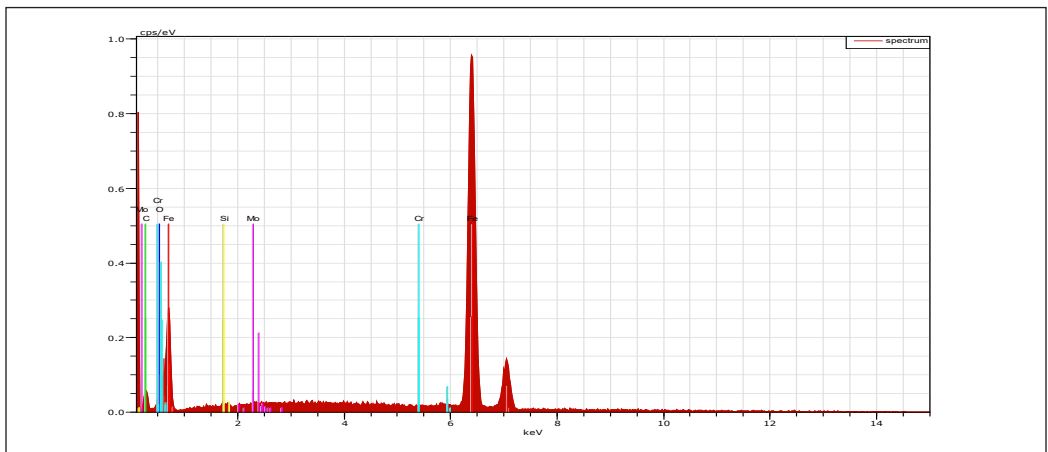
Figure 10. Volume loss of the steel balls lubricated with different greases



(a)



(b)



(c)

Figure 11. EDX spectra of (a) 0.25 wt.%, (b) 0.50 wt.% and (c) 0.75 wt.% MoS₂

that reported in (Wu et al., 2018), where an increase in the MoS₂ concentration increased the detected element percentage on the surface. However, the 0.25 wt.% MoS₂ yielded a slightly higher Mo percentage than the 0.50 wt.% MoS₂. It might be due to more grooves forming on the 0.25 wt.%, providing more space for the MoS₂ particles to be deposited (Du et al., 2018).

Table 2
Elemental composition on the worn surfaces

Element	Elemental percentage (wt.%)			
	Pure Grease	0.25 wt.% MoS ₂	0.50 wt.% MoS ₂	0.75 wt.% MoS ₂
C K	16.35	15.33	16.55	22.19
O K	0.24	0.69	1.34	1.28
Cr K	0.39	0.55	0.36	0.34
Fe K	83.02	82.59	80.10	75.23
Mo L	0	0.83	0.74	0.96

CONCLUSION

In this study, palm greases have been produced using lithium stearate as a thickener and micro-MoS₂ as an additive. Several tests have been conducted to evaluate grease performance, including the tribological test, surface morphology, and wear analysis. From the findings, the following conclusions can be drawn:

- The palm olein grease has a good friction performance and could be enhanced by the presence of a MoS₂ additive.
- The MoS₂ additive forms a protective layer on the contacting surfaces. The deposition of the additive on the wear scar surface was proven by the detection of the Mo element on the surfaces lubricated with the additive-added greases. This layer efficiently protects the contacting surfaces by reducing friction and wear.
- The value of 0.5 wt.% is the optimum MoS₂ concentration, reflecting the best performance of the grease. The lowest friction and wear scar diameters indicate, 0.0411 and 0.612 mm, respectively. Surface morphology analysis also revealed that shallower grooves were formed.
- The ability of the 0.5 wt.% MoS₂ to protect the surfaces is indicated by the smallest volume of material removed from the surface with a wear volume of $1.1361 \times 10^6 \mu\text{m}^3$ and 18.15 μm depth of wear scar.
- The average surface roughness of MoS₂-lubricated surfaces was slightly higher than that of pure palm grease. However, among the MoS₂ concentrations, the 0.50 wt.% produced the smoothest surface.
- The micro-MoS₂ additive has great potential for use as an additive in palm olein-based grease with superior friction and wear performance. The findings also

indicate a good synergistic effect between the palm olein grease and the MoS₂ additive, where the combination of both produced better surface protection than palm olein grease alone.

ACKNOWLEDGEMENTS

The authors express their appreciation to the government of Malaysia under the Ministry of Higher Education for providing research funding through the Fundamental Research Grant Scheme [FRGS/1/2019/TK03/USM/03/4].

REFERENCES

- Abdollah, M. F., Amiruddin, H., & Jamallulil, A. D. (2020). Experimental analysis of tribological performance of palm oil blended with hexagonal boron nitride nanoparticles as an environment-friendly lubricant. *The International Journal of Advanced Manufacturing Technology*, 106, 4183-4191. <https://doi.org/10.1007/s00170-019-04906-5>
- Abdulbari, H. A., & Zuhan, N. (2018). Grease formulation from palm oil industry wastes. *Waste and Biomass Valorization*, 9(12), 2447-2457. <https://doi.org/10.1007/s12649-018-0237-6>
- American Society for Testing and Materials. (2017). *Standard test methods for cone penetration of lubricating grease (ASTM D217-02)*. ASTM International.
- American Society for Testing and Materials. (2010). *Standard test method for dropping point of lubricating grease (ASTM D556-02)*. ASTM International.
- American Society for Testing and Materials. (2010). *Standard test method for wear preventive characteristics of lubricating grease (Four-ball method) (ASTM D 2266 – 01)*. ASTM International
- Bagi, S. D., & Aswath, P. B. (2015). Mechanism of friction and wear in MoS₂ and ZDDP/F-PTFE greases under spectrum loading conditions. *Lubricants*, 3(4), 687-711. <https://doi.org/10.3390/lubricants3040687>
- Blau, P. (2005). On the nature of running-in. *Tribology International*, 38(11-12), 1007-1012. <https://doi.org/10.1016/j.triboint.2005.07.020>
- Borda, F. L. G., Oliveira, S. J. R., Lazaro, L. M. S. M., & Leiroz, A. J. K. (2018). Experimental investigation of the tribological behavior of lubricants with additive containing copper nanoparticles. *Tribology International*, 117, 52-58. <https://doi.org/10.1016/j.triboint.2017.08.012>
- Chaurasia, S. K., Singh, N. K., & Singh, L. K. (2020). Friction and wear behavior of chemically modified Sal (*Shorea Robusta*) oil for bio based lubricant application with effect of CuO nanoparticles. *Fuel*, 282, Article 118762. <https://doi.org/10.1016/j.fuel.2020.118762>
- Du, S., Sun, J., & Wu, P. (2018). Preparation, characterization and lubrication performances of graphene oxide-TiO₂ nanofluid in rolling strips. *Carbon*, 140, 338-351. <https://doi.org/10.1016/j.carbon.2018.08.055>
- Fan, X., Li, W., Li, H., Zhu, M., Xia, Y., & Wang, J. (2018). Probing the effect of thickener on tribological properties of lubricating greases. *Tribology International*, 118, 128-139. <https://doi.org/10.1016/j.triboint.2017.09.025>

- Fox, N. J., & Stachowiak, G. W. (2007). Vegetable oil-based lubricants - A review of oxidation. *Tribology International*, 40(7), 1035-1046. <https://doi.org/10.1016/j.triboint.2006.10.001>
- Gong, L., Qian, S., Wang, W., Ni, Z., & Tang, L. (2021). Influence of nano-additives (nano-PTFE and nano-CaCO₃) on tribological properties of food-grade aluminum-based grease. *Tribology International*, 160, Article 107014. <https://doi.org/10.1016/j.triboint.2021.107014>
- Gulzar, M., Mahmood, K., Zahid, R., Alabdulkarem, A., Masjuki, H. H., Kalam, M. A., Varman, M., Zulkifli, N. W. M., Ahmad, P., & Malik, M. S. S. (2017). The effect of particle size on the dispersion and wear protection ability of MoS₂ particles in polyalphaolefin and trimethylolpropane ester. *Proceedings of the Institution of Mechanical Engineers, Part J: Journal of Engineering Tribology*, 232(8), 987-998. <https://doi.org/10.1177/1350650117749404>
- Gulzar, M., Masjuki, H. H., Varman, M., Kalam, M. A., Mufti, R., Mohd Zulkifli, N. W., Yunus, R., & Zahid, R. (2015). Improving the AW/EP ability of chemically modified palm oil by adding CuO and MoS₂ nanoparticles. *Tribology International*, 88, 271-279. <https://doi.org/10.1016/j.triboint.2015.03.035>
- He, Q., Li, A., Guo, Y., Liu, S., Zhang, Y., & Kong, L. (2018). Tribological properties of nanometer cerium oxide as additives in lithium grease. *Journal of Rare Earths*, 36(2), 209-214. <https://doi.org/10.1016/j.jre.2017.09.004>
- Heikal, E. K., Elmelawy, M. S., Khalil, S. A., & Elbasuny, N. M. (2017). Manufacturing of environment friendly biolubricants from vegetable oils. *Egyptian Journal of Petroleum*, 26(1), 53-59. <https://doi.org/10.1016/j.ejpe.2016.03.003>
- Holinski, R., & Gänsheimer, J. (1972). A study of the lubricating mechanism of molybdenum disulfide. *Wear*, 19(3), 329-342. [https://doi.org/10.1016/0043-1648\(72\)90124-X](https://doi.org/10.1016/0043-1648(72)90124-X)
- Hou, X., Jiang, H., Ali, M. K. A., Liu, H., Su, D., & Tian, Z. (2020). Dispersion behavior assessment of the molybdenum disulfide nanomaterials dispersed into poly alpha olefin. *Journal of Molecular Liquids*, 311, Article 113303. <https://doi.org/10.1016/j.molliq.2020.113303>
- Hu, E. Z., Xu, Y., Hu, K. H., & Hu, X. G. (2017). Tribological properties of 3 types of MoS₂ additives in different base greases. *Lubrication Science*, 29(8), 541-555. <https://doi.org/10.1002/ls.1387>
- Hu, X. (2005). On the size effect of molybdenum disulfide particles on tribological performance. *Industrial Lubrication and Tribology*, 57(6), 255-259. <https://doi.org/10.1108/00368790510622353>
- Jabal, M. H., Ani, F. N., & Syahrullail, S. (2014). The tribological characteristic of the blends of RBD palm olein with mineral oil using four-ball tribotester. *Jurnal Teknologi*, 69(6), 11-14. <https://doi.org/10.11113/jt.v69.3232>
- Koshy, C. P., Rajendrakumar, P. K., & Thottackkad, M. V. (2015). Evaluation of the tribological and thermo-physical properties of coconut oil added with MoS₂ nanoparticles at elevated temperatures. *Wear*, 330-331, 288-308. <https://doi.org/10.1016/j.wear.2014.12.044>
- Kozdrach, R., & Skowroński, J. (2018). The application of polyvinylpyrrolidone as a modifier of tribological properties of lubricating greases based on linseed oil. *Journal of Tribology*, 140(6), Article 061801. <https://doi.org/10.1115/1.4040054>

- Kumar, N., Saini, V., & Bijwe, J. (2020). Performance properties of lithium greases with PTFE particles as additive: Controlling parameter-size or shape? *Tribology International*, *148*, Article 106302. <https://doi.org/10.1016/j.triboint.2020.106302>
- Mannekote, J. K., & Kailas, S. V. (2012). The effect of oxidation on the tribological performance of few vegetable oils. *Journal of Materials Research and Technology*, *1*(2), 91-95. [https://doi.org/10.1016/S2238-7854\(12\)70017-0](https://doi.org/10.1016/S2238-7854(12)70017-0)
- Mushtaq, Z., & Hanief, M. (2021). Evaluation of tribological performance of jatropha oil modified with molybdenum disulphide micro-particles for steel-steel contacts. *Journal of Tribology*, *143*(2), Article 021401. <https://doi.org/10.1115/1.4047752>
- Nabhan, A., Rashed, A., Ghazaly, N. M., Abdo, J., & Haneef, M. D. (2021). Tribological properties of Al₂O₃ nanoparticles as lithium grease additives. *Lubricants*, *9*(1), Article 9. <https://doi.org/10.3390/lubricants9010009>
- Nagendramma, P., & Kumar, P. (2015). Eco-friendly multipurpose lubricating greases from vegetable residual oils. *Lubricants*, *3*(4), 628-636. <https://doi.org/10.3390/lubricants3040628>
- Nowak, P., Kucharska, K., & Kamiński, M. (2019). Ecological and health effects of lubricant oils emitted into the environment. *International Journal of Environmental Research and Public Health*, *16*(16), Article 3002. <https://doi.org/10.3390/ijerph16163002>
- Pande, G., Akoh, C. C., & Lai, O. M. (2012). 19 - Food uses of palm oil and its components. In O. M. Lai, C. P. Tan & C. C. Akoh (Eds.), *Palm Oil* (pp. 561-586). AOCS Press. <https://doi.org/10.1016/B978-0-9818936-9-3.50022-8>
- Qiang, H., Anling, L., Yangming, Z., Liu, S., & Yachen, G. (2017). Experimental study of tribological properties of lithium-based grease with Cu nanoparticle additive. *Tribology-Materials, Surfaces & Interfaces*, *11*(2), 75-82. <https://doi.org/10.1080/17515831.2017.1311560>
- Quinchia, L. A., Delgado, M. A., Reddyhoff, T., Gallegos, C., & Spikes, H. A. (2014). Tribological studies of potential vegetable oil-based lubricants containing environmentally friendly viscosity modifiers. *Tribology International*, *69*, 110-117. <https://doi.org/10.1016/j.triboint.2013.08.016>
- Razak, I. H. A., & Ahmad, M. A. (2021). Tribological behavior of calcium complex palm-biogrease with green additives. *Tribology in Industry*, *43*(1), 139-149. <https://doi.org/10.24874/ti.1002.11.20.02>
- Reeves, C. J., Menezes, P. L., Jen, T. C., & Lovell, M. R. (2015). The influence of fatty acids on tribological and thermal properties of natural oils as sustainable biolubricants. *Tribology International*, *90*, 123-134. <https://doi.org/10.1016/j.triboint.2015.04.021>
- Srinivas, V., Thakur, R. N., Jain, A. K., & Babu, M. S. (2017). Tribological studies of transmission oil dispersed with molybdenum disulfide and tungsten disulfide nanoparticles. *Journal of Tribology*, *139*(4), Article 041301. <https://doi.org/10.1115/1.4034766>
- Sukirno, Fajar, R., Bismo, S., & Nasikin, M. (2009). Biogrease based on palm oil and lithium soap thickener: Evaluation of antiwear property. *World Applied Sciences Journal*, *6*(30), 401-407.
- Sukirno, Ludi, Fajar, R., Bismo, & Nasikin. (2010). Anti-wear properties of bio-grease from modified palm oil and calcium soap thickener. *Agricultural Engineering International: The CIGR Journal*, *12*(2), 64-69.

- Tabee, E., Azadmard-Damirchi, S., Jägerstad, M., & Dutta, P. C. (2008). Effects of α -tocopherol on oxidative stability and phytosterol oxidation during heating in some regular and high-oleic vegetable oils. *Journal of the American Oil Chemists' Society*, 85(9), 857-867. <https://doi.org/10.1007/s11746-008-1274-2>
- Wang, W., Zhao, W., Ma, Q., Kouediatouka, A. N., Zhang, H., Dong, G., Hua, M., & Tam, H. Y. (2022). Synergistic lubrication for textured surfaces using polar and nonpolar lubricants. *Journal of Tribology*, 145(1), Article 012201. <https://doi.org/10.1115/1.4055715>
- Waqas, M., Zahid, R., Bhutta, M. U., Khan, Z. A., & Saeed, A. (2021). A review of friction performance of lubricants with nano additives. *Materials*, 14(21), Article 6310. <https://doi.org/10.3390/ma14216310>
- Winer, W. O. (1967). Molybdenum disulfide as a lubricant: A review of the fundamental knowledge. *Wear*, 10(6), 422-452. [https://doi.org/10.1016/0043-1648\(67\)90187-1](https://doi.org/10.1016/0043-1648(67)90187-1)
- Wu, H., Wang, L., Johnson, B., Yang, S., Zhang, J., & Dong, G. (2018). Investigation on the lubrication advantages of MoS₂ nanosheets compared with ZDDP using block-on-ring tests. *Wear*, 394-395, 40-49. <https://doi.org/10.1016/j.wear.2017.10.003>
- Xu, Z. Y., Hu, K. H., Han, C. L., Hu, X. G., & Xu, Y. F. (2013). Morphological influence of molybdenum disulfide on the tribological properties of rapeseed oil. *Tribology Letters*, 49(3), 513-524. <https://doi.org/10.1007/s11249-012-0092-8>
- Yahaya, W. M. A. W., Dandan, M. A., Samion, S., & Musa, M. N. (2018). A comprehensive review on palm oil and the challenges using vegetable oil as lubricant base-stock. *Journal of Advanced Research in Fluid Mechanics and Thermal Sciences*, 52(2), 182-197.
- Yu, R., Liu, J., & Zhou, Y. (2019). Experimental study on tribological property of MoS₂ nanoparticle in castor oil. *Journal of Tribology*, 141(10), Article 102001. <https://doi.org/10.1115/1.4044294>
- Zulhanafi, P., & Syahrullail, S. (2019). The tribological performances of super olein as fluid lubricant using four-ball tribotester. *Tribology International*, 130, 85-93. <https://doi.org/10.1016/j.triboint.2018.09.013>

Review Article

Supercritical Carbon Dioxide Extraction of Citronella Oil Review: Process Optimization, Product Quality, and Applications

Nicky Rahmana Putra^{1,2}, Ahmad Hazim Abdul Aziz^{3*}, Dwila Nur Rizkiyah², Mohd Azizi Che Yunus², Ratna Surya Alwi³, Reny Tri Anggraini¹, Siti Khodijah¹, Irianto Irianto⁴ and Lailatul Qomariyah⁵

¹National Research and Innovation Agency, Bogor, West Java 16911, Indonesia

²Centre of Lipid Engineering and Applied Research (CLEAR), Ibnu Sina Institute for Scientific and Industrial Research, Universiti Teknologi Malaysia, 81310 Skudai, Johor Bahru, Malaysia

³Faculty of Food Science and Nutrition, Universiti Malaysia Sabah, Kota Kinabalu 88400, Malaysia

⁴Department General Education, Faculty of Resilience, Rabdan Academy, Abu Dhabi, United Arab Emirates

⁵Department of Industrial Chemical Engineering, Institut Teknologi Sepuluh Nopember, 60111 Surabaya, Surabaya, Indonesia

ABSTRACT

This review paper explores the utilization of supercritical carbon dioxide (SC-CO₂) extraction to isolate citronella oil, delving into its multifaceted dimensions, including process optimization, product quality enhancement, and diverse potential applications. Citronella oil, renowned for its myriad bioactive compounds with demonstrated health benefits, is a coveted essential oil in the pharmaceutical, cosmetics, and food industries. The transition from traditional extraction techniques to SC-CO₂ extraction presents a paradigm shift due to its manifold advantages, such as heightened yield rates, expedited extraction

durations, and elevated product quality. However, the efficacy of SC-CO₂ extraction is intricately interwoven with an array of parameters encompassing pressure, temperature, flow rate, particle size, and co-solvent ratios. Accordingly, meticulous process optimization is indispensable in achieving the desired product quality while maximizing yield. Furthermore, the paper explores the extensive spectrum of potential applications for citronella oil, extending its reach into formulations with antimicrobial,

ARTICLE INFO

Article history:

Received: 19 May 2023

Accepted: 26 October 2023

Published: 01 April 2024

DOI: <https://doi.org/10.47836/pjst.32.3.04>

E-mail addresses:

nickyrahman1309@gmail.com (Nicky Rahmana Putra)

hazim.aziz@ums.edu.my (Ahmad Hazim Abdul Aziz)

dwila101@gmail.com (Dwila Nur Rizkiyah)

azizi@cheme.utm.my (Mohd Azizi Che Yunus)

ratn017@brin.go.id (Ratna Surya Alwi)

reny007@brin.go.id (Reny Tri Anggraini)

siti108@brin.go.id (Siti Khodijah)

iharny@ra.ac.ae (Irianto Irianto)

laila.qomariyah@its.ac.id (Lailatul Qomariyah)

* Corresponding author

insecticidal, and antioxidant properties. These applications underscore the versatility and commercial appeal of citronella oil. The review establishes SC-CO₂ extraction of citronella oil as a promising and sustainable alternative to conventional extraction methodologies, offering myriad applications across the pharmaceutical, cosmetics, and food sectors. This scholarly work provides valuable insights into the intricacies of process optimization and product quality. It outlines future perspectives and avenues for further exploration in SC-CO₂ extraction of citronella oil.

Keywords: Citronella, optimization, product quality, supercritical carbon dioxide

INTRODUCTION

The essential oil is extracted from the leaves and stems of certain species of citronella grass, including *Cymbopogon nardus* and *Cymbopogon winterianus*. The oil is frequently used to produce personal care products, fragrances, and insecticides due to its citrus-like aroma and insect-repelling properties (Wany et al., 2013). Citronella oil has a long history of use in traditional medicine and aromatherapy. Its popularity has increased in recent years as consumer interest in natural and organic products has increased (Carvalho et al., 2016). Traditional cultures have used citronella oil as an insect repellent for centuries, particularly against mosquitoes and other stinging insects (Tyagi, 2016). Geraniol, citronellol, and citronellal, all monoterpenes, are the active compounds in citronella oil responsible for their insect-repelling properties (Pohlit et al., 2011; Sarah et al., 2023). These compounds interfere with the insect's ability to locate its host, making it harder for insects to locate and bite humans and animals. Citronella oil is considered a safe and effective alternative to chemical insecticides, which can negatively impact the environment and human health.

Citronella oil is well-known for its aromatherapy benefits and insect-repelling properties. It is frequently used in fragrances, balms, and candles due to its fresh, invigorating aroma (Bell, 2012). Also believed to have a soothing effect on the mind and body, citronella oil is frequently employed in aromatherapy to promote relaxation and reduce tension. The oil is an alternative therapy for several illnesses, including migraines, muscle pains, and respiratory infections (Ali et al., 2015). Due to its popularity and versatility, citronella oil is now widely produced and used worldwide.

Steam distillation, solvent extraction, and cold pressing are the traditional techniques for extracting citronella oil (Hanif et al., 2019; Khan & Dwivedi, 2018). However, in recent years, supercritical fluid extraction has been a promising alternative method for extracting high-quality citronella oil (Sarah et al., 2023). Extraction of supercritical carbon dioxide requires its supercritical state, which possesses the properties of both a liquid and a gas. This technique is considered more efficient and environmentally favorable than traditional

methods because it does not require toxic solvents or high temperatures, which can degrade the extracted oil's quality (Aziz et al., 2022; Arsad et al., 2023; Rizkiyah et al., 2023).

This review paper presents several notable novelties compared to previously published papers. Firstly, it focuses on applying SC-CO₂ extraction to obtain citronella oil, highlighting its distinct advantages over conventional extraction methods. Notably, it delves into the crucial aspect of process optimization, recognizing that parameters such as pressure, temperature, flow rate, particle size, and co-solvent ratio influence the extraction process, offering potential insights into optimizing this technique.

Furthermore, the paper emphasizes product quality enhancement as a significant outcome of SC-CO₂ extraction. It is particularly pertinent for industries like pharmaceuticals, cosmetics, and food, where high-quality citronella oil is in demand. The review also explores the extensive range of potential applications for citronella oil, including its use in antimicrobial, insecticidal, and antioxidant formulations, underscoring its versatility and commercial value.

In addition to its benefits, the paper acknowledges the challenges associated with SC-CO₂ extraction, such as the high equipment and operational costs, as well as the need for standardization in the extraction methods. This comprehensive discussion of advantages, optimization strategies, product quality improvements, challenges, and future prospects ensures that this work offers valuable insights into the SC-CO₂ extraction of citronella oil, making it a significant contribution to the existing body of knowledge in this field.

CITRONELLA OIL AND ITS BIOACTIVITIES

Essential and regular oils, often referred to as carrier or vegetable oils, exhibit distinct differences in origin, composition, uses, aroma, and volatility. Essential oils are derived from aromatic parts of plants and contain concentrated volatile compounds like terpenes and phenols, giving them unique scents and therapeutic properties (Bakkali et al., 2008). They are commonly used for aromatherapy, perfumery, and flavoring, and they are diluted for topical applications due to their potency (Aziz et al., 2018). In contrast, regular oils, obtained from various sources such as seeds and nuts, consist primarily of fatty acids and lack the volatile aromatic compounds in essential oils. They possess mild, neutral scents, making them ideal base oils to dilute essential oils for skin application and culinary and industrial purposes. Essential oils are highly volatile and evaporate quickly, which enhances their aromatic qualities. In contrast, carrier oils are non-volatile and provide a stable medium for dilution and application of essential oils or other practical uses.

Citronella oil is primarily produced in tropical regions, particularly Indonesia, Sri Lanka, India, and China. The oil is extracted from the leaves and stems of citronella grass, a tall perennial grass with long, thin leaves and a characteristic lemon-like scent. The traditional method of extracting citronella oil is through steam distillation (Hamzah et al.,

2014). The plant material is placed in a distillation chamber and heated with steam. The steam causes the essential oil to evaporate and then condense into a liquid collected in a separate container. The resulting oil is filtered to remove impurities (Cassel et al., 2006).

Another method of extracting citronella oil is solvent extraction (Lim et al., 2021). This method involves using a solvent, such as hexane, to extract the oil from the plant material. The solvent is then removed from the oil using a distillation process, leaving behind pure citronella oil. Supercritical carbon dioxide extraction is a newer method of extracting citronella oil (Guedes et al., 2018). The carbon dioxide is used to extract the oil from the plant material, which is then separated from the carbon dioxide. Supercritical carbon dioxide extraction is considered more environmentally friendly than traditional extraction methods, as it does not require toxic solvents or high temperatures (Mohd-Nasir et al., 2021). The active compounds of citronella are shown in Table 1, and an explanation of its compounds is shown below. Citronella oil contains various compounds, including citronellal, geraniol, citronellol, limonene, and camphene. These compounds give citronella oil its characteristic aroma, insect-repelling properties, and other potential health benefits.

- Citronellal: Citronellal is the primary component of citronella oil, accounting for approximately 35%–45% of the oil’s total composition (Li et al., 2021). It has a strong lemon-like scent and is often used in fragrances and personal care products. Citronellal has also been found to have antimicrobial properties, making it helpful in treating various infections (Timung et al., 2016).
- Geraniol: Geraniol is another significant component of citronella oil, accounting for approximately 10%–20% of the oil’s total composition (El-Kholany, 2016). It has a floral, rose-like scent and is used in producing perfumes, soaps, and lotions. Geraniol has antioxidant and anti-inflammatory properties, potentially helpful in treating various inflammatory conditions (Ammar, 2023).
- Citronellol: Citronellol is present in citronella oil in smaller amounts, accounting for approximately 5%–15% of the oil’s total composition (Sreenath & Jagadishchandra, 2012). It has a rose-like scent and is used to produce perfumes and personal care products. Citronellol has also been found to have antimicrobial and anti-inflammatory properties (Chen & Viljoen, 2010).
- Limonene: Limonene is a minor component of citronella oil, accounting for approximately 2%–4% of the oil’s total composition

Table 1
Identification of interest compounds of citronella in the chromatogram oil by Silva et al. (2011)

Identification	Components	P(%)
1	Citronellal	98
2	Citronellol	95
3	Geraniol	86
4	β -Element	95
5	Germacrene-D	99
6	Endemol	83
7	Germacredien-5-ol	91

(Wijesekera et al., 1973). It has a citrus-like scent and is used in producing fragrances and cleaning products. Limonene has been found to have antioxidant and anti-inflammatory properties, as well as potential anti-cancer effects (Anandakumar et al., 2021).

- Camphene: Camphene is another minor component of citronella oil, accounting for less than 1% of the oil's total composition (Devi et al., 2021). It has a fresh, woody scent and is used in producing fragrances and flavorings. Camphene has been found to have anti-inflammatory properties and potential anti-cancer effects (Alesaeidi & Miraj, 2016).

SUPERCRITICAL CARBON DIOXIDE (SC-CO₂) OF CITRONELLA OIL

SC-CO₂ extraction is a technique for extracting essential oils from plant material. Carbon dioxide is a non-toxic, non-combustible, readily accessible solvent that can extract essential oils without leaving noxious residues or byproducts (Arumugham et al., 2021). When carbon dioxide is heated and pressurized beyond its critical point (73.8 bar and 31.1°C), it transforms into a supercritical fluid with a liquid's density and a gas's diffusion properties (Putra, Rizkiyah, Aziz, et al., 2023). In the case of citronella oil, SC-CO₂ extraction has proven to be an effective and eco-friendly technique for extracting essential oil from citronella grass (Sarah et al., 2023). The plant material is placed in a sealed extraction vessel and then exposed to carbon dioxide at a specific temperature and pressure. The supercritical carbon dioxide can permeate the plant material's cell walls, dissolving the essential oil and transporting it out of the extraction vessel (Sodeifian, Ardestani, et al., 2016; Sodeifian, Sajadian, & Ardestani, 2016).

SC-CO₂ extraction can selectively extract compounds from plant material, one of its benefits (Odunlami et al., 2022; Sodeifian et al., 2017). The solubility of various compounds in SC-CO₂ varies based on their chemical properties (Idham et al., 2021; Sodeifian, Ardestani, et al., 2018). For instance, compounds with high molecular weights and boiling points tend to be more soluble in SC-CO₂ than those with low molecular weights and boiling points (Aziz et al., 2022; Idham et al., 2021). In the case of citronella oil, SC-CO₂ extraction has proven effective at removing the oil's primary components, including citronellal, geraniol, and citronellol. It has also been discovered that the process produces a higher yield of essential oil than traditional steam distillation methods (Chai et al., 2020). In addition to its efficiency and selectivity, SC-CO₂ extraction of citronella oil has yielded a high-quality product with minimal chemical degradation (Odunlami et al., 2022). It is because neither high temperatures nor exposure to oxygen, which can cause chemical changes in the essential oil, are involved in the extraction process (de Melo et al., 2020). Overall, SC-CO₂ extraction is a prospective method for extracting citronella oil, as it provides a safe and environmentally friendly alternative to conventional

extraction techniques. This method is advantageous for producing citronella oil for various applications, including fragrances, personal care products, and insect repellents, due to the possibility of selective extraction and the production of high-quality essential oils. The parameters' influence on SC-CO₂ for citronella oil is shown in Table 2.

Effect of Pressure

The pressure in SC-CO₂ extraction can positively and negatively affect oil recovery, including citronella oil. Increasing the pressure in SC-CO₂ extraction can increase the oil yield by increasing the solubility of the oil components in the supercritical fluid. SC-CO₂ behaves like a gas at low pressure and a liquid at high pressure, which makes it an excellent solvent for extracting various organic compounds, including essential oils (Silva et al., 2021). When the pressure increases, the supercritical fluid's density and solubility increase. This increase in density and solubility allows the SC-CO₂ to penetrate deeper into the plant material and dissolve more oil components (de Oliveira et al., 2019; Sodeifian et al., 2022). The pressure also influences the polarity of the SC-CO₂, which can affect its ability to dissolve different compounds (Ahmad et al., 2019).

In the case of citronella oil extraction, citronellal and geraniol are the major components of the oil, which are responsible for its aroma and insect-repellent properties. These components have relatively high solubility in SC-CO₂, and increasing the pressure can enhance their solubility and, hence, the oil yield (Manaf et al., 2013; Sodeifian, Sajadian, et al., 2018). The pressure can also affect the phase behavior of the supercritical fluid and the oil, leading to changes in the partitioning of the oil components between the plant material and the supercritical fluid (Machado et al., 2022). It can result in more efficient extraction of the oil components, leading to higher oil yield.

Reducing the pressure during SC-CO₂ extraction can reduce oil recovery for various reasons. Initially, as the pressure decreases, the density and solubility of the supercritical fluid decrease (Sathasivam et al., 2022). Consequently, SC-CO₂'s ability to dissolve oil components decreases, resulting in a lower oil yield (Ongkasin et al., 2019; Sodeifian, Ardestani, et al., 2016). It occurs because the solubility of a compound in a supercritical fluid depends on the fluid's density, and a decrease in pressure causes a decrease in density, thereby decreasing solubility (Putra et al., 2022). Second, lowering the pressure can cause the supercritical fluid to expand, decreasing its concentration and density (Aziz et al., 2021, 2023; Putra, Rizkiyah, Aziz, Mamat et al., 2023; Putra, Rizkiyah, Aziz, Yunus et al., 2023; Wang et al., 2023). It can result in the formation of gas bubbles, which can inhibit the penetration of the supercritical fluid into the plant material and shorten the contact period between the supercritical fluid and the oil components. It reduces oil recovery. A decrease in pressure can also reduce the mass transfer coefficient, which is the rate at which the solute (oil components) diffuses from the solid matrix (plant material) into the

supercritical fluid (Soh et al., 2019). The mass transfer coefficient is affected by the density and diffusivity of the supercritical fluid, and a decrease in pressure causes both of these variables to decrease. It may result in a slower extraction rate and a reduced oil yield (Kim & Lim, 2020; Putra, Aziz, et al., 2018).

Effect of Temperature

In SC-CO₂ extraction, increasing the temperature can increase the oil yield by reducing the oil's viscosity and increasing the diffusion rate of the supercritical fluid in the plant material (Leila et al., 2022). However, increasing the temperature beyond a certain point can reduce the oil yield due to various factors. In SC-CO₂ extraction, when the temperature increases, the oil's viscosity decreases, making it more straightforward for the supercritical fluid to permeate the plant material and dissolve the oil components. Therefore, it will increase the oil yield. Increasing the temperature can also increase the diffusion rate of the supercritical fluid in the plant material, facilitating the mass transfer of the oil components from the plant material to the supercritical fluid, resulting in a greater oil yield (Moges et al., 2022; Putra, Aziz, et al., 2018).

However, if the temperature increases beyond the optimal range, the oil yield may decrease due to several factors. First, high temperatures can lead to the thermal degradation of oil components, resulting in the formation of undesirable byproducts and the loss of desirable oil components (Aprodu et al., 2020). High temperatures can also increase the volatility of oil components, resulting in their loss during extraction (Muhammad et al., 2022). In addition, elevated temperatures can reduce the solubility of oil components in SC-CO₂, decreasing the extraction efficiency and, consequently, the oil yield (Sodeifian et al., 2022).

Depending on various factors such as the pressure, solvent-to-feed ratio, and the properties of the plant material being extracted, a decrease in temperature during SC-CO₂ extraction can either decrease or increase the oil yield. The oil's viscosity increases at low temperatures, making it more difficult for the supercritical fluid to penetrate plant material and dissolve oil components (Dhara et al., 2022). Therefore, it can reduce oil recovery by SC-CO₂. In addition, decreasing the temperature can reduce the diffusion rate of the supercritical fluid in the plant material, which delays the mass transfer of oil components from the plant material to the supercritical fluid, resulting in a decreased oil yield (Dhara et al., 2022). On the other hand, in certain conditions, a decrease in temperature can also increase oil yield. For instance, at low temperatures, the solubility of specific oil components in SC-CO₂ may increase, resulting in greater extraction efficiency and, consequently, a greater oil yield (Aziz et al., 2022). In addition, low temperatures can diminish the vapor pressure of oil components, thereby minimizing their loss during extraction (Aziz et al., 2020).

It should be noted that the effect of temperature on oil yield is highly dependent on the pressure of the extraction process. Due to the causes above, decreasing the temperature

at moderate forces can reduce the oil yield. However, a temperature decrease at high pressures can increase oil yield as the solubility of oil components in SC-CO₂ rises with decreasing temperature (Putra et al., 2021). Consequently, the effect of temperature on oil yield during SC-CO₂ extraction is complex and highly variable. The temperature must be optimized alongside other extraction parameters to obtain the highest oil yield with desirable qualities. Depending on the pressure and other extraction parameters, the optimal temperature range for citronella oil extraction using SC-CO₂ is reported to be between 40 and 60°C, as shown in Table 2.

Table 2
Parameter conditions of SC-CO₂ extraction for citronella oil recovery

Conditions	Yield	Summary	References
T= 313.15 to 353.15 K P= 6.2, to 180.0 MPa	± 3%	essential oil more concentrated with rich active compounds. A high selectivity was obtained at 353.15K and 18.0MPa, with a pure	Silva et al. (2011)
Ext. time = 120 min P= 25 MPa T=35°C CO ₂ flow=18 L/h	4.40%	The antioxidant and antimicrobial activities of SFE oil are better than hydro distillation. Alcohols and aldehydes were the main compositions in the essential oils.	Wu et al. (2019)
P= 20 MPa T=40 °C	3.5%	Higher pressures significantly increased yield.	Guedes et al. (2018)
P= 15 MPa T= 50 °C Ext. time = 180 min.	1.4%	temperature is the most significant factor in maximizing citronella oil yield	Salea et al. (2018)
P =11 MPa T= 50 °C	1.92%	Higher pressures significantly increased the yield	Rosli et al. (2007)
P= 20 MPa T=40 °C	1.674%	oil yield was increased with increasing the pressure and decreasing the temperature	Abd Manaf et al. (2013)

Effect of Flowrate

Depending on various factors, increasing the flow rate of the supercritical fluid can have positive and negative effects on the oil yield. Increasing the flow rate can increase the mass transfer of the oil components from the plant material to the supercritical fluid, resulting in higher extraction efficiency and yield (Pavlić et al., 2020). Furthermore, it can increase the penetration of the supercritical fluid into the plant material, resulting in a quicker diffusion of the oil components into the supercritical fluid (Dimić et al., 2021). Increasing the flow rate can also diminish oil recovery. Increasing the flow rate decreases the contact duration between the supercritical fluid and the plant material, which may result in insufficient oil extraction. In addition, increasing the flow rate may also increase the pressure loss across the extraction vessel, reducing extraction efficacy (Peng et al., 2020).

On the other hand, decreasing the flow rate can also lead to a decrease in the oil yield. Decreasing the flow rate can increase the residence time of the supercritical fluid in the

extraction vessel, leading to a higher risk of thermal degradation of the oil components due to prolonged exposure to high temperatures (Dhakane-Lad & Kar, 2021). Notably, the effect of flow rate on oil yield is highly dependent on other extraction parameters such as pressure, temperature, and the ratio of solvent to feed. At high pressures, for instance, increasing the flow rate can result in a higher oil yield because the mass transfer rate of the oil components from the plant material to the supercritical fluid is already high (Argun et al., 2022). Increasing the flow rate can further improve it. However, increasing the flow rate may not inherently increase the oil yield at low pressures, as the pressure may limit the mass transfer rate (Rizkiyah et al., 2022; Soh et al., 2019).

Consequently, the influence of flow rate on oil yield in SC-CO₂ extraction is complex and highly variable. Optimizing the flow rate and other extraction parameters is essential to obtain the maximum oil yield with desirable qualities. According to reports (Table 2), the optimal flow rate range for citronella oil extraction using SC-CO₂ is 0.3 L/min, depending on the extraction pressure and other parameters.

Effect of Extraction Time

Depending on various factors, increasing the extraction time in SC-CO₂ extraction can also positively and negatively affect the oil yield. On the one hand, increasing the extraction time can increase the contact time between the supercritical fluid and the plant material, allowing the oil components to dissolve in the solvent for an extended period, resulting in a higher oil yield (Capuzzo et al., 2013; del Valle, 2015). Increasing the extraction time gives the supercritical fluid more time to penetrate the plant material and dissolve its oily components. On the other hand, increasing the extraction time can also reduce oil production because increasing the extraction time can increase the exposure of oil components to high-pressure and high-temperature conditions, potentially resulting in thermal degradation or oxidation of oil components, which can reduce the overall oil yield (Golmohammadi et al., 2018).

However, reducing the extraction time may also reduce the contact time between the supercritical fluid and the plant material, decreasing extraction efficiency and oil yield (Park et al., 2007; Wu et al., 2019). Therefore, the optimal extraction duration for SC-CO₂ extraction of citronella oil highly depends on the specific extraction conditions, such as pressure, temperature, and solvent-to-feed ratio. Depending on the pressure and other extraction parameters, the optimum extraction time for citronella oil extraction using SC-CO₂ is typically reported to be between 30 minutes and 3 hours (Table 2).

Effect of Particle Size

In the SC-CO₂ extraction of citronella oil, the particle size of the plant material has a complex effect on the oil yield. However, these parameters have yet to be investigated

by previous research. Therefore, this review will suggest that the effect of particle size in the extraction process can be applied to extract the citronella oil by SC-CO₂. When the particle size of the plant material is increased, the surface area of the material exposed to the supercritical fluid is decreased, which may decrease oil yield due to inefficient contact between the plant material and the solvent (Snyder et al., 1984; Sodeifian, Saadati Ardestani, et al., 2016). A larger particulate size will have a lower ratio of surface area to volume, resulting in lower extraction efficiency and, consequently, a lower oil yield. On the other hand, increasing the particle size can also increase the porosity of the plant material, allowing for greater solvent penetration and mass transfer of oil components from the plant material to the solvent (Uwineza & Waśkiewicz, 2020). It can result in a greater oil yield due to increased extraction efficacy.

Similarly, reducing the particle size can increase the surface area of the plant material, which can result in improved contact between the plant material and the solvent and, consequently, a greater oil yield (Jha & Sit, 2022). However, reducing the particle size can also increase the flow resistance of the supercritical fluid, which can reduce the mass transfer rate of oil components from the plant material to the solvent, resulting in a lower oil yield (Yousefi et al., 2019). Consequently, the optimal particle size for SC-CO₂ extraction of citronella oil depends on several variables, such as the extraction conditions, pressure, temperature, and solvent-to-feed ratio. SC-CO₂ extraction of plant material typically employs a particle size range of 0.5 to 3 mm (Putra, Rizkiyah, et al., 2018).

Effect of Co-solvent

In the SC-CO₂ extraction of citronella oil, using co-solvents can have complex effects on oil yield. However, these parameters have also yet to be investigated by previous research. Increasing the co-solvent ratio increases the solubility of the oil components in the supercritical fluid, resulting in a more significant mass transfer of the oil components from the plant material to the solvent and a higher oil yield (Sodeifian, Sajadian, & Saadati Ardestani, 2016). Co-solvents can also reduce the viscosity of SC-CO₂, thereby increasing the mobility of the solvent within the plant material and further improving extraction efficiency and oil yield (Benelli et al., 2010). The type of solvents that can be used in SC-CO₂ extraction is shown in Table 3. One of the safe co-solvents used in SFE for essential oils is ethanol. Ethanol is generally recognized as safe (GRAS) by the Food and Drug Administration (FDA) and is a common solvent in the food industry (Aziz et al., 2021). Ethanol has been used as a co-solvent in SFE for essential oils, and it has been found to increase the yield and quality of the extracted oil. However, using ethanol as a co-solvent in SFE requires careful optimization of the extraction parameters, such as temperature, pressure, and flow rate, to avoid denaturation of the essential oil components.

Table 3

Common co-solvent can be applied to assist SC-CO₂ extraction

Co-solvent	Chemical Formula	Source
Ethanol	C ₂ H ₅ OH	Daud et al., 2022
Methanol	CH ₃ OH	Marcus, 2018
Propanol	C ₃ H ₇ OH	Akkarawatkhoosith et al., 2019
Ethyl acetate	C ₄ H ₈ O ₂	Klein et al., 2019
Acetone	C ₃ H ₆ O	Byun, 2020
Dimethyl sulfoxide (DMSO)	C ₂ H ₆ OS	Zhou et al., 2022
Carbon disulfide	CS ₂	Daneshyan and Sodeifian, 2022

However, an excessive quantity of co-solvent can cause the density and solvation power of the SC-CO₂, thereby decreasing the solubility of the oil components in the solvent and resulting in a reduced oil yield (Ahmad et al., 2019; Moges et al., 2022). Increasing the co-solvent ratio may also increase the cost of the extraction process, thereby reducing the process's economic viability (Hayyan et al., 2022). Similarly, diminishing the co-solvent ratio can reduce the oil components' solubility in SC-CO₂, reducing oil yield. However, diminishing the co-solvent ratio can reduce the cost of the extraction process, thereby increasing the process's economic viability. In the SC-CO₂ extraction of plant materials, including citronella, a co-solvent ratio of 5% to 20% is typically used (Machmudah et al., 2006).

BIOACTIVITY OF CITRONELLA OIL

Citronella oil is known to have a range of bioactive properties that have been the subject of research for many years. Some of the most commonly studied bioactivities of citronella oil include:

- **Insect repellent:** Citronella oil is well-known for its insect-repelling properties, particularly against mosquitoes. It is effective in repelling several species of mosquitoes and has been used as a natural alternative to synthetic insect repellents (Nollet & Rathore, 2017).
- **Antimicrobial:** Citronella oil has exhibited antimicrobial activity against various bacteria and fungi (Nakahara et al., 2013). It is particularly effective against Gram-positive bacteria such as *Staphylococcus aureus*, *Bacillus subtilis*, and *Streptococcus pneumoniae*.
- **Antioxidant:** Citronella oil has been found to possess significant antioxidant activity, which can help to protect the body from oxidative damage caused by free radicals (Sinha et al., 2011). This activity may be due to phenolic compounds in the oil.
- **Anti-inflammatory:** Citronella oil has been found to exhibit anti-inflammatory

activity in both in vitro and in vivo studies. This activity may be due to geraniol and citronellal (Salaria et al., 2020).

- Analgesic: Citronella oil has been shown to possess analgesic properties, which can help to reduce pain and inflammation (Ganjewala, 2009). This activity may be due to compounds such as citronellal, which have been found to exhibit analgesic effects in animal studies.
- Anti-cancer: Some studies have suggested that citronella oil may possess anti-cancer activity, particularly against breast cancer cells (Manosroi et al., 2006). This activity may be due to geraniol and citronellol, which have been found to exhibit anti-cancer effects in vitro.

OPTIMIZATION METHODS FOR SC-CO₂ EXTRACTION PARAMETERS

SC-CO₂ extraction is a versatile and environmentally friendly method to obtain valuable compounds from various natural sources, including essential oils like citronella. The success of SC-CO₂ extraction depends on the precise control of multiple operating parameters, such as temperature, pressure, particle size, and co-solvent ratios. Achieving the desired product quality, maximum yield, and process efficiency necessitates optimizing these parameters systematically. In this context, optimization methods are pivotal in fine-tuning SC-CO₂ extraction processes. These methods offer structured frameworks to explore the complex interplay of variables and identify optimal conditions. Three commonly employed optimization approaches in SC-CO₂ extraction are Response Surface Methodology (RSM) with Central Composite Design (CCD), Box-Behnken Design (BBD), and the Taguchi method.

Response Surface Methodology with Central Composite Design

Response Surface Methodology (RSM) with Central Composite Design (CCD) is a robust statistical technique for optimizing complex processes with multiple variables. When applied to the supercritical carbon dioxide (SC-CO₂) extraction of citronella oil, RSM-CCD offers a structured and systematic approach to investigating and optimizing critical parameters like temperature, pressure, and flow rate.

RSM allows researchers to systematically vary the selected parameters within predetermined ranges. In the case of SC-CO₂ extraction, these parameters can include temperature (T), pressure (P), and flow rate, among others. By systematically altering these factors, researchers can evaluate their individual and interactive effects on the extraction process (Arumugham et al., 2022). The Central Composite Design (CCD) is employed within RSM to construct a response surface. This surface accounts for quadratic effects, enabling a comprehensive analysis of how parameter interactions affect the response variable (Moges et al., 2022). In this case, the yield and quality of citronella oil. The CCD

involves a series of experiments strategically placed within the parameter space, allowing for generating a mathematical model that approximates the relationship between the parameters and the response.

Once the response surface is constructed, researchers can analyze it to identify the optimal extraction conditions. These conditions represent the combination of parameters that maximize the desired outcome, such as citronella oil yield and product quality. By studying the response surface, researchers gain insights into the critical factors that significantly impact the extraction process. RSM-CCD has found practical application in SC-CO₂ extraction studies, as exemplified in Timung et al. (2016). This study employed the response surface to visualize the interplay between temperature and pressure, shedding light on their combined effects on citronella oil yield and quality. Researchers pinpointed the optimal conditions within the parameter space, enhancing process efficiency and product quality.

In summary, RSM-CCD is a valuable optimization methodology that offers a structured approach to fine-tune critical parameters in SC-CO₂ extraction processes. It leverages the construction of response surfaces to identify optimal conditions for citronella oil extraction. This statistical technique provides researchers with valuable insights into the complex interactions between parameters and their effects on yield and product quality, ultimately contributing to the advancement of SC-CO₂ extraction methods in various industries.

Box-Behnken Design

Box-Behnken Design (BBD) is a sophisticated experimental design method that efficiently optimizes SC-CO₂ extraction parameters (Rizkiyah et al., 2023). This methodology is particularly well-suited for situations where factors have three-level settings, making it a valuable tool for optimizing complex processes like SC-CO₂ extraction. BBD is designed to efficiently explore the design space by systematically varying critical parameters. In the case of SC-CO₂ extraction, researchers can select factors like temperature (T) and pressure (P) and explore multiple levels for each factor. BBD strategically places experiments at the low, middle, and high levels of these parameters, facilitating a thorough investigation of their effects on the extraction process (Putra, Rizkiyah, Idham, et al., 2023). Like RSM-CCD, BBD also involves the construction of a response surface. This mathematical model approximates the relationship between the selected parameters and the response variable, which includes factors like citronella oil yield and product quality. The response surface aids in visualizing how changes in parameter levels influence the response.

Researchers analyze the response surface generated through BBD to identify the optimal extraction conditions. These conditions represent the combination of parameter settings that maximize the desired outcome, such as achieving the highest yield of citronella oil with optimal product quality. BBD helps researchers navigate the parameter

space efficiently to reach these optimal conditions. Furthermore, BBD systematically investigates both the individual and interactive effects of parameters on the extraction process. It provides a comprehensive understanding of how each parameter contributes to the response and how they interact. Understanding these effects is crucial for fine-tuning the extraction process.

BBD is a powerful experimental design method that efficiently explores parameter settings in SC-CO₂ extraction. It offers a structured approach to identifying optimal conditions for citronella oil extraction, taking into account the individual and interactive effects of parameters. BBD aids researchers in navigating the complexities of the extraction process, ultimately contributing to enhanced process efficiency and product quality in various industrial applications.

Taguchi Method

The Taguchi Method is a robust optimization technique that prioritizes the robustness and performance of a process. When applied to SC-CO₂ extraction, it becomes a valuable tool for optimizing a range of parameters, including those critical for citronella oil extraction, such as particle size and co-solvent ratios. The Taguchi Method is rooted in the concept of robust optimization, which aims to achieve consistent and high-quality results while accounting for variability in process parameters. It is particularly well-suited for processes like SC-CO₂ extraction, where maintaining product quality and reliability are paramount.

The Taguchi Method allows for the systematic optimization of multiple parameters simultaneously. SC-CO₂ extraction might include factors such as particle size, co-solvent ratios, pressure, and temperature. By optimizing these parameters together, researchers can ensure that the extraction process is not overly sensitive to variations, thus enhancing its robustness. The Taguchi Method employs orthogonal arrays to organize experiments efficiently (Ramezani et al., 2020). These arrays help in planning a relatively small number of experiments while providing a comprehensive understanding of the parameter interactions and their effects on the response variable, which in this case would be citronella oil yield and quality.

A key aspect of the Taguchi Method is the use of Signal-to-Noise (S/N) ratios to assess the performance of different parameter combinations (Ribeiro et al., 2017). These ratios help identify which parameter settings result in the most desirable outcomes. Researchers aim to maximize the S/N ratios associated with the desired response, indicating optimal process conditions. In summary, the Taguchi Method is a powerful and structured optimization technique that is particularly useful for ensuring the robustness and quality of SC-CO₂ extraction processes, including citronella oil extraction. It offers a multi-factorial approach to parameter optimization, utilizing orthogonal arrays and S/N ratios to systematically fine-tune process conditions. This methodology is instrumental in

achieving consistent and desirable product characteristics while minimizing the impact of parameter variations.

COMPARISON OF SUPERCRITICAL CARBON DIOXIDE WITH TRADITIONAL EXTRACTION METHODS

Citronella oil has been traditionally extracted using steam distillation and hydrodistillation methods. However, the emergence of SC-CO₂ extraction has shown to be a promising alternative method for extracting essential oils, including citronella oil. The SC-CO₂ extraction method utilizes carbon dioxide in its supercritical state, where it behaves as both a gas and a liquid, to extract essential oils from plant materials.

Due to its many advantages, there has been a growing interest in using SC-CO₂ extraction as an alternative to traditional methods. Compared to traditional methods, SC-CO₂ extraction offers a more efficient and environmentally friendly process with higher yields and does not require toxic solvents. The SC-CO₂ extraction method is also highly tunable, optimizing extraction conditions to target specific compounds of interest in the extracted oil. Table 4 summarizes the advantages and disadvantages of conventional extraction and SC-CO₂ extraction.

Table 4

Advantages and disadvantages of conventional extraction and SC-CO₂ extraction

Extraction Method	Advantages	Disadvantages	Ref
Steam Distillation	<ul style="list-style-type: none"> • Low-cost and widely used • Preserves aroma and flavor 	<ul style="list-style-type: none"> • Low yield • Time-consuming • Sensitive to heat • Degradation of heat-sensitive compounds 	Hamzah et al., 2014; Weng et al., 2015
Solvent Extraction	<ul style="list-style-type: none"> • High yield • Can extract a wide range of compounds • Short extraction time 	<ul style="list-style-type: none"> • Use of toxic solvents • Residual solvent in the final product • Expensive and time-consuming solvent recovery 	Okpo and Otaraku, 2020
Hydrodistillation	<ul style="list-style-type: none"> • Efficient for extraction of high boiling point compounds • Preserves the aroma and flavor 	<ul style="list-style-type: none"> • High energy consumption • Low yield • Long extraction time 	Gavahian et al., 2018; Timung et al., 2016
SC-CO ₂ Extraction	<ul style="list-style-type: none"> • Non-toxic and environmentally friendly • High selectivity and purity • Short extraction time • High yield • No residual solvents in the final product 	<ul style="list-style-type: none"> • High equipment cost • Requires expertise to operate and optimize 	Wu et al., 2019

Several methods are employed to extract citronella oil, each with its advantages and disadvantages. Steam distillation, a widely used method, is characterized by its cost-effectiveness and ability to preserve the aroma and flavor of the oil. However, it suffers from drawbacks such as relatively low yields, time-consuming processes, and sensitivity to heat, which can degrade heat-sensitive compounds within the oil. Solvent extraction offers high yields and can quickly extract a wide range of compounds. Nevertheless, it involves toxic solvents, potentially resulting in residual solvents in the final product, and can be expensive due to the need for solvent recovery. Hydrodistillation is efficient for compounds with high boiling points and maintains the oil's aromatic and flavorful qualities. However, it comes with the trade-offs of high energy consumption, lower yields, and lengthy extraction times. In contrast, SC-CO₂ extraction offers a non-toxic and environmentally friendly alternative. It excels in purity, yield, and speed, with no residual solvents in the final product. Nonetheless, the method requires a substantial equipment investment and specialized expertise for optimal operation. The choice of extraction method hinges on specific project requirements and considerations, ranging from yield and product quality to environmental concerns and available resources.

APPLICATION CITRONELLA OIL

Due to its unique chemical composition and properties, citronella oil has numerous applications in numerous industries. The following are some of the most common applications of citronella oil:

Due to its delightful, fresh, and citrus aroma, Citronella oil is extensively employed in the fragrance industry. Popular in fragrances, balms, candles, and air fresheners (Ganjewala, 2009).

- Citronella oil is effective against mosquitoes, flies, and other insects as a natural insect repellent. It is commonly used in candles, perfumes, mists, and mosquito coils (Hsu et al., 2013).
- Aromatherapy utilizes citronella oil to promote relaxation, reduce tension, and enhance mood. Typical applications include diffusers, massage oils, and bath additives (Barbas et al., 2017).
- Citronella oil is a flavoring agent in the food and beverage industry (Neequaye et al., 2017). It is utilized frequently in soft beverages, ice creams, chocolates, and baked products.
- The antifungal, antibacterial, and antiseptic properties of citronella oil make it useful in the pharmaceutical industry (Kaur et al., 2021). It is incorporated into topical ointments, balms, and cosmetics.
- In veterinary medicine, citronella oil is used as an insect repellent and a natural treatment for various animal diseases.

- Citronella oil's antiseptic and astringent properties are utilized in cosmetics (Happy et al., 2021). It is commonly found in skin care products such as facial cleansers and toners.
- Citronella oil produces various industrial products, including insecticides, cleansing agents, and lubricants (Isman et al., 2011).

CHALLENGES AND FUTURE PERSPECTIVE IN SC-CO₂ EXTRACTION FOR CITRONELLA OIL

SC-CO₂ Extraction as an alternative to conventional methods for extracting essential oils, including citronella oil, has shown tremendous promise. However, some obstacles must be overcome for the widespread utilization of this technology in the citronella oil industry. Optimization of the extraction parameters is one of the most significant obstacles. Although the effects of pressure, temperature, flow rate, particle size, and co-solvent ratio on the extraction yield of citronella oil have been investigated, further optimization of these parameters is required to maximize the extraction yield and minimize operating costs. Additionally, the use of various co-solvents and their effects on the extraction yield and quality of the extracted oil should be investigated further.

Scaling up the SC-CO₂ extraction method presents further difficulty. While the laboratory-scale extraction yielded promising results, the scale-up process necessitates substantial investment and engineering expertise to ensure the process's efficacy and safety. In addition, the cost of the apparatus required for SC-CO₂ extraction is still comparatively high compared to conventional extraction techniques, which may prevent small-scale producers from adopting this technology.

The stability of the extracted citronella oil is an additional crucial factor to consider. The SC-CO₂ extraction method can yield high-quality essential oils with a minimal impurity content. To ensure the purity and efficacy of these oils, however, it is necessary to investigate their stability during storage and transportation. In addition, the effects of the extraction procedure on the bioactive compounds in citronella oil should be evaluated for their possible health benefits.

The future of SC-CO₂ extraction in the citronella oil industry appears promising despite these obstacles. The technology provides several advantages over conventional extraction techniques, including a higher yield, a lower impurity level, and a shorter extraction time. In addition, SC-CO₂ extraction has a lower environmental impact than conventional extraction methods because it does not require organic solvents, which can be detrimental to the environment. In addition, developing new technologies and optimizing existing ones can significantly enhance the SC-CO₂ extraction process's efficacy and cost-effectiveness (Chemat et al., 2020; De Oliveira et al., 2019). Using co-solvents and optimizing their ratio, for instance, can improve the extraction yield and the quality of the extracted oil.

Integrating SC-CO₂ extraction with other technologies, such as microwave and ultrasound, can improve the process's efficacy and selectivity.

The future of SC-CO₂ extraction for citronella oil appears promising, even though several obstacles still need to be addressed. Its future applications in the culinary, cosmetic, and pharmaceutical industries are extensive. Continued research and development in this field can significantly enhance the process's efficacy and cost-effectiveness, making it a viable alternative to conventional extraction techniques.

CONCLUSION

This review paper focused on the SC-CO₂ extraction of citronella oil, discussing topics such as the production and interesting compounds of citronella, the theory of SC-CO₂ extraction, and the various parameters that affect the yield and quality of the extracted oil. According to the review's findings, SC-CO₂ extraction is a promising alternative to conventional citronella oil extraction methods. It offers several advantages, including reduced solvent usage, shorter extraction times, and higher oil yields with a higher concentration of interesting compounds. However, there are still obstacles to maximizing the yield and quality of the extracted oil by optimizing the process parameters. Prospects for SC-CO₂ extraction of citronella oil include the development of new technologies and equipment, such as the use of co-solvents and the integration of ultrasound or microwave-assisted techniques, as well as the investigation of new applications for the extracted oil in various industries, such as the pharmaceutical, cosmetic, and food industries. This review provides valuable insights into the SC-CO₂ extraction of citronella oil, highlighting its potential as a sustainable and efficient alternative to traditional extraction methods and identifying research gaps.

ACKNOWLEDGEMENT

The authors acknowledged the Professional Development Research University grant (Q.J130000.21A2.07E06) from Universiti Teknologi Malaysia and Skim penyelidikan lantikan baru (SLB2242) from Faculty of Food Science and Nutrition, Universiti Malaysia Sabah, 88400 Kota Kinabalu, Sabah, Malaysia for supporting this work.

REFERENCES

- Ahmad, T., Masoodi, F., Rather, S. A., Wani, S., & Gull, A. (2019). Supercritical fluid extraction: A review. *Journal of Biological and Chemical Chronicles*, 5(1), 114-122.
- Akkarawatkhoosith, N., Kaewchada, A., & Jaree, A. (2019). Enhancement of continuous supercritical biodiesel production: influence of co-solvent types. *Energy Procedia*, 156, 48-52. <https://doi.org/10.1016/j.egypro.2018.11.085>

- Alesaeidi, S., & Miraj, S. (2016). A systematic review of anti-malarial properties, immunosuppressive properties, anti-inflammatory properties, and anti-cancer properties of *Artemisia annua*. *Electronic Physician*, *8*(10), Article 3150. <https://doi.org/10.19082/3150>
- Ali, B., Al-Wabel, N. A., Shams, S., Ahamad, A., Khan, S. A., & Anwar, F. (2015). Essential oils used in aromatherapy: A systemic review. *Asian Pacific Journal of Tropical Biomedicine*, *5*(8), 601-611. <https://doi.org/10.1016/j.apjtb.2015.05.007>
- Ammar, R. B. (2023). Potential effects of geraniol on cancer and inflammation-related diseases: A review of the recent research findings. *Molecules*, *28*(9), Article 3669. <https://doi.org/10.3390/molecules28093669>
- Anandakumar, P., Kamaraj, S., & Vanitha, M. K. (2021). D-limonene: A multifunctional compound with potent therapeutic effects. *Journal of Food Biochemistry*, *45*(1), Article e13566. <https://doi.org/10.1111/jfbc.13566>
- Aprodu, I., Milea, Ş. A., Enachi, E., Râpeanu, G., Bahrim, G. E., & Stănciuc, N. (2020). Thermal degradation kinetics of anthocyanins extracted from purple maize flour extract and the effect of heating on selected biological functionality. *Foods*, *9*(11), Article 1593. <https://doi.org/10.3390/foods9111593>
- Argun, M. E., Argun, M. Ş., Arslan, F. N., Nas, B., Ates, H., Tongur, S., & Cakmakcı, O. (2022). Recovery of valuable compounds from orange processing wastes using supercritical carbon dioxide extraction. *Journal of Cleaner Production*, *375*, Article 134169. <https://doi.org/10.1016/j.jclepro.2022.134169>
- Arsad, N. H., Putra, N. R., Idham, Z., Norodin, N. S. M., Yunus, M. A. C., & Aziz, A. H. A. (2023). Solubilization of eugenol from Piper betle leaves to supercritical carbon dioxide: Experimental and modelling. *Results in Engineering*, *17*, Article 100914. <https://doi.org/10.1016/j.rineng.2023.100914>
- Arumugham, T., AlYammahi, J., Rambabu, K., Hassan, S. W., & Banat, F. (2022). Supercritical CO₂ pretreatment of date fruit biomass for enhanced recovery of fruit sugars. *Sustainable Energy Technologies and Assessments*, *52*, Article 102231. <https://doi.org/10.1016/j.seta.2022.102231>
- Arumugham, T., K, R., Hasan, S. W., Show, P. L., Rinklebe, J., & Banat, F. (2021). Supercritical carbon dioxide extraction of plant phytochemicals for biological and environmental applications - A review. *Chemosphere*, *271*, Article 129525. <https://doi.org/10.1016/j.chemosphere.2020.129525>
- Aziz, Z. A. A., Ahmad, A., Setapar, S. H. M., Karakucuk, A., Azim, M. M., Lokhat, D., Rafatullah, M., Ganash, M., Kamal, M. A., & Ashraf, G. M. (2018). Essential oils: Extraction techniques, pharmaceutical and therapeutic potential - A review. *Current Drug Metabolism*, *19*(13), 1100-1110. <https://doi.org/10.2174/1389200219666180723144850>
- Aziz, A. H. A., Idrus, N. F. M., Putra, N. R., Awang, M. A., Idham, Z., Mamat, H., & Yunus, M. A. C. (2022). Solubility of rosmarinic acid in supercritical carbon dioxide extraction from *Orthosiphon stamineus* leaves. *ChemEngineering*, *6*(4), Article 59. <https://doi.org/10.3390/chemengineering6040059>
- Aziz, A. H. A., Putra, N. R., Kong, H., & Yunus, M. A. C. (2020). Supercritical carbon dioxide extraction of sinensetin, isosinensetin, and rosmarinic acid from *Orthosiphon stamineus* leaves: Optimization and modeling. *Arabian Journal for Science and Engineering*, *45*(9), 7467-7476. <https://doi.org/10.1007/s13369-020-04584-6>
- Aziz, A. H. A., Putra, N. R., Zaini, A. S., Idham, Z., Ahmad, M. Z., & Yunus, M. A. C. (2021). Solubility of sinensetin and isosinensetin from Cat's Whiskers (*Orthosiphon stamineus*) leaves in ethanol-assisted

supercritical carbon dioxide extraction: Experimental and modeling. *Chemical Papers*, 75(12), 6557-6563. <https://doi.org/10.1007/s11696-021-01822-5>

- Aziz, A. H. A., Rizkiyah, D. N., Qomariyah, L., Irianto, I., Yunus, M. A. C., & Putra, N. R. (2023). Unlocking the full potential of clove (*Syzygium aromaticum*) spice: An overview of extraction techniques, bioactivity, and future opportunities in the food and beverage industry. *Processes*, 11(8), Article 2453. <https://doi.org/10.3390/pr11082453>
- Bakkali, F., Averbeck, S., Averbeck, D., & Idaomar, M. (2008). Biological effects of essential oils - A review. *Food and Chemical Toxicology*, 46(2), 446-475. <https://doi.org/10.1016/j.fct.2007.09.106>
- Barbas, L. A. L., Hamoy, M., de Mello, V. J., Barbosa, R. P. M., de Lima, H. S. T., Torres, M. F., do Nascimento, L. A. S., da Silva, J. K. D. R., Andrade, E. H. D. A., & Gomes, M. R. F. (2017). Essential oil of citronella modulates electrophysiological responses in tambaqui *Colossoma macropomum*: A new anaesthetic for use in fish. *Aquaculture*, 479, 60-68. <https://doi.org/10.1016/j.aquaculture.2017.05.027>
- Bell, K. L. (2012). *Holistic aromatherapy for animals: A comprehensive guide to the use of essential oils & hydrosols with animals*. Simon and Schuster.
- Benelli, P., Riehl, C. A. S., Smânia, A., Smânia, E. F. A., & Ferreira, S. R. S. (2010). Bioactive extracts of orange (*Citrus sinensis* L. Osbeck) pomace obtained by SFE and low pressure techniques: Mathematical modeling and extract composition. *The Journal of Supercritical Fluids*, 55(1), 132-141. <https://doi.org/10.1016/j.supflu.2010.08.015>
- Byun, H. S. (2020). Co-solvent concentration influence of two-and three-component systems on the high pressure cloud-point behavior for the poly (vinyl stearate) under supercritical CO₂. *Journal of Industrial and Engineering Chemistry*, 90, 76-84. <https://doi.org/10.1016/j.jiec.2020.06.024>
- Capuzzo, A., Maffei, M. E., & Occhipinti, A. (2013). Supercritical fluid extraction of plant flavors and fragrances. *Molecules*, 18(6), 7194-7238. <https://doi.org/10.3390/molecules18067194>
- Carvalho, I. T., Estevinho, B. N., & Santos, L. (2016). Application of microencapsulated essential oils in cosmetic and personal healthcare products - A review. *International Journal of Cosmetic Science*, 38(2), 109-119. <https://doi.org/10.1111/ics.12232>
- Cassel, E., & Vargas, R. M. (2006). Experiments and modeling of the *Cymbopogon winterianus* essential oil extraction by steam distillation. *Journal of the Mexican Chemical Society*, 50(3), 126-129.
- Chai, Y. H., Yusup, S., Kadir, W. N. A., Wong, C. Y., Rosli, S. S., Ruslan, M. S. H., Chin, B. L. F., & Yiin, C. L. (2020). Valorization of tropical biomass waste by supercritical fluid extraction technology. *Sustainability*, 13(1), Article 233. <https://doi.org/10.3390/su13010233>
- Chemat, F., Vian, M. A., Fabiano-Tixier, A.-S., Nutrizio, M., Jambak, A. R., Munekata, P. E. S., Lorenzo, J. M., Barba, F. J., Binello, A., & Cravotto, G. (2020). A review of sustainable and intensified techniques for extraction of food and natural products. *Green Chemistry*, 22(8), 2325-2353. <https://doi.org/10.1039/C9GC03878G>
- Chen, W., & Viljoen, A. (2010). Geraniol - A review of a commercially important fragrance material. *South African Journal of Botany*, 76(4), 643-651. <https://doi.org/10.1016/j.sajb.2010.05.008>

- Daneshyan, S., & Sodeifian, G. (2022). Synthesis of cyclic polystyrene in supercritical carbon dioxide green solvent. *The Journal of Supercritical Fluids*, 188, Article 105679. <https://doi.org/10.1016/j.supflu.2022.105679>
- Daud, N. M., Putra, N. R., Jamaludin, R., Norodin, N. S. M., Sarkawi, N. S., Hamzah, M. H. S., Nasir, H. M., Zaidel, D. N. A., Yunus, M. A. C., & Salleh, L. M. (2022). Valorisation of plant seed as natural bioactive compounds by various extraction methods: A review. *Trends in Food Science & Technology*, 119, 201-214. <https://doi.org/10.1016/j.tifs.2021.12.010>
- de Melo, M. M., Carius, B., Simões, M. M., Portugal, I., Saraiva, J., & Silva, C. M. (2020). Supercritical CO₂ extraction of *V. vinifera* leaves: Influence of cosolvents and particle size on removal kinetics and selectivity to target compounds. *The Journal of Supercritical Fluids*, 165, Article 104959. <https://doi.org/10.1016/j.supflu.2020.104959>
- de Oliveira, M. S., Silva, S. G., da Cruz, J. N., Ortiz, E., da Costa, W. A., Bezerra, F. W. F., Cunha, V. M. B., Cordeiro, R. M., Neto, A. M. D. J. C., Andrade, E. H. D. A., & Junior, R. N. D. C. (2019). Supercritical CO₂ application in essential oil extraction. In R. M. Inamuddin & A. M. Asiri (Eds.), *Industrial Applications of Green Solvents* (Volume 2: pp. 1-28). Material Research Foundations. <https://doi.org/10.21741/97816449000314-1>
- del Valle, J. M. (2015). Extraction of natural compounds using supercritical CO₂: Going from the laboratory to the industrial application. *The Journal of Supercritical Fluids*, 96, 180-199. <https://doi.org/10.1016/j.supflu.2014.10.001>
- Devi, M. A., Sahoo, D., Singh, T. B., & Rajashekar, Y. (2021). Antifungal activity and volatile organic compounds analysis of essential oils from Cymbopogon species using solid-phase microextraction-gas chromatography-mass spectrometry. *Journal of Agriculture and Food Research*, 3, Article 100110. <https://doi.org/10.1016/j.jafr.2021.100110>
- Dhakane-Lad, J., & Kar, A. (2021). Supercritical CO₂ extraction of lycopene from pink grapefruit (*Citrus paradise* Macfad) and its degradation studies during storage. *Food Chemistry*, 361, Article 130113. <https://doi.org/10.1016/j.foodchem.2021.130113>
- Dhara, O., Rani, K. P., & Chakrabarti, P. P. (2022). Supercritical carbon dioxide extraction of vegetable oils: Retrospective and prospects. *European Journal of Lipid Science and Technology*, 124(8), Article 2200006. <https://doi.org/10.1002/ejlt.202200006>
- Dimić, I., Pezo, L., Rakić, D., Teslić, N., Zeković, Z., & Pavlić, B. (2021). Supercritical fluid extraction kinetics of cherry seed oil: kinetics modeling and ANN optimization. *Foods*, 10(7), Article 1513. <https://doi.org/10.3390/foods10071513>
- El-Kholany, E. A. (2016). Utilization of essential oils from citronella and geranium as natural preservative in mayonnaise. *International Journal of Microbiology and Biotechnology*, 1(1), 49-59.
- Ganjewala, D. (2009). Cymbopogon essential oils: Chemical compositions and bioactivities. *International Journal of Essential Oil Therapeutics*, 3(2-3), 56-65.
- Gavahian, M., Lee, Y. T., & Chu, Y. H. (2018). Ohmic-assisted hydrodistillation of citronella oil from Taiwanese citronella grass: Impacts on the essential oil and extraction medium. *Innovative Food Science & Emerging Technologies*, 48, 33-41. <https://doi.org/10.1016/j.ifset.2018.05.015>

- Golmohammadi, M., Borghei, A., Zenouzi, A., Ashrafi, N., & Taherzadeh, M. J. (2018). Optimization of essential oil extraction from orange peels using steam explosion. *Heliyon*, 4(11), Article e00893. <https://doi.org/10.1016/j.heliyon.2018.e00893>
- Guedes, A. R., de Souza, A. R. C., Zanoelo, E. F., & Corazza, M. L. (2018). Extraction of citronella grass solutes with supercritical CO₂, compressed propane and ethanol as cosolvent: Kinetics modeling and total phenolic assessment. *The Journal of Supercritical Fluids*, 137, 16-22. <https://doi.org/10.1016/j.supflu.2018.03.003>
- Hamzah, M. H., Man, H. C., Abidin, Z. Z., & Jamaludin, H. (2014). Comparison of citronella oil extraction methods from cymbopogon nardus grass by ohmic-heated hydro-distillation, hydro-distillation, and steam distillation. *BioResources*, 9(1), 256-272.
- Hanif, M. A., Nisar, S., Khan, G. S., Mushtaq, Z., & Zubair, M. (2019). Essential oils. In S. Malik (Ed.), *Essential Oil Research: Trends in Biosynthesis, Analytics, Industrial Applications and Biotechnological Production* (pp. 3-17). Springer. https://doi.org/10.1007/978-3-030-16546-8_1
- Happy, A. A., Jahan, F., & Momen, M. A. (2021). Essential oils: Magical ingredients for skin care. *Journal of Plant Sciences*, 9(2), Article 54.
- Hayyan, A., Samyudia, A. V., Hashim, M. A., Hizaddin, H. F., Ali, E., Hadj-Kali, M. K., Aldeehani, A. K., Alkandari, K. H., Etigany, H. T., Alajmi, F. D. H., Alhumaydhi, F. A., Aljohari, A. S. M., Zulkifli, M. Y., Halilu, A., & Yeow, A. T. H. (2022). Application of deep eutectic solvent as novel co-solvent for oil extraction from flaxseed using sonoenergy. *Industrial Crops and Products*, 176, Article 114242. <https://doi.org/10.1016/j.indcrop.2021.114242>
- Hsu, W. S., Yen, J. H., & Wang, Y. S. (2013). Formulas of components of citronella oil against mosquitoes (*Aedes aegypti*). *Journal of Environmental Science and Health, Part B*, 48(11), 1014-1019. <https://doi.org/10.1080/03601234.2013.816613>
- Idham, Z., Putra, N. R., Nasir, H., Yian, L. N., Idrus, N. F. M., & Yunus, M. A. C. (2021). Extraction and solubility modeling of anthocyanins rich extract from hibiscus sabdariffa l. using supercritical carbon dioxide. *Malaysian Journal of Fundamental and Applied Sciences*, 17(6), 720-730.
- Isman, M. B., Miresmailli, S., & Machial, C. (2011). Commercial opportunities for pesticides based on plant essential oils in agriculture, industry and consumer products. *Phytochemistry Reviews*, 10, 197-204. <https://doi.org/10.1007/s11101-010-9170-4>
- Jha, A. K., & Sit, N. (2022). Extraction of bioactive compounds from plant materials using combination of various novel methods: A review. *Trends in Food Science & Technology*, 119, 579-591. <https://doi.org/10.1016/j.tifs.2021.11.019>
- Kaur, H., Bhardwaj, U., Kaur, R., & Kaur, H. (2021). Chemical composition and antifungal potential of citronella (*Cymbopogon nardus*) leaves essential oil and its major compounds. *Journal of Essential Oil Bearing Plants*, 24(3), 571-581. <https://doi.org/10.1080/0972060X.2021.1942231>
- Khan, M. F., & Dwivedi, A. K. (2018). A review on techniques available for the extraction of essential oils from various plants. *International Research Journal of Engineering and Technology*, 5(5), 5-8.
- Kim, D. S., & Lim, S. B. (2020). Kinetic study of subcritical water extraction of flavonoids from citrus unshiu peel. *Separation and Purification Technology*, 250, Article 117259. <https://doi.org/10.1016/j.seppur.2020.117259>

- Klein, E. J., Nathia-Neves, G., Vardanega, R., Meireles, M. A. A., da Silva, E. A., & Vieira, M. G. A. (2019). Supercritical CO₂ extraction of α - β -amyryn from uvaia (*Eugenia pyriformis* Cambess.): Effects of pressure and co-solvent addition. *The Journal of Supercritical Fluids*, 153, Article 104595. <https://doi.org/10.1016/j.supflu.2019.104595>
- Leila, M., Ratiba, D., & Al-Marzouqi, A. H. (2022). Experimental and mathematical modelling data of green process of essential oil extraction: Supercritical CO₂ extraction. *Materials Today: Proceedings*, 49, 1023-1029. <https://doi.org/10.1016/j.matpr.2021.08.125>
- Li, C., Luo, Y., Zhang, W., Cai, Q., Wu, X., Tan, Z., Chen, R., Chen, Z., Wang, S., & Zhang, L. (2021). A comparative study on chemical compositions and biological activities of four essential oils: *Cymbopogon citratus* (DC.) Stapf, *Cinnamomum cassia* (L.) Presl, *Salvia japonica* Thunb. and *Rosa rugosa* Thunb. *Journal of Ethnopharmacology*, 280, Article 114472. <https://doi.org/10.1016/j.jep.2021.114472>
- Lim, S. F., Hamdan, A., David Chua, S. N., & Lim, B. H. (2021). Comparison and optimization of conventional and ultrasound-assisted solvent extraction for synthetization of lemongrass (*Cymbopogon*)-infused cooking oil. *Food Science & Nutrition*, 9(5), 2722-2732. <https://doi.org/10.1002/fsn3.2234>
- Machado, N. D., Mosquera, J. E., Martini, R. E., Goñi, M. L., & Gañán, N. A. (2022). Supercritical CO₂-assisted impregnation of cellulose microparticles with R-carvone: Effect of process variables on impregnation yield. *The Journal of Supercritical Fluids*, 188, Article 105671. <https://doi.org/10.1016/j.supflu.2022.105671>
- Machmudah, S., Sulaswatty, A., Sasaki, M., Goto, M., & Hirose, T. (2006). Supercritical CO₂ extraction of nutmeg oil: Experiments and modeling. *The Journal of Supercritical Fluids*, 39(1), 30-39. <https://doi.org/10.1016/j.supflu.2006.01.007>
- Manaf, M. A., Mustapa, A. N., & Mustapa, K. (2013). *Supercritical fluid extraction of Citronella oil from Cymbopogon nardus and its optimization*. [Paper presentation]. IEEE Business Engineering and Industrial Applications Colloquium (BEIAC), Langkawi, Malaysia. <https://doi.org/10.1109/BEIAC.2013.6560229>
- Manosroi, J., Dhumtanom, P., & Manosroi, A. (2006). Anti-proliferative activity of essential oil extracted from Thai medicinal plants on KB and P388 cell lines. *Cancer Letters*, 235(1), 114-120. <https://doi.org/10.1016/j.canlet.2005.04.021>
- Marcus, Y. (2018). Extraction by subcritical and supercritical water, methanol, ethanol and their mixtures. *Separations*, 5(1), Article 4. <https://doi.org/10.3390/separations5010004>
- Moges, A., Barik, C. R., Sahoo, L., & Goud, V. V. (2022). Optimization of polyphenol extraction from *Hippophae salicifolia* D. Don leaf using supercritical CO₂ by response surface methodology. *3 Biotech*, 12(11), Article 292. <https://doi.org/10.1007/s13205-022-03358-1>
- Mohd-Nasir, H., Putra, N. R., Chuo, S. C., Daud, N. M., Hartati, H., Bakeri, N., Ruslan, M. S. H., Mohd-Setapar, S. H., Ahmad, A., & Salleh, L. M. (2021). Optimization of the supercritical carbon dioxide extraction of *Quercus infectoria* galls extracts and its bioactivities. *Journal of Food Processing and Preservation*, 45(2), Article e15156. <https://doi.org/10.1111/jfpp.15156>
- Muhammad, S., Khalil, H. P. S. A., Hamid, S. A., Danish, M., Marwan, M., Yunardi, Y., Abdullah, C. K., Faisal, M., & Yahya, E. B. (2022). Characterization of bioactive compounds from patchouli extracted via supercritical carbon dioxide (SC-CO₂) extraction. *Molecules*, 27(18), Article 6025. <https://doi.org/10.3390/molecules27186025>

- Nakahara, K., Alzoreky, N. S., Yoshihashi, T., Nguyen, H. T., & Trakoontivakorn, G. (2013). Chemical composition and antifungal activity of essential oil from *Cymbopogon nardus* (citronella grass). *Japan Agricultural Research Quarterly: JARQ*, 37(4), 249-252. <https://doi.org/10.6090/jarq.37.249>
- Neequaye, K., Adonu, R., & Mensah, D. O. A. (2017). Production of cake using lemon grass as flavouring agent. *American Based Research Journal*, 6(11), 48-60.
- Nollet, L. M., & Rathore, H. S. (2017). Essential oil mixtures for pest control. In *Green Pesticides Handbook* (pp. 509-522). CRC Press.
- Odunlami, O. A., Vershima, D. A., Oladimeji, T. E., Nkongho, S., Ogunlade, S. K., & Fakinle, B. S. (2022). Advanced techniques for the capturing and separation of CO₂ - A review. *Results in Engineering*, 15, Article 100512. <https://doi.org/10.1016/j.rineng.2022.100512>
- Okpo, S. O., & Otaraku, I. J. (2020). Modelling of soxhlet extraction of lemongrass oil. *International Journal of Chemical Engineering Research*, 7(2), 24-29.
- Ongkasin, K., Sauceau, M., Masmoudi, Y., Fages, J., & Badens, E. (2019). Solubility of cefuroxime axetil in supercritical CO₂: Measurement and modeling. *The Journal of Supercritical Fluids*, 152, Article 104498. <https://doi.org/10.1016/j.supflu.2019.03.010>
- Park, H. S., Choi, H. K., Lee, S. J., Park, K. W., Choi, S. G., & Kim, K. H. (2007). Effect of mass transfer on the removal of caffeine from green tea by supercritical carbon dioxide. *The Journal of Supercritical Fluids*, 42(2), 205-211. <https://doi.org/10.1016/j.supflu.2007.03.002>
- Pavlič, B., Pezo, L., Marić, B., Tukuljac, L. P., Zeković, Z., Solarov, M. B., & Teslić, N. (2020). Supercritical fluid extraction of raspberry seed oil: Experiments and modelling. *The Journal of Supercritical Fluids*, 157, Article 104687. <https://doi.org/10.1016/j.supflu.2019.104687>
- Peng, W. L., Mohd-Nasir, H., Setapar, S. H. M., Ahmad, A., & Lokhat, D. (2020). Optimization of process variables using response surface methodology for tocopherol extraction from Roselle seed oil by supercritical carbon dioxide. *Industrial Crops and Products*, 143, Article 111886. <https://doi.org/10.1016/j.indcrop.2019.111886>
- Pohlit, A. M., Lopes, N. P., Gama, R. A., Tadei, W. P., & de Andrade Neto, V. F. (2011). Patent literature on mosquito repellent inventions which contain plant essential oils - A review. *Planta Medica*, 77(06), 598-617. <https://doi.org/10.1055/s-0030-1270723>
- Putra, N. R., Rizkiyah, D. N., Aziz, A. H. A., Yunus, M. A., Veza, I., Harny, I., & Tirta, A. (2023). Waste to wealth of apple pomace valorization by past and current extraction processes: A review. *Sustainability*, 15(1), Article 830. <https://doi.org/10.3390/su15010830>
- Putra, N. R., Rizkiyah, D. N., Aziz, A. H. A., Mamat, H., Jusoh, W. M. S. W., Idham, Z., Yunus, M. A. C., & Irianto, I. (2023). Influence of particle size in supercritical carbon dioxide extraction of roselle (*Hibiscus sabdariffa*) on bioactive compound recovery, extraction rate, diffusivity, and solubility. *Scientific Reports*, 13(1), Article 10871. <https://doi.org/10.1038/s41598-023-32181-8>
- Putra, N. R., Rizkiyah, D. N., Idham, Z., Zaini, M. A. A., Yunus, M. A. C., & Aziz, A. H. A. (2023). Optimization and solubilization of interest compounds from roselle in subcritical ethanol extraction (SEE). *Alexandria Engineering Journal*, 65, 59-74. <https://doi.org/10.1016/j.aej.2022.09.037>

- Putra, N. R., Rizkiyah, D. N., Idham, Z., Jumakir, J., Waluyo, W., Faizal, A. N. M., & Yunus, M. A. C. (2022). A new solubility model for competing effects of three solvents: Water, ethanol, and supercritical carbon dioxide. *Separation Science and Technology*, 57(14), 2269-2275. <https://doi.org/10.1080/01496395.2022.2045317>
- Putra, N. R., Rizkiyah, D. N., Zaini, A. S., Machmudah, S., & Yunus, M. A. C. (2021). Solubility of catechin and epicatechin from Arachis Hypogea skins wastes by using supercritical carbon dioxide-ethanol and its optimization. *Journal of Food Measurement and Characterization*, 15(2), 2031-2038. <https://doi.org/10.1007/s11694-020-00797-3>
- Putra, N. R., Aziz, A. H. A., Idham, Z., Ruslan, M. S. H., & Yunus, M. A. C. (2018). Diffusivity optimization of supercritical carbon dioxide extraction with co-solvent-ethanol from peanut skin. *Malaysian Journal of Fundamental and Applied Sciences*, 14(1), 9-14.
- Putra, N. R., Rizkiyah, D. N., Zaini, A. S., Yunus, M. A. C., Machmudah, S., Idham, Z. B., & Ruslan, M. S. H. (2018). Effect of particle size on yield extract and antioxidant activity of peanut skin using modified supercritical carbon dioxide and soxhlet extraction. *Journal of Food Processing and Preservation*, 42(8), Article e13689. <https://doi.org/10.1111/jfpp.13689>
- Ramezani, N., Raji, F., Rezakazemi, M., & Younas, M. (2020). Juglone extraction from walnut (*Juglans regia* L.) green husk by supercritical CO₂: Process optimization using Taguchi method. *Journal of Environmental Chemical Engineering*, 8(3), Article 103776. <https://doi.org/10.1016/j.jece.2020.103776>
- Ribeiro, J., Lopes, H., Queijo, L., & Figueiredo, D. (2017). Optimization of cutting parameters to minimize the surface roughness in the end milling process using the Taguchi method. *Periodica Polytechnica Mechanical Engineering*, 61(1), 30-35. <https://doi.org/10.3311/PPme.9114>
- Rizkiyah, D. N., Putra, N. R., Idham, Z., Aziz, A. H. A., Che Yunus, M. A., Veza, I., Irianto, Mamah, S. C., & Qomariyah, L. (2023). Recovery of anthocyanins from hibiscus sabdariffa L. Using a combination of supercritical carbon dioxide extraction and subcritical water extraction. *Processes*, 11(3), Article 751. <https://doi.org/10.3390/pr11030751>
- Rizkiyah, D. N., Putra, N. R., Idham, Z., Che Yunus, M. A., Veza, I., Harny, I., Syahlani, N., Aziz, A. H. A. (2022). Optimization of red pigment anthocyanin recovery from hibiscus sabdariffa by subcritical water extraction. *Processes*, 10(12), Article 2635. <https://doi.org/10.3390/pr10122635>
- Rosli, N. R., Daud, W. R. W., Md Jahim, J., & Markom, M. (2007). Supercritical fluid extraction of citronella (*Cymbopogon nardus*) essential oil: Modelling the effects of varying operating temperature and pressure. *Malaysian Journal of Chemical Engineering*, 1, 143-152.
- Salaria, D., Rolta, R., Sharma, N., Dev, K., Sourirajan, A., & Kumar, V. (2020). *In silico* and *in vitro* evaluation of the anti-inflammatory and antioxidant potential of *Cymbopogon citratus* from North-western Himalayas. *BioRxiv*. <https://doi.org/10.1101/2020.05.31.124982>
- Salea, R., Hiendrawan, S., Subroto, E., Veriansyah, B., & Tjandrawinata, R. R. (2018). Supercritical carbon dioxide extraction of citronella oil from cymbopogon winterianus using taguchi orthogonal array design. *International Journal of Applied Pharmaceutics*, 10(6), 147-151. <https://doi.org/10.22159/ijap.2018v10i6.28880>

- Sarah, M., Ardiansyah, D., Misran, E., & Madinah, I. (2023). Extraction of citronella oil from lemongrass (*Cymbopogon winterianus*) by sequential ultrasonic and microwave-assisted hydro-distillation. *Alexandria Engineering Journal*, 70, 569-583. <https://doi.org/10.1016/j.aej.2023.03.019>
- Sathasivam, R., Muthuraman, M. S., & Park, S. U. (2022). Intensification of supercritical fluid in the extraction of flavonoids: A comprehensive review. *Physiological and Molecular Plant Pathology*, 118, Article 101815. <https://doi.org/10.1016/j.pmpp.2022.101815>
- Silva, C. F., Moura, F. C., Mendes, M. F., & Pessoa, F. L. P. (2011). Extraction of citronella (*Cymbopogon nardus*) essential oil using supercritical CO₂: Experimental data and mathematical modeling. *Brazilian Journal of Chemical Engineering*, 28(2), 343-350. <https://doi.org/10.1590/S0104-66322011000200019>
- Silva, S. G., de Oliveira, M. S., Cruz, J. N., da Costa, W. A., da Silva, S. H. M., Maia, A. A. B., de Sousa, R. L., Junior R. F. C., & de Aguiar Andrade, E. H. (2021). Supercritical CO₂ extraction to obtain *Lippia thymoides* Mart. & Schauer (Verbenaceae) essential oil rich in thymol and evaluation of its antimicrobial activity. *The Journal of Supercritical Fluids*, 168, Article 105064. <https://doi.org/10.1016/j.supflu.2020.105064>
- Sinha, S., Biswas, D., & Mukherjee, A. (2011). Antigenotoxic and antioxidant activities of palmarosa and citronella essential oils. *Journal of Ethnopharmacology*, 137(3), 1521-1527. <https://doi.org/10.1016/j.jep.2011.08.046>
- Snyder, J., Friedrich, J., & Christianson, D. (1984). Effect of moisture and particle size on the extractability of oils from seeds with supercritical CO₂. *Journal of the American Oil Chemists' Society*, 61(12), 1851-1856. <https://doi.org/10.1007/BF02540816>
- Sodeifian, G., Ardestani, N. S., Sajadian, S. A., & Moghadamian, K. (2018). Properties of *Portulaca oleracea* seed oil via supercritical fluid extraction: Experimental and optimization. *The Journal of Supercritical Fluids*, 135, 34-44. <https://doi.org/10.1016/j.supflu.2017.12.026>
- Sodeifian, G., Sajadian, S. A., & Honarvar, B. (2018). Mathematical modelling for extraction of oil from *Dracocephalum kotschyi* seeds in supercritical carbon dioxide. *Natural Product Research*, 32(7), 795-803. <https://doi.org/10.1080/14786419.2017.1361954>
- Sodeifian, G., Ardestani, N. S., Sajadian, S. A., & Ghorbandoost, S. (2016). Application of supercritical carbon dioxide to extract essential oil from *Cleome coluteoides* Boiss: experimental, response surface and grey wolf optimization methodology. *The Journal of Supercritical Fluids*, 114, 55-63. <https://doi.org/10.1016/j.supflu.2016.04.006>
- Sodeifian, G., Sajadian, S. A., & Ardestani, N. S. (2016). Optimization of essential oil extraction from *Launaea acanthodes* Boiss: Utilization of supercritical carbon dioxide and cosolvent. *The Journal of Supercritical Fluids*, 116, 46-56. <https://doi.org/10.1016/j.supflu.2016.05.015>
- Sodeifian, G., Sajadian, S. A., & Saadati Ardestani, N. (2017). Supercritical fluid extraction of omega-3 from *Dracocephalum kotschyi* seed oil: Process optimization and oil properties. *The Journal of Supercritical Fluids*, 119, 139-149. <https://doi.org/10.1016/j.supflu.2016.08.019>
- Sodeifian, G., & Usefi, M. M. B. (2023). Solubility, Extraction, and nanoparticles production in supercritical carbon dioxide: A mini-review. *ChemBioEng Reviews*, 10(2), 133-166. <https://doi.org/10.1002/cben.202200020>

- Soh, S. H., Agarwal, S., Jain, A., Lee, L. Y., Chin, S. K., & Jayaraman, S. (2019). Mathematical modeling of mass transfer in supercritical fluid extraction of patchouli oil. *Engineering Reports*, 1(4), Article e12051. <https://doi.org/10.1002/eng2.12051>
- Sreenath, H. L., & Jagadishchandra, K. S. (2012). *Cymbopogon spreng* (Aromatic Grasses): In vitro culture, regeneration, and the production. In Y. P. S. Bajaj (Ed.), *Biotechnolog in Agriculture and Forestry 15: Medicinal and Aromatic Plants III* (pp. 211-234). Springer-Verlag.
- Timung, R., Barik, C. R., Purohit, S., & Goud, V. V. (2016). Composition and anti-bacterial activity analysis of citronella oil obtained by hydrodistillation: Process optimization study. *Industrial Crops and Products*, 94, 178-188. <https://doi.org/10.1016/j.indcrop.2016.08.021>
- Tyagi, B. K. (2016). Advances in vector mosquito control technologies, with particular reference to herbal products. In V. Veer & R. Gopalakrishnan (Eds.), *Herbal Insecticides, Repellents and Biomedicines: Effectiveness and Commercialization* (pp. 1-9). Springer. https://doi.org/10.1007/978-81-322-2704-5_1
- Uwineza, P. A., & Waśkiewicz, A. (2020). Recent advances in supercritical fluid extraction of natural bioactive compounds from natural plant materials. *Molecules*, 25(17), Article 3847. <https://doi.org/10.3390/molecules25173847>
- Wang, Q., Zhang, X., Cui, D., Bai, J., Wang, Z., Xu, F., & Wang, Z. (2023). Advances in supercritical water gasification of lignocellulosic biomass for hydrogen production. *Journal of Analytical and Applied Pyrolysis*, 170, Article 105934. <https://doi.org/10.1016/j.jaap.2023.105934>
- Wany, A., Jha, S., Nigam, V. K., & Pandey, D. M. (2013). Chemical analysis and therapeutic uses of citronella oil from *Cymbopogon winterianus*: A short review. *International Journal of Advanced Research*, 1(6), 504-521.
- Weng, D. C. J., Latip, J., Hasbullah, S. A., & Sastrohamidjojo, H. (2015). Optimal extraction and evaluation on the oil content of citronella oil extracted from *Cymbopogon nardus*. *Malaysian Journal of Analytical Sciences*, 19(1), 71-76.
- Wijesekera, R. O., Jayewardene, A. L., & Fonseka, B. D. (1973). Varietal differences in the constituents of citronella oil. *Phytochemistry*, 12(11), 2697-2704. [https://doi.org/10.1016/0031-9422\(73\)85083-6](https://doi.org/10.1016/0031-9422(73)85083-6)
- Wu, H., Li, J., Jia, Y., Xiao, Z., Li, P., Xie, Y., Zhang, A., Liu, R., Ren, Z., Zhao, M., Zeng, C., & Li, C. (2019). Essential oil extracted from *Cymbopogon citronella* leaves by supercritical carbon dioxide: Antioxidant and antimicrobial activities. *Journal of Analytical Methods in Chemistry*, 2019, Article 8192439. <https://doi.org/10.1155/2019/8192439>
- Yousefi, M., Rahimi-Nasrabadi, M., Pourmortazavi, S. M., Wysokowski, M., Jesionowski, T., Ehrlich, H., & Mirsadeghi, S. (2019). Supercritical fluid extraction of essential oils. *TrAC Trends in Analytical Chemistry*, 118, 182-193. <https://doi.org/10.1016/j.trac.2019.05.038>
- Zhou, T., Wang, Y., Zheng, H., Du, B., & Zheng, L. (2022). Sustainable and eco-friendly strategies for polyester-cotton blends dyeing in supercritical CO₂. *Journal of CO₂ Utilization*, 55, Article 101816. <https://doi.org/10.1016/j.jcou.2021.101816>

An Empirical Evaluation of Adapting Hybrid Parameters for CNN-based Sentiment Analysis

Mohammed Maree*, Mujahed Eleyat and Shatha Rabayah

Faculty of Engineering and Information Technology, Arab American University, P.O Box 240, Jenin, Palestine

ABSTRACT

Sentiment analysis aims to understand human emotions and perceptions through various machine-learning pipelines. However, feature engineering and inherent semantic gap constraints often hinder conventional machine learning techniques and limit their accuracy. Newer neural network models have been proposed to automate the feature learning process and enrich learned features with word contextual embeddings to identify their semantic orientations to address these challenges. This article aims to analyze the influence of different factors on the accuracy of sentiment classification predictions by employing Feedforward and Convolutional Neural Networks. To assess the performance of these neural network models, we utilize four diverse real-world datasets, namely 50,000 movie reviews from IMDB, 10,662 sentences from LightSide Movie_Reviews, 300 public movie reviews, and 1,600,000 tweets extracted from Sentiment140. We experimentally investigate the impact of exploiting GloVe word embeddings on enriching feature vectors extracted from sentiment sentences. Findings indicate that using larger dimensions of GloVe word embeddings increases the sentiment classification accuracy. In particular, results demonstrate that the accuracy of the CNN with a larger feature map, a smaller filter window, and the ReLU activation function in the convolutional layer was 90.56% using the IMDB dataset. In comparison, it was 80.73% and 77.64% using the sentiment140 and the 300 sentiment sentences dataset, respectively. However, it is worth mentioning that, with large-size sentiment sentences (LightSide's Movie Reviews) and using the same parameters, only a 64.44% level of accuracy was achieved.

ARTICLE INFO

Article history:

Received: 27 June 2023

Accepted: 05 December 2023

Published: 01 April 2024

DOI: <https://doi.org/10.47836/pjst.32.3.05>

E-mail addresses:

mohammed.maree@aaup.edu (Mohammed Maree)

mujahed.eleyat@aaup.edu (Mujahed Eleyat)

shatha.rabaia@student.aaup.edu (Shatha Rabaia)

* Corresponding author

Keywords: CNN, deep learning, GloVe word embedding, machine learning, sentiment classification

INTRODUCTION

In the Natural Language Processing (NLP) domain, Sentiment Analysis (SA) has gained significant attention (Hussein, 2018; Maree & Eleyat, 2020; Wang et al., 2018). SA is a classification task that analyzes textual sentences to classify their orientations (i.e., positive, negative or neutral). For individuals and organizations alike, SA provides an important source of valuable information. On the one hand, individuals can use SA to comprehend consumer opinions about products they want to purchase. On the other hand, an organization can use SA to visualize consumer opinions and make informed future decisions (Maree & Eleyat, 2020). Generally, two main SA approaches vary in strengths, weaknesses, and accuracy: (1) Lexicon-based and (2) Machine Learning-based SA models. Using sentiment lexicons comprising word sets paired with their respective sentiment polarities has gained prominence in lexicon-based approaches. Examples of such lexicons include SentiWordNet, SenticNet, and HowNet (Maree & Eleyat, 2020; Shaukat et al., 2020). In contrast, machine learning-based approaches rely on leveraging training samples to make predictions regarding the polarity of opinions. We recommend referring to the following references to delve deeper into these approaches and gain a comprehensive understanding (Yang & Chen, 2017).

Traditional methods, including Support Vector Machine (SVM), Maximum Entropy (ME), and Naïve Bayes (NB) classifiers, are commonly employed for sentiment analysis. These classifiers are often combined with intricate feature extraction techniques to achieve accurate predictions. Among the main limitations of these approaches are the incompleteness of the training data, lack of semantic information about the processed text, domain dependence, and huge computational cost. Newer deep-learning models have been proposed to address these limitations (Stojanovski et al., 2015; Vielma et al., 2020; Yenter & Verma, 2017). Among the main goals in this context are automating the feature learning process and incorporating semantic dimensions through word embedding techniques. We recommend reading a recent survey on the topic for more details on the main advantages of deep learning models (Zhang et al., 2018). An important aspect that we would like to highlight in the context of utilizing deep learning is the ability to couple discrete representations of text using One-hot vectors and distributional representations of words using Global Vectors (GloVe) or Word2Vec.

Starting from this position, we aim to experimentally investigate the impact of exploiting GloVe word embeddings on enriching feature vectors extracted from sentiment sentences and, subsequently, its impact on the quality of the utilized sentiment classifiers, namely FNN and CNN.

In particular, we summarize our contributions to this work as follows:

- Exploring and identifying the influence of various factors on the accuracy of sentiment classification predictions by employing ANN and CNN architectures, utilizing four diverse real-world datasets.

- We experimentally investigate the impact of exploiting GloVe word embeddings on enriching feature vectors extracted from sentiment sentences. Findings demonstrate that using larger dimensions of GloVe word embeddings increases the sentiment classification accuracy.

MATERIALS AND METHOD

Sentiment analysis is a classification problem that aims to identify, extract, and analyze the sentiment orientation of sentences (Hussein, 2018; Qaisar, 2020; Zhang et al., 2018). Among the commonly quoted definitions of the term Sentiment Analysis (SA) is highlighted by Alam and Yao (2019), where the authors define SA as “*a computational process which identifies and categorizes an opinion in a piece of text that expresses the positive, negative, or neutral attitude of a writer towards a particular product, event or personality*” (p. 321). Several approaches have been developed over the past years for analyzing sentiments. Among these approaches is the lexicon-based approach, which uses a dictionary that includes words with their polarities. This approach remains inaccurate as it depends on the word’s polarity to determine the text’s polarity (Maree & Eleyat, 2020). It can be attributed to the fact that the prior polarity of a word does not necessarily reflect its contextual polarity (Wilson et al., 2009). Recently, researchers witnessed a growing interest in developing machine-learning techniques for SA purposes. Some research works focused on using traditional machine learning techniques such as support vector machines SVMs, Maximum Entropy ME and Naïve Bayes NB models.

Horakova (2015) analyzed the sentiments of the text in the Czech language. The developed application collects data according to several criteria and then classifies user-generated reviews using machine learning. This application consists of three modules, each performing a specific task. The first module collects the data, and the second module pre-processes the raw data collected by the first module, including stop word removal and lemmatization. The third module uses machine learning to classify cleaned texts from the second module. The authors used Selenium Web Driver technology to collect the data, and they used the MorphoDiTa tool to perform morphological analysis to prepare the data for the classification stage. R programming language, namely RTextTools, was employed for the text classification task. Specifically, the authors employed the NB, SVM, Maximum Entropy, Decision Trees and Random Forest to classify sentiment sentences. The results showed the superiority of the Maximum Entropy and Random Forest classifiers over the rest of the classifiers when the lemmatization technique was used as part of the pre-processing pipeline. Despite this achievement, it is important to point out that traditional machine-learning techniques cannot learn features independently. In addition, only relying on the textual content of sentiment sentences will suffer from two main inherent problems.

First, latent semantic dimensions in texts will remain undiscovered and hidden under synonymy, polysemy and other semantically related dimensions, such as hypernyms and meronyms. Second, the dependence of traditional machine learning models on the training data and their domain will make them impractical for capturing the sentiment orientations of sentences in other domains of interest. In an attempt to address these limitations, researchers have recently shifted their focus to analyzing sentiments using deep learning techniques. For instance, Yang and Chen (2017) compared a variety of popular machine learning techniques for sentiment analysis: SVM, NB, ME and Artificial Neural Network method. Researchers discussed these methods in detail, provided an approximate comparison between them, and presented a set of challenges faced by that researchers in the field of sentiment analysis. Specifically, the researchers demonstrated that the NB method and neural networks are highly accurate, whereas the SVM and ME have lower accuracy.

However, despite the improvements introduced by newer deep learning methods, the authors still believe that one of the biggest challenges in this field is to study the various neural networks in depth and determine which features are most effective in sentiment analysis. In the same line of research, many researchers are focusing their efforts on the use of different neural networks, such as feedforward neural networks (FNN), convolutional neural networks (CNN), and recurrent neural networks (RNN) for SA purposes (Rusandi et al., 2021). In general, deep learning approaches follow two main phases: (1) the first phase focuses on word embedding (feature vectorization), and (2) the second phase is used for learning and classification of sentiment orientation of sentences. Stojanovski et al. (2015) attempted to study the importance of pre-trained word vectors to extract sentiments from a dataset of sentences obtained from Twitter. They proposed a deep convolutional neural network with one convolutional layer and two fully connected layers with dropout. A sigmoid activation function was used for the first layer, and a tangent activation function was used for the second layer. Lastly, the softmax activation function was applied to the output layer. The dropout rate that was used ranged between 0.7 and 0.5, respectively. The researchers generated word vectors using three pre-trained word embedding models that are word2vec, global vectors for word representation GloVe, and semantic-specific word embedding (SSWE).

The authors have used three sets from the SemEval Task 10 challenge for training and testing. A set of parameters was used to determine their effect on sentiment analysis accuracy. These parameters are filter window size, number of hidden units, feature maps size, patch size and activation function in the convolutional layer. Experiments showed that using hyperbolic activated tangent units in the convolutional layer, 500 hidden units in the first hidden layer, and 300 hidden units in the second hidden layer, and increasing the size of the feature maps to 300 improved the performance. Further, results indicated that the GloVe word embedding outperformed all other word embedding methods.

A traditional feedforward neural network extracts only the current time information and discards the useful information transmitted in the spatial and time arrangement of the data. To tackle this problem, researchers developed recurrent neural networks (RNNs). However, this type of network faces problems such as gradient explosion and gradient vanishing. As a result, researchers developed LSTM and GRU networks. LSTM can remember long-term information, and its sequential structure is more sophisticated and intelligent than RNN, while GRU is characterized by its high efficiency. Ni and Cao (2020) suggested a model combining LSTM and GRU to extract sentiment polarities. This study used pre-trained word embedding models to create word vectors. Researchers trained and tested their model using both IMDB and Review_Polarity datasets.

Three basic stages make up the model: (1) embedding words layer, during which text is converted into vectors in space using the GloVe model; (2) the output of the first stage is passed to the neural network layer consisting of 64 LSTM units and 64 GRU units in the second stage, and (3) the final stage is the output layer. The results showed that the proposed model performed better than the RNN model in accuracy. Cao et al. (2020) proposed a text sentiment classification based on the Attention Mechanism and Decomposition Convolutional Neural Network model. Parallel Decomposition Convolutional Neural Network (DCNN) was utilized to obtain comprehensive text features. An attention mechanism was integrated to extract important feature information and improve text sentiment classification. Experimental findings indicated that the proposed model performs better than the single-channel model, and the use of the Decomposed Convolutional Neural Network is better than the traditional Convolutional Neural Network. However, it may still be argued that the utilized combined approach may be hindered by high computational costs, especially when handling large-scale datasets. Another model used Bidirectional Encoder Representations from Transformers (BERT) to transform the words in the input sequence into a vector representation (He, 2023). A CNN was used to extract features where the output vector of BERT was convolved along the dimension of sequence length to extract the features in the sequence.

Bidirectional Long Short-Term Memory (BiLSTM) was used to encode the features and capture the long-term dependencies in the sequence. Accordingly, the results of the BiLSTM output were fed into a fully connected layer to make classification predictions. As discussed by the author, the proposed model has produced more precise sentiment classification results than conventional BERT, BiLSTM, CNN, and BERT-BiLSTM models. However, as we argued earlier, the complexity of such SA models can be at a very high computational cost, namely with large-scale datasets. In addition, comparable SA quality can be obtained using conventional models, which can be less complex on the one hand and more efficient on the other.

Identifying sentiment orientation in a given sentence involves several phases, beginning with data collection and pre-processing. It is followed by word vectorization, neural network training, and performance evaluation.

Dataset Collection and Pre-processing

Researchers often rely on Twitter and social media sites to gather datasets and sentiment sentences to test their approaches (Krouska et al., 2016). In our experiments, we used four datasets: the IMDB¹ dataset, which contains 10,662 movie reviews, and the Sentiment140² dataset, which contains 1,600,000 tweets collected from Twitter API. Both IMDB and Sentiment140 datasets are publicly available on Kaggle. Additionally, we collected the LightSide dataset consisting of 10,662 samples and 300 generic movie reviews from Twitter. Data collected is raw data that is not ready for use because it may contain unwanted characters, symbols and spelling mistakes (Haddi et al., 2013). In order to make raw data ready for use, it must be prepared by removing unwanted characters, such as numbers, white spaces, hashtags, punctuations and URLs.

Word Embedding

At this stage, the words are converted into vectors in space. The mathematical representations of the texts contribute greatly to the accuracy of the neural network results. Two main approaches can be used to represent word embeddings: discrete representations using One-hot vectors and distributional representations using Global Vectors (GloVe) or Word2Vec (Ni & Cao, 2020; Yang & Chen, 2017). There are many drawbacks to using One-hot vectors, including their extreme sparsity and huge feature vector size. It consumes enormous memory space requirements and makes algorithms more complex, in addition to the inability to show contextual connections among words. Researchers proposed an approach that uses dense vectors to represent features to overcome these limitations. Words are represented as n-dimensional dense vectors using the distributed approach. Where similar vectors represent similar words, relying on this approach, researchers used different approaches to represent words using Zhang and Wallace (2015), where they used random initialization for the word vectors. Then, they allowed the model to learn the most accurate representation of the words. However, this approach was ineffective for handling large-scale sentiment sentence datasets. Researchers recently utilized unsupervised learning to learn word representations from large text corpora (Dos-Santos & Gatti, 2014). This approach provides pre-trained vectors that can be used to perform various NLP tasks. Word2Vec and GloVe pre-trained embeddings are the most efficient and effective ways to convert

¹ <https://www.kaggle.com/lakshmi25npathi/imdb-dataset-of-50k-movie-reviews/>

² <https://www.kaggle.com/kazanova/sentiment140/>

words into corresponding dense vectors. In our experiments, we used GloVe³ because of its high scalability in speeding up parameter training (Ni & Cao, 2020). Once the words are converted to vectors, they are ready to be passed to the neural network.

Artificial Neural Networks

An artificial neural network can be defined as a mathematical model for the simulation of a network of biological neurons (e.g., human nervous system). It simulates different aspects related to the behavior and capacity of the human brain. Neural networks consist of basic units of computation called nodes or neurons. A neural network consists of a set of layers, each layer containing a set of nodes. Terminal nodes receive data (x). Each entry has a weight (w) determined according to the importance of the entry compared to other inputs. Internal nodes implement an activation function f like (sigmoid, ReLU & tanh) on the weighted sum of its inputs.

$$y = f(x_1 \cdot w_1 + x_2 \cdot w_2 + b) \quad (1)$$

Equation 1 illustrates how value Y is computed as the neuron's output. In the hidden layers, each neuron receives weighted inputs plus bias from each neuron in the previous layer, as shown by Equation 2.

$$O_i = \sum_{k=1}^{N_{j-1}} X_k^{j-1} W_{k,i} - b_k \quad (2)$$

where X_k^{j-1} denotes the input from k -th node in the j -th layer, $W_{k,i}$ is the weight of the link between node k and all the nodes in the previous layers, and b is the bias.

The activation function f plays a crucial role as a non-linear function, introducing non-linearity into the output of neurons. It is significant because real-world data often exhibits non-linear characteristics, necessitating neurons to learn and represent non-linear patterns. Many activation functions are used in neural networks, and perhaps the most commonly used are sigmoid, hyperbolic tangent, and Rectified Linear Unit ReLU activation functions. A sigmoid activation function adjusts input value into a 1 to 0 range. At the same time, the tangent function adjusts the input values into the range $[1, -1]$. The ReLU activation function replaces negative values with zero. b a.k.a. the bias represents a constant value that allows the shift of the activation function to better match the prediction with the data.

Based on Equation 2 above, O_i is passed along to an activation function to produce the node output, calculated as $Y_i = f(O_i)$. The sigmoidal function is the most commonly used activation function, defined as Equation 3.

³ <https://nlp.stanford.edu/projects/glove/>

$$f(O_i) = \frac{1}{1 + e^{-z_i}} \quad (3)$$

Feedforward Neural Network (FNN)

The feedforward neural network is the simplest type of artificial neural network. It consists of several neurons arranged in layers connected by connections with weights attached. A feedforward neural network has three types of layers: input, hidden, and output. In the input layer, input nodes receive input data and pass it on to the next layer without performing arithmetic operations. Hidden layers are behind input layers, so there is no direct connection to the data source. This layer forms a link between the input layer and the output layer. It performs calculations on the data and passes it to the output layer. A neural network may or may not have hidden layers. FFNs with hidden layers are called Multi-Layer Perceptron (MLP), while a network without any hidden layers is known as a Single Layer Perceptron. In a feedforward neural network containing hidden layers, data passes through them in one direction (forward). The output nodes in the output layer perform arithmetic operations on the data they receive from the network and then pass output to the outside world.

Convolutional Neural Networks

The Convolutional Neural Network (CNN) is among sentiment analysis's most widely used neural networks. Using CNNs automates feature generation, saving training time required by other conventional machine learning. CNNs consist of several layers: convolution, pooling and fully connected Multi-Layer Perceptron (MLP). The first layer in this architecture is a convolutional layer. The output of this layer is called a feature map. This layer uses a kernel, which acts as a sliding window over the feature map, where each piece of data in the convolutional layer is represented as one unit in the feature map. This layer acts as a feature extractor. By applying the max feature or averaging adjacent features on the feature map, the pooling layer reduces them to a single unit. The output of this layer is passed into a feedforward neural network. The general principle of neural networks is learning from errors, so the principle of neural networks can be summarized as follows: first, receiving data, making predictions, comparing the predictions with the real values, then adjusting the weights to predict with greater accuracy next time.

These steps lead to the neural network being trained. The next and final step is testing the model. To further explain the application of CNN in the context of our work, we first map tokens in sentences to their corresponding word vectors from a lookup table obtained based on GloVe term vector representations $L \in R^{k \times |V|}$, where k is the dimension of the word vectors, and V is a vocabulary of the words. Each token is projected to a vector $w_i \in R^k$. Consequently, a sentence concatenates the word embeddings $x = \{w_1, w_2, \dots, w_n\}$. After that, the convolution operation $x_i = h(W_c \cdot x_{i:i+h-1} + b_c)$ using windows of h sizes is performed

on each sentence to produce feature maps. Where $h(\cdot)$ is the hyperbolic tangent function and $x_{i:i+h-1}$ is the concatenation of word vectors from position i to position $i + h - 1$.

RESULTS AND DISCUSSION

For conducting the experiments, we employed the Python programming language to implement the proposed Neural Networks and utilized them to process the four publicly available datasets (Table 1). These datasets include LightSide's movie reviews dataset, a sentiment sentence dataset provided by Maree and Eleyat (2020), sentiment140, and the IMDB dataset. Below, we provide essential information about each of the datasets used.

Table 1
Statistics about the used sentiment review datasets

Dataset	Sentiment Sentences	Positive	Negative
IMDB	50,000	25,000	25,000
Sentiment Sentences from Reference(Maree & Eleyat, 2020)	10,662	5,331	5,331
LightSide's Movie Reviews	3000	150	150
Sentiment 140	1,600,000	800,000	800,000

After cleaning the data, the HTML tags, punctuation, numbers, and all unnecessary characters and white spaces were removed. It becomes ready for analysis. We have created a word-to-index dictionary using the tokenizer class in the Keras library. Each word in the corpus is a key, while a corresponding unique index is the value. We then loaded the GloVe word embeddings and created a dictionary to contain words as keys and their corresponding embedding lists as values. Creating the embedding matrix is the next step. Each row number corresponds to an index of words in the corpus. In addition, the matrix columns contain GloVe word embeddings for words in our corpus. Such word embeddings support four different vector representations, represented by four-dimension classes: 50, 100, 200 and 300. Thus, by using GloVe pertained model in our experiments, we have generated vectors using these four different representations. We classified the reviews using two types of neural networks. These are FNN and CNN.

Then, we have the training and testing phase using neural networks. Each dataset is broken down into a training set and a testing set. The training set makes up 70% of the total dataset. The testing set makes up the remaining 30%. Our experiments used FFNs with zero hidden and one, two, and three hidden layers. For CNNs, we have used it with different feature map sizes, filter window sizes, and activation functions in the convolution layer. After the convolution layer, we have a max pooling layer, followed by FFNs with a zero hidden layer, one hidden layer, two hidden layers, or three hidden layers. Finally, we have used the accuracy metric to compare these different cases. Tables 2 and 3 illustrate the FNN and CNN network parameters, respectively. In our experiments, we studied the effect of each of the

parameters listed below on FNN and CNN network classification accuracy.

- Using multidimensional vector representations of a word.
- Using different numbers of hidden layers.
- Utilizing different activation functions in hidden layers.
- Utilizing multiple activation functions in hidden layers.
- Using different activation functions in the convolution layer.
- Changing feature map sizes used in the convolution layer.
- Changing filter window sizes used in the convolution layer.

Tables 4 to 8 illustrate the variations in the accuracy results when utilizing each of the abovementioned parameters.

Table 2
Used FNN parameters

FNN parameters	
First hidden layer	300 unit
Dropout	0.3
Second hidden layer	50 unit
Dropout	0.2
Third hidden layer	10 unit
Dropout	0.2
Optimizer	Adam
Loss function	Binary-cross entropy
Activation function for the output layer	Sigmoid
Batch size	128
Epochs	6

Table 3
Used convolutional layer parameters

Convolutional layer parameters	
Filters	128, 384
Window size	3, 5
Activation function	Sigmoid, ReLU

Table 4
Experimental results using FNN and CNN without hidden layer

No hidden layers / epochs=6			
Input vector dimensions	Dataset	FNN	CNN 128/ ReLU
300	IMDB	76.33%	89.48%
	sentiment_sentences	70.60%	76.73%
	MovieReviews	51.11%4	52.22%
	Sentiment 140	72.75%	79.63%
200	IMDB	76.04%	89.10%
	sentiment_sentences	70.07%	75.45%7
	MovieReviews	53.33%6	51.11%4
	Sentiment 140	72.03%5	79.31%
100	IMDB	71.60%	88.07%
	sentiment_sentences	68.26%	74.92%
	MovieReviews	53.33%	51.11%
	Sentiment 140	70.49%	79.27%
50	IMDB	69.20%	85.94%
	sentiment_sentences	66.51	71.85%
	MovieReviews	57.77%	58.88%
	Sentiment 140	67.69%	77.21%

Table 5

Experimental results using CNN without hidden layer, using different feature maps, different filter sizes and different activation functions

Input vector dimensions	Dataset	CNN 128/ ReLU	CNN 384/ sigmoid/5	CNN 384/ ReLU/5	CNN 384/ ReLU/3
300	IMDB	89.48%	87.53%	90.20%	90.56%
	sentiment_sentences	76.73%	76.51%	76.76%	77.64%
	MovieReviews	52.22%	61.11%	63.33%	63.33%
	Sentiment 140	79.63%	79.24%	79.09%	79.98%

Table 6

Experimental results using FNN and CNN with one hidden layer

One hidden layer / epochs=6 /Dimensions = 300					
Activation function	Dataset	FNN	CNN 384/ sig/5	CNN 384/ ReLU/5	CNN 384/ ReLU/3
ReLU	IMDB	76.66%	89.50%	89.266%	88.48%
	sentiment_sentences	69.07%	77.11%	77.20%	77.11%6
	MovieReviews	46.66%	46.66%7	53.33%	53.33%
	Sentiment 140	75.68%	79.62%	79.72%	80.73%4
Sig	IMDB	77.14%	89.25%	89.72%	89.96%
	sentiment_sentences	68.63%	75.95%	76.860%	75.10%
	MovieReviews	46.66%	53.33%	46.66%	46.66%
	Sentiment 140	75.97%	79.60%	79.75%	80.21%
Tanh	IMDB	76.53%	89.26%	89.11%	89.5%
	sentiment_sentences	68.48%	76.54%	76.39%	76.67292
	MovieReviews	48.88%	64.44%	46.66%	54.44%
	Sentiment 140	75.70%	78.96%	79.69%	80.37%

Table 7

Experimental results using FNN and CNN with two hidden layers

Two hidden layers / epochs=6 /Dimensions = 300					
Activation function	Dataset	FNN	CNN 384/ sig/5	CNN 384/ ReLU/5	CNN 384/ ReLU/3
ReLU	IMDB	76.04%	89.10%	86.92%	86.26%
	sentiment_sentences	68.60%	76.61%	75.10%	76.01%
	MovieReviews	47.77%	46.66%	46.66%	52.22%
	Sentiment 140	75.66%	79.56%	79.99%	80.21%
Sig	IMDB	76.36%	89.07%	89.08%	87.34%
	sentiment_sentences	68.07%	77.01%	76.89%	77.45%
	MovieReviews	51.11%	53.33%	53.33%	46.66%
	Sentiment 140	76.08%	79.60%	79.52%	80.36%

Table 7 (continue)

Two hidden layers / epochs=6 /Dimensions = 300					
Activation function	Dataset	FNN	CNN 384/ sig/5	CNN 384/ ReLU/5	CNN 384/ ReLU/3
Tanh	IMDB	74.06%	89.36%	87.20%	89.26%
	sentiment_sentences	67.44%	76.64%	76.26%	76.70%
	MovieReviews	50.00%	53.33%	62.22%	53.33%
	Sentiment 140	75.07%	79.38%	80.10%	80.53%
sig, ReLU	IMDB	76.32%	88.51%	88.71%	89.026%
	sentiment_sentences	68.29%	75.51%	75.39%	76.61%
	MovieReviews	53.33%	46.66%	53.33%	53.33%
	Sentiment 140	75.82%	78.89%	80.00%	80.53%
ReLU,sig	IMDB	75.40%	89.36%	89.00%	89.20%
	sentiment_sentences	69.85%	76.57%	76.17%	77.14%
	MovieReviews	53.33%	53.33%	60.00%	53.33%
	Sentiment 140	75.71%	79.59%	80.10%	80.46%

Table 8

Experimental results using FNN and CNN with three hidden layers

Three hidden layers with / epochs=6 /Dimensions = 300					
Activation function	Dataset	FNN	CNN 384/ sig/5	Cnn 384/ ReLU/5	CNN 384/ ReLU/3
ReLU	IMDB	75.28%	89.16%	88.56%	85.14%
	sentiment_sentences	67.54%	76.51%	75.54%	76.23%5
	MovieReviews	53.33%	53.33%	50.00%	47.77%
	Sentiment 140	75.87%	79.49%	79.54%	80.57%
Sig	IMDB	76.35%	89.11%	88.94%	88.43%
	sentiment_sentences	69.04%	76.11%	76.86%	74.92%
	MovieReviews	52.22%	46.66%	46.66%	46.66%
	Sentiment 140	76.04%	79.36%6	79.74%	80.69%
Tanh	IMDB	75.93%	89.46%	88.96%	88.15%
	sentiment_sentences	67.54%	76.14134	74.67%	76.07%6
	MovieReviews	48.88%	46.66%	53.33%	46.66%
	Sentiment 140	75.06%	79.38%	79.75%	80.20%

Based on the results in Table 4, we notice that the accuracy increased when we used vectors of larger dimensions to represent the words. The highest classification accuracy was achieved when representing words using GloVe word embeddings with 300 dimensions. As a result, in our experiments, the rest of the runs were performed using GloVe word embeddings with 300 dimensions. As shown in Table 5, using the ReLU activation function in the convolution layer gives better results than using the sigmoid activation function. In

addition, the sentiment classification accuracy improved when bigger feature map sizes were used in the convolution layer. We obtained more accurate results in the convolutional layer when using feature maps with size 384 compared to those obtained using feature maps with size 128. Therefore, we used feature maps with size 384 in the convolutional layer in the rest of the experimental runs. Furthermore, we found that using a filter window with a smaller value improves the classification's accuracy, especially when using CNNs with zero hidden layers and one hidden layer.

As shown in Table 5, we obtained more accurate results when using a filter window with size 3 in the convolutional layer compared to using a filter window with size 5. Based on the results in Tables 6, 7 and 8, we notice that the FNN's classification accuracy was best when using sigmoid activation functions in the hidden layers. Nevertheless, the classification accuracy of the convolutional neural networks was better in most cases with the ReLU activation function in the hidden layers. As depicted in Table 7, using multiple activation functions in the hidden layers improves the classification accuracy. We obtained the best results using the ReLU activation function in the first hidden layer, followed by the Sigmoid activation function in the second hidden layer. Finally, according to the results, using FNN and CNN networks without hidden layers and one hidden layer produced more accurate results than using two and three hidden layers.

We obtained the best result using the FNN with the IMDB dataset (77.14%). In particular, we used one hidden layer with a sigmoid activation function and GloVe word embeddings with 300 dimensions. Considering the Sentiment Sentences dataset used by Maree and Eleyat (2020), we obtained the best result (70.60%) when using FNN without a hidden layer and GloVe word embeddings with 300 dimensions. We obtained the best result for the LightSide's Movie_Reviews dataset (57.77%) when we used FNN without a hidden layer and GloVe word embeddings with 50 dimensions. For Sentiment140, we obtained the best result (76.08%) when we used FNN with two hidden layers and a sigmoid activation function. Moreover, when we used CNN, all highly accurate results were obtained using a 384 feature filter with ReLU activation function and filter window with size 3 in the convolutional layer.

For the IMDB dataset, we obtained the best result (90.56%) when using CNN without a hidden layer and GloVe word embeddings with 300 dimensions. Considering the Sentiment Sentences dataset, we obtained the best result (77.64%) when we used CNN without a hidden layer and GloVe word embeddings with 300 dimensions. We obtained the best result for the LightSide's Movie_Reviews dataset (64.44%) using CNN flowed by FNN with one hidden layer with the tanh activation function. For Sentiment140, we obtained the best result (80.73%) when we used a convolutional layer flowed by FNN with one hidden layer with a ReLU activation function.

Comparison with Other SA Models

The results obtained using the IMDB dataset were compared with previous works conducted by Shaukat et al. (2020), Qaisar (2020), Vielma et al. (2020), and Yenter and Verma (2017). These researchers utilized different types of neural networks, including Long Short-Term Memory (LSTM), Single and Multi-branch CNN-Bidirectional LSTM, and CNN-LSTM. The respective results achieved by these researchers are presented in Table 9. As observed in Table 9, the LSTM network demonstrated superior performance to other neural network models, achieving an accuracy of 89.9%. Furthermore, our model surpasses the performance of similar models, with an accuracy of 90.56% (Table 9).

Table 9
Comparison with existing SA models

System	Employed Classifier	Accuracy
Our Result	CNN	90.56%
Sentiment analysis on IMDB using lexicon and neural networks (Shaukat et al., 2020)	lexicon and neural networks	86.67%
Sentiment Analysis of IMDB Movie Reviews Using Long Short-Term Memory (Qaisar, 2020)	Long Short-Term Memory	89.90%
Single and Multi-branch CNN-Bidirectional LSTM for IMDB Sentiment Analysis (Vielma et al., 2020)	Single and Multi-branch CNN-Bidirectional LSTM	89.54%
Deep CNN-LSTM with combined kernels from multiple branches for IMDB review sentiment analysis (Yenter & Verma, 2017)	CNN-LSTM	89.50%

CONCLUSION

Social networking sites and websites have become important platforms for individuals to express their opinions about products and services. Analyzing sentiments is one of the most important techniques to help analyze this large volume of comments. So that individuals and institutions can make informed decisions based on them. Thus, we see that researchers are interested in developing the various techniques used in sentiment analysis. It includes machine learning techniques based on neural networks. This paper employed two types of neural networks for sentiment analysis: the Convolutional neural network CNN and the feedforward neural network (FNN). We studied a set of variables in the neural network to determine how they affect sentiment classification accuracy. These variables include the number of hidden layers used in the network, the activation function used in these layers, the size of the feature maps, the size of the filter window, and the activation function used in the convolutional neural network. In addition, we used glove embedding for word vectorization, whereby we used the different representations supported by the glove.

To test our model, we used four data sets, which included 50,000 movie reviews, 10,662 sentences, 300 public movie reviews, and 1,600,000 tweets. Results show that GloVe word

embedding increases accuracy with a large word dimension. Moreover, we found that the convolutional neural network's accuracy improved with a larger feature map, a smaller filter window, and using ReLU activation functions. The neural network's classification accuracy was improved using multiple activation functions in the hidden layers. It is important to point out, however, that among the limitations of our current work are the incompleteness of the training data, lack of semantic information about the processed text, and the domain dependence of the training data utilized for training the SA model. As a future extension of our current work, we will consider comparing the current model with dynamic embeddings using transformer architectures such as the BERT model.

ACKNOWLEDGEMENT

The authors thank the Arab American University of Palestine for funding and support for the research work published based on this research project.

REFERENCES

- Alam, S., & Yao, N. (2019). The impact of preprocessing steps on the accuracy of machine learning algorithms in sentiment analysis. *Computational and Mathematical Organization Theory*, 25, 319-335. <https://doi.org/10.1007/s10588-018-9266-8>
- Cao, D., Huang, Y., Li, H., Zhao, X., Chen, H., & Fu, Y. (2020, August 25-27). *Text sentiment classification based on attention mechanism and decomposition convolutional neural network model*. [Paper presentation]. IEEE International Conference on Advances in Electrical Engineering and Computer Applications (AEECA), Dalian, China. <https://doi.org/10.1109/AEECA49918.2020.9213672>
- Dos-Santos, C., & Gatti, M. (2014, August 23-29). *Deep convolutional neural networks for sentiment analysis of short texts*. [Paper presentation]. Proceedings of COLING 2014, the 25th International Conference on Computational Linguistics: Technical Papers, Dublin, Ireland.
- Haddi, E., Liu, X., & Shi, Y. (2013). The role of text pre-processing in sentiment analysis. *Procedia Computer Science*, 17, 26-32. <https://doi.org/10.1016/j.procs.2013.05.005>
- He, Y. (2023, July 14-16). *BERT-CNN-BiLSTM: A Hybrid Deep Learning Model for Accurate Sentiment Analysis*. [Paper presentation]. IEEE 5th International Conference on Power, Intelligent Computing and Systems (ICPICS), Shenyang, China. <https://doi.org/10.1109/ICPICS58376.2023.10235335>
- Horakova, M. (2015). Sentiment analysis tool using machine learning. *Global Journal on Technology*, 2015(5), 195-204.
- Hussein, D. M. E. D. M. (2018). A survey on sentiment analysis challenges. *Journal of King Saud University - Engineering Sciences*, 30(4), 330-338. <https://doi.org/10.1016/j.jksues.2016.04.002>
- Krouska, A., Troussas, C., & Virvou, M. (2016, July 13-15). *The effect of preprocessing techniques on Twitter sentiment analysis*. [Paper presentation]. 7th International Conference on Information, Intelligence, Systems & Applications (IISA), Chalkidiki, Greece. <https://doi.org/10.1109/IISA.2016.7785373>

- Maree, M., & Eleyat, M. (2020). Semantic graph based term expansion for sentence-level sentiment analysis. *International Journal of Computing* 19(4), 647-655. <https://doi.org/10.47839/ijc.19.4.2000>
- Ni, R., & Cao, H. (2020, July 27-29). *Sentiment analysis based on GloVe and LSTM-GRU*. [Paper presentation]. 39th Chinese Control Conference (CCC), Shenyang, China. <https://doi.org/10.23919/CCC50068.2020.9188578>
- Qaisar, S. M. (2020, October 13-15). *Sentiment analysis of IMDb movie reviews using long short-term memory*. [Paper presentation]. 2nd International Conference on Computer and Information Sciences (ICCIS), Sakaka, Saudi Arabia. <https://doi.org/10.1109/ICCIS49240.2020.9257657>
- Rusandi, M. R., Sutoyo, E., & Widartha, V. P. (2021, November 3-4). *Convolutional neural network for predicting sentiment: Case study in tourism*. [Paper presentation]. Sixth International Conference on Informatics and Computing (ICIC), Jakarta, Indonesia.
- Shaukat, Z., Zulfikar, A. A., Xiao, C., Azeem, M., & Mahmood, T. (2020). Sentiment analysis on IMDB using lexicon and neural networks. *SN Applied Sciences*, 2(2), Article 148. <https://doi.org/10.1007/s42452-019-1926-x>
- Stojanovski, D., Strezoski, G., Madjarov, G., & Dimitrovski, I. (2015). Twitter sentiment analysis using deep convolutional neural network. In E. Onieva, I. Santos, E. Osaba, H. Quintian & E. Carchado (Eds.), *Hybrid Artificial Intelligence Systems* (pp. 726-737). Springer. https://doi.org/10.1007/978-3-319-19644-2_60
- Vielma, C., Verma, A., & Bein, D. (2020). Single and multibranch CNN-bidirectional LSTM for IMDb sentiment analysis. In S. Latifi. (Ed.), *17th International Conference on Information Technology–New Generations* (pp. 401-406). Springer. https://doi.org/10.1007/978-3-030-43020-7_53
- Wang, M., Chen, S., & He, L. (2018). Sentiment classification using neural networks with sentiment centroids. In D. Phung, V. S. Tseng, G. O. Webb, B. Ho, M. Ganji & L. Rashidi (Eds.), *Advances in Knowledge Discovery and Data Mining* (pp. 56-67). Springer. https://doi.org/10.1007/978-3-319-93034-3_5
- Wilson, T., Wiebe, J., & Hoffmann, P. (2009). Recognizing contextual polarity: An exploration of features for phrase-level sentiment analysis. *Computational Linguistics*, 35(3), 399-433. <https://doi.org/10.1162/coli.08-012-R1-06-90>
- Yang, P., & Chen, Y. (2017, December 15-17). *A survey on sentiment analysis by using machine learning methods*. [Paper presentation]. IEEE 2nd Information Technology, Networking, Electronic and Automation Control Conference (ITNEC), Chengdu, China. <https://doi.org/10.1109/ITNEC.2017.8284920>
- Yenter, A., & Verma, A. (2017, October 19-21). *Deep CNN-LSTM with combined kernels from multiple branches for IMDb review sentiment analysis*. [Paper presentation]. IEEE 8th Annual Ubiquitous Computing, Electronics and Mobile Communication Conference (UEMCON), New York, USA. <https://doi.org/10.1109/UEMCON.2017.8249013>
- Zhang, L., Wang, S., & Liu, B. (2018). Deep learning for sentiment analysis: A survey. *Wiley Interdisciplinary Reviews: Data Mining and Knowledge Discovery*, 8(4), Article e1253. <https://doi.org/https://doi.org/10.1002/widm.1253>
- Zhang, Y., & Wallace, B. (2015). *A Sensitivity Analysis of (and practitioners' guide to) Convolutional Neural Networks for Sentence Classification*. arXiv preprint arXiv:1510.03820. <https://doi.org/10.48550/arXiv.1510.03820>

Mathematical Modelling of Scission Electrospun Polystyrene Fibre by Ultrasonication Scission

Cheryl Rinai Raja^{1*}, Marini Sawawi¹, Shirley Johnathan Tanjong¹ and Nurliyana Truna²

¹Faculty of Engineering, Universiti Malaysia Sarawak, Jalan Datuk Mohammad Musa, Kota Samarahan, 94300, Sarawak, Malaysia

²Pusat Pengajian Pra Universiti, Kampus Timur, Universiti Malaysia Sarawak, Kota Samarahan, 94300, Sarawak, Malaysia

ABSTRACT

This study investigates the effects of time and diameter on the final scission length of the electrospun polystyrene (PS) fibres, whereby the fibres were ultrasonicated for 1, 2, 3, 4, and 8 minutes. The ultrasonic probe stimulates bubble cavitation followed by bubble implosion as scission occurs. Factors affecting the scissionability of the electrospun PS fibres are primarily the diameter of the fibre and the sonication run time. The scission final fibre length range is approximately 23.7 μm to 1.1 μm . SEM images show that the fibre breaks into shorter lengths as sonication run time increases. Conversely, fibre diameter exhibits a positive relationship with fibre length. The model gives an R-squared value of 0.44 and 0.59 for linear and non-linear regression, thus suggesting that the non-linear model provides a better fit for the data. The validation of the model is achieved by conducting a hypothesis test. Through hypothesis testing, the mean of the experimental average final length value and the predicted average fibre length from the regression model were not significant, indicating that the model can generally predict a relatively accurate average final fibre length value. The model derived from this study enables researchers to estimate the time required to sonicate the PS fibre (with a specific diameter) to achieve the short fibre length needed in their application. As

research progresses, refining the model and incorporating additional parameters will be essential to ensure the broad reliability and applicability of these models across a variety of practical contexts.

ARTICLE INFO

Article history:

Received: 27 June 2023

Accepted: 20 November 2023

Published: 01 April 2024

DOI: <https://doi.org/10.47836/pjst.32.3.06>

E-mail addresses:

cheryl.raja@gmail.com (Cheryl Rinai Raja)

smarini@unimas.my (Marini Sawawi)

jtshirley@unimas.my (Shirley Johnathan Tanjong)

tliyana@unimas.my (Nurliyana Truna)

* Corresponding author

Keywords: Electrospinning, mathematical modelling, polystyrene, regression, scission, ultrasonication

INTRODUCTION

The process of using electrostatic forces to produce synthetic fibres with diameters and lengths of the submicron scale (Doshi & Reneker, 1995) has piqued the interest of researchers over the past century, especially due to its wide range of applications. In this procedure, referred to as electrospinning, a high-voltage source is used to induce a certain polarity of charge into a polymer solution or melt, which is subsequently accelerated toward a collector of a different polarity (Subbiah et al., 2005). However, the electrospinning process is limited to producing only long, thin, continuous fibres with a limited range of applications compared to that of discontinuous, short electrospun fibres. Unlike the length, the diameter, as well as other characteristics of the electrospun fibre, can be manipulated by optimising the electrospinning parameters (Valizadeh & Farkhani, 2014).

The tailorable parameters include the type of solvents, solution concentration, collection rate, gap distance, applied voltage, drop height, and fibre orientation. These processing parameters will highly influence the characteristics of the electrospun nanofibers, such as fibre diameter (Khanlou et al., 2015), morphology (Megelski et al., 2002), porosity (Baker et al., 2008), mechanical properties (O'Connor et al., 2021), chemical composition (Lima et al., 2020) and uniformity (Zhang et al., 2021). Such characteristics require optimising these parameters to maximise their performance for specific applications. For instance, Zhang et al. (2021) reported that 1000rpm was the optimal rotational speed in creating electrospun PCL fibres with aligned topography, which would serve as a promising candidate for nerve guidance conduits (NGCs) and other tissue engineering applications. Furthermore, different solvents have also been reported by Maleki et al. (2013), where electrospun PLLA yarns produced had the highest tensile strength as well as Young's modulus and a higher elongation at break when using chloroform and dichloromethane respectively. However, producing short continuous fibres through electrospinning is impossible just by adjusting the parameters.

A secondary process is needed to produce the desired discontinuous short fibres (Luo et al., 2011). Such secondary process includes mechanical cutting (Thieme et al., 2011), ultra-violet (UV) cutting (Li et al., 2010), microtome cutting (Oksman et al., 2009), micro cutting under liquid nitrogen (Magill & Gunning, 1969), cryogenic milling (Morkavuk et al., 2018), ball milling (Hrabalova et al., 2011) as some of the less popular scission methods. One method which has been widely reported for the scission of carbon nanotubes or even electrospun nanofibers is by means of ultrasonication (Chew et al., 2011; Hennrich et al., 2007; Liu et al., 2017; Niemczyk-Soczynska et al., 2021; Pagani et al., 2012).

Ultrasonication is widely used in the dispersion of solutes, especially carbon nanotubes (Ahir et al., 2008; Kharissova & Kharisov, 2017). Studies employing the ultrasonication technique for exfoliating carbon nanotubes (CNTs) have reported scission as an unwanted

side effect (Stegen, 2014), which later garnered more attention from researchers. This technique allows for scission of the carbon nanotubes through the mechanism of bubble cavitation and implosion. When ultrasound is used to insonify a liquid medium, a sequence of compression and rarefaction cycles results, creating regions with high and low local pressures (Lucas et al., 2009). Existing gas nuclei expand as a result of the dissolved gas's desorption to create cavitation bubbles. High local temperatures and pressures are caused by these transient cavities, which first grow before rapidly collapsing in subsequent compression cycles. When cavitation bubbles collide close to an interface, liquid jets are expelled, causing an impact with a mechanical effect on the surrounding material (Ando, 1991; Sander et al., 2014; Tsochatzidis et al., 2001). The van der Waals forces and other nonbonding interactions between the nanofibers, which are essentially bound to one other through nonbonding interactions, can be broken by said impact. This approach offers a practical, adaptable, and eco-friendly fabrication technique for the large-scale production of short nanofibers.

Discontinuous short electrospun fibres are versatile and can be used for various applications such as scaffolds (Li et al., 2006) or carrier matrices in tissue engineering (Lannutti et al., 2007), drug delivery (Zeng et al., 2003), wound healing (Casper et al., 2005), filtration systems (Bortolassi et al., 2019), micro-electronic (Luzio et al., 2014) applications, fibre reinforcement (Chen et al., 2011) and many more (Bhardwaj & Kundu, 2010; Jiang et al., 2018; Schiffman & Schauer, 2008). Therefore, it is important to study the process of producing these electrospun short fibres.

Several works of literature discuss the theoretical process of the scission caused by the shear stress and strain forces imposed on the carbon nanotubes (CNTs) by the imploding bubble in ultrasonication (Ahir et al., 2008; Heller et al., 2004; Hennrich et al., 2007; Huang et al., 2009; Pagani et al., 2012; Stegen, 2014). While some of these were derived with comparison to the scission modelling of polymer fibres whereby the fractures were deemed non-random as the point of scission typically occurs at the centre of mass (Kuijpers et al., 2004; Price & Smith, 1991), another study have discussed the degradation of polymer fibres with respect to time (Van Der Hoff & Glynn, 1974). Through this research, very few have addressed the simultaneous effects of several variables as predictors for the final fibre length. A mathematical model that predicts the final fibre length and predictor variables will be useful to pre-determine the exact input parameters to achieve the desired length. Hence, this research aims to predict the average final length of scission electrospun polystyrene (PS) nanofiber by ultrasonication while considering the scission time and diameter (the predictor variables) of the polymer fibre. A multiple regression model could provide a foundation for further research, potentially paving the way for precise control of submicron-length fibres on a large scale.

METHOD AND MATERIALS

Electrospinning

The parameters of the electrospinning and ultrasonication process to produce the short electrospun fibres were optimised from the previous works (Sawawi et al., 2013). The electrospinning process was conducted using an electrospinner built in the laboratory, which used a high voltage supply from Gamma High Voltage Research (USA), whilst the syringe pump was from Razel Scientific Instruments, Inc. (USA).

The PS fibres were produced by varying the concentration to obtain three sizes of fibre diameter to investigate the effect of fibre diameter on ultrasonication scission. The thinner PS fibres were electrospun at 8 wt/v%, whilst the larger fibre diameter was achieved when electrospun was at 16 wt/v%. All the fibres for these comparative purposes were electrospun in the same solvent solution, a mixture of chloroform and DMF (1:1) with 1 mM DTAB at the same speed of rotating mandrel of 6.8 m/s surface velocity. After collection, the non-woven web was stored in a desiccator under vacuum prior to further use. The other electrospinning parameters were kept the same: a 1.6 mL/hr feed rate, 20 kV accelerating voltage, 6 cm working distance and 18G gauged needle. The optimum voltage for 8 wt/v% is 15 kV. The electrospinning parameters are listed in Table 1.

Table 1
Electrospinning parameters (Sawawi et al., 2013)

Material	Solvent	Concentration (%) (w/v)	Feed rate (ml/hr)	Voltage (+kV)	Needle size (G)	Working distance (cm)	Mandrel speed (m/s)
PS	Chloroform + DMF (1 mM DTAB)	8	1.6	15	18	6	6.3
PS	Chloroform + DMF (1 mM DTAB)	12	1.6	20	18	6	6.3
PS	Chloroform + DMF (1 mM DTAB)	16	1.6	20	18	6	6.3

Ultrasonication

In the scissioning process, the electrospun webs were peeled off the collection plate, and a 1 cm² area was cut with a sharp knife before being placed randomly in a glass vial (25 mm in diameter) containing 15 mL of MiliQ water. The sonication was carried out using a Vibracell 750W (Sonics & Materials, Inc, USA) sonicator probe with a probe diameter of 13 mm and a working frequency of 20 kHz. The probe was positioned ca. 1 cm from the bottom of the vial. The processing parameters varied, such as total run time, amplitude percentage, and lapsed ON/OFF time. The water used for this study was at ambient

conditions. In general, ultrasonication was conducted in a beaker cooled by water-ice slurry to maintain the processing temperatures below 30°C since ongoing sonication raises the solvent temperature, even when using ON/OFF pulsed exposure.

After completion of the ultrasonic treatment, short fibres in the solvent suspension were placed on a scanning electron microscope (SEM) stub, which was covered with double-sided carbon tape to allow adhesion to the stub. Prior to SEM imaging, the sample was dried overnight in the fumehood followed by 2 hr in a vacuum oven at 60°C and platinum-coated at 1 nm thickness with a sputter coater, Cressington 208HR, (UK).

Mathematical Modelling

In this study, the mathematical model is designed through model assumptions that sonication run time and the diameter of the electrospun fibre influence the final fibre length. The relationship between the sonication run time, the diameter and the limiting length is studied through the regression analysis. A general multiple linear regression model (Zain et al., 2012) is expressed as Equation 1:

$$y = b_0 + b_1x_1 + b_2x_2 + b_3x_3 + \dots b_nx_n \quad [1]$$

whereby y is the dependent variable, b_0 is the intercept parameter, $b_1, b_2, b_3 \dots, b_n$ are the slope parameters, and x_n is the independent variable. This model is suitable for describing a linear relationship between the independent and dependent variables. In this model, the data used for the analysis was based on the quantified experimental data of the electrospun aligned PS 8wt% and 16wt% to generate a model covering the range of diameter, d from 240 μm to 930 μm respectively. The regression mathematical models developed in this study are produced using the Minitab and Microsoft Excel software. Multiple linear and non-linear regression analysis was used to develop the mathematical model, and the two models were compared. Data for the ultrasonicated electrospun 12wt% PS fibre was used to conduct the hypothesis testing. Table 2 summarises the descriptive statistics of the data obtained from the experiment used to construct the model.

Table 2
Summary of experimental data statistics

Variable	N	N*	Mean	SE Mean	StDev	Minimum	Q1	Median	Q3	Maximum
Y	406	0	6.820	0.386	7.780	0.450	2.083	3.758	8.241	46.666
X1	406	0	585.0	17.1	345.4	240.0	240.0	585.0	930.0	930.0
X2	406	0	4.254	0.113	2.285	2.000	2.000	3.500	8.000	8.000

CHARACTERISATION

Scanning Electron Microscopy

Scanning electron microscopy (SEM) is used to study the morphology and microstructure of a solid surface, which is important in understanding the structure-property relationship of a material. In this method, the sample surface is scanned by a high-energy electron beam where the incident electrons interact with the specimen atoms and cause extensive scattering. The SEM was conducted using a Scanning Electron Microscope (JEOL840A JEOL Ltd, Japan). The short fibre samples were dried overnight in the fumehood, followed by heating at 60°C in a vacuum oven for 2 hr prior to platinum coating of the sample (1 nm thickness) using a sputter coater (Cressington 208HR, UK).

RESULTS AND DISCUSSION

Scanning Electron Microscopy

SEM was performed on the as-spun PS fibre before and after ultrasonication to compare the surface morphology and quantify the average fibre length of the short fibres. Figure 1 shows the electrospun fibres before and after sonication for what we define in this work as the “minimum sonication time,” which was found to be 1 minute. This minimum sonication time is defined as the first time that the web was visually observed to significantly fragment, which was found. The sonicated fibres are of 732 ± 312 nm diameters in aligned orientation having 12wt/v%.

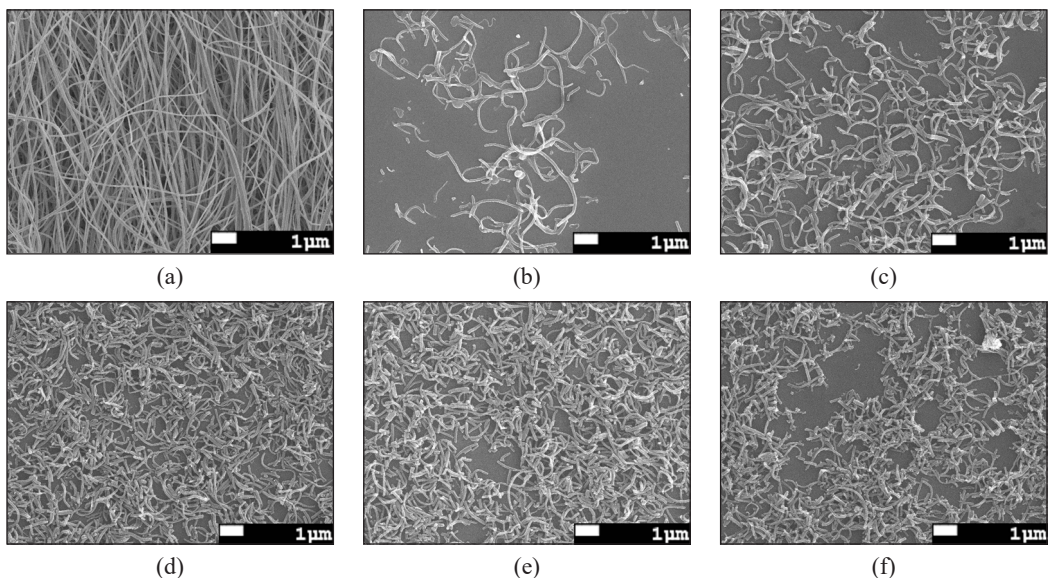


Figure 1. SEM images of electrospun PS fibres with aligned orientation under various sonication times at $\times 1.5k$ magnification: (a) as-spun PS fibre; (b) 1 minute; (c) 2 minutes; (d) 3 minutes; (e) 4 minutes; and (f) 8 minutes

Figure 1(a) is the as-spun un-ultrasonicated electrospun PS fibre which appears as a continuous web or mesh of fibres when compared to the ultrasonicated fibres in Figures 1(b), 1(c), 1(d), 1(e) and 1(f). In this study, the fibres are found to be scissioned with a minimum time of 1 minute. However, comparing Figures 1(b) to 1(c), 1(d), 1(e) and 1(f), the discontinuous fibres are still long and do not have enough discrete discontinuous fibres to be quantified. Fibres sonicated at 2, 3, 4 and 8 minutes show discrete, discontinuous fibres where the end-to-end of the singular fibres can be observed. The average final fibre length reduces as sonication run time increases, with the longest length being $5.63 \pm 4.38 \mu\text{m}$ at 2 minutes and the shortest average final length of $2.17 \pm 0.75 \mu\text{m}$ at 8 minutes (Table 3). Factors affecting the scissionability of the fibres include the diameter and time.

Figure 2 compares the average final fibre length of ultrasonicated electrospun PS fibres with different diameters. The concentration of the polymer influences the variance of diameter. The 8wt/v%, 12wt/v% and 16wt/v% have diameters of $d_1 = 240 \pm 70 \text{ nm}$, $d_2 = 732 \pm 312 \text{ nm}$ and $d_3 = 930 \pm 290 \text{ nm}$ respectively (images not shown here). It can be observed in the graph that the electrospun fibre with the largest diameter, d_3 (16wt/v%), has a longer final fibre length after sonication. In contrast, the shortest length is achieved by the fibre with the smallest diameter, d_1 (8wt/v%). Regardless of diameter size, a negative trend can

Table 3
Average final aligned PS fibre length after ultrasonication

Diameter, d (nm)	732 ± 312	732 ± 312	732 ± 312	732 ± 312
Time, t (minutes)	2	3	4	8
Average final fibre length, L_{avg} (microns)	5.625 ± 4.384	3.922 ± 2.092	2.915 ± 0.999	2.174 ± 0.749

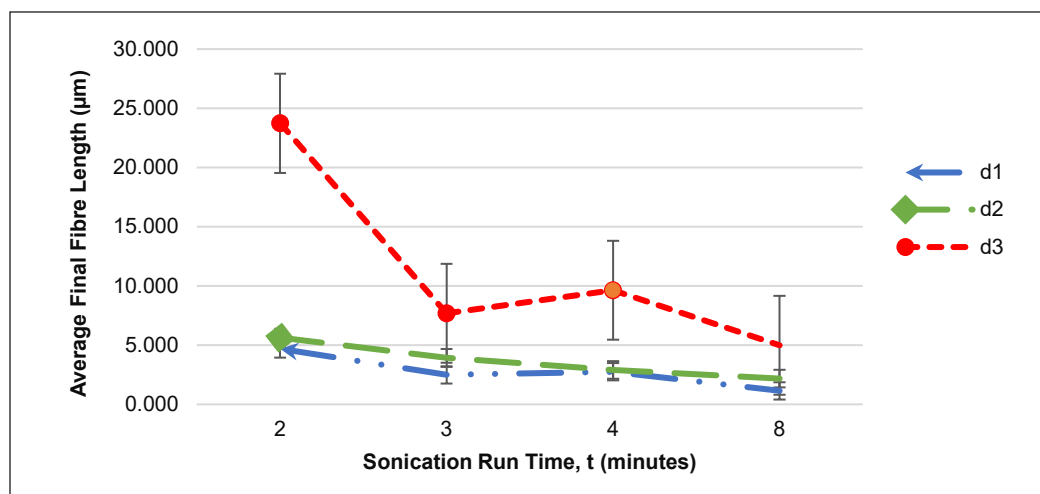


Figure 2. Average final fibre length against the sonication run time of electrospun PS fibres with different diameters

be observed from the graph, which also concludes the negative relationship between the sonication run time and final length. The opposite is implied for the relationship between the diameter and the average final fibre length.

Multiple Regression Modelling

Equation 2 shows the multiple linear regression model obtained using the Minitab software.

$$L_{avg} = 5.349 + 0.012125d - 1.322t \quad [2]$$

The linear regression model analysis resulted in an R^2 value of 0.44 and $p < 0.001$, which indicates that the relationship between x_1 (diameter, d) and x_2 (time, t) and y (average fibre length, L_{avg}) is statistically significant. This model may not accurately represent the relationship between the effects of time and diameter on the final fibre length; therefore, as a comparison, a non-linear regression model was also generated using the Minitab software, resulting in Equation 3.

$$L_{avg} = 14.30 + 0.02278d - 7.404t + 0.7257t^2 - 0.002500dt \quad [3]$$

where Y is the average final length, X_1 is the diameter (μm), and X_2 is the sonication time (min). Equation 3 represents a non-linear regression model of the relationship between L_{avg} , d and t . According to the analysis, the model R^2 value is 0.5989. It means that 59.89% of the variation in the response variable can be explained by the predictor variables (d and t). The relationship between the variables in this model is statistically significant with $p < 0.001$, less than 0.05. It means that a relationship exists between the response and predictor variables. According to Vilorina et al. (2016), if the R-squared value is above 80%, it indicates that the independent variables are enough to explain the relationship to the dependent variable. However, for the models in this study, the parameters may not be enough to explain the behaviour of the fibre scission by ultrasonication given that the R^2 is less than 80% because ultrasonication is a random process in terms of positions of bubble cavitation, which causes the scission of the fibre. It can also be explained by the high standard deviation obtained from sonication, which shows the variability of the data. However, at a higher sonication time, the R^2 value is significantly higher at 65.9% since a longer sonication run time will produce shorter fibres up to a point where it stabilises.

Referring to Equations 2 and 3, the coefficient of the variable for time, t , shows a negative value, which indicates that as the sonication run time increases, the final fibre length decreases. In contrast, the positive value for the diameter variable, d , suggests that the average final length increases as the diameter increases. This non-linear regression model concludes that it better fits the data with the trend aligned with the initial model

assumptions. Although regression analysis can help identify the type and strength of correlations, it is unable to differentiate between indirect and direct effects or consider the complex interaction between cause and effect.

Average Length vs Model Length

The mathematical model in Equation 3 was verified using the 12wt/v% of PS concentration, in which the data is tabulated in Table 4. The graphical output is shown in Figure 3; the difference in values between the model and the actual average final fibre length at 2 minutes is large, whereby even the maximum final length value does not overlap with the modelled value. However, it should be noted that in the sonication experiment, the fibre length varies significantly. For example, when calculating the maximum length for 2 minutes of sonication time, the length was 10 μm , about 50% of the estimated fibre length, using Equation 3. It is also true for other sonication times. As the sonication increases (such as at 8 minutes), the maximum fibre length was found to be 2.92 μm (about 20% difference). The average final fibre length after 8 minutes of sonication is $2.17 \pm 0.749 \mu\text{m}$, and the modelled fibre length is $\sim 3.54 \mu\text{m}$. If the maximum value is 2.92 μm , it is closer to the modelled length. The difference can be neglected as it is $\sim 0.62 \mu\text{m}$. Furthermore, as the sonication run-time approaches 8 minutes, the model has a similar trend to the actual data.

Table 4
Actual final length and predicted final length using the model

Time	2	3	4	8
Mathematical Model (Equation 3)	15.37	9.77	5.62	3.54
Actual experiment average final fibre length L_{avg}	5.63 ± 4.384	3.69 ± 2.092	2.86 ± 0.999	2.17 ± 0.749

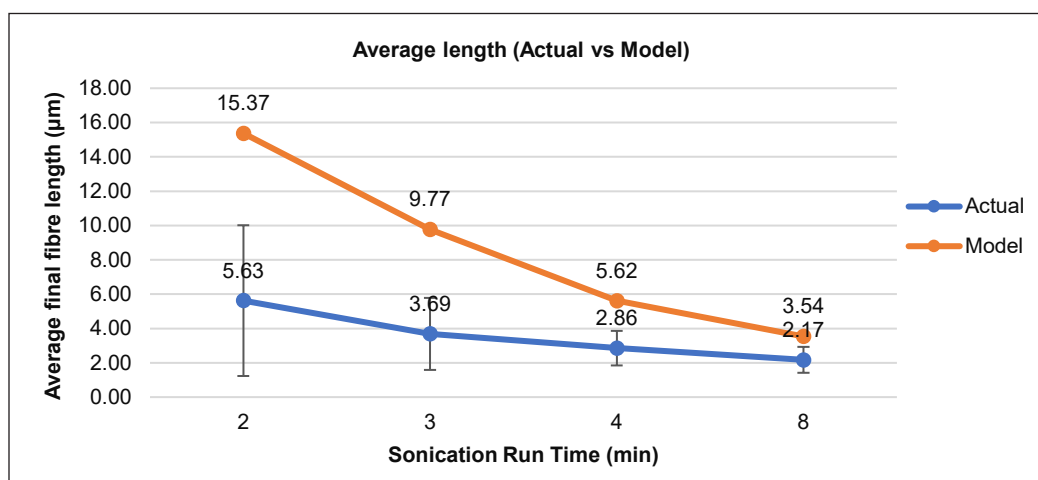


Figure 3. Graph of average final fibre length based on experiment (actual) and prediction (model)

To validate the model, a 2-sample independent t-test was conducted. It was highlighted that there is no significant difference ($p > 0.05$) between the mean of the experimental value and the average fibre length predicted from the regression model (Figure 4). It indicates that the model describes the fibre length generally accurately. This test concludes that it is possible to develop the model for the scission of electrospun fibres to determine the final fibre length given the diameter and sonication run time. However, precaution needs to be taken whereby the fibre length can vary from 50% to 20%. The fibre length that resulted from this process is in tens-micron size, which does not make a significant difference when only 2-5-micron length differs.

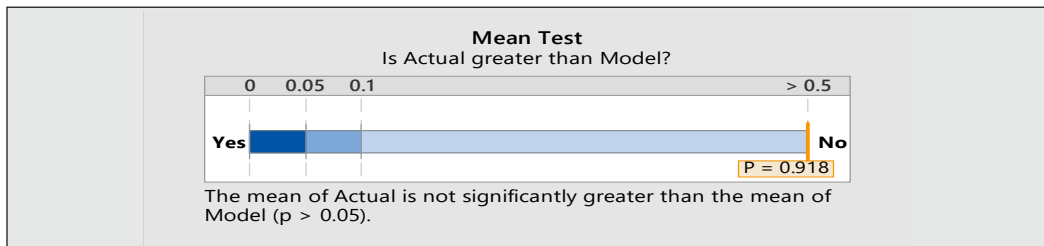


Figure 4. 2-sample independent t-test

Limitations and Recommendations

Though the model does show a relation between the variables, it does have a few notable limitations, such as its reliance on a specific experimental setting. Since this model is based on electrospun fibres from the previous study, the variables involved are limited, thus making the model only applicable to the difference in diameter for PS. It limits the model's generalizability, which does not allow it to fully capture the complexity of all possible scenarios and variations in the scissioning process. Furthermore, the model shows equipment dependency, which can only be used for PS electrospun nanofibers being sonicated using specific equipment with specific parameters. Variations in equipment specifications or configurations may not be accounted for, potentially restricting the model's applicability in a broader range of experimental setups. The generated model is also based on only one type of material, which limits its application in studying the scission effects of other materials as different materials have different characteristics.

In future research, the model's robustness can be improved by including additional parameters, such as the variables related to both the sonication process and the type of materials, which allows a better understanding of their effects on one another. Each material has distinct characteristics which would facilitate a more inclusive analysis. Including diverse materials would also enhance the model's reliability by using it for validation to increase its accuracy in a broader context. Furthermore, the model can be improved by considering the inherent variability in real-world processes, such as a safety factor, to

account for the unpredictability of certain experimental conditions. Conducting sensitivity analysis can also help in providing insight into the model's responsiveness to parameter variations. It would help identify critical factors that significantly impact the outcomes, guiding the experimental efforts and model refinement.

CONCLUSION

This study has applied a regression analysis to produce a model equation of ultrasonicated electrospun PS fibres. It is found that a quadratic multiple regression model better fits the data as the correlation between the diameter and time with respect to the final fibre length do not linearly respond to one another. As observed, the average final fibre length decreases when the sonication run time increases. The opposite is concluded for the relationship between the diameter and the final fibre length; as the diameter increases, the fibre length also increases. The quadratic regression model is statistically significant, whereby the model can explain 59.89% of the data. Furthermore, through hypothesis testing, the mean of the experimental value and the average fibre length predicted from the regression model are not significant, which indicates that the model can generally predict a relatively accurate average final fibre length value. While acknowledging the model's limitations, such as equipment and material dependencies, it provides a foundation for further research. In the future, the mathematical model might be more refined to provide an exact length value to ease the production of these submicron-length fibres on a large scale. More variables can be added to the modelling to produce a higher R^2 value feasible for large-scale production. The ability to create short, discontinuous electrospun fibres through ultrasonication holds tremendous promise for a wide range of applications, including tissue engineering, drug delivery, filtration systems, and more. As we move forward, refining the model and incorporating additional parameters to enhance its robustness is imperative. Exploring the effects of different materials, conducting sensitivity analyses, and accounting for real-world variability are essential steps to ensure the reliability and broad applicability of these models. Ultimately, this research contributes to our understanding of electrospinning and paves the way for more precise control of fibre properties in various practical contexts.

ACKNOWLEDGEMENTS

The authors thank the Ministry of Higher Education, Malaysia, Fundamental Research Grant Scheme (FRGS/1/2020/TK0/UNIMAS/02/12 and Universiti Malaysia Sarawak (F02/FRGS/1999/2020) for supporting this work.

REFERENCES

- Ahir, S. V., Huang, Y. Y., & Terentjev, E. M. (2008). Polymers with aligned carbon nanotubes: Active composite materials. *Polymer*, 49(18), 3841–3854. <https://doi.org/10.1016/j.polymer.2008.05.005>

- Ando, T. (1991). Ultrasonic organic synthesis involving non-metal solids. *Advances in Sonochemistry*, 2, 211-251.
- Baker, B. M., Gee, A. O., Metter, R. B., Nathan, A. S., Marklein, R. A., Burdick, J. A., & Mauck, R. L. (2008). The potential to improve cell infiltration in composite fiber-aligned electrospun scaffolds by the selective removal of sacrificial fibers. *Biomaterials*, 29(15), 2348–2358. <https://doi.org/10.1016/J.BIOMATERIALS.2008.01.032>
- Bhardwaj, N., & Kundu, S. C. (2010). Electrospinning: A fascinating fiber fabrication technique. *Biotechnology Advances*, 28(3), 325–347. <https://doi.org/10.1016/j.biotechadv.2010.01.004>
- Bortolassi, A. C. C., Nagarajan, S., de Araújo Lima, B., Guerra, V. G., Aguiar, M. L., Huon, V., Soussan, L., Cornu, D., Miele, P., & Bechelany, M. (2019). Efficient nanoparticles removal and bactericidal action of electrospun nanofibers membranes for air filtration. *Materials Science and Engineering C*, 102, 718–729. <https://doi.org/10.1016/j.msec.2019.04.094>
- Casper, C. L., Yamaguchi, N., Kiick, K. L., & Rabolt, J. F. (2005). Functionalizing electrospun fibers with biologically relevant macromolecules. *Biomacromolecules*, 6(4), 1998–2007. <https://doi.org/10.1021/bm050007e>
- Chen, D., Wang, R., Tjiu, W. W., & Liu, T. (2011). High performance polyimide composite films prepared by homogeneity reinforcement of electrospun nanofibers. *Composites Science and Technology*, 71(13), 1556–1562. <https://doi.org/10.1016/j.compscitech.2011.06.013>
- Chew, H. B., Moon, M. W., Lee, K. R., & Kim, K. S. (2011). Compressive dynamic scission of carbon nanotubes under sonication: Fracture by atomic ejection. *Proceedings of the Royal Society A: Mathematical, Physical and Engineering Sciences*, 467(2129), 1270–1289. <https://doi.org/10.1098/rspa.2010.0495>
- Doshi, J., & Reneker, D. H. (1995). Electrospinning process and applications of electrospun fibers. *Electrospinning Process and Applications of Electrospun Fibres*, 3(2-3), 151–160. <https://doi.org/10.1109/ias.1993.299067>
- Heller, D. A., Mayrhofer, R. M., Baik, S., Grinkova, Y. V., Usrey, M. L., & Strano, M. S. (2004). Concomitant length and diameter separation of single-walled carbon nanotubes. *Journal of the American Chemical Society*, 126(44), 14567–14573. <https://doi.org/10.1021/ja046450z>
- Henrich, F., Krupke, R., Arnold, K., Stütz, J. A. R., Lebedkin, S., Koch, T., Schimmel, T., & Kappes, M. M. (2007). The mechanism of cavitation-induced scission of single-walled carbon nanotubes. *Journal of Physical Chemistry B*, 111(8), 1932–1937. <https://doi.org/10.1021/jp065262n>
- Hrabalova, M., Schwanninger, M., Wimmer, R., Gregorova, A., Zimmermann, T., & Mundigler, N. (2011). Fibrillation of flax and wheat straw cellulose: Effects on thermal, morphological, and viscoelastic properties of poly(vinylalcohol)/fibre composites. *BioResources*, 6(2), 1631–1647. <https://doi.org/10.15376/biores.6.2.1631-1647>
- Huang, Y. Y., Knowles, T. P. J., & Terentjev, E. M. (2009). Strength of nanotubes, filaments, and nanowires from sonication-induced scission. *Advanced Materials*, 21(38–39), 3945–3948. <https://doi.org/10.1002/adma.200900498>
- Jiang, S., Chen, Y., Duan, G., Mei, C., Greiner, A., & Agarwal, S. (2018). Electrospun nanofiber reinforced composites: A review. *Polymer Chemistry*, 9(20), 2685–2720. <https://doi.org/10.1039/c8py00378e>

- Khanlou, H. M., Ang, B. C., Talebian, S., Barzani, M. M., Silakhori, M., & Fauzi, H. (2015). Multi-response analysis in the processing of poly (methyl methacrylate) nano-fibres membrane by electrospinning based on response surface methodology: Fibre diameter and bead formation. *Measurement*, *65*, 193–206. <https://doi.org/10.1016/j.measurement.2015.01.014>
- Kharissova, O. V., & Kharisov, B. I. (2017). *Solubilization and dispersion of carbon nanotubes*. Springer. <https://doi.org/10.1007/978-3-319-62950-6>
- Kuijpers, M. W. A., Iedema, P. D., Kemmere, M. F., & Keurentjes, J. T. F. (2004). The mechanism of cavitation-induced polymer scission; experimental and computational verification. *Polymer*, *45*(19), 6461–6467. <https://doi.org/10.1016/j.polymer.2004.06.051>
- Lannutti, J., Reneker, D., Ma, T., Tomasko, D., & Farson, D. (2007). Electrospinning for tissue engineering scaffolds. *Materials Science and Engineering C*, *27*(3), 504–509. <https://doi.org/10.1016/j.msec.2006.05.019>
- Li, M., Mondrinos, M. J., Chen, X., Gandhi, M. R., Ko, F. K., & Lelkes, P. I. (2006). Co-electrospun poly(lactide-co-glycolide), gelatin, and elastin blends for tissue engineering scaffolds. *Journal of Biomedical Materials Research - Part A*, *79*(4), 963–973. <https://doi.org/10.1002/jbm.a.30833>
- Li, Z. L., Zheng, H. Y., Lim, G. C., Chu, P. L., & Li, L. (2010). Study on UV laser machining quality of carbon fibre reinforced composites. *Composites Part A: Applied Science and Manufacturing*, *41*(10), 1403–1408. <https://doi.org/10.1016/j.compositesa.2010.05.017>
- Lima, L. L., Bierhalz, A. C. K., & Moraes, Â. M. (2020). Influence of the chemical composition and structure design of electrospun matrices on the release kinetics of Aloe vera extract rich in aloin. *Polymer Degradation and Stability*, *179*, 109233. <https://doi.org/10.1016/j.polymdegradstab.2020.109233>
- Liu, C., Shi, H., Yang, H., Yan, S., Luan, S., Li, Y., Teng, M., Khan, A. F., & Yin, J. (2017). Fabrication of antibacterial electrospun nanofibers with vancomycin-carbon nanotube via ultrasonication assistance. *Materials and Design*, *120*, 128–134. <https://doi.org/10.1016/j.matdes.2017.02.008>
- Lucas, A., Zakri, C., Maugey, M., Pasquali, M., Schoot, P. V. D., & Poulin, P. (2009). Kinetics of nanotube and microfiber scission under sonication. *Journal of Physical Chemistry C*, *113*(48), 20599–20605. <https://doi.org/10.1021/jp906296y>
- Luo, C. J., Stride, E., Stoyanov, S., Pelan, E., & Edirisinghe, M. (2011). Electrospinning short polymer microfibres with average aspect ratios in the range of 10-200. *Journal of Polymer Research*, *18*(6), 2515–2522. <https://doi.org/10.1007/s10965-011-9667-6>
- Luzio, A., Canesi, E. V., Bertarelli, C., & Caironi, M. (2014). Electrospun polymer fibers for electronic applications. *Materials*, *7*(2), 906-947. <https://doi.org/10.3390/ma7020906>
- Magill, H., & Gunning, B. (1969). A simple microtome capable of cutting sections of plastic-embedded material down to 1 µm in thickness. *Journal of Microscopy*, *89*(2), 217–223. <https://doi.org/10.1111/j.1365-2818.1969.tb00667.x>
- Maleki, H., Gharehaghaji, A. A., Moroni, L., & Dijkstra, P. J. (2013). Influence of the solvent type on the morphology and mechanical properties of electrospun PLLA yarns. *Biofabrication*, *5*(3), Article 035014. <https://doi.org/10.1088/1758-5082/5/3/035014>

- Megelski, S., Stephens, J. S., Bruce Chase, D., & Rabolt, J. F. (2002). Micro- and nanostructured surface morphology on electrospun polymer fibers. *Macromolecules*, 35(22), 8456–8466. <https://doi.org/10.1021/ma020444a>
- Morkavuk, S., Köklü, U., Bağcı, M., & Gemi, L. (2018). Cryogenic machining of carbon fiber reinforced plastic (CFRP) composites and the effects of cryogenic treatment on tensile properties: A comparative study. *Composites Part B: Engineering*, 147, 1–11. <https://doi.org/10.1016/j.compositesb.2018.04.024>
- Niemczyk-Soczynska, B., Dulnik, J., Jeznach, O., Kolbuk, D., & Sajkiewicz, P. (2021). Shortening of electrospun PLLA fibers by ultrasonication. *Micron*, 145, Article 103066. <https://doi.org/10.1016/j.micron.2021.103066>
- O'Connor, R. A., Cahill, P. A., & McGuinness, G. B. (2021). Effect of electrospinning parameters on the mechanical and morphological characteristics of small diameter PCL tissue engineered blood vessel scaffolds having distinct micro and nano fibre populations – A DOE approach. *Polymer Testing*, 96, Article 107119. <https://doi.org/10.1016/j.polymertesting.2021.107119>
- Oksman, K., Mathew, A. P., Långström, R., Nyström, B., & Joseph, K. (2009). The influence of fibre microstructure on fibre breakage and mechanical properties of natural fibre reinforced polypropylene. *Composites Science and Technology*, 69(11–12), 1847–1853. <https://doi.org/10.1016/j.compscitech.2009.03.020>
- Pagani, G., Green, M. J., Poulin, P., & Pasquali, M. (2012). Competing mechanisms and scaling laws for carbon nanotube scission by ultrasonication. *Proceedings of the National Academy of Sciences of the United States of America*, 109(29), 11599–11604. <https://doi.org/10.1073/pnas.1200013109>
- Price, G. J., & Smith, P. F. (1991). Ultrasonic degradation of polymer solutions. 1. Polystyrene revisited. *Polymer International*, 24(3), 159–164. <https://doi.org/10.1002/pi.4990240306>
- Sander, J. R. G., Zeiger, B. W., & Suslick, K. S. (2014). Sonocrystallization and sonofragmentation. *Ultrasonics Sonochemistry*, 21(6), 1908–1915. <https://doi.org/10.1016/j.ultsonch.2014.02.005>
- Sawawi, M., Wang, T. Y., Nisbet, D. R., & Simon, G. P. (2013). Scission of electrospun polymer fibres by ultrasonication. *Polymer*, 54(16), 4237–4252. <https://doi.org/10.1016/j.polymer.2013.05.060>
- Schiffman, J. D., & Schauer, C. L. (2008). A review: Electrospinning of biopolymer nanofibers and their applications. *Polymer Reviews*, 48(2), 317–352. <https://doi.org/10.1080/15583720802022182>
- Stegen, J. (2014). Mechanics of carbon nanotube scission under sonication. *Journal of Chemical Physics*, 140(24), Article 244908. <https://doi.org/10.1063/1.4884823>
- Subbiah, T., Bhat, G. S., Tock, R. W., Parameswaran, S., & Ramkumar, S. S. (2005). Electrospinning of nanofibers. *Journal of Applied Polymer Science*, 96(2), 557–569. <https://doi.org/10.1002/app.21481>
- Thieme, M., Agarwal, S., Wendorff, J. H., & Greiner, A. (2011). Electrospinning and cutting of ultrafine bioerodible poly(lactide-co-ethylene oxide) tri- and multiblock copolymer fibers for inhalation applications. *Polymers for Advanced Technologies*, 22(9), 1335–1344. <https://doi.org/10.1002/pat.1617>
- Tsochatzidis, N. A., Guiraud, P., Wilhelm, A. M., & Delmas, H. (2001). Determination of velocity, size and concentration of ultrasonic cavitation bubbles by the phase-Doppler technique. *Chemical Engineering Science*, 56(5), 1831–1840. [https://doi.org/10.1016/S0009-2509\(00\)00460-7](https://doi.org/10.1016/S0009-2509(00)00460-7)

- Valizadeh, A., & Farkhani, S. M. (2014). Electrospinning and electrospun nanofibres. *IET Nanobiotechnology*, 8(2), 83–92. <https://doi.org/10.1049/iet-nbt.2012.0040>
- Van Der Hoff, B. M. E., & Glynn, P. A. R. (1974). The Rate of degradation by ultrasonation of polystyrene in solution. *Journal of Macromolecular Science: Part A - Chemistry*, 8(2), 429–449. <https://doi.org/10.1080/00222337408065839>
- Viloria, A., Urbina, M. C., Rodríguez, L. G., & Muñoz, A. P. (2016). Predicting of behavior of escherichia coli resistance to Imipenem and Meropenem, using a simple mathematical model regression. *Indian Journal of Science and Technology*, 9(46), 1-5. <https://doi.org/10.17485/ijst/2016/v9i46/107379>
- Zain, A. M., Haron, H., Qasem, S. N., & Sharif, S. (2012). Regression and ANN models for estimating minimum value of machining performance. *Applied Mathematical Modelling*, 36(4), 1477–1492. <https://doi.org/10.1016/j.apm.2011.09.035>
- Zeng, J., Xu, X., Chen, X., Liang, Q., Bian, X., Yang, L., & Jing, X. (2003). Biodegradable electrospun fibers for drug delivery. *Journal of Controlled Release*, 92(3), 227–231. [https://doi.org/10.1016/S0168-3659\(03\)00372-9](https://doi.org/10.1016/S0168-3659(03)00372-9)
- Zhang, J., Zhang, X., Wang, C., Li, F., Qiao, Z., Zeng, L., Wang, Z., Liu, H., Ding, J., & Yang, H. (2021). Conductive composite fiber with optimized alignment guides neural regeneration under electrical stimulation. *Advanced Healthcare Materials*, 10(3), Article 2000604. <https://doi.org/10.1002/adhm.202000604>

An Accident Prediction Model Based on ARIMA in Kuala Lumpur, Malaysia, Using Time Series of Actual Accidents and Related Data

Boon Chong Choo¹, Musab Abdul Razak^{1*}, Mohd Zahirasri Mohd Tohir¹, Dayang Radiah Awang Biak¹ and Syafie Syam²

¹Safety Engineering Interest Group, Department of Chemical & Environmental Engineering, Universiti Putra Malaysia, 43400 UPM, Serdang, Selangor, Malaysia

²Department of Chemical and Materials Engineering, Faculty of Engineering Rabigh Brang, King Abdulaziz University, Jeddah, Kingdom of Saudi Arabia

ABSTRACT

Recently, there has been an emerging trend to analyse time series data and utilise sophisticated tools for optimally fitting time series models. To date, Malaysian industrial accident data is underutilised and lacks informative records. Thus, this paper aims to investigate the Malaysian accident database and further evaluate the optimal forecasting models in accident prediction. The model's input was based on available data from the Department of Occupational Safety and Health, Malaysia (DOSH), from 2018 until 2021, with 80% of the dataset to train the models and the remaining 20% for validation. The negative binomial and Poisson distribution prediction showed a mean absolute percentage error (MAPE) of 33% and 51%, respectively. It indicated that the negative binomial performed better than the Poisson distribution in accident frequency prediction. The available time series accident data were gathered for four years, and stationarity was checked in R Studio software for the Augmented Dickey-Fuller test. The lowest Akaike Information Criterion (AIC), Bayesian

Information Criterion (BIC) and other error values were used to justify the best model, which was the ARIMA(2,0,2)(2,0,0)(12) model. The ARIMA models were considered after the data showed autocorrelation. The MAPE for both ARIMA in R and manual time series were 40% and 49%, respectively. Therefore, the accident prediction by using R Studio would outperform the manually negative binomial and Poisson distribution.

ARTICLE INFO

Article history:

Received: 18 July 2023

Accepted: 06 December 2023

Published: 01 April 2024

DOI: <https://doi.org/10.47836/pjst.32.3.07>

E-mail addresses:

boonchong93@gmail.com (Boon Chong Choo)

musab@upm.edu.my (Musab Abdul Razak)

zahirasri@upm.edu.my (Mohd Zahirasri Mohd Tohir)

dradiah@upm.edu.my (Dayang Radiah Awang Biak)

ssmahmoud@kau.edu.sa (Syafie Syam)

* Corresponding author

Based on the findings, industrial safety practitioners should report accidents to DOSH truthfully in the era of digitalisation. It could enable future data-driven accident predictions to be carried out.

Keywords: Accident models, accident prediction, digitalisation, Malaysia's accidents, R studio

INTRODUCTION

The rapid growth of industrialisation and the global economy in developing countries like Malaysia has constantly led to industrial accidents, which have emerged as a social problem (Kim et al., 2021). It had been reported by Kim et al. (2021) that the Asian occupational fatality per 100,000 workers was higher than in EU countries, and Malaysia required more effective safety regulations and programmes. There is a legal requirement in Malaysia under the Occupational Safety and Health Act (OSHA) 1994 for accident reporting to the Department of Occupational Safety and Health (DOSH) Malaysia via JKPP 6 or myKKP website. In view of the statistical field and machine learning, such accident reporting can provide continuous analysis and learning processes to prevent unwanted occurrences (Freivalds & Johnson, 1990). Click or tap here to enter text. On accident cost estimation, Rohani et al. (2015) found that the ratio of accident prevention to accident cost is 1:19.6 in Malaysia. However, Kidam et al. (2015) and Choo et al. (2022) highlighted that weakness in Malaysian accident reporting led to poor learning.

The statistical data and analysis of the accident database would be more reliable in the research on accident prevention (Chong & Low, 2014). For example, Abdullah and Wern (2011) studied the accident frequency and revealed the factors of high levels of injuries and fatalities encountered in the construction industry based on accident statistics. Ayob et al. (2018) conducted a descriptive study through a survey to identify the cause (poor risk management) and accident agent (fall from height) in the construction industry. Chong and Low (2014), through statistical data and court cases in the period of 2000-2009, identified and tabulated the causes that contributed to health issues, and the reported main cause of construction accidents were striking objects and falls. Hadi et al. (2017) conducted a survey that found that 94.7% of the workers did not report any accidents to their management and revealed a prevalence of non-reporting accidents in construction sites. As a result, the safety officer in the company may be unaware of the near-miss that happened and not record it in the safety system. Apart from the construction industry, Ali et al. (2017) studied the trend of accidents in the manufacturing industry using descriptive data and found that the number of fatalities and permanent and non-permanent disability increased by 26%, 71% and 64%, respectively. Zein et al. (2015) completed a survey on working postures, revealing the most prominent work involving bending forward and lifting heavy loads, which showed the most significant physical body injury.

In accident prediction, Rohayu et al. (2012) predicted the road accident fatalities for 2020 using the ARIMA model, and the data showed autocorrelation. Manan et al. (2013) reported the first motorcycle accident prediction model in Malaysia using the negative binomial regression model. Malaysia has actively conducted road transportation safety research, but to our knowledge, no industrial accident prediction has been reported in Malaysia. Choo et al. (2022) conducted a literature review on supervised machine learning, and the concept of accident prediction is applied in this paper. Thus, this paper aims to utilise the Malaysian accident database and fit the data for modelling, namely Poisson and negative binomial distribution, for frequency modelling. The time series prediction by using R Studio was also evaluated. The findings of this study can set a foundation for industrial accident prediction in Malaysia.

METHODOLOGY

This study utilised accident data obtained from DOSH in Kuala Lumpur, Malaysia. A total of 1131 industrial accidents reported to DOSH from January 2018 to December 2021 were used in this study. As Zermane et al. (2022) highlighted, the accident data were incomplete, with fewer details, and repetitive with unclear descriptions. Thus, the data were screened pre-processed by removing invalid data (Hajakbari & Minaei-Bidgoli, 2014), resulting in 1047 accident data for this study. The incomplete, redundant, and invalid data, such as non-word text-type data, was excluded from the table. The number of days lost was created from the injuries suffered. For modelling purposes, 80% of the dataset was used in training, whereas the remaining 20% was used as validation.

Frequency Modelling

The number of accidents can be described as the statistical safety indicators (Jian, 2021) and applied in prediction (Attwood et al., 2006). In this research, the primary variable for frequency modelling was the time elapsed between the date of the latest accident and the previous one (Hajakbari & Minaei-Bidgoli, 2014; Esmaili et al., 2021). The frequency distribution was selected based on the relationship between the mean (Attwood et al., 2006) and the variance of annual incidents. Several researchers demonstrated a constant failure rate and assumed no safety-related changes were made (Attwood et al., 2006); therefore, two distributions, Poisson and negative binomial distributions, were used in this study as below.

Poisson distribution as expressed in Equation 1 (If mean and variance of the data are in closed proximity) (Attwood et al., 2006; Ismail & Zamani, 2013; Manan et al., 2013)

$$y \sim p(y = y_i) = \left\{ \frac{\lambda^{y_i} e^{-\lambda}}{y_i!} \right\}, y_i \in \{1^1\}, y_i \geq 0, \lambda > 0, \quad [1]$$

where y_i is the number of incidents in the year i , and λ is the annual average number of incidents, with the expected value, $E(y)$, and variance, $V(y)$, equal to λ .

The prior distribution for λ is assumed to follow Gamma-distribution, $\lambda \sim (\alpha, \beta)$ due to uncertainty (Meel & Seider, 2006; Meel et al., 2007) as expressed in Equation 2:

$$p(\lambda) \propto \lambda^{\alpha-1} e^{-\beta\lambda}, \alpha > 0, \beta > 0 \tag{2}$$

From Baye’s theorem, the posterior distribution, which permits a projection of accident frequency in the future (Meel & Seider, 2006), $p(\lambda | \text{Data})$, is expressed in Equation 3:

$$p(\lambda | \text{Data}) \propto \ell(\text{Data} | \lambda) p(\lambda) \\ \propto (\lambda^s e^{-N_t \lambda})(\lambda^{\alpha-1} e^{-\beta\lambda}) \propto \lambda^{(\alpha+s)-1} e^{-(\beta+N_t)\lambda}, \tag{3}$$

where $\text{Data} = (y_0, y_1, \dots, y_{N_t})$, $s = \sum_{i=0}^{N_t} y_i$, N_t is the number of years, and $\ell(\text{Data} | \lambda)$ is the Poisson likelihood distribution. Note that $p(\lambda | \text{Data})$ is also a Gamma distribution, Gamma $(\alpha + S, \beta + N_t)$, because λ is distributed according to Gamma (α, β) , which is conjugate prior to the Poisson distribution. The mean of the posterior distribution is the weighted average of the means of the prior and likelihood distributions, as expressed in Equation 4:

$$\frac{\alpha+s}{\beta+N_t} = \frac{\beta}{\beta+N_t} \left(\frac{\alpha}{\beta}\right) + \frac{N_t}{\beta+N_t} \frac{s}{N_t}, \tag{4}$$

and the variance of the posterior distribution is $\frac{\alpha+s}{(\beta+N_t)^2}$.

Negative binomial distribution (Poisson-gamma) (Thakali et al., 2016) is used when the Poisson distribution is poor. Denham (2020) and Warner (2015) reported that when the variance exceeds its mean, the data are considered over-dispersed and need a different model instead of Poisson distribution. The number of incidents that occurred in a year is a non-negative and integer-valued result that can be estimated using a negative binomial distribution in Equation 5 for y :

$$y \sim (q)^\mu (1 - q)^{y_i} \quad y_i \in \{I^1\}, y_i \geq 0, \mu > 0, q \geq 0, \tag{5}$$

where y_i is the number of incidents in year i th, $\mu(1-q)/q$ is the expected annual (mean) of incidents, $E(y)$, and $\mu(1-q)/q^2$ is the expected variance, $V(y)$. Due to uncertainty, the prior distribution for μ is assumed to follow a Gamma distribution as expressed in Equation 6, $\sim \text{Gamma}(\alpha, \beta)$:

$$p(\mu) \propto \mu^{\alpha-1} e^{-\beta\mu}, \alpha > 0, \beta > 0, \tag{6}$$

and that for q is assumed to follow a Beta distribution in Equation 7, $q \sim \text{Beta}(a, b)$:

$$p(q) \propto q^{a-1}(1-q)^{b-1}, a > 0, b > 0. \tag{7}$$

From Baye’s theorem, the posterior distribution in Equation 8, which permits a projection of accident frequency in the future, $p(\mu, q | \text{Data})$, is

$$\begin{aligned} p(\mu, q | \text{Data}) &\propto l(\text{Data} | \mu, q)p(\mu)p(q) \\ &\propto q^{n\mu} (1-q)^s (\mu^{\alpha-1} e^{-\beta\lambda}) q^{a-1} (1-q)^{b-1} \\ &\propto q^{n\mu+a-1} (1-q)^{s+b-1} (\mu^{\alpha-1} e^{-\beta\mu}), \end{aligned} \tag{8}$$

where $\text{Data} = (y_0, y_1, \dots, y_{N_t})$, $s = \sum_{i=0}^{N_t} y_i$, N_t is the number of years, and $l(\text{Data} | \mu, q)$ is the Negative Binomial likelihood distribution.

Time Series Accident Prediction

Freivalds and Johnson (1990) described that the time series of accident data from the previous week or month would influence the next week or month’s data. They reported that accident data varies about a mean value, which applied the concept of time series in accident prediction. The manual time series prediction was analysed in Excel, where the mean value of previous months was the predicted value.

The R package applied in this research was the library “forecast” and “tseries” with “Box-test”. The frequency of accidents was expressed in terms of a time series model due to its capability to forecast, interpret, and test hypotheses concerning the data (Sari et al., 2009). The behaviour and pattern of past observations will be assumed to continue in the future. The Augmented Dickey-Fuller test (ADF) confirmed the stationarity of data in R. With the nature of accident data received, the number of accidents did not show a significant relationship among the variables such as date of accident and nationality. Thus, linear regression was not considered in accident prediction. Auto-Regression Integrated Moving Average (ARIMA) was used to predict future values using auto-arima in the forecast package in R. The ARIMA (p, d, q) model consists of expressions identified as the order (p) of the auto-regressive part (AR), with an order of differentiation model (d) and an order (q) for moving average (MA). The seasonal ARIMA (p, d, q) (P, D, Q)_s is a time series model with recurring peaks that represent the order or period of seasonality (Melchior et al., 2021).

Several analyses in R were used for model selection, such as the autocorrelation function (ACF), partial autocorrelation function (PACF), the Akaike Information Criterion (AIC) and Bayesian Information Criterion (BIC). AIC and BIC are the criteria that balance

the model’s goodness of fit and complexity and achieve a trade-off between fitting the available data and preventing over-fitting (Esmaili et al., 2021). Therefore, it is reported that it is preferable to have a lower value of AIC and BIC (Abdulqader et al., 2020). The Box-Ljung statistical test in R was used to confirm the correlation of the data.

Model Performance Measure

Two goodness-of-fit measures (Kuşkapan et al., 2021; Thakali et al., 2016) were used to check the model’s performance. The first one is the mean absolute error (MAE) (Equation 9), and the other one is the RMSE (Equation 10).

$$MAE = \frac{\sum_{i=1}^n |\hat{y}_i - y_i|}{n} \tag{9}$$

$$RMSE = \sqrt{\frac{\sum_{i=1}^n (\hat{y}_i - y_i)^2}{n}} \tag{10}$$

where y_i is the i th observed accident frequency, \hat{y}_i is the estimated accident frequency for the i th observation, and n is the total observations.

Mean absolute percentage error (MAPE) was used to determine the model accuracy by using the formula as depicted in Equation 11 and evaluating its accuracy in accordance with Table 1 (Weng et al., 2015).

$$MAPE = \frac{\sum_{i=1}^n \left| \frac{y_i - \hat{y}_i}{y_i} \right|}{n} \times 100\% \tag{11}$$

Table 1
Scale of evaluation of prediction accuracy

Condition	Assessment
$MAPE \leq 10\%$	Highly accurate prediction
$10\% < MAPE \leq 20\%$	Good prediction
$20\% < MAPE \leq 50\%$	Reasonable prediction
$MAPE > 50\%$	Inaccurate prediction

RESULTS AND DISCUSSION

In Malaysia, any accident with four lost days must be reported to DOSH through the myKKP website. The database received from DOSH was a relational database stored in a table with accidents recorded in a row and various attributes in columns. An accident dataset of four years (2018-2021) in Kuala Lumpur consisting of the accidents’ date, details of injured persons, classification of accidents, incident descriptions, injured parts, type of industries, and related coding for each variable was acquired from DOSH for this study. However, the data were incomplete because containing fewer details and were repetitive with very short descriptions, as highlighted by Zermane et al. (2022). In addition, Mohamad et al. (2019) and Muhamad et al. (2021) highlighted that Malaysian manufacturing companies still lack awareness and are not accustomed to implementing big data analytics due to the high cost of cloud computing services and worry the companies’ database being stolen or compromised.

The data were normalised to reduce redundancy and eliminate undesirable data. It was done by removing the duplicated rows in the Excel spreadsheet. In addition, the dataset received had many missing values in various attributes, which is considered the extent of the error. It may be due to several individual and organisational shortcomings in data reporting, collection, management, and processing (Ahmed et al., 2020).

Table 2
Number of accidents in the year 2018 to 2021

Year	Number of Attributes (Column in database)	Number of Accidents	
		Raw Data	Normalised
2018	16	190	188
2019	6	375	338
2020	23	322	305
2021	22	244	216
Total		1131	1047

As shown in Table 2, out of 1131 accident cases reported to DOSH, about 84 cases (7.43%) were missing vital information in the available reported cases. In 2019, the least number of attributes were reported, and most information was missing. It means that a researcher would face difficulty analysing the root causes and the contributing factors to accidents. The number of attributes is the table column found in the database from DOSH. The attributes include age, victim status, date of the accident, accident classification by employers and DOSH officers, a short description of accidents, gender, nationality, type of injuries, accident agent, type of industries, work sector, body part injured and each code of above mentioned which had been defined by DOSH. Hadi et al. (2017) revealed that non-reporting accidents are prevalent in industries where 94.7% of construction workers did not report accidents.

On the other hand, limited research utilised publicly available data from the DOSH website. For example, Rafindadi et al. (2022) and Zermane et al. (2022) analysed data from the DOSH website for fatal fall-related accidents. Their finding showed the limitation in missing vital information in DOSH data. It was urged to adequately document and make the record up to date and international standard. In general, it was observed that 2021 accident reporting was more detailed compared to previous years. It has been discovered that the upper limbs are the most registered injury, followed by the lower limbs. However, the accident records showed a general injury sustained without providing detailed analysis, also reported by Rafindadi et al. (2022).

Frequency Modelling

Different accident prediction models are developed using econometric models such as ARIMA, negative binomial and Poisson models, as Quddus (2008) reported. Due to

the availability of accident data, the distribution was based on the time elapsed between accident dates, as shown in Figure 1. It is the time interval between the date of the latest accident and the previous occurrence (Hajakbari & Minaei-Bidgoli, 2014). Based on Figure 1, accidents were reported daily (shortest time interval between two accidents) in Kuala Lumpur, Malaysia. It was recorded that no accident was reported in two consecutive weeks, and the longest interval was 15 days, which can be considered “zero accident” and is extremely difficult to achieve (Attwood et al., 2006).

The frequency of accidents had been modelled statistically by fitting two distributions, Poisson and negative binomial distribution, as shown in Figures 2(a) and 2(b), respectively. From the data, everyday accidents are reported to DOSH. Both models are mathematical equations through statistical modelling of accident data and show the same right-skewed pattern. The distributions are to be used as the base condition for model development, where the frequency of an accident is significant in risk analysis. By having such a quantitative approach based on past reports, safety practitioners may be able to present unique safety practices to reduce accident frequency since Attwood et al. (2006) highlighted that the prediction of annual accidents was expected to be around the mean value. It indicates that given the same accident data, the impact of the variables on the different models is similar, but the expected frequency obtained from each model is slightly different. In other words, the model could estimate how many accidents would occur under average situations because, to date, no organisation has established a major change in the safety culture. Weng et al. (2015) highlighted the difficulty in predicting accidents with perfect confidence due to their uncertainty. Khattak et al. (2021) reported that the Poisson regression model is the first choice of researchers to adopt for the count data model in the beginning, and the negative binomial model is still in great popularity in the modelling process.

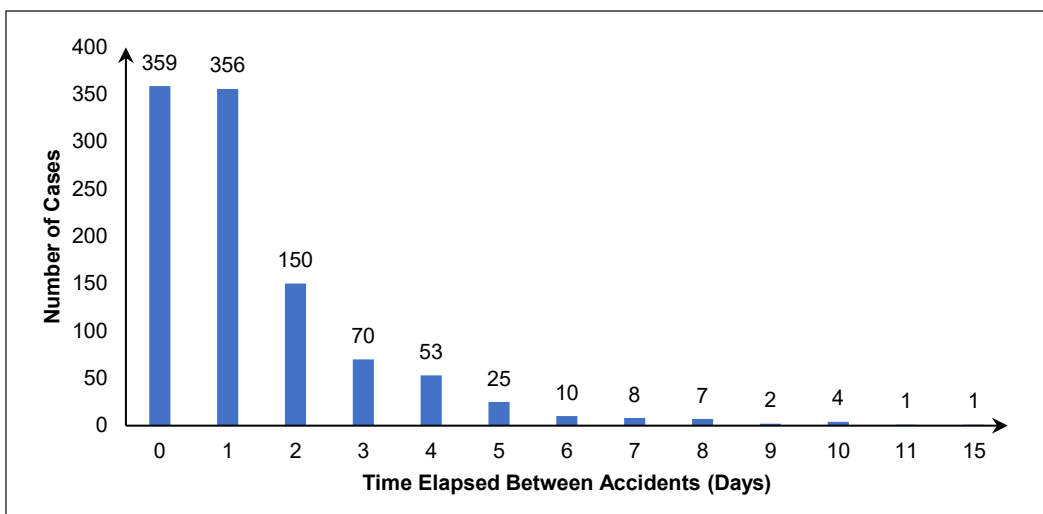
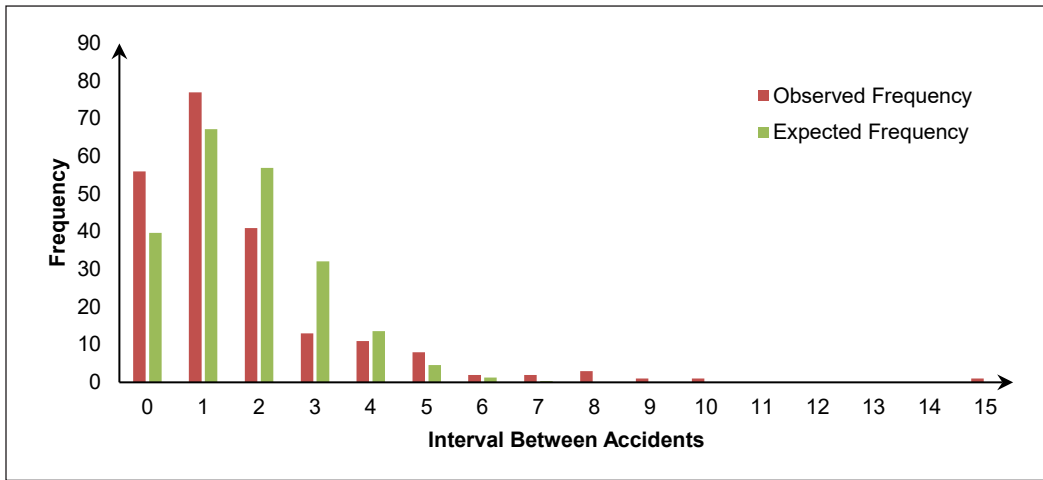
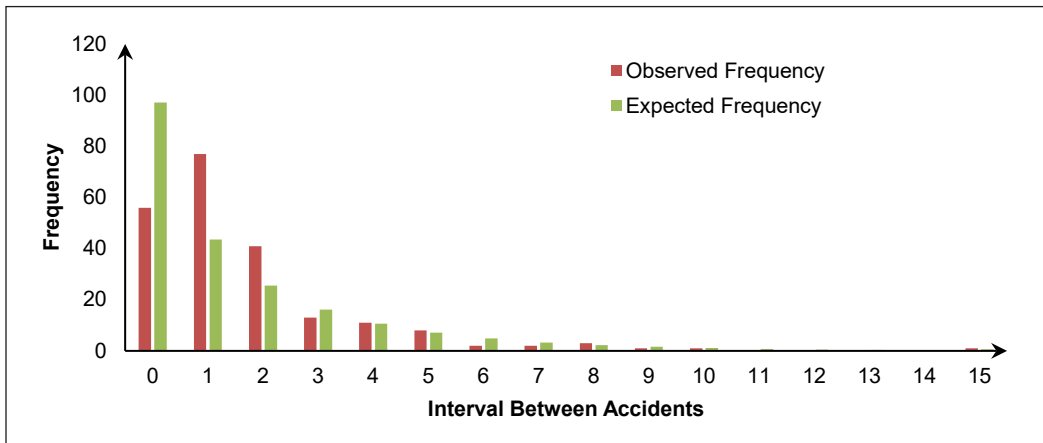


Figure 1. Distribution of the number of accidents for various intervals



(a)



(b)

Figure 2. Frequency modelling: (a) Poisson distribution; (b) Negative binomial distribution

Table 3 tabulated the performance of prediction based on Poisson and negative binomial. The predicted number of accidents using both distributions resulted in 216 cases. The MAPE based on monthly accident cases for the Poisson distribution is 51%, whereas the negative binomial distribution is 33%. The result shows that the negative binomial distribution makes a reasonable prediction compared to the Poisson distribution.

Table 3
Results of distribution accuracy

Distribution	Predicted Accident	MAE	RMSE	MAPE (%)
Poisson	216	4.721	7.974	51
Negative binomial	216	6.393	1.253	33

This finding is consistent with the research by Khattak et al. (2021), where the negative binomial model performed better than the Poisson model. Furthermore, Quddus (2008) found that the negative binomial model application is not statistically significant in serial correlation and non-stationarity in time series of accident data. On the other hand, Meel et al. (2007) utilised the National Response Centre (NRC) database for incident prediction through frequency modelling. Their findings found significantly different predictions using Poisson and negative binomial distribution in different companies. Therefore, the same distribution may not agree better across various companies.

Hajakbari and Minaei-Bidgoli (2014) reported that analysing occupational accident databases using data mining could reveal meaningful patterns that are unable to be provided by traditional statistical methods. Radzuan et al. (2020) believed that the accuracy of the prediction model for road traffic accidents in Malaysia could be increased with more features included, such as vehicle types, gender of driver and others. It is also supported by Alawad et al. (2019), where an increase in the dataset and more attributes would contribute to significant analysis and results. However, Choo et al. (2022) reported that the accident database in DOSH Malaysia is still relatively underutilised, and the data received for this study found many missing values, which may affect the accuracy of the modelling. In addition, Koc et al. (2022) highlighted that their finding for the best occupational accident prediction model for short-term and mid-term was the W-ANN model, and the long-term was the W-MARS model. They also reported that the developed predictive model might show different accuracy for different countries due to the country-specific dataset. In addition, Zhu et al. (2023) revealed that the recent text-based AI tool, ChapGPT, frequently obtained mistakes and errors and needs more effective research. Thus, Malaysians must develop an occupational predictive model to manage safety issues more efficiently and understand what national conditions cause more or fewer accidents.

Time Series Prediction

The ARIMA model is a stochastic time series prediction for short-term forecasting with high accuracy and applies to stationary time series (Li et al., 2021). Figure 3 shows the observed monthly accident data reported to DOSH based on the time between accident dates from January 2018 to December 2021. This period was chosen due to the availability, accuracy and quality of the data received from DOSH. The data fluctuates around the mean value, with no noticeable data sequence trend. Therefore, it is preliminarily determined that the data remains stable and does not change over time.

The ACF and PACF plots from R use a 95% confidence level, as shown in Figures 4(a) and 4(b), which are dashed blue lines indicating the significant threshold level. There are many spikes above the threshold level, and both plots observed tail-off patterns. It is observed that the values of AFC coefficients are gradually declining, and the AFC analysis

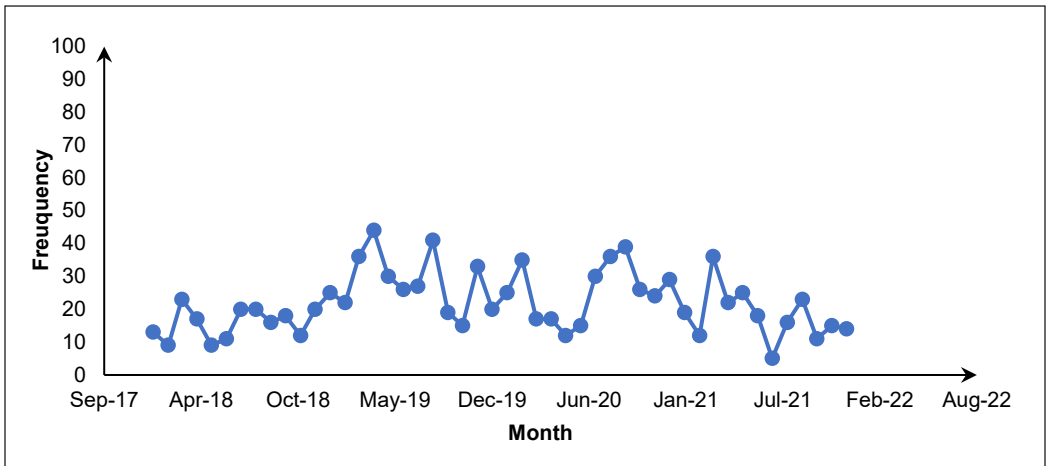
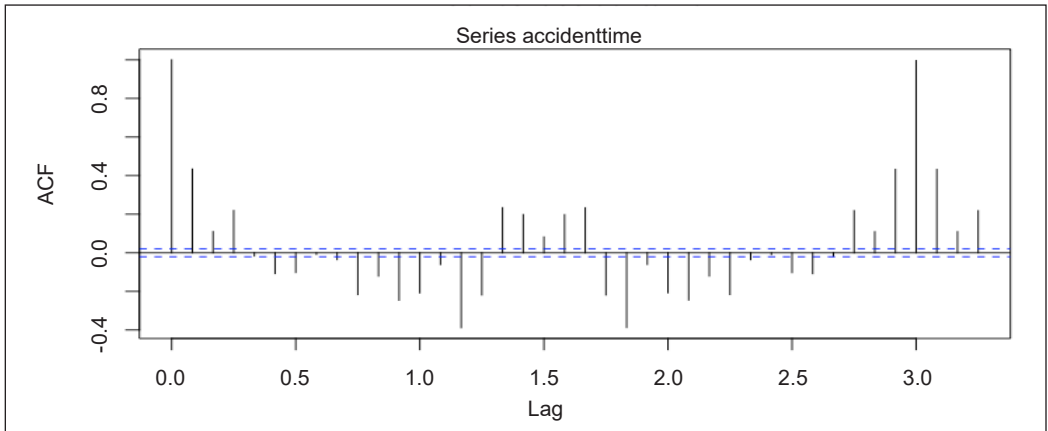
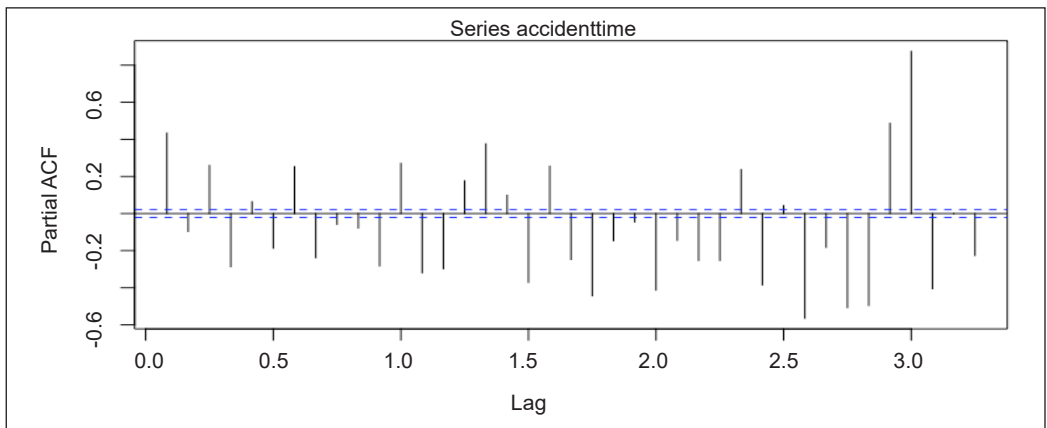


Figure 3. Original time series accident data in KL from January 2018 until December 2021



(a)



(b)

Figure 4. (a) ACF plot; (b) PACF plot

indicates stationary data since the auto-correlation function's fast decay. As highlighted by Alabdulrazzaq et al. (2021), the inspection to visual observation of the data in ACF and PACF helps determine the values for parameters p and q in ARIMA.

The ADF was tested with stationary alternative hypothesis using `adf.test` in the `tseries` package. The ADF test in R showed a printed value of -42.701 , which is smaller than the p -value of 0.01 and indicates a significant autocorrelation pattern (Abdulqader et al., 2020). Therefore, the null hypothesis was rejected, and the stationary trend was verified. Quddus (2008) also studied the ARIMA model with stationarity time series data based on traffic accidents in Great Britain, UK. On the other hand, Al-Hasani et al. (2019) and Abdulqader et al. (2020) investigated a non-stationary time series of monthly road traffic accidents in Oman and Erbin City of Iraq, respectively. It suggests that different time series accident data must confirm their stationarity before applying the modelling process.

Since the series does not have a trend (it is stationary), it is not applied differencing for ARIMA models. The `auto.arima` function of the forecast library in R Studio was used to identify the best-suited series data. This function returned the ARIMA model based on the model's generality, which characterises the sample data and the entire population over a given period. Table 4 presents the ARIMA model that best fits the time series data identified, where ARIMA(2,0,2)(2,0,0)(12) was the best-fit model. The selection of the best-fitting model is based on the lowest rate of AIC, corrected AIC (AICc) or BIC, which denotes better generality and more significant potential for maximising the likelihood function (de Souza et al., 2022). Based on the R Studio models fitting, the lowest AIC reported was 58295.35 for ARIMA(2,0,2)(2,0,0)(12). In addition, the forecast package in R had automatically conducted re-fitting without approximation to confirm the best model, with an AIC value of 58313.39 , which is also lower compared to other models.

The first part of the model has a second-order self-regression ($p = 2$), no differentiation ($d = 0$) and a second-order moving average ($q = 2$). The $p=2$ indicates that two previous periods are used in the auto-regression of the time series, $q=2$ indicates two lags of the error component, and $d=0$ indicates no differencing transformation required to turn the time series into stationary (Alabdulrazzaq et al., 2021). The other part of the model indicates the developed model for the seasonal component, whose elements only have second-order seasonal self-regression ($P = 2$, $D = 0$ and $Q = 0$). The index of 12 refers to the number of periods per season and the corresponding months for different years. Since the input was monthly time series data, the length of seasonality is 12. Based on Table 4, the ARIMA(0,0,0) with zero mean shows the highest AIC value compared to a non-zero mean of the same model. Alabdulrazzaq et al. (2021) reported that the manual model tends to overfit the data.

Interestingly, Abdulqader et al. (2020) reviewed the studies by other researchers in several countries. For example, in Saudi Arabia, the best fatality forecasting model was

Table 4
Results of ARIMA in R

Models Fitting	Mean	AIC
ARIMA(2,0,2)(1,0,1)(12)	Non-zero	60971.19
ARIMA(0,0,0)	Non-zero	64635.14
ARIMA(0,0,0)	Zero	82371.27
ARIMA(1,0,0)(1,0,0)(12)	Non-zero	62606.65
ARIMA(0,0,1)(0,0,1)(12)	Non-zero	61116.68
ARIMA(2,0,2)(0,0,1)(12)	Non-zero	60989.85
ARIMA(2,0,2)(1,0,0)(12)	Non-zero	61018.40
ARIMA(2,0,2)	Non-zero	61281.70
ARIMA(2,0,2)(2,0,0)(12)	Non-zero	58295.35
ARIMA(2,0,1)(2,0,0)(12)	Non-zero	58749.84
ARIMA(1,0,1)(2,0,0)(12)	Non-zero	60348.56
ARIMA(3,0,1)(2,0,0)(12)	Non-zero	58742.65
ARIMA(2,0,2)(2,0,0)(12)	Non-zero (re-fitting without approximation)	58313.39

ARIMA(1,1,3)(0,1,0) by using historical traffic accident data from 2013 to 2017; the AR of order one also showed the best model to analyse traffic accidents in Al-Qadisiya. On the other hand, ARIMA(1,0,0)(2,1,0)12 showed a good performance model for monthly traffic accidents in India, and ARIMA(1,0,2)(1,0,0)12 for motorcycle injuries study. Several works using different statistical methods have been done with traffic accidents worldwide, where each researcher reported their best model for forecasting. However, it is reported that the best model varies from application to application (Domingos, 2012), although many researchers are trying various models and believe in their efforts' superiority. Li et al. (2021) studied highway transportation accidents in China from 2013 to 2019 and applied the ARIMA modelling process.

Freivalds and Johnson (1990) presented ARIMA's Box-Jenkins modelling procedures, where model selection is based on the sum of errors with less than infinity. Thus, ARIMA(2,0,2)(2,0,0) was selected by R. The model established may not be perfect but best suits the available data set and returned the smallest standard error. After fitting the best prediction model, a residual analysis indicated a serial correlation in the data (Quddus, 2008). The statistical tests of Box-Ljung were performed in R, and the p-value is less than the 5% significance level; the residuals are dependent on each other where there is serial correlation and without white noise.

Based on Figure 5 and Table 5, the number of predicted accidents in R (214 cases) and manual time series (229 cases) are low compared to the number of actual accidents (216 cases). Each month, the prediction in R and manual time series was not equal to the actual accident. The number of accidents in actual and prediction shows less difference in April 2021 compared to other months. For the nature of time-series accident data, the

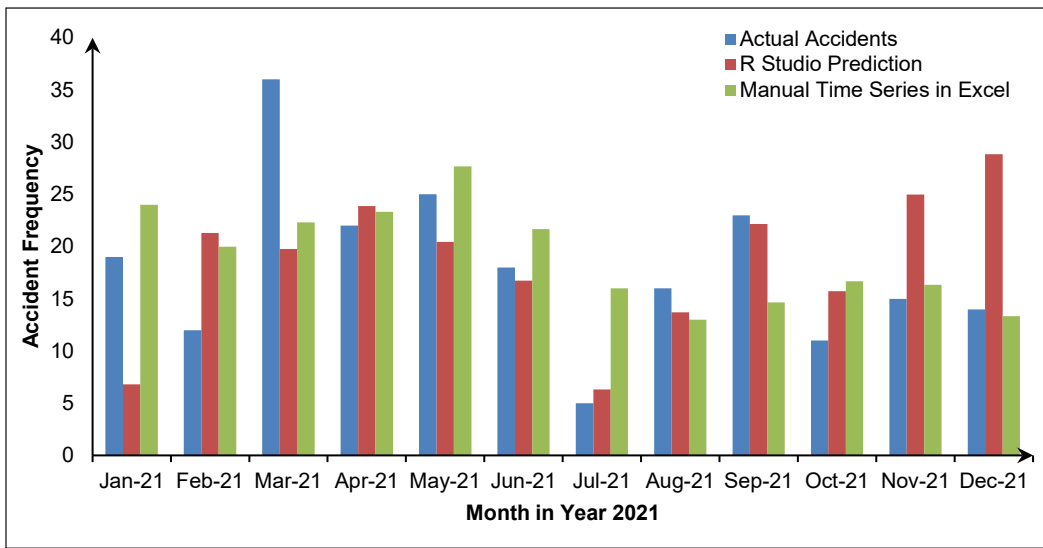


Figure 5. Comparison of actual and predicted accidents

Table 5
Comparison of manual time series and R Studio prediction accuracy

Model	Predicted Accident	MAE	RMSE	MAPE (%)
Manual time series	229	6.181	7.784	49
R Studio	214	6.621	8.537	40

predicted number will vary around the mean of previous months. The predicted number of accidents in R was observed to be a difference of 2 cases from the actual reported cases at 95% confidence, which shows that ARIMA(2,0,2)(2,0,0) produced a reasonably accurate prediction. Compared to the manual time series method, there was a 13-case difference from the actual reported cases. It shows that R Studio is able to forecast more accurately than manual time series. Alabdulrazzaq et al. (2021) presented their forecast for COVID-19 cases using the ARIMA model, which was accurate despite the dynamic conditions of the daily disease data.

They highlighted that utilisation of software packages to facilitate the automated selection of ARIMA’s model in R Studio returned the best-fit model. Table 5 tabulates the prediction accuracy based on MAE, RSME, and MAPE. The MAPE of the prediction in R is 40%, and the manual time series is 49%, which shows that the ARIMA model can make a reasonable prediction. The finding was supported by Attwood et al. (2006), where the number of accidents prediction indicated that the number of future accidents happened was around the mean value of the past number of accidents. Alabdulrazzaq et al. (2021) highlighted that predicted values will not necessarily equal actual observed values but use scale-dependent accuracy measurement, as shown in Table 1. Rohayu et al. (2012) also

found that the ARIMA model performed better than Poisson and Negative Binomial for road accident prediction. Quddus (2008) highlighted that the performance of the model could be measured based on MAE, MAPE and RMSE, where the smaller the value, the better the fit of the model.

On the other hand, Abdulqader et al. (2020) reported that their best model was ARIMA(0,1,1)(1,0,1)₁₂ with an MAE of 23.11, which fits predicted accident injuries. In this study, the number of accidents from April 2021 until September 2021 was close to the forecast values, and there were also decreased and increased forecasted values reported. There are the same mean values of actual accident cases and forecasted accidents in 2021, which is 18 cases. This research used time series analysis to contribute to accident modelling and forecasting, which agrees with Marhavidas et al. (2013). It was also supported by de Souza et al. (2022), where ARIMA successfully applied modelling for time series forecasting.

Table 6 shows the performance of accident data for actual and predicted data using different approaches. From the data analysis, the mean value for R Studio and manual time series prediction is comparable to actual accident data, whereas both negative binomial and Poisson distributions recorded lower values. The negative binomial and Poisson distribution variance significantly differed from the actual accident data. Besides that, the negative binomial and Poisson standard deviation also show a large difference compared to the actual accident data. However, the standard deviation of both R Studio and manual time series prediction is lower than the actual accident data, showing that the R Studio prediction is more accurate than other approaches. On the other hand, in a modelling study conducted by Bora et al. (2020), they observed that lower standard error was considered precise, and the model developed from R was reasonably accurate.

Table 6
Statistical performance of the actual accident and predicted data

Statistical Analysis	Actual Data	R Studio	Manual Time Series	Negative Binomial	Poisson
Mean	18.0	18.4	19.0	14.0	13.0
Variance	58.2	43.6	20.5	596.5	479.2
Standard Deviation	8.0	6.9	4.7	25.2	22.6

CONCLUSION AND FUTURE RESEARCH

This paper investigated the DOSH accident data across various industries in KL and pointed out that the database was incomplete with missing values. This study analyses the accident data and time series models generated by the `auto.arima` function in R. The time series data considered in the study represented monthly industrial accidents in KL from January 2018 to December 2021, totalling 1047 cases. Upon investigation, the stakeholders in accident reporting shall report more detailed information, which could be useful for future

research. The data fit the stationary time series curve, as the Augmented Dickey-Fuller test confirmed. The ARIMA(2,0,2)(2,0,0)(12) model fits predicted numbers and results in the best model in this time series data. The model has been validated against 20% of the actual accident data. The model generated in R outperformed the Poisson and negative binomial model with the lowest MAPE (40%). The MAPE for the manually calculated time series model was 49%.

The results of this study support the idea that auto.arima function from the forecast R package would be a significant improvement in forecasting accident frequency from a safety perspective. Based on the findings, industrial safety practitioners should report accidents truthfully in the era of digitalisation. It could enable future data-driven accident predictions to be carried out. The main bottleneck of the study was the lack of informative records reported and the access to data in DOSH, which resulted in the underutilisation of DOSH data. In addition, the number of datasets used in training can influence the study's results. It can be verified in future by including more data and adjustments to the model. The same data could be tested using Python or Matlab to compare their accuracy.

ACKNOWLEDGEMENT

We thank the Master of Process Safety and Loss Prevention, Department of Chemical and Environmental Engineering, Universiti Putra Malaysia, for providing beneficial insight into improving safety culture in Malaysian industries. This research received no specific grant from funding agencies in the public, commercial, or not-for-profit sectors.

REFERENCES

- Abdulqader, Q. M., Hassan, M. T., & Ahmad, K. H. (2020). Building a mathematical SARIMA model for forecasting the number of monthly injured people by traffic accidents in Erbil City. *Technology Reports of Kansai University*, 62(3), Article 909916.
- Abdullah, D. N. M. A., & Wern, G. C. M. (2011). An analysis of accidents statistics in Malaysian construction sector. *International Conference on E-Business, Management and Economics*, 3(1), 1–4.
- Ahmed, A., Sadullah, A. F. M., Yahya, A. S., Akhtar, M. N., & Azam, Q. (2020). How accurate are locations in Malaysian accident data? Development of a rectification procedure based on nested filtered search technique. *Transportation Research Procedia*, 48, 1125–1141. <https://doi.org/10.1016/j.trpro.2020.08.138>
- Alabdulrazzaq, H., Alenezi, M. N., Rawajfih, Y., Alghannam, B. A., Al-Hassan, A. A., & Al-Anzi, F. S. (2021). On the accuracy of ARIMA based prediction of COVID-19 spread. *Results in Physics*, 27, Article 104509. <https://doi.org/10.1016/j.rinp.2021.104509>
- Alawad, H., Kaewunruen, S., & An, M. (2019). Learning from accidents: Machine learning for safety at railway stations. *IEEE Access*, 8, 633–648. <https://doi.org/10.1109/ACCESS.2019.2962072>
- Al-Hasani, G., Khan, A. M., & Al Reesi, H. (2019). Diagnostic time series models for road traffic accidents data modelling, analysis and forecasting road traffic accidents view project design and verification of

- safety critical embedded systems view project. *International Journal of Applied Statistics and Economics*, 2, 19–26.
- Ali, D., Yusof, Y., & Adam, A. (2017). Safety culture and issue in the Malaysian manufacturing sector. *MATEC Web of Conferences*, 135, Article 00031. <https://doi.org/10.1051/mateconf/201713500031>
- Attwood, D., Khan, F., & Veitch, B. (2006). Validation of an offshore occupational accident frequency prediction model - A practical demonstration using case studies. *Process Safety Progress*, 25(2), 160–171. <https://doi.org/10.1002/prs.10128>
- Ayob, A., Shaari, A. A., Zaki, M. F. M., & Munaaim, M. A. C. (2018). Fatal occupational injuries in the Malaysian construction sector-causes and accidental agents. *IOP Conference Series: Earth and Environmental Science*, 140(1), Article 012095. <https://doi.org/10.1088/1755-1315/140/1/012095>
- Bora, B., Chattopadhyaya, S., & Kumar, R. (2020). Development of mathematical model for friction stir welded joint using “R” programming. *Materials Today: Proceedings*, 27(3), 2142–2146. <https://doi.org/10.1016/j.matpr.2019.09.083>
- Chong, H. Y., & Low, T. S. (2014). Accidents in Malaysian construction industry: Statistical data and court cases. *International Journal of Occupational Safety and Ergonomics*, 20(3), 503–513. <https://doi.org/10.1080/10803548.2014.11077064>
- Choo, B. C., Razak, M. A., Radiah, A. B. D., Tohir, M. Z. M., & Syafie, S. (2022). A review on supervised machine learning for accident risk analysis: Challenges in Malaysia. *Process Safety Progress*, 41(S1), S147-S158. <https://doi.org/10.1002/prs.12346>
- Denham, B. E. (2020). Poisson and negative binomial regression. In *Categorical Statistics for Communication Research* (1st ed.: pp. 74–94). John Wiley & Sons.
- de Souza, J. A. F., Silva, M. M., Rodrigues, S. G., & Santos, S. M. (2022). A forecasting model based on ARIMA and artificial neural networks for end-of-life vehicles. *Journal of Environmental Management*, 318, Article 115616. <https://doi.org/10.1016/j.jenvman.2022.115616>
- Domingos, P. (2012). A few useful things to know about machine learning. *Communications of the ACM*, 55(10), 78–87. <https://doi.org/10.1145/2347736.2347755>
- Esmaili, N., Buchlak, Q. D., Piccardi, M., Kruger, B., & Giroso, F. (2021). Multichannel mixture models for time-series analysis and classification of engagement with multiple health services: An application to psychology and physiotherapy utilization patterns after traffic accidents. *Artificial Intelligence in Medicine*, 111, Article 101997. <https://doi.org/10.1016/j.artmed.2020.101997>
- Freivalds, A., & Johnson, A. B. (1990). Time-series analysis of industrial accident data. *Journal of Occupational Accidents*, 13(3), 179–193. [https://doi.org/10.1016/0376-6349\(90\)90020-V](https://doi.org/10.1016/0376-6349(90)90020-V)
- Hadi, N. A. A., Tamrin, S. B. M., Guan, N. Y., How, V., & Rahman, R. A. (2017). Association between non-reporting of accident and contributing factors in Malaysia’s construction industry. *The Japanese Journal of Ergonomics*, 53(Supplement2), S648-S651. <https://doi.org/10.5100/jje.53.S648>
- Hajakbari, M. S., & Minaei-Bidgoli, B. (2014). A new scoring system for assessing the risk of occupational accidents: A case study using data mining techniques with Iran’s Ministry of labor data. *Journal of Loss Prevention in the Process Industries*, 32, 443–453. <https://doi.org/10.1016/j.jlp.2014.10.013>

- Ismail, N., & Zamani, H. (2013). Estimation of claim count data using negative binomial, generalized Poisson, zero-inflated negative binomial and zero-inflated generalized Poisson regression models. *Casualty Actuarial Society E-Forum*, 41(20), 1–28.
- Jian, T. (2021, October 22–24). *Statistical analysis and countermeasures study on major accidents of highway and waterway in China*. [Paper presentation]. 6th International Conference on Transportation Information and Safety (ICTIS), Wuhan, China. <https://doi.org/10.1109/ICTIS54573.2021.9798527>
- Khattak, M. W., Pirdavani, A., De Winne, P., Brijs, T., & De Backer, H. (2021). Estimation of safety performance functions for urban intersections using various functional forms of the negative binomial regression model and a generalized Poisson regression model. *Accident Analysis and Prevention*, 151, Article 105964. <https://doi.org/10.1016/j.aap.2020.105964>
- Kidam, K., Abidin, Z. Z., Sulaiman, Z., Hashim, M. H., Ripin, A., Ali, M. W., Safuan, H. M., Haron, S., Othman, N., Zakaria, Z. Y., Fandi, F. M., Masri, M. F., Hassan, S. A. H. S., Ali, N. M., Ahmad, A., & Asri, H. (2015). Current status of industrial accident learning in Malaysia. *Journal of Occupational Safety and Health*, 12(1), 1–4.
- Kim, S., Lee, J., & Kang, C. (2021). Analysis of industrial accidents causing through jamming or crushing accidental deaths in the manufacturing industry in South Korea: Focus on non-routine work on machinery. *Safety Science*, 133, Article 104998. <https://doi.org/10.1016/j.ssci.2020.104998>
- Koc, K., Ekmekcioğlu, Ö., & Gurgun, A. P. (2022). Accident prediction in construction using hybrid wavelet-machine learning. *Automation in Construction*, 133, Article 103987. <https://doi.org/10.1016/j.autcon.2021.103987>
- Kuşkapan, E., Çodur, M. Y., & Atalay, A. (2021). Speed violation analysis of heavy vehicles on highways using spatial analysis and machine learning algorithms. *Accident Analysis and Prevention*, 155, Article 106098. <https://doi.org/10.1016/j.aap.2021.106098>
- Li, X., Liu, Y., Fan, L., Shi, S., Zhang, T., & Qi, M. (2021). Research on the prediction of dangerous goods accidents during highway transportation based on the ARMA model. *Journal of Loss Prevention in the Process Industries*, 72, Article 104583. <https://doi.org/10.1016/j.jlp.2021.104583>
- Manan, M. M. A., Jonsson, T., & Várhelyi, A. (2013). Development of a safety performance function for motorcycle accident fatalities on Malaysian primary roads. *Safety Science*, 60, 13–20. <https://doi.org/10.1016/j.ssci.2013.06.005>
- Marhavilas, P. K., Koulouriotis, D. E., & Spartalis, S. H. (2013). Harmonic analysis of occupational-accident time-series as a part of the quantified risk evaluation in worksites: Application on electric power industry and construction sector. *Reliability Engineering and System Safety*, 112, 8–25. <https://doi.org/10.1016/j.res.2012.11.014>
- Meel, A., O'Neill, L. M., Levin, J. H., Seider, W. D., Oktem, U., & Keren, N. (2007). Operational risk assessment of chemical industries by exploiting accident databases. *Journal of Loss Prevention in the Process Industries*, 20(2), 113–127. <https://doi.org/10.1016/j.jlp.2006.10.003>
- Meel, A., & Seider, W. D. (2006). Plant-specific dynamic failure assessment using Bayesian theory. *Chemical Engineering Science*, 61(21), 7036–7056. <https://doi.org/10.1016/j.ces.2006.07.007>

- Melchior, C., Zanini, R. R., Guerra, R. R., & Rockenbach, D. A. (2021). Forecasting Brazilian mortality rates due to occupational accidents using autoregressive moving average approaches. *International Journal of Forecasting*, 37(2), 825–837. <https://doi.org/10.1016/j.ijforecast.2020.09.010>
- Mohamad, E., Shern, T. Y., Jamli, M. R., Mohamad, N. A., Rahman, M. A. A., Salleh, M. R., Oktavianty, O., & Ito, T. (2019, September 25-27). *Readiness of Malaysian manufacturing firms in implementing industry 4.0*. [Paper presentation]. Proceedings of the 29th Design Engineering and Systems Division Lecture Meeting of the Japan Society of Mechanical Engineers, Sendai, Japan. <https://doi.org/10.1299/jsmesd.2019.29.1201>
- Muhamad, M. Q. B., Syed Mohamad, S. J. A. N., & Mat Nor, N. (2021). When digital intelligent taking over: Addressing SMEs readiness on Industry 4.0 in Malaysia. *International Journal of Academic Research in Business and Social Sciences*, 11(1), 543-551. <https://doi.org/10.6007/ijarbss/v11-i1/8335>
- Quddus, M. A. (2008). Time series count data models: An empirical application to traffic accidents. *Accident Analysis and Prevention*, 40(5), 1732–1741. <https://doi.org/10.1016/j.aap.2008.06.011>
- Radzuan, N. Q., Hassan, M. H. A., Majeed, A. P. P. A., Musa, R. M., Razman, M. A. M., & Kassim, K. A. A. (2020). Predicting serious injuries due to road traffic accidents in Malaysia by means of artificial neural network. In Z. Jamaludin & M. N. A. Mokhtar (Eds.), *Intelligent Manufacturing and Mechatronics* (pp. 75-80) Springer. https://doi.org/10.1007/978-981-13-9539-0_8
- Rafindadi, A. D. U., Napiah, M., Othman, I., Mikić, M., Haruna, A., Alarifi, H., & Al-Ashmori, Y. Y. (2022). Analysis of the causes and preventive measures of fatal fall-related accidents in the construction industry. *Ain Shams Engineering Journal*, 13(4), Article 101712. <https://doi.org/10.1016/j.asej.2022.101712>
- Rohani, J. M., Atan, H., Hamid, W. H. W. Johari, M. F., & Ramly, E. (2015). Occupational accident cost estimation: A case study in wood based related industries. *Journal of Occupational Safety and Health*, 12(1), 109–116.
- Rohayu, S., Rahim, S. A. S. M., Marjan, J. M., & Voon, W. S. (2012). *Predicting Malaysian road fatalities for year 2020*. Malaysian Institute of Road Safety Research (MIROS)
- Sari, M., Selcuk, A. S., Karpuz, C., & Duzgun, H. S. B. (2009). Stochastic modeling of accident risks associated with an underground coal mine in Turkey. *Safety Science*, 47(1), 78–87. <https://doi.org/10.1016/j.ssci.2007.12.004>
- Thakali, L., Fu, L., & Chen, T. (2016). Model-based versus data-driven approach for road safety analysis: Do more data help? *Transportation Research Record*, 2601(1), 33–41. <https://doi.org/10.3141/2601-05>
- Warner, P. (2015). Poisson regression. *Basic Biostatistics for Medical and Biomedical Practitioners*, 41(3), 591-595.
- Weng, J., Qiao, W., Qu, X., & Yan, X. (2015). Cluster-based lognormal distribution model for accident duration. *Transportmetrica A: Transport Science*, 11(4), 345–363. <https://doi.org/10.1080/23249935.2014.994687>
- Zein, R. M., Halim, I., Azis, N. A., Saptari, A., & Kamat, S. R. (2015). A survey on working postures among Malaysian industrial workers. *Procedia Manufacturing*, 2, 450–459. <https://doi.org/10.1016/j.promfg.2015.07.078>

Zermane, A., Tohir, M. Z. M., Baharudin, M. R., & Yusoff, H. M. (2022). Risk assessment of fatal accidents due to work at heights activities using fault tree analysis: Case study in Malaysia. *Safety Science*, *151*, Article 105724. <https://doi.org/10.1016/j.ssci.2022.105724>

Zhu, J. J., Jiang, J., Yang, M., & Ren, Z. J. (2023). ChatGPT and environmental research. *Environmental Science & Technology*, *57*(46), 17667–17670. <https://doi.org/10.1021/acs.est.3c01818>

Effects of NaOH Concentration and Plate Surface Texture on the Performance of the HHO Generator

Asmawi Marullah Ridwan^{1,2}, Muhd Ridzuan Mansor^{1*}, Noreffendy Tamaldin¹, Fahamsyah Hamdan Latief² and Viktor Vekky Ronald Repi³

¹*Faculty of Mechanical Technology and Engineering, Universiti Teknikal Malaysia Melaka, Hang Tuah Jaya, Durian Tunggal 76100, Melaka, Malaysia*

²*Department of Mechanical Engineering, Faculty of Engineering and Science, Universitas Nasional, Jakarta 12520, Indonesia*

³*Department of Engineering Physics, Faculty of Engineering and Science, Universitas Nasional, Jakarta 12520, Indonesia*

ABSTRACT

The need for clean energy as an alternative is inevitable. HHO gas has received much attention lately. In addition to electrolyte concentration, the breakthrough with a diverse electrode surface texture approach has not been extensively performed. Therefore, this study aims to determine the effects of NaOH concentration and plate surface texture on the performance of the HHO generator. In general, the increase in electrolyte concentration combined with surface texture caused an increase in output current, HHO gas production, and output temperature. As for the applied voltage variation with various surface textures, the increase in output current, HHO gas production, and output temperature also took place, similar to the case of increasing NaOH concentration. Either an increase in electrolyte concentration or an increase in applied voltage triggers faster ion movement, leading to

an increase in conductivity, thus effectively assisting the electrolysis of water. Regarding the output current and HHO gas production, the textured surface had a much higher value than the plain surface in terms of increasing NaOH concentration or applied voltage variations. However, according to the R^2 results, the linear surface has a stronger relationship with the output current and HHO gas production than the cross surface. In the case of the output temperature, the linear surface was slightly lower than the

ARTICLE INFO

Article history:

Received: 19 July 2023

Accepted: 20 November 2023

Published: 01 April 2024

DOI: <https://doi.org/10.47836/pjst.32.3.08>

E-mail addresses:

asmawi@civitas.unas.ac.id (Asmawi Marullah Ridwan)

muhd.ridzuan@utem.edu.my (Muhd Ridzuan Mansor)

noreffendy@utem.edu.my (Noreffendy Tamaldin)

fhlatief@civitas.unas.ac.id (Fahamsyah Hamdan Latief)

vekky_repi@civitas.unas.ac.id (Viktor Vekky Ronald Repi)

* Corresponding author

cross surface. It is possibly due to impurities in the electrolyte solution that contaminate the electrode surface, resulting in a lower output temperature on the linear surface.

Keywords: HHO generator, hydrogen, NaOH, performance, surface texture

INTRODUCTION

The ongoing problem of global warming and ozone layer depletion has prompted a search for renewable energy alternatives that do not emit harmful pollutants to human health and the environment. In addition, this is also inspired by the availability of fossil fuels that have begun to deplete; thus, the development and discovery of renewable energy must get more serious attention for the benefit of human life in the future (Dufour et al., 2011; Muritala et al., 2020). One alternative energy introduced lately through the development of oxyhydrogen (HHO) generators has an economic advantage and a main resource easily obtained and available in nature, namely water (Dincer & Zamfirescu, 2012).

Among the various types of alternative fuels that exist, hydrogen gas is the cleanest energy source. The hydrogen gas can be principally produced using electrolysis (Grigoriev et al., 2020), which is achieved by separating the atoms contained in water molecules by applying electric current to the cathode and anode, acting as negative and positive poles, respectively, immersed in water, resulting in chemical reactions in accordance with the concept of redox. The interesting things about HHO gas are its lightness, colourlessness, easy reaction with other chemicals, and flammability. However, the improvements in the performance of the generator are still needed. The proposed method to improve its performance is either increasing the concentration of the catalyst, which is made of an electrolyte solution (Hassan et al., 2022; Soler et al., 2009), or, more recently, manipulating the effective surface of the electrode plate (Ayub et al., 2022).

Meanwhile, surface texture engineering has been introduced in recent years to optimise engine performance and is expected to expand its practical applications (Rao et al., 2021). For example, in a study conducted by Borghi et al. (2008), the effect of surface modification by laser texturing on the tribological performance of nitrided steels for high-performance engine applications was thoroughly investigated. The original idea of surface texture engineering was to improve the mechanical and tribological properties of engine metal components (Naat et al., 2023; Rajput et al., 2021). It is noted that the chemical composition and surface hardness of objects have an important influence on the wear resistance of materials under sliding conditions. Many components made of steel or other ferrous materials are nitrided to improve their wear resistance, fatigue strength, and corrosion resistance (Fahy, 2014; Kato et al., 1994). Moreover, surface texture fabrication has been carried out by various techniques, i.e., chemical etching, atomic layer deposition, ultrasonic-assisted milling, laser surface texturing, micro-milling, and electrical discharge

(EDM) (Ayub et al., 2022; Li et al., 2018; Li et al., 2022). Based on the literature review, surface texture engineering provides several advantages, including lowering friction and wear, increasing load-carrying capacity, and increasing fluid layer stiffness. Previous studies hinted that the surface texture of the electrode impacts electrolysis, which in turn impacts the rate of hydrogen gas production (Xu et al., 2021; Zeng & Zhang, 2014).

An equally important variable for increasing hydrogen gas production is the type of electrolyte solution and concentration levels used. Among the types of electrolytes that have been used previously in HHO generators are potassium hydroxide (KOH) (Karthik, 2017; Manu et al., 2016) and sodium hydroxide (NaOH) (Alam & Pandey, 2017; Ismail et al., 2018). Many studies have been conducted to find the relationship between the electrolyte type and the HHO gas production rate. The results show that the electrolyte concentration is important in increasing the HHO gas flow rate. It was also found that an increase in electrolyte concentration by 1% molality led to increased current consumption (Yilmaz et al., 2010). Fiala et al. (2013) have conducted a comparative study on the use of KOH and NaOH in HHO generators. The conclusion obtained is that the use of a KOH electrolyte concentration of 10% was able to achieve optimal conditions because KOH has better chemical stability and more efficient HHO gas production when compared to NaOH. Santilli (2006) reported that sulfuric acid and other electrolytes are sometimes added to KOH and NaOH to promote water electrolysis.

Apart from what has been described above, it turns out that other important parameters also affect the production of HHO gas, such as the cross-sectional area of the electrodes used, the distance between electrodes, the configuration of the plate arrangement, and the type of electrode plate materials, (Ridhuan et al., 2021). With regard to the lack of research on the effect of surface texture on electrode plates that have been carried out, the combination of the two variables, in this case, the type of electrolyte and the surface texture of the electrode, is a very interesting and promising topic for further study in efforts to develop HHO generators in the future. Therefore, the main objective of this study is to evaluate the effects of varying NaOH concentrations and the surface texture of the electrode plates on the performance of the HHO generator.

MATERIALS AND METHODS

Materials

In this study, the first stage involves modifying the surface of the electrode plate to be installed on the HHO generator. Following the modification, performance testing of the HHO generator was conducted with variations in NaOH catalyst concentrations, specifically 10 g, 20 g, 30 g, 40 g, 50 g, and 60 g, respectively, at 12V applied voltage. Subsequently, the applied voltage was kept constant at 12V for all test parameters. The research then proceeded to test the performance of the HHO generator using electrode cell plates with

different surface textures. These surface textures of the electrode plate consist of plain, linear, and cross patterns (Figure 1). The output parameters analysed based on the catalyst concentration and application voltage input include the HHO gas production rate, output current, and output temperature.

The electrode plate base material is made of commercial 316 stainless steel labelled “SS316L,” which has a chemical composition as shown in Table 1. The electrode plates used in this study have dimensions of 100 mm × 100 mm × 1 mm and three different types of plate surface textures, as illustrated in Figure 1. Based on the prepared design, the HHO generator was equipped with five SS316L electrode plates with 2 mm between each plate.

Table 1
The chemical composition of SS316L (in wt.%)

Fe	Cr	Ni	Mo	Mn	C	P	S	Si	N
Bal.	16	10	2	2	0.03	0.045	0.03	0.75	0.1

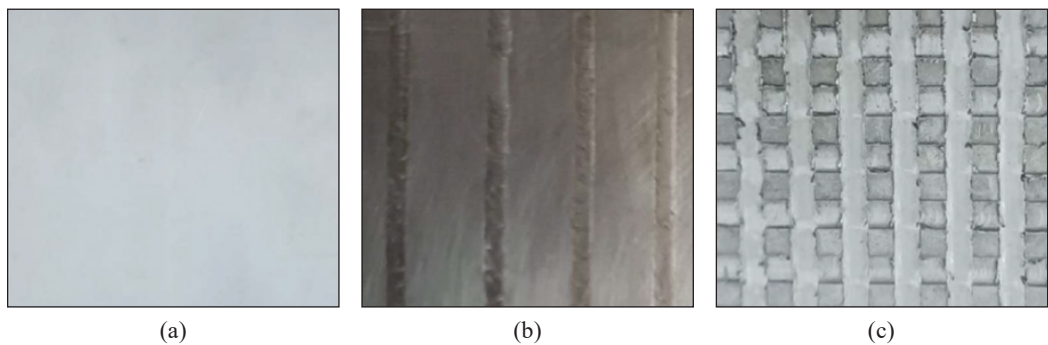


Figure 1. Surface texture types of electrode plates used in HHO generators: (a) plain; (b) linear; and (c) cross-surface

Fabrication of Electrode Surface Textures

The texturing of the electrode surface was performed using a machining process. The first step starts with creating patterns for each design using CAD software called CATIA V5 R20 to produce patterns with good precision and accuracy, as presented in Figures 2 and 3. The second step is to use the patterns prepared to proceed with the machining process and obtain the program codes for each pattern. In the third step, the program codes were input into the CNC machine to create the desired texture on the surface of each electrode plate. Electrode surface texturing was performed using a machining process. The first step was to create patterns for each design using CAD software, CATIA V5 R20, to produce patterns with precision and accuracy. In the second step, based on the created patterns, the machining process was continued to obtain the program codes for each pattern. In the third step, the program codes are input into the CNC machine to create the desired texture on the

surface of each electrode plate. In the fourth step, the fabrication process for texturing was carried out at 1150 mm/min for about 20 minutes for each type of plate. In the fifth step, coolant was continuously applied during the machining process to lubricate the contact area between the surface of the plate and the tool and to cool the temperature arising from

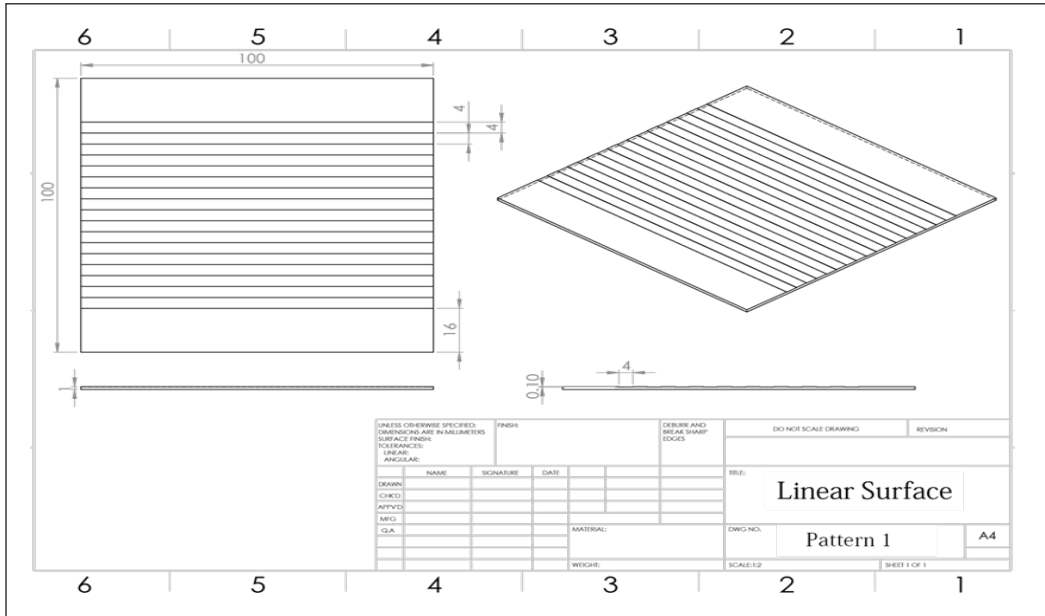


Figure 2. The surface texture design of the electrode plate with a linear pattern (unit dimension = mm)

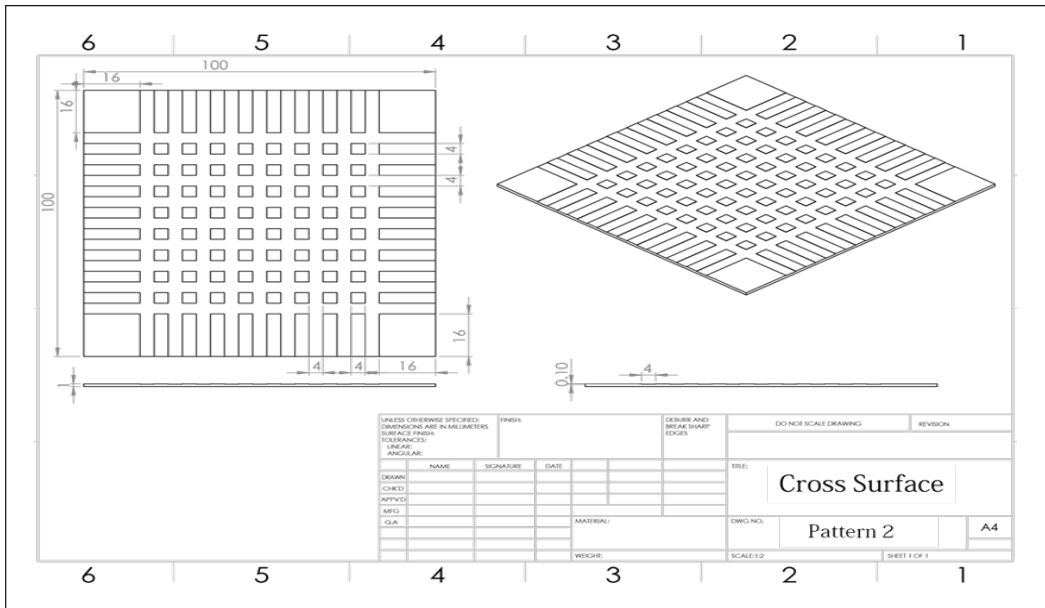


Figure 3. The surface texture design of the electrode plate with a cross-pattern (unit dimension = mm)

the contact, thus preventing tool wear and producing a good surface finish. The last step was to ensure that the surface of the electrode plate was free from any remaining cutting residue with the aid of a tool file before polishing with isopropyl.

Setup of the HHO Generator

In this study, the designed HHO generator combines wet cells and dry cells since both cell types have advantages over each other that are interesting to observe. It should be noted that the calibration method was used to assess the performance of the HHO generator in producing the desired HHO gas. A detailed schematic of the HHO generator parts is shown in Figure 4. The following steps need to be taken to set up the HHO generator: NaOH electrolyte solution is put into the container to submerge the electrode plates completely. Then, the power supply is connected to the HHO generator by providing a constant input voltage of 12 V. After the voltage is supplied, the electrolysis process takes place, and bubbles begin to appear slowly as a sign of HHO gas production. The calibration method is used to evaluate the performance of the HHO generator in producing the HHO gas.

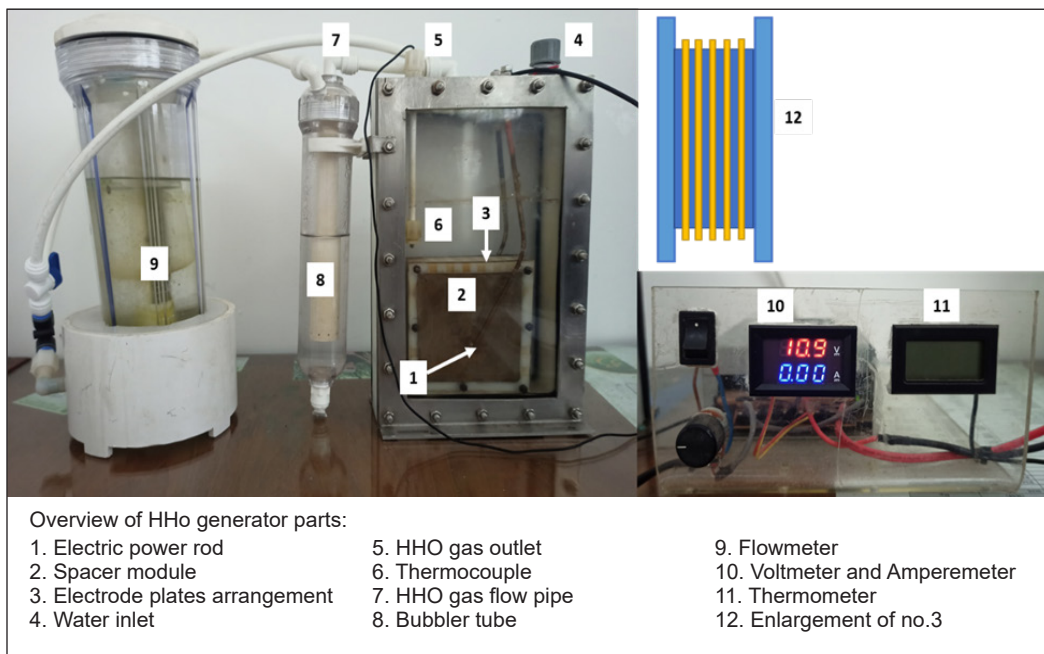


Figure 4. Schematic arrangement of the parts of the HHO generator

Measurement Procedures

The procedure of measuring the output current, HHO gas production rate, output temperature, and operating time is important to understand. Systematically, it starts filling the container with NaOH electrolyte with a predetermined concentration ranging from 10

g/L to 60 g/L so that the installed electrode plates are thoroughly and evenly submerged. Then, the “on” button on the generator is pressed to activate the electricity needed for the electrolysis process to take place as expected. After pressing the on button, the HHO generator is allowed to stand for approximately 30 minutes to stabilise its condition. After a stable condition has been achieved, the voltage is kept constant at 12 V, and the stopwatch starts to be activated at the beginning of the calculation.

Furthermore, the HHO gas production process runs as the operating time increases, which causes a gradual increase in the volume of water in the flowmeter so that the scale shows a value of 10 ml (assumed to be the maximum value), which indicates that the hydrogen production rate is running well and is usually followed by an increase in temperature due to the chemical reactions taking place. After reaching the maximum condition, the HHO generator engine was immediately deactivated, the amount of output current produced was visible on the power supply screen, the volume of hydrogen gas produced was easily identified, and the output temperature was also read on the screen via the thermocouple connection connected to the generator. The operating time is calculated from the start of the generator being turned on until it is turned off, which can be read through a stopwatch. The results of each determined parameter are obtained from the various observations made. In the final stage, data analysis is needed to be able to find out how variations in NaOH electrolyte concentration and electrode plate surface texture affect the actual performance of the HHO generator.

RESULTS AND DISCUSSION

Effect of NaOH Concentration on Output Current at Varying Plate Surface Textures

Figure 5 shows the relationship between the output current and NaOH concentration at various surface textures of the electrode plate under the condition of a constant voltage of 12 V. It is obviously seen that the output current increases with increasing NaOH concentrations from 10 g/L to 60 g/L, which occurs in all types of plate surface textures. From the results obtained, increasing the electrolyte concentration plays an important role in producing the output current obtained. It is understandable that the NaOH electrolyte will decompose into Na^+ and OH^- ions, resulting in electron

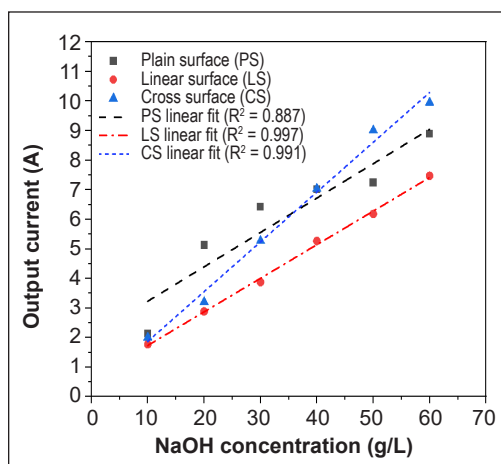


Figure 5. Output current vs. NaOH concentration under varying plate surface textures at 12V applied voltage

transfer and increased water conductivity (Rusdianasari et al., 2019). Increasing the electrolyte concentration has an impact on increasing the rate of electron transfer between the installed electrode plates.

Even further, the conductance generated by the electrodes also increased. Because of these two things, the output current achieved will vary, and if observed carefully, it comes down to the rate of water dissociation (Wang et al., 2021). In contrast, increasing electrolyte concentration decreases the electrical resistance and increases the current. On the other hand, decreasing electrolyte resistance can cause an increase in electrical conductivity and a decrease in potential simultaneously. Besides that, the resistance in the electrolyte and electrodes can affect the resulting current output values due to side reactions, inverse reactions, and the factor of impurities attached to the electrode surface. The impurities in the electrolyte, such as magnesium, calcium, and chloride ions, can also cause side reactions. On the other hand, the resistances in the electrolytic solution and electrodes brought on by inverse reactions, side reactions, and impurities in electrode material also influence the electric current values obtained (Zeng & Zhang, 2010).

Another reason to consider is the distance between the electrode plates. In this study, the distance between the electrodes was 2 mm, indicating a much closer distance between the electrodes. As mentioned in the previous study, close spacing between electrodes effectively reduces the electrical resistance between the electrodes, increasing the amount of current generated (Galama et al., 2016). Still related to Figure 5, the increase in output current at electrolyte concentrations of 10 g/L to 60 g/L is above 300% for all electrode surface textures. However, from a linear regression perspective, the highest R² value is for the linear surface texture of 0.997, which means the accuracy is very good for this linear surface. The results also indicated that using different electrode surface texture types affects the output current achieved by the HHO generator. The surface textures created make a difference in the effective surface area of the electrodes. The surface area calculation of each surface texture is summarised in Table 2.

Table 2 shows that the cross-sectional area for the linear surface is 101.8 cm², which is the highest compared to the other types. The relationship between electrode cross-sectional area and electrical resistance is given in Equation 1 (Mazloomi & Sulaiman, 2012).

$$R = \frac{\rho l}{A} \tag{1}$$

where R is the electrical resistance of the material, ρ is the electrode material’s resistivity, A is the cross-sectional area of the electrode and l is the distance between the electrodes used to do the measurement. The

Table 2
Cross-section area of the electrode plate with varying surface textures

Type of surface textures	Texture labelling	Cross-section area (cm ²)
Plain surface	PS	100.00
Linear surface	LS	101.80
Cross surface	CS	102.30

large cross-sectional area allows the resulting electrical resistance to be small. It is known that electrical resistance is the opposite of electric current; thus, when electrical resistance decreases, the resulting output current will increase. It is also necessary to understand that the surface area of the electrode plate refers to the area of the conducting plate, which functions to transmit electric current. The broader the cross-section area, the greater the electric current that can be delivered (Poimenidis et al., 2021).

Effect of NaOH Concentration on HHO Production Rate at Varying Plate Surface Textures

Figure 6 illustrates the HHO gas production rate against the NaOH electrolyte concentration at different electrode surface textures. Similar to the output current, the same trend is also shown by the HHO gas production rate, where the increase fully influences the increase in HHO gas production in electrolyte concentration. The results showed that the increase in HHO gas production rate was above 200% for all electrode surface textures. As for the 60 g/L electrolyte concentration, the HHO gas production rate value is 305.93 L/min, 291.09 L/min, and 218.08 L/min for cross, linear, and plain surface textures, respectively. It should be noted that increasing the electrolyte concentration can generally accelerate the movement of molecules in the water so that a higher-intensity collision process occurs between molecules available in it, such as hydrogen and oxygen. The higher the intensity of collisions between molecules in the water, the greater the amount of HHO gas produced (El Soly et al., 2021). However, based on the statistical approach, the linear surface texture had the highest R^2 value of 0.991. In addition to the increase in electrolyte concentration, it appears that the difference in electrode surface texture has a positive impact on the rate of HHO gas production. Texturing the surface of the electrode plates has affected their surface roughness, which results in a difference in cross-sectional area between each other. The results obtained align with the achievements Fahy reported (2014).

Another important factor is the type of electrode plate material. This study used SS316L, which has a high nickel concentration (about 10 per cent by weight), as the electrode. The electrode made of SS316L is in an alkaline environment because it uses NaOH as the electrolyte, where the hydrogen evolution reaction (HER) takes place at the cathode, which acts

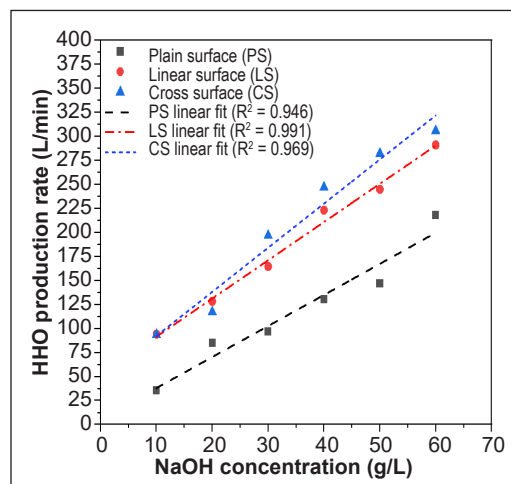
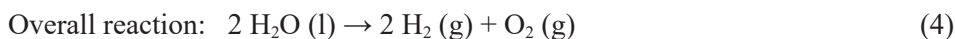
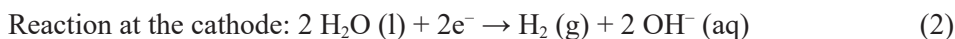


Figure 6. HHO production rate vs. NaOH concentration under varying plate surface textures at 12 V applied voltage

as the negative pole. In contrast, at the anode, which acts as the positive pole, the oxygen formation reaction (OER) takes place. As a function of time, the hydrogen evolution rate (HER) increases with rising electrolyte concentration. However, the HER rate tends to be slower in NaOH compared to KOH. The characteristics of the electrocatalytic surface significantly influence the HER rate. Electrochemical analysis of stainless steel indicates that 316 steel is the optimal choice for a cathodic electrode in inducing HER within the solution.

The HER rate is not only affected by the concentration of the electrolyte but also impacts the formation of metal hydrides in stainless steel, minimising corrosive effects on the material. Meanwhile, oxygen hydroxide (OH) originates from the water structure and surfaces of OER. The presence of OH serves a dual purpose: firstly, an excess of OH can detrimentally affect conductivity and structural integrity. Secondly, moderate OH levels with the right level of acidity at the electrode/electrolyte interface can positively influence the fundamental oxygen evolution reaction and thermodynamically reduce the ion release rate. It is based on the non-electrocatalytic activity in oxygen evolution reactions, as well as the identification of crystalline defects and stoichiometric oxide anode levels, which contribute to the oxygen evolution reactions.

Of course, this phenomenon is most likely inseparable from the formation of the nickel hydrate layer, which acts as a protective layer on the electrode surface, allowing the corrosion rate to be suppressed, which results in a fairly high HHO gas production rate (Olivares-Ramírez et al., 2007). The minimum corrosion effect greatly contributes to the smoothness of the hydrogen formation reaction (Vračar & Conway, 1990). Coupled with surface texture engineering, this will be a promising technique and should be taken into account for the development of further enhancements of HHO gas production. The details of the chemical reaction Equations 2, 3 and 4 at each pole are shown as follows gas (Subramanian & Thangavel, 2020):



According to stoichiometry, the above chemical reaction shows that the production of hydrogen gas is double that of oxygen gas (Subramanian & Thangavel, 2020).

Effect of NaOH Concentration on Output Temperature at Varying Plate Surface Textures

The results of the output temperature versus NaOH concentration at different surface textures are shown in Figure 7. The output temperature generally shows an increasing trend

with increasing NaOH concentration at all types of electrode surface textures, where the temperature increase ranges above 40 per cent for NaOH electrolyte concentrations of 0–60 g/L. The final output temperatures at 60 g/L concentration were 42.5°C for the plain surface, 45.13°C for the linear surface, and 46.55°C for the cross surface. However, there was some temperature instability for each type of surface texture. The most obvious instability is for the electrode with cross-surface texture, where there is a decrease in the output temperature at two different concentrations, one from 39.05°C to 24°C and the other from 50.18°C to 46.55°C.

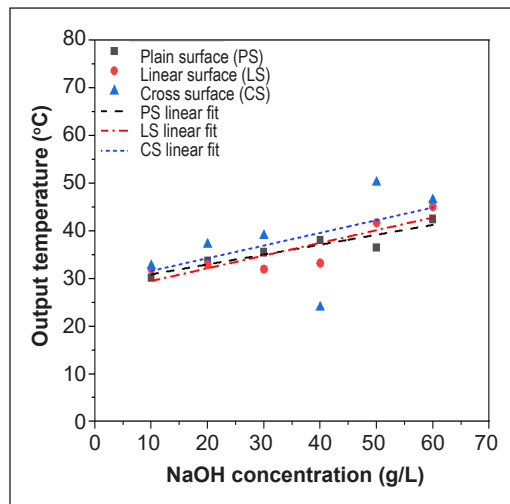


Figure 7. Output temperature vs. NaOH concentration under varying plate surface textures at 12 V applied voltage

This instability phenomenon may be due to the type of electrolyte used, NaOH. The basic principle of an electrolyte solution is that it is influenced by the mobility and conductivity of ions that decompose in the solution. As already stated, the mobility and conductivity of Na⁺ ions are lower than those of K⁺ ions (Cao et al., 2009). It is likely to cause instability in the resulting output temperature, and the presence of impurities in the electrolyte solution that could contaminate the electrode surface must also be considered (Doche et al., 1999).

The type of electrolyte and electrolyte concentration play an important role in water electrolysis. NaOH is strong as a type of electrolyte; it decomposes completely into ions when dissolved in water, so it has a fairly high conductivity. When the electrolyte concentration is increased, it increases the intensity of collisions between ions, making them more intense. The resulting impact is increased conductivity, accompanied by higher ion mobility during the water electrolysis process. Due to the increased conductivity, it produces an electrolyte solution temperature that is much hotter than its initial condition, and thus, the output temperature of the HHO generator also rises (Sun & Hsiau, 2018; Yuvaraj & Santhanaraj, 2014).

Effect of Applied Voltage on Output Current at Varying Plate Surface Textures

Figure 8 shows the applied voltage and output current at varying electrode surface textures. Their relationship shows good linearity, where the output current increases with increasing input current. Upon further observation, the increase in output temperature is more prominent on textured electrode surfaces, with an increase of over 300% on both types

of textured electrode surfaces. In contrast, the increase in output current is only about 148% for plain surfaces with increasing applied voltage. Beyond that, the largest R^2 value of 0.982 was experienced by the electrode with a linear surface. This value indicates a strong relationship between the input voltage variation and the output current.

Figure 8 shows that a higher applied input voltage will accelerate the decomposition reaction in water electrolysis. The supplied applied voltage causes faster electron movement, producing a higher output current (Zhao et al., 2016).

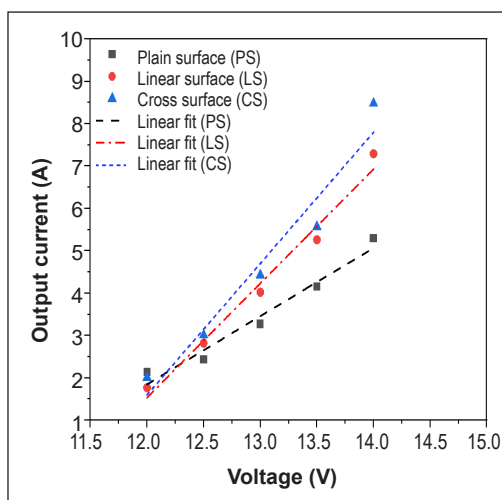


Figure 8. Applied voltage variations vs. output current under varying plate surface textures at 30g/L catalyst concentration

Effect of Applied Voltage on HHO Production Rate at Varying Plate Surface Textures

Figure 9 shows the HHO gas production as a function of applied voltage with variations in electrode surface texture. The results showed a significant increase in the HH gas production rate on the electrodes with linear and cross textures, namely 508.74 L/min and 573.82 L/min, respectively. A striking difference is seen for electrodes with plain surfaces, where the HHO gas rate is only 147.66 L/min. The increased applied voltage resulted in a uniform increase in charge density, promoting the acceleration of chemical reaction rates on the electrode surface by ion exchange (Lin et al., 2012). It is clearly seen that electrodes with textured surfaces are more effective in accommodating the ion exchange process to increase the rate of kinetics of the decomposition reaction in water electrolysis, which in turn can increase the rate of HHO gas production. The highest R^2 value was 0.979, achieved by the electrode with a linear surface texture. Lastly, this is also supportive evidence that HHO gas production is more promising on

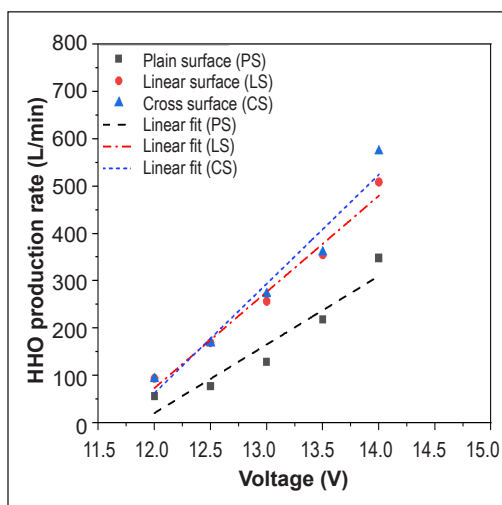


Figure 9. Applied voltage variations vs HHO production gas under varying plate surface textures at 30 g/L catalyst concentration

textured electrode surfaces. The results obtained are in accordance with the results stated by Mounir and Bellel (2011), where it is explained that the rate of hydrogen gas production will continue to increase as the voltage variation used increases.

Effect of Applied Voltage on Output Temperature at Varying Plate Surface Textures

Figure 10 shows various plate surface textures' applied voltage and output temperatures. At an applied voltage of 12 V, the resulting output temperature is 27.88°C for plain surfaces, 33.66°C for linear surfaces, and 32.71°C for cross surfaces. Interestingly, with increasing applied voltage, the output temperature increased slowly. At an input voltage of 14 V, the output temperature values achieved are 39.67°C for the plain surface, 37.52°C for the linear surface, and 44.11 °C for the cross surface. The increase in output temperature on the linear surface is the slowest compared to other electrode surfaces; the increase is only about 11.47% with an applied voltage range of 12 V–14 V. It seemed that increasing the input voltage had a lower impact on the output temperature at the linear surface compared with other surfaces. Increasing the output temperature may reduce the possibility of splitting water molecules. However, on the other hand, it can increase the reaction of the electrode surface and the ionic conductivity of electrolytes (El Kady et al., 2020). In addition, the accelerated mobility of ions due to increased applied voltage was also a reason for the increased output temperature.

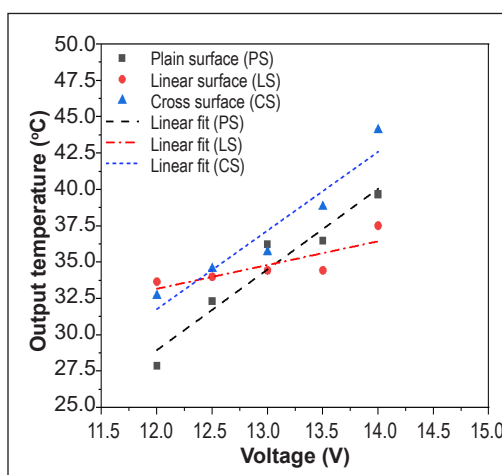


Figure 10. Applied voltage variations vs. output temperature under varying plate surface textures at 30 g/L catalyst concentration

CONCLUSION

The effect of varying NaOH electrolyte concentration in a range of 10 g/L to 60 g/L and electrode surface texture on the performance of the HHO generator was investigated. Several important points can be drawn from the present study as follows:

1. Overall, the output current, HHO gas production, and output temperature increase with increasing NaOH concentration and are also influenced by different electrode surface textures.
2. At a NaOH concentration of 60 g/L, the output currents on the linear and cross surfaces were 7.46 A and 9.95 A, respectively. Meanwhile, the HHO gas production for the linear and cross surfaces was 219.08 L/min and 305.93 L/min, respectively.

However, in terms of R² value, the linear surface is better than the cross surface, where the R² value is greater than 0.991 for both the output current and HHO gas production on the linear surface.

3. Additionally, the output temperature of the linear surface (i.e., 45.12 °C) was slightly lower than that of the cross surface (i.e., 46.55 °C) at a NaOH concentration of 60 g/L.
4. Similar to the NaOH concentration increment, the output current, HHO gas production, and output temperature also increased linearly with increasing applied voltage at varying electrode surface textures and a constant NaOH concentration of 30 g/L.
5. The HHO gas production on the linear surface and cross surface increased drastically at an output voltage of 14 V, to be about 508.74 L/min and 573.82 L/min, respectively. However, the R² value of the linear surface is higher than that of the cross surface, which is 0.979 and 0.955, respectively.

ACKNOWLEDGEMENT

The authors thank Universiti Teknikal Malaysia Melaka, as well as Universitas Nasional, Indonesia, for the financial support they provided throughout the completion of this study.

REFERENCES

- Alam, N., & Pandey, K. M. (2017). Experimental Study of hydroxy gas (HHO) production with variation in current, voltage and electrolyte concentration. *IOP Conference Series: Materials Science and Engineering*, 225(1), Article 012197. <https://doi.org/10.1088/1757-899X/225/1/012197>
- Ayub, M. S., Yusof, S. N. A., Mohamed, S. B., Said, M. S., Asako, Y., Sidik, N. A. C., Kashim, M. S., & Mohamad, A. T. (2022). Effect of electrode plates on the engine performance and gas emissions of a four-stroke petrol engine. *Journal of Advanced Research in Fluid Mechanics and Thermal Sciences*, 90(2), 90–108. <https://doi.org/10.37934/arfmts.90.2.90108>
- Borghini, A., Gualtieri, E., Marchetto, D., Moretti, L., & Valeri, S. (2008). Tribological effects of surface texturing on nitriding steel for high-performance engine applications. *Wear*, 265(7), 1046–1051. <https://doi.org/10.1016/j.wear.2008.02.011>
- Cao, X. D., Kim, B. H., & Chu, C. N. (2009). Micro-structuring of glass with features less than 100µm by electrochemical discharge machining. *Precision Engineering*, 33(4), 459–465. <https://doi.org/10.1016/j.precisioneng.2009.01.001>
- Dincer, I., & Zamfirescu, C. (2012). Sustainable hydrogen production options and the role of IAHE. *International Journal of Hydrogen Energy*, 37(21), 16266–16286. <https://doi.org/10.1016/j.ijhydene.2012.02.133>
- Doche, M. L., Rameau, J. J., Durand, R., & Novel-Cattin, F. (1999). Electrochemical behaviour of aluminium in concentrated NaOH solutions. *Corrosion Science*, 41(4), 805–826. [https://doi.org/10.1016/S0010-938X\(98\)00107-3](https://doi.org/10.1016/S0010-938X(98)00107-3)

- Dufour, J., Serrano, D. P., Gálvez, J. L., Moreno, J., & González, A. (2011). Hydrogen production from fossil fuels: life cycle assessment of technologies with low greenhouse gas emissions. *Energy & Fuels*, *25*(5), 2194–2202. <https://doi.org/10.1021/ef200124d>
- El Kady, M. A., Farrag, A. E. F., Gad, M. S., El Soly, A. K., & Abu Hashish, H. M. (2020). Parametric study and experimental investigation of hydroxy (HHO) production using dry cell. *Fuel*, *282*, Article 118825. [/https://doi.org/10.1016/j.fuel.2020.118825](https://doi.org/10.1016/j.fuel.2020.118825)
- El Soly, A. K., El Kady, M. A., Farrag, A. E. F., & Gad, M. S. (2021). Comparative experimental investigation of oxyhydrogen (HHO) production rate using dry and wet cells. *International Journal of Hydrogen Energy*, *46*(24), 12639–12653. <https://doi.org/10.1016/j.ijhydene.2021.01.110>
- Fahy, K. F. (2014). Enhancement of water electrolyzer efficiency. *Journal of Energy Technologies and Policy*, *4*(11), 1–2.
- Fiala, J., Kuracina, M., Hrušovský, I., & Soldan, M. (2013). Study of basic characteristics of hydrogen generator. *Applied Mechanics and Materials*, *448–453*, 3078–3081. <https://doi.org/10.4028/www.scientific.net/AMM.448-453.3078>
- Galama, A. H., Hoog, N. A., & Yntema, D. R. (2016). Method for determining ion exchange membrane resistance for electrodialysis systems. *Desalination*, *380*, 1–11. <https://doi.org/10.1016/j.desal.2015.11.018>
- Grigoriev, S. A., Fateev, V. N., Bessarabov, D. G., & Millet, P. (2020). Current status, research trends, and challenges in water electrolysis science and technology. *International Journal of Hydrogen Energy*, *45*(49), 26036–26058. <https://doi.org/10.1016/j.ijhydene.2020.03.109>
- Hassan, H., Aissa, W. A., Eissa, M. S., & Abdel-Mohsen, H. S. (2022). Enhancement of the performance and emissions reduction of a hydroxygen-blended gasoline engine using different catalysts. *Applied Energy*, *326*, Article 119979. <https://doi.org/10.1016/j.apenergy.2022.119979>
- Ismail, T. M., Ramzy, K., Abelwhab, M. N., Elnaghi, B. E., El-Salam, M. A., & Ismail, M. I. (2018). Performance of hybrid compression ignition engine using hydroxy (HHO) from dry cell. *Energy Conversion and Management*, *155*, 287–300. <https://doi.org/10.1016/j.enconman.2017.10.076>
- Karthik, N. B. V. S. R. (2017). Better performance of vehicles using HHO gas. *American Journal of Mechanical Engineering*, *5*(4), 167–174. <https://doi.org/10.12691/ajme-5-4-9>
- Kato, H., Eyre, T. S., & Ralph, B. (1994). Sliding wear characteristics of nitrided steels. *Surface Engineering*, *10*(1), 65–74. <https://doi.org/10.1179/sur.1994.10.1.65>
- Li, H., Xu, W., Li, L., Xia, H., Chen, X., Chen, B., Song, X., & Tan, C. (2022). Enhancing the wettability for 4043 aluminum alloy on 301L stainless steel via chemical-etched surface texturing. *Journal of Materials Processing Technology*, *305*, Article 117577. <https://doi.org/10.1016/j.jmatprotec.2022.117577>
- Li, Z., Bai, J., & Tang, J. (2018). Micro-EDM method to fabricate three-dimensional surface textures used as SERS-active substrate. *Applied Surface Science*, *458*, 810–818. <https://doi.org/10.1016/j.apsusc.2018.07.132>
- Lin, M. Y., Hourng, L. W., & Kuo, C. W. (2012). The effect of magnetic force on hydrogen production efficiency in water electrolysis. *International Journal of Hydrogen Energy*, *37*(2), 1311–1320. <https://doi.org/10.1016/j.ijhydene.2011.10.024>

- Manu, P. V., Sunil, A., & Jayaraj, S. (2016). Experimental investigation using an on-board dry cell electrolyzer in a CI engine working on dual fuel mode. *Energy Procedia*, 90, 209–216. <https://doi.org/10.1016/j.egypro.2016.11.187>
- Mazloomi, S. K., & Sulaiman, N. (2012). Influencing factors of water electrolysis electrical efficiency. *Renewable and Sustainable Energy Reviews*, 16(6), 4257–4263. <https://doi.org/10.1016/j.rser.2012.03.052>
- Mounir, S., & Bellel, N. (2011). Hydrogen production by electrolysis of brine using a source of renewable energy. *International Review of PHYSICS*, 5(4), 158–161.
- Muritala, I. K., Guban, D., Roeb, M., & Sattler, C. (2020). High temperature production of hydrogen: Assessment of non-renewable resources technologies and emerging trends. *International Journal of Hydrogen Energy*, 45(49), 26022–26035. <https://doi.org/10.1016/j.ijhydene.2019.08.154>
- Naat, N., Boutar, Y., Naïmi, S., Mezlini, S., & Da Silva, L. F. M. (2023). Effect of surface texture on the mechanical performance of bonded joints: A review. *The Journal of Adhesion*, 99(2), 166–258. <https://doi.org/10.1080/00218464.2021.2008370>
- Olivares-Ramírez, J. M., Campos-Cornelio, M. L., Uribe Godínez, J., Borja-Arco, E., & Castellanos, R. H. (2007). Studies on the hydrogen evolution reaction on different stainless steels. *International Journal of Hydrogen Energy*, 32(15), 3170–3173. <https://doi.org/10.1016/j.ijhydene.2006.03.017>
- Poimenidis, I. A., Tsanakas, M. D., Papakosta, N., Klini, A., Farsari, M., Moustazis, S. D., & Loukakos, P. A. (2021). Enhanced hydrogen production through alkaline electrolysis using laser-nanostructured nickel electrodes. *International Journal of Hydrogen Energy*, 46(75), 37162–37173. <https://doi.org/10.1016/j.ijhydene.2021.09.010>
- Rajput, H., Atulkar, A., & Porwal, R. (2021). Optimization of the surface texture on piston ring in four-stroke IC engine. *Materials Today: Proceedings*, 44(1), 428–433. <https://doi.org/10.1016/j.matpr.2020.09.752>
- Rao, X., Sheng, C., Guo, Z., Zhang, X., Yin, H., Xu, C., & Yuan, C. (2021). Effects of textured cylinder liner piston ring on performances of diesel engine under hot engine tests. *Renewable and Sustainable Energy Reviews*, 146, Article 111193. <https://doi.org/10.1016/j.rser.2021.111193>
- Ridhuan, A., Osman, S. A., Fawzi, M., Alimin, A. J., & Osman, S. A. (2021). A review of comparative study on the effect of hydroxyl gas in internal combustion engine (ICE) on engine performance and exhaust emission. *Journal of Advanced Research in Fluid Mechanics and Thermal Sciences*, 87(2), 1–16. <https://doi.org/10.37934/arfmts.87.2.116>
- Rusdianasari, Bow, Y., & Dewi, T. (2019). HHO gas generation in hydrogen generator using electrolysis. *IOP Conference Series: Earth and Environmental Science*, 258(1), Article 012007. <https://doi.org/10.1088/1755-1315/258/1/012007>
- Santilli, R. M. (2006). A new gaseous and combustible form of water. *International Journal of Hydrogen Energy*, 31(9), 1113–1128. <https://doi.org/10.1016/j.ijhydene.2005.11.006>
- Soler, L., Candela, A. M., Macanás, J., Muñoz, M., & Casado, J. (2009). In situ generation of hydrogen from water by aluminum corrosion in solutions of sodium aluminate. *Journal of Power Sources*, 192(1), 21–26. <https://doi.org/10.1016/j.jpowsour.2008.11.009>

- Subramanian, B., & Thangavel, V. (2020). Analysis of onsite HHO gas generation system. *International Journal of Hydrogen Energy*, 45(28), 14218–14231. <https://doi.org/10.1016/j.ijhydene.2020.03.159>
- Sun, C. W., & Hsiau, S. S. (2018). Effect of electrolyte concentration difference on hydrogen production during pem electrolysis. *Journal of Electrochemical Science and Technology*, 9(2), 99–108. <https://doi.org/10.5229/JECST.2018.9.2.99>
- Vračar, L., & Conway, B. E. (1990). Hydride formation at Ni-containing glassy-metal electrodes during the H₂ evolution reaction in alkaline solutions. *Journal of Electroanalytical Chemistry and Interfacial Electrochemistry*, 277(1), 253–275. [https://doi.org/10.1016/0022-0728\(90\)85106-F](https://doi.org/10.1016/0022-0728(90)85106-F)
- Wang, S., Lu, A., & Zhong, C. J. (2021). Hydrogen production from water electrolysis: Role of catalysts. *Nano Convergence*, 8(1), 1-23. <https://doi.org/10.1186/s40580-021-00254-x>
- Xu, Y., Wang, C., Huang, Y., & Fu, J. (2021). Recent advances in electrocatalysts for neutral and large-current-density water electrolysis. *Nano Energy*, 80, Article 105545. <https://doi.org/10.1016/j.nanoen.2020.105545>
- Yilmaz, A. C., Uludamar, E., & Aydin, K. (2010). Effect of hydroxy (HHO) gas addition on performance and exhaust emissions in compression ignition engines. *International Journal of Hydrogen Energy*, 35(20), 11366–11372. <https://doi.org/10.1016/j.ijhydene.2010.07.040>
- Yuvaraj, A. L., & Santhanaraj, D. (2014). A systematic study on electrolytic production of hydrogen gas by using graphite as electrode. *Materials Research*, 17(1), 83–87. <https://doi.org/10.1590/S1516-14392013005000153>
- Zeng, K., & Zhang, D. (2010). Recent progress in alkaline water electrolysis for hydrogen production and applications. *Progress in Energy and Combustion Science*, 36(3), 307–326. <https://doi.org/10.1016/j.pecs.2009.11.002>
- Zeng, K., & Zhang, D. (2014). Evaluating the effect of surface modifications on Ni based electrodes for alkaline water electrolysis. *Fuel*, 116, 692–698. <https://doi.org/10.1016/j.fuel.2013.08.070>
- Zhao, Z., Zhang, Y., Quan, X., & Zhao, H. (2016). Evaluation on direct interspecies electron transfer in anaerobic sludge digestion of microbial electrolysis cell. *Bioresource Technology*, 200, 235–244. <https://doi.org/10.1016/j.biortech.2015.10.021>

Effect of Bimetallic Co-Cu/Dolomite Catalyst on Glycerol Conversion to 1,2-Propanediol

Norsahida Azri^{1,2,3}, Ramli Irmawati^{2,3,4*}, Usman Idris Nda-Umar^{2,5}, Mohd Izham Saiman^{2,3}, Yun Hin Taufiq-Yap^{2,3} and Ghassan Abdulkareem-Alsultan^{2,3}

¹Preparatory Centre for Science and Technology, Universiti Malaysia Sabah, 88400 Kota Kinabalu, Sabah, Malaysia

²Department of Chemistry, Faculty of Science, Universiti Putra Malaysia, 43400 UPM, Serdang, Selangor, Malaysia

³Catalysis Science and Technology Research Centre (PutraCat), Faculty of Science, Universiti Putra Malaysia, 43400 UPM, Serdang, Selangor, Malaysia

⁴Laboratory of Processing and Product Development, Institute of Plantation Studies, Universiti Putra Malaysia, 43400 UPM, Serdang, Selangor, Malaysia

⁵Department of Chemical Sciences, Federal Polytechnic, PMB 55, Bida, Niger State, Nigeria

ABSTRACT

This present study examines the efficacy of using dolomite (Dol, $\text{CaMg}(\text{CO}_3)_2$)-supported copper (Cu) and cobalt (Co) bimetallic and monometallic catalysts for the hydrogenolysis of glycerol to propylene glycol (PG; 1,2-PDO). The proposed catalysts were generated using the impregnation process before they were calcined at 500°C and reduced at 600°C. Advanced analytical techniques namely Brunauer, Emmett, and Teller (BET) method; the Barrett, Joyner, and Halenda (BJH) method; temperature-programmed desorption of ammonia (NH_3 -TPD), hydrogen-temperature programmed reduction (H_2 -TPR), X-ray diffraction (XRD) analysis, and scanning electron microscopy (SEM) were then used to characterise the synthesised catalysts, whose performance was then tested in the hydrogenolysis of

glycerol. Of all the synthesised catalysts tested in the hydrogenolysis process, the Co-Cu/Dol bimetallic catalyst performed best, with an 80.3% glycerol conversion and 85.9% PG selectivity at a pressure of 4 MPa, a temperature of 200°C, and a reaction time of 10 hours. Its high catalytic performance was attributed to effective interactions between its Co-Cu-Dol species, which resulted in acceptable acidity, good reducibility of metal oxide species at low

ARTICLE INFO

Article history:

Received: 21 July 2023

Accepted: 02 November 2023

Published: 01 April 2024

DOI: <https://doi.org/10.47836/pjst.32.3.09>

E-mail addresses:

norsahidaazri@gmail.com (Norsahida Azri)

irmawati@upm.edu.my (Ramli Irmawati)

uindaumar@gmail.com (Usman Idris Nda-Umar)

mohdizham@upm.edu.my (Mohd Izham Saiman)

taufiq@upm.edu.my (Yun Hin Taufiq-Yap)

kreem.alsultan@yahoo.com (Ghassan Abdulkareem-Alsultan)

* Corresponding author

temperatures, larger surface area ($15.3 \text{ m}^2 \text{ g}^{-1}$), large-sized particles, fewer pores ($0.032 \text{ cm}^3 \text{ g}^{-1}$), and smaller pore diameter (0.615 nm).

Keywords: Cobalt, copper, dolomite support, acidity, glycerol hydrogenolysis, 1,2-propanediol

INTRODUCTION

Glycerol, an important by-product of the biodiesel production process, can be utilised for the production of value-added chemicals such as propylene glycol (PG), which is also called propane-1,2-diol or 1,2-propanediol (1,2-PDO); 1,3-propanediol (1,3-PDO), glycerol carbonates, cyclic acetals/ketals, glycerol esters, glyceric acid, glycerol ethers, acrolein/acrylic acid, and other speciality chemicals (Liu et al., 2019; Pandhare et al., 2016). Of all these speciality chemicals, PG has a huge market demand owing to its application as a monomer or component in the pharmaceutical industries, as well as a solvent in cosmetics, food, and polyester resins (Gallegos-Suarez et al., 2015; Pudi et al., 2015). The predicted global output of PG is ≈ 1.4 million tonnes per year, with an annual market growth rate of 4% (Vasiliadou et al., 2011). Traditionally, propylene oxide, generated from various petroleum processing techniques, undergoes the hydration process for synthesising PG (Bagheri et al., 2015; Mallesham et al., 2016; Rajkhowa et al., 2017).

However, as the financial returns from petroleum have decreased and environmental concerns have increased, there are increased efforts to develop a more practical and sustainable method of producing PG. If catalyst-driven hydrogenolysis of glycerol can be successfully developed, it would significantly alter the price of PG due to the benefits of the manufacturing process. According to multiple extant studies, glycerol hydrogenolysis to PG is a dual-step reaction. In the first step, glycerol is converted to acetol by dehydrating it over the catalyst's acidic sites before the resultant acetol is hydrogenated to synthesise PG over the active metallic sites in the catalysts in the second step. The procedure prioritises cleaving the C-O bonds in the glycerol molecules while preventing the cleaving of its C-C bonds to prevent the production of by-products (Zheng et al., 2015).

The hydrogenolysis of glycerol to PG is significantly more efficient with the use of noble-based catalysts, such as platinum (Pt), ruthenium (Ru), palladium (Pd), and cerium (Ce) (Soares et al., 2016; Yu et al., 2010). However, as these catalysts are costly, they are not feasible for industrial applications. Non-noble metal catalysts, such as zinc (Zn), nickel (Ni), copper (Cu), aluminium (Al), iron (Fe), cobalt (Co), and magnesium (Mg) have demonstrated good performance, of which Cu-based catalysts have been used most frequently as they perform best and very efficiently activate the cleaving of C-O bonds instead of C-C bonds (Freitas et al., 2018). Apart from that, Co-based catalysts are also active catalysts that have high PG selectivity (Guo et al., 2009). However, the activity and stability of Cu and Co-based catalysts warrant further investigation to maximise their potential.

As such, bimetallic catalysts are more frequently used as they significantly increase the conversion of glycerol and the selectivity of PG. Bimetallic catalysts are highly effective due to their metal-metal interactions, which enhance their chemical strengths, thermal strengths, acidity, surface area, metallic phase dispersion, and reducibility or oxygen ion mobility (Jiang et al., 2016; Pandhare et al., 2016). More specifically, a catalyst containing Cu, zinc oxide (ZnO), and aluminium oxide (Al_2O_3) was able to completely convert glycerol at a PG selectivity of 80% at a temperature of 240°C and a hydrogen (H_2) pressure of 0.1 MPa (Feng et al., 2011). Meanwhile, a catalyst containing a 1:1 ratio of Cu to Ni as well as Al_2O_3 yielded 89% PG selectivity and converted 60% of the glycerol at a temperature of 210°C and H_2 pressure of 4.5 MPa over a reaction duration of 12 hours (Pudi et al., 2015).

A catalyst containing a 1:3 ratio of Ce to Ni-Co was able to convert 71.3% of the glycerol and select 68.5% of the PG at a temperature of 220°C and a H_2 pressure of 6 MPa over a reaction duration of 10 hours when the glycerol concentration was 20 wt% (Jiang et al., 2016). Similarly, a Cu-Ni/ Al_2O_3 catalyst converted 70.5% of the glycerol with a PG selectivity of 70% at 4.5 MPa H_2 pressure, 220°C , and 16-hour reaction duration when the glycerol concentration was 4 wt% (Gandarias et al., 2012). Furthermore, Ru-Cu/ Al_2O_3 and Ru-Cu/ ZrO_2 catalysts were able to convert 45% and 13.7% of the glycerol and select 94% and 100% of the PG, respectively, using 2.5 H_2 pressure, 200°C , a reaction duration of 24 hours, and a glycerol concentration of 20 wt% (Soares et al., 2016).

During glycerol hydrogenolysis, acid sites and metal surfaces serve dual functions as active reaction sites for dehydration and hydrogenation processes. Therefore, metal-based catalysts with bifunctional sites carry significant potential. These properties enable a catalyst to increase the surface area for depositing the active phase. It also serves as a reservoir for the extra hydrogen molecules that help hydrogenate surface species by enabling hydrogen ions from the dolomite (Dol) support to migrate to the metal particles and create more active sites that are interfacial in the metal support, all of which help increase its catalytic activity (Rajkhowa et al., 2017).

Therefore, this present study prepared three separate Dol-supported Co and Cu catalysts. The Dol support mostly contained magnesium carbonate (MgCO_3), calcium carbonate (CaCO_3), and varying concentrations of high quantities of ferric oxide (Fe_2O_3), silicon dioxide (SiO_2), and Al_2O_3 that did not exceed 5% w/w. Dolomite (Dol) has grown in popularity as it is cheap and possesses acidic properties. Furthermore, Dol contains Mg and Ca ions, which are well-known as effective reducers for electrochemical series, so Dol may help reduce metal oxides to metallic species. It has also been found to outperform its more conventional, expensive, and time-consuming counterparts, for instance, HZSM-5 zeolites, Mobil® composition of matter no. 41 (MCM-41), Santa Barbara amorphous-15 (SBA-15), and Santa Barbara amorphous-16 (SBA-16) (Vanama et al., 2015).

Dolomite (Dol) is abundantly available and can easily be procured from the state of Perlis in Malaysia. As such, this present study used the impregnation method to synthesise Dol-supported Co and Cu monometallic and Co-Cu bimetallic catalysts. These three catalysts were used to conduct the hydrogenolysis of glycerol before multiple characterisation methods were used to analyse the correlations between their performance and properties. The impregnation method was used instead of the co-precipitation method as it is significantly easier to control the size of the metal particles in the catalyst (Karelovic & Ruiz, 2015).

MATERIALS AND METHODS

Chemicals

Perlis Dolomite Industries, Malaysia, supplied dolomite. Copper nitrate hexahydrate ($\text{Cu}(\text{NO}_3)_2 \cdot 6\text{H}_2\text{O}$) ($\geq 99\%$) and cobalt nitrate hexahydrate ($\text{Co}(\text{NO}_3)_2 \cdot 6\text{H}_2\text{O}$) ($\geq 99\%$) were purchased from R&M Chemical Company, Malaysia. Glycerol ($\geq 99.5\%$) was acquired from Sigma-Aldrich. The chemicals were used without further purification.

Catalyst Preparation

Every catalyst was synthesised using the impregnation procedure. The Co and Cu loading concentrations were set at 20 wt%. During the standard synthesis mechanism, copper nitrate ($\text{Cu}(\text{NO}_3)_2$, 3.8 g) and cobalt nitrate ($\text{Co}(\text{NO}_3)_2$, 4.9 g) were individually dissolved in distilled water (10 ml) and added to Dol powder (4 g) to produce Solution 1. A magnetic stirrer was used to stir the solution at 300 rpm before transferring it to a hot plate and left to dry at 90°C for 3 hours. It was then transferred to drying over to further age for 24 hours at 120°C . The catalyst was placed in a tube furnace to be calcined for 3 hours at 500°C with a temperature ramp rate of $10^\circ\text{C}/\text{min}$ and static airflow to eliminate nitrate salt. Without removing the catalyst from the tube furnace, a 5% hydrogen/argon (H_2/Ar) gas mixture was then used to reduce it for 3 hours at 600°C and a temperature ramp rate of $2^\circ\text{C}/\text{min}$. The two catalysts produced were labelled “Cu/Dol” and “Co/Dol” for future use. A similar method was used to prepare the bimetallic catalyst by adding 20 wt% of the respective metal precursors to Solution 1, which was then stirred, dried, aged, calcined, and reduced. The bimetallic catalyst produced was labelled “Co-Cu/Dol”. The performance of all three synthesised catalysts was examined by using them to conduct the hydrogenolysis of glycerol.

Catalyst Characterisation

A Micromeritics® accelerated surface area and porosimetry (ASAP) 2010 system was used to observe the isotherms of nitrogen (N_2) adsorption-desorption of the synthesised catalysts and determine their textural characteristics (pore diameter, BET surface area, and

pore size) while their crystallite sizes and the structure of their phase compositions were determined by analysing their X-ray diffraction (XRD). Meanwhile, a Thermo-Finnigan® 1100 series TPDRO analyser equipped with a thermal conductivity detector (TCD) was used to observe their H₂-TPR and assess their metal reducibility as well as evaluate their distribution of acid sites and total acidity. Lastly, a Shimadzu® RayNy™ energy dispersive X-ray (EDX)-720 spectrometer was used to conduct SEM and examine their morphological characteristics. The analysis conducted in this present study has already been explained in great detail in our previous study (Azri et al., 2020).

Experimental Setup

The performance of the synthesised catalysts for the hydrogenolysis of glycerol was tested in a 150 mL capacity stainless steel (SS-316L) autoclave reactor and was explained in our previous study (Azri et al., 2020). Figure 1 depicts a schematic layout of the reactor setup used to examine the reactions.

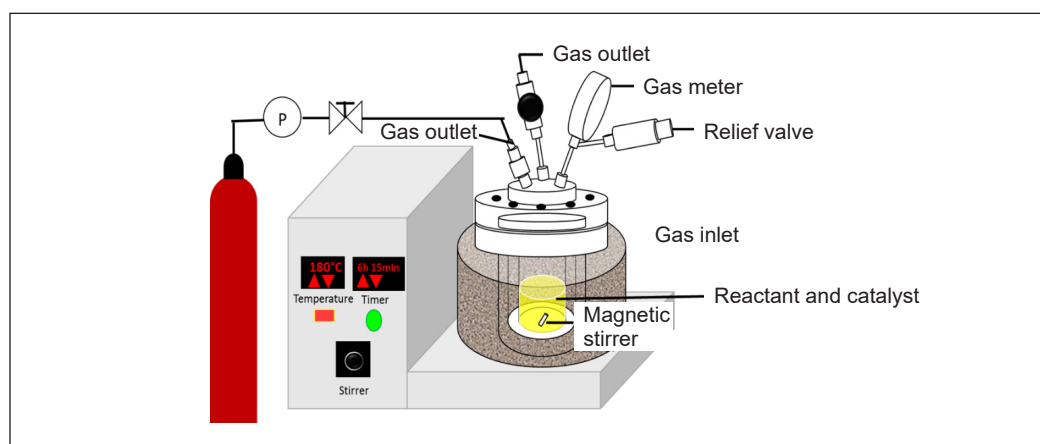


Figure 1. The experimental setup for glycerol hydrogenolysis reaction

Product Analysis

A flame ionisation detector (FID) fitted with an HP-5 capillary column was used to conduct gas chromatography (GC) on the liquid output of the experiment after it had been extracted thrice using ethyl acetate. The analytical procedure was similar to that of our previous study (Azri et al., 2020).

RESULTS AND DISCUSSION

Catalyst Characterisation

Table 1 presents the textural characteristics of the Dol, Co/Dol, Cu/Dol, and Co-Cu/Dol catalysts, such as the pore diameter, Brunauer, Emmett, and Teller (BET) surface area, and

pore size. The bimetallic catalyst showed an increase in the BET surface area to $21.9 \text{ m}^2 \text{ g}^{-1}$ from the $13.3 \text{ m}^2 \text{ g}^{-1}$ of the Dol. On the other hand, the surface area of the 20% Cu/Dol catalyst and 20% Ni/Dol catalyst showed a decrease to $9.7 \text{ m}^2 \text{ g}^{-1}$ and $3.5 \text{ m}^2 \text{ g}^{-1}$, respectively. These results could be attributed to the fact that the metal ions were filling the pores of the Dol support. Thirupathi et al. (2012) presented a similar finding and observed that the decreased surface area of the study's 0.4 manganese-nickel (Mn–Ni) and titanium dioxide (TiO_2) catalyst could be due to the nickel oxide (NiO) ions that were loaded onto the support material. The BET surface area showed the following trend: Co-Cu/Dol > Dol > Cu/Dol > Co/Dol.

In terms of pore volume, all Dol-supported catalysts have a smaller pore volume than Dol ($0.276 \text{ cm}^3 \text{ g}^{-1}$). According to Zhao et al. (2013), this occurs because the metal species embeds and clogs the Dol matrix that covers the pores of the catalyst. The pore sizes of all Dol-supported catalysts (6.15 \AA) were, similarly, smaller than that of Dol (156.34 \AA). It is noteworthy that both the diameter and volume of the pores of the bimetallic catalyst were small. It may be attributed to the presence of fresh active sites or new pores on the surface of the bimetallic catalyst. During a catalytic reaction, the active sites on the surface of a catalyst initially adsorb or react before they move into the pores of the catalyst. However, in this case, the small pores of the catalyst may prevent leaching from occurring easily at the active sites, increasing the amount of adsorption-desorption that occurs there throughout the catalytic reaction. Furthermore, the active sites within the tiny pores may be beneficial when determining the reusability of a catalyst. It may also preserve the catalyst's stability throughout the subsequent cycle of reactions.

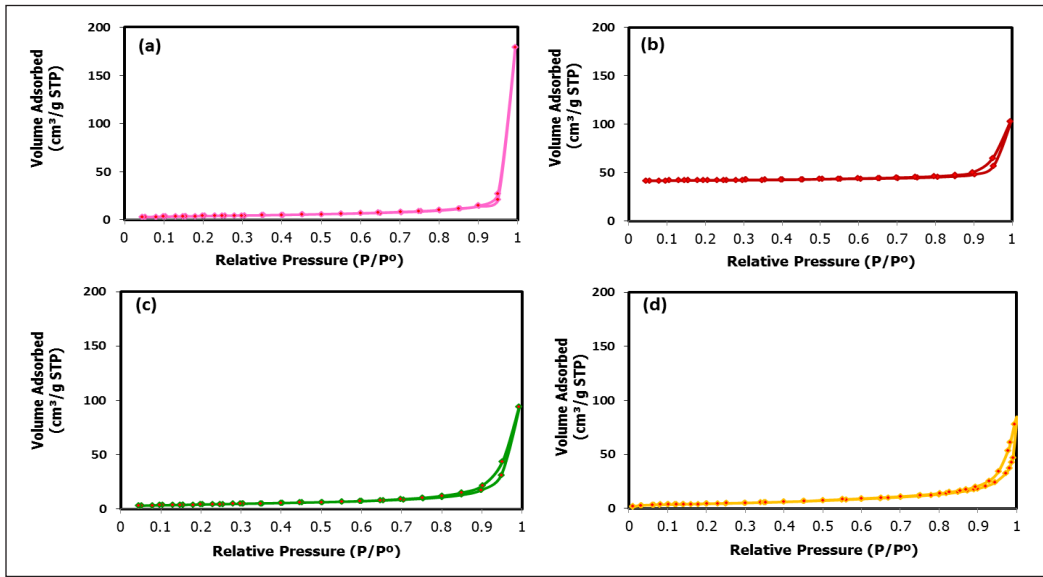
According to the IUPAC classification system, the isotherms of the N_2 adsorption-desorption, seen in Figure 2A, indicate that the synthesised catalysts had type III isotherms typical of macro-porous solids. The weak adsorption-desorption interaction between

Table 1
Physicochemical properties of the catalysts

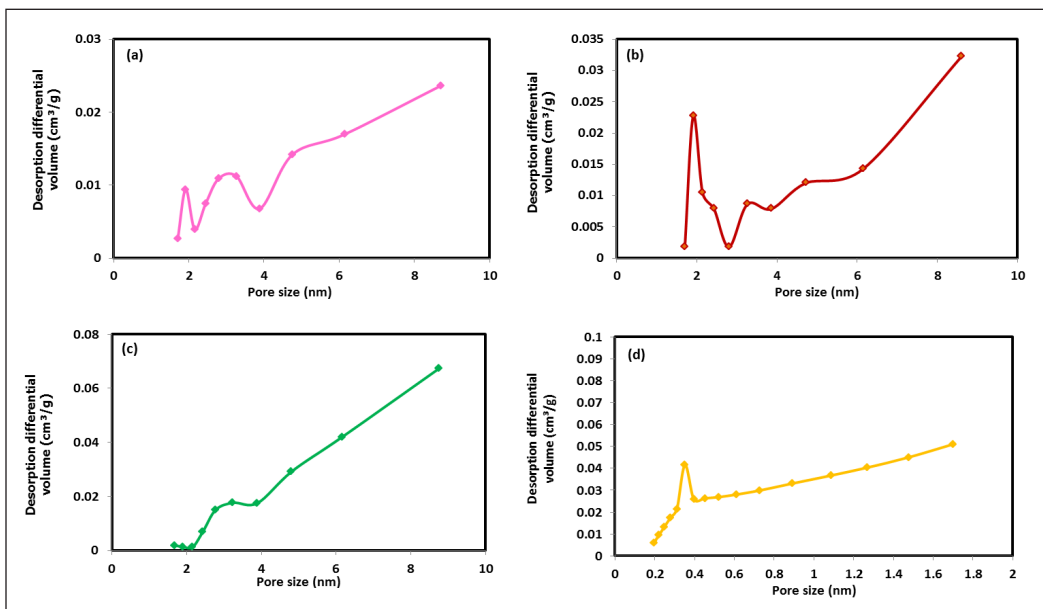
Catalyst	BET	XRD	H ₂ -TPR		NH ₃ -TPD			
	Surface area ($\text{m}^2 \text{ g}^{-1}$)		Pore volume ($\text{cm}^3 \text{ g}^{-1}$)	Pore diameter (\AA)		Crystallite size (nm) ^a	H ₂ consumed at different temp ($\mu\text{mol/g}$)	Total amount H ₂ consumed ($\mu\text{mol/g}$)
					150-550°C	> 550°C		> 550°C
Dolomite	13.3	0.276	152.02	27.4	-	1005	1005	16149
Cu/Dol	9.7	0.098	19.07	54.8	23582, 17919	10268	51769	19528
Co/Dol	7.8	0.145	156.34	22.9	19250	54712	73962	11172
Co-Cu/Dol	15.3	0.032	6.15	72.3	3719	1705	5424	11724

Note. ^aThe data were estimated according to the Debye Scherrer equation using the FWHM of the dolomite peak at $2\theta = 62^\circ$

adsorbed and desorbed molecules from the clustered solid catalyst was responsible for the isotherm results. Furthermore, similarities between the isotherms of the metal-supported catalysts and Dol indicate that the addition of metal ions did not significantly alter the structure of the Dol. As hysteresis developed in all the synthesised catalysts when the



(A)



(B)

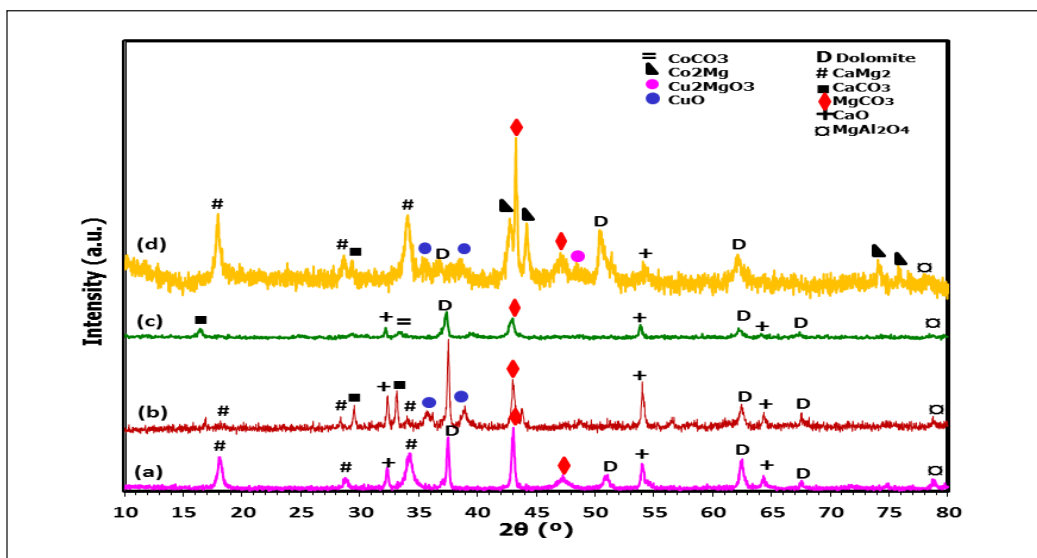
Figure 2. N₂-physorption isotherms (A) and pore size distribution (B) of (a) Dolomite, (b) Cu/Dol, (c) Co/Dol, and (d) Co-Cu/Dol catalyst

relative pressure (p/p°) exceeded 0.8, their aggregates had the non-rigid characteristics of plate-shaped particles and a non-uniform size (Luna et al., 2018). It is commonly attributed to the capillary or delayed condensation capabilities of solid catalysts, as their multilayer pore network causes weak adsorption (Lopez et al., 2019). As all the synthesised catalysts, except the Cu/Dol catalyst, adsorbed little N_2 ($\sim 1 \text{ cm}^3 \text{ g}^{-1}$), it underscored that the macroporosity of the Cu/Dol catalyst was that of a solid catalyst. The Cu/Dol catalyst may have adsorbed more N_2 as its structure certain mesopores. The Barrett, Joyner, and Halenda (BJH) method was used to determine the curves of the pore size distributions of all the catalysts (Figure 2B). The distributions of the pore sizes of the Dol, Co/Dol, and Cu/Dol catalysts ranged between 2 to 10 nm, while that of the bimetallic Co-Cu/Dol catalyst was less than 2 nm.

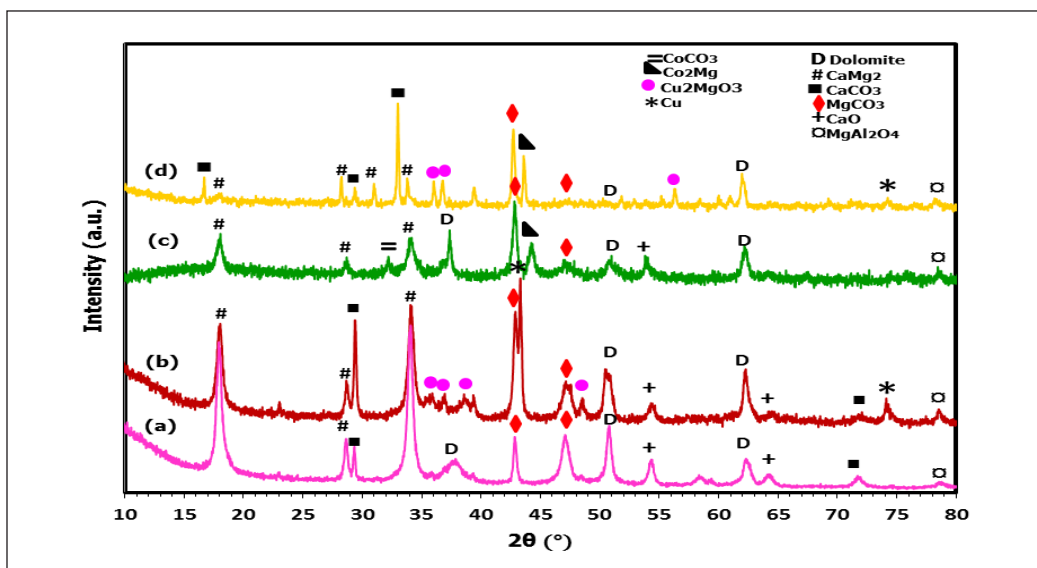
Figure 3A depicts the XRD patterns of the calcined catalysts, while Figure 3B shows those of the reduced catalysts. Diffraction peaks in the Dol support were identified with heterogeneous crystalline phases. The peaks observed at $2\theta = 18.1^\circ$, 28.3° and 33.8° were attributed to the calcium-magnesium (1:2) phase (CaMg_2 , Joint Committee on Powder Diffraction Standards (JCPDS) 01-1070) and the peaks observed at $2\theta = 37.51^\circ$, 50.76° , and 62.20° were attributed to the phase of the Dol (JCPDS 02-0767). Furthermore, the two peaks observed at $2\theta = 44.2^\circ$ and 47.4° were attributed to the phase of MgCO_3 (JCPDS 02-0871). The peaks observed at $2\theta = 32.4^\circ$ and 54.2° were attributed to the calcium oxide (CaO) phase (JCPDS 01-1160), and the lower intensity peak observed at $2\theta = 78.7^\circ$ was attributed to the magnesium aluminate (MgAl_2O_4) phase (JCPDS 03-1160).

With regards to the monometallic and bimetallic catalysts, the XRD patterns indicated that the novel phases corresponded to the corresponding metal oxide molecules as the metal oxide species had become embedded in the matrix of the Dol support; more specifically, copper oxide (CuO) at $2\theta = 35.5^\circ$ and 38.8° (JCPDS 44-0706) and cobalt carbonate (CoCO_3) at $2\theta = 33.5^\circ$ (JCPDS 01-1020). Alloy phases were also observed in the bimetallic catalysts; more specifically, the guggenite (Cu_2MgO_3) phase at $2\theta = 48^\circ$ (JCPDS 21-0291) and the cobalt-magnesium (2:1) (Co_2Mg) phase at $2\theta = 42^\circ$, 44.5° , 74.5° and 76° (JCPDS 29-0486). Extant studies have similarly concluded that metal oxide species are more likely to produce spinel when supported by limestone or clay materials containing Mg and Ca ions (Kovanda et al., 2001; Pardeshi et al., 2010). However, the calcined catalysts did not show the presence of any peaks that correlate with metallic species.

As seen in Figure 3B, the CuO diffraction peaks ($2\theta = 35.5^\circ$ and 38.8°) had vanished, whereas the peaks of the Cu ($2\theta = 43.5^\circ$ and 74.3°) (JCPDS; 085-1326), which is metallic, appeared in the bimetallic and monometallic catalysts. The metallic copper (Cu^0) species may have appeared due to the effective transfer of electrons between the oxide species and the Dol support, which would destabilise the bonds of the metal oxide and help reduce the metal species. The interfacial sites of the metal-support material helped coordinate



(A)



(B)

Figure 3. XRD diffractograms of calcined (A) and reduced samples (B) of (a) Dolomite, (b) Cu/Dol, (c) Co/Dol, and (d) Co-Cu/Dol catalyst

the oxygen atoms with the help of a single pair of electrons, which facilitates electron migration and helps reduce the metal oxide species (Nagaraja et al., 2007). As Ca and Mg are good reducers, this study hypothesised that the CaMg(CO₃)₂, CaO, and MgCO₃ surface species of the Dol reduced the metal oxide (Tasyurek et al., 2018). Furthermore, the peak of the Co₂Mg phase was observed at $2\theta = 44.5^\circ$, while those of the Cu₂MgO₃ phase were

observed at $2\theta = 35.3^\circ, 37.5^\circ, 38.2^\circ,$ and 48° . However, the reduced catalysts did not present any characteristic peak associated with the Co and Cu oxide species.

As seen in Table 1, the crystallites of the bimetallic catalyst were larger than those of the monometallic catalysts. Therefore, the higher concentration of metal oxide, which increased the amount of intercalated Cu and Co in the catalyst, caused the metal species to fill the interstitial spaces of the Dol bulk and increased the size of the crystallites. The crystallite sizes were, in descending order, Co-Cu/Dol > Cu/Dol > Co/Dol. The higher intensity non-shifting peaks of MgCO_3 observed at $2\theta = 47.4^\circ$ and 43.5° in the Dol indicate the increase in the size of the crystallites. The non-shifting characteristic of the peaks also indicates that the metal species had incorporated into the support well (Asikin-Mijan et al., 2017). The size of the particles of a catalyst may directly affect H_2 adsorption or activation and hydrogenation, especially during the hydrogenolysis of glycerol.

Figure 4 depicts all the catalysts' H_2 -TPR profiles, while Table 1 lists their H_2 adsorption. The reduction profiles indicate that incorporating Cu and/or Co species into the Dol caused reduction peaks that were lower than that of the Dol to appear. The reduction peaks observed at 291 and 455°C, 444°C only, and 277 and 435°C were attributed to the Cu/Dol, Co/Dol, and bimetallic catalysts, respectively. The appearance of a reduction peak at low temperatures indicates weakly bonded or dispersed metal oxide species (species). In contrast, the appearance of a reduction peak at temperatures that exceed 400°C indicates the reduction of metal oxides as a complex species as a consequence of increased interactions between the metals and the support material (Shozi et al., 2017; Wen et al., 2013; Zhao et al., 2017). The presence of Cu in the aluminate spinel (CuAl_2O_4) and complex Cu phases of $\text{Cu}_x\text{Mg}_x\text{Al}_2\text{O}_4$ led to the reduction of the mixed oxides that contained Cu at 400 to 750°C (Tanasoi et al., 2009). This present study observed the two peaks at 277 and 291°C, which could be attributed to the dispersed CuO species reducing to Cu^0 . On the other hand, the peak observed between 435 to 455°C was attributed to the Cu or Co species-containing mixed oxides reducing (Tanasoi et al., 2009; Vargas-Hernández et al., 2014).

As Cu_2MgO_3 and Co_2Mg peaks were observed in the XRD pattern, the results of this present study could be attributed to the Co and Cu oxides reducing the defects present in the interstitial spaces of the Dol phase. The peaks observed at 616 to 638°C were attributed to the Dol reducing as they were similar to that of a Dol bulk (639°C) (Azri et al., 2020). Furthermore, compared to the monometallic catalysts, the reduction of the bimetallic catalyst effectively shifted toward the lower temperatures (277°C). It was attributed to significant interactions between the Co-Cu-Dol species of the bimetallic catalyst, which enhanced and altered its metal reducibility. However, the reduction peaks observed at 638°C in the Co/Dol catalyst were broader and higher than that of the Dol peak. It may be due to the reduction of the Co species, which significantly interacted with the Dol support and is also supported by the findings of the XRD analysis, which detects the CoCO_3

species. Extant studies have similarly concluded that taller and wider peaks appear when strong metal-support species reduce as it requires more H₂ adsorption, which broadens the reduction peak (Li et al., 2009). The interphase H₂ adsorption or the slow diffusion of the hydrogen ions in a thoroughly sintered metal species may also cause a wider reduction peak (Soares et al., 2016).

As seen in Table 1, the Dol adsorbed less total H₂ than the monometallic and bimetallic catalysts. Extant studies have similarly found that a catalyst containing CuO and ceric oxide (CeO₂) adsorbed significantly more H₂ than required to completely reduce unadulterated CuO (Zhao et al., 2019). Therefore, the Ce may have played a role in the reduction. It suggests that metal species with larger exposure areas are more reducible but increase the H₂ consumption of the catalyst. The monometallic and bimetallic catalysts had wider and taller reduction peaks than the Dol as they adsorbed more H₂. Furthermore, it was advantageous that the metal species were reduced to under 300°C as the metallic species remained stable and active throughout the catalytic reaction process, which occurred at 200°C. It would significantly improve H₂ adsorption on the surface of the catalyst and expedite the hydrogenolysis reaction. As alloy instead of metallic species appeared in the monometallic and bimetallic catalysts, the presence and reduction of CaO, MgCO₃, CaCO₃, and MgAl₂O₄ phases of the Dol warrant further investigation as a source of chemisorption in H₂ atoms and higher H₂ uptake.

Acid sites are required to activate the C-O bonds of glycerol molecules through dehydration (Zhu et al., 2013). The NH₃ adsorption and dissociation ability of a catalyst can be used to determine its acidity. Acid strengths are classified as weak if they remain below 250°C, medium between 250 to 500°C, and strong if they exceed 500°C (Srivastava

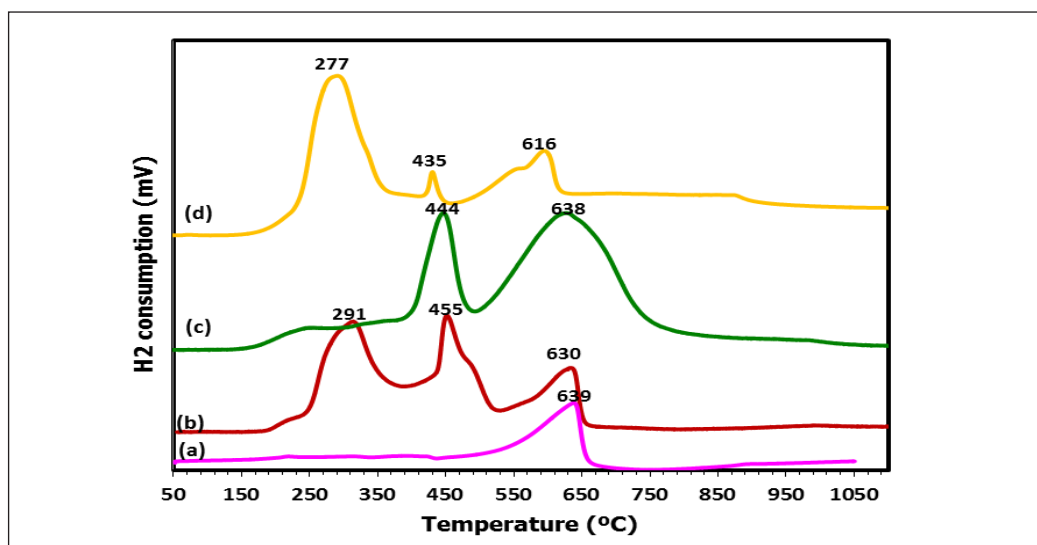


Figure 4. H₂-TPR profiles of (a) Dolomite, (b) Cu/Dol, (c) Co/Dol, and (d) Co-Cu/Dol catalyst

et al., 2017). Figure 5 displays the NH_3 desorption profiles of the three synthesised catalysts, whereas Table 1 presents their acidity data, which is the concentration of ammonia absorption. All three catalysts contained significant acid sites, with desorption peaks that exceeded 500°C . More specifically, the desorption peaks of the Dol were observed at 805 and 874°C , that of the Cu/Dol catalyst at 718 and 948°C , and that of the Co/Dol catalyst at 712 and 815°C while the bimetallic catalyst had the lowest desorption peak (589°C). Stronger acid sites were present on the surface of the catalyst, as evidenced by the high desorption temperature of the Cu/Dol catalyst (948°C) over the Dol. It matched the total NH_3 desorption amount (Table 1).

The Cu/Dol catalyst had the highest acidity of all three catalysts. As such, the acidity of the catalysts was, in descending order, $\text{Cu/Dol} > \text{Dol} > \text{Co-Cu/Dol} > \text{Co/Dol}$. As the Co-Cu/Dol and Co/Dol catalysts were less acidic than the Dol, the metal species in the Dol may have encased and blocked its surface, thereby limiting the amount of NH_3 it desorbed (Priya et al., 2017). The decreased acidity with loading of Co-Cu can also be attributed to increased agglomeration on the surface of the catalyst upon incorporation of the metals, thereby hindering the surface from absorption of ammonia into catalyst pores, leading to decreased pore volume and diameter as indicated in Table 1. The acidity of the catalysts may also be due to the MgCO_3 and CaCO_3 phases of the Dol (Azri et al., 2020).

Figure 6 depicts the SEM-based surface morphology of the catalysts. The SEM photomicrographs showed that all the catalysts contained irregular agglomerated structures that measured $10\ \mu\text{m}$ on average on a scale bar. Therefore, the macro-porous solids had formed tightly clustered crystals.

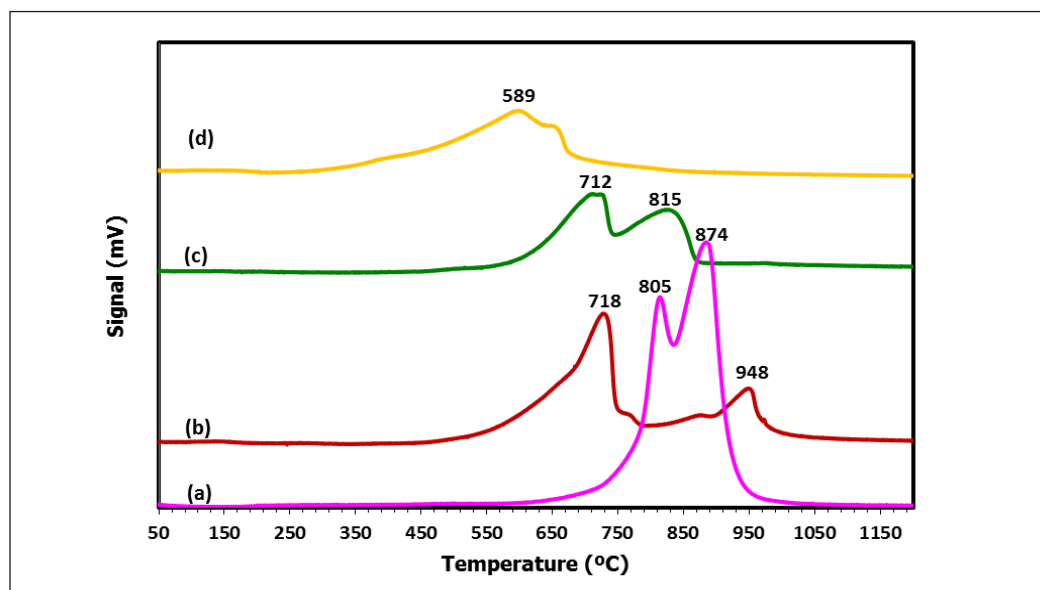


Figure 5. NH_3 -TPD profiles of (a) Dolomite, (b) Cu/Dol, (c) Co/Dol, and (d) Co-Cu/Dol catalyst

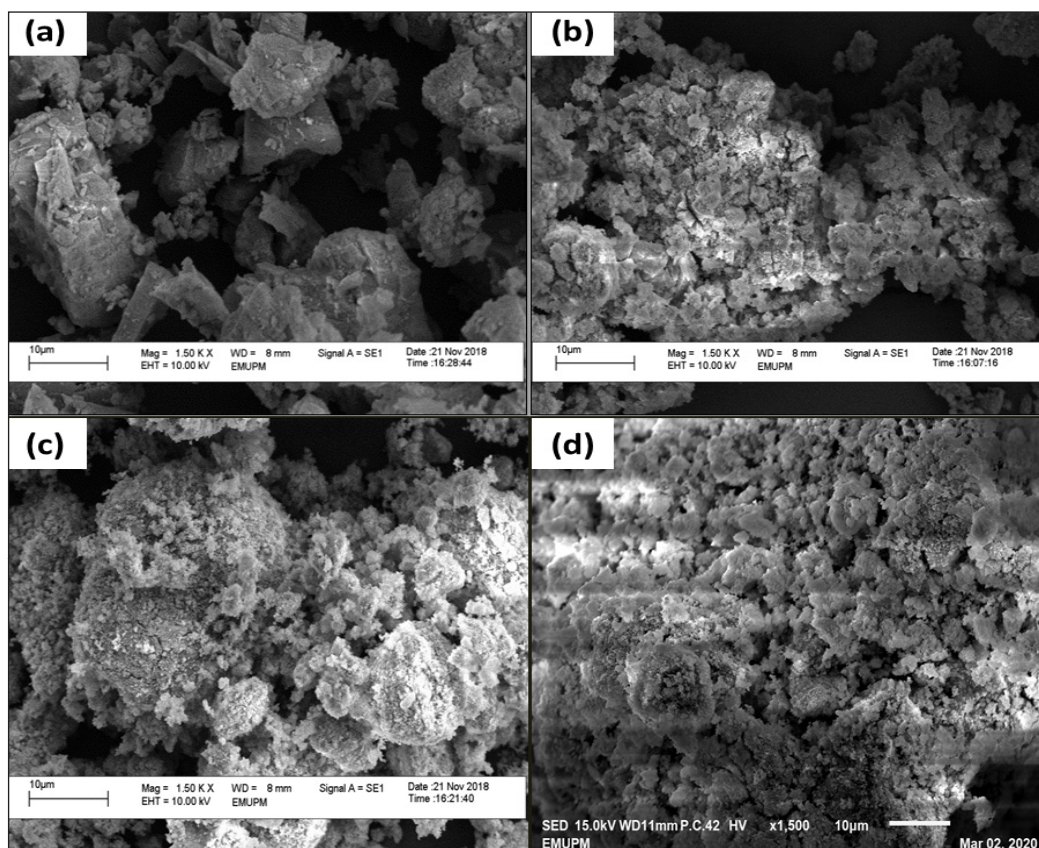


Figure 6. SEM images of (a) Dolomite, (b) Cu/Dol, (c) Co/Dol, and (d) Co-Cu/Dol catalyst

Catalytic Activity

Table 2 presents the catalytic activities of glycerol hydrogenolysis using each catalyst. A blank reaction or control experiment was also carried out, which meant conducting the hydrogenolysis sans a catalyst and/or support. The conversion of glycerol and selectivity of PG, acetol, and methanol were used to evaluate the performance of each catalyst. Without a catalyst and/or support, the control experiment could only convert 8.7% of the glycerol and did not select the PG. The introduction of a catalyst had a profound impact. Although the Dol was able to convert 10.6% of the glycerol, it lacked selectivity for PG.

Therefore, the Dol could not catalyse glycerol to PG hydrogenolysis on its own. The catalytic reaction was significantly influenced by adding metal ions to the Dol. The bimetallic Co-Cu/Dol catalyst outperformed the other catalysts in terms of glycerol conversion (80.3%) and PG selectivity (85.9%). Its elevated turnover frequency (TOF) also confirmed its significant catalytic activity. Compared to the bimetallic catalyst, the glycerol conversion and PG selectivity of the monometallic catalysts were poorer; more specifically, 78.5% and 79% for the Cu/Dol catalyst and 60.9% and 58.1% for the Co/Dol

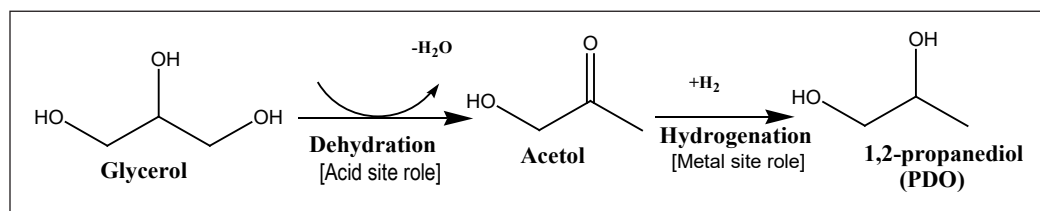
Table 2
Performance of the synthesised catalysts

Sample	Conversion (%)	Selectivity (%)			TOF (h ⁻¹)
		Acetol	1,2-PDO	Methanol	
Blank	8.7	0	0	0	-
Dolomite	10.6	6.3	0	93.7	0.46
Cu/Dol	78.5	18.9	79	2.1	3.41
Co/Dol	60.9	14.2	58.1	27.6	2.65
Co-Cu/Dol	80.3	4.3	85.9	9.9	3.49

Note. Reaction conditions: 20 ml of aqueous glycerol (20wt%); reaction temperature 200 °C; H₂ pressure 4 MPa; catalyst dosage 1g; reaction time 10 hr

catalyst, respectively. Therefore, the glycerol hydrogenolysis performance of the catalysts was, in descending order, Co-Cu/Dol > Cu/Dol > Co/Dol > Dol. It also proves that the inclusion of Co and Cu in Dol increases its glycerol conversion and PG selectivity.

The bimetallic catalyst outperformed the other catalysts, potentially, because it possessed adequate acidity (11724 μmol/g), a high surface area (15.3 m²g⁻¹), fewer pores (0.032 cm³g⁻¹), and smaller pores (0.615 nm). The presence of sufficient surface acid sites aided in the dehydration of the glycerol molecules to generate acetol, which resulted in PG. Extant studies indicate that acid sites significantly affect hydrogenolysis (Putrakumar et al., 2015; Yuan et al., 2009). Metallic sites on the surface of a catalyst are also essential as they enable hydrogenation to occur by breaking H₂ down to hydride, which helps hydrogenate the intermediate acetol to PG. The catalytic performance of a bimetallic catalyst correlates to the presence of Cu metallic species. The results of this present study demonstrate that the presence of bifunctional sites on the bimetallic catalysts led to the simultaneous and rapid dehydration of glycerol to acetol and the hydrogenation of acetol to PG, as also proposed in the literature (Scheme 1).



Scheme 1. Glycerol hydrogenolysis pathway over metal-acid condition (Mallesham et al., 2016)

However, H₂ adsorption or activation may determine if a hydrogenation reaction is high or low, as H₂ supplies the hydride required to hydrogenate the intermediate product during a catalytic reaction. The ability of a catalyst to adsorb high amounts of H₂ may correlate with the size of its metal particles. Extant studies have similarly indicated a linear correlation between the catalytic activity and the H₂ adsorption of catalysts with large-sized

metal particles (Karelovic & Ruiz, 2015). Catalysts with large-sized metal particles have larger surface areas and interfacial exposure, which improves H₂ adsorption as more H₂ can be activated on the surface of the catalyst, and there is better accessibility to metallic reaction sites. In turn, it significantly encourages the cleaving of the C-O bond during hydrogenation.

As seen in Table 1, the crystallite particle sizes of the bimetallic catalyst were larger than those of the other catalysts, which may have facilitated its high PG selectivity. Hydrogen (H₂) adsorption is believed to be more active in large-sized metal particles as the surface exposure of the metal is larger. Therefore, more H₂ can be activated on the surface of the catalyst. It also increases accessibility to metallic sites, which, in turn, increases its reactivity towards the C-O bonds *via* hydrogenation, which increases the amount of PG produced. Conversely, the smaller particle sizes of the monometallic catalysts decreased their PG selectivity.

The results reveal that the bimetallic catalyst had better catalytic performance than the monometallic catalysts. The catalytic efficiency of the bimetallic Co-Cu/Dol catalysts could have been influenced by different factors such as appropriate acidity, large particle size, good metal reducibility, high surface area, fewer pores, and smaller pore diameters. The bimetallic catalyst had good glycerol conversion and PG selectivity when factors such as pressure, reaction temperature, and reaction duration were optimised, in comparison to the results of extant studies (Table 3).

Table 3

Comparison of the result obtained in this work with other results from the literature

Catalyst	Reaction parameters				Conv (%)	Sel (%) 1,2-PDO	References
	Temp (°C)	H ₂ (MPa)	Time (h)	Cat Dosage (g)			
Cu-Ni/Al ₂ O ₃	210	4.5	12	2	60	89	Pudi et al., 2015
Cu/Ce/Mg	200	6	10	1	56.4	97.4	Mallesham et al., 2016
Cu-Ni/Al ₂ O ₃	220	4.5	16	0.9	70.5	70	Gandarias et al., 2012
Ru-Cu/Al ₂ O ₃	200	2.5	24	2	45	94	Soares et al., 2016
Ru-Cu/ZrO ₂	200	2.5	24	2	13.7	100	Soares et al., 2016
Ni-Co/Al ₂ O ₃	220	6	10	2	63.5	60.4	Jiang et al., 2016
Ni-Co/Ce	220	6	10	2	71.3	68.5	Jiang et al., 2016
Ni-Cu/Dol ^a	200	4	10	1	80	88.4	Present work

CONCLUSION

The bimetallic Co-Cu/Dol catalyst that this present study proposed had a maximum glycerol conversion of 80.3% and a maximum PG selectivity of 85.9% at a reaction temperature of 200°C, reaction pressure of 4 MPa, and a reaction duration of 10 hours. It performed the best as it had effective Cu-Co-Dol interactions, an optimal acidity of 11724 μmol/g,

a large surface area of $15.3 \text{ m}^2 \text{ g}^{-1}$, a good ability to reduce metal oxide species at a low temperature of 277°C , a pore diameter of 0.615 nm , fewer pores ($0.032 \text{ cm}^3 \text{ g}^{-1}$), and large particle sizes (72.3 nm).

ACKNOWLEDGEMENTS

The authors thank Universiti Putra Malaysia for funding the study with a Research Grant under Initiative Putra Student Grants (No.: 9619500) and (No.: 9692400).

REFERENCES

- Asikin-Mijan, N., Lee, H. V., Juan, J. C., Noorsaadah, A. R., & Taufiq-Yap, Y. H. (2017). Catalytic deoxygenation of triglycerides to green diesel over modified CaO-based catalysts. *RSC Advances*, *7*(73), 46445-46460. <https://doi.org/10.1039/C7RA08061A>
- Azri, N., Ramli, I., Nda-Umar, U. I., Shamsuddin, M. Razali., Saiman, M. I., & Taufiq-Yap, Y. H. (2020). Copper-dolomite as effective catalyst for glycerol hydrogenolysis to 1,2-propanediol. *Journal of the Taiwan Institute of Chemical Engineers*, *112*, 34-51. <https://doi.org/10.1016/j.jtice.2020.07.011>
- Bagheri, S., Muhd, N., & Yehye, W. A. (2015). Catalytic conversion of biodiesel derived raw glycerol to value added products. *Renewable and Sustainable Energy Reviews*, *41*, 113-127. <https://doi.org/10.1016/j.rser.2014.08.031>
- Feng, Y., Yin, H., Wang, A., Shen, L., Yu, L., & Jiang, T. (2011). Gas phase hydrogenolysis of glycerol catalyzed by Cu/ZnO/MO_x (MO_x = Al₂O₃, TiO₂, and ZrO₂) catalysts. *Chemical Engineering Journal*, *168*(1), 403-412. <https://doi.org/10.1016/j.cej.2011.01.049>
- Freitas, I. C., Manfro, R. L., & Souza, M. M. V. M. (2018). Hydrogenolysis of glycerol to propylene glycol in continuous system without hydrogen addition over Cu-Ni catalysts. *Applied Catalysis B: Environmental*, *220*, 31-41. <https://doi.org/10.1016/j.apcatb.2017.08.030>
- Gallegos-Suarez, E., Guerrero-Ruiz, A., Rodriguez-Ramos, I., & Arcoya, A. (2015). Comparative study of the hydrogenolysis of glycerol over Ru-based catalysts supported on activated carbon, graphite, carbon nanotubes and KL-zeolite. *Chemical Engineering Journal*, *262*, 326-333. <https://doi.org/10.1016/j.cej.2014.09.121>
- Gandarias, I., Requies, J., Arias, P. L., Armbruster, U., & Martin, A. (2012). Liquid-phase glycerol hydrogenolysis by formic acid over Ni-Cu/Al₂O₃ catalysts. *Journal of Catalysis*, *290*, 79-89. <https://doi.org/10.1016/j.jcat.2012.03.004>
- Guo, X., Li, Y., Shi, R., Liu, Q., Zhan, E., & Shen, W. (2009). Co/MgO catalysts for hydrogenolysis of glycerol to 1, 2-propanediol. *Applied Catalysis A: General*, *371*(1-2), 108-113. <https://doi.org/10.1016/j.apcata.2009.09.037>
- Jiang, T., Kong, D., Xu, K., & Cao, F. (2016). Hydrogenolysis of glycerol aqueous solution to glycols over Ni-Co bimetallic catalyst: Effect of ceria promoting. *Applied Petrochemical Research*, *6*, 135-144. <https://doi.org/10.1007/s13203-015-0128-8>

- Karelovic, A., & Ruiz, P. (2015). The role of copper particle size in low pressure methanol synthesis via CO₂ hydrogenation over Cu/ZnO catalysts. *Catalysis Science & Technology*, 5(2), 869–881. <https://doi.org/10.1039/C4CY00848K>
- Kovanda, F., Jiratova, K., Rymes, J., & Kolousek, D. (2001). Characterization of activated Cu/Mg/Al hydrotalcites and their catalytic activity in toluene combustion. *Applied Clay Science*, 18(1-2), 71-80. [https://doi.org/10.1016/S0169-1317\(00\)00032-6](https://doi.org/10.1016/S0169-1317(00)00032-6)
- Li, Y., Guo, Y., & Xue, B. (2009). Catalytic combustion of methane over M (Ni, Co, Cu) supported on ceria-magnesia. *Fuel Processing Technology*, 90(5), 652-656. <https://doi.org/10.1016/j.fuproc.2008.12.002>
- Liu, Y., Guo, X., Rempel, G. L., & Ng, F. T. T. (2019). The promoting effect of Ni on glycerol hydrogenolysis to 1,2propanediol with in situ hydrogen from methanol steam reforming using a Cu/ZnO/Al₂O₃ catalyst. *Catalysts*, 9(5), Article 412. <https://doi.org/10.3390/catal9050412>
- Luna, F. M. T., Cecilia, J. A., Saboya, R. M. A., Barrera, D., Sapag, K., Rodríguez-Castellón, E., & Jr, C. C. L. (2018). Natural and modified montmorillonite clays as catalysts for synthesis of biolubricants. *Materials*, 11(9), Article 1764. <https://doi.org/10.3390/ma11091764>
- Lopez, A., Aragon, J. A., Hernandez-Cortez, J. G., Mosqueira, M. L., & Martinez-Palou, R. (2019). Study of hydrotalcite-supported transition metals as catalysts for crude glycerol hydrogenolysis. *Molecular Catalysis*, 468, 9–18. <https://doi.org/10.1016/j.mcat.2019.02.008>
- Mallesham, B., Sudarsanam, P., Reddy, B. V. S., & Reddy, B. M. (2016). Development of cerium promoted copper–magnesium catalysts for biomass valorization: Selective hydrogenolysis of bioglycerol. *Applied Catalysis B: Environmental*, 181, 47–57. <https://doi.org/10.1016/j.apcatb.2015.07.037>
- Nagaraja, B. M., Padmasri, A. H., Seetharamulu, P., Reddy, K. H. P., Raju, B. D., & Rao, K. R. (2007). A highly active Cu-MgO-Cr₂O₃ catalyst for simultaneous synthesis of furfuryl alcohol and cyclohexanone by a novel coupling route-Combination of furfural hydrogenation and cyclohexanol dehydrogenation. *Journal of Molecular Catalysis A: Chemical*, 278(1-2), 29-37. <https://doi.org/10.1016/j.molcata.2007.07.045>
- Pandhare, N. N., Pudi, S. M., Biswas, P., & Sinha, S. (2016). Vapor phase hydrogenolysis of glycerol to 1, 2-propanediol over γ -Al₂O₃ supported copper or nickel monometallic and copper–nickel bimetallic catalysts. *Journal of the Taiwan Institute of Chemical Engineers*, 61, 90–96. <https://doi.org/10.1016/j.jtice.2015.12.028>
- Pardeshi, S. K., & Pawar, R. Y. (2010). Optimization of reaction conditions in selective oxidation of styrene over fine crystallite spinel-type CaFe₂O₄ complex oxide catalyst. *Materials Research Bulletin*, 45(5), 609-615. <https://doi.org/10.1016/j.materresbull.2010.01.011>
- Priya, S. S., Selvakannana, Komandur, P. R., Chary, V. R., Kantam, M. L., & Bhargava, S. K. (2017). Solvent-free microwave-assisted synthesis of solketal from glycerol using transition metal ions promoted mordenite solid acid catalysts. *Molecular Catalysis*, 434, 184–193. <https://doi.org/10.1016/j.mcat.2017.03.001>
- Pudi, S. M., Biswas, P., Kumar, S., & Sarkar, B. (2015). Selective hydrogenolysis of glycerol to 1,2 propanediol over bimetallic Cu-Ni catalysts supported on γ -Al₂O₃. *Journal of the Brazilian Chemical Society*, 26(8), 1551–1564. <https://doi.org/10.5935/0103-5053.20150123>

- Putrakumar, B., Nagaraju, N., Kumar, V. P., & Chary, K. V. R. (2015). Hydrogenation of levulinic acid to valerolactone over copper catalysts supported on Al_2O_3 . *Catalysis Today*, 250, 209–217. <https://doi.org/10.1016/j.cattod.2014.07.014>
- Rajkhowa, T., Marin, G. B., & Thybaut. J. W. (2017). A comprehensive kinetic model for Cu catalyzed liquid phase glycerol hydrogenolysis. *Applied Catalysis B: Environmental*, 205, 469–480. <https://doi.org/10.1016/j.apcatb.2016.12.042>
- Shozi, M. L., Dasireddy, V. D. B. C., Singh, S., Mohlala, P., Morgan, D. J., Iqbal, S., & Friedrich, H. B. (2017). An investigation of Cu–Re–ZnO catalysts for the hydrogenolysis of glycerol under continuous flow conditions. *Sustainable Energy & Fuels*, 1(6), 1437–1445. <https://doi.org/10.1039/C7SE00199A>
- Soares, A. V., Perez, G., & Passos, F. B. (2016). Alumina supported bimetallic Pt–Fe catalysts applied to glycerol hydrogenolysis and aqueous phase reforming. *Applied Catalysis B: Environmental*, 185, 77–87. <https://doi.org/10.1016/j.apcatb.2015.11.003>
- Soares, A. V. H., Salazar, J. B., Falcone, D. D., Vasconcellos, F. A., Davis, R. J., & Passos, F. B. (2016). A study of glycerol hydrogenolysis over Ru–Cu/ Al_2O_3 and Ru–Cu/ ZrO_2 catalysts. *Journal of Molecular Catalysis A: Chemical*, 415, 27–36. <https://doi.org/10.1016/j.molcata.2016.01.027>
- Srivastava, S., Jadeja, G. C., & Parikh, J. (2017). Synergism studies on alumina-supported copper nickel catalysts towards furfural and 5-hydroxymethylfurfural hydrogenation. *Journal of Molecular Catalysis A: Chemical*, 426(Part A), 244–256. <https://doi.org/10.1016/j.molcata.2016.11.023>
- Tanasoi, S., Tanchoux, N., Adriana, U., Tichit, D., Sandulescu, I., Fajula, F., & Marcu, I. C. (2009). New Cu-based mixed oxides obtained from LDH precursors, catalysts for methane total oxidation. *Applied Catalysis A: General*, 363(1-2), 135–142. <https://doi.org/10.1016/j.apcata.2009.05.007>
- Tasyurek, K. C., Bugdayci, M., & Yucel, O. (2018). Reduction conditions of metallic calcium from magnesium production residues. *Metals*, 8(6), Article 383. <https://doi.org/10.3390/met8060383>
- Thirupathi, B., & Smirniotis, P. G. (2012). Nickel-doped Mn/ TiO_2 as an efficient catalyst for the low-temperature SCR of NO with NH_3 : Catalytic evaluation and characterizations. *Journal of Catalysis*, 288, 74–83. <https://doi.org/10.1016/j.jcat.2012.01.003>
- Vanama, P. K., Kumar, A., Ginjaipalli, S. R., & Komandur, V. R. C. (2015). Vapor-phase hydrogenolysis of glycerol over nanostructured Ru/MCM-41 catalysts. *Catalysis Today*, 250, 226–238. <https://doi.org/10.1016/j.cattod.2014.03.036>
- Vargas-Hernández, D., Rubio-Caballero, J. M., Santamaría-González, J., Moreno-Tost, R., Mérida-Robles, J. M., Pérez-Cruz, M. A., Jiménez-López, A., Hernández-Huesca, R., & Maireles-Torres, P. (2014). Furfuryl alcohol from furfural hydrogenation over copper supported on SBA-15 silica catalysts. *Journal of Molecular Catalysis A: Chemical*, 383–384, 106–113. <https://doi.org/10.1016/j.molcata.2013.11.034>
- Vasiliadou, E. S., & Lemonidou, A. A. (2011). Investigating the performance and deactivation behaviour of silica-supported copper catalysts in glycerol hydrogenolysis. *Applied Catalysis A: General*, 396(1-2), 177–185. <https://doi.org/10.1016/j.apcata.2011.02.014>
- Wen, C., Yin, A., Cui, Y., Yang, X., Dai, W. L., & Fan, K. (2013). Enhanced catalytic performance for SiO_2 – TiO_2 binary oxide supported Cu-based catalyst in the hydrogenation of dimethyl oxalate. *Applied Catalysis A: General*, 458, 82–89. <https://doi.org/10.1016/j.apcata.2013.03.021>

- Yu, W., Zhao, J., Ma, H., Miao, H., Song, Q., & Xu, J. (2010). Aqueous hydrogenolysis of glycerol over Ni–Ce/AC catalyst: Promoting effect of Ce on catalytic performance. *Applied Catalysis A: General*, 383(1-2), 73-78. <https://doi.org/10.1016/j.apcata.2010.05.023>
- Yuan, Z., Wu, P., Gao, J., & Lu, X. (2009). Pt/solid-base: A predominant catalyst for glycerol hydrogenolysis in a base-free aqueous solution. *Catalysis Letters*, 130, 261-265. <https://doi.org/10.1007/s10562-009-9879-0>
- Zhao, F., Li, S., Wu, X., Yue, R., Li, W., Zha, X., Deng, Y., & Chen, Y. (2019). Catalytic behaviour of flame-made CuO-CeO₂ nanocatalysts in efficient co oxidation. *Catalysts*, 9(3), Article 256. <https://doi.org/10.3390/catal9030256>
- Zhao, S., Yue, H., Zhao, Y., Wang, B., Geng, Y., Lv, J., Wang, S., Gong, J., & Ma, X. (2013). Chemoselective synthesis of ethanol via hydrogenation of dimethyl oxalate on Cu/SiO₂: Enhanced stability with boron dopant. *Journal of Catalysis*, 297, 142-150. <https://doi.org/10.1016/j.jcat.2012.10.004>
- Zhao, Y., Zhang, Y., Wang, Y., Zhang, J., Xu, Y., Wang, S., & Ma, X. (2017). Structural evolution of mesoporous silica supported copper catalyst for dimethyl oxalate hydrogenation. *Applied Catalysis A: General*, 539, 59–69. <https://doi.org/10.1016/j.apcata.2017.04.001>
- Zheng, L., Xia, S., & Hou, Z. (2015). Hydrogenolysis of glycerol over Cu-substituted hydrocalumite mediated catalysts. *Applied Clay Science*, 118, 68–73. <https://doi.org/10.1016/j.clay.2015.09.002>
- Zhu, S., Gao, X., Zhu, Y., Zhu, Y., Zheng, H., & Li, Y. (2013). Promoting effect of boron oxide on Cu/SiO₂ catalyst for glycerol hydrogenolysis to 1,2-propanediol. *Journal of Catalysis*, 303, 70–79. <https://doi.org/10.1016/j.jcat.2013.03.018>

Evaluation of Microalgae *Chlorella vulgaris* and *Tetradesmus bernardii* for Cultivation and Nutrient Removal in Palm Oil Mill Effluent

Mohammad Navid Wais^{1,2}, Shahrizim Zulkifly^{1*}, Mohd Hafiz Ibrahim¹, Afiqah Mohamed¹ and Zana Ruhaizat Zana Rudin¹

¹Department of Biology, Faculty of Science, Universiti Putra Malaysia, 43400 UPM, Serdang, Selangor, Malaysia

²Department of Botany, Faculty of Biology, Kabul University, Kart-e-Char, Kabul 1006, Afghanistan

ABSTRACT

The palm oil industry is one of the key players in contributing to Malaysia's economy. Palm oil mill effluent (POME), a significant by-product of the oil extraction process, requires mandatory remediation to ensure proper treatment and disposal. Bioremediation using microalgae is a cost-effective and sustainable approach. This study aims to utilise pure and mixed microalgal species, *Chlorella vulgaris* and *Tetradesmus bernardii*, in phycoremediation and biomass production in different concentrations of POME (20%, 40%, 60%, and 80%). Cultivation of microalgae was carried out in 200 mL medium with pH 7–7.8, room temperature of $25 \pm 1^\circ\text{C}$ for 21 days and continuous light illumination at 2000 lux. The highest biomass productivity was observed in 20% POME for mixed microalgae (mean = $0.1733 \text{ mg.mL}^{-1} \pm 0.0057$), followed by *C. vulgaris* ($0.1633 \text{ mg.mL}^{-1} \pm 0.0057$) and *T. bernardii* ($0.1603 \text{ mg.mL}^{-1} \pm 0.0020$). Similarly, the highest nutrient removal was observed in 20% POME for mixed microalgae (COD:66.9801%, TN:86.9565%, TP:86.9655%), followed by *C. vulgaris* and *T. bernardii*. The results showed positive

effects on growth, increased biomass production, and nutrient removal, with 20% POME being the optimal concentration for microalgae. Valuable by-products, such as high-quality pigments and biomass, are also generated by applying microalgae for remediation. Mixed microalgae are superior in the remediation of POME compared to single-culture algae. Treating wastewater through microalgal bioremediation is

ARTICLE INFO

Article history:

Received: 23 July 2023

Accepted: 20 November 2023

Published: 01 April 2024

DOI: <https://doi.org/10.47836/pjst.32.3.10>

E-mail addresses:

waismohammadnavid007@gmail.com (Mohammad Navid Wais)

shahrizim@upm.edu.my (Shahrizim Zulkifly)

mhafiz_ibrahim@upm.edu.my (Mohd Hafiz Ibrahim)

haqifa.dhom@gmail.com (Afiqah Mohamed)

zruhaizat@upm.edu.my (Zana Ruhaizat Zana Rudin)

* Corresponding author

highly efficient in nutrient removal. This research has contributed towards the use of mixed microalgae to achieve effective nutrient removal and biomass for future industrial applications.

Keywords: Biomass, *Chlorella vulgaris*, growth, Malaysia, microalgae, palm oil mill effluent (POME), phycoremediation, *Tetrademus bernardii*

INTRODUCTION

Malaysia is the second-largest producer and exporter of palm oil globally. (Khatun et al., 2017). Manufacturing of palm oil 2020 was 19.14 million tonnes, with the total export of palm products amounting to 26.73 million tonnes (Haryati et al., 2022). Palm oil manufacturing is expected to raise production by 25 million tonnes in 2035. According to the Food and Agriculture Organization (FAO), the demand for palm oil is anticipated to hit 156 million tonnes by 2050 (Chew et al., 2021). The palm oil expansion has contributed to a large portion of the country's Gross National Income (GNI), contributing towards 47% of global production (Rowland et al., 2022).

The palm oil industry by-products include empty fruit bunches, mesocarps, fibres, shells, and palm oil mill effluent (POME) (Singh et al., 2010). Manufacturing palm oil requires an extensive amount of water. One tonne of palm oil requires 5–7 tonnes of water for processing, with 2.5 m³ of POME produced (Ratnasari et al., 2021). Wastewater produced by POME contains various dissolved and suspended contaminants consisting of 95%–96% water, 4%–5% total solids, and 0.6%–0.7% oil (Kamyab et al., 2015). POME consists of a high level of nutrients such as nitrogen, phosphorus, and ammonia; exceeding the level of these nutrients will cause contamination of the aquatic zone (Karim et al., 2021). The production of huge volumes of by-products during oil extraction may contaminate water bodies (Ahmad et al., 2016). Furthermore, the release of untreated POME can have a crucial impact on the diversity of phytoplankton, a disorder in the aquatic ecosystems' reproductive and physiological systems of fishes (Bala et al., 2015).

The conventional way of removing nutrients from palm oil mill effluent include using an open pond, phytoremediation, supercritical water gasification, aerobic-anaerobic process, coagulation-flocculation, and another option is using electrochemical advanced oxidation process (Kamyab et al., 2022). This paper focuses on the use of microalgae for the remediation and nutrient removal of palm oil mill effluent. Valuable by-products, such as high-quality pigments and biomass, are also generated by applying microalgae for remediation.

Several unconventional methods exist for POME treatment but are not without problems. These include adsorption, membrane filtration and electrochemical oxidation. The adsorption technique uses adsorbing materials such as activated carbon, clay, or other

porous substances with a high surface area that can attract and trap pollutants through physical and chemical interactions. However, the adsorbent has a limited capacity to adsorb contaminants. Once saturated, they need to be replaced or regenerated, which can be costly and require additional energy input, impacting the overall environmental footprint of the treatment process. The adsorption selection and specific contaminant removal can complicate the process (Mohammed, 2013).

Membrane filtration is a separation process that uses a semipermeable membrane to remove suspended solids, oils, and other impurities from the effluent. The membrane can become fouled or clogged over time, reducing their efficiency. Pre-treatment, regular cleaning, and maintenance have caused the elevation of the operational cost for the membrane filtration method (Azmi & Yunus, 2014; Udaiyappan et al., 2021). Electrochemical advanced oxidation processes (EAOPs) are innovative techniques that harness the in situ electro-generation of reactive oxygen species (ROS) and other powerful oxidant species, enabling the efficient mineralisation of organic compounds into carbon dioxide CO₂, water, and essential inorganic ions (Kamyab et al., 2021). The choice of (EAOPs) and the system's complexity should be carefully considered in terms of energy consumption, cost, and expertise.

Biological treatment, especially microalgal treatment methods, offers unique advantages compared to other methods. Microalgae are highly efficient at removing nutrients such as nitrogen and phosphorous from POME. They can reduce nutrient content to a level that meets environmental discharge standards, potentially facilitating nutrient recovery to reuse (Khalid et al., 2016). Microalgae can rapidly grow and multiply in POME, leading to biomass production; during the process, it can sequester the CO₂. Microalgae are adaptable to a wide range of environmental conditions and can thrive in different POME compositions, making them a versatile option for treatment (Hazman et al., 2018). The microalgae-based treatment of POME offers unique benefits related to nutrient removal, biomass production, carbon capture, and resource recovery. It represents a promising and environmentally sustainable approach for POME treatment, especially. In the context of sustainability and circular economy goals (Anto et al., 2020; Cheah et al., 2018).

Microalgae serve as multifunctional agents in wastewater treatment, with capabilities encompassing the efficient removal of excess nutrients, reduction of chemical oxygen demand (COD), and the accumulation of heavy metals through biosorption. These microorganisms also effectively inhibit harmful pathogen growth and, notably, enhance the visual appeal of treated water. Their comprehensive role is pivotal in preventing eutrophication, enhancing water quality, and beautifying treated water, underscoring their significance in sustainable wastewater remediation. Studies used microalgae species, *Chlorella vulgaris*, *Characium* sp., and *Scenedesmus* sp. for remediation of POME, municipal and polluted surface water (Talib et al., 2023).

Microalgae effectively capture carbon dioxide (CO₂) during photosynthesis and store it as biomass in the form of complex carbohydrates and lipids. Lipids can be used for biofuel applications, such as biodiesel, offering a renewable energy source. Among the microalgal species, *Chlorella* sp., *Chlamydomonas* sp., and *Nannochloropsis* were used in remediating palm oil mill effluent (POME), CO₂ sequestration, and biomass production (Ding et al., 2016; Hariz et al., 2018; Resdi et al., 2021). *Haematococcus pluvialis* and *Chromochloris zofingiensis* were used for phycoremediation of POME and producing valuable by-product, pigment astaxanthin (Fernando et al., 2021). Applications of astaxanthin can be used in diverse industries such as healthcare, cosmetics, and aquaculture.

Microalgae Roles in Wastewater Treatment and Bioremediation

***Chlorella vulgaris/Chlorella* sp.** *Chlorella vulgaris* has been widely studied due to its potential in various industries, such as supplementary food that provides essential nutrients (Orusmurzaeva et al., 2022). Mass cultivation of *Chlorella* sp. has produced a large amount of biomass that has been incorporated into various products such as animal feed (Medvedeva et al., 2022), aquaculture (Ahmad et al., 2020), cosmetics (Morais et al., 2020) and pharmaceutical as it contains a significant concentration of carotenoids that associated with anti-inflammatory and antioxidant properties (Velmurugan & Muthukaliannan, 2022). Another sector that has benefited from this alga is wastewater treatment and bioremediation. Studies have been conducted to assimilate them in heavy metal treatment of aqueous environment, such as removing cadmium and zinc (Al-Khiat et al., 2023; Ahmad et al., 2017).

In Malaysia, the palm oil industry has contributed to a large amount of wastewater from palm oil mill effluent's by-products. *Chlorella* sp. has been proven to have tolerance towards high pollutants and nutrients from the POME and managed to sequester the carbon content through the carbon fixation process (Hariz et al., 2019), apart from nutrient removal such as total nitrogen (TN) and total phosphorus (TP) along with biological oxygen demand (BOD) and chemical oxygen demand (COD) (Ahmad et al., 2017; Kamarudin et al., 2013; Tan et al., 2022).

Tetradesmus bernardii

Tetradesmus bernardii is another species of green algae of Phylum Chlorophyta, classified under Chlorophyceae. This species is the basionym of an earlier identified species, *Scenedesmus bernardii* (Wynne & Hallan, 2015). This genus has previously been studied as one of the bioindicators of water quality assessment (El-Din et al., 2022), as different water quality levels impacted the size and shape of the cells and organelles (Bauer et al., 2012) and due to its rich components of lipids, protein, and carbohydrates made them suitable to be incorporated as the raw materials for bioplastics production (Song et al.,

2022). The potential of *Tetradesmus* sp. for the application of wastewater treatment and bioremediation has also been studied extensively. A study conducted to assess the capacity for nutrient removal from hydroponic greenhouse wastewater has discovered this genus to acquire a complete removal of N and T from the medium (Salazar et al., 2023). With a similar capability as the *Chlorella*, it has also been applied to include this alga in the studies of nutrient removal in POME (Kamarudin et al., 2013; Tan et al., 2022).

Most research focuses on using unialgal cultures for the bioremediation of wastewater. Limited work was done on using mixed algal species for remediation. In this study, we are testing the effects of using unialgal cultures of microalgae versus a mixed culture of microalgae. We hypothesised that using a mixture of two microalgae species will benefit wastewater remediation (POME). Unialgal cultures, *C. vulgaris* and *T. bernardii*, were isolated from the remediation ponds and will be tested for remediation as unialgal cultures versus a mixed culture. The cultures were tested towards different concentrations of POME to evaluate the efficiency of microalgae growth, biomass accumulation, and nutrient removal.

MATERIALS AND METHODS

Experimental Design

All the experiments in this research study were conducted in the plant physiology laboratory, Department of Biology, University Putra Malaysia (UPM). Microalgae *C. vulgaris* and *T. bernardii*, collected from the remediation ponds, were isolated into pure cultures. The cultures were grown in a 250 mL conical flask with a light intensity of 2000 lux, pH 7-7.8, and room temperature of $25\pm 1^{\circ}\text{C}$ for 21 days in triplicates. Palm oil mill effluents (POME) were collected in two 5 L plastic containers from the aerobic pond Bell Sri Lingga palm oil mill industry, Melaka ($2^{\circ}22'40.3''$ N $101^{\circ}59'10.4''$ E). The POME was transferred to the Plant Physiology lab, Department of Biology, University Putra Malaysia and stored at 4°C to avoid microbial degradation. Mixed microalgae *C. vulgaris* and *T. bernardii* were cultivated in different concentrations of POME (20%, 40%, 60%, and 80%). The concentrations were based on preliminary research that included 100% POME concentration; however, microalgae cultivation was unsuccessful. The POME was prepared at different concentrations by dilution with autoclaved distilled water.

Purification and Identification of Microalgae

The microalgal cultures are from the Plant Physiology Lab UPM. The cultures were purified on agar plates to obtain single colonies. Isolated microalgal cultures were subjected to DNA extraction using DNeasy PowerSoil pro kit Qiagen (Qiagen GmbH, Qiagen Strasse 1, 40724 Hilden, Germany). The eukaryotic

primer for V8 forward 5'-ATAACAGGTCTGTGATGCCCT-3', and for V9 reverse 5'-CCTTCYGCAGGTTACCTAC-3' were used to amplify the 18S ribosomal RNA genes (Bradley et al., 2016). The primer synthesis and PCR product sequencing were carried out by Apical Scientific (Seri Kembangan, Selangor). The 18S sequences were compared against the National Centre for Biotechnology Information (NCBI) BLAST database.

Growth Rate of Microalgae (Optical Density)

The growth rate of mixed microalgae (*C. vulgaris* and *T. bernardii*), *C. vulgaris*, and *T. bernardii* were measured in different concentrations of POME (20%, 40%, 60%, 80%) in triplicates by using optical density (OD) spectrophotometer (HITACHI U-1900). The OD was measured at three different wavelengths (680 nm, 685 nm, and 700 nm). The 680 nm was chosen as the optimum wavelength for this study (Hazman et al., 2018; Jasni et al., 2020). Cultivation of microalgae was carried out in 200 mL medium with pH 7–7.8, room temperature of 25±1°C for 21 days and continuous light illumination at 2000 lux.

Biomass of Microalgae (Dry Weight)

The biomass, in terms of dry weight, of microalgae was quantified on both day zero and day 21 of the study. Initially, the palm oil mill effluent (POME) underwent a filtration process employing 150 µm filters to eliminate undesired particles. Subsequently, the filtrate was subjected to a secondary filtration step utilising 0.45 µm autoclaved glass membrane filters (Schleicher & Schuell, Germany) to capture the microalgal cells. These samples were then transferred to sterile petri dishes and subjected to desiccation in an oven set at 60°C for 24 hours. The filter papers were weighed using an analytical balance with 0.1 mg sensitivity (AL204, Mettler Toledo) (Ding et al., 2016; Hazman et al., 2018). The biomass (dry weight) of microalgae was calculated in gL⁻¹ as in the following Equation 1:

$$\text{DCW (gL}^{-1}\text{)} = \frac{(WF+s)-Wf}{V} \quad [1]$$

where WF+s is the weight of the filter plus sample, Wf is the weight of the filter, and V is the volume of the sample collected.

Pigment Content of Microalgae

Microalgal chlorophyll *a* and carotenoid were determined following trichromatic spectrophotometry methods with some modifications (Johan et al., 2014). Samples (25 mL) were centrifuged at 4000 rpm for 10 minutes. Then, 5 mL of 99% acetone was added to the samples and ground by mortar and pestle. Three mL of samples were transferred to a glass cuvette, and the chlorophyll *a* was measured using a spectrophotometer (HITACHI U-1900) (Aminot & Rey, 2000; Johan et al., 2014). Chlorophyll *a* was measured at three

wavelengths (630, 647, 664 nm) and (452 nm) for carotenoids. Chlorophyll *a* and carotenoid were calculated in mgL^{-1} as in Equations 2, 3 and 4.

$$\text{Chlorophyll-}a = (\text{mgm}^{-3}) \frac{(\text{Ca}) * (\text{Va})}{\text{Va}} \quad [2]$$

where, $\text{Ca} = (11.6 * \text{OD664}) - (1.31 * \text{OD647}) - (0.14 * \text{OD630})$; Va = Volume of acetone used for extraction (mL); and Vc = Volume of algal culture filtered (mL)

$$\text{Chlorophyll-}a \text{ (mgL}^{-1}\text{)} = \frac{\text{Chl } a \text{ (mgm}^{-3}\text{)}}{1000} \quad [3]$$

$$\text{Carotenoid (mgL}^{-1}\text{)} = \frac{(\text{OD452}) * (3.86) * (\text{Va})}{\text{Vb}} \quad [4]$$

where, Va = Volume of acetone used for extraction (mL); and Vb = Volume of algal culture filtered (mL)

Nutrient Removal

The chemical parameter measurements of palm oil mill effluent (POME), including nutrients such as total nitrogen (TN), total phosphorous (TP) and chemical oxygen demand (COD), were measured in the laboratory at day 0 and day 21 by using Hach Multiparameter Portable Colorimeter (DR900, HACH). The chemical profiles of the sample collected were assessed based on the instructions: TN (Persulfate digestion method – 10072), TP (Molybdovanadate with Persulfate digestion acid method – 10127), COD (Reactor digestion method – 8000).

Statistical Analysis

Statistical analysis was performed using Statistical Packages for the Social Sciences (SPSS) software (version 21.0, SPSS Inc., Chicago, IL). The data was assessed using One-way ANOVA to determine the differences in the mean value of the dependent variable associated with the effect of the controlled independent variable. The standard deviation was used to measure variability, and post-hoc analysis (Duncan) was performed to determine the significant difference between species of algae in different concentrations of POME with the significant level for the p-value ($p < 0.05$).

RESULTS

Isolation and Identification

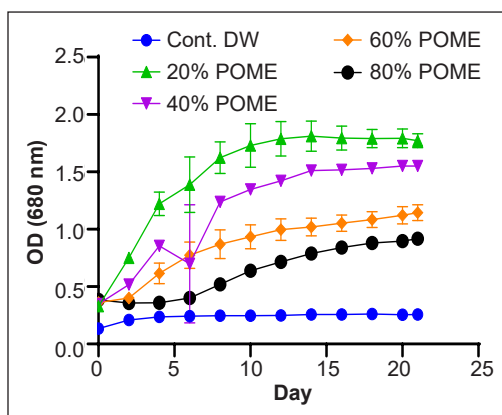
Unialgal cultures were identified as *C. vulgaris* and *T. bernardii* species, with 100% similarity. The gene sequences have been deposited in the NCBI GenBank with accession numbers (ON158767) for *C. vulgaris* and (OP804515) for *T. bernardii* (Figure S1).

Growth Rate, Optical Density (OD) of Microalgae in Different Concentrations of POME

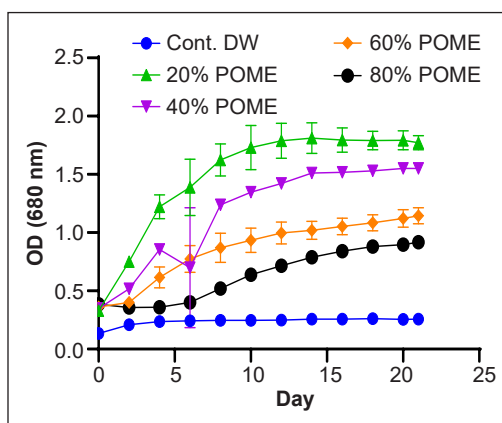
The microalgae cultured in treatment batches showed relatively similar growth patterns for microalgae. Figure 1 indicates the growth performance of mixed microalgae, *C. vulgaris*, and *T. bernardii* in various concentrations of POME. It was shown that the highest growth rate was observed in 20% POME for mixed microalgae, followed by *C. vulgaris* and *T. bernardii*. The lowest growth was found in 80% POME for *T. bernardii*, followed by *C. vulgaris* and mixed microalgae, respectively. The trend showed that the reduction of POME concentration increases the growth rate of mixed microalgae, *C. vulgaris*, and *T. bernardii*, with 20% POME being the optimal concentration.

Biomass of Microalgae (Dry Weight)

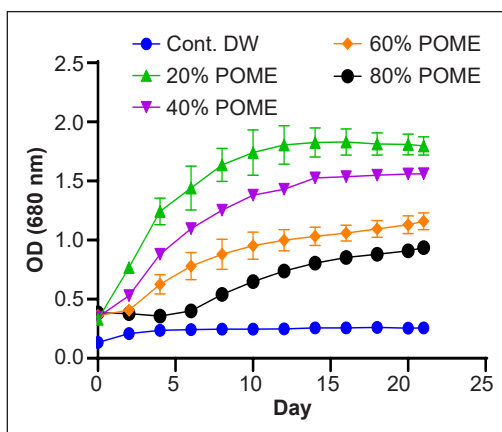
Figure 2(a) shows biomass accumulation in different concentrations of POME for mixed microalgae, *C. vulgaris*, and *T. bernardii*. The microalgal species biomass accumulation cultivated in POME in different concentrations was described by mean biomass (dry weight). The result obtained from dry-weight cells of microalgae in different concentrations of POME indicates that the highest biomass was significantly observed in 20% POME for mixed microalgae ($p < 0.05$). At the same time, unialgal cultures of *C. vulgaris* and *T. bernardii* were not significant. The lowest biomass was found in 80% POME for all groups between the treatment groups. It



(a)



(b)



(c)

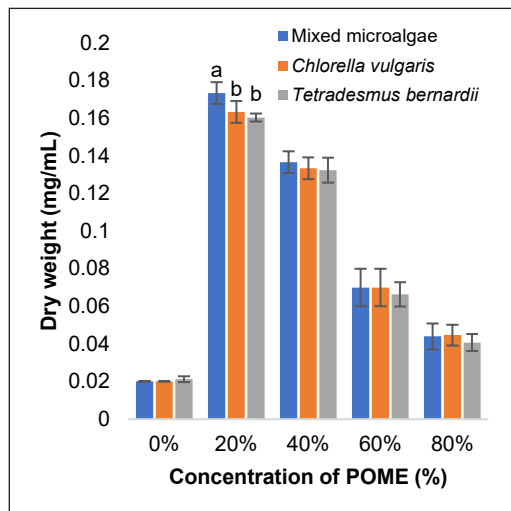
Figure 1. The growth of (a) mixed microalgae, (b) unialgal cultures of *Chlorella vulgaris*, and (c) unialgal cultures of *Tetradesmus bernardii* in different POME concentrations

was shown that by decreasing POME concentration, the biomass accumulation of mixed microalgae, *C. vulgaris* and *T. bernardii* increased, with the optimal concentration of 20% POME for all microalgae species.

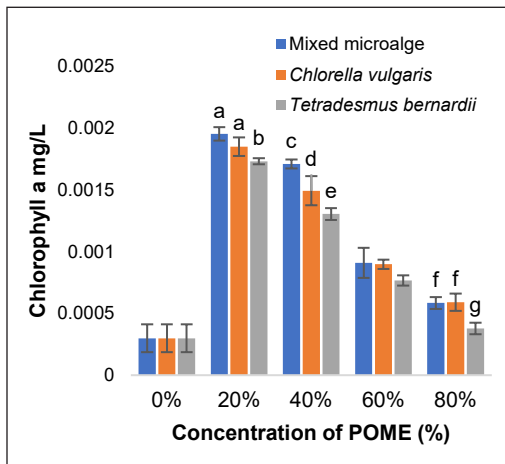
Microalgae Pigments (Chlorophyll *a* and Carotenoids)

The productivity of algal pigments such as chlorophyll *a* and carotenoids was also noted in Figure 2(b); the highest chlorophyll *a* was recorded in mixed microalgae culture and *C. vulgaris* at 20% POME concentrations. The lowest chlorophyll *a* was recorded in 80% POME concentration.

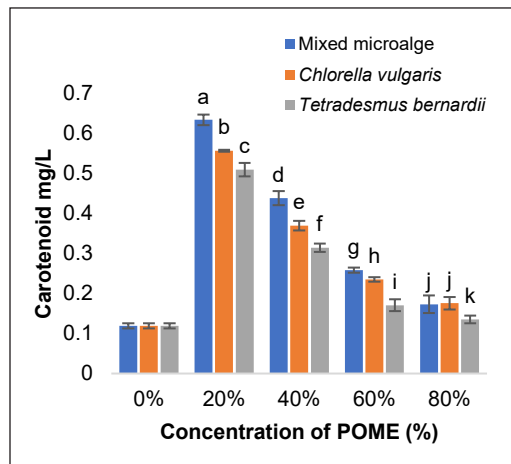
As for the carotenoids Figure 2(c), mixed microalgae show the highest concentration of carotenoids, followed by *C. vulgaris* and *T. bernardii* ($p < 0.05$) at 20% POME. The lowest carotenoids were found in 80% POME. Cultures of 20% POME were found to have the highest chlorophyll *a* and carotenoid levels of mixed microalgae, *C. vulgaris*, and *T. bernardii*.



(a)



(b)



(c)

Figure 2. (a) Biomass, (b) chlorophyll *a*, and (c) carotenoids of mixed microalgae, unialgal cultures of *Chlorella vulgaris*, and *Tetradesmus bernardii* in different POME concentrations. Values are presented as average \pm standard deviation ($n = 3$). Lowercase letters indicate significant differences between mixed microalgae, *C. vulgaris* and *T. bernardii* (One-way ANOVA, $p < 0.05$, Duncan test). Error bars without lowercase letters indicate no significant difference

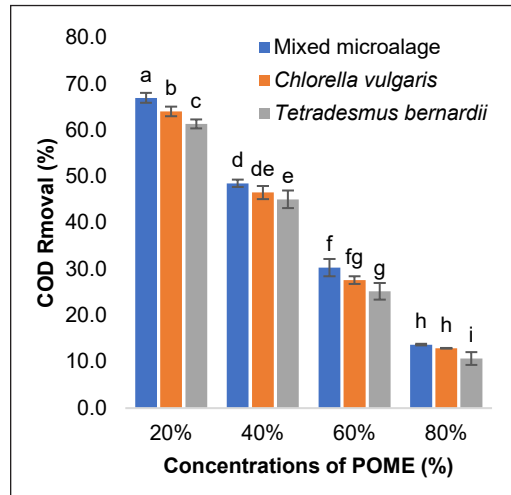
Nutrient Removal

Figure 3(a) shows the nutrient removal from POME in different concentrations of POME by mixed microalgae, *C. vulgaris*, and *T. bernardii*. Mixed microalgae showed significantly the highest COD removal percentage ($p < 0.05$) in comparison to unialgal cultures. All treatments found the lowest growth in 80% POME concentration. At 20% POME concentration, mixed microalgae were most efficient at removing COD.

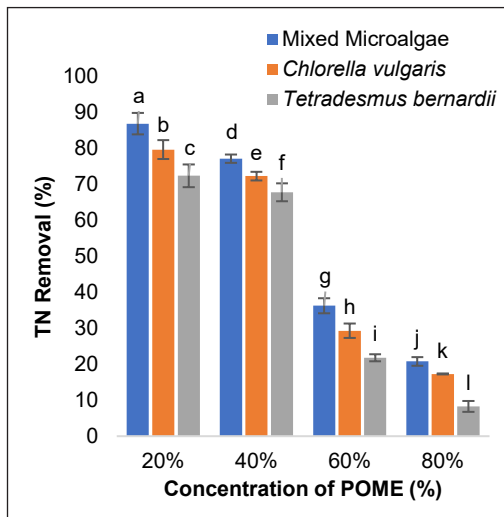
Mixed microalgae were also found to be efficient at removing total nitrogen at 20% POME concentration ($p < 0.05$) in comparison to the two unialgal cultures of *C. vulgaris* and *T. bernardii* (Figure 3(b)).

For total phosphorus, the mixed microalgae cultures were also found to be significantly higher in removing total phosphorus ($p < 0.05$), while the unialgal cultures were not significantly different (Figure 3(c)).

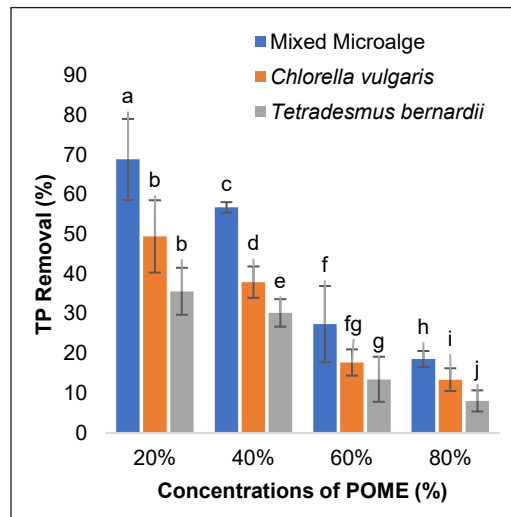
Table 1 describes the nutrient removal of POME using various microalgae species. From this research, mixed microalgae removed 66% of COD, 86% of TN, and 68%



(a)



(b)



(c)

Figure 3. (a) COD, (b) TN, and (c) TP removal efficiency of mixed microalgae, unialgal cultures of *Chlorella vulgaris*, and *Tetradesmus bernardii* in different POME concentrations. Values are presented as average \pm standard deviation ($n = 3$). Lowercase letters indicate significant differences between mixed microalgae, *C. vulgaris* and *T. bernardii* (One-way ANOVA, $p < 0.05$, Duncan test)

Table 1

Comparison of nutrient removal of POME using various microalgal species

Microalgae	COD (%)	TN (%)	TP (%)	Description	References
Mixed Microalgae	66	86	68	This study	
<i>Chlorella vulgaris</i>	61	80	56	This study	
<i>Tetradesmus bernardii</i>	64	79	49	This study	
<i>Scenedesmus</i> sp. strain UKM9	57	100	91	Cultivation and application for nutrient removal	Udaiyappan et al., 2021
<i>Haematococcus pluvialis</i> and <i>Chromochloris zofingiensis</i>	50.9%	49.3	3.95	Phycoremediation and astaxanthin production	Fernando et al., 2021
<i>Nannochloropsis</i> sp.	71% 48%	-	-	Cultivation and application for nutrient removal with and without beads	Emparan et al., 2020)
<i>Chlorella sorokiniana</i> sp.	47.09%	62.07	30.77	Cultivation and application for nutrient removal for lipid production	Cheah et al., 2018
<i>Chlamydomonas</i> sp. UKM6	15-20%	-	5-20	Microalgae-bacteria interaction in palm oil mill effluent treatment	Udaiyappan et al., 2020
<i>Chlorella</i> sp.	-	80.9	-	CO ₂ sequestration by using microalgae sustainable strategies for environmental protection	Hariz et al., 2018
<i>Chlamydomonas</i> sp UKM6, <i>Chlorella sorokiniana</i>	56%	65	34	CO ₂ fixation capability of <i>Chlorella</i> sp. and treating POME	Hazman et al., 2018
<i>Chlamydomonas</i> sp. UKM6	8.59- 29.13%	43.5- 72.97	58.58- 100	Cultivation and application for nutrient removal and biomass production	Ding et al., 2016
<i>Chlamydomonas</i>	67.35%	-	-	Efficiency of microalgae in nutrient removal from POME	Kamyab et al., 2015
Micro and macroalgae	71	-	-	Micro-macroalgae mixture as a promising agent for treating POME	Kamyab et al., 2014

of TP. The nutrient removal efficiency of POME by mixed microalgae was higher than *C. vulgaris* or *T. bernardii* unialgal cultures (see supplementary data Tables S1, S2, and S3). The comparison of other research using microalgae is also shown in Table 1.

DISCUSSION

Growth Rate

Wastewater originates from a range of agriculture, domestic, and industrial water activities, and it encompasses contaminants along with inorganic and organic compounds (Ahmed

et al., 2022). Treating wastewater before releasing it into the environment is essential to prevent contamination from entering natural water systems and harming the environment (Otondo et al., 2018). The utilisation of microalgae in biological wastewater treatment is widely applied due to their environmental advantages and cost-effectiveness.

Particulate and suspension substances of POME affect microalgae growth and significantly decrease the growth rate. In this study, by increasing the concentration of POME, the growth of microalgae is limited and influenced by the physical characteristics of POME. High suspensions of POME gradually limited light penetration for microalgae growth. The dark colour of POME also inhibits the light intensity from the bottom of the culture flasks. As a result, it disrupts photosynthesis and limits algal growth (Talib et al., 2023).

Microalgae cultures cultivated in highly concentrated wastewater POME require a long time to reach the stationary phase because the growth is slower than in low concentrations. The dark colour of POME affected the growth rate of microalgae. *Coelastrrella* sp., *Chlamydomonas* sp., and *Scenedesmus* sp. cultures showed a low growth rate in high concentrations, resulting in algae cells staying longer in the adaptation phase (Ding et al., 2016; Udaiyappan et al., 2020). Diluting POME in different concentrations reduces the effect of higher concentrations of POME in the culture media, limiting the growth rate and reducing the lag phase for the algae (Cheah et al., 2018; Khalid et al., 2016). Diluted palm oil effluent (POME) effectively grew microalgae *Characium* sp. (Khalid et al., 2016).

POME is rich in organic compounds such as nitrogen, phosphorus, and ammonia, with high levels of chemical oxygen demand (COD) and low levels of biological oxygen demand (BOD) (Fernando et al., 2021). On the other hand, these organic compounds are still essential for microalgae growth at a certain concentration range (Emparan et al., 2020).

In conclusion, the results indicate that the highest growth was for 20% concentration for mixed microalgae. As the concentration of POME decreases, the growth rate increases. It suggests that POME can be cost-effective and is readily available for microalgae cultivation. However, the physical characteristics of POME, such as dark colour and high levels of suspended solids, have negatively affected microalgae growth by limiting light penetration and inhibiting photosynthesis. Diluting POME in different concentrations can mitigate these effects and improve the growth profile of microalgae in wastewater treatment applications.

Biomass

For this study, low concentrations of POME for microalgae revealed a significantly higher biomass production because of adequate light intensity for the cell to speed up growth and biomass accumulation. In other studies, low concentrations of POME also showed higher biomass production in microalgae *Chlamydomonas*, whereas high concentrations of POME (100% and 50%) limit biomass accumulation (Ding et al., 2016).

Meanwhile, high concentrations of POME indicate less biomass accumulation, which may be due to the dark colour of POME and inadequate light intensity at the bottom of culture flasks. Additionally, the high number of cells prevents light penetration for other cells. Excessive number of algal cells causes self-shading on the cells. Therefore, it causes low light intensity for algal growth and biomass production. Furthermore, it will reduce photosynthesis, resulting in less biomass production (Kumaran et al., 2023). It is possible to correlate the CO₂ amount with biomass production. Higher biomass production results from high CO₂ fixation in low POME concentrations, and less biomass accumulation is due to poor CO₂ absorption (Hariz et al., 2018).

Microalgal biomass cultivated in POME has much potential to be utilised in various applications. Microalgal biomass has the potential to produce biofuel because of its low lignin content, a higher growth rate than plants and a high range of nutrient absorption from wastewater (Ahmad et al., 2016). Microalgae are emerging as a highly promising option for biofuel production, mainly attributable to their exceptional photosynthetic efficiency, which enables efficient CO₂ sequestration. They also exhibit remarkable attributes such as elevated biomass yields, significant lipid and carbohydrate accumulation, robust adaptability to various environmental conditions, resistance to contamination, and the presence of valuable components that hold significant potential for the development of non-fuel bioproduct (Cheah et al., 2016; Saidu et al., 2017).

Numerous species of algae are cultivated as human food sources and used as a biofertiliser, animal feed, and pharmaceuticals (Michalak et al., 2019). Consequently, less growth and biomass yield in higher concentrations of POME directly affected the amount of chlorophyll *a* and carotenoid in culture batches (Hazman et al., 2018). POME may contain various nutrients, including nitrogen and phosphorus compounds essential for microalgae growth. However, the specific impact on microalgae growth can depend on the composition and concentration of nutrients within the POME (Hadiyanto & Nur, 2014).

Microalgal Pigments (Chlorophyll *a* and Carotenoids)

Microalgal biomass contains essential pigments such as chlorophyll *a*, carotenoid, and other components, which might be useful for various industrial applications (Aburai et al., 2013). The chlorophyll *a* concentration is a significant indicator for assessing the nutritional state of water (Johan et al., 2014). Accurate measuring of algal chlorophyll *a* is crucial to predict the biomass production and the photosynthetic rate of algae (Simon & Helliwell., 1998). Chlorophyll *a* is an important element indicating the photosynthetic level in microalgae (Hariz et al., 2018). The concentration of chlorophyll *a* and other pigments available in algae implies the algal growth and biomass production (Aminot & Rey, 2000).

Photosynthetic organisms such as plants and algae utilise carotenoids within the photosynthesis light-harvesting complex. They serve as supplementary pigments and

are recognised for safeguarding photosystems against oxidative harm, acting as a photoprotective shield (Aburai et al., 2013). Microalgae contain several types of carotenoids that act as free-radical foragers or antioxidants (Nobre et al., 2013; Takaichi., 2011). Various colourants derived from microalgae, such as phycocyanin (the blue pigment from *Spirulina*), β - carotene (the yellow pigment from *Dunaliella*), and astaxanthin (ranging from yellow to red, obtained from *Haematococcus*), are increasingly valued over synthetic alternatives due to their non-toxic and non-carcinogenic properties (Begum et al., 2016).

Microalgae grown in wastewater were used for the production of astaxanthin from *H. pluvialis* and *C. zoofingiensis* (Fernando et al., 2021), phycocyanins from *Nostoc* sp., and *Arthrospira platensis*; as well as phycoerythrin from *Porphyridium purpureum* (Arashiro et al., 2020).

Nutrient Removal

A comparison of nutrient removal efficiencies of microalgae in POME is shown in Table 1. From this study, we found that mixed microalgae removed the highest COD (66%), followed by *C. vulgaris* (64%) and *T. bernardii* (61%) in concentrations of 20% POME. Other studies have reported COD percentage removal of 15%–71%. As indicated in Table 1, various microalgae species perform differently when removing COD (Ding et al., 2016; Emparan et al., 2020; Kamyab et al., 2014).

The highest removal of total nitrogen (TN) using mixed microalgae was 86%. Other studies have reported between 43.5 % (*Chlamydomonas* sp. UKM6) (Ding et al., 2016) to 100% (*Scenedesmus* sp. UKM9) (Udaiyappan et al., 2021). The highest removal of total phosphorus (TP) in this study was mixed microalgae at 68%. Other studies have reported between 3.95% (*H. pluvialis* and *C. zoofingiensis*) (Fernando et al., 2021) to 100% (*Chlamydomonas* sp. UKM6) (Ding et al., 2016). In *Nannochloropsis*, 60% POME and Walnes medium effectively removed 62% COD (Resdi et al., 2021).

Nitrogen is a necessary compound for algal growth and metabolism. POME contains high amounts of nutrients, which are viable for algal growth. In this study, microalgae exhibit substantial nitrogen removal efficiency when exposed to low concentrations of POME. In contrast, their nitrogen removal capacity decreased as the POME concentration increased, in alignment with prior research findings on mono species of *H. pluvialis* and *C. zoofingiensis* (Fernando et al., 2021), as well as on mono species of *Chlorella* UKM8 and *Chlamydomonas* UKM6 (Hazman et al., 2018).

Microalgae assimilate phosphorus as phosphate for algal growth, biomass production, and metabolism (Goh et al., 2022; Nakarmi et al., 2023). Microalgae can thrive in lower concentrations of POME because nitrogen and phosphorus, which are vital nutrients for their growth, may be scarce. In such conditions, microalgae can efficiently absorb and use these limited nutrients since they are not in surplus, facilitating their growth (Dominic

& Baidurah., 2022). The high concentrations of wastewater and POME can encompass diverse organic compounds and heavy metals, including recalcitrant and potentially harmful organic substances (Al-Amshawee et al., 2020). These compounds possess the capacity to impede the growth of microalgae and their uptake of nutrients.

Toxic compounds have the potential to disrupt the microalgal capacity to efficiently assimilate and utilise nutrients and heavy metals (Zhao et al., 2023). Microalgae are capable of environmental adaptation; for instance, at lower POME concentrations, they demonstrate the ability to acclimate by adjusting their physiological processes and nutrient uptake mechanisms, thereby optimising nutrient utilisation. Conversely, when confronted with higher POME concentrations, microalgae may encounter challenges adapting to fluctuating and potentially more hostile conditions (Saidu et al., 2017).

Consortium species might have superior nitrogen removal than the mono species as different microalgae species can have varying growth rates and responses to environmental conditions (Fallahi et al., 2020). If one species faces unfavourable conditions, the other species may continue to thrive and contribute to nutrient removal. Mixed microalgae are more effective at removing nutrients due to the diverse nutrient needs of each species and can compensate for the nutrient loss of another. If one species is highly efficient at utilising nitrogen but less so at using phosphorus, and another species is the opposite (efficient at phosphorus but not nitrogen), they can complement each other's nutrient demand. It means that mixed microalgae can effectively utilise the available nutrients in the POME, leading to higher overall nutrient removal and reduction of COD. Higher nutrient removal and COD reduction in agricultural wastewater using mixed microalgae were due to microalgal selection, medium composition, and physicochemical variables (Qin et al., 2016).

The research findings reveal the effectiveness of microalgae-based treatment as a highly efficient biological method for substantially removing nutrients and organic loads. The variability in bioremediation of palm oil mill effluent (POME) efficiency using microalgae is affected by several factors: (1) POME composition, (2) microalgal selection, (3) inoculum size, (4) POME physicochemical state after collection and treatment, and (5) duration of the remediation.

In terms of POME composition, the starting material for POME was different for each experiment (for example, 2.5%–100% for anaerobic ponds and 20%–80% for aerobic ponds). POME composition indicates diverse nutrient levels in different ponds (cooling, anaerobic and aerobic) as well as sampling time (wet or dry season). The source of palm oil and the condition of the trees and fruits during the oil extraction and residue can directly affect the viability of the nutrients in POME.

The selection of microalgae significantly affects the bioremediation of POME due to their capacity for nutrient absorption, tolerance towards adverse seasons (dry and wet) and toxic substances in POME. Inoculum size (the number of microalgae introduced

into the culture media) can also affect the bioremediation of POME. A higher amount of inoculum is essential for acclimatising the culture that undergoes the lag phase after some time (Khalid et al., 2016). A high amount of inoculum also contributes to controlling the cultivation and remediation of POME by microalgae (Lau et al., 1995).

The physicochemical state of POME after collection and treatment differs in terms of pH, temperature, suspended solids, and heavy metals concentration. Raw POME samples were collected from the cooling pond, and the treated POME samples were collected from anaerobic and aerobic ponds. Untreated POME from cooling ponds is highly acidic and contains particles (sand, wood, residue from extraction of oil) that can cause a reduction in microalgal growth and nutrient removal. The experimental design and duration in each research differed in terms of nutrient removal, growth, and biomass accumulation. These factors make comparing the current study findings with previous research difficult.

CONCLUSION

Mixed microalgae are superior in the remediation of POME compared to single-culture algae. This research reports for the first time a mixed microalgae combination of *C. vulgaris* and *T. bernardii* in bioremediating wastewater from the palm oil mill effluent. Mixed microalgae have the benefit of fulfilling each other's specific nutrient demands for growth. This research found a significant reduction in COD, TN and TP levels from the palm oil mill effluent. Based on the data, the optimal concentration for effective nutrient reduction was 20% of POME.

The research was conducted indoors in controlled lab conditions. The results may vary if conducted on a large scale outdoors. When evaluating the performance of microalgae in nutrient removal efficiencies, the parameters are usually different in terms of the growth parameters, algae selection and cultivation or time of remediation.

Treating wastewater through microalgal bioremediation is effective at nutrient removal and environmentally friendly. This research has contributed towards the use of mixed microalgae to achieve effective nutrient removal and biomass for future industrial applications. Further research is needed on lower concentrations of POME as well as different microalgal consortia on effective palm oil waste effluent wastewater remediation.

ACKNOWLEDGEMENTS

The authors acknowledge The Ministry of Higher Education Malaysia (MOHE), under the Fundamental Research Grant Scheme (FRGS) (FRGS/1/2020/STG03/UPM/02/09), as well as Universiti Putra Malaysia under the PUTRA IPM (GP/2017/9568100) and UPM PUTRA IPS grants (GP-IPS/2018/9664300). The authors acknowledge the contribution of Naweedullah Amin in helping with the technical details of the paper.

REFERENCES

- Aburai, N., Ohkubo, S., Miyashita, H., & Abe, K. (2013). Composition of carotenoids and identification of aerial microalgae isolated from the surface of rocks in mountainous districts of Japan. *Algal Research*, 2(3), 237-243. <https://doi.org/10.1016/j.algal.2013.03.001>
- Ahmad, A., Bhat, A. H., & Buang, A. (2017). Immobilized *Chlorella vulgaris* for efficient palm oil mill effluent treatment and heavy metals removal. *Desalination and Water Treatment*, 81, 105-117. <https://doi.org/10.5004/dwt.2017.20991>
- Ahmad, A., Buang, A., & Bhat, A. H. (2016). Renewable and sustainable bioenergy production from microalgal co-cultivation with palm oil mill effluent (POME): A review. *Renewable and Sustainable Energy Reviews*, 65, 214–234. <https://doi.org/10.1016/j.rser.2016.06.084>
- Ahmad, M. T., Shariff, M., Yusoff, F. M., Goh, Y. M., & Banerjee, S. (2020). Applications of microalga *Chlorella vulgaris* in aquaculture. *Reviews in Aquaculture*, 12(1), 328-346. <https://doi.org/10.1111/raq.12320>
- Ahmed, S. F., Mofijur, M., Parisa, T. A., Islam, N., Kusumo, F., Inayat, A., Van, G. L., Badruddin, I. A., Khan, T. M. Y., & Ong, H. C. (2022). Progress and challenges of contaminate removal from wastewater using microalgae biomass. *Chemosphere*, 286(1), Article 131656. <https://doi.org/10.1016/j.chemosphere.2021.131656>
- Al-Amshawee, S. K., Yunus, M. Y., & Azoddein, A. A. (2020). A review study of biofilm bacteria and microalgae bioremediation for palm oil mill effluent: Possible approach. *IOP Conference Series: Materials Science and Engineering* 736(2), Article 02203. <https://doi.org/10.1088/1757-899X/736/2/022034>
- Al-Khiat, S. H., Bukhari, N. A., Ameen, F., & Abdel-Raouf, N. (2023). Comparison of the microalgae *Phormidium tenue* and *Chlorella vulgaris* as biosorbents of Cd and Zn from aqueous environments. *Environmental Research*, 235, Article 116675. <https://doi.org/10.1016/j.envres.2023.116675>
- Aminot, A., & Rey, F. (2000). Standard procedure for the determination of chlorophyll *a* by spectroscopic methods. *International Council for the Exploration of the Sea*, 112, Article 25.
- Anto, S., Mukherjee, S. S., Muthappa, R., Mathimani, T., Deviram, G., Kumar, S. S., Verma, T. N., & Pugazhendhi, A. (2020). Algae as green energy reserve: Technological outlook on biofuel production. *Chemosphere*, 242, Article 125079. <https://doi.org/10.1016/j.chemosphere.2019.125079>
- Arashiro, L. T., Boto-Ordóñez, M., Van Hulle, S. W., Ferrer, I., Garfí, M., & Rousseau, D. P. (2020). Natural pigments from microalgae grown in industrial wastewater. *Bioresource Technology*, 303, Article 122894. <https://doi.org/10.1016/j.biortech.2020.122894>
- Azmi, N. S., & Yunus, K. F. M. (2014). Wastewater treatment of palm oil mill effluent (POME) by ultrafiltration membrane separation technique coupled with adsorption treatment as pre-treatment. *Agriculture and Agricultural Science Procedia*, 2, 257-264. <https://doi.org/10.1016/j.aaspro.2014.11.037>
- Bala, J. D., Lalung, J., & Ismail, N. (2015). Studies on the reduction of organic load from palm oil mill effluent (POME) by bacterial strains. *International Journal of Recycling of Organic Waste in Agriculture*, 4, 1-10. <https://doi.org/10.1007/s40093-014-0079-6>
- Bauer, D. E., Conforti, V., Ruiz, L., & Gómez, N. (2012). An in-situ test to explore the responses of *Scenedesmus acutus* and *Lepocinlis acus* as indicators of the changes in water quality in lowland streams. *Ecotoxicology and Environmental Safety*, 77, 71-78. <https://doi.org/10.1016/j.ecoenv.2011.10.021>

- Begum, H., Yusoff, F. M., Banerjee, S., Khatoon, H., & Shariff, M. (2016). Availability and utilization of pigments from microalgae. *Critical Reviews in Food Science and Nutrition*, 56(13), 2209-2222. <https://doi.org/10.1080/10408398.2013.764841>
- Bradley, I. M., Pinto, A. J., & Guest, J. S. (2016). Design and evaluation of Illumina MiSeq-compatible, 18S rRNA gene-specific primers for improved characterization of mixed phototrophic communities. *Applied and Environmental Microbiology*, 82(19), 5878-5891. <https://doi.org/10.1128/AEM.01630-16>
- Cheah, W. Y., Show, P. L., Juan, J. C., Chang, J. S., & Ling, T. C. (2018). Microalgae cultivation in palm oil mill effluent (POME) for lipid production and pollutants removal. *Energy Conversion and Management*, 174, 430-438. <https://doi.org/10.1016/j.enconman.2018.08.057>
- Chew, C. L., Ng, C. Y., Hong, W. O., Wu, T. Y., Lee, Y. Y., Low, L. E., Kong, P. S., & Chan, E. S. (2021). Improving sustainability of palm oil production by increasing oil extraction rate: A review. *Food and Bioprocess Technology*, 14, 573-586. <https://doi.org/10.1007/s11947-020-02555-1>
- Ding, G. T., Yaakob, Z., Takriff, M. S., Salihon, J., & Rahaman, M. S. A. (2016). Biomass production and nutrients removal by a newly-isolated microalgal strain *Chlamydomonas* sp. in palm oil mill effluent (POME). *International Journal of Hydrogen Energy*, 41(8), 4888-4895. <https://doi.org/10.1016/j.ijhydene.2015.12.010>
- Dominic, D., & Baidurah, S. (2022). Recent developments in biological processing technology for palm oil mill effluent treatment. *Biology*, 11(4), Article 525. <https://doi.org/10.3390/biology11040525>
- El-Din, N. G. S., El-Sheekh, M. M., El-Kassas, H. Y., Essa, D. I., & El-Sherbiny, B. A. (2022). Biological indicators as tools for monitoring water quality of a hot spot area on the Egyptian Mediterranean Coast. *Arabian Journal of Geosciences*, 15(18), Article 1485. <https://doi.org/10.1007/s12517-022-10701-6>
- Empanan, Q., Jye, Y. S., Danquah, M. K., & Harun, R. (2020). Cultivation of *Nannochloropsis* sp. microalgae in palm oil mill effluent (POME) media for phycoremediation and biomass production: Effect of microalgae cells with and without beads. *Journal of Water Process Engineering*, 33, Article 101043. <https://doi.org/10.1016/j.jwpe.2019.101043>
- Fallahi, A., Hajinajaf, N., Tavakoli, O., & Sarrafzadeh, M. H. (2020). Cultivation of mixed microalgae using municipal wastewater: biomass productivity, nutrient removal, and biochemical content. *Iranian Journal of Biotechnology*, 18(4), Article e2586. <https://doi.org/10.30498/IJB.2020.2586>
- Fernando, J. S. R., Premaratne, M., Dinalankara, D. M. S. D., Perera, G. L. N. J., & Ariyadasa, T. U. (2021). Cultivation of microalgae in palm oil mill effluent (POME) for astaxanthin production and simultaneous phycoremediation. *Journal of Environmental Chemical Engineering*, 9(4), Article 105375. <https://doi.org/10.1016/j.jece.2021.105375>
- Goh, P. S., Lau, W. J., Ismail, A. F., Samawati, Z., Liang, Y. Y., & Kanakaraju, D. (2022). Microalgae-enabled wastewater treatment: A sustainable strategy for bioremediation of pesticides. *Water*, 15(1), Article 70. <https://doi.org/10.3390/w15010070>
- Hadiyanto, & Nur, M. M. A. (2014). Lipid extraction of microalga *Chlorella* sp. cultivated in palm oil mill effluent (POME) medium. *World Applied Sciences Journal*, 31(5), 959-967. <https://doi.org/10.5829/idosi.wasj.2014.31.05.2006>

- Hariz, H. B., Takriff, M. S., Ba-Abbad, M. M., Yasin, N. H. M., & Hakim, N. I. N. M. (2018). CO₂ fixation capability of *Chlorella* sp. and its use in treating agricultural wastewater. *Journal of Applied Phycology*, *30*, 3017-3027. <https://doi.org/10.1007/s10811-018-1488-0>
- Hariz, H. B., Takriff, M. S., Yasin, N. H. M., Ba-Abbad, M. M., & Hakimi, N. I. N. M. (2019). Potential of the microalgae-based integrated wastewater treatment and CO₂ fixation system to treat palm oil mill effluent (POME) by indigenous microalgae; *Scenedesmus* sp. and *Chlorella* sp. *Journal of Water Process Engineering*, *32*, Article 100907. <https://doi.org/10.1016/j.jwpe.2019.100907>
- Haryati, Z., Subramaniam, V., Noor, Z. Z., Hashim, Z., Loh, S. K., & Aziz, A. A. (2022). Social life cycle assessment of crude palm oil production in Malaysia. *Sustainable Production and Consumption*, *29*, 90-99. <https://doi.org/10.1016/j.spc.2021.10.002>
- Hazman, N. A. S., Yasin, N. H. M., Takriff, M. S., Hasan, H. A., Kamarudin, K. F., & Hakimi, N. I. N. M. (2018). Integrated palm oil mill effluent treatment and CO₂ sequestration by microalgae. *Sains Malaysiana*, *47*(7), 1455-1464. <https://doi.org/10.17576/jsm-2018-4707-13>
- Jasni, J., Arisht, S. N., Yasin, N. H. M., Abdul, P. M., Lin, S. K., Liu, C. M., & Takriff, M. S. (2020). Comparative toxicity effect of organic and inorganic substances in palm oil mill effluent (POME) using native microalgae species. *Journal of Water Process Engineering*, *34*, Article 101165. <https://doi.org/10.1016/j.jwpe.2020.101165>
- Johan, F., Jafri, M. Z., Lim, H. S., & Maznah, W. W. (2014, December 9-12). *Laboratory measurement: Chlorophyll-a concentration measurement with acetone method using spectrophotometer*. [Paper presentation]. IEEE International Conference on Industrial Engineering and Engineering Management, Selangor, Malaysia. <https://doi.org/10.1109/IEEM.2014.7058737>
- Justine, I., Chin, G. J. W. L., Yong, W. T. L., & Misson, M. (2023). Characterization and optimization of *Rhodotorula toruloides* and *Ankistrodesmus falcatus* co-culture in palm oil mill effluent for efficient COD removal and lipid production. *Biocatalysis and Agricultural Biotechnology*, *51*, Article 102782. <https://doi.org/10.1016/j.bcab.2023.102782>
- Kamarudin, K. F., Yaakob, Z., Rajkumar, R., & Tasirin, S. M. (2013). Bioremediation of palm oil mill effluents (POME) using *Scenedesmus dimorphus* and *Chlorella vulgaris*. *Advanced Science Letters*, *19*(10), 2914-2918. <https://doi.org/10.1166/asl.2013.5044>
- Kamyab, H., Din, M. F. M., Keyvanfar, A., Majid, M. Z. A., Talaiekhosani, A., Shafaghath, A., & Ismail, H. H. (2015). Efficiency of microalgae *Chlamydomonas* on the removal of pollutants from palm oil mill effluent (POME). *Energy Procedia*, *75*, 2400-2408. <https://doi.org/10.1016/j.egypro.2015.07.190>
- Kamyab, H., Fadhil, M., Lee, C., Ponraj, M., Soltani, M., & Eva, S. (2014). Micro-macro algal mixture as a promising agent for treating POME discharge and its potential use as animal feed stock enhancer. *Jurnal Teknologi*, *68*(5), 1-4.
- Kamyab, H., Yuzir, M. A., Riyadi, F. A., Ostadrahimi, A., Khademi, T., Ghfar, A. A., & Kirpichnikova, I. (2022). Electrochemical oxidation of palm oil mill effluent using platinum as anode: Optimization using response surface methodology. *Environmental Research*, *214*(3), Article 113993. <https://doi.org/10.1016/j.envres.2022.113993>

- Karim, A., Islam, M. A., Khalid, Z. B., Yousuf, A., Khan, M. M. R., & Faizal, C. K. M. (2021). Microbial lipid accumulation through bioremediation of palm oil mill effluent using a yeast-bacteria co-culture. *Renewable Energy*, 176, 106-114. <https://doi.org/10.1016/j.renene.2021.05.055>
- Khalid, A. A. H., Yaakob, Z., Abdullah, S. R. S., & Takriff, M. S. (2016). Enhanced growth and nutrients removal efficiency of *Characium* sp. cultured in agricultural wastewater via acclimatized inoculum and effluent recycling. *Journal of Environmental Chemical Engineering*, 4(3), 3426-3432. <https://doi.org/10.1016/j.jece.2016.07.020>
- Khatun, R., Reza, M. I. H., Moniruzzaman, M., & Yaakob, Z. (2017). Sustainable oil palm industry: The possibilities. *Renewable and Sustainable Energy Reviews*, 76, 608-619. <https://doi.org/10.1016/j.rser.2017.03.077>
- Kumaran, M., Palanisamy, K. M., Bhuyar, P., Maniam, G. P., Rahim, M. H. A., & Govindan, N. (2023). Agriculture of microalgae *Chlorella vulgaris* for polyunsaturated fatty acids (PUFAs) production employing palm oil mill effluents (POME) for future food, wastewater, and energy nexus. *Energy Nexus*, 9, Article 100169. <https://doi.org/10.1016/j.nexus.2022.100169>
- Lau, P. S., Tam, N. F. Y., & Wong, Y. S. (1995). Effect of algal density on nutrient removal from primary settled wastewater. *Environmental Pollution*, 89(1), 59-66. [https://doi.org/10.1016/0269-7491\(94\)00044-E](https://doi.org/10.1016/0269-7491(94)00044-E)
- Medvedeva, L. N., Zorkina, O. V., & Moskovets, M. V. (2022). Use of *Chlorella vulgaris* as a dietary supplement for quails bred at private farms. *Journal of Agronomy and Animal Industries*, 17(4), 499-513. <https://doi.org/10.22363/2312-797X-2022-17-4-499-513>
- Michalak, I., Baśladyńska, S., Mokrzycki, J., & Rutkowski, P. (2019). Biochar from a freshwater macroalga as a potential biosorbent for wastewater treatment. *Water*, 11(7), Article 1390. <https://doi.org/10.3390/w11071390>
- Mohammed, R. R. (2013). Decolourisation of biologically treated palm oil mill effluent (POME) using adsorption technique. *International Refereed Journal of Engineering and Science*, 2(10), 1-11.
- Morais, F. P., Simões, R. M. S., & Curto, J. M. R. (2020). Biopolymeric delivery systems for cosmetic applications using *Chlorella vulgaris* algae and tea tree essential oil. *Polymers*, 12(11), Article 2689. <https://doi.org/10.3390/polym12112689>
- Nakarmi, K. J., Daneshvar, E., Mänttari, M., & Bhatnagar, A. (2023). Removal and recovery of nutrients from septic tank wastewater using microalgae: Key factors and practical implications. *Journal of Environmental Management*, 345, Article 118922. <https://doi.org/10.1016/j.jenvman.2023.118922>
- Nobre, B. P., Villalobos, F., Barragan, B. E., Oliveira, A. C., Batista, A. P., Marques, P. A. S. S., Mendes, R. L., Savova, H., Palavra, A. F., & Gouveia, L. (2013). A biorefinery from *Nannochloropsis* sp. microalga-extraction of oils and pigments. Production of biohydrogen from the leftover biomass. *Bioresource Technology*, 135, 128-136. <https://doi.org/10.1016/j.biortech.2012.11.084>
- Orusmurzaeva, Z., Maslova, A., Tambieva, Z., Sadykova, E., Askhadova, P., Umarova, K., Merzhoeva, A., Albogachieva, K., Ulikhanyan, K., & Povetkin, S. (2022). Investigation of the chemical composition and physicochemical properties of *Chlorella vulgaris* biomass treated with pulsed discharges technology for potential use in the food industry. *Slovak Journal of Food Sciences*, 16, 777-789.

- Otondo, A., Kokabian, B., Stuart-Dahl, S., & Gude, V. G. (2018). Energetic evaluation of wastewater treatment using microalgae, *Chlorella vulgaris*. *Journal of Environmental Chemical Engineering*, 6(2), 3213-3222. <https://doi.org/10.1016/j.jece.2018.04.064>
- Qin, L., Wang, Z., Sun, Y., Shu, Q., Feng, P., Zhu, L., & Yuan, Z. (2016). Microalgae consortia cultivation in dairy wastewater to improve the potential of nutrient removal and biodiesel feedstock production. *Environmental Science and Pollution Research*, 23, 8379-8387. <https://doi.org/10.1007/s11356-015-6004-3>
- Ratnasari, A., Zaidi, N. S., Syafiuddin, A., Boopathy, R., Kueh, A. B. H., Amalia, R., & Prasetyo, D. D. (2021). Prospective biodegradation of organic and nitrogenous pollutants from palm oil mill effluent by acidophilic bacteria and archaea. *Bioresource Technology Reports*, 15, Article 100809. <https://doi.org/10.1016/j.biteb.2021.100809>
- Resdi, R., Lim, J. S., & Idris, A. (2021). Batch kinetics of nutrients removal for palm oil mill effluent and recovery of lipid by *Nannochloropsis* sp. *Journal of Water Process Engineering*, 40, Article 101767. <https://doi.org/10.1016/j.jwpe.2020.101767>
- Rowland, D., Zanello, G., Waliyo, E., & Ickowitz, A. (2022). Oil palm and gendered time use: A mixed-methods case study from West Kalimantan, Indonesia. *Forest Policy and Economics*, 137, Article 102682. <https://doi.org/10.1016/j.forpol.2021.102682>
- Saidu, H., Jamaluddin, H., & Mohamad, S. E. (2017). Nutrient removal and biokinetic study of freshwater microalgae in palm oil mill effluent (POME). *Indian Journal of Science and Technology*, 10(24), 1-10. <https://doi.org/10.17485/ijst/2017/v10i24/114584>
- Salazar, J., Santana-Sánchez, A., Näkkilä, J., Sirin, S., & Allahverdiyeva, Y. (2023). Complete N and P removal from hydroponic greenhouse wastewater by *Tetradesmus obliquus*: A strategy for algal bioremediation and cultivation in Nordic countries. *Algal Research*, 70, Article 102988. <https://doi.org/10.1016/j.algal.2023.102988>
- Simon, D., & Helliwell, S. (1998). Extraction and quantification of chlorophyll *a* from freshwater green algae. *Water Research*, 32(7), 2220-2223. [https://doi.org/10.1016/S0043-1354\(97\)00452-1](https://doi.org/10.1016/S0043-1354(97)00452-1)
- Singh, R. P., Ibrahim, M. H., Esa, N., & Iliyana, M. S. (2010). Composting of waste from palm oil mill: A sustainable waste management practice. *Reviews in Environmental Science and Biotechnology*, 9(4), 331-344. <https://doi.org/10.1007/s11157-010-9199-2>
- Song, X., Bo, Y., Feng, Y., Tan, Y., Zhou, C., Yan, X., Ruan, R., Xu, Q., & Cheng, P. (2022). Potential applications for multifunctional microalgae in soil improvement. In *Frontiers in Environmental Science*, 10, Article 1035332. <https://doi.org/10.3389/fenvs.2022.1035332>
- Takaichi, S. (2011). Carotenoids in algae: Distributions, biosynthesis and functions. *Marine Drugs*, 9(6), 1101-1118. <https://doi.org/10.3390/md9061101>
- Talib, S. L. A., Yasin, N. H. M., Takriff, M. S., & Japar, A. S. (2023). Comparative studies on phycoremediation efficiency of different water samples by microalgae. *Journal of Water Process Engineering*, 52, Article 103584. <https://doi.org/10.1016/j.jwpe.2023.103584>

- Tan, K. A., Lalung, J., Wijaya, D., Ismail, N., Omar, W. M. W., Wabaidur, S. M., Siddiqui, M. R., Alam, M., & Rafatullah, M. (2022). Removal of nutrients by using green microalgae from lab-scale treated palm oil mill effluent. *Fermentation*, 8(11), Article 658. <https://doi.org/10.3390/fermentation8110658>
- Udaiyappan, A. F. M., Hasan, H. A., Takriff, M. S., Abdullah, S. R. S., Yasin, N. H. M., & Ji, B. (2021). Cultivation and application of *Scenedesmus* sp. strain UKM9 in palm oil mill effluent treatment for enhanced nutrient removal. *Journal of Cleaner Production*, 294, Article 126295. <https://doi.org/10.1016/j.jclepro.2021.126295>
- Udaiyappan, A. F., Hasan, H. A., Takriff, M. S., Abdullah, S. R. S., Maeda, T., Mustapha, N. A., Mohd Yasin, N. H., & Hakimi, N. I. N. M. (2020). Microalgae-bacteria interaction in palm oil mill effluent treatment. *Journal of Water Process Engineering*, 35, Article 101203. <https://doi.org/10.1016/j.jwpe.2020.101203>
- Velmurugan, A., & Muthukaliannan, G. K. (2022). Genetic manipulation for carotenoid production in microalgae an overview. *Current Research in Biotechnology*, 4, 221-228. <https://doi.org/10.1016/j.crbiot.2022.03.005>
- Wynne, M. J., & Hallan, J. K. (2015). Reinstatement of *Tetradismus* GM Smith (Sphaeropleales, Chlorophyta). *Feddes Repertorium*, 126(3-4), 83-86. <https://doi.org/10.1002/fedr.201500021>
- Zhao, D., Cheah, W. Y., Lai, S. H., Ng, E. P., Khoo, K. S., Show, P. L., & Ling, T. C. (2023). Symbiosis of microalgae and bacteria consortium for heavy metal remediation in wastewater. *Journal of Environmental Chemical Engineering*, 11(3), Article 109943. <https://doi.org/10.1016/j.jece.2023.109943>

Table S1
Nutrient removal efficiency in different dilutions of POME by mixed microalgae

	Parameter	20%	40%	60%	80%
COD	Initial value	319.0000 ± 1.0000	408.0000 ± 6.5574	579.6667 ± 4.0414	729.6667 ± 3.5118
	Terminal value	105.3333 ± 3.51188	210.0000 ± 3.0000	403.6667 ± 8.0208	629.6667 ± 4.0414
	Removal efficiency	66.98016%	48.52941%	30.36228%	13.52215%
TN	Initial value	69.0000 ± 1.0000	103.6667 ± 1.5275	119.3333 ± 1.5275	133.0000 ± 1.0000
	Terminal value	9.0000 ± 2.0000	23.6667 ± 1.5275	76.0000 ± 2.0000	105.3333 ± 2.0816
	Removal efficiency	86.95652%	75.88452%	36.31283%	20.80203%
TP	Initial value	0.9667 ± 0.0577	1.2867 ± 0.088	1.8000 ± 0.1000	2.5000 ± 0.1000
	Terminal value	0.3000 ± 0.1000	0.5567 ± 0.0513	1.3000 ± 0.1000	2.0367 ± 0.1305
	Removal efficiency	68.96553%	56.73574%	27.77778%	18.53332%
N	Initial value	16.3000 ± 0.2000	21.4000 ± 0.3000	28.7333 ± 0.2087	33.3667 ± 0.2516
	Terminal value	3.1000 ± 0.1000	6.1333 ± 0.3055	17.5333 ± 0.3511	23.4667 ± 0.2516
	Removal efficiency	80.9816%	71.33957%	38.97912%	29.67033%
P	Initial value	0.8267 ± 0.0404	1.1000 ± 0.2000	1.5700 ± 0.1212	2.2000 ± 0.1000
	Terminal value	0.2433 ± 0.0450	0.4500 ± 0.0458	1.1400 ± 0.0529	1.6767 ± 0.0305
	Removal efficiency	64.84017808%	81.84931102%	40.72163163%	31.37653211%

Table S2
Nutrient removal efficiency in different dilutions of POME by Chlorella vulgaris

	Parameter	20%	40%	60%	80%
COD	Initial value	319.0000 ± 1.0000	408.0000 ± 6.5574	579.6667 ± 4.0414	729.6667 ± 3.5118
	Terminal value	114.6667 ± 3.5118	218.0000 ± 3.0000	419.3333 ± 2.5166	635.3333 ± 3.5118
	Removal efficiency	64.05433%	46.56863%	27.65958%	12.92829%
TN	Initial value	69.0000 ± 1.0000	103.6667 ± 1.5275	119.3333 ± 1.5275	133.0000 ± 1.0000
	Terminal value	14.0000 ± 2.0000	28.6667 ± 1.5275	84.3333 ± 2.0816	110.0000 ± 1.0000
	Removal efficiency	79.71014%	72.34724%	29.32962%	17.29323%
TP	Initial value	0.9667 ± 0.0577	1.2867 ± 0.088	1.8000 ± 0.1000	2.5000 ± 0.1000
	Terminal value	0.4867 ± 0.0808	0.8000 ± 0.1000	1.4800 ± 0.0721	2.1667 ± 0.1527
	Removal efficiency	49.65516%	37.82385%	17.77778%	13.33332%
N	Initial value	16.3000 ± 0.2000	21.4000 ± 0.3000	28.7333 ± 0.2087	33.3667 ± 0.2516
	Terminal value	4.5000 ± 0.2000	7.3667 ± 0.2081	18.7667 ± 0.1527	24.5000 ± 0.2645
	Removal efficiency	72.39264%	65.57632%	34.68676%	26.57343%
P	Initial value	0.8267 ± 0.0404	1.1000 ± 0.2000	1.5700 ± 0.1212	2.2000 ± 0.1000
	Terminal value	0.3367 ± 0.0251	0.5533 ± 0.0251	1.1767 ± 0.0152	1.7800 ± 0.0360

Table S3

Nutrient removal efficiency in different dilutions of POME by Tetrademus bernardii

	Parameter	20%	40%	60%	80%
COD	Initial value	319.0000 ± 1.0000	408.0000 ± 6.5574	579.6667 ± 4.0414	729.6667 ± 3.5118
	Terminal value	123.3333 ± 3.5118	224.0000 ± 5.0000	433.3333 ± 7.3711	651.6667 ± 7.5718
	Removal efficiency	61.33752%	45.52941%	30.36228%	13.52215%
TN	Initial value	69.0000 ± 1.0000	103.6667 ± 1.5275	119.3333 ± 1.5275	133.0000 ± 1.0000
	Terminal value	19.0000 ± 2.000	33.3333 ± 3.0550	93.3333 ± 2.0816	122.0000 ± 2.6445
	Removal efficiency	72.46377%	67.8457%	21.78772%	8.270677%
TP	Initial value	0.9667 ± 0.0577	1.2867 ± 0.088	1.8000 ± 0.1000	2.5000 ± 0.1000
	Terminal value	0.6200 ± 0.0200	0.9000 ± 0.1000	1.5533 ± 0.0152	2.2967 ± 0.0513
	Removal efficiency	35.86209%	30.05183%	13.88889%	8.13332%
N	Initial value	16.3000 ± 0.2000	21.4000 ± 0.3000	28.7333 ± 0.2087	33.3667 ± 0.2516
	Terminal value	6.1533 ± 0.0503	9.2667 ± 0.1527	19.4333 ± 0.3055	26.3000 ± 0.1000
	Removal efficiency	62.24949%	56.69782%	32.36659%	21.17883%
P	Initial value	0.8267 ± 0.0404	1.1000 ± 0.2000	1.5700 ± 0.1212	2.2000 ± 0.1000
	Terminal value	0.3833 ± 0.0152	0.6167 ± 0.0251	1.2533 ± 0.0152	1.8367 ± 0.0305
	Removal efficiency	53.62909%	43.93936%	20.16987%	17.19242%

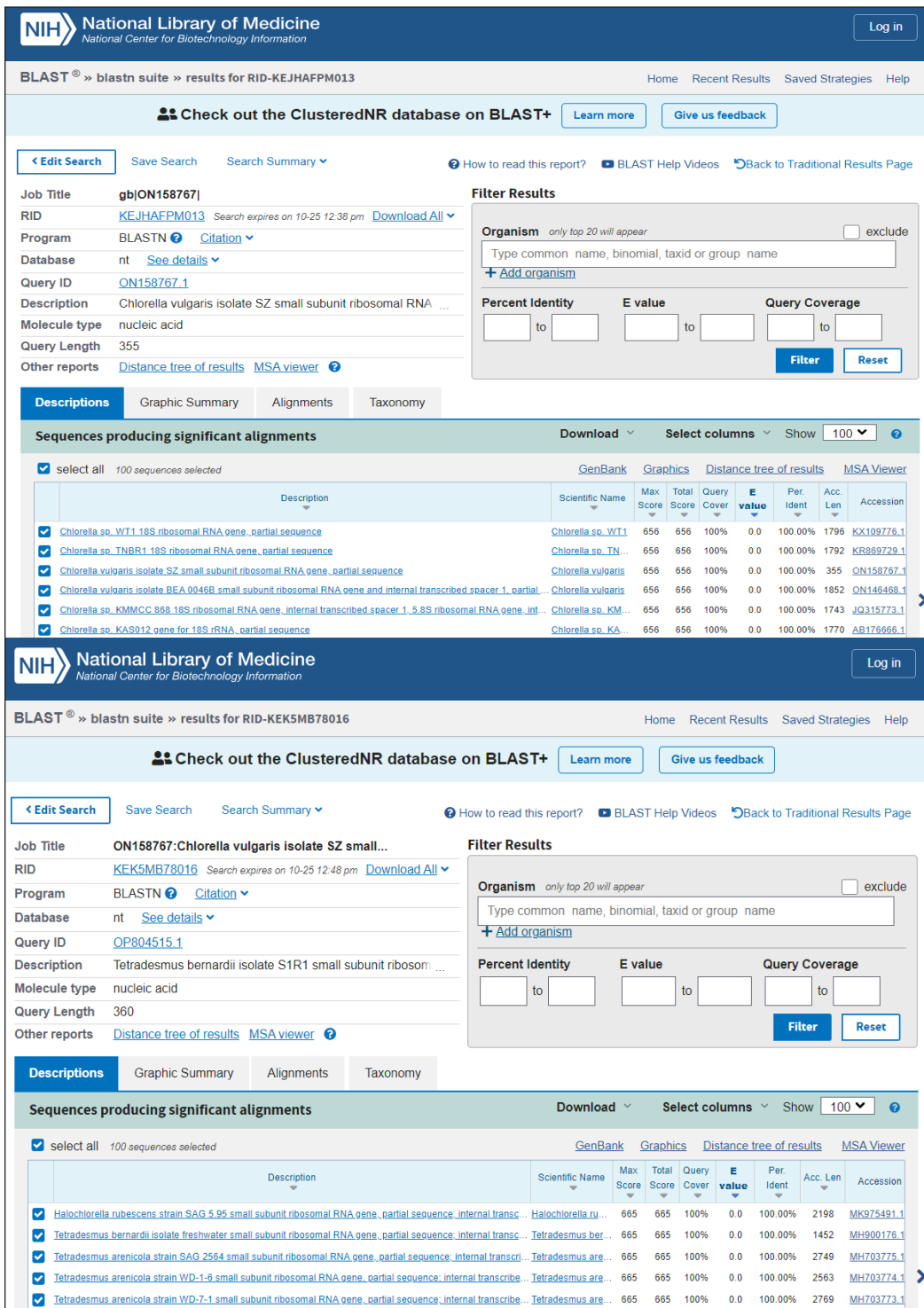


Figure S1. The NCBI blast results for *Chlorella vulgaris* (ON158767) and *Tetradesmus bernardii* (OP804515)

Study of LED Retrofit Lamps in HSPV Luminaires Based on Photometric Method for Road Lighting

Mohd Hanif Jamaludin^{1,2}, Wan Zakiah Wan Ismail^{1,2*}, Elina Mohd Husini³ and Nor Ain Mohd Bahrer²

¹Advanced Device and System, Faculty of Engineering and Built Environment, Universiti Sains Islam Malaysia, 71800 Nilai, Negeri Sembilan, Malaysia

²Centre of Excellence for Engineering and Technology JKR (CREaTE), Jabatan Kerja Raya Malaysia, 78000, Alor Gajah, Melaka, Malaysia

³Sustainable Energy Technology, Faculty of Engineering and Built Environment, Universiti Sains Islam Malaysia, 71800 Nilai, Negeri Sembilan, Malaysia

ABSTRACT

Energy reduction is a great challenge in road lighting applications. Replacing high-pressure sodium vapor (HPSV) with light-emitting diodes (LED) is a viable approach to reducing energy consumption. However, a total replacement can incur a significant capital cost. This study aims to investigate the effects on light distribution by replacing HPSV lamps with LED lamps in HPSV luminaires using Light Intensity Distribution (LID) curve measurement and Backlight, Uplight and Glare (BUG) rating evaluation to reduce the adoption costs. While LED lamps have high illumination rates, the structural differences from HPSV lamps can affect the LID curve and original lighting design. Therefore, it is crucial to study photometric dispersion after retrofitting light sources. Both lamps were installed into similar HPSV luminaires to assess photometric performance using goniophotometer measurements. The HPSV lamp outperforms the LED lamp in terms of luminous flux (11.13%) and light intensity (7.69%), whereas the LED lamp outperforms the HPSV lamp in terms of efficacy rating (68.67%) and wattage used (47.61%). The findings

indicate that retrofit LED luminaires have an LOR of 46.77% lower than the HPSV luminaires. The light distribution pattern is maintained but reduced to 40 to 50% for the main usable light angles. The reduced performance is caused by the lamp structure, which occupies a large area inside the luminaire housing, obstructing proper light distribution. Although overall energy consumption is reduced, similar illumination

ARTICLE INFO

Article history:

Received: 31 March 2023

Accepted: 12 September 2023

Published: 04 April 2024

DOI: <https://doi.org/10.47836/pjst.32.3.11>

E-mail addresses:

mhanif@jkr.gov.my (Mohd Hanif Jamaludin)

drwanzakiah@usim.edu.my (Wan Zakiah Wan Ismail)

elina@usim.edu.my (Elina Mohd Husini)

norain@jkr.gov.my (Nor Ain Mohd Bahrer)

*Corresponding author

levels cannot be maintained. These outcomes can assist authorities and manufacturers with alternative methods of reducing costs while maintaining lighting levels.

Keywords: High-pressure sodium vapor, light emitting diode, light intensity distribution curve, light output ratio

INTRODUCTION

Choosing a light source that defines the cost, visual performance, and energy consumption is one of the main components of the lighting system (Rofaie et al., 2022). High-pressure sodium vapor (HPSV) lamp is currently used for road lighting in Malaysia due to its lower price. However, the current trend is moving towards energy-efficient lighting, such as light-emitting diodes (LEDs) and plasma induction (Grau et al., 2021). In 2018, Tenaga Nasional Berhad (TNB), one of the main electrical energy providers in Peninsular Malaysia, replaced over 212 639 units of 150W HSPV luminaire with LED luminaire, which has contributed to 30 to 40 % energy reduction (BERNAMA, 2023). The Public Works Department of Malaysia (PWD) also released a guideline in 2013, revised in 2018, on using energy-efficient light sources such as LED, induction lighting and eco-sodium light lamps (Jabatan Kerja Raya, 2018). In 2015, the EU decided to phase out light sources with hazardous material from 2021 to 2027 (https://eur-lex.europa.eu/eli/dir_del/2022/275/oj). By the year 2027, current HPSV lamps will be phased out and replaced by more energy-efficient light sources. The current method of using LED light source is a comprehensive conversion, which involves replacing the entire HPSV luminaire with a new complete LED luminaire, which comes at a high upfront expense (Bamisile et al., 2016; Kovačević et al., 2022). Even though this is a promising factor, the total replacement of HPSV luminaires with LED luminaires for each road requires a large capital cost.

Another approach lighting manufacturers introduced is replacing the HPSV lamps with LED replacement lamps while maintaining the original HPSV luminaire housing (Philips, 2023). Lamp conversion is common for indoor installations but rarely carried out in road lighting installations (Braga et al., 2014). Even though there are many types of LED retrofit lamps, research on the light distribution impact for road lighting applications is limited compared to indoor applications due to many safety requirements involving road lighting applications (Gordic et al., 2021; Rofaie et al., 2022). Thus, photometric parameters that describe the light performance of luminaire, such as the light intensity distribution, light intensity at angle, light output ratio and total luminous flux, are important to design the required illumination level for a given space, whether for indoor or outdoor lighting designs (Abdullah et al., 2021). For road lighting or public lighting, sufficient illumination is required to reduce traffic accidents (Li et al., 2023; Setyaningsih & Candra, 2023). Two roadway photometric criteria (horizontal illuminance and lighting uniformity) were investigated, and the matched case-control method was applied to decouple the illuminance

average and standard deviation (Li et al., 2023). DIALux software simulation was used to find the most optimum photometric illuminance in road lighting freeways in Indonesia to comply with the standard SNI 7391:2008 and eventually reduce accidents at night (Setyaningsih & Candra, 2023). Compliance with safety requirements is an important factor and should not be neglected. DIALux software has also been used to analyze the changes in road lighting in terms of luminaire and pole spacing (Zima & Cieplucha, 2023). Besides general properties of luminaires such as total luminous flux, wattage, and power factor, the luminous intensity distribution (LID) curve, which describes the output of luminaires at various angles, is one of the main pieces of information for calculating or simulating lighting designs (Bergen, 2012). LEDs are also superior to HPSV lamps in terms of visual acuity due to the higher color rendering index (CRI) and visual capabilities. Studies have shown that a lower lumen output of LED lamps is sufficient to match higher lumen values from HPSV lamps (Brons et al., 2021). Modeling techniques on comparison of HPSV and LED luminaires concluded that LEDs are marginally higher in average luminance per watt increment of luminaire power than HPSV luminaires (Bhattacharya et al., 2023). Studies on the photometric impact of replacing the original light source are limited (Abdullah et al., 2021). Recent studies regarding LED measurement have shown that LED has different characteristics than conventional luminaires and may require different measurement approaches for correct evaluation (Czyżewski, 2023).

HPSV is the current lamp utilized nationwide but is shifting towards energy-efficient light, such as LED lamps (BERNAMA, 2023). Fully LED road lighting requires a high investment cost for full implementation, including the lamp, luminaire and circuit (Rofaie et al., 2022). Back in 2012, when Malaysia started implementing LED lighting on roads, The Electrical and Electronics Association of Malaysia (TEAAM) did not recommend the usage of LEDs due to factors such as energy savings, cost savings, safety and security and environmental impact (TEEAM, 2012). However, advancements in lighting technology and updated standards in ensuring the safety of road LED light sources have become one of the main options for replacing HPSV lighting to reduce energy usage. In order to ensure the safety of road users, the laminated road has to meet the requirements of MS 825:2007; Code of Practice for The Design of Road Lighting-Part 1: Lighting of Roads and Public Amenity Area and BS EN 13201-2:2015 Road lighting Part 2: Performance requirements, in terms of performance parameters such as luminance value, overall uniformity, longitudinal uniformity, glare rating and glare index class. In contrast to the HPSV lighting system, LEDs are point light sources that are prone to cause glare toward road users if designed incorrectly (Ying & Lim, 2022).

This research aims to study the performance of LED and HSPV lamps based on photometric methods to look at the suitability of the LED lamp in HSPV luminaire. Replacing the HSPV lamp with an LED lamp in the HSPV luminaire housing can reduce

cost compared to replacing the whole unit, but the lighting needs to be sufficient to ensure the safety of road users. Thus, a photometric analysis of LED and HPSV was implemented to observe both lamps' light distribution properties and performance. Light Intensity Distribution Curve (LIDC) changes were observed for both lamps based on photometric measurement. This study focuses on efficacy rating, wattage, luminous flux and light output ratio of the luminaire using the goniophotometric method and comparative analysis.

METHODS

Figure 1 shows the flow chart of the experimental method. The measurement process consists of equipment calibration and setting of equipment, measurement of bare lamps, and measurement of lamps inside light fittings. The comparison focuses mainly on the LID curve and Backlight, Up-light and Glare (BUG) rating. The test samples consist of an HPSV lamp (150W) and an LED Lamp (68W), as in Figure 2 (a and b), where the 150 W HPSV lamp was used as the basis for analysis of the 68 W LED lamp. The 68 W LED lamp is a surface-mounted device (SMD) type LED chip mounted on a circuit board with

a heat sink (Philips, 2023). The light fixtures of both lamps are similar, as shown in Figure 2(c). Specification of the test sample is shown in Table 1.

This study was conducted in a laboratory environment at an ambient temperature of $25 \pm 2^\circ\text{C}$ and relative air humidity of $<50\%$ with reference to standards CIE 121:1996 (International Commission on Illumination, 1996) and CIE DIS S025:2015 (Bredemeier, 2017) to ensure stability and reliability of the measurement. Figure 3 (a and b) show the photometer sensor and light baffles used in the experiment. The test sample was mounted and measured on the Rotating Luminaire Goniophotometer (Figure 3c) and tested based on C- γ coordinate system measurement. Measurement was repeated 10 times with a standard error of 0.01 to look at any reading discrepancies and to ensure the reliability of the experiment.

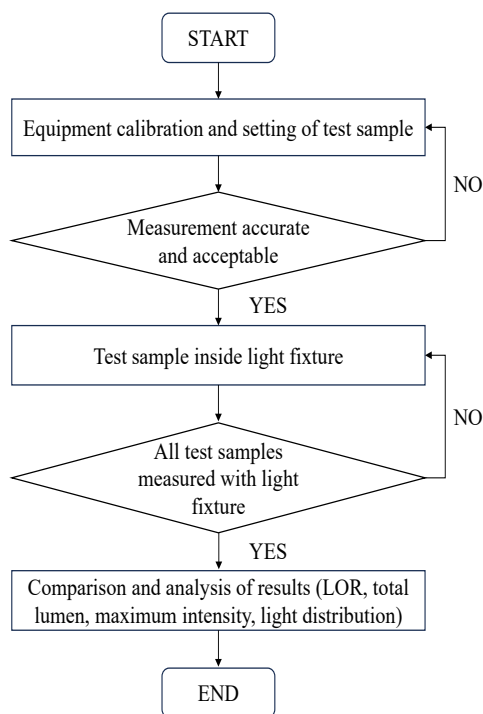


Figure 1. Flow chart of experimental measurement

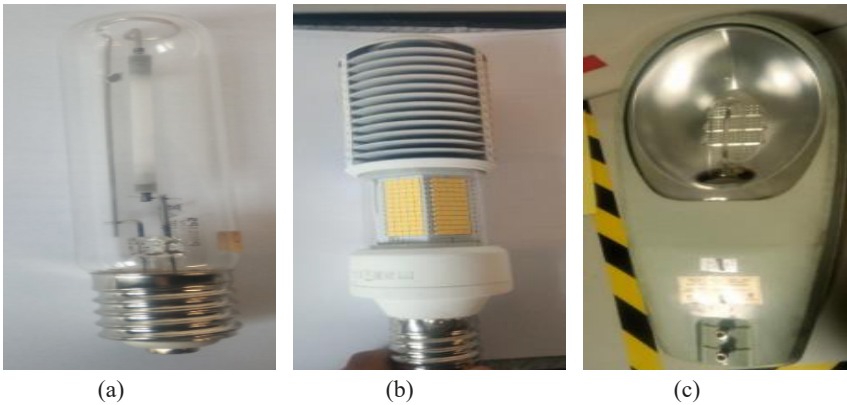


Figure 2. Test sample used in the study: (a) HPSV lamp, (b) LED retrofit lamp, (c) 150 W HPSV light fixture

Table 1
Specification of the light sources

PARAMETER	HPSV LAMP	LED LAMP
Wattage	150 W@240 V	68 W@ 240 V
Rated Luminous Flux	13,500 lm	12,000 lm
Correlated Color Temperature (CCT)	2000K	4000K
Burning Orientation	Any	N/A
Screw Head Type	E40	E40



Figure 3. The main components of a goniophotometer: (a) a Photometer sensor, (b) light baffles, (c) a Goniometer sample mounting stage and test sample

The LED replacement lamp utilizes the same lamp base as the original HPSV lamp, allowing easy installation without any modifications to the existing luminaire. The test

sample installed in the HPSV road light fitting is shown in Figures 4 and 5. The test was conducted by initially measuring the LID curve of each lamp before installing it into the sample road light fittings to compare both light distribution characteristics prior to installation into the luminaires. The luminaires were mounted vertically on a Rotating Luminaire Goniophotometer to the C-axis as in Figure 3(a), with starting coordinates based on the measurement of the C- γ coordinate system. Scan intervals were set at 15° for the C angle and 1° for γ angle.



Figure 4. LED lamp in 150W HPSV light fixture



Figure 5. 150W HPSV lamp inside 150W HPSV light fixture

Analysis Methods

Results were analyzed based on a comparison of the original HPSV lamp and LED retrofit lamp in terms of the light output ratio (LOR) (International Commission on Illumination, 1996) and light output distribution angle percentage value based on the backlight- uplight- glare rating value (Chinnis et al., 2011).

Calculation of LOR is done based on Equation 1.

$$\text{LOR} = \frac{\text{Luminaire Total Luminous Flux}}{\text{Bare Lamp Total Luminous Flux}} \quad [1]$$

Zoning classification regarding the light output region was based on the luminaire classification system zoning, also known as Backlight-Uplight-Glare (BUG) classification (LCS). The BUG system provides a numerical rating of luminaire based on the photometric distribution tested by the manufacturer. The BUG rating system was proposed due to its ability to evaluate luminaire distributions in the context of the impact of light emitted in

the various solid angles of the LCS as they apply to light trespass, sky-glow, and glare. The zones are divided into three major zones, shown by the alphabet U, which applies to sky glow, G to glare and B to backlight or light trespass Figure 6.

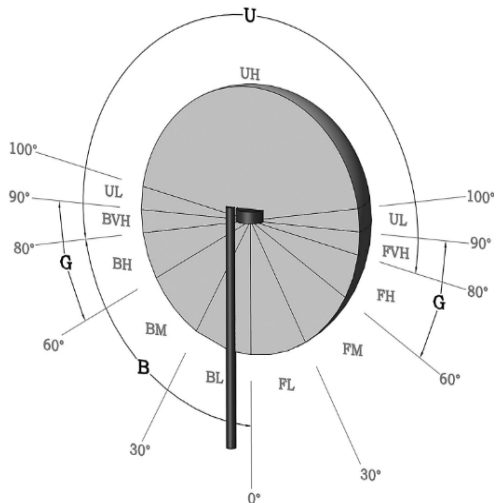


Figure 6. Zones for luminaires classification: UL (Up Light), FVH (Front Very High), FH (Front High), FM (Front Mid), FL (Front Low), BVH (Back Very High), BH (Back High), BM (Back Mid), and BL (Back Low) (IES TM-15:2007)

The light distribution has a slight dent or valley due to the frame structure blocking the light output, which can be seen in the 2-dimensional polar plot diagram at 90° vertical axis.

Figure 8 shows the 3-dimensional rendering of the LED retrofit lamp's Light Intensity Distribution (LID) Curve. The light distribution is a form of hexagonal shape with a similar resemblance to the HPSV bare lamp distribution results. The hexagonal shape shown in Figure 8(a) is due to the construction of the LED retrofit lamp comprising 6 faces of LEDs.

Table 2
Luminous flux output of HPSV lamp and LED lamp

Parameters	HPSV Lamp		LED Lamp	
	Measured Value	Manufacturer's Value	Measured Value	Manufacturer's Value
Luminous Flux	13,350 lm	13,500 lm	11,864 lm	11,200 lm
Efficacy Rating	83 lm/w	98 lm/w	140 lm/w	164 lm/w
Wattage	160.8 W	147.0 W	84.7 W	68.0 W

RESULTS

Light Output of Light Source

Table 2 shows the measured photometric properties of the HPSV lamp and LED lamp. The difference between the measured and manufacturer's values is attributed to the different measurement methods where the measured values are from goniophotometric measurements. The integrating sphere method is normally used to measure the total luminous flux. Goniophotometric measurement is chosen here to monitor and analyze the light distribution pattern.

Figure 7 shows the 3-dimensional (3D) rendering of the Light Intensity Distribution (LID) Curve of a bare HPSV lamp. The light distribution is a doughnut shape with no light from the base and tip of the lamp.

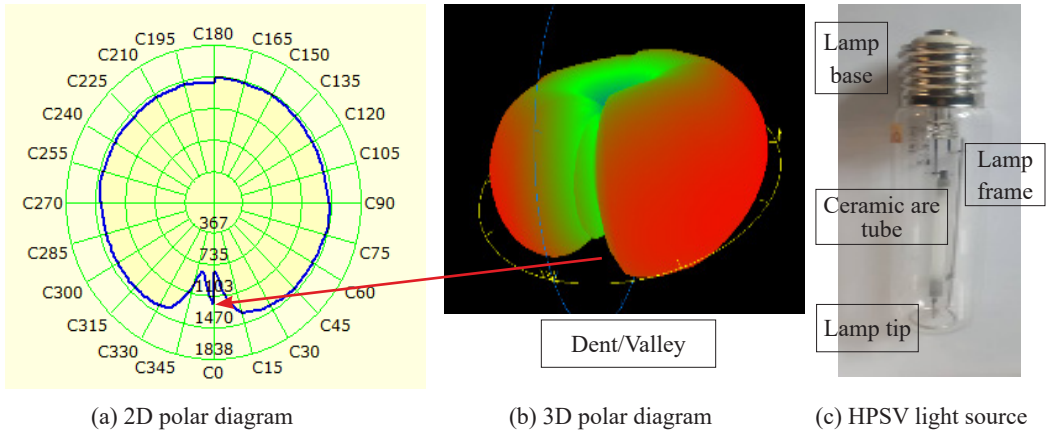


Figure 7. Polar diagram of HPSV lamp light at 90 vertical axis output and equivalent 3D rendering

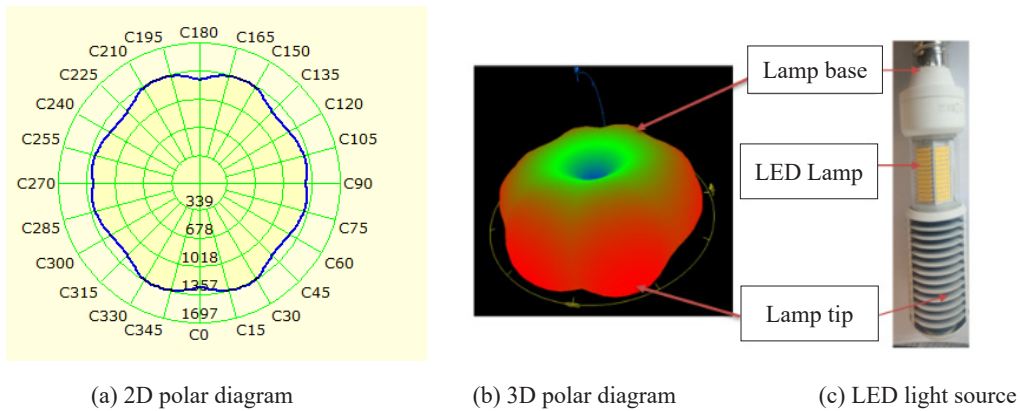


Figure 8. Polar diagram of LED lamp at 90 vertical axis output and equivalent 3D rendering

Comparison of HPSV and LED Retrofit Lamp

Figure 9 shows the 3D line rendering and 2D polar plot comparison of both HPSV and LED lamps. The green rendered line is for the HPSV lamp, while the red is for the LED retrofit lamp. The LED retrofit lamp has a similar doughnut-shaped output to the HPSV lamp. It shows the compatibility of replacing the LED retrofit lamp with the HPSV fitting due to similar luminous flux. The characteristics of luminous output value are shown in Table 3.

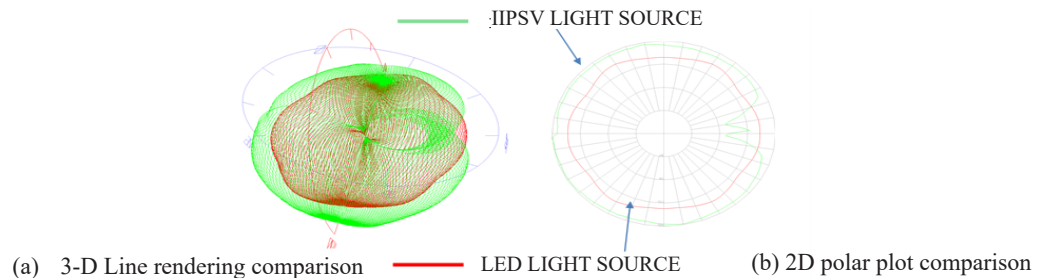


Figure 9. Polar diagram of LED lamp at 90 vertical axis output and equivalent 3D rendering

Table 3
Luminous output comparison of HPSV and LED retrofit lamp

	HPSV Lamp	LED Retrofit Lamp	% Difference
Luminous Flux	13,350 lm	11,864 lm	- 11.13%
Efficacy Rating	83 lm/w	140 lm/w	+ 68.67%
Wattage	161.78 W	84.75 W	- 47.61%
Maximum Intensity	1470.93 cd	1357.72 cd	- 7.69%

LIDC Comparison of HPSV And LED Retrofit HPSV Luminaires (150 W)

The LID curve of the LED retrofit lamp and the original LID curve of the HPSV lamp are compared in Figure 10. The original LID curve of the HPSV luminaire is represented by the red shade of the LID curve, while the green shade of the LID curve represents the LED lamp retrofitted HPSV luminaire. A significant drop in the luminaire's light distribution can be observed from almost all angles. The decline is visible in the 0°–180° and 90°–270° regions. Table 4 compares the HPSV and LED retrofit lamps used in 150W HPSV fitting. From the results, a reduction of total lumen output from 11,146 lm to 5,807 lm can be seen clearly. There is an insignificant change in the efficacy rating of 67 lm/w for HPSV lamps compared to 69 lm/w for LED retrofit lamps, possibly due to the higher wattage of the HPSV lamp. The efficiency of the fitting has also reduced to 49% from an initial efficiency of 83% by using the LED retrofit lamp. Then, Figure 11 shows the lumen pie chart for (a) HPSV lamp and (b) LED retrofit lamp luminaire.

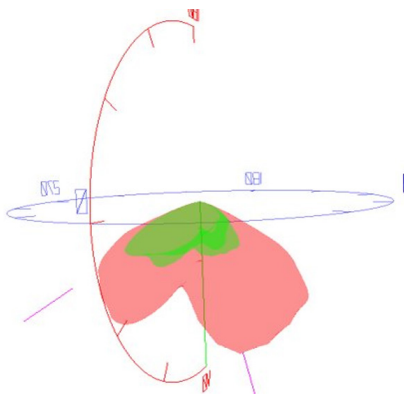


Figure 10. Comparison of HPSV lamp and LED lamp polar diagram with each lamp is placed inside 150 W HPSV light fitting using goniophotometric measurement

Table 4
Comparison of lumen output for HPSV lamp and LED retrofit lamp in 150W HPSV fitting

Description	150W HPSV LAMP	LED Lamp (Philips Trueforce LED Lamp 68 W)
Lumens Per Lamp	13,350 (1 lamp)	11,858 (1 lamp)
Total Lamp Lumens	13,350	11,858
Luminaire Lumens	11,146	5,807
Downward Total Efficiency	83%	49%
Total Luminaire Efficiency (LOR)	83%	49%
Luminaire Efficacy Rating (LER)	67	69
Total Luminaire Watts	166.72	84.18
LCS: Total Lumens	11,146	5,807

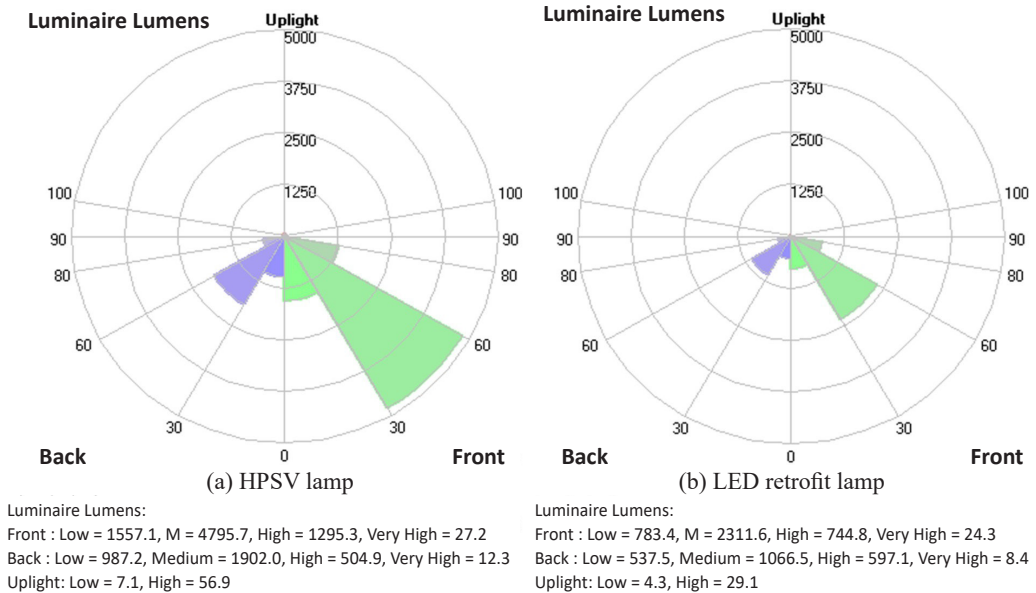


Figure 11. (a) HPSV lamp, (b) LED retrofit lamp luminaire lumen pie chart

Based on the two-lumen pie charts in Figure 11, it can clearly be seen that the proportion of lumen output per distribution angle is almost identical, with the luminaire maintaining its forward and backward light distribution. However, there is a reduction to about half of the original light distribution for the retrofit LED lamp. The front-mid angle has decreased from 4,795.7 lumens to 2,311.6 lumens, a 51% reduction in lumen output. The average drop of 40% is similar to other elevation angles. Table 5 compares the HSPV lamp and LED lamp based on elevation angle. There is no significant change in glare rating when the HPSV lamp is changed to an LED lamp except for reduced glare from G1 to G0 at "Back Very High Elevation." A lower glare rating indicates a lower level of glare.

Table 5
 Light output comparison of HPSV and LED retrofit lamp per elevation angle

Elevation Angle	Hpsv Lamp (Lumen)	Lamp Glare Rating	Retrofit LED Lamp (Lumen)	LED Lamp Glare Rating	% Reduction
Front Low	1557.1	-	783.4	-	49.68
Front Medium	4795.7	-	2311.6	-	51.7
Front High	1295.3	G1	744.8	G1	42.4
Front Very High	27.2	G1	24.3	G1	11.02
Back Low	987.2	-	537.5	-	45.55
Back Medium	1902.0	-	1066.5	-	43.92

Table 5 (Continue)

Elevation Angle	Elevation Angle	Lamp Glare Rating	Retrofit LED Lamp (Lumen)	LED Lamp Glare Rating	% Reduction
Back High	504.9	G0	297.1	G0	41.11
Back Very High	12.3	G1	8.4	G0	31.70
LCS: Total Lumens	11,146	-	5,807	-	46.77

Due to the lamp structure, which occupies a large area inside the luminaire's housing, the output performance of the LED retrofit lamp is significantly reduced. Figures 3 and 4 show the retrofit LED and HPSV lamps inside the luminaire housing, respectively. Compared to the HPSV lamp, the LED retrofit lamp has taken up more than half of the space inside the HPSV luminaire, obstructing the LED lamp's light output.

DISCUSSION

In this research, a much cheaper method is utilized where the HPSV lamp is replaced with an LED lamp of similar luminous output to determine the suitability of using such a method. The different solutions can be utilized and give benefits in terms of better color rendering visibility at a cheaper cost. The lamp replacement may be an alternative method to total luminaire replacement by the local government. The study uses photometric measurement to analyze changes in light distribution, and analysis is also done based on Backlight-Uplight and Glare ratings.

From the results of the photometric measurement, it was found that installing the LED lamp inside the luminaire caused a reduction in the total light output ratio. The light distribution pattern was maintained but with a 40–50 % reduction at all backlight and front light angles. The glare was still controlled, whereas the rating was still maintained. It also resulted in an overall luminance value of 52% based on the lighting simulation.

The main focus of the study is to compare the light output ratio (LOR) using two types of lamps applied in Malaysia, HSPV and LED lamps. The LED lamp replaces the original HPSV lamp in the HSPV luminaire. The LOR value is chosen as an indicator of the ability of the road lighting fixture to produce output light from the installed lamp towards the illuminated area. In terms of construction, both lamps have different lamp structures where the LED lamp is larger compared to the HSPV. The LOR and backlight, uplight and glare (BUG) rating parameters can be applied as an initial stage to choose a suitable road lighting system without any energy waste. Other parameters such as average road luminance, brightness uniformity, longitudinal uniformity, glare, surround ratio (SR), color rendering index (CRI) and visual inducement are also important for road lighting. However, LOR and BUG rating parameters are much needed for the initial stage of lamp selection.

The LOR and BUG rating parameters differ from the street lighting design parameters, such as average luminance, uniformity and glare, where those parameters require a longer lighting simulation or measurement for the analysis.

The latest road lighting standard has implemented the scotopic /photopic ratio in evaluating road lighting measurement and design. This value will benefit light sources with a spectral distribution tilted towards the lower wavelength, such as LEDs. The mid-range mesopic visibility region for road lighting is evaluated at low luminance values. It enables designers to design a system with lower electrical consumption while maintaining the required lighting levels. The luminous intensity class and glare ratings requirements have also been included (British Standard, 2015).

In general, LED lighting is a solid-state device with no moving parts. Based on the manufacturer's data, the LED lamp has a lifetime capability of 50,000 hours, whereas the HPSV lamp has a lifetime capability of 25,000 (Philips, 2023). However, LEDs are prone to failure due to electrical control gear components, which will require thorough investigation (Lewotsky, 2011).

LED has a color rendering index (CRI) of above 70, while the HPSV lamp has a CRI of 35, much lower than that of LED (Philips, 2023). It shows that the LED has a better visual perception than the HPSV lamp, resulting in a lower luminance value requirement. Factors such as low luminance level illumination where the mesopic region is more sensitive to human sight will affect the visibility of road users. Further study on implementing mesopic evaluation for road lighting may increase the usability of LED lighting systems even at lower lighting levels. Then, the Light Intensity Distribution (LID) Curve of the light source describes the light propagation, which will directly impact the light falling on the road surface and direct surroundings. From the LIDC of the light source, important parameters such as total luminous flux of the light, luminaire efficacy (lm/w) and efficiency based on light output ratio (LOR) and Backlight-uplight dan Glare indicators can be identified and measured as well.

This research can assist the authorities in choosing whether to replace the whole HSPV luminaire with an LED luminaire or only the lamps. It is important to save installation costs while ensuring the required lighting level is sufficient. Previous studies indicated high capital cost in changing from HPSV to LED systems, and its feasibility depends on the energy conservation potential (Kovačević et al., 2022; Yousif et al., 2018). Due to limited resources, the study used HPSV luminaires with a "cobra head" design with only a single type of LED retrofit sample. Various types of luminaires, such as compound post-top luminaires and different LED retrofit lamp structures, may produce different outcomes.

CONCLUSION

In conclusion, the study shows the possibility of replacing HPSV lamps with LED retrofit lamps rather than replacing entire luminaires to save costs. Using more efficient lighting,

such as LED, at a lower cost can be a promising solution. The photometric output of original HPSV lamps fitted streetlight and LED retrofit lamps are compared in this study.

According to the photometric results of the bare light sources, both have similar light output distribution, with most of the light coming from the sides of the lamps and almost no light from the tips. Thus, the retrofit method is a compatible replacement in terms of light distribution of the light source. The entire luminous flux of both lamps is similar, with a total lumen difference of 1492 lumens between the HPSV lamp and the LED retrofit lamp.

When the HPSV lamp fitting is retrofitted with the LED lamp source, the luminaire's performance is reduced to a 49% light output ratio (LOR) from an initial 83%. The proportion of lumen output per distribution angle is approximately identical for the luminaire's forward and backward light distribution. Compared to the HPSV lamp, which has a smaller structure, the LED retrofit lamp causes a considerable decrease in output performance since the lamp structure occupies a large area inside the luminaire housing, preventing the light output from the luminaire.

The findings can assist the government in looking at the advantages of LED over HSPV in upgrading road lighting that can finally benefit humans and the environment. Thus, local authorities and manufacturers can work together to study the best structure of luminaire housing. In the future, more LED samples will be tested to compare their performance based on photometric methods.

ACKNOWLEDGEMENTS

We acknowledge the Malaysian Public Works Department (JKR), Ministry of Education Malaysia under FRGS grant (FRGS/1/2021/WAB02/USIM/02/1) and Universiti Sains Islam Malaysia (USIM) for the funding and support.

REFERENCES

- Abdullah, A., Aziz, M., & Huda, M. (2021). Redesigning public street lighting using photometric method. *Indonesian Journal of Computing, Engineering and Design (IJoCED)*, 3(1), 54–67. <https://doi.org/10.35806/ijoced.v3i1.153>
- Bamisile, O. O., Dagbasi, M., & Abbasoglu, S. (2016). Economic feasibility of replacing sodium vapor and high pressure mercury vapor bulbs with LEDs for street lighting. *Energy and Policy Research*, 3(1), 27–31. <https://doi.org/10.1080/23815639.2016.1201442>
- Bergen, A. S. J. (2012). A practical method of comparing luminous intensity distributions. *Lighting Research & Technology*, 44(1), 27-36. <https://doi.org/10.1177/1477153511435769>
- BERNAMA. (2023). *212,639 Street Bulbs Replaced with LED Lights - TNB*. Bernama Energy.com. <http://energy.bernama.com/news.php?id=1737759>
- Bhattacharya, S., Majumder, S., & Roy, S. (2023). Modelling of the effects of luminaire installation geometries and other factors on road illumination system photometric parameters and energy efficiency. *World Journal of Engineering*. <https://doi.org/10.1108/WJE-09-2022-0372>

- Braga, M. F., Nogueira, F. J., Campos, M. F. C., Gouveia, L. H. B., & Braga, H. A. C. (2014). *A comparative study regarding linear fluorescent and LED lamps for indoor lighting*. [Paper presentation]. 11th IEEE/IAS International Conference on Industry Applications, Juiz de Fora, Brazil. <https://doi.org/10.1109/INDUSCON.2014.7059469>
- Bredemeier, K. (2017). *Photometric Data for the Development of Lighting Components*. Universitätsbibliothek Ilmenau.
- British Standard. (2015). *BS-EN 13201-2 Road Lighting: Performance Requirements*. BSI Standards Publication
- Brons, J. A., Bullough, J. D., & Frering, D. C. (2021). Rational basis for light emitting diode street lighting retrofit luminaire selection. *Transportation Research Record*, 2675(9), 634-638. <https://doi.org/10.1177/03611981211003890>
- Chinnis, D., Mutmansky, M., & Clanton, N. (2011). IES TM-15 BUG value-setting and adjustment methodology. *Leukos*, 8(1), 25-39. <https://doi.org/10.1080/15502724.2011.10732155>
- Czyżewski, D. (2023). The photometric test distance in luminance measurement of light-emitting diodes in road lighting. *Energies*, 16(3), Article 1199. <https://doi.org/10.3390/en16031199>
- Gordic, D., Vukasinovic, V., Kovacevic, Z., Josijevic, M., & Zivkovic, D. (2021). Assessing the techno-economic effects of replacing energy-inefficient street lighting with LED corn bulbs. *Energies*, 14(13), Article 3755. <https://doi.org/10.3390/en14133755>
- Grau, F., Cervantes, J., Vázquez, L., & Nuñez, J. R. (2021). Effect of LED technology on technical losses in public lighting circuits. A case study. *Journal of Engineering Science and Technology Review*, 14(2), 198–206. <https://doi.org/10.25103/jestr.142.24>
- International Commission on Illumination. (1996). *CIE 121 1996: The Photometry and Goniophotometry of Luminaires*. International Commission on Illumination.
- Jabatan Kerja Raya. (2018). *Garis Panduan Penggunaan Lampu Jalan Jenis Cepak Tenaga untuk Pemasangan Baharu dan Sedia Ada Projek Kerajaan (CKE.GP.01.54.(00).2018)* [Guidelines for the Use of Energy-Efficient Road lighting for New and Existing Installations for Government Projects (CKE.GP.01.54.(00).2018)]. Jabatan Kerja Raya. <https://dokumen.tips/documents/garis-panduan-penggunaan-lampu-jalan-jenis-cekap-epsmgjkr.gov.my/images669garispanduanlampujalancekaptenaga.html?page=2>
- Kovačević, Z., Vukašinić, V., & Gordić, D. (2022). Piecewise techno-economic analysis of led corn bulbs for street lighting. *Applied Engineering Letters*, 7(2), 74–80. <https://doi.org/10.18485/aletters.2022.7.2.4>
- Lewotsky, K. (2011, November 22). *Understanding and Preventing LED Failure*. DigiKey. <https://www.digikey.com/en/articles/techzone/2011/nov/understanding-and-preventing-led-failure>
- Li, Q., Wang, Z., Kolla, R. D. T. N., Li, M., Yang, R., Lin, P. S., & Li, X. (2023). Modeling effects of roadway lighting photometric criteria on nighttime pedestrian crashes on roadway segments. *Journal of Safety Research*, 86, 253-261. <https://doi.org/10.1016/J.JSR.2023.07.004>
- Philips. (2023). *The Best LED Replacement for HID and SON Road Lamps with TrueForce LED TrueForce LED Public (Road-SON)*. Philips. https://www.lighting.philips.co.uk/api/assets/v1/file/PhilipsLighting/content/comf7165342-pss-en_gb/LP_CF_7165342_EU.en_GB.PROF.CF.pdf
- Rofaie, N. S. A., Phoong, S. W., & Mutalib, M. A. T. A. (2022). Light-emitting diode (LED) versus high-pressure sodium vapour (HPSV) efficiency: A data envelopment analysis approach with undesirable output. *Energies*, 15(13), Article 4589. <https://doi.org/10.3390/en15134589>

- Rofaie, N. S. A., Phoong, S. W., & Mutalib, M. A. T. A. (2022). Light-emitting diode (LED) versus high-pressure sodium vapour (HPSV) efficiency: A data envelopment analysis approach with undesirable output. *Energies*, *15*(13), Article 4589. <https://doi.org/10.3390/en15134589>
- Setyaningsih, E., & Candra, H. (2023). Optimization of photometric quantities for road lighting freeways in Indonesia. *Journal of Theoretical and Applied Information Technology*, *31*(6), 2433-2441.
- TEEAM. (2012). *The Electrical and Electronics Association of Malaysia* [Technical report]. <https://www.scribd.com/document/707493031/Technical-Report-Suitability-of-LED-for-Road-Lighting-in-Malaysia-Manualzz>
- Ying, J. K. X., & Lim, W. F. (2022). Study and optimization of lens shape affecting light patterns of light-emitting surface based LED street lighting. *Optik*, *260*, Article 169083. <https://doi.org/10.1016/j.ijleo.2022.169083>
- Yousif, O. S., Majid, M. Z. A., Aminudin, E., Zakaria, R., Wahid, C. M. F. H. C., Neardey, M., & Ramli, M. R. (2018, October 24-26). *Energy and economic benefits of LED adoption in Malaysia highway lighting system*. [Paper presentation]. Proceedings of the 4th International Conference on Low Carbon Asia, Johor Bahru, Malaysia.
- Zima, K., & Cieplucha, W. (2023). Efficiency analysis of roadway lighting replacement in a selected polish municipality. *Applied Sciences*, *13*(5), Article 3257. <https://doi.org/10.3390/app13053257>

Application of Membrane-less Microbial Fuel Cell in Reducing Human Hazards from Dewatered Sludge

Fatin Nur Izzati Mohd Fadzil¹, Chen Sep Ngee¹, Mohammed Zharif Asyrani
Mohammed Alias¹, Muhammad Adib Fadhlullah Muhammad Lukman²,
Amira Suriaty Yaakop³, Muaz Mohd Zaini Makhtar¹ and Ana Masara Ahmad
Mokhtar^{1,4*}

¹Small G Protein Research Group, School of Industrial Technology, Universiti Sains Malaysia, 11800 Penang, Malaysia

²National Poison Centre, Universiti Sains Malaysia, 11800 Penang, Malaysia

³School of Biological Sciences, Universiti Sains Malaysia, 11800 Penang, Malaysia

⁴Green Biopolymer Coating and Packaging Centre, School of Industrial Technology, Universiti Sains Malaysia, 11800, Penang, Malaysia

ABSTRACT

Membrane-less microbial fuel cell (ML-MFC) technology has emerged as a potential for wastewater treatment and electricity generation. Despite its benefit in green energy production, studies have yet to determine its role in minimizing the human hazards stemming from dewatered sludge (DS). Hence, this research aims to investigate the effects of ML-MFC-treated DS on cell toxicity and its benefits in reducing protein-denaturation-related inflammation and antimicrobial resistance (AMR) dissemination. MTT assay was performed to determine the cytotoxic effect of ML-MFC-treated DS on 3T3-L1 and Hep G2 cells at 24 h. The anti-inflammatory property of ML-MFC-treated DS was determined using a protein denaturation assay. Next, the antibiotic susceptibility

of bacteria isolated from ML-MFC-treated samples was determined using the disk-diffusion method. All the data obtained were statistically analyzed using GraphPad Prism software (Version 9.2.0) with a p -value ≤ 0.05 was considered significant. Interestingly, ML-MFC-treated DS showed 80% cell viability on 3T3-L1 and slight toxicity on Hep G2 cells. ML-MFC-treated DS exhibited anti-inflammatory properties with 62.43% protein denaturation inhibition and displayed fewer antibiotic-resistance

ARTICLE INFO

Article history:

Received: 08 May 2023

Accepted: 23 October 2023

Published: 04 April 2024

DOI: <https://doi.org/10.47836/pjst.32.3.12>

E-mail addresses:

fatinfadzil@student.usm.my (Fatin Nur Izzati Mohd Fadzil)

sepngee@gmail.com (Chen Sep Ngee)

zharif.asyrani.alias@gmail.com (Muhammad Zharif Asyrani)

Mohammed Alias)

adib.padolah@gmail.com (Muhammad Adib Fadhlullah

Muhammad Lukman)

amirasuriaty@usm.my (Amira Suriaty Yaakop)

muazzaini@usm.my (Muaz Mohd Zaini Makhtar)

anamasara@usm.my (Ana Masara Ahmad Mokhtar)

*Corresponding author

bacteria than the untreated. Overall, the ML-MFC technology showed novel applications by decreasing DS-related health hazards.

Keywords: Antimicrobial resistance (AMR), cytotoxicity, dewatered sludge, inflammation, microbial fuel cell (MFC)

INTRODUCTION

Over the years, rapid development and growing population in Malaysia have led to increased sewage sludge production. It generates approximately 3 million cubic meters of sewage sludge annually within wastewater treatment plants and is expected to increase substantially in the future (Safuan et al., 2014). Generally, sewage sludge, or biosolids, refers to the residual, semi-solid substances produced as a by-product during the treatment of municipal or industrial wastewater (Kumar & Chopra, 2016). Sewage sludge normally contains high water content (92–99.5%), which contributes to the high costs of its further treatment (Górka et al., 2018). Hence, dewatering becomes a crucial step in sludge treatment by reducing the water content, consequently minimizing its weight and volume, resulting in a more economical disposal operating cost. The yield of this process is commonly referred to as dewatered sludge (DS). DS potentially benefits industries and communities, as demonstrated by its conversion into fertilizers and application in various land uses, including agriculture, landfills and composting (Gerba & Pepper, 2009). There is also a growing interest in deriving renewable energy from DS as it has a high potential to be converted into energy and reduce hazardous emissions compared to fossil fuel (Yacob et al., 2006). However, when managing waste from various sources, sewage workers are routinely exposed to harmful components within the sewage or sewage sludge, including biological and chemical irritants such as toxic gases, pathogens, genotoxic agents, and harmful organic chemicals (Straub et al., 1993). Despite treatment, the sewage sludge might retain resilient pathogens and bacteria capable of surviving the current treatment methods. For example, certain pathogens, such as *C. perfringens*, can remain in treated sewage sludge, displaying resistance to various disinfection methods (Al-Gheethi et al., 2018; Alonso et al., 2004).

Furthermore, the hepatitis A virus (HAV) is stable in the environment for an extended period and is resistant to current wastewater treatment practices (Ouardani et al., 2016). These pathogens, associated with food poisoning and hepatitis, can be transmitted to humans through various routes, ingesting contaminated vegetables or water, inhalation or direct skin contact. Acute and continuous exposure to these harmful substances may initiate inflammatory reactions and enhanced nitric oxide or pro-inflammatory cytokines production, leading to various inflammation-related diseases such as skin irritation, pulmonary diseases, and even cancer (Straub et al., 1993).

Moreover, the implications of wastewater treatment plants (WWTPs) are noteworthy. These plants serve as a major reservoir of antimicrobial resistance (AMR) amplification because they provide an ideal environment for the survival of AMR bacteria (ARBs) with AMR genes (ARGs) (Osińska et al., 2020). AMR, also known as drug resistance, is widely recognized as a global threat to human health that demands immediate action in countries worldwide. AMR has emerged as a significant concern in recent years, as it could lead to a post-antibiotic era in which antibiotics are no longer effective, impacting humans, animals, and the environment (Hocking et al., 2021). Although the wastewater treatment process can aid in eliminating or minimizing the ARB load, some remaining surviving ARBs with non-biodegradable ARGs will spread the genes to other bacteria via horizontal gene transfer (HGT) (Sun et al., 2019). Ultimately, it will facilitate the transmission of pathogenic AMR or ARBs to animals and humans via several routes, endangering their health (Osińska et al., 2020). Consequently, the dissemination of AMR in the environment could result in the inability to effectively treat infections, exacerbating inflammation and leading to prolonged illnesses such as cancer (Michael et al., 2014; Mokhtar et al., 2022).

Therefore, an alternative is needed to reduce the human hazards stemming from the land application of DS, and one of the potential technologies is Microbial Fuel Cell (MFC). MFC is a bioelectrical device that operates electrochemically by incorporating electrogenic bacteria (EB), an organism that can transfer electrons to extracellular electron acceptors to generate electricity (Mahmoud et al., 2022; Oibileke et al., 2021). Previous studies show the potential use of MFC treatment in providing electricity and reducing chemical oxygen demand (COD) in DS (Makhtar & Tajarudin, 2020; Makhtar & Vadivelu, 2019; Muaz et al., 2019). Additionally, MFC technology can also effectively replace conventional non-renewable resources such as natural gas and coal that are continuously depleted through time (Muaz et al., 2019) and could reduce the emission of greenhouse gases that can cause global warming and climate change (Anderson et al., 2016). In line with this, the utilization of EB, such as *B. subtilis*, demonstrated its capacity to secrete anti-inflammatory metabolites like exopolysaccharide (EPS), that can stimulate the development of anti-inflammatory M2 macrophages to inhibit T cell activation *in vivo* (Paynich et al., 2017; Rhayat et al., 2019).

Nevertheless, in the current research landscape, the emphasis within MFC studies has predominantly revolved around its electricity generation capabilities, leaving a notable gap in understanding its potential to mitigate DS-related human hazards. Hence, exploring the potential of MFC technology in DS treatment gained significant attention, particularly for its role in mitigating inflammation and countering the spread of antimicrobial resistance (AMR) in forthcoming research endeavors. Therefore, this study investigated the promise of ML-MFC as a functional approach to producing electricity and concurrently reducing the long-term risk of human hazards stemming from DS.

MATERIALS AND METHODS

Collection and Preparation of ML-MFC-treated DS Samples

DS was obtained from the Juru municipal wastewater treatment plant. The ML-MFC setup was constructed following Muaz et al. (2019)'s approach. *B. subtilis* served as the EB. This study considered two sets of samples: ML-MFC-untreated DS (T0) and ML-MFC-treated DS obtained after 120 hours (T120). 1 g of sample was mixed with 10 mL sterile distilled water. Subsequently, centrifugation at 3500 rpm for 15 min was conducted to obtain the supernatant. The supernatant was then filtered with a 0.22 µm membrane filter and stored in a -20°C freezer for further analysis.

Cell Maintenance

Mouse fibroblast, 3T3-L1 cell and hepatocellular carcinoma, Hep G2 cancer cell was maintained in Dulbecco's Modified Eagle Medium (DMEM) and Minimum Essential Medium (MEM), respectively, supplemented with 10% fetal bovine serum (FBS) and 1% antibiotics-antimycotic, in the incubator with 5% CO₂ at 37°C. Cells were subcultured after reaching 80-90% confluency.

MTT Assay

The toxic effect of ML-MFC-treated DS on 3T3-L1 and Hep G2 cells was identified using an MTT assay adapted from Horiuchi et al. (1988) with slight adjustments. Briefly, cells were seeded in a 96-well plate at a cell density of 50,000 cells/mL overnight. The cells were treated with 25 mg/mL, diluted, filtered samples before being further incubated for 24 h. 5 mg/mL MTT solution was added to each well and incubated for another 4 h at 37°C. After 4 h, the media was removed, and DMSO solution was added to dissolve the MTT-formazan crystals. Finally, the absorbance value for each sample was measured at 540 nm with 620 nm as a reference. The percentage of cell viability of each sample was calculated as Equation 1:

$$\text{Percentage of cell viability} = \frac{(A_{\text{treatment}} - A_{\text{blank}})}{(A_{\text{control}} - A_{\text{blank}})} \times 100\% \quad [1]$$

where A = absorbance value for each sample

Protein Denaturation Assay

The ability of MFC technology to reduce DS-induced protein denaturation-related inflammation was determined via bovine serum albumin denaturation assay as described by Padmanabhan and Jangle (2012), with slight modifications. Firstly, the mixtures were prepared by mixing DS samples, 7% BSA solution and PBS solution (pH 6.9) before being heated at 75°C for 20 min. A mixture of PBS and BSA was used to form the control tube. Then, the mixtures were left to cool down at room temperature for 5 minutes. After

the mixtures were cooled down, each sample's absorbance values were measured at 660 nm in triplicate, and the readings were recorded. The percentage of inhibition of protein denaturation was calculated based on Equation 2 to identify the anti-inflammatory activity of the samples involved.

$$\% \text{ Inhibition of protein denaturation} = \left(1 - \frac{[\text{Abs}(\text{sample})]}{[\text{Abs}(\text{control})]} \right) \times 100 \quad [2]$$

Antibiotic Susceptibility Testing

The Kirby-Bauer disk diffusion susceptibility test was performed to determine the sensitivity or resistance of bacteria to various antibiotics in ML-MFC-treated DS samples. Firstly, the ML-MFC-treated DS samples were diluted up to 10^{-3} dilutions. The bacterial colonies were then isolated using the spread plate method and incubated at 37°C for a week. The well-isolated bacterial colonies obtained from the isolation step were further purified on the streak plate and then further incubated overnight. After incubation, a loopful of pure culture from different dewatered samples was diluted and spread onto the nutrient agar plate. Then, the antibiotic discs (streptomycin sulfate, kanamycin monosulphate, tetracycline free base, chloramphenicol, amoxicillin, penicillin G, and ampicillin) were applied to the nutrient agar plate, followed by incubating the plate in the incubator at 37°C for 24 h. After 24 h, the diameter of the zone of inhibition (ZOI), in mm, for each antibiotic was measured and determined according to the guidelines published by the Clinical and Laboratory Standards Institute (CLSI, 2020). Zone diameters of susceptibility testing results were categorized as sensitive, intermediate, or resistant based on the CLSI breakpoint.

Bacterial Identification of Selected Isolates

The colony PCR method was used to identify the selected isolates genetically. The 16S rRNA gene of selected bacteria was amplified by using a forward primer (27F: 5'-AGAGTTTGATCCTGGCTCAG-3') and a reverse primer (1492R: 5'-GGTACCTTGTTACGACTT-3'), as described by Lane (1991). The quality of the PCR product was quantified using NanoDrop (Thermo Fisher Scientific). Centre for Chemical Biology (CCB) USM performed gene sequencing. Sequences obtained were run in the Basic Local Alignment Search Tool (BLAST) feature from the National Center for Biotechnology Information (NCBI) to find regions of local similarity between sequences for identification.

Statistical Analysis

The statistical analysis was performed using GraphPad Prism version 9.2.0. All results were presented as mean \pm standard deviation (SD) of three independent experiments. An unpaired t-test was used to compare the means between groups with a p -value less than or equal to 0.05 ($p \leq 0.05$) considered significant.

RESULTS AND DISCUSSION

ML-MFC-treated DS Showed Slight Toxicity to Cancer Cells

ML-MFC-treated DS at 120 h was chosen in this research because it was when the power generation and biomass were in the log phase (Makhtar et al., 2021). Besides, according to Sabri et al. (2021), MFC-treated DS at 120 h (day 5) shows an increment of voltage at peak (88 mV). It indicates that *B. subtilis* reacted positively in ML-MFC on day 5, resulting in the fast growth of the bacteria and high voltage output due to the acceleration of the metabolic rate of *B. subtilis*. The toxic effect of ML-MFC-treated DS on normal cell, 3T3-L1 cell was identified using MTT assay for 24 h. As shown in Figure 1, both samples show more than 60% cell viability, with 67.74% for T0 and 65.99% for T120, respectively. There was no statistical difference between both samples, indicating that with or without ML-MFC treatment, there was no toxic effect on normal cells.

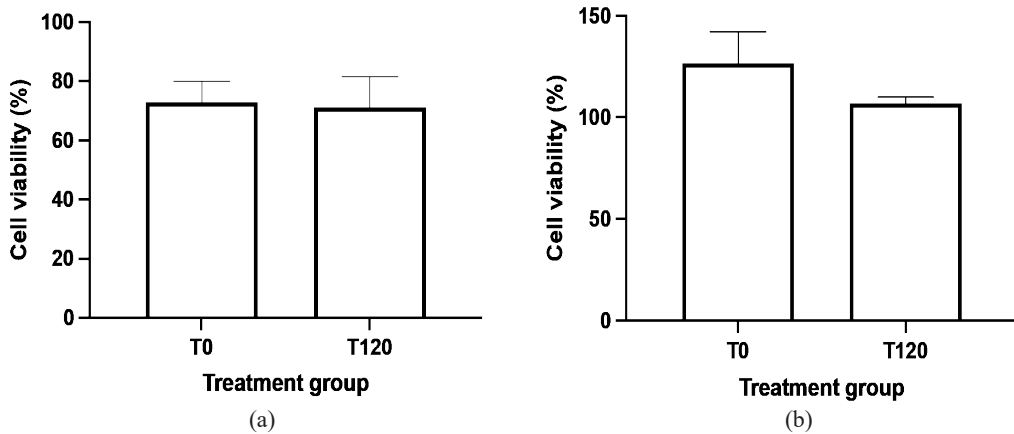


Figure 1. The determination of cell viability percentage using MTT assay for (a) 3T3-L1 and (b) Hep G2 cells. Values were expressed as the mean \pm standard deviation ($n=3$). T0: untreated DS at 0 h; T120: MFC-treated DS at 120 h.

Next, the effect of ML-MFC-treated DS on hepatocellular carcinoma cell toxicity, Hep G2, was determined using an MTT assay for 24 h. According to Figure 1, although it is not significant, there is a slight decrease in cancer cell viability after being treated with T120. Hence, the data suggests that ML-MFC treatment can potentially reduce the number of cancer cells. The inhibitory effect observed in ML-MFC-treated DS may be due to the activity of *B. subtilis*-secreted bacteriocins such as lipopeptides, surfactin, and iturin (Zhao et al., 2018). This bacteriocin was found to kill cancer cells such as K562 (myelogenous leukemia cells) (Zhao et al., 2018), LoVo (human colon carcinoma cell) (Kim et al., 2007), MCF-7 (breast cancer cells) (Cao et al., 2010), and 95D (human lung cancer cell line) (Yin et al., 2013). Bacteriocin exerts its activity by inducing paraptosis, a planned cell death characterized by cytoplasmic vacuoles and swelling of the mitochondria and endoplasmic

reticulum (ER). It is comparable to cell necrosis, but necrosis is generally followed by blebbing of the cell membrane (Zhao et al., 2018). Kim et al. (2007) also reported that surfactin from *B. subtilis* has an anti-proliferation effect on LoVo cells by promoting proapoptotic activity and interrupting the cell cycle. Nevertheless, the effect was expected to increase if we prolonged the incubation time, such as up to 72 h. However, caution must be taken as normal cells might also be affected.

Potential Anti-Inflammatory Properties of ML-MFC-Treated DS

Protein denaturation has been linked to inflammation and the development of various inflammatory-associated-disorders (Osman et al., 2016). During protein denaturation, the biological characteristics of a protein are impaired, contributing to a disruption in its functional activity. Therefore, a BSA protein denaturation assay was performed to determine the potential of ML-MFC-treated DS in reducing protein denaturation and, hence, its ability to reduce inflammation. Interestingly, as *B. subtilis* has been supplemented as a catalyst in the ML-MFC treatment process, the macromolecules or metabolites secreted by *B. subtilis* may have some anti-inflammatory properties. As postulated, Figure 2 shows an increasing percentage of protein denaturation inhibition with increased treatment times, wherein 32.77% and 62.43% were recorded for T0 and T120, respectively. The high percentage of protein denaturation inhibition observed on day five is probably due to the increased metabolic rate of *B. subtilis*, which leads to the high secretion of macromolecules or metabolites with anti-inflammatory properties (Sabri et al., 2021).

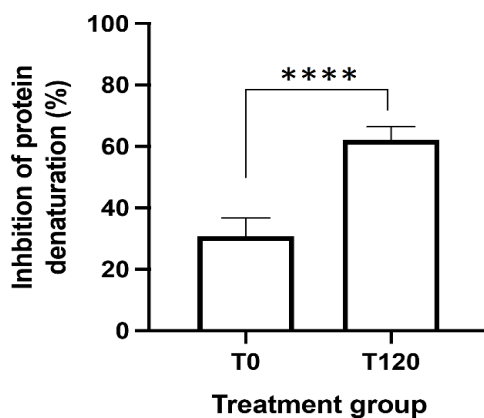


Figure 2. Protein Denaturation inhibition of ML-MFC-treated DS. An unpaired t-test was used to compare the means between groups with **** $p \leq 0.0001$. Values were expressed as the mean \pm standard deviation ($n=3$). T0: untreated DS at 0 h; T120: MFC-treated DS at 120 h.

Based on Figure 2, the T0 sample recorded a lower percentage of protein denaturation inhibition than the ML-MFC-treated DS. Nevertheless, treatments with ML-MFC significantly decreased protein denaturation compared to the untreated samples. The release of anti-inflammatory metabolites, EPS by *B. subtilis* that act as a catalyst during the ML-MFC treatment process might contribute to it. EPS are high-molecular-weight polymers produced by microorganisms outside their cell wall. EPS may stabilize the BSA protein by modifying its functional properties, leading to lower protein denaturation levels (Deep et al., 2012). It is supported by the high percentage of protein denaturation inhibition compared to the untreated.

ML-MFC Technology Promotes Bacteria Sensitivity Against Antibiotics

Eight types of antibiotics were involved in the testing, including streptomycin sulfate, kanamycin monosulphate, tetracycline free base, chloramphenicol, amoxicillin, penicillin G, and ampicillin. The distilled water and ethanol extract acted as the negative.

The diameter of the zone of inhibition (ZOI), in mm, for each antibiotic was measured and compared to the CLSI breakpoint criteria published by CLSI to determine the bacteria's susceptibility to specific antibiotics. Table 1 shows the size of the ZOI for each sample and control.

Table 1
Size of the zone of inhibition (ZOI) for negative control and different antibiotics

Group	Size of Zone of Inhibition (ZOI) (mm)		Antibiotic Resistance (Sensitive/Intermediate/Resistant)	
	Sample			
	T0	T120	T0	T120
	Mean ± S.D	Mean ± S.D		
Negative Control				
Distilled Water (DW)	-	-	-	-
Ethanol (EtOH)	-	-	-	-
Antibiotics				
Streptomycin sulfate (S)	20 ± 0	25 ± 1.41	Sensitive	Sensitive
Kanamycin mono sulfate (K)	28 ± 2.83	30 ± 2.83	Sensitive	Sensitive
Amoxicillin (AX)	20 ± 0	20 ± 0	Sensitive	Sensitive
Penicillin (P)	27 ± 1.41	33 ± 1.41	Resistant	Sensitive
Ampicillin (Amp)	-	24 ± 0	Resistant	Sensitive
Chloramphenicol (C)	33 ± 2.83	18 ± 0	Sensitive	Sensitive

Based on the disk diffusion antibiotic susceptibility test, the bacteria growth in the T0 and T120 samples were generally sensitive to Streptomycin sulfate (S), Kanamycin monosulphate (K), Amoxicillin (AX) and Chloramphenicol (C). It can be seen with a larger zone of inhibition around an antibiotic-containing disk than the standard zone of inhibition, indicating the presence of ARBs with ARGs (supplementary data). Interestingly, the bacterial colonies isolated from the T0 sample were shown resistance to both Penicillin (P) and Ampicillin (Amp). However, after treatment with ML-MFC, the bacteria found

in the T120 sample were susceptible to them, indicating that the ML-MFC technology is beneficial in reducing ARBs with ARGs, which could help reduce AMR distribution to the environment.

It is probably due to MFC's ability to break down antibiotics and ARGs, as proven by Ondon et al. (2020) and Xue et al. (2019), who found MFC technology to be able to remove 85.1% and 65.5% of sulfamethoxazole (SMX) and norfloxacin (NFLX), respectively. Additionally, the number of ARGs and integrons after MFC treatment was significantly less than that discovered in WWTPs. For example, the relative abundance of the *intI1* is between 63.11 and 652.00 copies/mL(g) in the MFC product compared to 109 to 1011 copies/mL in WWTPs (Chen et al., 2021; Mandal & Das, 2018).

MFC's ability to promote the susceptibility of certain bacteria in DS might also be due to the release of certain bacteriocin from *B. subtilis* that will help kill those ARBs (Joseph et al., 2013). Bacteriocins are a group of ribosomally synthesized antimicrobial peptides produced by bacteria, capable of controlling bacterial pathogens and clinically relevant susceptible and drug-resistant bacteria (Benitez-Chao et al., 2021). Alternatively, *B. subtilis* produces subtilin and subtilosin, which are active against many strains of gram-positive bacteria and act as antimicrobial or killing peptides, directly inhibiting competing strains or pathogens (Joseph et al., 2013).

Microbes Isolated from MFC-Treated DS and Its Potential as Anti-Inflammatory Agents

Four isolates were obtained from the T120 sample, and upon analysis, they were found to share more than 90% similarities with *Bacillus licheniformis* (*B. licheniformis*), *Bhargavaea beijingensis* (*B. beijingensis*), *Oceanobacillus caeni* (*O. caeni*) and *Oceanobacillus caeni* (*O. caeni*) (Table 2).

Interestingly, among these bacteria, *B. licheniformis* is known as one of the most important bacteria to produce bacitracin to combat pathogens, promote balance in the intestinal flora, and also enhance the nutritional quality of animal feeds (Lan & Kim, 2019; Wang et al., 2020). In addition, *B. licheniformis* has also been shown to exhibit anti-inflammatory properties by reducing the production of pro-inflammatory cytokines, Interleukin (IL)-8, upon induction with *Salmonella enterica* serovar Typhimurium (Aperce et al., 2010). Other microbes isolated from ML-MFC-treated DS were *B. beijingensis* and *O. caeni*. There were no reports on *O. caeni*'s benefits in regulating inflammation. However, interestingly, *B. beijingensis* DSM19038, isolated from the internal tissue of ginseng roots, was shown to affect nitrite production (Verma et al., 2012), suggesting its potential as an anti-inflammatory agent.

Intriguingly, the absence of isolated *B. subtilis* from the DS sample, particularly at T120, can be attributed to the complex and competitive nature of the microbial community present

within the DS. This environment fosters intense competition among various microorganisms for limited resources, potentially leading to the dominance of certain species (Bauer et al., 2018). Notably, it is conceivable that *B. licheniformis* could outcompete *B. subtilis* and other bacterial counterparts, further influencing the composition of the microbial community observed. This phenomenon underscores the dynamic interplay between microbial species within the DS ecosystem, where ecological factors and resource availability shape the prevalence of specific bacteria over others. In addition to the observed outcomes, there is potential for improvement by employing bacterial identification of the chosen isolates through 16S rRNA gene sequencing at multiple time points rather than solely relying on a single time point. This expanded approach would provide a more comprehensive understanding of the dynamic changes in the microbial composition within the DS ecosystem over time.

Table 2

16S rRNA identification of bacteria isolated from ML-MFC-treated DS at 120 h

Test strain	Representative species	Percentage similarity (%) (BLAST)	Query coverage (%)	Proven anti-inflammatory properties	References
A	<i>Bacillus licheniformis</i>	90.80	13	Decrease Salmonella-induced IL-8 secretion Improve subhealth state by reshaping gut microbiota, lowering inflammation, suppressing hypothalamic-pituitary-adrenal axis hyperactivity, regulating neurotransmitter levels, and relieving a negative mood. Enhance isovaleric acid in the colon, which alleviates abdominal pain and diarrhea.	Aperce et al. (2010); Feng et al. (2022); Lan and Kim (2019); Li et al. (2022); Roselli et al. (2017)

Table 2 (Continue)

Test strain	Representative species	Percentage similarity (%) (BLAST)	Query coverage (%)	Proven anti-inflammatory properties	References
B	<i>Bhargavaea beijingensis</i>	98.05	97	Positive for nitrite reduction	Verma et al. (2012)
C	<i>Oceanobacillus caeni</i>	97.69	94	N/A	
E	<i>Oceanobacillus caeni</i>	96.67	96	N/A	

Note. Not applicable denoted by N/A

CONCLUSION

To conclude, ML-MFC technology demonstrates remarkable anti-inflammatory properties in a time-dependent manner, exhibiting its highest inhibitory effect on protein denaturation (62.43%) at T120. Furthermore, this treatment successfully restored the sensitivity of previously resistant bacteria to penicillin and ampicillin. Additionally, ML-MFC-treated DS exhibited minimal cytotoxicity towards normal cells while demonstrating moderate effectiveness against cancer cells, thus indicating its potential as an anti-cancer agent. These noteworthy benefits may be attributed to the secretion of numerous metabolites, including but not limited to bacteriocins, subtilin, EPS, and subtilosin. However, further in-depth research, encompassing both *in vitro* and *in vivo* studies, is necessary to fully elucidate the underlying mechanisms responsible for these properties. Undoubtedly, this research holds significant promise for applications in healthcare and pharmaceuticals.

ACKNOWLEDGEMENT

This work was supported by Universiti Sains Malaysia (Apex ERA) (Grant numbers No. 1001.PTEKIND.881006) granted to Ana Masara Ahmad Mokhtar (AMAM), Universiti Sains Malaysia, Penang, Malaysia.

REFERENCES

- Al-Gheethi, A. A., Efaq, A. N., Bala, J. D., Norli, I., Abdel-Monem, M. O., & Ab. Kadir, M. O. (2018). Removal of pathogenic bacteria from sewage-treated effluent and biosolids for agricultural purposes. *Applied Water Science*, 8(2), Article 74. <https://doi.org/10.1007/s13201-018-0698-6>
- Alonso, E., Santos, A., & Riesco, P. (2004). Micro-organism re-growth in wastewater disinfected by UV radiation and ozone: A micro-biological study. *Environmental Technology*, 25(4), 433–441. <https://doi.org/10.1080/09593332508618452>

- Anderson, T. R., Hawkins, E., & Jones, P. D. (2016). CO₂, the greenhouse effect and global warming: From the pioneering work of Arrhenius and Callendar to today's Earth System Models. *Endeavour*, 40(3), 178–187. <https://doi.org/https://doi.org/10.1016/j.endeavour.2016.07.002>
- Aperce, C. C., Burkey, T. E., KuKanich, B., Crozier-Dodson, B. A., Dritz, S. S., & Minton, J. E. (2010). Interaction of *Bacillus* species and *Salmonella enterica* serovar Typhimurium in immune or inflammatory signaling from swine intestinal epithelial cells1. *Journal of Animal Science*, 88(5), 1649–1656. <https://doi.org/10.2527/jas.2009-2263>
- Bauer, M. A., Kainz, K., Carmona-Gutierrez, D., & Madeo, F. (2018). Microbial wars: Competition in ecological niches and within the microbiome. *Microbial Cell*, 5(5), 215-219. <https://doi.org/10.15698/mic2018.05.628>
- Benítez-Chao, D. F., León-Buitimea, A., Lerma-Escalera, J. A., & Morones-Ramírez, J. R. (2021). Bacteriocins: An overview of antimicrobial, toxicity, and biosafety assessment by *in vivo* models. *Frontiers in Microbiology*, 12, Article 630695. <https://doi.org/10.3389/fmicb.2021.630695>
- Cao, X. H., Wang, A. H., Wang, C. L., Mao, D. Z., Lu, M. F., Cui, Y. Q., & Jiao, R. Z. (2010). Surfactin induces apoptosis in human breast cancer MCF-7 cells through a ROS/JNK-mediated mitochondrial/caspase pathway. *Chemico-Biological Interactions*, 183(3), 357–362. <https://doi.org/10.1016/j.cbi.2009.11.027>
- Chen, P., Guo, X., Li, S., & Li, F. (2021). A review of the bioelectrochemical system as an emerging versatile technology for reduction of antibiotic resistance genes. *Environment International*, 156, Article 106689. <https://doi.org/10.1016/j.envint.2021.106689>
- CLSI. (2020). *Performance Standard for Antimicrobial Susceptibility Testing*. Clinical and Laboratory Standards Institute. <https://www.nih.org.pk/wp-content/uploads/2021/02/CLSI-2020.pdf>
- Deep, G., Hassan, A. N., & Metzger, L. (2012). Exopolysaccharides modify functional properties of whey protein concentrate. *Journal of Dairy Science*, 95(11), 6332–6338. <https://doi.org/10.3168/JDS.2012-5649>
- Feng, S., Meng, C., Hao, Z., & Liu, H. (2022). *Bacillus licheniformis* reshapes the gut microbiota to alleviate the subhealth. *Nutrients*, 14(8), Article 1642. <https://doi.org/10.3390/nu14081642>
- Gerba, C. P., & Pepper, I. L. (2009). Chapter 24 - Wastewater treatment and biosolids reuse. In R. M. Maier, I. L. Pepper & C. P. Gerba (Eds.), *Environmental Microbiology* (2nd ed.: pp. 503–530). Academic Press. <https://doi.org/https://doi.org/10.1016/B978-0-12-370519-8.00024-9>
- Górka, J., Cimochoicz-Rybicka, M., & Kryłów, M. (2018). Use of a water treatment sludge in a sewage sludge dewatering process. *E3S Web of Conferences*, 30, Article 02006. <https://doi.org/10.1051/e3sconf/20183002006>
- Hocking, L., Ali, G.-C., d'Angelo, C., Deshpande, A., Stevenson, C., Virdee, M., & Guthrie, S. (2021). A rapid evidence assessment exploring whether antimicrobial resistance complicates non-infectious health conditions and healthcare services, 2010–20. *JAC-Antimicrobial Resistance*, 3(4), dlab171. <https://doi.org/10.1093/jacamr/dlab171>
- Horiuchi, N., Nakagawa, K., Sasaki, Y., Minato, K., Fujiwara, Y., Nezu, K., Ohe, Y., & Saijo, N. (1988). *In vitro* antitumor activity of mitomycin C derivative (RM-49) and new anticancer antibiotics (FK973) against lung cancer cell lines determined by tetrazolium dye (MTT) assay. *Cancer Chemotherapy and Pharmacology*, 22(3), 246–250. <https://doi.org/10.1007/BF00273419>

- Joseph, B., Dhas, B., Hena, V., & Raj, J. (2013). Bacteriocin from *Bacillus subtilis* as a novel drug against diabetic foot ulcer bacterial pathogens. *Asian Pacific Journal of Tropical Biomedicine*, 3(12), 942–946. [https://doi.org/10.1016/S2221-1691\(13\)60183-5](https://doi.org/10.1016/S2221-1691(13)60183-5)
- Kim, S., Kim, J. Y., Kim, S.-H., Bae, H. J., Yi, H., Yoon, S. H., Koo, B. S., Kwon, M., Cho, J. Y., Lee, C. E., & Hong, S. (2007). Surfactin from *Bacillus subtilis* displays anti-proliferative effect via apoptosis induction, cell cycle arrest and survival signaling suppression. *FEBS Letters*, 581(5), 865–871. <https://doi.org/10.1016/j.febslet.2007.01.059>
- Kumar, V., & Chopra, A. K. (2016). Agronomical performance of high yielding cultivar of eggplant (*Solanum melongena* L.) grown in sewage sludge amended soil. *Research in Agriculture*, 1(1), 1-24. <https://doi.org/10.22158/ra.v1n1p1>
- Lan, R., & Kim, I. H. (2019). Effects of *Bacillus licheniformis* and *Bacillus subtilis* complex on growth performance and faecal noxious gas emissions in growing-finishing pigs. *Journal of the Science of Food and Agriculture*, 99(4), 1554–1560. <https://doi.org/10.1002/jsfa.9333>
- Lane, D. J. (1991). 16S/23S rRNA sequencing. In *Nucleic Acid Techniques in Bacterial Systematics* (pp. 115–175). John Wiley and sons.
- Li, Q., Li, L., Chen, Y., Yu, C., Azevedo, P., Gong, J., & Yang, C. (2022). *Bacillus licheniformis* PF9 improves barrier function and alleviates inflammatory responses against enterotoxigenic *Escherichia coli* F4 infection in the porcine intestinal epithelial cells. *Journal of Animal Science and Biotechnology*, 13(1), Article 86. <https://doi.org/10.1186/s40104-022-00746-8>
- Mahmoud, R. H., Gomaa, O. M., & Hassan, R. Y. A. (2022). Bio-electrochemical frameworks governing microbial fuel cell performance: Technical bottlenecks and proposed solutions. *RSC Advances*, 12(10), 5749–5764. <https://doi.org/10.1039/D1RA08487A>
- Mandal, S. K., & Das, N. (2018). Application of microbial fuel cells for bioremediation of environmental pollutants: An overview. *Journal of Microbiology, Biotechnology and Food Sciences*, 7(4), 437–444. <https://doi.org/10.15414/jmbfs.2018.7.4.437-444>
- Michael, C. A., Dominey-Howes, D., & Labbate, M. (2014). The antimicrobial resistance crisis: Causes, consequences, and management. *Frontiers in Public Health*, 2, Article 145. <https://doi.org/10.3389/fpubh.2014.00145>
- Makhtar, M. M. Z., & Tajarudin, H. A. (2020). Electricity generation using membrane-less microbial fuel cell powered by sludge supplemented with lignocellulosic waste. *International Journal of Energy Research*, 44(4), 3260–3265. <https://doi.org/10.1002/er.5151>
- Makhtar, M. M. Z., Tajarudin, H. A., Samsudin, M. D. M., Vadivelu, V. M., Shoparwe, N. F., & Zainuddin, N. 'Izzah. (2021). Membrane-less microbial fuel cell: Monte Carlo simulation and sensitivity analysis for COD removal in dewatered sludge. *AIP Advances*, 11(6), Article 065016. <https://doi.org/10.1063/5.0039014>
- Makhtar, M. M. Z., M., & Vadivelu, V. M. (2019). Membraneless microbial fuel cell: Characterization of electrogenic bacteria and kinetic growth model. *Journal of Environmental Engineering*, 145(5), Article 04019015. [https://doi.org/10.1061/\(ASCE\)EE.1943-7870.0001522](https://doi.org/10.1061/(ASCE)EE.1943-7870.0001522)

- Mokhtar, A. M. B. A., Makhtar, M. M. Z., & Mokhtar, A. M. A. (2022). Waste and health: Sewage sludge and its hazard to human. In A. Z. Yaser, H. A. Tajarudin & A. Embrandiri (Eds.), *Waste Management, Processing and Valorisation* (pp. 135–158). Springer. https://doi.org/10.1007/978-981-16-7653-6_8
- Muaz, M. Z. M., Abdul, R., & Vadivelu, V. M. (2019). Recovery of energy and simultaneous treatment of dewatered sludge using membrane-less microbial fuel cell. *Environmental Progress & Sustainable Energy*, 38(1), 208–219. <https://doi.org/10.1002/ep.12919>
- Obileke, K. C., Onyeaka, H., Meyer, E. L., & Nwokolo, N. (2021). Microbial fuel cells, a renewable energy technology for bio-electricity generation: A mini-review. *Electrochemistry Communications*, 125, Article 107003. <https://doi.org/10.1016/j.elecom.2021.107003>
- Ondon, B. S., Li, S., Zhou, Q., & Li, F. (2020). Simultaneous removal and high tolerance of norfloxacin with electricity generation in microbial fuel cell and its antibiotic resistance genes quantification. *Bioresource Technology*, 304, Article 122984. <https://doi.org/10.1016/j.biortech.2020.122984>
- Osińska, A., Korzeniewska, E., Harnisz, M., Felis, E., Bajkacz, S., Jachimowicz, P., Niestępski, S., & Konopka, I. (2020). Small-scale wastewater treatment plants as a source of the dissemination of antibiotic resistance genes in the aquatic environment. *Journal of Hazardous Materials*, 381, Article 121221. <https://doi.org/10.1016/j.jhazmat.2019.121221>
- Osman, N. I., Sidik, N. J., Awal, A., Adam, N. A. M., & Rezali, N. I. (2016). In vitro xanthine oxidase and albumin denaturation inhibition assay of *Barringtonia racemosa* L. and total phenolic content analysis for potential anti-inflammatory use in gouty arthritis. *Journal of Intercultural Ethnopharmacology*, 5(4), 343–349. <https://doi.org/10.5455/jice.20160731025522>
- Ouardani, I., Turki, S., Aouni, M., & Romalde, J. L. (2016). Detection and molecular characterization of hepatitis A virus from tunisian wastewater treatment plants with different secondary treatments. *Applied and Environmental Microbiology*, 82(13), 3834–3845. <https://doi.org/10.1128/AEM.00619-16>
- Padmanabhan, P., & Jangle, S. N. (2012). Evaluation of in-vitro anti-inflammatory activity of herbal preparation, a combination of four medicinal plants. *International Journal of Basic and Applied Medical Sciences*, 2(1), 109-116.
- Paynich, M. L., Jones-Burrage, S. E., & Knight, K. L. (2017). Exopolysaccharide from bacillus subtilis induces anti-inflammatory M2 macrophages that prevent T cell-mediated disease. *The Journal of Immunology*, 198(7), 2689–2698. <https://doi.org/10.4049/jimmunol.1601641>
- Rhayat, L., Maresca, M., Nicoletti, C., Perrier, J., Brinch, K. S., Christian, S., Devillard, E., & Eckhardt, E. (2019). Effect of bacillus subtilis strains on intestinal barrier function and inflammatory response. *Frontiers in Immunology*, 10, Article 564. <https://doi.org/10.3389/fimmu.2019.00564>
- Roselli, M., Pieper, R., Rogel-Gaillard, C., de Vries, H., Bailey, M., Smidt, H., & Lauridsen, C. (2017). Immunomodulating effects of probiotics for microbiota modulation, gut health and disease resistance in pigs. *Animal Feed Science and Technology*, 233, 104–119. <https://doi.org/10.1016/j.anifeedsci.2017.07.011>
- Sabri, M. N. I. M., Shamsuddin, N. A., Alias, M. F. A., Tajaruddin, H. A., & Makhtar, M. Z. (2021). Assessment of power generation from dewatered sludge using membrane-less microbial fuel cell. *IOP Conference Series: Earth and Environmental Science*, 765(1), Article 012060. <https://doi.org/10.1088/1755-1315/765/1/012060>

- Safuan, Z. M., Hassan, S., & Faizairi, M. (2014). Penerbit akademia baru thermal drying of Malaysian sewage sludge [Thermal drying of Malaysian sewage sludge]. *Journal of Advanced Research in Fluid Mechanics and Thermal Sciences ISSN*, 3(1), 2289–7879.
- Straub, T. M., Pepper, I. L., & Gerba, C. P. (1993). Hazards from pathogenic microorganisms in land-disposed sewage sludge. In G. W. Ware (Ed.), *Reviews of Environmental Contamination and Toxicology: Continuation of Residue Reviews* (pp. 55-91). Springer. https://doi.org/10.1007/978-1-4684-7065-9_3
- Sun, D., Jeannot, K., Xiao, Y., & Knapp, C. W. (2019). Editorial: Horizontal gene transfer mediated bacterial antibiotic resistance. *Frontiers in Microbiology*, 10, Article 1933. <https://doi.org/10.3389/fmicb.2019.01933>
- Verma, P., Pandey, P. K., Gupta, A. K., Seong, C. N., Park, S. C., Choe, H. N., Baik, K. S., Patole, M. S., & Shouche, Y. S. (2012). Reclassification of *Bacillus beijingensis* Qiu et al. 2009 and *Bacillus ginsengi* Qiu et al. 2009 as *Bhargavaea beijingensis* comb. nov. and *Bhargavaea ginsengi* comb. nov. and emended description of the genus *Bhargavaea*. *International Journal of Systematic and Evolutionary Microbiology*, 62(Pt_10), 2495–2504. <https://doi.org/10.1099/ijs.0.034850-0>
- Wang, S., Hou, Q., Guo, Q., Zhang, J., Sun, Y., Wei, H., & Shen, L. (2020). Isolation and characterization of a *Deoxyvalenol-Degrading Bacterium Bacillus licheniformis* YB9 with the capability of modulating intestinal microbial flora of mice. *Toxins*, 12(3), Article 184. <https://doi.org/10.3390/toxins12030184>
- Xue, W., Li, F., & Zhou, Q. (2019). Degradation mechanisms of sulfamethoxazole and its induction of bacterial community changes and antibiotic resistance genes in a microbial fuel cell. *Bioresource Technology*, 289, Article 121632. <https://doi.org/10.1016/j.biortech.2019.121632>
- Yacob, S., Ali Hassan, M., Shirai, Y., Wakisaka, M., & Subash, S. (2006). Baseline study of methane emission from anaerobic ponds of palm oil mill effluent treatment. *Science of the Total Environment*, 366(1), 187–196. <https://doi.org/10.1016/j.scitotenv.2005.07.003>
- Yin, H., Guo, C., Wang, Y., Liu, D., Lv, Y., Lv, F., & Lu, Z. (2013). Fengycin inhibits the growth of the human lung cancer cell line 95D through reactive oxygen species production and mitochondria-dependent apoptosis. *Anti-Cancer Drugs*, 24(6), 587–598. <https://doi.org/10.1097/CAD.0b013e3283611395>
- Zhao, H., Yan, L., Xu, X., Jiang, C., Shi, J., Zhang, Y., Liu, L., Lei, S., Shao, D., & Huang, Q. (2018). Potential of *Bacillus subtilis* lipopeptides in anti-cancer I: Induction of apoptosis and paraptosis and inhibition of autophagy in K562 cells. *AMB Express*, 8(1), 1-16. <https://doi.org/10.1186/s13568-018-0606-3>

Review Article

Weed Management Using UAV and Remote Sensing in Malaysia Paddy Field: A Review

Zaid Ramli¹, Abdul Shukor Juraimi^{1*}, Mst. Motmainna¹, Nik Norasma Che'Ya², Muhammad Huzaifah Mohd Roslim³, Nisfariza Mohd Noor⁴ and Anuar Ahmad⁵

¹Department of Crop Science, Faculty of Agriculture, Universiti Putra Malaysia, 43400 UPM Serdang, Selangor, Malaysia

²Department of Agriculture Technology, Faculty of Agriculture, Universiti Putra Malaysia, 43400 UPM Serdang, Selangor, Malaysia

³Department of Crop Science, Faculty of Agricultural and Forestry Sciences, Universiti Putra Malaysia Bintulu Sarawak Campus, 97008 Bintulu, Sarawak, Malaysia

⁴Department of Geography, Faculty of Arts and Social Sciences, Universiti Malaya, 50603 Kuala Lumpur, Malaysia

⁵Department of Geoinformation, Faculty of Built Environment & Surveying, Universiti Teknologi Malaysia, 81310 Johor Bahru, Johor, Malaysia

ABSTRACT

Controlling weed infestation is pivotal to achieving the maximum yield in paddy fields. At a time of exponential human population growth and depleting arable land mass, finding the solution to this problem is crucial. For a long time, herbicides have been the most favoured approach for weed control due to their efficacy and ease of application. However, adverse effects on the environment due to the excessive use of herbicides have prompted more cautious and effective herbicide usage. Many weed species tend to dominate the field, and the weed thrived in patches, rendering conventional broad herbicide spraying futile.

Site-specific weed management (SSWM) consists of two strategies: weed mapping and selective herbicide application. Since its introduction into the agriculture sector, unmanned aerial vehicles (UAV) have become the platform of choice for carrying both the remote sensing system for weed mapping and the selective application of herbicide. Red-Green-Blue (RGB), multispectral and hyperspectral sensors on UAVs enable highly accurate weed mapping. In Malaysia, adopting this technology is

ARTICLE INFO

Article history:

Received: 03 June 2023

Accepted: 20 November 2023

Published: 04 April 2024

DOI: <https://doi.org/10.47836/pjst.32.3.13>

E-mail addresses:

gs60804@student.upm.edu.my (Zaid Ramli)

ashukur@upm.edu.my (Abdul Shukor Juraimi)

motmainna@upm.edu.my (Mst. Motmainna)

niknorasma@upm.edu.my (Nik Norasma Che'Ya)

muhammadhuzaifah@upm.edu.my

(Muhammad Huzaifah Mohd Roslim)

nish@um.edu.my (Nisfariza Mohd Noor)

anuarahmad@utm.my (Anuar Ahmad)

*Corresponding author

highly possible, given the nature of government-administrated rice cultivation. This review provides insight into the weed management practice using remote sensing techniques on UAV platforms with potential applications in Malaysia's paddy field. It also discusses the recent works on weed mapping with imaging remote sensing on a UAV platform.

Keywords: Hyperspectral remote sensing, paddy field, unmanned aerial vehicle (UAV), weed management

INTRODUCTION

As the global population is fast approaching the 8 billion mark, ensuring sufficient food supply has become a top priority for the world economies. Rice (*Oryza sativa* L), which feeds half of the world's population daily, accounts for 20% of the annual cereal grain production (Cai et al., 2022). In Asian countries, the role of rice as the staple food is more monumental as it supplies an astounding 70% of the daily calorie need (Rahman & Zhang, 2022). According to the latest data, global rice production stood at 508.7 million tons (Nawaz et al., 2022).

Rice cultivation is one of the main agriculture sectors in Malaysia, apart from rubber and oil palm plantations (Sulaiman et al., 2022). Approximately one million people are directly employed under the rice cultivation ecosystem. In terms of daily consumption, Malaysia's average rice consumption per capita in 2016 stood at 80 kilograms per person (Abidin et al., 2022). It is equivalent to 2.7 million tons of rice requirement per year. However, as of 2020, the local rice production was insufficient to fulfil the demand, with a total production of only 1.51 million tons. This situation has caused Malaysia to depend on rice imports from Thailand, Vietnam, and Pakistan to compensate for the deficit.

Numerous efforts have been undertaken to increase the production of rice. However, the infestation of weeds has proven to be the main biological hindrance in achieving the full rice yield potential, reducing cultivation profitability. Weeds compete for nutrients, light, space and moisture (Hasan, Ahmad-Hamdani et al., 2021). The extent of damage caused by weeds in rice cultivation depends on several factors. Among the most prominent are the weed species, their density in the planting area, and the competition duration. Meanwhile, the weed type and its persistence are determined by the type of crop, climate and season, date of sowing, and the cultivating methodology.

The loss of rice production in Malaysia is mainly due to the weedy rice (*Oryza sativa* f. *spontanea* Roshev) species infestation (Motmainna et al., 2021a; Mispan et al., 2019). Similar to other developing countries that produce rice, the shift from planting techniques to direct seeding methods in the last 35 years has amplified the weedy rice infestation. Though it is estimated that the rice loss in Malaysia is between 10–15%, the final extent of the loss can be much higher depending on the infestation level. At a high infestation level, defined by the presence of 21–30 weedy rice panicles per square meter, the loss can

amount to 30% (Dilipkumar et al., 2021). In contrast, half of the cultivation can be lost once the infestation reaches a heavy level (≥ 31 panicles).

The control measures for weeds range from cultural, physical, biological and mechanical methods. However, chemical control involving the use of the herbicide has been preferred since it is the most effective and easiest to perform (Motmainna et al., 2021b; Hasan, Mokhtar et al., 2021). Herbicide is distinguished into different categories based on several criteria: its chemical family and formulation, mechanism of action, selectivity, site of uptake by the targeted weed, and based on its application times, whether it is pre-plant, pre-emergence or post-emergence (Monteiro & Santos, 2022). Unfortunately, excessive usage of herbicides causes harmful and detrimental environmental effects. Therefore, there is a need for a more sustainable weed management strategy.

Site-specific weed management (SSWM) is a method that enables accurate and site-specific application of herbicides on weeds of interest (Huang et al., 2020). It involves the process of weed mapping using specific remote sensing tools integrated into a suitable platform before the herbicide spraying process. Imaging remote sensors, namely Red-Green-Blue (RGB), multispectral, and hyperspectral, are the three different image sensors used widely in the agriculture industry (Roslim et al., 2021). Data gathered by the sensors is processed and interpreted by a suitable machine learning (ML) approach to produce a workable and precise weed mapping used for the site-specific herbicide application (Guo et al., 2022). Meanwhile, Unmanned Aerial Vehicles (UAVs) have gained attention among the available platforms for their brevity and precision (Monteiro & Santos, 2022). Through SSWM via remote sensing, the need for herbicide application can be determined based on the economic weed threshold, at which yield gain outweighed the overall cost of the chemical and its spraying operation. Numerous studies on cereals, maize, sugar, beat and peas have reported a 23–89% saving on herbicides (Gerhards et al., 2022). This paper reviews the weed problem involving rice plantations, with particular attention to weedy rice, and the solution via SSWM using remote sensing technology and the UAV platform for application in Malaysian rice fields.

RICE CULTIVATION IN MALAYSIA AND THE WEED PREDICAMENT

Rice is a seasonal crop with two cultivation cycles, with the first one beginning in April till September, followed by October and ending in March. A complete rice growth cycle lasts for 120-125 days. The cycle consists of three growth stages: (1) vegetative (1–41 days after planting), (2) reproductive (42–77 days), and (3) maturative (83–99 days). To boost rice production, Malaysia's government introduced a rice granary, arable land, with a centralised canal irrigation system that the federal government administrates (Ruzmi et al., 2021). To date, 12 rice granaries have been developed that cover a total area of 425,613 hectares. Most of the rice cultivation undertaken in Malaysia takes place in these granaries.

The manual rice transplanting method was used at the beginning of large-scale cultivation. Unfortunately, the shrinking workforce in the agriculture sector has made the transplanting method less practical (Alam et al., 2020). It is reported that the labour workforce has experienced a prolonged decline since the 1980s and eventually shrunk by 0.1% between 2010–2019 due to several factors, such as rapid urbanisation and an ageing farming population. The direct-seeded rice (DSR) technique was adopted to overcome this, in which the seed is sown directly into the soil (Shekhawat et al., 2020). Apart from requiring fewer workforces, it has become a method of choice since it is more rapid, has a low water requirement, and requires minimal mechanisation. It has also been reported that DSR experienced a 7–10 days early maturity (Nagargade et al., 2018). DSR has been adopted in Malaysia since the late 1980s (Ruzmi et al., 2021). In Asia, DSR is practised in 21% or 29 million hectares of the total cultivated area (Alam et al., 2020). Meanwhile, in Malaysia, due to the intensive adoption of mechanisation for rice cultivation, 90% of the total area is planted using DSR (Sulaiman et al., 2022).

In tropical Asian rice fields, yield loss caused by weeds is more significant than that caused by pathogens and insects. Rice is a naturally weak competitor and, under duress, will experience uneven flowering and non-uniform maturity. The severity of yield loss depends on the duration of competition with weed. Throughout the entire growth cycle, the first 41 days after sowing are the most critical, though keeping the cultivation free from weed for up to 70 days has been shown to guarantee a high yield (Shekhawat et al., 2020). If proper weed management is not practised during this critical period, yield loss could range from 15% to a complete loss (Busi et al., 2017). Major weed flora in DSR for the Asia region consists of 3 broad groups: grassy, sedges, and broadleaf (Table 1).

Table 1
Major weed species in Asia's rice field (Nagargade et al., 2018)

Grassy weeds	Sedges	Broadleaf weeds
<i>Digitaria setigera</i> Roth	<i>Cyperus iria</i> L.	<i>Commelina benghalensis</i> L.
<i>Digitaria sanguinalis</i> (L.) Scop.	<i>Cyperus difformis</i> L.	<i>Caesulia axillaris</i> Roxb.
<i>Digitaria ciliaris</i> (Retz.) Koeler	<i>Cyperus rotundus</i> L.	<i>Eclipta prostrata</i> (L.) L.
<i>Echinochloa colona</i> (L.) Link	<i>Fimbristylis miliacea</i> (L.) Vahl	<i>Ipomoea aquatica</i> Forssk.
<i>Echinochloa crus-galli</i> (L.) P. Beauv.		<i>Ludwigia octovalvis</i> (Jacq.) P. H. Raven
<i>Eleusine indica</i> (L.) Gaertn.		<i>Ludwigia adscendens</i> (L.) H. Hara
<i>Ischaemum rugosum</i> Salisb.		<i>Monochoria vaginalis</i> (Burm.f.) C. Presl

Table 1 (Continue)

Grassy weeds	Sedges	Broadleaf weeds
<i>Leptochloa chinensis</i> (L.) Nees <i>O. sativa</i> <i>Paspalum conjugatum</i> P. J.Bergius		<i>Sphenoclea zeylanica</i> Gaertn.

Despite its numerous advantages in advancing the rice cultivation sector, DSR has given rise to severe weed infestation worldwide. Due to prolonged and continuous DSR implementation, the original weed flora in Southeast Asia rice fields has shifted towards the more aggressive grassy and sedge weed species. The most notable species that has caused the most damage is the weedy rice, which belongs to the same genus and species as cultivated rice (Motmainna et al., 2021a). Severe weedy rice infestations have been reported in China, India, Bangladesh, Bhutan, Nepal, Sri Lanka, the Philippines, Vietnam, Thailand, Malaysia, and the USA. In Malaysia, weedy rice is known by its local name, *padi angin*, translated as wind rice, for its grains are often shattered by wind gusts (Motmainna et al., 2021c). The first case of weedy rice infestation was reported in 1988 in the Northwest Selangor Project rice field in Sekinchan (Mispan et al., 2019). It then spread to the rest of the rice granaries. In some of the granaries, an infestation rate of more than 50% of the total cultivated land has been reported. Weedy rice possessed numerous characteristics that made it possible for it to survive and thrive in the rice area. Morphologically, weedy rice is taller than cultivated rice, making it more efficient in capturing sunlight. It also has higher tillering when competing for space. The photosynthetic rate and the nitrogen uptake efficiency of weedy rice are also superior, depriving the cultivated rice of enough nutrients for growth. Higher stress tolerance is also associated with the weed plant (Motmainna et al., 2021d). The weedy rice seed has a faster germination rate and can stay dormant in the soil bed for a consecutively long period of up to 10 years.

Weed control is pivotal to ensure maximum yield and avoid crop destruction. Manual weed control, though effective, is not preferred on the commercial scale since it depends on a large labour workforce. Chemical control via herbicide is the most applied method in rice cultivation. Herbicide is a chemical substance formulated to pass through the plant's membrane surface and exerts toxic and lethal effects inside the cell (Hasan et al., 2022). Generally, there are two types of herbicides: (1) pre-emergence and (2) post-emergence with varying chemical active ingredients (Table 2). Pre-emergence is sprayed within three days following the seed sowing. As for the post-emergence herbicide, an early application takes place 10–12 days after sowing, while a late application is made 25–30 days after sowing.

Table 2

Commonly used herbicide in paddy fields based on the active ingredients (Hafeez-ur-Rehman et al., 2019; Shekhawat et al., 2020)

Pre-emergence	Trade name	Post-emergence	Trade name
Nitrofen	Tok E-25	Bispyribac sodium	Adora 10 SC
Butachlor	Machete	Pyrazosulfuron	Ojika
Pendimethalin	Stomp	Ethoxysulfuron	Sunrice
Thiobencarb	Bolero	Penoxsulam	Granite
Oxyflorfen	Goal	Glyphosate	Roundup
Oxadiazon	Ronstar	2,4-D	Weedar 64
Oxadiargyl	Topstar	Fenoxaprop	Acclaim Extra
Pretilachlor	Sofit	Azimsulfuron	Gulliver
Acetochlor	Harness	Propanil	Stamp F-34

Unfortunately, applying herbicides in agriculture is associated with various detrimental effects. It causes contamination to the soil surface, which, as a result, reduces soil microbial communities and earthworm populations. Consequently, the naturally occurring soil nutrient enrichment process is affected, and the overall soil biodiversity is altered. Herbicides can seep deep into the ground and contaminate the groundwater reservoir (Monteiro & Santos, 2022). The residue of the chemicals can also be traced in the food supply. Meanwhile, continuous application of similar herbicides on the same field site triggers weed flora shift and develops herbicide-resistance weeds (Motmainna et al., 2021e). The on-field growth pattern of the weed creates another challenge for an efficient application of the herbicide. Weed grows heterogeneously and is spread throughout the entire field in patches. Without proper weed control, the weed aggregates in the designated patches over time and eventually becomes dominant over the cultivated species. Furthermore, flat spraying, in which herbicide is sprayed indiscriminately on the entire field, contributes to the thriving of a specific weed flora on specific patches. Therefore, a more prudent way is required to achieve satisfactory control over the weed infestation via herbicide application.

SITE-SPECIFIC WEED MANAGEMENT WITH REMOTE SENSING AND UAV

A better chemical weed control strategy through herbicide application involves two strategies. The first is identifying and selecting the zones or patches inside the rice field that require herbicide spraying. Secondly, the herbicide is applied exclusively on the determined site. These strategies of weed identification and selective herbicide application are known as site-specific weed management (SSWM) (Eddy et al., 2014). Meanwhile, the economic weed threshold is the decision-making process that determines the necessary herbicide spraying. Herbicide is sprayed only when the expected yield increase following

the herbicide treatment exceeds the overall cost of the herbicide application. SSWM eliminates unnecessary herbicide usage, lowers production costs, and reduces contamination related to herbicides being released into the environment (Eddy et al., 2014). Remote sensing imaging technologies used in agriculture are the Red-Green-Blue (RGB) sensor, multispectral and hyperspectral.

Meanwhile, UAVs are becoming the preferred platform for carrying imaging sensors. It offers flexibility in its flying program due to its swift and fast deployment, which shortens the planning-to-flight time (Roslim et al., 2021). However, there are limitations related to UAVs in terms of their limited flight time and data processing speed (Huang, Reddy et al., 2018). Three operators are required to accomplish the surveying operation. First is a radio control pilot responsible for manually launching and landing the UAV and activating the flight path. The second ground station operator controls the UAV position, flying altitude, flight speed, wind speed, radio control signal quality and battery level. Finally, a third operator is a visual observer to assess possible collision and obstruction. When coupled with UAV, the surveying and documentation process consists of three phases: (1) pre-flight planning, (2) in-flight image acquisition, and (3) dataset extrapolation. Besides the surveying task, UAVs have also been utilised for selective herbicide spraying. A specified herbicide is applied directly to the weed patch, and excessive chemical usage can be avoided using data feed based on the weed mapping. The overall SSWM process is depicted in Figure 1.

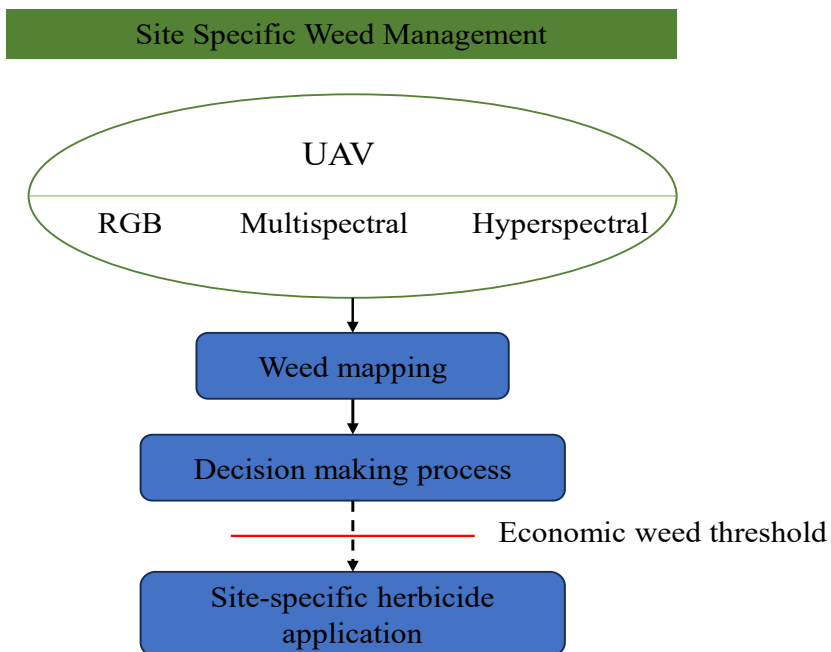


Figure 1. The overall process of site-specific weed management using herbicide via UAV and remote sensing

SSWM with remote sensing and UAV may solve the problem of weed infestation. However, the adoption rate of the technology for on-field applications is relatively slow. Economic feasibility, particularly the return on investment, is a critical factor that worsens the situation. There are costs associated with hardware and software procurement and data acquisition. In addition, a large land area of more than 500 hectares is required to make the technology economically feasible (Hunt & Daughtry, 2018). Other factors contributing to the low adoption rate are the farmer's age, educational background, and ownership status of the land.

AVAILABLE SENSORS FOR REMOTE SENSING

RGB Sensor

RGB is the most basic imaging remote sensing technology currently in use. A normal consumer camera with a red-green-blue visual spectrum can be readily utilised (Roslim et al., 2021). This type of sensor can measure vegetation indices (VI) such as the Greenness Index (GI), Excessive Greenness (EG), and Green/Red Vegetation Index (GRVI). RGB has the lowest cost and a shallow learning curve, making it easy for a novice to familiarise themselves and apprehend the process. Unlike the multispectral and hyperspectral sensors, RGB does not require radiometric calibration (Esposito et al., 2021). However, it is susceptible to low lighting conditions. Moreover, the ability of RGB to distinguish the weed from the cultivated plant depends on the degree of apparent and significant disparity between both plants (Zhang et al., 2019).

Before the flight, parameters such as the area coverage, flight altitude, topography, weather conditions and any related local regulations have to be determined (Esposito et al., 2021). During the flight, the operator needs to ensure that sufficient data is gathered to produce meaningful analysis. During the third phase, the individual images collected undergo rectification before being stitched together to generate a single image (orthomosaic) of the covered study area. The orthomosaic image can be represented by either the RGB values or the intended VI. In the broad agriculture application, the RGB sensor has been used to type the phenotypic features of plants such as the flower, fruit, branch, and trunk. In addition, information such as the leaf count, shape, colour, position and overall plant size has also been gathered via the RGB sensory process (Roslim et al., 2021). Meanwhile, the UAV-mounted RGB has been utilised for several purposes, such as producing the field map, identifying plants that experienced abiotic stress, and performing biomass estimation.

Multispectral Sensor

Multispectral sensor imagery ranges from 5–12 radiometric bands and can detect spectra in the visible spectrum and near-infrared region. Due to the additional bands,

the range of VI that a multispectral sensor can monitor is expanded compared to an RGB sensor (Esposito et al., 2021). Multispectral sensor requires radiometric calibration and atmospheric correction. Unlike the RGB sensor, which captures images, the multispectral sensor records the radiance from the field and converts it to digital numbers (Tu et al., 2018). The digital numbers are not exactly representative of the surface reflectance since the light illumination condition, and the consistency of the sensor influence the recorded numbers. Therefore, radiometric calibration is a prerequisite to obtaining consistent spectral information throughout the entire area of mapping. During the flight, the sensor will gather a high dataset volume. Input/output errors and missing data must be avoided to ensure sufficient and satisfactory data can be collected (Esposito et al., 2021). Finally, multiple images collected are rectified and georeferenced before they are stacked together to produce a single image with varying radiometric levels.

VI are algebraic combinations of several spectra at particular bands that indicate vegetation vigour and properties. Since the reflectance in the near-infrared region is more abundant than in the visible spectrum, many non-visible recognitions, such as early-stage plant disease and soil water content, can be harnessed (Esposito et al., 2021). Moreover, the accuracy of VI generated by the multispectral sensor is superior to the RGB sensor (Furukawa et al., 2021).

Hyperspectral Sensor

The hyperspectral sensor differs from the multispectral sensor in terms of the number of spectral bands and the bandwidth (Adão et al., 2017). The total number of spectral bands in hyperspectral imaging can extend to the thousands range with a bandwidth ranging from 5–20 nm, respectively. The enormous dataset gathered from the almost continuous spectra of the hyperspectral sensor enables a more in-depth and specific field characteristic compared to the multispectral sensor (Esposito et al., 2021). Processes and steps involved during the three phases of flight operation are almost similar to the multispectral sensor; however, they are more complex due to the greater complexity of the hyperspectral technology. Through hyperspectral imagery, narrowband VI, such as modified vegetation stress ratio (MVSR), transformed chlorophyll absorption ratio index (TCARI), and modified soil-adjusted vegetation index (MSAVI), can be calculated (Adão et al., 2017).

MACHINE LEARNING FOR WEED IDENTIFICATION

The initial step of a successful SSWM with remote sensing is detecting and recognizing weeds. The sensors' massive data must be processed to produce a workable and accurate weed mapping. Machine learning (ML), a subset of artificial intelligence, uses the current high computing performance to interpret the big data generated (Benos et al., 2021). ML involves a computer learning process based on data input without strict programming

limitations (Liakos et al., 2018). The learning process occurs via various machine learning models and algorithms, and the performance of the ML process is validated using appropriate statistical measures.

ML is widely applied in various precision agriculture practices, including weed management. A typical ML takes place in four steps: data input, data pre-processing, model building, and generalisation (Sharma et al., 2021), as shown in Figure 2. The performance of ML improved over time with a gain in new data and experience, making it possible for the model and algorithm to come up with better and correct predictions (Domingos, 2012).

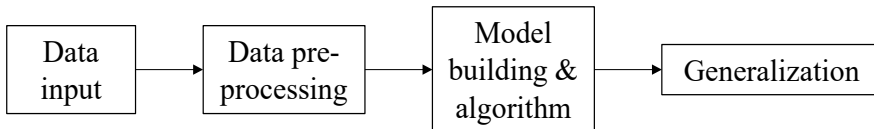


Figure 2. A general machine learning approach

RECENT PROGRESS ON WEED MAPPING VIA IMAGING REMOTE SENSING

The first part of a successful SSWM strategy is identifying and locating the weed infestation site and determining the necessity of selective herbicide application. Countless research on SSWM via remote sensing has been reported using multiple platforms. However, there is an increasing preference for UAVs as the platform of choice. Here, the latest works on this specific subject are compiled to present the current progress (Table 3). Only publications dated from 2018 are included in the compilation.

RGB sensors dominate the research realm regarding weed mapping using UAVs. Although a multispectral sensor is more stable and relatively unaffected by the surrounding conditions, it is more expensive than RGB. The RGB sensor's performance can be improved by modifying the camera. The near-infrared filter can be replaced with a red filter to make it more sensitive to the near-infrared spectrum (Maes & Steppe, 2019). Weed detection on the field can be achieved by employing two approaches. The first is detection via row crops, and the second is through spectral discrimination. In the first approach, the weed that flourishes between the row crops can be detected and identified through advanced algorithms analysis, most notably OBIA methodology that identifies spatially and spectrally similar objects through adjacent pixel grouping. Modified RGB cameras have been utilised for inter-row weed detection with high overall accuracy (Maes & Steppe, 2019). However, this approach is less effective in detecting weeds growing within the crop rows and for high-density crop cultivation such as wheat.

In the spectral discrimination approach, the weed is distinguished from the crop through disparity in the spectral signal (Maes & Steppe, 2019). Differential spectral-based discrimination allows for mapping multiple weeds (Eide et al., 2021). Multispectral and

hyperspectral sensors work on this principle. Modified RGB cameras exhibited the same property; however, simultaneous detection of multiple weeds has yielded a low accuracy due to the limited number of spectral bands available. Several studies were done with multispectral, including on rice, where discrimination of barnyard and common purslane weeds was achieved with 94% accuracy (Stroppiana et al., 2018). However, only works on maize were reported for the hyperspectral sensor. One of the stumbling blocks hampering the progress of hyperspectral imagery-related research is the substantial cost of procuring the sensors. One unit of hyperspectral sensor would cost USD 175,000, compared to a multispectral sensor that costs just around USD 6,000. Moreover, accurate quantification of spectral indices of crops and weeds can be obtained through the cheaper multispectral sensor (Askari et al., 2019). An inherent limitation associated with the hyperspectral image is that it captures images at a low spatial and temporal resolution. This phenomenon occurs because the hyperspectral sensor captures images in a very narrow wavelength band, consequently limiting the number of photons able to imp the sensor per unit of time.

Furthermore, the instability of the sensor during the flight due to the vibrating nature of the UAV has further worsened the problem (Esposito et al., 2021). Regardless of the limitation, there has been a study to distinguish rice, weedy rice and barnyard grass based on spectral recognition using hyperspectral line-scanning images (Zhang et al., 2019). As a result, six wavelengths (415 nm, 561 nm, 687 nm, 705 nm, 735 nm, and 1007 nm) have been identified as the most important spectral features that enabled weedy rice and barnyard grass discrimination with 100% accuracy.

Table 3
Recent works on weed mapping with imaging remote sensing on a UAV platform

Type of sensor	Crops	Vegetation / spectral indices	Flying altitude (m)	Scopes and main findings	References
		Not applicable	0.8 – 1.2	Weed (<i>Sagittaria trifolia</i> L.) identification. Weed mapping through the FCN method. Accuracy of 92.7%	Ma et al. (2019)
		ExG, ExR, GRVI, CIVE	20	Spatial weed distribution. Accuracy of 91.5%	Kawamura et al. (2021)
		Not applicable	6	Weed mapping through FCN. Accuracy of 88.3%	Huang et al. (2018b)
RGB	Rice	Not applicable	10	Weed mapping comparison between OBIA and FCN methods. FCN performs better in terms of accuracy (83.3% vs 72.2%)	Huang et al. (2020)
		Not applicable	6	Weed (<i>L. chinensis</i> and <i>C. iria</i>) mapping via FCN. Accuracy of 94%	Huang, Lan et al. (2018)

Table 3 (Continue)

Type of sensor	Crops	Vegetation / spectral indices	Flying altitude (m)	Scopes and main findings	References
		Not applicable	6	Real-time image processing onboard a UAV using the FCN method. Accuracy of 80.9%	Deng et al. (2020)
		Not applicable	10	Weed (<i>L. chinensis</i> and <i>C. iria</i>) mapping via FCN. Accuracy of 86%	Huang et al. (2018a)
	Oat	VARI, GLI, NGRDI, BI, CI, RI	10	Weed mapping. Accuracy of 87.1 – 89%	Gašparović et al. (2020)
		ExG, ExR, ExGR	30	Weed mapping through the OBIA method. Overall accuracy of 83%	Mateen (2019)
	Wheat	Not applicable	1–6	Individual classification of 4 types of weeds: <i>Matricaria chamomilla</i> L., <i>Papaver rhoeas</i> L., <i>Veronica hederifolia</i> L., <i>Viola arvensis</i> Murray., <i>Arvensis</i> using the DCNN method. Overall accuracy of 94%.	de Camargo et al. (2021)
RGB		Not applicable	20	Weed against soybean mapping using the CNN method. Accuracy of 0.66	Sivakumar et al. (2020)
	Soybean	Not applicable	4	The existing imagery dataset was analysed using two established CNN methods and three custom CNNs. Custom 5-layer CNN has the highest accuracy at 97.7%, with the lowest latency and memory usage.	Razfar et al. (2022)
		Not applicable	4	Classification of soybean, grass and broadleaf weed. Overall accuracy of 99.4%	Haq (2021)
	Marigold	ExG, ExR, ExGR	20	Weed mapping and corresponding density on field infested with green bristlegrass, milkweed and sedge. The accuracy of weed mapping was 93.5%. The accuracy for weed density was 0.94.	Zou et al. (2021)

Table 3 (Continue)

Type of sensor	Crops	Vegetation / spectral indices	Flying altitude (m)	Scopes and main findings	References
RGB	Bean spinach	ExG	20	Weed mapping using a similar CNN method on two crops on different fields. Overall accuracy of 0.95	Bah et al. (2018)
	Sunflower & cotton	Not applicable	30 & 60	Early season weed mapping against two types of crops of different fields using a similar OBIA method. Accuracy of 81% (sunflowers) and 84% (cotton).	de Castro et al. (2018)
	Beet, parsley & spinach	Not applicable	20 & 30	Weed discrimination using the CNN method. Overall accuracy of 99%	Reedha et al. (2022)
	Pea & strawberry	Not applicable	2	Weed mapping using GAN method. Accuracy of 90% and comparable to the CNN method	Khan et al. (2021)
	Grassland	Not applicable	10	Mapping of <i>Rumex obtusifolius</i> L. from production grasslands via CNN method. 90% accuracy	Valente et al. (2019)
		Not applicable	10 & 20	Mapping of <i>R. obtusifolius</i> by combining OBIA and CNN method. Accuracy of 92.1%	Lam et al. (2021)
		Not applicable	25	Weed mapping through the CNN method. Overall accuracy of 87%	Pei et al. (2022)
	Maize	ExG	20	Weed mapping via OBIA with an accuracy of 0.945	Gao et al. (2018)
		Not applicable	Variable height	Weed mapping with augmented data via CNN method. Improved accuracy to 95.7% from 92.9%	Bullock et al. (2019)
	Tobacco	Not applicable	4	Weed mapping through 2-stage segmentation CNN. Improved accuracy from 0.76 (single stage segmentation) to 0.91 (two-stage)	Moazzam et al. (2023)
	Sesame	Not applicable	5	Mapping of weed using the newly established CNN method. Accuracy of 96.7%	Moazzam et al. (2022)
		Not applicable	120-240	Weed mapping through Mask R-CNN with augmented data. Accuracy of 0.803	Mini et al. (2020)

Table 3 (Continue)

Type of sensor	Crops	Vegetation / spectral indices	Flying altitude (m)	Scopes and main findings	References
		ExG	125-200	Comparison of weed mapping accuracy between machine learning and CNN method. CNN performed slightly better	Júnior et al. (2020)
	Wheat, maize & peanut	Not applicable	2	Mapping of three weeds: <i>Chenopodium album</i> L., <i>Humulus scandens</i> (Lour.) Merr., <i>Xanthium sibiricum</i> Patr. ex Widder on three separate farmlands. Weed mapping was generated using the CNN method. Overall accuracy of 99.39% (RGB) and 99.53% (MS). Weed density accuracy was near the Ground truth values	Wang et al. (2022)
RGB & multispectral	Maise & sugar beet	NDVI (multispectral) & ExGR (RGB)	15 & 30	Mapping of creeping thistle and curled dock by combining data set from RGB and multispectral. Accuracy of 96% (maise) and 80% (sugar beetz)	Mink et al. (2018)
	Winter wheat	Not applicable	45	Large scale mapping of blackgrass from 31 fields (205 hectares) using the CNN method with an accuracy of above 0.9	Fraccaro et al. (2022)
RGB & multispectral	Maise & sugar beet	NDVI (multispectral) & ExGR (RGB)	15 & 30	Mapping of creeping thistle and curled dock by combining data set from RGB and multispectral. Accuracy of 96% (maise) and 80% (sugar beetz)	Mink et al. (2018)
	Winter wheat	Not applicable	45	Large scale mapping of blackgrass from 31 fields (205 hectares) using the CNN method with an accuracy of above 0.9	Fraccaro et al. (2022)
	Rice	SAVI, NDVI, RGRI, CVI, NDRE	70	Distinguishing <i>Echinochloa</i> spp. and <i>Portulaca oleracea</i> L.). Overall accuracy of 94%	Stroppiana et al. (2018)
		NDVI	60	Weed mapping on cultivated rice field	Rosle et al. (2022)

Table 3 (Continue)

Type of sensor	Crops	Vegetation / spectral indices	Flying altitude (m)	Scopes and main findings	References
Multispectral	Maise	NDVI	50	Weed mapping of <i>C. album</i> and <i>Cirsium arvense</i> (L.) Scop. Accuracy of 80%	Louargant et al. (2017)
	Wheat	18 Vis were adopted, with the best performing being TGI	20	Mapping of <i>Alopecurus myosuroides</i> Huds. infecting wheat fields. Overall accuracy of 93%	Su et al. (2022)
	Soybean	NDVI	10	Detecting and mapping glyphosate resistance weeds of kochia, ragweed and amaranth after glyphosate application. The highest mapping accuracy scores were attained after 8 days of application. Respective accuracy score: kochia (0.752), ragweed (0.872), and amaranth (0.935)	Eide et al. (2021)
	Sorghum	Not applicable	10–38	Spectral data of sorghum and 6 types of weeds were collected with a handheld hyperspectral device. Data from identified bands were loaded into a multispectral sensor on a UAV for field surveying. Successful identification of sorghum, amaranth, liver seed grass, mallow weed, and nutgrass.	Che'ya et al. (2021)
	Green onion	Not applicable	4–5	Weed detection using CNN based on images curated from a video recording. Accuracy of 93.81%	Parico and Ahamed (2020)
	Sugar beet	NDVI	10	Production of high-resolution weed mapping on large area coverage using DNN. Accuracy of 0.782	Sa et al. (2018)
Hyperspectral		CNORM, GRDB, OSAVI	30	Maise field infested with 5 weeds. Analysis based on chlorophyll and carotenoid leaf behaviour. Introduction of two new spectral indices. Successful mapping of maise, Amaranthus and Cyperus-based on comparison with ground-based dry biomass and LAI index	Pignatti et al. (2019)
	Maise	CNORM, GRDB	30	Broad discrimination between weed and crop and dataset analysis using 3 methods. Amaranthus and Cyperus can be separated from maise using the CNORM/GRDB index and CNN methods. The quality of spectral images was compromised due to the instability of the UAV during the image-taking process	Casa et al. (2019)

SELECTIVE HERBICIDE SPRAYING USING UAV

The final strategy for a successful SSWM with herbicide is the ability to selectively apply a specific herbicide on weed patches based on the information relayed by the weed mapping. UAV has been widely employed for this purpose. Generally, there are three types of UAVs: fixedwing, single rotor, and multiple rotors (Hanif et al., 2022). As for the multiple rotors UAV, the naming is based on the number of rotors: quadcopter (4 rotors), hexacopter (6 rotors) and octocopter (8 rotors). Multirotor is the most employed UAV in agricultural practices, with the quadcopter being the most preferred due to its greater stability (Rahman et al., 2021). UAVs allow selective herbicide spraying and expedite the application process, vital in large-scale cultivation where timely herbicide application is vital. The simultaneous deployment of multiple drones has also been explored to fulfil the timely herbicide spraying requirement (Chen et al., 2022). UAVs used in SSWM are equipped with numerous technological features, namely Global Positioning System (GPS), automatic path planning, high accuracy positioning, obstacle avoidance ability, real-time kinematics, automatic spraying system, and pulse width modulation system.

However, using UAV for herbicide spraying on the field is associated with drift and downwash airflow of the herbicide droplets associated with the vortex pulse created by the rotor. Consequently, uniform droplet deposition, the key to successful herbicide application, is not achieved (Hao et al., 2022). Studies have been done to minimise or eliminate the drift and downwash effects by studying the spraying parameters, such as the droplet size and the spraying rate (Chen et al., 2020). Apart from the spraying parameters, the droplet deposition is also influenced by several other factors: the UAV flight condition (altitude and speed), environmental factors (humidity, temperature, and wind speed), and the liquid properties (type and concentration) (Hao et al., 2022).

CONCLUSION AND FUTURE PROSPECT

Weed infestation will continue to become one of the biggest hurdles in achieving maximum crop production. SSWM is a formidable approach to solving the weed predicament. The induction of remote sensing and UAV as part of the SSWM strategy has offered a promising solution for the ongoing weed infestation. Implementing this technology in Malaysia's rice field can increase rice production and reduce its dependency on rice imports. Nevertheless, research related to this technology in Malaysia is either non-existent or insufficient to provide insight into its real-time application on local climate and conditions. Therefore, research is imperative to implementing this technology in Malaysia's paddy field.

ACKNOWLEDGEMENTS

The authors are grateful to the Research Project entitled "Pest and Disease Monitoring Using Artificial Intelligence for Risk Management of Rice Under Climate Change" under the Long-term Research Grant Scheme (LRGS), Ministry of Higher Education, Malaysia

(LRGS/1/2019/UPM01/2/5; vote number: 5545002) also sincerely acknowledges the University Putra Malaysia for providing facilities.

REFERENCES

- Abidin, I. S. Z., Haseeb, M., Islam, R., & Chiat, L. W. (2022). Role of technology adoption, labor force and capital formation on the rice production in Malaysia. *AgBioForum*, *24*(1), 41–49.
- Adão, T., Hruška, J., Pádua, L., Bessa, J., Peres, E., Morais, R., & Sousa, J. J. (2017). Hyperspectral imaging: A review on UAV-based sensors, data processing and applications for agriculture and forestry. *Remote Sensing*, *9*(11), Article 1110. <https://doi.org/10.3390/rs9111110>
- Alam, M. K., Bell, R. W., Hasanuzzaman, M., Salahin, N., Rashid, M. H., Akter, N., Akhter, S., Islam, M. S., Islam, S., Naznin, S., Anik, M. F. A., Mosiur Rahman Bhuyin Apu, M., Saif, H. Bin, Alam, M. J., & Khatun, M. F. (2020). Rice (*Oryza sativa* L.) establishment techniques and their implications for soil properties, global warming potential mitigation and crop yields. *Agronomy*, *10*(6), Article 888. <https://doi.org/10.3390/agronomy10060888>
- Askari, M. S., McCarthy, T., Magee, A., & Murphy, D. J. (2019). Evaluation of grass quality under different soil management scenarios using remote sensing techniques. *Remote Sensing*, *11*(15), Article 1835. <https://doi.org/10.3390/rs11151835>
- Benos, L., Tagarakis A. C., Dolias G., Berruto R., Kateris D., & Bochtis D. (2021) Machine learning in agriculture: A comprehensive updated review. *Sensors*, *21*(11), Article 3758. <https://doi.org/10.3390/s21113758>
- Bullock, D., Mangeni, A., Kolkman, J. M., Nelson, R. J., & Gore, M. A. (2019). *Automated weed detection in aerial imagery with context*. ArXiv Preprint. <https://doi.org/10.48550/arXiv.1910.00652>
- Busi, R., Nguyen, N. K., Chauhan, B. S., Vidotto, F., Tabacchi, M., & Powles, S. B. (2017). Can herbicide safeners allow selective control of weedy rice infesting rice crops? *Pest Management Science*, *73*(1), 71–77. <https://doi.org/10.1002/ps.4411>
- Cai, C., Yang, H., Zhang, L., & Cao, W. (2022). Potential yield of world rice under global warming based on the ARIMA-TR model. *Atmosphere*, *13*(8), Article 1336. <https://doi.org/10.3390/atmos13081336>
- Casa, R., Pascucci, S., Pignatti, S., Palombo, A., Nanni, U., Harfouche, A., Laura, L., Di Rocco, M., & Fantozzi, P. (2019). UAV-based hyperspectral imaging for weed discrimination in maize. In J. V. Stafford (Ed.), *Precision Agriculture 2019* (pp. 365-371). Wageningen Academic Publishers. https://doi.org/10.3920/978-90-8686-888-9_45
- Che'ya, N. N., Dunwoody, E., & Gupta, M. (2021). Assessment of weed classification using hyperspectral reflectance and optimal multispectral UAV imagery. *Agronomy*, *11*(7), Article 1435. <https://doi.org/10.3390/agronomy11071435>
- Chen, P., Ouyang, F., Zhang, Y., & Lan, Y. (2022). Preliminary evaluation of spraying quality of multi-unmanned aerial vehicle (UAV) close formation spraying. *Agriculture*, *12*(8), Article 1149. <https://doi.org/10.3390/agriculture12081149>

- Chen, S., Lan, Y., Zhou, Z., Ouyang, F., Wang, G., Huang, X., Deng, X., & Cheng, S. (2020). Effect of droplet size parameters on droplet deposition and drift of aerial spraying by using plant protection UAV. *Agronomy*, *10*(2), Article 195. <https://doi.org/10.3390/agronomy10020195>
- de Camargo, T., Schirrmann, M., Landwehr, N., Dammer, K. H., & Pflanz, M. (2021). Optimized deep learning model as a basis for fast UAV mapping of weed species in winter wheat crops. *Remote Sensing*, *13*(9), Article 1704. <https://doi.org/10.3390/rs13091704>
- de Castro, A. I., Torres-Sánchez, J., Peña, J. M., Jiménez-Brenes, F. M., Csillik, O., & López-Granados, F. (2018). An automatic random forest-OBIA algorithm for early weed mapping between and within crop rows using UAV imagery. *Remote Sensing*, *10*(2), Article 285. <https://doi.org/10.3390/rs10020285>
- Deng, J., Zhong, Z., Huang, H., Lan, Y., Han, Y., & Zhang, Y. (2020). Lightweight semantic segmentation network for real-time weed mapping using unmanned aerial vehicles. *Applied Sciences*, *10*(20), Article 7132. <https://doi.org/10.3390/app10207132>
- Bah, M. D., Hafiane, A., & Canals, R. (2018). Deep learning with unsupervised data labeling for weed detection in line crops in UAV images. *Remote Sensing*, *10*(11), Article 1690. <https://doi.org/10.3390/rs10111690>
- Dilipkumar, M., Ahmad-Hamdani, M. S., Rahim, H., Chuah, T. S., & Burgos, N. R. (2021). Survey on weedy rice (*Oryza* spp.) management practice and adoption of Clearfield® rice technology in Peninsular Malaysia. *Weed Science*, *69*(5), 558–564. <https://doi.org/10.1017/wsc.2021.16>
- Domingos, P. (2012). A few useful things to know about machine learning. *Communications of the ACM*, *55*(10), 78-87. <https://doi.org/10.1145/2347736.2347755>
- Eddy, P. R., Smith, A. M., Hill, B. D., Peddle, D. R., Coburn, C. A., & Blackshaw, R. E. (2014). Weed and crop discrimination using hyperspectral image data and reduced bandsets. *Canadian Journal of Remote Sensing*, *39*(6), 481–490. <https://doi.org/10.5589/m14-001>
- Eide, A., Koparan, C., Zhang, Y., Ostlie, M., Howatt, K., & Sun, X. (2021). UAV-Assisted thermal infrared and multispectral imaging of weed canopies for glyphosate resistance detection. *Remote Sensing*, *13*(22), Article 4606. <https://doi.org/10.3390/rs13224606>
- Esposito, M., Crimaldi, M., Cirillo, V., Sarghini, F., & Maggio, A. (2021). Drone and sensor technology for sustainable weed management: A review. *Chemical and Biological Technologies in Agriculture*, *8*(1), 1–11. <https://doi.org/10.1186/s40538-021-00217-8>
- Fraccaro, P., Butt, J., Edwards, B., Freckleton, R. P., Childs, D. Z., Reusch, K., & Comont, D. (2022). A deep learning application to map weed spatial extent from unmanned aerial vehicles imagery. *Remote Sensing*, *14*(17), Article 973. <https://doi.org/10.3390/rs14174197>
- Furukawa, F., Laneng, L. A., Ando, H., Yoshimura, N., Kaneko, M., & Morimoto, J. (2021). Comparison of RGB and multispectral unmanned aerial vehicle for monitoring vegetation coverage changes on a landslide area. *Drones*, *5*(3), Article 97. <https://doi.org/10.3390/drones5030097>
- Gao, J., Liao, W., Nuyttens, D., Lootens, P., Vangeyte, J., Pižurica, A., He, Y., & Pieters, J. G. (2018). Fusion of pixel and object-based features for weed mapping using unmanned aerial vehicle imagery. *International Journal of Applied Earth Observation and Geoinformation*, *67*, 43–53. <https://doi.org/10.1016/j.jag.2017.12.012>

- Gašparović, M., Zrinjski, M., Barković, Đ., & Radočaj, D. (2020). An automatic method for weed mapping in oat fields based on UAV imagery. *Computers and Electronics in Agriculture*, *173*, Article 105385. <https://doi.org/10.1016/j.compag.2020.105385>
- Gerhards, R., Andújar Sanchez, D., Hamouz, P., Peteinatos, G. G., Christensen, S., & Fernandez-Quintanilla, C. (2022). Advances in site-specific weed management in agriculture - A review. *Weed Research*, *62*(2), 123–133. <https://doi.org/10.1111/wre.12526>
- Guo Y, Chen S, Li X, Cunha M, Jayavelu S, Cammarano D, Fu Y. (2022). Machine learning-based approaches for predicting SPAD values of maize using multi-spectral images. *Remote Sensing*, *14*(6), Article 1337. <https://doi.org/10.3390/rs14061337>
- Hanif, A. S., Han, X., & Yu, S. H. (2022). Independent control spraying system for UAV-based precise variable sprayer: A review. *Drones*, *6*(12), Article 383. <https://doi.org/10.3390/drones6120383>
- Hao, Z., Li, M., Yang, W., & Li, X. (in press). Evaluation of UAV spraying quality based on 1D-CNN model and wireless multi-sensors system. *Information Processing in Agriculture*. <https://doi.org/10.1016/j.inpa.2022.07.004>
- Haq, M. A. (2021). CNN based automated weed detection system using UAV imagery. *Computer Systems Science and Engineering*, *42*(2), 837–849. <https://doi.org/10.32604/csse.2022.023016>
- Hasan, M., Mokhtar, A. S., Mahmud, K., Berahim, Z., Rosli, A. M., Hamdan, H., Motmainna, M., & Ahmad-Hamdani, M. S. (2022). Physiological and biochemical responses of selected weed and crop species to the plant-based bioherbicide WeedLock. *Scientific Reports*, *12*(1), Article 19602. <https://doi.org/10.1038/s41598-022-24144-2>
- Hasan, M., Ahmad-Hamdani, M. S., Rosli, A. M., & Hamdan, H. (2021). Bioherbicides: An eco-friendly tool for sustainable weed management. *Plants*, *10*(6), Article 1212. <https://doi.org/10.3390/plants10061212>
- Hasan, M., Mokhtar, A. S., Rosli, A. M., Hamdan, H., Motmainna, M., & Ahmad-Hamdani, M. S. (2021). Weed control efficacy and crop-weed selectivity of a new bioherbicide WeedLock. *Agronomy*, *11*(8), Article 1488. <https://doi.org/10.3390/agronomy11081488>
- Huang, H., Deng, J., Lan, Y., Yang, A., Deng, X., Wen, S., Zhang, H., & Zhang, Y. (2018a). Accurate weed mapping and prescription map generation based on fully convolutional networks using UAV imagery. *Sensors*, *18*(10), Article 3299. <https://doi.org/10.3390/s18103299>
- Huang, H., Deng, J., Lan, Y., Yang, A., Deng, X., & Zhang, L. (2018b). A fully convolutional network for weed mapping of unmanned aerial vehicle (UAV) imagery. *PLoS ONE*, *13*(4), Article e0196302. <https://doi.org/10.1371/journal.pone.0196302>
- Huang, H., Lan, Y., Deng, J., Yang, A., Deng, X., Zhang, L., & Wen, S. (2018). A semantic labeling approach for accurate weed mapping of high resolution UAV imagery. *Sensors*, *18*(7), Article 2113. <https://doi.org/10.3390/s18072113>
- Huang, Y., Reddy, K. N., Fletcher, R. S., & Pennington, D. (2018). UAV low-altitude remote sensing for precision weed management. *Weed Technology*, *32*(1), 2–6. <https://doi.org/10.1017/wet.2017.89>
- Huang, H., Lan, Y., Yang, A., Zhang, Y., Wen, S., & Deng, J. (2020). Deep learning versus object-based image analysis (OBIA) in weed mapping of UAV imagery. *International Journal of Remote Sensing*, *41*(9), 3446–3479. <https://doi.org/10.1080/01431161.2019.1706112>

- Hunt, E. R., & Daughtry, C. S. T. (2018). What good are unmanned aircraft systems for agricultural remote sensing and precision agriculture? *International Journal of Remote Sensing*, 39(15–16), 5345–5376. <https://doi.org/10.1080/01431161.2017.1410300>
- Júnior, P. C. P., Monteiro, A., Ribeiro, R. da L., Sobieranski, A. C., & von-Wangenheim, A. (2020). Comparison of classical computer vision vs. Convolutional neural networks for weed mapping in aerial images. *Revista de Informatica Teorica e Aplicada*, 27(4), 20–33. <https://doi.org/10.22456/2175-2745.97835>
- Kawamura, K., Asai, H., Yasuda, T., Soisouvanh, P., & Phongchanmixay, S. (2021). Discriminating crops/weeds in an upland rice field from UAV images with the SLIC-RF algorithm. *Plant Production Science*, 24(2), 198–215. <https://doi.org/10.1080/1343943X.2020.1829490>
- Khan, S., Tufail, M., Khan, M. T., Khan, Z. A., Iqbal, J., & Alam, M. (2021). A novel semi-supervised framework for UAV based crop/weed classification. *PLoS ONE*, 16(5), Article e0251008. <https://doi.org/10.1371/journal.pone.0251008>
- Lam, O. H. Y., Dogotari, M., Prüm, M., Vithlani, H. N., Roers, C., Melville, B., Zimmer, F., & Becker, R. (2021). An open source workflow for weed mapping in native grassland using unmanned aerial vehicle: Using *Rumex obtusifolius* as a case study. *European Journal of Remote Sensing*, 54(sup1), 71–88. <https://doi.org/10.1080/22797254.2020.1793687>
- Liakos, K. G., Busato, P., Moshou, D., Pearson, S., & Bochtis, D. (2018) Machine learning in agriculture: A review. *Sensors*, 18(8), 2674. <https://doi.org/10.3390/s18082674>
- Louargant, M., Villette, S., Jones, G., Vigneau, N., Paoli, J. N., & Gée, C. (2017). Weed detection by UAV: Simulation of the impact of spectral mixing in multispectral images. *Precision Agriculture*, 18(6), 932–951. <https://doi.org/10.1007/s11119-017-9528-3>
- Ma, X., Deng, X., Qi, L., Jiang, Y., Li, H., Wang, Y., & Xing, X. (2019). Fully convolutional network for rice seedling and weed image segmentation at the seedling stage in paddy fields. *PLoS ONE*, 14(4), Article e0215676. <https://doi.org/10.1371/journal.pone.0215676>
- Maes, W. H., & Steppe, K. (2019). Perspectives for Remote Sensing with Unmanned Aerial Vehicles in Precision Agriculture. *Trends in Plant Science*, 24(2), 152–164. <https://doi.org/10.1016/j.tplants.2018.11.007>
- Mateen, A. (2019). Weed detection in wheat crop using UAV for precision agriculture. *Pakistan Journal of Agricultural Sciences*, 56(03), 775–784. <https://doi.org/10.21162/pakjas/19.8036>
- Mini, G. A., Oliva Sales, D., & Luppe, M. (2020, December 16-18). *Weed segmentation in sugarcane crops using Mask R-CNN through aerial images*. [Paper presentation]. International Conference on Computational Science and Computational Intelligence (CSCI), Las Vegas, USA. <https://doi.org/10.1109/CSCI51800.2020.00088>
- Mink, R., Dutta, A., Peteinatos, G. G., Sökefeld, M., Engels, J. J., Hahn, M., & Gerhards, R. (2018). Multi-temporal site-specific weed control of *Cirsium arvense* (L.) scop. and *Rumex crispus* L. in maize and sugar beet using unmanned aerial vehicle based mapping. *Agriculture*, 8(5), Article 65. <https://doi.org/10.3390/agriculture8050065>
- Mispan, M. S., Bzoor, M. I., Mahmud, I. F., Md-Akhir, A. H. B., & Zulrushdi, A. Q. (2019). Managing weedy rice (*Oryza sativa* L.) in Malaysia: Challenges and ways forward. *Journal of Research in Weed Science*, 2, 149–167. <https://doi.org/10.26655/JRWEEDSCI.2019.3.6>

- Moazzam, S. I., Khan, U. S., Qureshi, W. S., Nawaz, T., & Kunwar, F. (2023). Towards automated weed detection through two-stage semantic segmentation of tobacco and weed pixels in aerial Imagery. *Smart Agricultural Technology*, 4, Article 100142. <https://doi.org/10.1016/j.atech.2022.100142>
- Moazzam, S. I., Khan, U. S., Qureshi, W. S., Tiwana, M. I., Rashid, N., Hamza, A., Kunwar, F., & Nawaz, T. (2022). Patch-wise weed coarse segmentation mask from aerial imagery of sesame crop. *Computers and Electronics in Agriculture*, 203, Article 107458. <https://doi.org/10.1016/j.compag.2022.107458>
- Monteiro, A., & Santos, S. (2022). Sustainable approach to weed management: The role of precision weed management. *Agronomy*, 12(1), Article 118. <https://doi.org/10.3390/agronomy12010118>
- Motmainna, M., Juraimi, A. S., Uddin, M. K., Asib, N. B., Islam, A. K. M. M., & Hasan, M. (2021a). Allelopathic potential of Malaysian invasive weed species on Weedy rice (*Oryza sativa* f. *spontanea* Roshev). *Allelopathy Journal*, 53, 53-68. <https://doi.org/10.26651/allelo.j/2021-53-1-1327>
- Motmainna, M., Juraimi, A. S., Uddin, M. K., Asib, N. B., Islam, A. K. M. M., & Hasan, M. (2021b). Bioherbicidal properties of *Parthenium hysterophorus*, *Cleome rutidosperma* and *Borreria alata* extracts on selected crop and weed species. *Agronomy*, 11(4), Article 643. <https://doi.org/10.3390/agronomy11040643>
- Motmainna, M., Juraimi, A. S., Uddin, M. K., Asib, N. B., Islam, A. K. M. M., & Hasan, M. (2021c). Assessment of allelopathic compounds to develop new natural herbicides: A review. *Allelopathy Journal*, 52, 21-40. <https://doi.org/10.26651/allelo.j/2021-52-1-1305>
- Motmainna, M., Juraimi, A. S., Uddin, M. K., Asib, N. B., Islam, A. K. M. M., Ahmad-Hamdani, M.S., Berahim, Z., & Hasan, M. (2021d). Physiological and Biochemical Responses of *Ageratum conyzoides*, *Oryza sativa* f. *spontanea* (Weedy Rice) and *Cyperus iria* to *Parthenium hysterophorus* Methanol Extract. *Plants*, 10(6), Article 1205. <https://doi.org/10.3390/plants10061205>
- Motmainna, M., Juraimi, A. S., Uddin, M. K., Asib, N. B., Islam, A. M., Ahmad-Hamdani, M. S., & Hasan, M. (2021e). Phytochemical constituents and allelopathic potential of *Parthenium hysterophorus* L. in comparison to commercial herbicides to control weeds. *Plants*, 10(7), Article 1445. <https://doi.org/10.3390/plants10071445>
- Nagargade, M., Singh, M., & Tyagi, V. (2018). Ecologically sustainable integrated weed management in dry and irrigated direct-seeded rice. *Advances in Plants & Agriculture Research*, 8(3), 319-331. <https://doi.org/10.15406/apar.2018.08.00333>
- Nawaz, A., Rehman, A. U., Rehman, A., Ahmad, S., Siddique, K. H. M., & Farooq, M. (2022). Increasing sustainability for rice production systems. *Journal of Cereal Science*, 103, Article 103400. <https://doi.org/10.1016/j.jcs.2021.103400>
- Parico, A. I. B., & Ahamed, T. (2020). An aerial weed detection system for green onion crops using the you only look once (YOLOv3) deep learning algorithm. *Engineering in Agriculture, Environment and Food*, 13(2), 42–48. https://doi.org/10.37221/eaef.13.2_42
- Pei, H., Sun, Y., Huang, H., Zhang, W., Sheng, J., & Zhang, Z. (2022). Weed detection in maize fields by UAV images based on crop row preprocessing and improved YOLOv4. *Agriculture*, 12(7), Article 975. <https://doi.org/10.3390/agriculture12070975>
- Pignatti, S., Casa, R., Harfouche, A., Huang, W., Palombo, A., & Pascucci, S. (2019, July 18-August 2). *Maize crop and weeds species detection by using UAV VNIR hyperpectral data*. [Paper presentation].

- International Geoscience and Remote Sensing Symposium (IGARSS), Yokohama, Japan. <https://doi.org/10.1109/IGARSS.2019.8900241>
- Rahman, A. N. M. R. B., & Zhang, J. (2022). Trends in rice research: 2030 and beyond. *Food and Energy Security, 12*(2), Article e390. <https://doi.org/10.1002/fes3.390>
- Rahman, M. F. F., Fan, S., Zhang, Y., & Chen, L. (2021). A comparative study on application of unmanned aerial vehicle systems in agriculture. *Agriculture, 11*(1), Article 22. <https://doi.org/10.3390/agriculture11010022>
- Razfar, N., True, J., Bassiouny, R., Venkatesh, V., & Kashef, R. (2022). Weed detection in soybean crops using custom lightweight deep learning models. *Journal of Agriculture and Food Research, 8*, Article 100308. <https://doi.org/10.1016/j.jafr.2022.100308>
- Reedha, R., Dericquebourg, E., Canals, R., & Hafiane, A. (2022). Transformer neural network for weed and crop classification of high resolution UAV images. *Remote Sensing, 14*(3), Article 592. <https://doi.org/10.3390/rs14030592>
- Rosle, R., Sulaiman, N., Che'Ya, N. N., Radzi, M. F. M., Omar, M. H., Berahim, Z., Ilahi, W. F. F., Shah, J. A., & Ismail, M. R. (2022). Weed detection in rice fields using UAV and multispectral aerial imagery. *Chemistry Proceedings, 10*(1), Article 44. <https://doi.org/10.3390/IOCAG2022-12519>
- Roslim, M. H. M., Juraimi, A. S., Che'ya, N. N., Sulaiman, N., Manaf, M. N. H. A., Ramli, Z., & Motmainna, M. (2021). Using remote sensing and an unmanned aerial system for weed management in agricultural crops: A review. *Agronomy, 11*(9), Article 1809. <https://doi.org/10.3390/agronomy11091809>
- Ruzmi, R., Ahmad-Hamdani, M. S., Abidin, M. Z. Z., & Roma-Burgos, N. (2021). Evolution of imidazolinone-resistant weedy rice in Malaysia: The current status. *Weed Science, 69*(5), 598–608. <https://doi.org/10.1017/wsc.2021.33>
- Sa, I., Popović, M., Khanna, R., Chen, Z., Lottes, P., Liebisch, F., Nieto, J., Stachniss, C., Walter, A., & Siegwart, R. (2018). WeedMap: A large-scale semantic weed mapping framework using aerial multispectral imaging and deep neural network for precision farming. *Remote Sensing, 10*(9), Article 1423. <https://doi.org/10.3390/rs10091423>
- Sharma, A., Jain, A., Gupta, P., & Chowdary, V. (2020). Machine learning applications for precision agriculture: A comprehensive review. *IEEE Access, 9*, 4843–4873. <https://doi.org/10.1109/ACCESS.2020.3048415>
- Shekhawat, K., Rathore, S. S., & Chauhan, B. S. (2020). Weed management in dry direct-seeded rice: A review on challenges and opportunities for sustainable rice production. *Agronomy, 10*(9), Article 1264. <https://doi.org/10.3390/agronomy10091264>
- Sivakumar, A. N. V., Li, J., Scott, S., Psota, E., Jhala, A. J., Luck, J. D., & Shi, Y. (2020). Comparison of object detection and patch-based classification deep learning models on mid-to late-season weed detection in UAV imagery. *Remote Sensing, 12*(13), Article 2136. <https://doi.org/10.3390/rs12132136>
- Stroppiana, D., Villa, P., Sona, G., Ronchetti, G., Candiani, G., Pepe, M., Busetto, L., Migliazzi, M., & Boschetti, M. (2018). Early season weed mapping in rice crops using multi-spectral UAV data. *International Journal of Remote Sensing, 39*(15–16), 5432–5452. <https://doi.org/10.1080/01431161.2018.1441569>
- Su, J., Yi, D., Coombes, M., Liu, C., Zhai, X., McDonald-Maier, K., & Chen, W. H. (2022). Spectral analysis and mapping of blackgrass weed by leveraging machine learning and UAV multispectral imagery. *Computers and Electronics in Agriculture, 192*, Article 106621. <https://doi.org/10.1016/j.compag.2021.106621>

- Sulaiman, N., Norasma, N., Ya, C., Huzaifah, M., Roslim, M., Juraimi, A. S., Noor, N. M., Fazilah, W., & Ilahi, F. (2022). The application of hyperspectral remote sensing imagery (HRSI) for weed detection analysis in rice fields. A review. *Applied Sciences*, *12*(5), Article 2570. <https://doi.org/10.3390/app12052570>
- Tu, Y. H., Phinn, S., Johansen, K., & Robson, A. (2018). Assessing radiometric correction approaches for multi-spectral UAS imagery for horticultural applications. *Remote Sensing*, *10*(11), Article 1684. <https://doi.org/10.3390/rs10111684>
- Valente, J., Doldersum, M., Roers, C., & Kooistra, L. (2019). Detecting Rumex obtusifolius weed plants in grasslands from UAV RGB imagery using deep learning. *ISPRS Annals of the Photogrammetry, Remote Sensing and Spatial Information Sciences*, *4*, 179-185. <https://doi.org/10.5194/isprs-annals-IV-2-W5-179-2019>
- Wang, S., Han, Y., Chen, J., He, X., Zhang, Z., Liu, X., & Zhang, K. (2022). Weed density extraction based on few-shot learning through UAV remote sensing RGB and multispectral images in ecological irrigation area. *Frontiers in Plant Science*, *12*, Article 735230. <https://doi.org/10.3389/fpls.2021.735230>
- Zhang, Y., Gao, J., Cen, H., Lu, Y., Yu, X., He, Y., & Pieters, J. G. (2019). Automated spectral feature extraction from hyperspectral images to differentiate weedy rice and barnyard grass from a rice crop. *Computers and Electronics in Agriculture*, *159*, 42–49. <https://doi.org/10.1016/j.compag.2019.02.018>
- Zou, K., Chen, X., Zhang, F., Zhou, H., & Zhang, C. (2021). A field weed density evaluation method based on uav imaging and modified u-net. *Remote Sensing*, *13*(2), Article 310. <https://doi.org/10.3390/rs13020310>

SPICE Modeling and Performance Analysis of Enhancement-Mode GaN HEMTs for Augmented Hard-Switching Energy Conversion Efficiency

Xinzhi Liu^{1,2}, Suhaidi Shafie^{1,3,4*}, Mohd Amran Mohd Radzi^{1,2}, Norhafiz Azis^{1,2}, Nurbahirah Norddin¹, Ismail Lawal³, Normaziah Zulkifli² and Abdul Hafiz Abdul Karim^{1,2}

¹Department of Electrical and Electronic Engineering, Faculty of Engineering, Universiti Putra Malaysia, 43400 UPM Serdang, Selangor, Malaysia

²Advanced Lightning, Power, and Energy Research (ALPER) Centre, Universiti Putra Malaysia, 43400 UPM Serdang, Selangor, Malaysia

³Institute of Nanoscience and Nanotechnology, Universiti Putra Malaysia, 43400 UPM Serdang, Selangor, Malaysia

⁴Institute of Nano Electronic Engineering, Universiti Malaysia Perlis, 01007 Kangar, Malaysia

ABSTRACT

The advancement of renewable energy sources necessitates the development of effective power electronic devices. Enhancement-mode Gallium Nitride (E-GaN) high-electron-mobility transistors (HEMTs), an emerging wide-bandgap semiconductor device, demonstrate potential in photovoltaic (PV) energy converting applications to enhance power transfer efficiency. This paper discusses the enhanced semiconducting characteristics of GaN HEMT over conventional silicon power devices by analyzing spontaneous and piezoelectric polarizations of wurtzite GaN crystalline structure and the formation of two-dimensional electron gas (2DEG). The lateral device structure of E-GaN HEMT and normally

switched-on depletion mode GaN HEMT are compared. A device-under-test (DUT) equivalent model incorporating parasitic components is proposed, adopting the EPC2204 Level 3 SPICE model. The model is simulated in a novel Double Pulse Test (DPT) topology with clamping and snubber subcircuits using LTSPICE software. The performance of GaN E-HEMT is compared to a MOSFET with similar parameters, and the impact of parasitic inductances and stray capacitances is evaluated through switching

ARTICLE INFO

Article history:

Received: 07 June 2023

Accepted: 27 November 2023

Published: 04 April 2024

DOI: <https://doi.org/10.47836/pjst.32.3.14>

E-mail addresses:

berryxinzhi@hotmail.com (Xinzhi Liu)

suhaidi@upm.edu.my (Suhaidi Shafie)

amranmr@upm.edu.my (Mohd Amran Mohd Radzi)

norhafiz@upm.edu.my (Norhafiz Azis)

gs65460@student.upm.edu.my (Nurbahirah Norddin)

ismo4faty2015@gmail.com (Ismail Lawal)

normaziah@upm.edu.my (Normaziah Zulkifli)

akahafiz@unimas.my (Abdul Hafiz Abdul Karim)

*Corresponding author

analysis. Findings support the potential of E-GaN HEMTs and indicate the DC-DC converter design considerations for portable solar PV system applications.

Keywords: DPT, E-GaN HEMT, parasitic inductance, power electronics, SPICE modeling, switching power losses

INTRODUCTION

Renewable energy development has significant implications for the global environment and economy. Among various sources, solar energy presents a promising solution for diverse applications (Ahmad et al., 2011). The escalating demand for sustainable and efficient energy conversion and transfer has spurred the need for innovative semiconductor devices and technologies in power electronics for renewable energy applications. Nonetheless, conventional silicon-based power semiconductors, such as Metal Oxide Silicon Field Effect Transistors (MOSFETs), which are frequently employed in DC renewable energy power electronic systems, exhibit constraints in power density, on-resistance, temperature resilience, and switching speeds (Roccaforte et al., 2018). These limitations lead to considerable power switching losses and protracted switching response times. To overcome these obstacles, wide bandgap semiconductor devices, especially Gallium Nitride (GaN) and Silicon Carbide (SiC), have emerged as popular substitutes for solid-state device operation under high voltage and power conditions (Chow, 2015; Jones et al., 2016). As illustrated in Figure 1, GaN demonstrates superior material properties in comparison to silicon (Si), encompassing a higher electric critical breakdown field, energy bandgap, saturated electron velocity, and electron mobility.

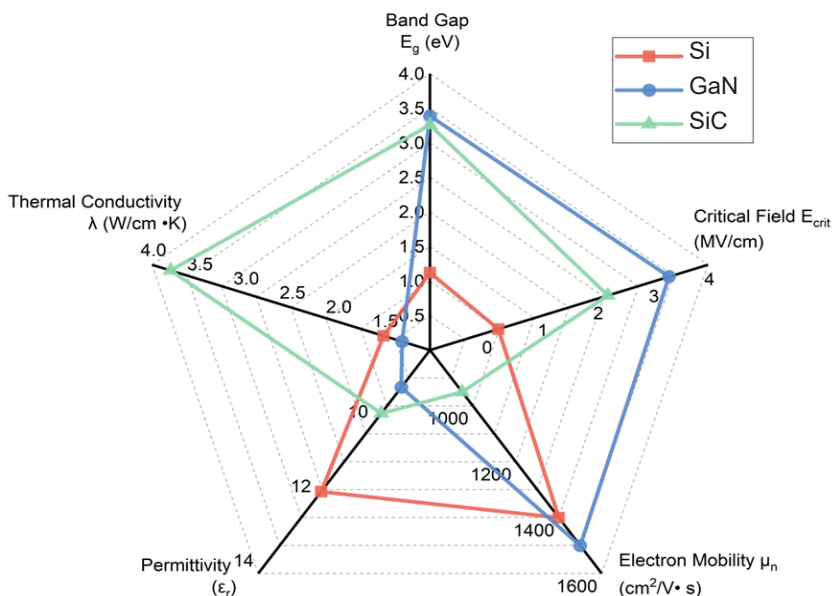


Figure 1. Properties of GaN comparing with Si and SiC

This numerical value in the bandgap signifies the energy level disparity between the valence and conduction bands, closely related to how strong the atomic bonds within the lattice are. These stronger connections imply that it will be more challenging for electrons to move between sites. It leads to lower intrinsic leakage currents and higher operating temperatures for semiconductors with greater band gaps, making it possible for them to have smaller depletion areas and produce device architectures with many carriers. These architectures have little resistance and capacitance because they have smaller transistors and shorter current channels. These qualities enable devices to operate at speeds up to 100 times quicker than those of conventional designs (Lidow et al., 2019). As indicated by the data presented in Figure 1, GaN exhibits a larger bandgap compared to silicon, which is advantageous for high voltage and power applications.

Moreover, the more robust chemical bonds, which contribute to an increased bandgap, also necessitate a greater critical electric field to instigate impact ionization, thereby leading to a heightened breakdown voltage. This relationship can be articulated through the subsequent Equation 1.

$$V_{BD} = \frac{1}{2} w_{drift} \cdot E_{critical} \tag{1}$$

The device's breakdown voltage (V_{BD}) is consequently proportional to the drift region's width (W_{drift}) and the critical breakdown field ($E_{critical}$). GaN could feature a drift area that is an order of magnitude smaller than silicon while maintaining an equivalent breakdown voltage. Carriers must exist in the drift area and be depleted when the device reaches the required field to sustain this electric field. This feature emphasizes a significant benefit for devices with exhibited elevated critical fields. The one-dimensional simplified form of Poisson's equation under constant relative permittivity could be potentially employed to determine the number of electrons between two terminals (presuming an N-type doped device, most carriers are electrons) (Equations 2 & 3).

$$\frac{d^2V_{BD}}{dw_{drift}^2} = - \frac{q \cdot N}{\epsilon_0 \cdot \epsilon_r} \tag{2}$$

$$q \cdot N = \epsilon_0 \cdot \epsilon_r \cdot \frac{E_{critical}}{w_{drift}} \tag{3}$$

Within Equations 2 and 3, q represents the electron's charge ($1.602 \times 10^{-19}C$), N denotes the aggregate numbers of electrons in the device dimensions, ϵ_0 signifies the vacuum permittivity ($8.854 \times 10^{-12}F/m$), and ϵ_r corresponds to the relative permittivity as compared to the vacuum. Under stable direct current (DC) conditions, permittivity is identical to the crystal's dielectric constant. The charge density in the drift area must be much higher, according to the second-order derivative connection between the electric potential and the width of the drift region. This fundamental principle underpins the superior semiconducting performance of GaN over Silicon in power conversion applications. Nonetheless, GaN

exhibits inferior thermal conductivity in comparison to Silicon. Incorporating GaN semiconductors in power electronic applications directed at renewable energy sources requires striking a balance between material attributes to ensure exceptional performance and considerable downsizing of passive and magnetic constituents.

In this paper, the GaN crystalline and the GaN HEMT device structures, including depletion-mode GaN (D-GaN), the gate injection transistor (GIT) E-GaN, and Schottky E-GaN, are primarily introduced. Secondly, the HEMT DUT circuit topology with parasitic components is then developed. Furthermore, LTSPICE simulation software is utilized, integrating the GaN E-HEMT manufacturer model for optimal switching performance analysis against a comparable MOSFET. Finally, the DUT model is combined with the designed DPT circuit to investigate the effects of parasitic inductances and stray capacitances.

PROPERTIES OF GAN HEMT

Wurtzite GaN Polarization and 2DEG Generation

GaN, a widely investigated III-V binary compound wide bandgap semiconductor material, predominantly exhibits a wurtzite crystal structure under standard conditions, making it a prime candidate for semiconducting applications. As illustrated in Figure 2, created using VESTA 3D visualization software, this stable structure, identifiable by its unique hexagonal lattice, leads to superior growth quality and electrical properties, particularly on the c-plane (0001), widely employed in HEMT applications. Alternative planes, such as the non-polar (1120) and semi-polar (1011), offer potential advantages like mitigating piezoelectric polarization effects, thus reducing defect impacts and improving device performance. The inherent polarization of the wurtzite structure contributes to GaN's superior conductivity over silicon, further enhanced by its notable chemical stability and thermal resilience.

Wurtzite GaN compounds exhibit spontaneous polarization due to electronegativity variations in their constituent atoms, which depends on the crystal growth direction. Piezoelectric polarization, on the other hand, arises from mechanical strain when two materials with different lattice constants coalesce. This strain triggers a slight atomic shift within the lattice, creating an electric field. The extent of polarization is directly linked to the in-plane strain and is determined by the mismatch in lattice constants (Wonglakhon & Zahn, 2020).

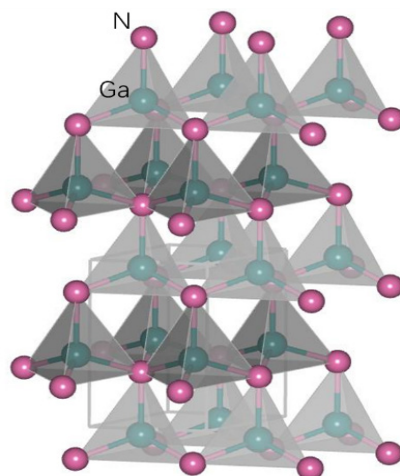


Figure 2. Wurtzite GaN crystal structure

Based on the intrinsic property of GaN, by incorporating a heterostructure comprising a thin, high electron mobility material layer of Aluminum Gallium Nitride (AlGa_N), strain is then introduced at the contact, producing a two-dimensional electron gas (2DEG) that compensates at the interface (Delagebeaudeuf & Linh, 1982). Electrons can be successfully conducted when an electric field is placed over this 2DEG. The confinement of electrons in a narrow area at the interface contributes to the 2DEG's outstanding conductivity. The AlGa_N/Ga_N heterointerface produces a fixed charge stemming from spontaneous and piezoelectric polarization, resulting in a polarization magnitude difference between the layers and an abrupt polarization shift at the interface. The induced charge density can be either positive or negative, leading to the formation of 2DEG or two-dimensional hole gas (2DHG) at the heterointerface to preserve charge neutrality (Nakajima et al., 2010).

GaN HEMT Architectures

The standard configuration of GaN HEMT incorporating a 2DEG channel at the heterojunction is depicted in Figure 3(a) and is commonly referred to as D-GaN HEMT. This device typically operates in an on-state without gate voltage and can be switched off by applying a negative gate bias below the turn-on threshold gate voltage. However, it is crucial to avoid leaving the gate terminal unconnected, as this may inadvertently activate the device and potentially result in catastrophic failure. Generally, GaN HEMTs employed in power converters need to be normally off devices to guarantee safe operation. If the gate driver is deactivated or malfunctions, and its output drops to zero, the HEMT must switch off (Greco et al., 2018).

Given these properties, D-GaN HEMTs are not recommended as independent switches in renewable energy power conversion applications.

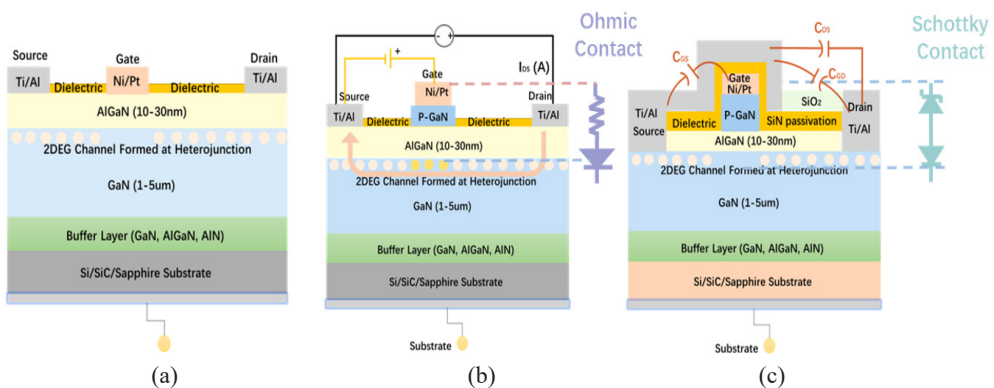


Figure 3. Structure of (a) Conventional GaN HEMT and (b) Gate Injection Transistor (GIT) E-GaN HEMT and (c) EPC Schottky type E-GaN HEMT with locating the internal capacitances

As a solution, commercially available configurations of E-GaN HEMTs are illustrated in Figures 3(b) and 3(c). Figure 3(b) presents the conventional cross-sectional representation

of a gate injection transistor (GIT) structure. The 2DEG underlying the gate is efficiently depleted with $V_{GS}=0$ by adding a p-type GaN layer to the AlGaN barrier layer within the ohmic contact with the Gate. It facilitates efficient hole injection and raises the conduction band energy. It changes the GaN-HEMT into a typically off-E-mode device. According to this method, the p-GaN area must be removed selectively using plasma etching, which might damage the AlGaN surface and worsen the electrical characteristics of the 2DEG in the device access region (Greco et al., 2018). P-type conductivity in GaN has been achieved at both the laboratory and manufacturing levels. A high doping concentration is necessary for the p-type GaN layer. Magnesium (Mg) replaces the Ga lattice and serves as an acceptor when integrated into the nitrogen lattice, making it the conventional p-type dopant for GaN and AlGaN. Many leading manufacturers, such as GaN Systems Inc., have adopted this structure.

The Schottky-type p-GaN configuration shown in Figure 3(c) also attains a normally off-device operation. Under this structure, the p-GaN layer forms a Schottky contact with the gate metal. This design also incorporates dielectric and passivation layers to insulate the gate, which is deposited on P-GaN and insulated from other contacts. This interlayer dielectric deposition methodology substantially enhances the insulation between the gate and source, improving device stability (Chen et al., 2017). While C_{DS} stands for the effective capacitance between the drain terminal and the field plate, C_{GS} indicates the effective capacitance seen from the channel created by the 2DEG to the field plate atop the gate terminal. Finally, C_{GD} is less significant in size than C_{GS} and C_{DS} , which is in a modest area of the gate terminal. These E-GaN HEMTs display diminished vulnerability to unwanted transient dv/dt voltage spikes, which have the potential to cause unintended turn-on at the transistor's gate terminal, owing to the larger magnitude of C_{GS} in comparison to C_{GD} .

E-GaN HEMT as Power Switching Devices

The E-GaN HEMT devices operate as critical current and voltage switches in the energy system, aiming at power conversion applications. Therefore, the transient switching characteristics of these devices are significant in determining power conversion efficiency (PCE) and high-power performance, which are critical aspects influencing their high-performance capabilities. The parasitic nonlinear junction capacitances affect the switching dynamics of the power electronics device. Key capacitances encompass the input capacitance (C_{ISS}), output capacitance (C_{OSS}), and reverse transfer capacitance (C_{RSS}) (Zhang et al., 2018). These capacitances are correlated with the internal capacitances of the E-GaN HEMTs demonstrated in Figure 3(c), as the Equations 4, 5 and 6 (Wang et al., 2020).

$$C_{ISS} = C_{GS} + C_{GD} \quad [4]$$

$$C_{OSS} = C_{DS} + C_{GD} \quad [5]$$

$$C_{RSS} = C_{GD} \quad [6]$$

Parasitic capacitances are essential for determining switching losses and evaluating gate driver performance in power-switching devices. These parameters are accounted for in the corresponding model in relation to the SPICE models derived from manufacturers.

GaN HEMT Spice Modeling

The dynamic characterization of HEMT switching behavior or power conversion-oriented circuit design requires a double-pulse tester (DPT) circuit with PCB featuring various topologies. However, transient analysis of these devices, particularly GaN HEMTs, can be challenging due to the nanosecond testing intervals when the gate pulse frequency reaches GHz levels, demanding advanced testing equipment. Therefore, electronic simulations are typically employed for efficient pre-experimental circuit design assessment. Simulation Program with Integrated Circuit Emphasis (SPICE), a widely used circuit simulation platform, provides a solution for analyzing and designing complex electronic circuits. The E-GaN HEMT equivalent sub-circuit, illustrated in Figure 4, normally includes a .lib file provided by the manufacturer containing all necessary SPICE model settings. The model comprises a voltage-dependent current source (I_{DS}), three voltage-dependent capacitances (C_{GD} , C_{DS} , and C_{GS}), and three parasitic resistances (R_G , R_S , and R_D). I_{DS} models the static I-V characteristics for both forward and reverse conduction. The parasitic capacitances significantly influence the device's switching performance, while R_G , a relatively small constant, often helps reduce transient oscillations during switching events. R_D and R_S are temperature-dependent resistances representing the terminal topology's distributed nature. EPC and GaN Systems provide E-GaN HEMT SPICE models, with GaN Systems also including thermal resistance connector pins for temperature measurements.

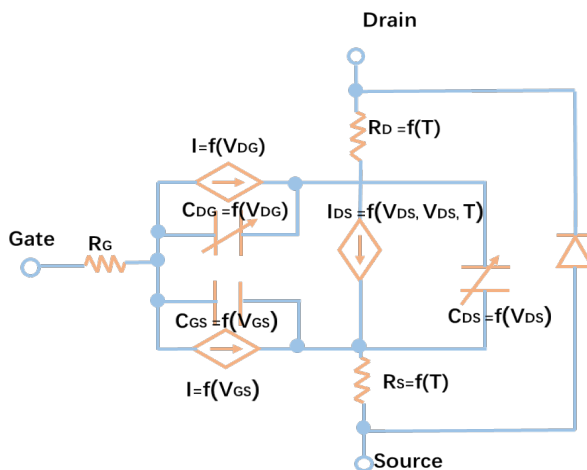


Figure 4. SPICE equivalent of E-GaN HEMT sub-circuit

Parasitic Inductances of E-GaN HEMT

The SPICE model adeptly simulates HEMT switching dynamics, facilitating the study of transient waveforms. However, achieving precise simulation results akin to real-world tests necessitates considering external variables, such as parasitic inductance-induced oscillations. Parasitic inductances in E-GaN HEMTs, undesirable byproducts of device design and assembly, can instigate detrimental outcomes like transient voltage spikes and electromagnetic interference. The primary parasitic inductance sources in E-GaN HEMTs encompass internal device inductance, originating from intra-device current paths, and packaging inductance, stemming from device packaging and interconnections. External inductance, related to device and circuit interconnections, also contributes significantly (Liu et al., 2014). This study chiefly concentrates on internal device and packaging inductance to analyze HEMT switching characteristics at the device level.

METHODOLOGY

The objectives of the simulation design encompass three key aspects: (1) examining the static characteristics of the device, (2) assessing the enhancement in power efficiency through double pulse testing while scrutinizing the switching transients, such as V_{DS} , I_D , V_{GS} , and instantaneous switching power losses in comparison to MOSFETs, and (3) evaluating the influence of parasitic inductance on the switching behavior of the device. The simulation process employs LTSPICE as the software, utilizing the EPC2204 GaN E-HEMT model provided by Efficient Power Conversion (EPC). To facilitate a comparison of switching performance and power loss conditions, the IPA086N10N3 MOSFET is also selected for analysis.

Table 1 presents a silicon FET and a GaN E-HEMT chosen for a performance comparison based on their similar voltage V_{DS} and drain-source on-state resistance $R_{DS(on)}$ ratings. It is crucial to underscore that the GaN E-HEMT has a maximum gate voltage limitation of 6V, substantially lower than the 20V limit of the silicon FET, due to its smaller gate threshold. This characteristic makes gate voltage control more challenging and renders the transistor susceptible to damage should the gate voltage exceed this limitation during peak overshoots or oscillations.

Table 1
Key parameters of silicon and E-GaN FETs

FET Types	Part Number	V_{DS} (V)	I_{DS} (A)	$R_{DS(on)}$ (m Ω)	Q_G (nC)	V_{GS} (V)
E-GaN FET	EPC2204	100	29	6	5.7	-4/6
MOSFET	IPA086N10N3	100	45	8.6	42	± 20

Static simulations of the GaN HEMT were conducted based on the detailed parameter settings presented in Table 2. The results are presented in Figure 5. Figure 5(a) illustrates the output characteristics elucidating the relationship between the drain current (I_D) and the forward directional drain-to-source voltage (V_{DS}) under varying gate-to-source voltage (V_{GS}) conditions. Figure 5(b) portrays the static on-resistance in the linear drain current region. Figure 5(c) depicts the typical transfer characteristics, accentuating the variations in I_D across different junction temperatures. It is observable that an elevation in junction temperature yields a reduction in current, attributable to amplified lattice vibrations and diminished charge carrier mobility. Additionally, a subtle yet discernible shift in the threshold voltage is noted. Figure 5(d) presents the reversed curves of I_D - V_{DS} for various V_{GS} levels. Notably, when the freewheeling current $I_D = -20A$, adjusting V_{GS} from -4V to 6V reduces the on-state V_{DS} magnitude from 6.4V to 0.2V. Distinct from P-N junction reverse bias, the GaN HEMT exhibits resistive behavior through the formation of 2DEG, resulting in tangible losses and indicating substantial reverse conduction losses in power circuit applications. Minimizing reverse conduction loss is advisable, potentially achieved by optimizing the dead time between turning off one switch and turning on another to diminish shoot-through currents and related losses (Niu et al., 2018).

Table 2
EPC 2204 static simulation parameters

Forward Output characteristics	Static On-Resistance R_{ON}	Transfer Characteristics	Reverse Output Characteristics
DC Sweep Junction Temperature: 25°C Type of sweep: Linear 1 st source: V_{DS} ; Start value:0V; Stop value: 6V; Increment: 0.2V 2 nd source: V_{GS} ; Start value:1V; Stop value:6V; Increment: 1V	DC Sweep Junction Temperature: 25°C Type of sweep: Linear 1 st source: V_{DS} ; Start value:0V; Stop value: 6V; Increment: 0.2V 2 nd source: V_{GS} ; Start value:3V; Stop value:6V; Increment: 1V	DC Sweep Junction Temperature: Step up of 25°C, 75°C, 125°C, accordingly Type of sweep: Linear 1 st source: V_{GS} ; Start value:-2V; Stop value: 10V; Increment: 0.2V	DC Sweep Junction Temperature: 25°C Type of sweep: Linear 1 st source: V_{DS} ; Start value:-10V; Stop value: 2V; Increment: 0.2V 2 nd source: V_{GS} ; Start value:-4V; Stop value:6V; Increment: 2V

DPT Circuit Design for Switching Performance Analysis

The switching performance of GaN HEMT and MOSFET is evaluated using a DPT circuit, which includes a DC power source, a double pole switch, a gate driver circuit, the device under test (DUT), an inductive load, and clamping circuits. An RC snubber circuit

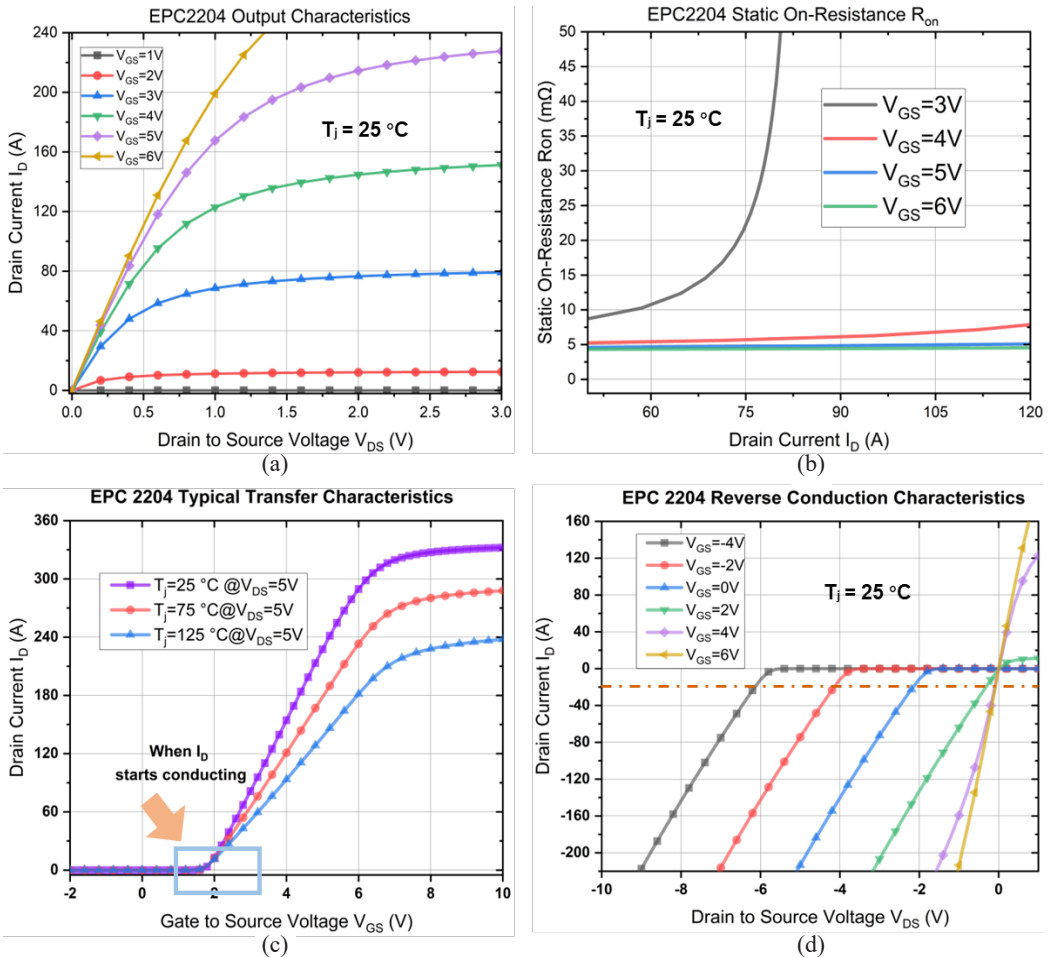


Figure 5. EPC2204 HEMT static analysis: (a) forward output characteristics, (b) static on-resistance R_{on} during linear current region, (c) typical transfer characteristics with junction temperature variation, and (d) reverse output characteristics

is also incorporated to mitigate oscillations from parasitic inductances and capacitances during high-speed switching (Wang et al., 2021). Bulk capacitance maintains a consistent DC voltage across the power supply, preventing sudden DUT switching that could cause voltage oscillations. A decoupling capacitor filters high-frequency noise that rapid DUT switching might generate, ensuring accurate measurements.

Figure 6 presents the LTSPICE schematic employed for the specified simulation. The EPC2204 GaN HEMT is assessed alongside the IPA086N10N3 MOSFET as the DUT while implementing the LTC7001 gate driver. Subsequently, external parasitic inductances, including L_{gs} , L_{ds} , and L_{cm} (Common-Mode Inductance) originating from package inductance, PCB trace inductance, and ground plane inductance, are considered (Jiang et al., 2022). Additionally, stray capacitances emerging from the physical structure of the device,

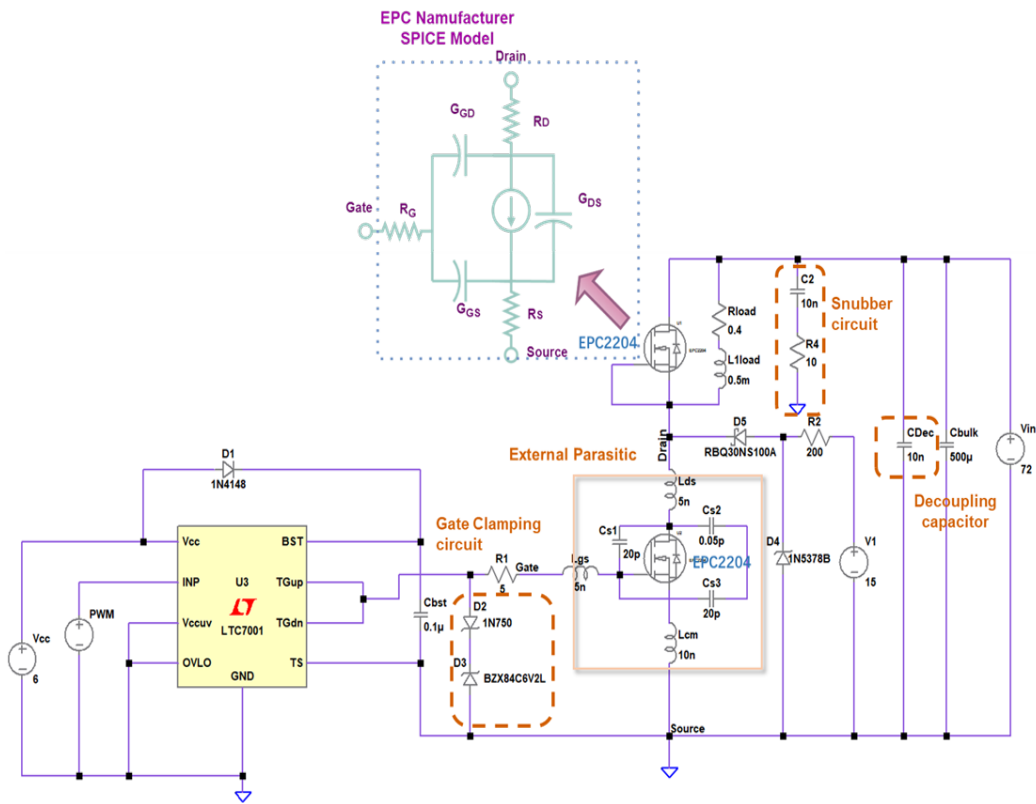


Figure 6. LTSPICE simulation schematic of the proposed DPT circuit with external parasitic

its packaging, and adjacent circuit components are incorporated and simulated, referencing values from prior research. The I_D and V_{DS} transit waveforms between the ideal and parasitic conditions are evaluated. Ultimately, an RC snubber circuit is integrated to evaluate its efficacy in mitigating switching oscillations, as evidenced through waveform comparison (Nakajima et al., 2008). For optimal voltage overshoot attenuation, the snubber capacitor must strike a balance: sufficiently large and perceptive in energy dissipation. Given the EPC2204's C_{OSS} under 1nF, a 10nF capacitor is chosen for simulations. The resistor, tasked with dissipating energy from the snubber capacitor, necessitates suitable value selection depending on load inductance and snubber capacitance. Simulative iterations lead to the selection of a 10-ohm resistor.

RESULTS AND DISCUSSION

The transient simulation parameters are detailed in Table 3. Under ideal conditions, free of external parasitic influences, the turn-on and turn-off transitions of the EPC2204 GaN HEMT and IPA086N10N3 MOSFET are examined in a single cycle, as depicted in Figure 7. LTC7001 filtered gate signal generated full switching-on gate voltages of 5.4V for the EPC2204 GaN HEMT and 8.3V for the IPA086N10N3 MOSFET.

Table 3

Simulation settings for hard switching transient analysis

EPC2204 E-GaN FET	IPA086N10N3 MOSFET
PWM pulse setting: $V_{initial}=-4V$; $V_{on}=6V$; $T_{delay}=0$; $T_{rise}=1ns$; $T_{fall}=1ns$; $T_{(on)}=1.25\mu s$; $T_{period(s)}=2.5\mu s$; $f_{sw}=0.4$ MHz Stray capacitance: $C_{S1}=20pF$; $C_{S2}=0.05pF$; $C_{S3}=20pF$; External parasitic inductance: $L_{CM}=10nH$; $L_{GS}=5nH$; $L_{DS}=5nH$	PWM pulse setting: $V_{initial}=-10V$; $V_{on}=10V$; $T_{delay}=0$, $T_{rise}=1ns$; $T_{fall}=1ns$; $T_{(on)}=1.25\mu s$; $T_{period(s)}=2.5\mu s$; $f_{sw}=0.4$ MHz
Power Setting: $V_{in}=72V$; $L_{load}=0.75mH$; $R_{Lload}=1.3\Omega$ Gate driver: LTC7001; Transient stop time: 2ms; Time to start saving data: 1.98m; Maximum time step: 1 μs	

According to Figure 7(a), under the specified load parameters ($R_L=1.3 \Omega$, $L_L=0.75$ mH) and an input voltage of $V_{in}=72$ V, approximating the output of two series-connected solar panels under open-circuit voltage (V_{OC}) conditions, the GaN HEMT displayed a transient current spike of 49 A before reverting to a load current of 26A. This transition was characterized by smooth oscillatory curves that helped mitigate current overshoot. The entire turn-on phase lasted 4.28ns, while the turn-off phase took 5.91ns. Conversely, as per Figure 7(b), the current in the MOSFET spiked sharply to 445A during the switching-on process before abruptly falling to the load current. The respective durations of the on-and-off switching processes were 22.8ns and 23.3ns. The data reveals that the GaN HEMT's on-and-off switching responses were 5.3 and 3.9 times faster.

Apart from the exceptional switching time and relatively minor current spike, the GaN HEMT surpasses the MOSFET in switching power losses for the DUTs under DPT. As shown in Figure 8(a), the waterfall plot highlights the maximum peak instantaneous power losses for both the GaN HEMT and MOSFET, representing the sum of the product of gate voltage and gate current, as well as the product of drain voltage and drain current. Notably, there is a significant difference in the magnitude of switching power losses between the two devices. The MOSFET's highest instantaneous power losses reach 16,000 W, while the GaN HEMT dissipates approximately 3,000 W within a nanosecond interval. With respect to off-switching power losses, the MOSFET dissipates nearly 580 W. At the same time, the GaN HEMT exhibits a peak power of 530 W. Figures 8(b) and 8(c) present a comparison of average power losses, calculated by integrating the area and dividing by the time interval. The GaN HEMT delivers a remarkable reduction in switching power loss for both on and off-half cycles. Those advantages of lower instantaneous peak current and quicker switching times, as well as reduced switching power losses, can be ascribed to GaN's inherently higher electron mobility, diminished C_{OSS} , reduced gate charge and Miller charge, which further underscore GaN's superiority in hard-switching power conversion applications.

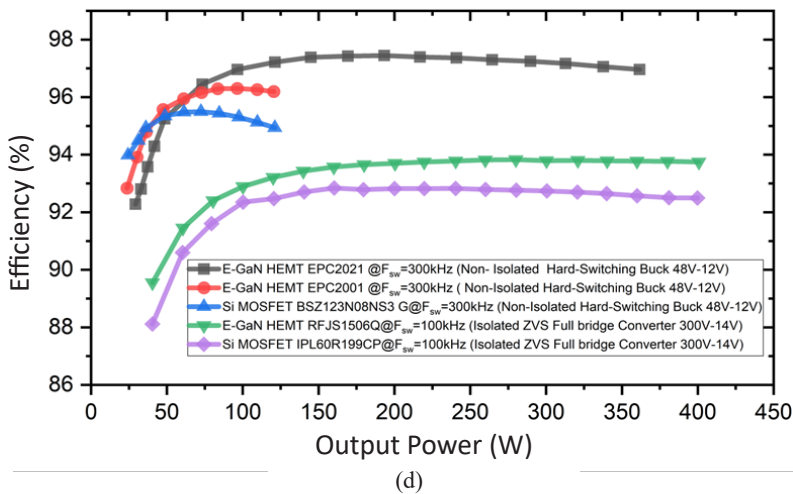


Figure 8. (Continue) (d) validation of efficiency enhancement through comparison with existing research findings

Examining E-GaN HEMT Solutions for Improved Threshold Voltage Stability

Despite the superior switching behavior and reduced power losses associated with E-GaN HEMT, DC analysis reveals a notable imperfection: a narrow gate voltage threshold. This occurrence might lead to challenges in gate pulse control and, in some cases, even failure. As illustrated in Figure 9, upon initiating hard switching of EPC2204 E-GaN HEMT, I_D begins to conduct when $V_{GS(ON)}$ reaches 1.70 V, while its switching off process at a $V_{GS(OFF)}$ of 2.25V. In synchronous DC-DC converter designs, the gate pulse for one switching device is customarily the logical inverse of the other's pulse signal. Given the prevailing challenges associated with a low gate threshold voltage, an extended dead time is necessary to preclude both transistors' concurrent activation within a half-bridge topology. Inadequate deadtime management can exacerbate losses and jeopardize the device's integrity, potentially compromising the circuit's stability.

A solution to address the imperfections of E-GaN HEMTs involves applying cascading GaN HEMTs. This configuration involves the series connection of a low-voltage silicon MOSFET with the GaN HEMT, where the silicon MOSFET serves as a level shifter to regulate the gate voltage of the GaN device, preventing it from surpassing its threshold voltage. This configuration effectively mitigates the issue of gate leakage current that is often associated with standalone E-GaN HEMTs. Nonetheless, challenges related to packaging parasitics and associated costs persist.

An alternative approach involves adapting the gate driver to provide meticulous control over the gate voltage. The integration of the LTC7001 gate driver, which generates robust pull-up and pull-down currents to the gate of GaN HEMT and precisely controls the temporal lag between the gate pulse signal and HEMT drain response, introduces a delay

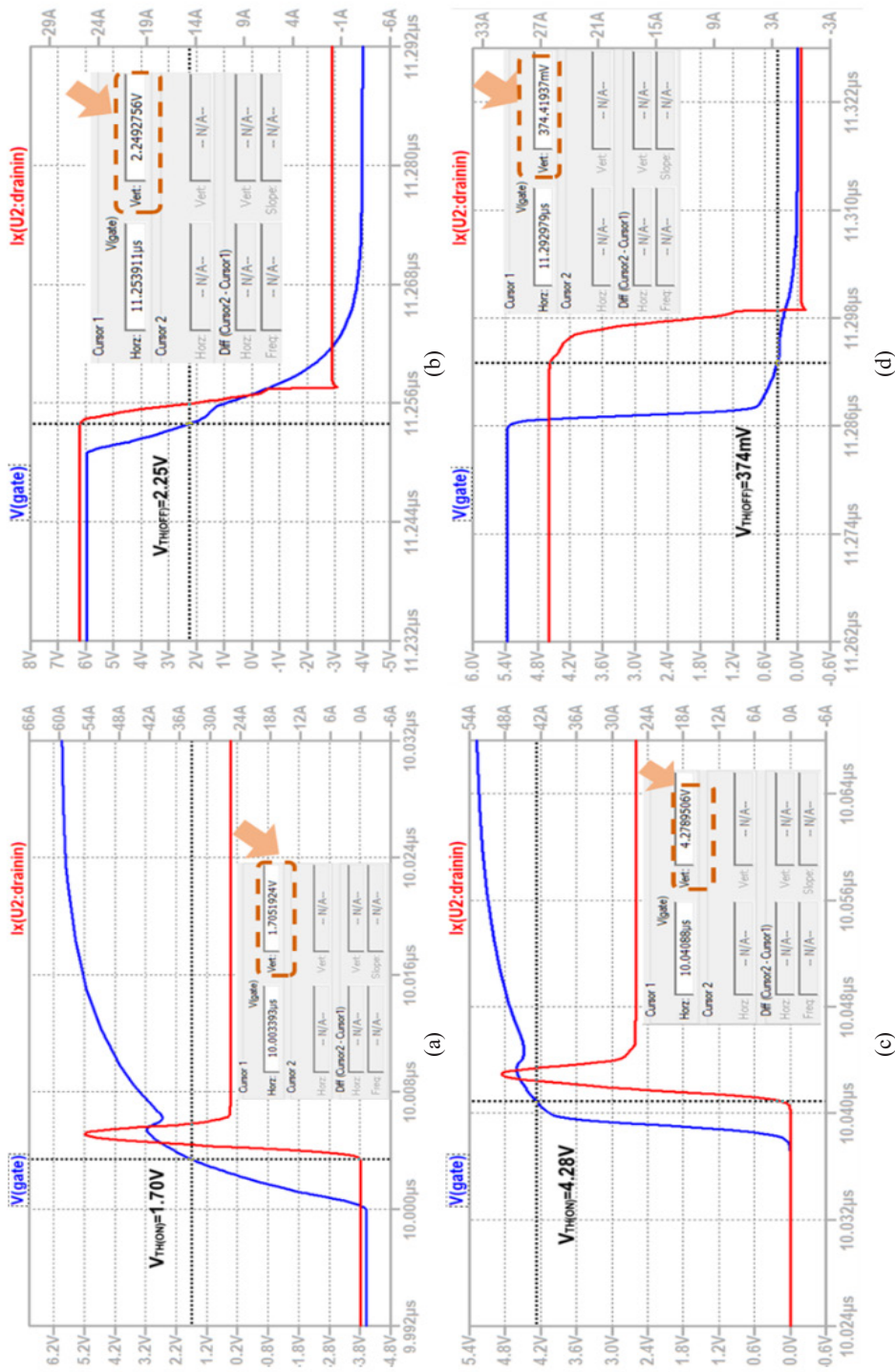


Figure 9. Observation of EPC2204 E-GaN HEMT threshold gate voltage under (a) turning-on without LTC7001, (b) turning-off without LTC7001, (c) turning-on with gate signal processed by LTC7001, and (d) turning-off with gate signal processed by LTC7001

to both on-switching and off-switching processes. This delay significantly mitigates the aforementioned issues. Figure 9(c) illustrates that when the HEMT initiates the turn-on process, the gate voltage reaches 4.28 V, aligning closely with the upper threshold gate voltage in the linear and saturation region. Conversely, when the HEMT begins the off-switching process, the gate voltage has already dropped to 0.374 V. This advancement effectively eliminates the crosstalk of gate signals between the two transistors of the synchronous converter.

Influences of Parasitic Inductances and Stray Capacitances

While the EPC2204 E-GaN HEMT exhibits optimal performance characteristics, such as faster switching speed, fewer current spikes, and reduced power losses, its operation under LTSPICE simulation, which considers internal capacitance and parasitic resistances only, is significantly influenced by parasitic inductances and stray capacitances, as discussed before. This influence becomes apparent in Figures 10(a) and (b), where substantial oscillations are seen in V_{GS} , V_{DS} , and I_D . Dense oscillations are followed by a second set of oscillation

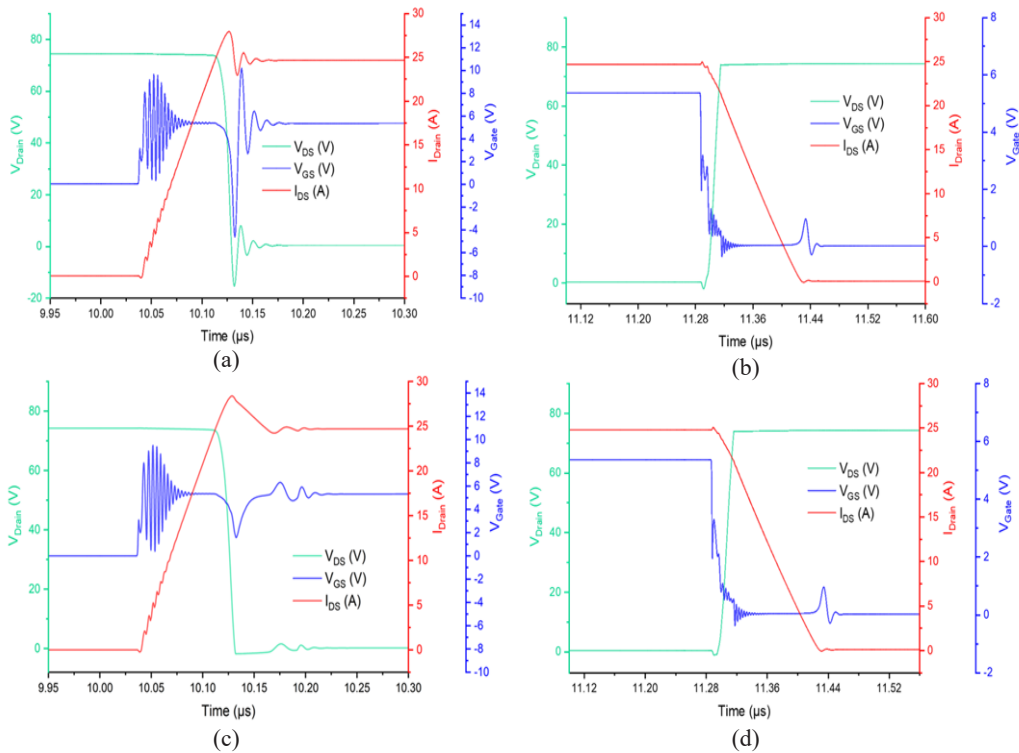


Figure 10. Influences of Parasitic Inductances and Stray Capacitances for GaN HEMT during (a) on-switching without clamping and snubber circuit, (b) off-switching without clamping and snubber circuit, (c) on-switching within clamping and snubber circuit and (d) off-switching within clamping and snubber circuit

spikes that range from -5V to $+10\text{V}$, beginning with the gate pulse. This range surpasses the maximum gate threshold of EPC2204 (-4V to $+6\text{V}$) and could potentially lead to device damage. Furthermore, the initial V_{DS} spikes exhibit a high negative value of -17V , indicative of a reverse bias condition. This negative bias could also lead to power loss and potential functional discrepancies in the circuit. Although the peak overshoot in I_{D} appears to be lower, the duration of oscillations increases the overall switching speed, potentially compromising the stability of constant current output for DC-DC converter applications.

These parasitic effects can be mitigated by integrating snubber and clamping circuits for gate-source and drain-source, as depicted in Figures 10(c) and (d). The gate-source clamping circuit, which incorporates a reverse-connected zener diode with a rated voltage identical to the maximum threshold of the GaN HEMT gate, truncates the peak overshoot and buffers the oscillation. Regarding V_{DS} , the negative spike is eliminated by the drain-source clamping circuit, in addition to the buffered I_{D} oscillation waveform, which enhances current stability. It is also observed that the gate oscillation magnitude is reduced during the off-switching cycle. In addition, when designing HEMT circuits, it is essential to minimize parasitic inductances and stray capacitances by optimizing the layout and routings of the PCB.

CONCLUSION

In this study, a detailed examination of the E-GaN HEMT was undertaken, particularly focusing on its 2DEG output property, which differentiates it from traditional P-N junction devices. The unique behavior of this 2DEG semiconducting property was characterized through static DC analysis. A comparative hard-switching transient simulation was conducted using a half-bridge circuit schematic, highlighting the pronounced performance of GaN over MOSFET in power converter applications. This superior performance is attributed to the absence of reverse conduction losses inherent to the 2DEG characteristic and reduced output capacitances due to device size and packaging considerations. Furthermore, the influences of external parasitic inductances and stray capacitances on transient performances were examined, offering insights for PCB design in real-world applications. The findings underscore the potential of E-GaN HEMTs to enhance the efficiency of DC-DC converters, particularly for photovoltaic energy delivery.

ACKNOWLEDGEMENT

The authors would like to extend our deepest gratitude to Universiti Putra Malaysia for the support provided through the Geran Putra (GP)-IPM/2022/9732100 grant, which has been instrumental in funding and facilitating our research.

REFERENCES

- Ahmad, S., Kadir, M. Z. A. A., & Shafie, S. (2011). Current perspective of the renewable energy development in Malaysia. *Renewable and Sustainable Energy Reviews*, 15(2), 897–904. <https://doi.org/10.1016/j.rser.2010.11.009>
- Chen, K. J., Haberlen, O., Lidow, A., Tsai, C. lin, Ueda, T., Uemoto, Y., & Wu, Y. (2017). GaN-on-Si power technology: Devices and applications. *IEEE Transactions on Electron Devices*, 64(3), 779–795. <https://doi.org/10.1109/TED.2017.2657579>
- Chow, T. P. (2015, November 2-4). *Wide bandgap semiconductor power devices for energy efficient systems*. [Paper presentation]. IEEE 3rd Workshop on Wide Bandgap Power Devices and Applications (WiPDA), Blacksburg, USA. <https://doi.org/10.1109/WiPDA.2015.7369328>
- Delagebeaudeuf, D., & Linh, N. T. (1982). Metal-(n) AlGaAs-GaAs two-dimensional electron gas FET. *IEEE Transactions on Electron Devices*, 29(6), 955–960. <https://doi.org/10.1109/T-ED.1982.20813>
- Greco, G., Iucolano, F., & Roccaforte, F. (2018). Review of technology for normally-off HEMTs with p-GaN gate. *Materials Science in Semiconductor Processing*, 78, 96–106. <https://doi.org/10.1016/j.mssp.2017.09.027>
- Jiang, Z., Hua, M., Huang, X., Li, L., Wang, C., Chen, J., & Chen, K. J. (2022). Negative gate bias induced dynamic on-resistance degradation in schottky-type p-gan gate HEMTs. *IEEE Transactions on Power Electronics*, 37(5), 6018–6025. <https://doi.org/10.1109/TPEL.2021.3130767>
- Jones, E. A., Wang, F. F., & Costinett, D. (2016). Review of commercial GaN power devices and GaN-based converter design challenges. *IEEE Journal of Emerging and Selected Topics in Power Electronics*, 4(3), 707–719. <https://doi.org/10.1109/JESTPE.2016.2582685>
- Kim, D. S., Joo, D. M., Lee, B. K., & Kim, J. S. (2015, June 1-5). *Design and analysis of GaN FET-based resonant dc-dc converter*. [Paper presentation]. 9th International Conference on Power Electronics and ECCE Asia (ICPE-ECCE Asia), Seoul, Korea. <https://doi.org/10.1109/ICPE.2015.7168196>
- Lidow, A., Rooij, M., Strydom, J., Reusch, D., & Glaser, J. (2019). *GaN Transistors for Efficient Power Conversion*. Wiley. <https://doi.org/10.1002/9781119594406>
- Liu, Z., Huang, X., Lee, F. C., & Li, Q. (2014). Package parasitic inductance extraction and simulation model development for the high-voltage cascode GaN HEMT. *IEEE Transactions on Power Electronics*, 29(4), 1977–1985. <https://doi.org/10.1109/TPEL.2013.2264941>
- Nakajima, A., Takao, K., Shimizu, M., Okumura, H., Ohashi, H. (2008 September, 14-18). *Equivalent circuit model for GaN-HEMTs in a switching simulation*. [Paper presentation]. IEEE 30th International Telecommunications Energy Conference, San Diego, USA. <https://doi.org/10.1109/INTLEC.2008.4664095>
- Nakajima, A., Sumida, Y., Dhyani, M. H., Kawai, H., & Narayanan, E. M. S. (2010). High density two-dimensional hole gas induced by negative polarization at GaN/AlGaIn heterointerface. *Applied Physics Express*, 3(12), Article 121004. <https://doi.org/10.1143/APEX.3.121004>
- Niu, Y. C., Huang, Y. T., Chen, C. L., & Chen, Y. M. (2018, October 30-November 2). *Design considerations of the gate drive circuit for GaN HEMT Devices*. [Paper presentation]. Asian Conference on Energy, Power and Transportation Electrification (ACEPT), Singapore. <https://doi.org/10.1109/ACEPT.2018.8610849>

- Reusch, D., Strydom, J., & Lidow, A. (2015, March 15-19). *A new family of GaN transistors for highly efficient high frequency DC-DC converters*. [Paper presentation]. IEEE Applied Power Electronics Conference and Exposition (APEC), Charlotte, USA. <https://doi.org/10.1109/APEC.2015.7104619>
- Roccaforte, F., Fiorenza, P., Greco, G., Lo Nigro, R., Giannazzo, F., Iucolano, F., & Saggio, M. (2018). Emerging trends in wide band gap semiconductors (SiC and GaN) technology for power devices. *Microelectronic Engineering*, 187–188, 66–77. <https://doi.org/10.1016/j.mee.2017.11.021>
- Wang, F., Chen, W., Li, X., Sun, R., Xu, X., Xin, Y., Wang, Z., Shi, Y., Xia, Y., Liu, C., Zhou, J., Zhou, Q., & Zhang, B. (2020). Charge storage impact on input capacitance in p-GaN gate AlGaIn/GaN power high-electron-mobility transistors. *Journal of Physics D: Applied Physics*, 53(30), Article 305106. <https://doi.org/10.1088/1361-6463/ab86e7>
- Wang, W., Liang, Y., Zhang, M., Lin, F., Wen, F., & Wang, H. (2021). Mechanism analysis of dynamic on-state resistance degradation for a commercial GaN HEMT using double pulse test. *Electronics*, 10(10), Article 1202. <https://doi.org/10.3390/electronics10101202>
- Wonglakhon, T., & Zahn, D. (2020). Interaction potentials for modelling GaN precipitation and solid state polymorphism. *Journal of Physics: Condensed Matter*, 32(20), Article 205401. <https://doi.org/10.1088/1361-648X/ab6cbe>
- Zhang, Y., Sun, M., Perozek, J., Liu, Z., Zubair, A., Piedra, D., Chowdhury, N., Gao, X., Shepard, K., & Palacios, T. (2018). Large area 1.2 kV GaN vertical power FinFETs with a record switching figure-of-merit. *IEEE Electron Device Letters*, 40(1), 75-78. <https://doi.org/10.1109/LED.2018.2880306>

Optimisation of the Distribution System Reliability with Shielding and Grounding Design Under Various Soil Resistivities

Jia-Wen Tang¹, Chin-Leong Wooi^{1,2*}, Wen-Shan Tan³, Hadi Nabipour Afrouzi⁴, Hana Abdull Halim² and Syahrin Nizam Md Arshad@Hashim^{1,2}

¹Faculty of Electrical Engineering Technology, Universiti Malaysia Perlis, Pauh Putra Campus, 02600 Arau, Perlis, Malaysia

²Centre of Excellence for Renewable Energy (CERE), Universiti Malaysia Perlis, Pauh Putra Campus, 02600 Arau, Perlis, Malaysia

³School of Engineering and Advance Engineering Platform, Monash University Malaysia, Jalan Lagoon Selatan, 47500 Bandar Sunway, Selangor, Malaysia

⁴Faculty of Engineering, Computing and Science, Swinburne University of Technology Sarawak, 93350 Kuching, Sarawak, Malaysia

ABSTRACT

Lightning strikes can cause equipment damage and power outages, so the distribution system's reliability in withstanding lightning strikes is crucial. This research paper presents a model that aims to optimise the configuration of a lightning protection system (LPS) in the power distribution system and minimise the System Average Interruption Frequency Index (SAIFI), a measure of reliability, and the associated cost investment. The proposed lightning electromagnetic transient model considers LPS factors such as feeder shielding, grounding design, and soil types, which affect critical current, flashover rates, SAIFI, and cost. A metaheuristic algorithm, PSO-GSA, is used to obtain the optimal solution. The paper's main contribution is exploring grounding schemes and soil resistivity's impact on SAIFI. Using 4 grounding rods arranged in a straight line under the soil with 10 Ωm resistivity reduces

grounding resistance and decreases SAIFI from 3.783 int./yr (no LPS) to 0.146 int./yr. Unshielded LPS has no significant effect on critical current for soil resistivity. Four test cases with different cost investments are considered, and numerical simulations are conducted. Shielded LPSs are more sensitive to grounding topologies and soil resistivities, wherein higher investment, with 10 Ωm soil resistivity, SAIFI decreases the most by 73.34%. In contrast, SAIFIs for

ARTICLE INFO

Article history:

Received: 14 June 2023

Accepted: 18 December 2023

Published: 04 April 2024

DOI: <https://doi.org/10.47836/pjst.32.3.15>

E-mail addresses:

jiawen@studentmail.unimap.edu.my (Jia-Wen Tang)

clwooi@unimap.edu.my (Chin-Leong Wooi)

tan.wenshan@monash.edu (Wen-Shan Tan)

HAfrouzi@swinburne.edu.my (Hadi Nabipour Afrouzi)

hanahalim@unimap.edu.my (Hana Abdull Halim)

syahrin@unimap.edu.my (Syahrin Nizam Md Arshad@Hashim)

*Corresponding author

1 k Ω m and 10 k Ω m soil resistivities show minor decreases compared to SAIFIs with no LPS. The study emphasises the importance of considering soil resistivity and investment cost when selecting the optimal LPS configuration for distribution systems, as well as the significance of LPS selection in reducing interruptions to customers.

Keywords: Distribution system reliability, grounding system design, lightning protection system, lightning transient model, metaheuristic optimisation

INTRODUCTION

Lightning strikes can result in substantial consequences for power distribution systems, leading to power blackouts, equipment impairment, and potentially endangering public safety. Lightning can cause power outages by directly impacting overhead lines or inducing an overvoltage in the wiring. Researchers worldwide are continuously working to enhance the dependability of power distribution systems by improving lightning protection systems (LPS), aiming to decrease power outages caused by dangerous weather conditions (Executive Office of the President, 2013). When people plan how to protect distribution systems from lightning strikes, deciding on the appropriate lightning protection system (LPS) and its placement can be challenging. Therefore, the utilities use much information like past experiences and reliability data, as well as technical knowledge to make good decisions for LPS design (Katic & Savic, 1998; Orille-Fernández et al., 2004; Shariatinasab et al., 2014).

According to IEEE 1410-2010 (2011), one approach to enhance the distribution system's reliability is to make it resistant to lightning by installing lightning arresters in appropriate locations. Another method to minimise the risk of power outages involves using insulators with high critical flashover (CFO) voltage and installing a shielding wire above the phase conductors. Additionally, reducing the grounding resistance of the system is crucial, necessitating a study of soil resistivity and the design of the grounding system to impact grounding resistance.

The IEEE 998-2012 (2013) says that adding shielding wires can help improve the lightning protection performance of transmission lines. Some researchers have studied these shielding effects and found that installing shielding wires can reduce the number of flashovers or overvoltage caused by lightning strikes on transmission lines (Metwally & Heidler, 2003; Paolone et al., 2004).

The previous paper (Shariatinasab et al., 2014) proposed a method for optimising arrester location based on a risk assessment approach that considers both the probability and consequences of overvoltage events to mitigate the risk of lightning-induced overvoltage. The authors noted that while an arrester was installed, it could reduce the risk of overvoltage, but improper location of arresters could result in inadequate protection and increased costs.

However, using the hybrid approach for risk assessment and arrester optimisation in this paper is complex compared with recent studies.

A recent study by Zhang et al. (2020) proposed a model that simulates the electromagnetic transients caused by indirect lightning in a distribution network. The model considered scenarios with and without protection measures, such as lightning wires and lightning arrestors, and found the optimal LPS configuration with cost constraints using mixed-integer linear programming (MILP). Zhang et al. (2021) have also recognised the character of the problem of multiple objectives interacting with each other and proposed an optimised multi-objective interdependency model while considering the combination of LPSs with cost constraints. However, only three LPSs are combined, so the selectivity of LPSs can be increased to further optimise the system's reliability.

In previous studies (Cabral et al., 2012, 2013), the lightning electromagnetic transient model can simulate the electromagnetic transient process caused by lightning in distribution networks. The authors used a feeder model to simulate and evaluate the performances of shielding of feeders and grounding resistances against lightning. The system with a shielded feeder and lower soil resistivity can withstand larger lightning currents. Based on the studies above, Cabral et al. (2018) and Bretas et al. (2018) have developed an optimisation strategy for the combination of shield wires and grounding designs as a lightning protection system (LPS) that considers multiple distribution reliability indexes. Additionally, the authors have considered constraint conditions to ensure the best possible protection for the system. These two papers analysed the effectiveness of lightning rods and lightning wires on the distribution system's reliability based on cost constraints. Neither of these references mentioned the effect of soil resistivity on various soil types. These two papers only considered 5 types of grounding design; many more grounding designs described in IEEE 142-2007 (2007) can be further studied.

In summary, the publications above have indicated that optimising LPS for distribution networks remains a subject of ongoing research. Lightning strikes can significantly impact power distribution systems, and proper lightning protection measures are essential to prevent damage and ensure system reliability. Grounding, surge protection, and shielding are essential components of lightning protection systems, and their effectiveness should be evaluated through simulations and field testing.

This paper presents a MILP model to minimise a reliability index that quantifies the average frequency of sustained interruptions in a distribution system while considering the associated costs. An 80-line section distribution system (Bretas et al., 2018) is utilised in the model to assess the effectiveness of the proposed LPS design model. The model incorporates an LPS design strategy that takes into account both sustained interruptions and the number of affected customers for every line section. By utilising the PSOGSA (Particle Swarm Optimisation with Gravitational Search Algorithm) metaheuristic algorithm,

globally optimal LPS configurations are able to be obtained for the distribution system. The test results confirm the feasibility and robustness of our optimisation model.

This paper explains the proposed approach for determining the critical current using the ATPDraw transient model, estimates the fault rate resulting from lightning strikes, and introduces the optimisation model. Firstly, only one type of LPS configuration is applied to the whole system. Then, 4 test cases with different investment costs are compared to find the best LPS solutions under the costs. Finally, the inferences drawn from our research are summarised.

METHODOLOGY

The main objective of the proposed optimisation is to find the best Lightning Protection System (LPS) for the distribution network while minimising both the System Average Interruption Frequency Index (SAIFI) and the cost investment. The study by Cabral et al. (2012) provides information on the characteristics, specific parameters, and models related to the overhead distribution feeder and the system's transient response. The LPS optimisation models and parameters proposed by Cabral et al. (2018) and Bretas et al. (2018) are also reviewed and referenced.

Figure 1 illustrates the methodology employed for optimising the distribution system's reliability. It elucidates the system's response characteristics to lightning under different LPS conditions, which are taken into account when deriving and optimising the system reliability model.

ATPDraw Lightning Simulation

Grounding resistance is the resistance of the connection between the electrical system and the earth. In a power distribution system, grounding is an essential safety measure that helps to protect people and equipment from the harmful effects of electrical faults and lightning strikes. When a fault occurs in an electrical system, such as a short circuit, excess current flows through the ground, which can be dangerous to people and equipment. Grounding provides a low-resistance path for this current to flow to the earth, minimising the risk of electrical shock or damage to equipment.

The arrangement of grounding rods and the type of soil can significantly affect the grounding resistance of a power distribution system. The grounding rod is the electrode that is buried in the earth and provides the connection between the electrical system and the ground. The soil surrounding the grounding rod determines the resistance of the grounding system. The effect of soil resistivity on the ground resistance of power distribution systems is an important consideration in designing effective lightning protection systems. The soil resistivities of various soil types used in this paper can be found in IEEE 80-2013 (2015), as shown in Table 1.

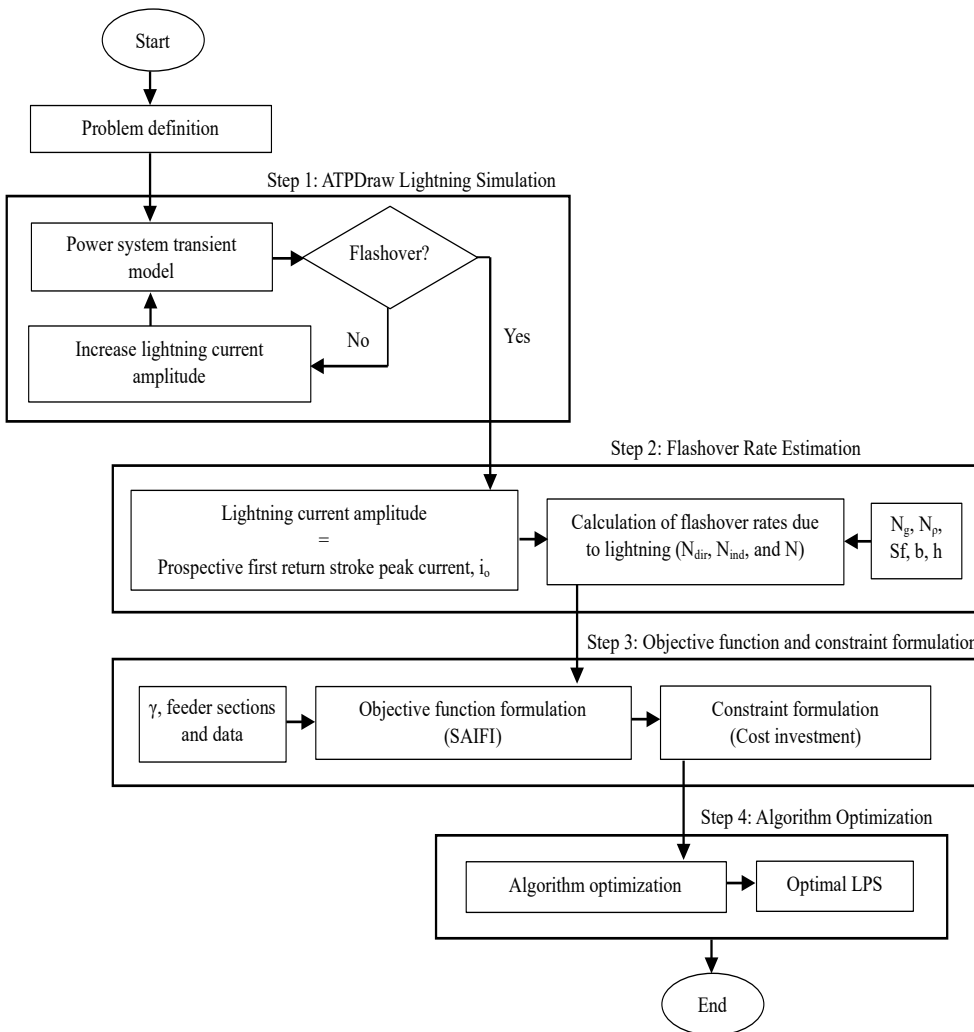


Figure 1. Data flow chart of distribution system reliability optimisation

Table 1
Soil resistivity of different soil types (IEEE, 2015)

Soil Type	Soil Resistivity (Ωm)
Wet organic soil	10
Moist soil	100
Dry soil	1k
Bedrock	10k

Five types of grounding designs are considered in this paper, and Equations 1 to 5 are used to determine the grounding resistance of each design, respectively. The arrangement of grounding rods can be found in IEEE Std. 142 and Military Handbook MIL-HDBK-419A (Department of Defense, 1987).

1. Single vertical rod

$$R_g = \frac{\rho}{2\pi L} \left(\ln \frac{4L}{r} - 1 \right) \tag{1}$$

2. Single horizontal rod

$$R_g = \frac{\rho}{\pi L} \left(\ln \frac{2L}{\sqrt{2rd}} - 1 \right) \tag{2}$$

3. Two vertical rods

$$R_g = \frac{\rho}{4\pi L} \left[\ln \left(\frac{2L + \sqrt{s^2 + 4L^2}}{s} \right) + \frac{s}{2L} - \frac{\sqrt{s^2 + 4L^2}}{2L} + \ln \frac{4L}{r} - 1 \right] \tag{3}$$

4. Straight line of multiple vertical rods

$$R_g = \frac{\rho}{2\pi L N_1} \left(\ln \frac{4L}{r} + \frac{2L}{s} \ln \frac{2N}{\pi} - 1 \right) \tag{4}$$

5. Square array of vertical rods

$$R_g = \frac{\rho}{2\pi L} \left(\ln \frac{4L}{r} - 1 \right) \times + \frac{K}{N_2} \tag{5}$$

Where R_g is ground resistance in Ω , ρ is soil resistivity in Ωm , L is the length of the grounding rod in m, r is the radius of the grounding rod in m, d is the horizontal rod depth in m, s the spacing between the rods in m, and N_1 is the number of straight-line rods, N_2 is the number of square array rods, and K is the resistance ratio for a square array equally spaced of equal length rods, in $s=L$ curve can be obtained in Figure 2. The ground resistances for each grounding topology under different soil resistivity are calculated and tabulated in Table 2. In the case of the feeder without shielding and an ungrounded system, the grounding resistance remained consistently at 1000 Ω , irrespective of the changes in soil resistivity, which ranged from 10 Ωm to 10 $\text{k}\Omega\text{m}$ (Cabral et al., 2014).

The placement of shielded guard wire near the phase conductors on overhead distribution feeders aims to lower the occurrence of lightning strikes and mitigate induced voltages from external sources (Comassetto et al., 2008). Figure 3 illustrates various pole structures for the LPSs. At the same time, Table 3 details the LPS configuration marked as "j", which comprises a combination of unshielded or shielded feeders and different grounding designs.

Flashover Rates due to Lightning

Lightning strikes can have both direct and induced effects on electrical systems, including power distribution systems. Direct lightning effects occur when lightning strikes an electrical component or conductor, such as a power line or transformer. Direct lightning strikes can cause damage to the component or conductor and can result in an electrical fault or outage. The high voltage and current associated with a lightning strike can cause

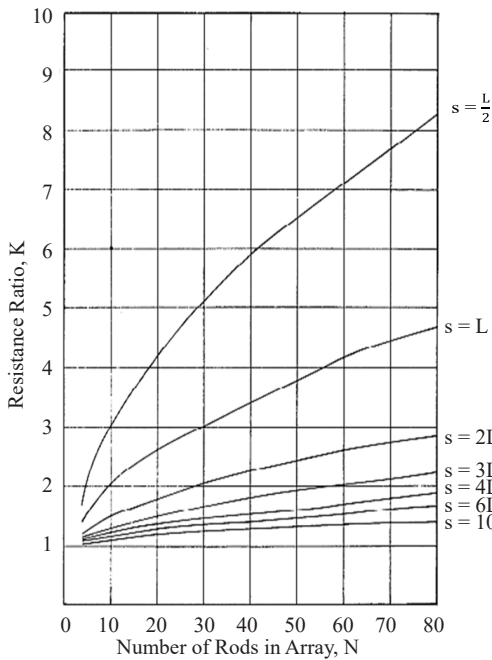


Table 2
Ground resistance in Ohm (Ω) for grounding designs under various soil resistivities

Grounding Resistance (Ω)	Soil Resistivity (Ωm)			
	10	100	1k	10k
Ungrounded	1000	1000	1000	1000
Single vertical rod	3.60	35.99	359.86	3598.62
Single horizontal rod	2.92	29.15	291.55	2915.48
Two vertical rods	1.97	19.74	197.43	1974.27
Straight line of 4 vertical rods	1.09	10.86	108.56	1085.61
Square array of 4 vertical rods	1.26	12.60	125.95	1259.52

Figure 2. The ratio of the actual resistance of a rod array to the ideal resistance of N rods in parallel (Department of Défense, 1987)

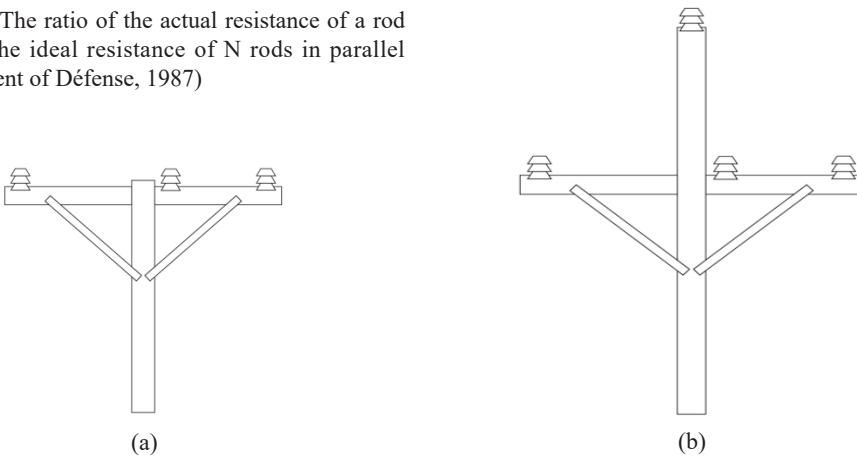


Figure 3. Pole structures of (a) unshielded and (b) shielded with wire guard

Table 3
LPS configuration for a combination of pole structure and grounding designs

Pole Structures	Grounding Designs	j
Unshielded feeder	Ungrounded (no LPS)	1
	Single vertical rod	2
	Single horizontal rod	3
	Two vertical rods	4
	Straight line of 4 vertical rods	5
	Square array of 4 vertical rods	6

Table 3 (Continue)

Pole Structures	Grounding Designs	j
Shielded feeder	Single vertical rod	7
	Single horizontal rod	8
	Two vertical rods	9
	Straight line of 4 vertical rods	10
	Square array of 4 vertical rods	11

insulation breakdown and create arcing, leading to equipment failure and posing a risk to public safety.

Induced lightning effects occur when lightning strikes nearby, and the resulting electromagnetic fields induce voltages or currents in nearby conductors. These induced effects can result in transient overvoltage and current surges, damaging equipment and leading to electrical faults or outages. Induced lightning effects are more common than direct ones and can occur even if the lightning strike is not close to the electrical system.

The process involves establishing a specific threshold current, the critical current, which triggers a flashover event for a given LPS. This critical current serves as the potential peak current (i_0) for the first return stroke. It is utilised in reference [6] to determine the likelihood of the first return stroke having a peak current (I_0) that surpasses i_0 . By substituting the critical current of the LPS, it becomes possible to compute the direct and induced flashover rates, as well as the flashover rate (N) for each section of the feeder, based on different LPS configurations.

The failure rate of the feeder caused by the direct and indirect impacts of lightning strikes can be evaluated by examining the characteristic parameters and the amplitude of the first return stroke current by Equation 6, which is the probability law specified in the IEEE 1410-2010 (2011) guidelines:

$$P(I_0 \geq i_0) = \frac{1}{1 + \left(\frac{i_0}{31}\right)^{2.6}} \quad [6]$$

where $P(I_0 \geq i_0)$ is the probability that the first return stroke has a peak current I_0 that exceeds i_0 , and i_0 is the prospective first return stroke peak current (kA).

The estimation of direct impact flashovers on the overhead distribution system can be achieved using Equation 7 by taking into account the distances between the distribution feeders and nearby structures, as well as the probability of lightning current occurrence. This assessment allows for considering the impact of neighbouring structures on safeguarding the distribution system against lightning strikes. If no structures like buildings or trees are nearby, the shielding factor (Sf) is regarded as zero in those regions. Nonetheless, flashovers can still happen even when nearby structures fully shield distribution lines (Sf = 1).

$$N_{dir} = N_g \left(\frac{b + 28h^{0.6}}{10} \right) P(I_0 \geq i_0)(1 - Sf) \tag{7}$$

where N_{dir} represents the number of flashovers caused by direct impacts (flashes/100 km/yr), N_g denotes the ground flash density (GFD) measured in flashes per km² per year and estimated based on the keraunic level, h represents the height of the highest conductor at the pole (m), b represents the width of the structure (m), and Sf represents the environmental shielding factor, which ranges from 0 to 1.

When a structure located close to an energised line is struck by lightning, it can create an induced overvoltage and lead to power failures. Consequently, when nearby structures shield the line from direct lightning strikes, it also affects the number of indirect flashovers. Equation 8, provided by IEEE 1410-2010 (2011), can be utilised to estimate the number of induced flashovers for distribution circuits:

$$N_{ind} = N_p N_g \left(\frac{h}{10} \right) P(I_0 \geq i_0) \tag{8}$$

where N_{ind} represents the number of flashovers caused by induced overvoltage (flashes/100 km/yr), N_g denotes GFD measured in flashes per km² per year, h represents the height of the highest conductor at the pole (m), and N_p is the induced flashover rate (flashes/100 km/yr).

Figure 4 displays the occurrence rate of flashover in relation to the critical flashover (CFO) voltage. The flashover data pertains to a 10 m tall, infinitely long line comprising a single conductor positioned above a conductive ground. The values have been normalised based on a ground flash density (GFD) of $N_g = 1$ flash/km²/yr and can be proportionally adjusted according to the GFD.

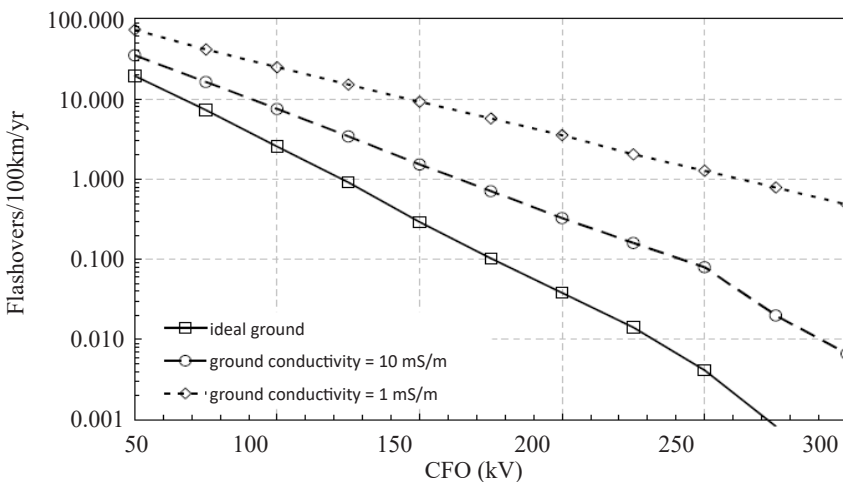


Figure 4. Number of induced-voltage flashovers versus distribution-line insulation level (IEEE1410-2010, 2011)

Hence, as Equation 9 shows, the total number of flashovers caused by lightning can be determined by considering the rates of both direct and indirect flashovers:

$$N = N_{dir} + N_{ind} \tag{9}$$

where N represents the total number of flashovers due to lightning (flashes/100 km/yr).

Therefore, it is possible to establish a matrix N that incorporates the flashover rates N_{ij} , taking into account the LPS topology "j" for each line section "i". Flashovers typically cause momentary faults that are resolved within a few seconds, as well as sustained faults that may last until human intervention for repair. This research concentrates on permanent interruptions that can arise in distribution systems, assuming that flashovers will lead to sustained faults as a conservative estimate. The sustained failure rates for each feeder are determined using Equation 10.

$$\gamma = \bar{\gamma} \cdot N \tag{10}$$

where γ is the permanent failure rates (failures/100 km/yr), $\bar{\gamma}$ is the ratio between the number of permanent faults and total faults.

System Reliability Index and Constraint Formulation

Reliability measures for system services are determined by how often the system experiences interruptions. The widely used reliability index for measuring permanent interruptions is the System Average Interruption Frequency Index (SAIFI). In general, overcurrent protection plays a crucial role in minimising the adverse impact of lightning events on the reliability of electric power distribution. When lightning strikes a wire, it can cause a fault, but with proper distribution system design, overcurrent protection can swiftly resolve the fault before any harm occurs. This study assumes that the coordination between protection devices in the distribution systems remains intact, regardless of the fault's location (Cabral et al., 2018). This paper proposes the reliability index SAIFI as the objective function by constructing a mathematical model in Equation 11 for each line section and Equation 12 for the whole system, which takes into account the affected customers in each section, relying on Equations 6 to 10. The average SAIFI of 80-line sections measures the reliability of the whole distribution system.

$$sai fi_{-ij} = \frac{\gamma_{ij} C_i^P}{C_T} \tag{11}$$

$$SAIFI = \frac{\sum_{i=1}^{ns} \sum_{j=1}^{ne} SAIFI_{ij}}{ns} \tag{12}$$

Where γ_{ij} refers to the rate at which permanent faults occur in the LPS "j" on feeder section "i" as defined in Equation 10, C_i^P represents the count of customers who are located

downstream from line section i and closest to the protective device upstream whose service is interrupted by fault P , C_T indicates the total number of customers being served, and n_s denotes the overall number of distribution network sections, and n_e represents the total number of different LPS conditions.

The cost investment is the constraint of the LPS optimisation for the distribution system, including the cost of the shielded wire and the grounding rods, and the labour cost is not considered in this paper. The market price of the lightning shield wire is about 800 dollars/km, the lightning rod costs 300 dollars/unit, and the grid conductor cost for a 2x2 square array of 4 vertical rod designs is 5 dollars/m. There are 4 test cases with different investment costs have been presented.

Algorithm Optimisation

Talbi (2002) discussed various hybridisation techniques for heuristic algorithms, each with pros and cons. One such method is PSO-GSA, which is an optimisation algorithm that merges Particle Swarm Optimisation (PSO) with the Gravitational Search Algorithm (GSA). PSO-GSA combines the capabilities of both algorithms, running them simultaneously to generate the best solutions (Mirjalili & Hashim, 2010). It uses PSO for exploration and diversity while incorporating GSA for exploitation and convergence towards optimal solutions. This hybrid approach better balances exploration and exploitation, improving optimisation performance.

PSO-GSA demonstrates superior convergence and robustness compared to other evolutionary methods like PSO (Sadati et al., 2009), genetic algorithm (Katic & Savic, 1998), ordinal optimisation (Orille-Fernández et al., 2004), and imperialist competition (Soroudi & Ehsan, 2012). Although mixed integer linear programming (MILP) (Bretas et al., 2018; Jooshaki et al., 2023) achieves the global optimum solution quickly, PSO-GSA has advantages over MILP: it handles continuous and discrete problems without requiring linear programming formulation, has good global search capability, has a simpler implementation, handles non-linear objectives, and is naturally parallelisable for faster optimisation in distributed computing.

RESULTS AND DISCUSSION

After simulation using ATPDraw, the critical lightning current is obtained for each LPS configuration. The critical lightning current values are then used to calculate flashover rates, and the distribution system's reliability is further optimised by a metaheuristic algorithm, PSO-GSA, using MATLAB.

An 81-bus distribution system in Brazil is used for testing purposes, and Figure 5 depicts the single-line diagram of the radial distribution feeder, which consists of 80 sections ($n_s = 80$). The number of customers for each line section is shown in Table 4, and

the relevant system data can be found in a study by Bretas et al. (2018). In this study, the permanent fault rate (λ) is set at 0.2, with N_g being 10 lightning flashes/100km/yr and S_f being 0, according to a study by Cabral et al. (2014). The wood cross-arm (b) is 1.8 m for the overhead distribution feeder, and the pole height (h) is 9 m for the unshielded feeder and 10 m for the shielded feeder.

The characteristics and data of aluminium conductor steel reinforced ACSR LYNX is used as the line conductor, and the aluminium clad steel ACS 7/8 AWG is used as shield wire. With consideration of bare conductors and a 180 kV CFO voltage, the critical current (i_0), SAIFI and the total cost under unshielded and shielded distribution feeders and various grounding topologies for the whole distribution system against soil resistivity are tabulated in Table 5.

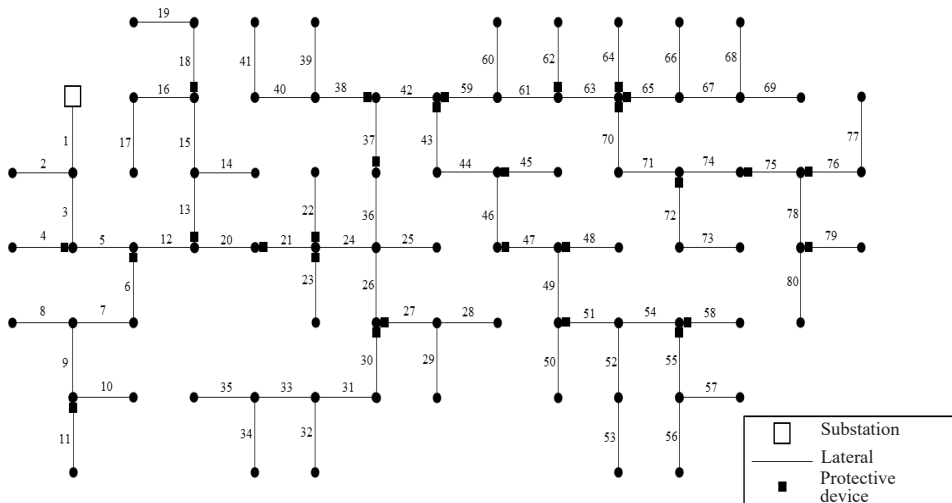


Figure 5. Radial distribution system with 80-line sections

Table 4
Number of customers for each line section

No. Sec	No. Cust.						
1	0	21	401	41	235	61	74
2	104	22	44	42	85	62	240
3	99	23	145	43	124	63	85
4	63	24	141	44	120	64	97
5	43	25	125	45	318	65	0
6	249	26	0	46	50	66	46
7	266	27	186	47	22	67	79
8	139	28	81	48	85	68	0
9	410	29	86	49	92	69	105
10	187	30	100	50	1	70	21

Table 4 (Continue)

No. Sec	No. Cust						
11	172	31	217	51	7	71	20
12	143	32	84	52	58	72	0
13	359	33	19	53	55	73	0
14	488	34	100	54	1	74	28
15	115	35	199	55	1	75	20
16	40	36	96	56	1	76	32
17	12	37	65	57	3	77	1
18	14	38	67	58	31	78	0
19	1	39	197	59	68	79	27
20	392	40	45	60	216	80	13

Table 5 presents the results when the system only applies one LPS configuration. The unshielded LPS does not significantly affect the critical current for soil resistivity ranging from 10 Ωm to 10 $\text{k}\Omega\text{m}$. In contrast, SAIFIs between the soil resistivities are gapped due to different induced flashover rates measured by the soil resistivities. SAIFI for the feeder without LPS is 3.783 int./yr for 10 Ωm of soil resistivity, 3.813 int./yr for 100 Ωm of soil resistivity, 5.471 int./yr for 1 $\text{k}\Omega\text{m}$ of soil resistivity, and 8.232 int./yr for 10 $\text{k}\Omega\text{m}$ of soil resistivity. The best LPS configuration is the shielded feeder with the straight line of 4 vertical rods ($j = 10$) where the SAIFIs are 0.146 int./yr and 0.774 int./yr for 10 Ωm and 100 Ωm respectively, decreased by 96% and 80% from SAIFIs of no LPS and unshielded LPSs. The LPS with a shielded structure has excellent sensitivity to the grounding topologies and the soil resistivities, in which the critical current is affected by the 10 $\text{k}\Omega\text{m}$ of soil resistivity, ranging from 43.59 to 5.98% less than which of an unshielded-structure LPSs.

In the 2x2 square array ($j=11$), there is a greater likelihood of current crowding and interference between adjacent rods, affecting the current flow and leading to higher resistance. On the other hand, the configuration with four rods aligned in a straight line ($j = 10$) does not experience this interference problem, as each rod functions independently. The electrical current tends to distribute more evenly along the line of rods. It can result in a more efficient current dissipation into the ground, leading to lower ground resistance. However, it is important to note that when soil resistivity is exceptionally high, such as in this case (10 $\text{k}\Omega\text{m}$), the influence of grounding systems becomes less pronounced because high soil resistivity limits the effect of a grounding system by increasing ground resistance, reducing the area of influence, and impeding the system's ability to provide a low-resistance path for current dissipation. Therefore, $j=10$ tends to get lower SAIFI compared to $j=11$ for all three-soil resistivity except for 10 $\text{k}\Omega\text{m}$ or higher soil resistivity.

Table 5
Simulation results for each LPS configuration

LPS configuration, j	Cost (US\$)	Soil Resistivity (Ωm)							
		10 Ωm		100 Ωm		1 k Ωm		10 k Ωm	
		i_0 (kA)	SAIFI (int./yr)	i_0 (kA)	SAIFI (int./yr)	i_0 (kA)	SAIFI (int./yr)	i_0 (kA)	SAIFI (int./yr)
1	0	1.18	3.783	1.18	3.813	1.17	5.471	1.17	8.232
2	24000	1.18	3.783	1.18	3.813	1.17	5.471	1.17	8.232
3	24000	1.18	3.783	1.18	3.813	1.17	5.471	1.17	8.232
4	48000	1.18	3.783	1.18	3.813	1.17	5.471	1.17	8.232
5	96000	1.18	3.783	1.18	3.813	1.17	5.471	1.17	8.232
6	103200	1.18	3.783	1.18	3.813	1.17	5.471	1.17	8.232
7	57097.6	90.17	0.227	23.80	2.593	2.42	3.994	0.66	5.056
8	57097.6	94.52	0.203	29.06	2.112	2.89	3.991	0.70	5.056
9	81097.6	101.09	0.172	36.84	1.519	4.12	3.978	0.81	5.056
10	129097.6	107.74	0.146	53.02	0.774	7.40	3.905	1.10	5.056
11	136297.6	106.41	0.151	48.61	0.923	6.37	3.935	1.01	5.056

j = 1: No LPS; j = 2: Unshielded feeder + single vertical rod; j = 3: Unshielded feeder + single horizontal rod; j = 4: Unshielded feeder + two vertical rods; j = 5: Unshielded feeder + straight line of 4 vertical rods; j = 6: Unshielded feeder + square array of 4 vertical rods; j=7: Shielded feeder + single vertical rod; j = 8: Shielded feeder + single horizontal rod; j = 9: Shielded feeder + two vertical rods; j = 10: Shielded feeder + straight line of 4 vertical rods; j = 11: Shielded feeder + square array of 4 vertical rods

In order to validate the optimisation model, 4 test cases are considered and subjected to different investment costs as described below, while the objective is the minimisation of SAIFI under these constraints.

- Case 1: Investment = US\$ 10,000
- Case 2: Investment = US\$ 30,000
- Case 3: Investment = US\$ 50,000
- Case 4: Investment = US\$ 70,000

The main concept identifies the LPS configuration plan that can result in the lowest SAIFI and cost investment when implemented in the feeder sections. The outcomes are shown in Table 6. This paper utilises the PSO GSA heuristic algorithm to obtain the best solution, which requires initialising various parameters. These parameters include a population size of 200, weighting factors with c_1 set to 1 and c_2 set to 2, a random number between 0 and 1 for the weight factor w , a descending coefficient α of 20, and an initial value of G_0 set to 100. The algorithm will iterate a maximum of 300 times, and it will terminate once this maximum iteration is reached.

The results of the cases are taken the best from 30 independent runs each. Table 6 presents the best LPS configurations for the 80-line section distribution system under various soil resistivities and investment cases. Compared to the no LPS plan for all line sections, up to 91% of line sections are unprotected ($j = 1$) in Case 1, up to 78%, 64%, and 50% of line sections are unprotected in Case 2, Case 3, and Case 4 respectively. As the investment increased by the cases, the selection of no LPS configuration to the line sections decreased. In contrast, the shielded feeder grounded by a square array of 4 vertical rods ($j = 11$) becomes more chosen with the increased investment, and up to 48% of line sections apply this LPS configuration in Case 4.

Table 6 provides the SAIFI values and their corresponding costs for different cases. It also reveals the percentage reduction in SAIFI values compared to the no LPS ($j=1$) base case in Table 5 under the same soil resistivities. In Case 1, a budget constraint of US\$ 10,000 leads to excluding LPS installations in most line sections, resulting in reduced reliability compared to the other three cases. For Case 1, under soil resistivities of 10 Ωm and 100 Ωm , the SAIFI is reduced by 26.23% and 21.24%, respectively, compared to scenarios with no LPS. Case 2 shows 46.11% and 34.44% reductions, while Case 3 achieves 56.88% and 51.03% reductions. Case 4 attains the most substantial SAIFI reduction, with decreases of 73.34% and 56.10% for soil resistivities of 10 Ωm and 100 Ωm .

For 1 $\text{k}\Omega\text{m}$ and 10 $\text{k}\Omega\text{m}$ of soil resistivities, all SAIFIs under these soil resistivities have minor decreases from SAIFIs of no LPS, wherein SAIFIs in Case 1 are decreased by 0.07% and 0.09%. In contrast, 1.23% and 2.24% in Case 2, 3.38% and 4.56% in Case 3, and SAIFIs in Case 4 are decreased by 4.29% and 4.87%, respectively, because the higher the soil resistivities, the harder the lightning current discharge to the ground, therefore, there are no notable changes in SAIFIs between the cases. Since the LPSs with shielded structures are sensitive to soil resistivity, the SAIFI increases as the soil resistivity increases. Table 6 also presents that the higher the cost investment, the lower the SAIFI and the higher the reliability of the distribution system. The location of the LPS is important, and the number of customers in the line sections affects the SAIFI. Since the LPS can reduce customer interruptions, if the LPS is located at the feeder section with more customers, the SAIFI can be reduced.

For better understanding, based on Table 6, Figures 6 and 7 are graphed to show the SAIFIs for the test cases and the percentages of SAIFIs of the cases compared to the SAIFI with no LPS, respectively. Figure 6 clearly shows the drops of SAIFIs as the cost investment is increased to implement LPS for soil resistivities 10 Ωm and 100 Ωm . In contrast, there are no significant changes in SAIFIs between the cases of 1 $\text{k}\Omega\text{m}$ and 10 $\text{k}\Omega\text{m}$ of soil resistivities, respectively. Again, it has been proven that there is a limitation to mitigating interruptions under high soil resistivity. Among the soil resistivities, it can be seen that the SAIFIs are rising as the soil resistivity becomes higher.

Table 6
Numerical results for test cases

j	Soil Resistivity (Ωm)															
	10 Ωm				100 Ωm				1 k Ωm				10 k Ωm			
	Case 1	Case 2	Case 3	Case 4	Case 1	Case 2	Case 3	Case 4	Case 1	Case 2	Case 3	Case 4	Case 1	Case 2	Case 3	Case 4
	Percentage of Line Section Applying j (%)															
1	91.25	76.25	62.50	48.75	91.25	77.50	62.50	50	86.25	76.25	63.75	47.50	90	76.25	58.75	41.25
2	0	0	0	0	0	0	0	0	1.25	1.25	0	0	1.25	0	1.25	2.50
3	0	0	0	0	0	0	0	0	5.00	0	0	0	0	0	0	1.25
4	1.25	0	0	0	1.25	0	0	0	1.25	0	1.25	1.25	0	0	1.25	1.25
5	0	0	1.25	0	0	0	0	0	0	2.50	1.25	1.25	3.75	0	2.50	5.00
6	0	0	0	0	0	0	0	0	1.25	0	0	0	2.50	2.50	5.00	3.75
7	0	0	0	0	0	0	0	0	0	0	0	0	0	0	0	0
8	0	1.25	0	0	0	1.25	1.25	0	0	0	0	0	0	0	0	1.25
9	0	1.25	0	1.25	0	0	0	1.25	0	0	0	0	0	0	0	1.25
10	0	1.25	1.25	2.50	1.25	2.50	2.50	2.50	0	0	1.25	2.50	0	2.50	1.25	2.50
11	7.50	20.00	35.00	47.50	6.25	18.75	33.75	46.25	5.00	20.00	32.50	47.50	2.50	18.75	30	40
SAIFI (int/yr)	2.790	2.038	1.631	1.008	3.003	2.500	1.868	1.674	5.466	5.403	5.286	5.236	8.225	8.048	7.857	7.832
COST (US\$)	9957.6	29949	49964	69973	9901.2	29957	49961	69910	9906.8	29982	49913	69959	9968	29934	49920	69987
SAIFI Reduct. (%)	26.23	46.11	56.88	73.34	21.24	34.44	51.03	56.10	0.07	1.23	3.38	4.29	0.09	2.24	4.56	4.87

Case 1: US\$ 10,000 investment constraint; Case 2: US\$ 30,000 investment constraint; Case 3: US\$ 50,000 investment constraint;
Case 4: US\$ 70,000 investment constraint

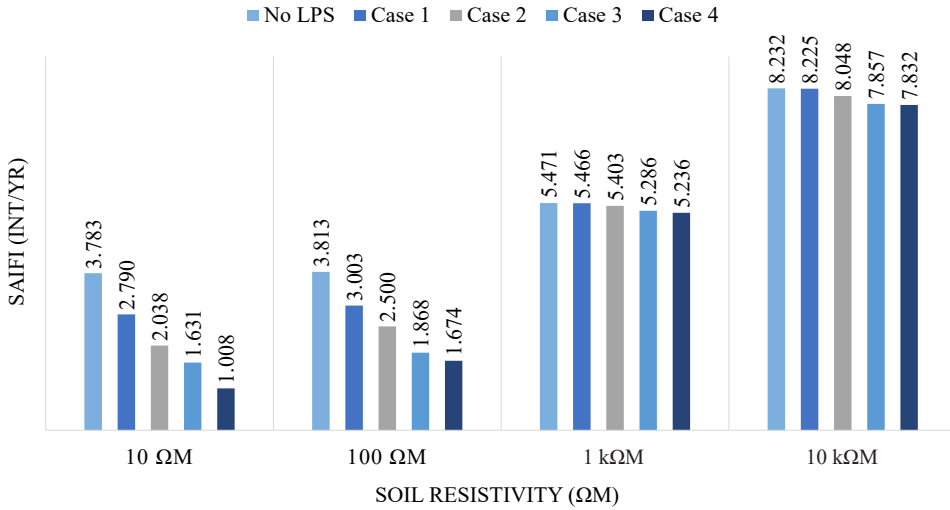


Figure 6. SAIFI against soil resistivity for test cases compared to no lightning protection system

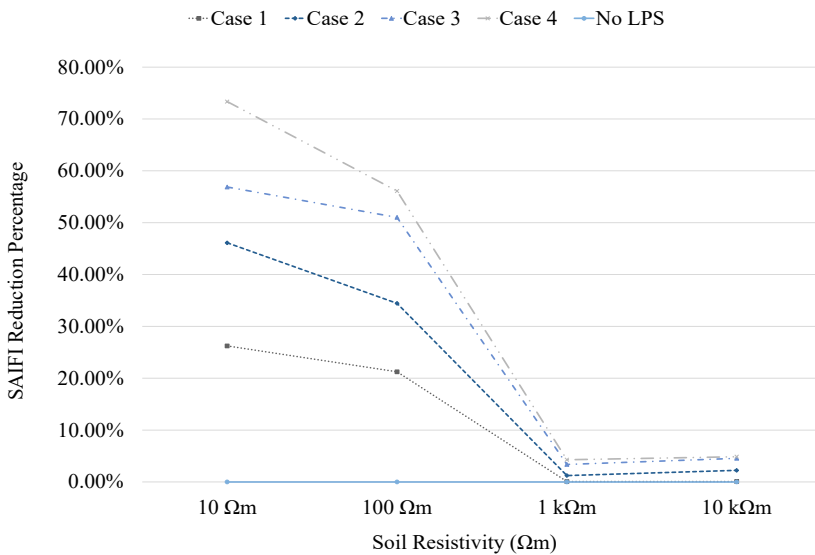


Figure 7. Percentage of SAIFI reduction against soil resistivity for test cases compared to no lightning protection system

Figure 7 demonstrates the differences in SAIFI in percentage for each case to those with no LPS under soil resistivities. SAIFIs for 10 Ωm soil resistivity drop the most. They are followed by 100 Ωm, wherein the SAIFI in Case 4 under 10 Ωm soil resistivity decreases the most by 73.34% as it has the lowest soil resistivity to discharge the lightning current and decreases the flashover rate, as well as the case of the highest cost investment to apply LPS which with lower ground resistance but higher costing. The SAIFIs for 1 kΩm and

10 k Ω m soil resistivities have minor decreases from SAIFIs with no LPS, ranging from 0.07 to 4.87%.

Figures 6 and 7 show that when the soil resistivity is high, it is hard for the lightning to be discharged to the ground. Therefore, with higher soil resistivity (1 k Ω m and 10 k Ω m), LPS cannot help much to discharge the lightning current to the ground and mitigate the interruption to the customers.

In comparison to the previous research papers (Bretas et al., 2018; Zhang et al., 2021), a distinctive contribution of our study is the in-depth exploration of grounding schemes and soil resistivity's impact on SAIFI, which is particularly pertinent when selecting the optimal LPS configuration. By considering various soil resistivities and investment costs, our study provides valuable insights into how these factors influence SAIFI and the reduction of interruptions to customers. This consideration of diverse scenarios and soil conditions enhances the practical applicability of our findings, making them relevant to real-world distribution systems.

CONCLUSION

This paper highlights the importance of protective measures to ensure the reliability and safety of power distribution systems. Lightning protection systems, good shielding and grounding practices can help mitigate lightning's effects on power distribution systems. A grounding system is essential for lightning protection in power distribution systems, and a grounding system with lower grounding resistance means that the system is better grounded and more effective at dissipating fault currents. On the other hand, high soil resistivity means the soil does not conduct electricity as easily. As a result, the ground has a higher resistance to the current flow. This increased ground resistance can make it more challenging for a grounding system to effectively dissipate electrical faults or lightning strikes into the earth.

Among the presented grounding rod configurations, 4 grounding rods arranged in a straight line ($j=10$) under the soil with lower resistivity, which is 10 Ω m, results in a better grounding performance of 1.09 Ω grounding resistance. The combination with shielded feeders results in the highest withstand current of 107.74 kA, and the SAIFI was further decreased from 3.783 int./yr (no/unshielded LPS) to 0.146 int./yr. The results in Table 5 showed that shielded LPS ($j=7-11$) were more sensitive to the soil resistivities, as the SAIFI increases with soil resistivity for grounding topologies. At the same time, unshielded LPS ($j=2-6$) had no significant effect and no differences from no LPS ($j=1$) on the critical current for soil resistivity, as well as the SAIFIs between the grounding topologies.

The study also analysed the impact of lightning protection systems on the reliability of distribution systems for different soil resistivities and investment costs. The study validated an optimisation model using PSO-GSA to minimise SAIFI under different investment cost

constraints. The results showed that the higher the cost investment, the lower the SAIFI and the higher the reliability of the distribution system. However, the location of the LPS was also important, as placing the LPS at the feeder section with more customers could further reduce SAIFI. The study demonstrated the importance of considering both soil resistivity and investment cost when selecting the optimal LPS configuration for distribution systems, as well as the significance of LPS location in reducing interruptions to customers.

The study reveals that the relationship between the SAIFI and cost is inversely proportional, which means that higher investment costs can achieve lower SAIFI. Therefore, future studies plan to explore the multi-objective optimisation algorithms to find an optimal solution that simultaneously reduces cost and improves SAIFI. This approach should enable striking an optimal solution between SAIFI and cost. Lastly, obtaining comprehensive Malaysian data can be challenging. Thus, the 81-bus test system (Bretas et al., 2018) was chosen as it offered complete and accessible information for the optimisation algorithm's development and evaluation in this study. To reflect the Malaysian situation, the authors aim to validate the approach with Malaysian data in future studies to address this concern.

ACKNOWLEDGEMENTS

The authors acknowledged the Fundamental Research Grant Scheme (FRGS) support under a grant number of (Ref: FRGS/1/2022/TK08/UNIMAP/02/72) from the Ministry of Higher Education Malaysia. This work is supported by the Collaborative Research Grant (CRG), Grant No. 9023-00017 from Universiti Malaysia Perlis (UniMAP).

REFERENCES

- Bretas, A. S., Cabral, R. J., Leborgne, R. C., Ferreira, G. D., & Morales, J. A. (2018). Multi-objective MILP model for distribution systems reliability optimization: A lightning protection system design approach. *Electrical Power and Energy Systems*, 98, 256–268. <https://doi.org/10.1016/j.ijepes.2017.12.006>
- Cabral, R. J., Gazzana, D. S., Leborgne, R. C., Bretas, A. S., Dias, G. A. D., & Telló, M. (2012, September 2-7). *Improvement of an overhead distribution feeder performance against lightning considering the wire-guard protection*. [Paper presentation]. International Conference on Lightning Protection (ICLP), Vienna, Australia. <https://doi.org/10.1109/ICLP.2012.6344291>
- Cabral, R. J., Gazzana, D. S., Leborgne, R. C., Bretas, A. S., Dias, G. A. D., Schwanz, D., & Telló, M. (2013, September 22-24). *Effect of shielding and grounding on lightning performance of 23 kV distribution feeders*. [Paper presentation]. North American Power Symposium (NAPS), Manhattan, USA. <https://doi.org/10.1109/NAPS.2013.6666939>
- Cabral, R. J., Bretas, A. S., Leborgne, R. C., Morales, J. A., & Orduna E. A. (2014, March 31-April 3). *Sensitivity assessment of lightning-induced surges in distribution feeders using ATP*. [Paper presentation]. 12th IET International Conference on Development in Power System Protection (DPSP), Copenhagen, Denmark. <https://doi.org/10.1049/cp.2014.0094>

- Cabral, R. J., Leborgne, R. C., Bretas, A. S., Ferreira, G. D., & Morales, J. A. (2018). Lightning protection system design for distribution networks based on System Average Interruption Frequency minimization. *Electric Power Systems Research, 160*, 1-12. <https://doi.org/10.1016/j.epsr.2018.01.018>
- Comassetto, L., Bernardon, D. P., Canha, L. N., & Abaide, A. R. (2008). Automatic coordination of protection devices in distribution system. *Electric Power Systems Research, 78*(7), 1210–1216. <https://doi.org/10.1016/j.epsr.2007.10.004>
- Department of Defense. (1987). *Military handbook (MIL-HDBK-419A) grounding, bonding, and shielding for electronic equipments and facilities volume I: Basic theory*. Defense Technical Information Center. <https://apps.dtic.mil/sti/citations/tr/ADA239565>
- Executive Office of the President (2013). *Economic benefits of increasing electric grid resilience to weather outages*. The White House. <chrome-extension://efaidnbmnnnibpcajpcglclefindmkaj/https://www.energy.gov/articles/economic-benefits-increasing-electric-grid-resilience-weather-outages>
- IEEE 142-2007. (2007). *IEEE recommended practice for grounding of industrial and commercial power systems*. IEEE Publishing. <https://doi.org/10.1109/IEEESTD.2007.4396963>.
- IEEE 1410-2010. (2011). *IEEE guide for improving the lightning performance of electric power overhead distribution lines*. IEEE Publishing. <http://doi.org/10.1109/IEEESTD.2011.5706451>
- IEEE 998-2012. (2013). *IEEE guide for direct lightning stroke shielding of substations*. IEEE Publishing. <http://doi.org/10.1109/IEEESTD.2013.6514042>
- IEEE 80-2013. (2015). *IEEE guide for safety in AC substation grounding*. IEEE Publishing. <http://doi.org/10.1109/IEEESTD.2015.7109078>
- Jooshaki, M., Karimi-Arpanahi, S., Millar, R. J., Lehtonen, M., & Fotuhi-Firuzabad, M. (2023). On the MILP modeling of remote-controlled switch and field circuit breaker malfunctions in distribution system switch placement. *IEEE Access, 11*, 40905-40915. <http://doi.org/10.1109/ACCESS.2023.3268993>
- Katic, N. A., & Savic, M. S. (1998). Technical and economical optimisation of overhead power distribution line lightning protection. *IEE Proceedings. Generation, Transmission and Distribution, 145*(3), 239–244. <https://doi.org/10.1049/ip-gtd:19981897>
- Metwally, I. A., & Heidler, F. H. (2003). Improvement of lightning shielding performance of overhead transmission lines by passive shield wires. *IEEE Transactions on Electromagnetic Compatibility, 45*(2), 378-392. <http://doi.org/10.1109/TEMC.2003.811300>
- Mirjalili, S., & Hashim, S. Z. M. (2010, December 3-5). *A new hybrid PSO-GSA algorithm for function optimization*. [Paper presentation]. International Conference on Computer and Information Application, Tianjin, China. <http://doi.org/10.1109/ICCIA.2010.6141614>
- Orille-Fernández, A. L., Rodríguez, S. B., & Gotés, M. A. G. (2004). Optimization of surge arrester's location. *IEEE Transactions on Power Delivery, 19*(1), 145-150. <http://doi.org/10.1109/TPWRD.2003.820213>
- Paolone, M., Nucci, C. A., Petrache, E., & Rachidi, F. (2004). Mitigation of lightning-induced overvoltages in medium voltage distribution lines by means of periodical grounding of shielding wires and of surge arresters: Modelling and experimental validation. *IEEE Transactions on Power Delivery, 19*(1), 423-431. <http://doi.org/10.1109/TPWRD.2003.820196>

- Sadati, N., Amraee, T., & Ranjbar, A. M. (2009). A global particle swarm-based simulated annealing optimization technique for under-voltage load shedding problem. *Applied Soft Computing*, 9(2), 652–657. <https://doi.org/10.1016/j.asoc.2008.09.005>
- Shariatinasab, R., Safar, J. G., & Falaghi, H. (2014). Optimisation of arrester location in risk assessment in distribution network. *IET Generation, Transmission & Distribution*, 8(1), 151–159. <http://doi.org/10.1049/iet-gtd.2013.0166>
- Soroudi, A., & Ehsan, M. (2012). Imperialist competition algorithm for distributed generation connections. *IET Generation, Transmission & Distribution*, 6(1), 21–29. <http://doi.org/10.1049/iet-gtd.2011.0190>
- Talbi, E. G. (2002). A taxonomy of hybrid metaheuristic. *Journal of Heuristics*, 8(5), 541–546. <https://doi.org/10.1023/A:1016540724870>
- Zhang, L., Zhang, Z., Fang, S., & Bretas, A. S. (2020, August 2-6). An optimization model for distribution networks lightning protection system design: A reliability indexes and cost-based solution. [Paper presentation]. *IEEE Power & Energy Society General Meeting (PESGM)*, Montreal, Canada. <http://doi.org/10.1109/PESGM41954.2020.9281988>
- Zhang, Z., Zhang, L., Liu, X., Zhao, T., & Zou, L. (2021). A reliability-based optimization model for comprehensive lightning protection system design. *IOP Conference Series: Earth and Environmental Science*, 838(1), Article 012005. <http://doi.org/10.1088/1755-1315/838/1/012005>

Identifying Communities with Modularity Metric Using Louvain and Leiden Algorithms

Siti Haryanti Hairol Anuar¹, Zuraida Abal Abas^{2*}, Norhazwani Md Yunos², Mohd Fariduddin Mukhtar³, Tedy Setiadi⁴ and Abdul Samad Shibghatullah⁵

¹Faculty of Technology and Engineering Electronic & Computer, Universiti Teknikal Malaysia Melaka (UTeM), Melaka, Malaysia

²Faculty of Information & Communication Technology, Universiti Teknikal Malaysia Melaka (UTeM), Melaka, Malaysia

³Faculty of Mechanical Technology & Engineering, Universiti Teknikal Malaysia Melaka (UTeM), Melaka, Malaysia

⁴Faculty of Science, Fakultas Teknologi Industri (FTI), Ahmad Dahlan University (UAD), Yogyakarta, Indonesia

⁵School of Information Technology, Faculty of Business & Information Science (FoBIS), UCSI University Kuala Lumpur, Malaysia

ABSTRACT

Over the past 20 years, there has been a significant increase in publication in complex network analysis research, especially in community detection. Many methods were proposed to identify community structure. Each community identification algorithm has strengths and weaknesses due to the complexity of information. Among them, the optimisation methods are widely focused on. This paper focuses on an empirical study of two community detection algorithms based on agglomerative techniques using modularity metric: Louvain and Leiden. In this regard, the Louvain algorithm has been shown to produce a bad connection in the community and disconnected when executed iteratively. Therefore, the Leiden algorithm is designed to successively resolve the weaknesses. Performance comparisons between the two and their concept were summarised in

detail, as well as the step-by-step learning process of the state-of-the-art algorithms. This study is important and beneficial to the future study of interdisciplinary data sciences of network analysis. First, it demonstrates that the Leiden method

ARTICLE INFO

Article history:

Received: 15 July 2023

Accepted: 26 October 2023

Published: 04 April 2024

DOI: <https://doi.org/10.47836/pjst.32.3.16>

E-mail addresses:

sitharyanti@utem.edu.my (Siti Haryanti Hairol Anuar)

zuraidaa@utem.edu.my (Zuraida Abal Abas)

wanie.my@utem.edu.my (Norhazwani Md Yunos)

fariduddin@utem.edu.my (Mohd Fariduddin Mukhtar)

tedyasni@gmail.com (Tedy Setiadi)

abdulsamad@ucsiuniversity.edu.my (Abdul Samad Shibghatullah)

* Corresponding author

Current Affiliation:

Abdul Samad Shibghatullah

College of Computing & Informatics (CCI), Universiti Tenaga Nasional, 43000 Kajang, Selangor, Malaysia

outperformed the Louvain algorithm in terms of modularity metric and running time. Second, the paper displays the use of these two algorithms on synthetic and real networks. The experiment was successful as it identified better performance, and future work is required to confirm and validate these findings.

Keywords: Community detection, Leiden, Louvain, modularity, network structure

INTRODUCTION

Systems in many real-world data can be modelled as a complex network. Based on Scopus online database, the number of research studies about network analysis is projected to grow by more than 148 873 publications from 1994 until now. Scopus is a large database of peer-reviewed literature and the citation and publication index owned by Elsevier, including journals, books, and conference proceedings. The concept of community detection is crucial to both graph theory and social network analysis. A network is composed of nodes as objects, as well as edges as the interaction or relation between the objects in a particular community. Community detection is one of the methods used to represent information in a complex real-world structural network. A community is described as a set of nodes that share common properties such as affiliations, similar interests, and similar information. Community detection is used to identify low-density communities with a high density within edges.

There are several different social network analysis techniques to characterise the structural network, investigate the relationship, or determine the social network group structure, depending on the application of the communities. In that sense, several studies have provided recommendations concerning algorithm selection using criteria such as network parameters, computation time, or overlap with a simulated community structure.

Generally, community detection can be categorised into global and local scopes. Global scope is dependent on prior knowledge of the entire network. Various perspectives have been developed to detect the community structure, such as hierarchical, spectral, and fuzzy clustering, as well as optimisation methods. Among them, the optimisation methods are widely focused on (Cheng et al., 2019). These class methods define community detection as the optimisation problem of an objective function.

For the performance testing of each community detection algorithm, it is preferable to run on networks that can be modified regarding the mesoscopic characteristics, including the distribution of degrees, the extent of local clustering, and the modularity of the global structure (LaRock et al., 2020). First, the degree distribution is important in determining whether learning is feasible or beneficial. Distributions of degree in complex networks can be characterised by two simplified extremes, which are homogenous and heterogeneous distributions. Second is the extension of the local clustering coefficient. It measures the degree of connectivity between two nodes and finds the important node.

The third is modularity, also known as quality function and denoted as Q (Newman, 2006; Newman & Girvan, 2004). The modularity function can be used to determine a community's strength. In this way, modularity measures can be applied to community detection to find the density of connections within communities rather than between communities (Blondel et al., 2008). Several community detection algorithms utilise modularity as an objective function to be maximised (Yuan & Liu, 2021). Modularity can be leveraged only in undirected, static, and non-overlapping networks. It is also used to denote the dendrogram's line and mark the conclusion of the algorithm that shows the values of effective partitions.

This paper forms a relationship between degree distribution and modularity metric from these three properties. This paper mainly evaluates Louvain and Leiden, two community detection algorithms based on agglomerative methods using modularity metric as an objective function. Numerous graph analysis software uses the well-known Louvain algorithm. Despite the fact that both techniques use similar steps at the start of the two phases, the Leiden algorithm performs better than Louvain because of improvements made during the refining phase before the identification of the community.

The main contributions of this paper can be summarised as follows:

- Through experimental comparison, this study demonstrated that Leiden is a superior algorithm to Louvain concerning performance comparison by focusing on the modularity metric and running time.
- This paper displays the use of these two algorithms on synthetic and real networks.

Consequently, this would aid other users in selecting the best community detection algorithm based on the results that showed the Leiden approach is the latest and faster than the Louvain algorithm.

LITERATURE REVIEW

Hierarchical Clustering

In the past 20 years, several community detection techniques have been created and implemented (Gilad & Sharan, 2023). One of the approaches in community analytics methods is hierarchical clustering. Hierarchical clustering can be classified into divisive and agglomerative methods (Newman & Girvan, 2004). The divisive method uses a split-process mechanism and contains two community detection algorithms: Girvan-Newman and the leading eigenvector algorithm. Meanwhile, the agglomerative method uses a merge process consisting of four community detection algorithms: fast greedy, walktrap, Louvain, and Leiden.

Each of the past research initiatives analysed the network's content from a unique perspective and then used this analysis to discover communities by considering the topological information of a network (Ullah et al., 2022). Recent trends in the practical application of community detection in network structure especially using the Louvain

and Leiden algorithm, are in healthcare (Chatterjee & Sanjeev, 2023; Evans et al., 2022; Jin et al., 2020; Kabir et al., 2019; Kramer et al., 2020; Nallusamy & Easwarakumar, 2023; Nicolini et al., 2017; Rahiminejad et al., 2019), social network (Chessa et al., 2023; Irsyad & Rakhmawati, 2019; Li et al., 2023; Park & Kwon, 2022; Torene et al., 2022), telecommunication (Ding et al., 2022; Zu et al., 2021), economic (Han et al., 2018; Wang et al., 2022), intelligent (Karyotis et al., 2018; Singhal et al., 2020) and nature (Peeples & Bischoff, 2023; Wang & Wang, 2022; Xie et al., 2022).

MATERIALS AND METHOD

Preliminary

We formulate some preliminaries and notations used in the proposed method in the form of definitions listed in Table 1.

The definition of modularity, Q , is represented in Equation 1 as follows:

$$Q = \frac{1}{2m} \sum_{ij} \left(A_{ij} - \frac{k_i k_j}{2m} \right) \delta(C_i, C_j) \quad (1)$$

In $G = (V, E)$, an undirected and unweighted network, the quality function of community structure can be measured by modularity metric, Q where A_{ij} represent the adjacency matrix, k_i and k_j is the degree of node i and j , respectively, C_i and C_j are the community of node i and j , respectively, and $\delta(\circ)$ represents Kronecker function as in Equation 2.

$$\delta(C_i, C_j) = \begin{cases} 1, & \text{if } C_i = C_j \\ 0, & \text{if } C_i \neq C_j \end{cases} \quad (2)$$

The purpose of the Kronecker-delta function is to ensure that if nodes i and j are in different communities, then Q is zero. Otherwise, the value of 1, provided that both node i and j belong to the same community C_i and C_j .

Framework

After introducing the key notations and description, we begin to run the experiment based on this framework in Figure 1, which summarises the complete flow of the experiment.

Network datasets from synthetics and real-world networks were collected in the first stage. An artificial network termed Lancichinetti-Fortunato-Radicchi (LFR) was adopted as a benchmark for the synthetic type with three different network sizes consisting of small, medium, and large. Similar network sizes were also applied for the six real-world networks utilised.

Table 1

Notations used in this paper

Notation	Description
E	The set of edges
G	The whole network
m	The number of edges
n	The number of nodes
Q	The modularity
t	The running time in seconds
V	The set of nodes

The three network sizes are used to evaluate the performance algorithm, and the network parameters were set up earlier based on the benchmark network. The small size contains less than one thousand nodes, the medium size network contains between one thousand and ten thousand nodes, and the large size is more than that.

The input dataset was read as an edge list for the next step and transformed into adjacency matrices using Python. Three popular graph libraries with Python bindings, namely `cdlib`, `NetworkX` and `igraph`, were used for performance comparison between the two techniques. `cdlib` is a powerful Python package that allows the extraction, comparison, and evaluation of communities from complex networks. `NetworkX` was implemented using pure Python methods, whereas `igraph` was run using C language. In this paper, the Louvain and Leiden algorithms were applied using the three libraries and tested in the same network. The details of two representative algorithms have been explained in comparison to the algorithm.

For the final step, both algorithms were evaluated through modularity metrics, and the running time was set up in unit seconds.

Comparison of Algorithms

A hierarchical clustering strategy can rapidly generate highly modular communities in a large network. There are two phases in the Louvain algorithm (Blondel et al., 2008). The first stage is the local moving of nodes for modularity optimisation, while the second stage is the community merging or network aggregation process. A static network is required for Louvain to produce an efficient output. In a large network, this approach, which belongs to the hierarchical clustering category, may quickly create communities with a high degree of modularity.

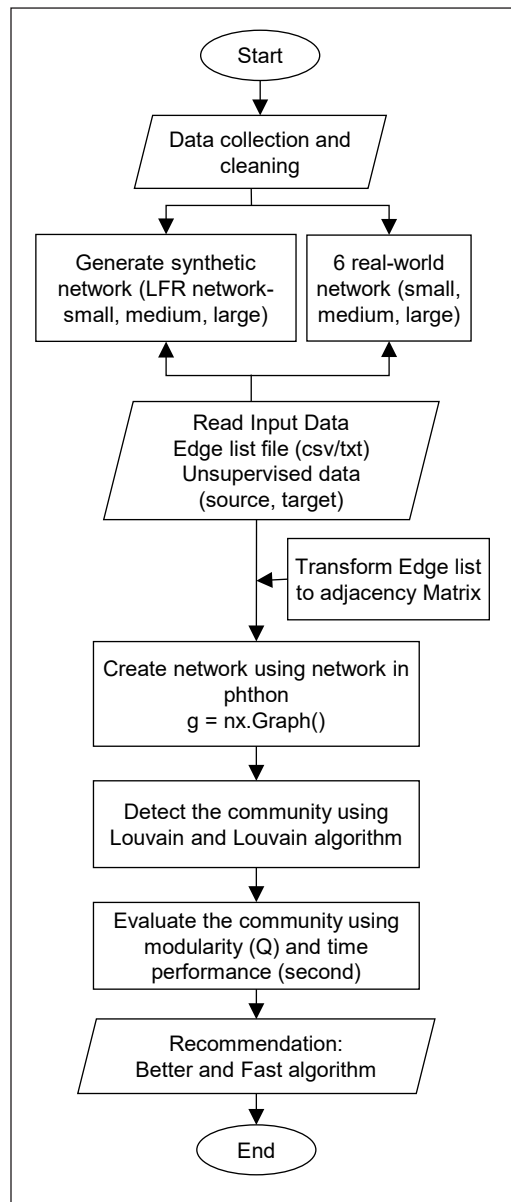


Figure 1. Workflow of the experiment

Meanwhile, the Leiden algorithm enhances the Louvain algorithm (Traag et al., 2019). Despite the fact that it is more complicated than its counterpart, this algorithm is able to derive a faster and more precise computation time. As opposed to Louvain's, the Leiden algorithm comprises three phases, with the modularity optimisation process being the first, followed by partition refinement, and the community aggregation process in the last step. In addition, this algorithm works well on large-scale, medium, and small networks. Figure 2 compares hierarchical clustering, and Figure 3 shows the infographic of the Louvain and Leiden algorithms.

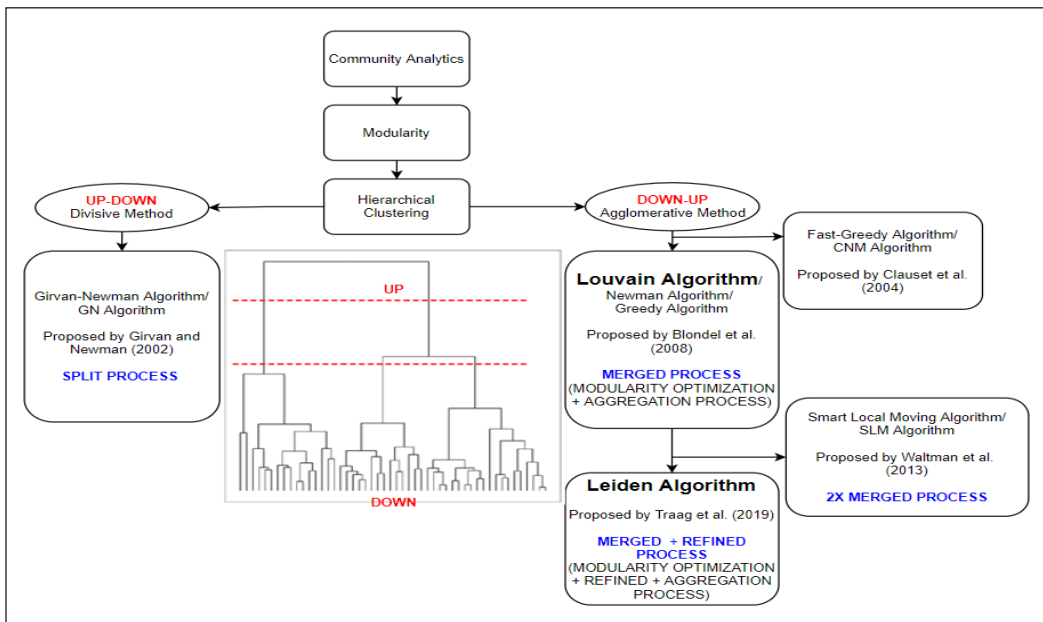


Figure 2. Hierarchical clustering (Anuar et al., 2021)

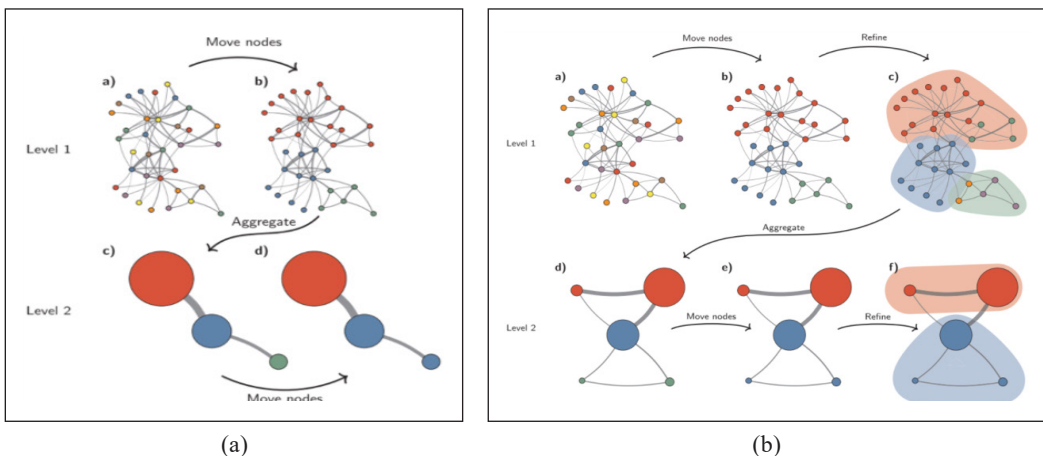


Figure 3. Infographic of: (a) Louvain; and (b) Leiden algorithms method (Traag et al., 2019)

EXPERIMENTS

Experimental Environment

All the algorithms were executed on a device with installed Python running on an Intel Core i7-7700 CPU @ 2.8GHz and 24GB of RAM.

Experimental Data

Many researchers have proposed their community detection and experiment on various types of networks as a benchmark. (Chunaev, 2020) The small dataset consists of less than 10^3 nodes, the medium dataset consists of nodes between 10^3 and 10^5 , while the large dataset consists of nodes of more than 10^5 . (Chunaev, 2020) For convenience, the datasets were distinguished by size, namely, small, medium, and large. Louvain and Leiden's algorithms were tested on a range of synthetic networks, as well as six real-world datasets.

Synthetic Networks

To evaluate the performance of two community detection algorithms, Louvain and Leiden, we generated a synthetic network with a known ground truth called extended LFR. The details are shown in Table 2. Three artificial network data sets were constructed. The difference between the six artificial network data sets lies in the blend factor number of nodes, representing the small, medium, and large networks.

LFR network as a benchmark of synthetic network can be built very quickly, and the complexity of the construction algorithms is linear in the number of links of the graph. So, one can perform tests on very large systems, provided the study method is fast enough to analyse them.

Table 2
Synthetic network used in experiment

LFR Network	Parameters					
	n	τ_1	τ_2	c_{min}	k	μ
Small	500	3	1.5	20	5	0.1-1.0
Medium	7000	3	1.5	20	5	0.1-1.0
Large	10000	3	1.5	20	5	0.1-1.0

Real-world Networks

We also performed experiments on six real-world networks. The dataset retrieved from the UCI machine learning library is detailed in Table 3.

Real-world datasets can include complex networks from sociology, communication, biology, and transportation domains. Fundamentally, real-world or empirical networks are unknown ground truths. The description of each network is provided as follows:

1. Zachary network: A social network of connections formed by 34 karate club members of a US university's karate club in the 1970s.
2. Democratic National Committee (DNC): The official administration body of the United States Democratic Party. It undirected a network of individuals who received the same email in 2016.
3. Cora: A seven-class network of scientific publications in the citation network. The classes include genetic algorithms, case-based reasoning, neural networks, probabilistic techniques, rule learning, reinforcement learning, and theory.
4. Wikipedia: A Wikipedia voting for the promotion of administrator ship. A to B directed edge indicates that user A voted on B to become a Wikipedia administrator.
5. Enron email: An undirected network of communication emails sent around 500,000 emails from the Federal Energy Regulatory Commission.
6. Amazon: A network of products derived from the process of crawling the Amazon website. It is based on the feature 'Customers Who Bought This Item Also Bought' on the Amazon website.

Table 3
The real-world network features

Size datasets	Network	Domain	Feature	
			Nodes (<i>n</i>)	Edges (<i>m</i>)
Small	Zachary	Social network	34	78
	DNC	Communication network	906	12100
Medium	Cora	Publication network	2,708	5,429
	Wikipedia	Wiki-vote network	7,115	103689
Large	Email Enron	Communication network	36,692	183,831
	Amazon	Product network	334,863	925,872

RESULTS AND DISCUSSION

The result elaboration is divided into performance evaluation index and statistical analysis.

Performance Evaluation Index

The detailed performance result of Louvain and Leiden algorithms is explained for the 36 datasets of networks with different nodes and mixing parameters in the form of modularity metrics and running time. First, tests are performed on well-known synthetic networks.

Synthetic Networks

A set of networks was created by the LFR benchmark (Lancichinetti & Fortunato, 2009). LFR generation consists of network size N , the mixing parameters, the average degree k ,

the maximum degree, the minimum, and the maximum community size. Generally, the degrees of the nodes are governed by power laws with an exponent of $\tau_1=3$ and $\tau_2=1.5$, respectively. The parameters of LFR networks are set as shown in Table 2. Figure 4 shows the detection effect in the LFR networks with $n = 500, 7000, \text{ and } 10000$.

The modularity values range between 0 and 1 (Needham & Hodler, 2021). Larger values indicate better communities, while a modularity value of less than 1 signifies that each node is a community. However, the optimal partition indicates 0.41 and above, which is the best value of partition using modularity metrics.

By comparison, both the Louvain and Leiden algorithms have good performance at the value of μ from 0.1 to 1.0 in terms of modularity. However, in terms of running time,

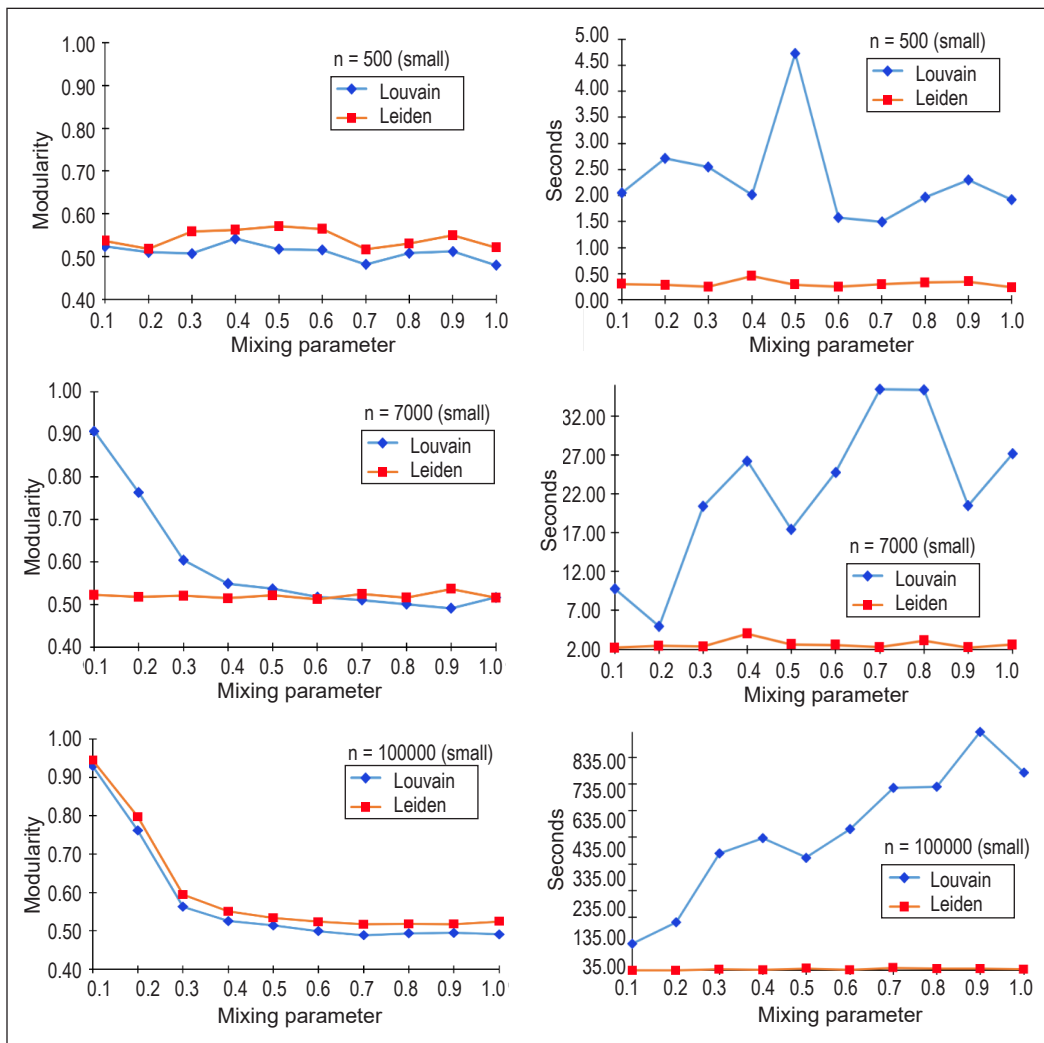


Figure 4. Results on LFR benchmark networks. Small, medium, and big notation indicates that the community sizes are in the range mixing parameter $\mu [0.1, 1.0]$

Leiden performed well and fast. With increasing of μ , the Leiden algorithm has stable performance in the networks with $k = 5$ and $c_{min} = 20$. The algorithm has no significant difference in the networks with varying numbers of nodes. It indicates that the Leiden algorithm is stable in dense networks and is unaffected by the number of nodes and the scale of mixing parameters. However, when $\mu < 0.4$ with a big network scale, the value of modularity increases in the network with $k = 5$ and $c_{min} = 20$. When $\mu > 0.4$, the modularity value is suddenly stable at the optimal range $[0.5, 0.6]$ for both the Louvain and Leiden algorithms.

When the mixing parameter is increased, each node is more closely connected to a local central node. This situation allows too many nodes to be merged into the same community, rapidly deteriorating the detection effect.

Real-world Networks

The selected networks include Zachary Karate Club, DNC, Cora, Wikipedia, email Enron and Amazon, which are in Table 3. Figures 5 to 7 show the detection effect in real networks with small, medium, and large sizes.

By comparison, both the Louvain and Leiden algorithms perform well in real-world networks in terms of modularity. However, in terms of running time, Leiden still performed

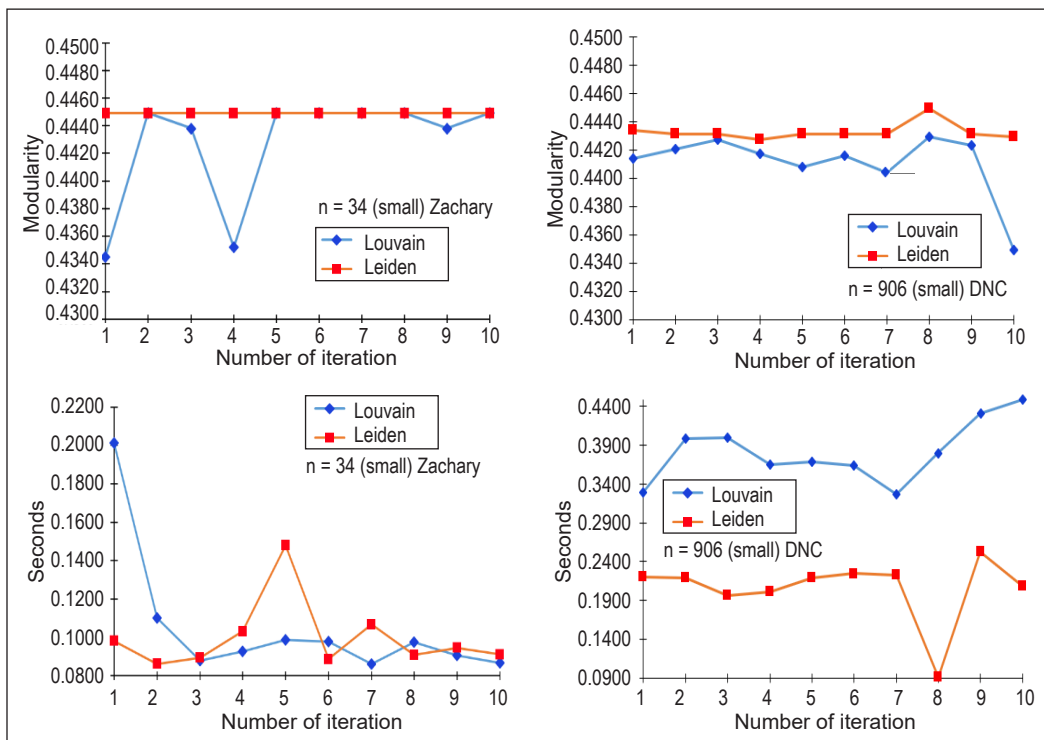


Figure 5. Results on real-world networks (small scale $< 10^3$ nodes)

Comparison of Community Detection Algorithm Based on Modularity

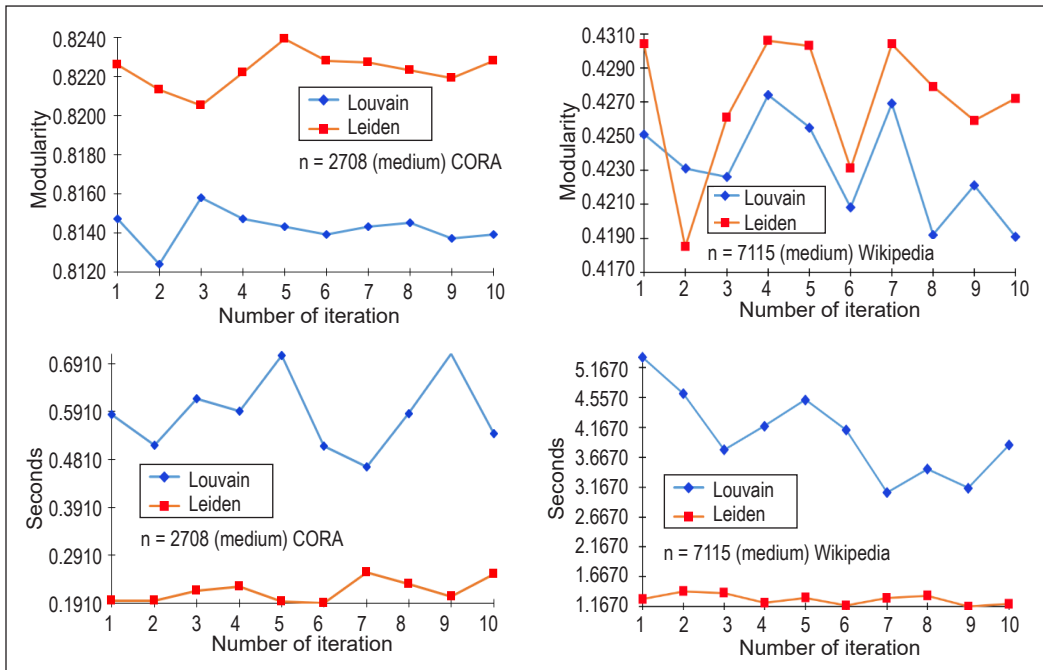


Figure 6. Results on real-world networks (medium scale $10^3 < \text{nodes} < 10^5$)

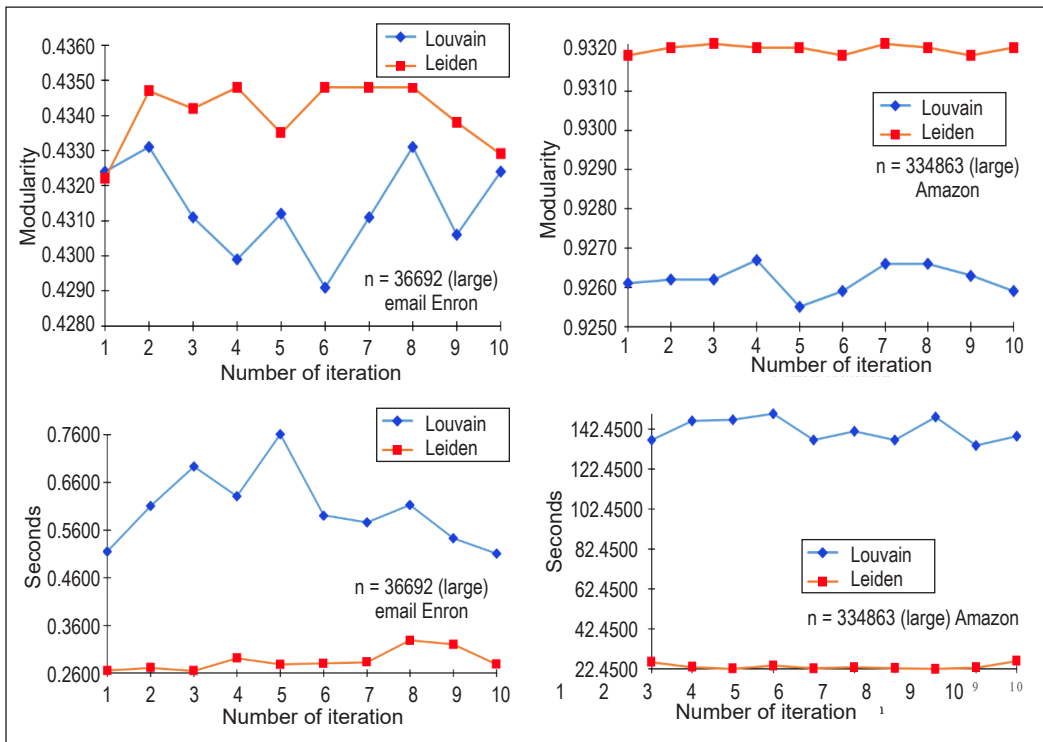


Figure 7. Results on real-world networks (large-scale nodes $> 10^5$)

well and fast compared to Louvain. The algorithm has no significant difference in the networks, with varying types of networks of different sizes. It indicates that the Leiden algorithm is more stable in dense networks and is unaffected by the number of nodes in the ground truth dataset.

Statistical Analysis

Statistical analysis was performed to demonstrate that the Leiden algorithm has a higher quality function (modularity metric) than the Louvain algorithm. Leiden algorithm takes less running time, as measured in seconds. Thus, a hypothesis test of unknown standard deviation, σ , and a small sample size ($n < 30$) was carried out based on the critical value technique. The standard test statistic, t , was applied following a t -distribution with a degree of freedom ($d.f.$) equal to $n - 1$.

The significance level (α) was first identified to produce the total area under the rejection region's distribution curve before determining the $d.f. = - 1$. IBM SPSS software was used to calculate the value of t and derive the conclusion from the results.

The hypothesis tests for null and alternative are denoted by:

Null hypothesis (H0): There is no difference (equal) for the value in modularity and running time between Louvain and Leiden algorithms.

Alternative hypothesis (H1): There is a difference in the value for the modularity and running time between the Louvain and Leiden algorithms.

An independent t -test on a small-size Zachary network of 34 nodes showed no difference in modularity value and time performance for the statistically significant Louvain algorithm with $t(9) = -0.17$ and $p = 0.123$. The value of $p = 0.123$ was chosen because Levene's test produced a statistically significant p -value, where $p < 0.001$ and was less than 0.05. Otherwise, $p = 0.106$ would be chosen. $p = 0.123$ is greater than 0.05, thus failing to reject the null hypothesis that there is no difference in modularity value between the Louvain and Leiden algorithms for a small-size network (Zachary and LFR 500).

However, the results of medium- and large-size networks contradict the small-size network. This test proved a difference in modularity value and execution time performance between Louvain and Leiden algorithms. For the LFR network with 7000 nodes, the test generated a statistically significant result with $t(18) = -4.064$ and $p = 0.001$. Thus, the null hypothesis was rejected due to the statistical difference in value in modularity and running time between Louvain and Leiden algorithms.

These results might provide insight into the impact of the number of nodes against the modularity metric's value and how long each community detection technique takes to run. The Louvain and Leiden algorithms may be suitable for usage in any network size.

CONCLUSION

This research focuses on two community detection algorithms, the Louvain and Leiden methods, which are based on agglomerative techniques using modularity. A detailed summary of the concept and benefit is provided through an experimental comparison. This study demonstrates the state-of-the-art algorithm's step-by-step learning. This study presents two-fold contributions. First, it demonstrates that the Leiden method performs better in modularity and running time than the Louvain algorithm. Second, it shows the application of both synthetic and real networks using these two approaches.

This study exhibits the experimental findings of several different-sized networks using Louvain and Leiden algorithms. Both Louvain and Leiden have an optimal value of the result, but there is an improvement from Leiden. The Leiden method was found to perform better in terms of execution time and the modularity metric. The researchers may consider this information for their project. Future research on network analysis using interdisciplinary data sciences would benefit from these findings, especially in the healthcare field.

ACKNOWLEDGEMENT

This work was supported by the Faculty Publication Fund (Fakulti Teknologi dan Kejuruteraan Elektronik dan Komputer, FTKEK) and Centre for Research and Innovation Management (CRIM), Universiti Teknikal Malaysia Malacca (UTeM).

REFERENCES

- Anuar, S. H. H., Abas, Z. A., Yunos, N. M., Mohd Zaki, N. H., Hashim, N. A., Mokhtar, M. F., Asmai, S. A., Abidin, Z. Z., & Nizam, A. F. (2021). Comparison between Louvain and Leiden algorithm for network structure: A review. *Journal of Physics: Conference Series*, 2129(1), Article 012028. <https://doi.org/10.1088/1742-6596/2129/1/012028>
- Blondel, V. D., Guillaume, J. L. L., Lambiotte, R., & Lefebvre, E. (2008). Fast unfolding of communities in large networks. *Journal of Statistical Mechanics: Theory and Experiment*, 2008(10), 1–12. <https://doi.org/10.1088/1742-5468/2008/10/P10008>
- Chatterjee, S., & Sanjeev, B. S. (2023). Community detection in Epstein-barr virus associated carcinomas and role of tyrosine kinase in etiological mechanisms for oncogenesis. *Microbial Pathogenesis*, 180, Article 106115. <https://doi.org/10.1016/j.micpath.2023.106115>
- Cheng, J., Su, X., Yang, H., Li, L., Zhang, J., Zhao, S., & Chen, X. (2019). Neighbor similarity based agglomerative method for community detection in networks. *Complexity*, 2019, Article 8292485. <https://doi.org/10.1155/2019/8292485>
- Chessa, A., D'Urso, P., De Giovanni, L., Vitale, V., & Gebbia, A. (2023). Complex networks for community detection of basketball players. *Annals of Operations Research*, 325(1), 363–389. <https://doi.org/10.1007/s10479-022-04647-x>

- Chunaev, P. (2020). Community detection in node-attributed social networks: A survey. *Computer Science Review*, 37, Article 100286. <https://doi.org/10.1016/j.cosrev.2020.100286>
- Ding, R., Fu, J., Du, Y., Du, L., Zhou, T., Zhang, Y., Shen, S., Zhu, Y., & Chen, S. (2022). Structural evolution and community detection of china rail transit route network. *Sustainability*, 14(19), Article 12342. <https://doi.org/10.3390/su141912342>
- Evans, J. C., Lindholm, A. K., & König, B. (2022). Family dynamics reveal that female house mice preferentially breed in their maternal community. *Behavioral Ecology*, 33(1), 222–232. <https://doi.org/10.1093/beheco/arab128>
- Gilad, G., & Sharan, R. (2023). From Leiden to Tel-Aviv University (TAU): Exploring clustering solutions via a genetic algorithm. *PNAS Nexus*, 2(6), Article pgad180. <https://doi.org/10.1093/pnasnexus/pgad180>
- Han, Z., Mo, R., Yang, H., & Hao, L. (2018). Module partition for mechanical CAD assembly model based on multi-source correlation information and community detection. *Journal of Advanced Mechanical Design, Systems, and Manufacturing*, 12(1), Article JAMDSM0023. <https://doi.org/10.1299/jamdsm.2018jamdsm0023>
- Irsyad, A., & Rakhmawati, N. A. (2019). Community detection in twitter based on tweets similarities in Indonesian using cosine similarity and Louvain Algorithms. *Register: Jurnal Ilmiah Teknologi Sistem Informasi*, 6(1), Article 22. <https://doi.org/10.26594/register.v6i1.1595>
- Jin, D., Li, R., & Xu, J. (2020). Multiscale community detection in functional brain networks constructed using dynamic time warping. *IEEE Transactions on Neural Systems and Rehabilitation Engineering*, 28(1), 52–61. <https://doi.org/10.1109/TNSRE.2019.2948055>
- Kabir, K., Hassan, L., Rajabi, Z., Akhter, N., & Shehu, A. (2019). Graph-based community detection for decoy selection in template-free protein structure prediction. *Molecules*, 24(5), Article 854. <https://doi.org/10.3390/molecules24050854>
- Karyotis, V., Tsitseklis, K., Sotiropoulos, K., & Papavassiliou, S. (2018). Big data clustering via community detection and hyperbolic network embedding in IoT applications. *Sensors*, 18(4), Article 1205. <https://doi.org/10.3390/s18041205>
- Kramer, J., Boone, L., Clifford, T., Bruce, J., & Matta, J. (2020). Analysis of medical data using community detection on inferred networks. *IEEE Journal of Biomedical and Health Informatics*, 24(11), 3136–3143. <https://doi.org/10.1109/JBHI.2020.3003827>
- Lancichinetti, A., & Fortunato, S. (2009). Community detection algorithms: A comparative analysis. *Physical Review E*, 80(5), Article 056117. <https://doi.org/10.1103/PhysRevE.80.056117>
- LaRock, T., Sakharov, T., Bhadra, S., & Eliassi-Rad, T. (2020). Understanding the limitations of network online learning. *Applied Network Science*, 5(1), Article 60. <https://doi.org/10.1007/s41109-020-00296-w>
- Li, S., Zhao, C., Li, Q., Huang, J., Zhao, D., & Zhu, P. (2023). BotFinder: A novel framework for social bots detection in online social networks based on graph embedding and community detection. *World Wide Web*, 26(4), 1793–1809. <https://doi.org/10.1007/s11280-022-01114-2>
- Needham, M., & Hodler, A. E. (2021). *Graph algorithms Practical examples in Apache Spark and Neo4j*. O'Reilly. O'Reilly Media.

- Nallusamy, K., & Easwarakumar, K. S. (2023). Classifying schizophrenic and controls from fMRI data using graph theoretic framework and community detection. *Network Modeling Analysis in Health Informatics and Bioinformatics*, 12(1), Article 19. <https://doi.org/10.1007/s13721-023-00415-4>
- Newman, M. E. J., & Girvan, M. (2004). Finding and evaluating community structure in networks. *Physical Review E - Statistical, Nonlinear, and Soft Matter Physics*, 69(2), Article 026113. <https://doi.org/10.1103/PhysRevE.69.026113>
- Newman, M. E. J. (2006). Modularity and community structure in networks. *Proceedings of the National Academy of Sciences*, 103(23), 8577–8582. <https://doi.org/10.1073/pnas.0601602103>
- Nicolini, C., Bordier, C., & Bifone, A. (2017). Community detection in weighted brain connectivity networks beyond the resolution limit. *NeuroImage*, 146, 28–39. <https://doi.org/10.1016/j.neuroimage.2016.11.026>
- Park, J. H., & Kwon, H. Y. (2022). Cyberattack detection model using community detection and text analysis on social media. *ICT Express*, 8(4), 499–506. <https://doi.org/10.1016/j.icte.2021.12.003>
- Peebles, M. A., & J. Bischoff, R. (2023). Archaeological networks, community detection, and critical scales of interaction in the U.S. Southwest/Mexican Northwest. *Journal of Anthropological Archaeology*, 70, Article 101511. <https://doi.org/10.1016/j.jaa.2023.101511>
- Rahiminejad, S., Maurya, M. R., & Subramaniam, S. (2019). Topological and functional comparison of community detection algorithms in biological networks. *BMC Bioinformatics*, 20(1), 1-25. <https://doi.org/10.1186/s12859-019-2746-0>
- Singhal, A., Cao, S., Churas, C., Pratt, D., Fortunato, S., Zheng, F., & Ideker, T. (2020). Multiscale community detection in Cytoscape. *PLOS Computational Biology*, 16(10), Article e1008239. <https://doi.org/10.1371/journal.pcbi.1008239>
- Torene, S., Follmann, A., Teague, T., Chang, P., & Howald, B. (2022). Automated hashtag hierarchy generation using community detection and the Shannon Diversity Index, with applications to Twitter and Parler. *International Journal of Semantic Computing*, 16(04), 473–496. <https://doi.org/10.1142/S1793351X22500052>
- Traag, V. A., Waltman, L., & van Eck, N. J. (2019). From Louvain to Leiden: Guaranteeing well-connected communities. *Scientific Reports*, 9(1), Article 5233. <https://doi.org/10.1038/s41598-019-41695-z>
- Ullah, A., Wang, B., Sheng, J. F., Long, J., Khan, N., & Ejaz, M. (2022). A novel relevance-based information interaction model for community detection in complex networks. *Expert Systems with Applications*, 196, Article 116607. <https://doi.org/10.1016/j.eswa.2022.116607>
- Wang, C., & Wang, F. (2022). GIS-automated delineation of hospital service areas in Florida: From Dartmouth method to network community detection methods. *Annals of GIS*, 28(2), 93–109. <https://doi.org/10.1080/19475683.2022.2026470>
- Wang, J., Zhou, C., Rong, J., Liu, S., & Wang, Y. (2022). Community-detection-based spatial range identification for assessing bilateral jobs-housing balance: The case of Beijing. *Sustainable Cities and Society*, 87, Article 104179. <https://doi.org/10.1016/j.scs.2022.104179>

- Xie, L., Cui, J., Qin, Y., & Qiu, L. (2022). Analysis of deformation characteristics of reverse slope under the influence of reservoir water based on community detection. *Environmental Earth Sciences*, 81(4), Article 110. <https://doi.org/10.1007/s12665-022-10252-9>
- Yuan, Q., & Liu, B. (2021). Community detection via an efficient nonconvex optimization approach based on modularity. *Computational Statistics and Data Analysis*, 157, Article 107163. <https://doi.org/10.1016/j.csda.2020.107163>
- Zu, J., Hu, G., Yan, J., & Tang, S. (2021). A community detection based approach for service function chain online placement in data center network. *Computer Communications*, 169, 168–178. <https://doi.org/10.1016/j.comcom.2021.01.014>

Elicitation of Cryptic Secondary Metabolites and Antibacterial Activities from Mangrove and Cave Soil Actinomycetes

Intan Azzween Natasha Ahmad Razi^{1,2}, Nurunajah Ab Ghani^{1,2}, Siti Hajar Sadiran^{1,2}, Suhaidi Ariffin³, Sharifah Aminah Syed Mohamad^{1,2} and Anis Low Muhammad Low^{1,3*}

¹*Atta-ur-Rahman Institute for Natural Products Discovery (AuRIns), Universiti Teknologi MARA (UiTM) Puncak Alam Campus, 42300 Puncak Alam, Selangor, Malaysia*

²*Faculty of Applied Sciences, Universiti Teknologi MARA (UiTM) Shah Alam, 40450 Shah Alam, Selangor, Malaysia*

³*Faculty of Applied Sciences, Universiti Teknologi MARA (UiTM) Negeri Sembilan Branch, Kuala Pilah Campus, 72000 Kuala Pilah, Negeri Sembilan, Malaysia*

ABSTRACT

Actinomycetes' secondary metabolites have received considerable attention due to their many beneficial biological activities. However, many biosynthetic gene clusters in actinomycetes remain silent as they are not transcribed under standard laboratory conditions. Therefore, this study aims to introduce antibiotic elicitors to activate cryptic secondary metabolites in soil actinomycetes and screen them for antibacterial potential. A total of 20 cave and 10 mangrove soil actinomycete isolates were exposed to streptomycin or erythromycin at subinhibitory concentration (0.5–1048 µg/mL) in minimal media. The ethyl acetate extracts were subjected to high-performance liquid chromatography (HPLC) profiling to observe the effect of elicitors towards secondary metabolite production. As a result, 61.7% of the isolates showed a positive impact (appearance of 'new'/increase in metabolite production) when elicitors were supplemented. These changes were more pronounced in erythromycin-induced media (63.3%) than in streptomycin (60.0%).

Two isolates (CS3PT50 and CS3PT53) exhibited significant changes in the profile, with additional peaks detected at 210 and 245 nm, which may indicate the production of new metabolites. More antibacterial activities were observed from stimulated (26.7%) as opposed to non-stimulated isolates (10.0%), including 6 new activities, 1 improved, and 1 decrease in inhibitory. Furthermore, isolate

ARTICLE INFO

Article history:

Received: 17 July 2023

Accepted: 26 October 2023

Published: 04 April 2024

DOI: <https://doi.org/10.47836/pjst.32.3.17>

E-mail addresses:

intanazzween@gmail.com (Intan Azzween Natasha Ahmad Razi)

nurunajah@uitm.edu.my (Nurunajah Ab Ghani)

hajarsadiran@uitm.edu.my (Siti Hajar Sadiran)

suhaidi@uitm.edu.my (Suhaidi Ariffin)

sharifah459@uitm.edu.my (Sharifah Aminah Syed Mohamad)

anislow3085@uitm.edu.my (Anis Low Muhammad Low)

* Corresponding author

CS3PT53 (0.5 mg/disc) displayed broad-spectrum activities, inhibiting *S. aureus* ATCC 25923 and *S. Typhimurium* ATCC 14028. The hit actinomycete isolates belonged to the genus *Streptomyces* (55.6%), *Nocardia* (22.2%), *Nocardioopsis*, and *Saccharomonospora* (11.1%). Overall, this study demonstrated that incorporating antibiotic elicitor at subinhibitory concentration could effectively trigger the production of cryptic secondary metabolites with antibacterial properties in soil actinomycetes.

Keywords: Antibacterial activities, cryptic secondary metabolites, elicitors, soil actinomycetes

INTRODUCTION

Actinomycetes are a diverse group of filamentous, spore-forming Gram-positive bacteria broadly distributed in nature. They are factories of many important secondary metabolites, biologically useful enzymes, and lead molecules, which have found application, particularly in the medical, pharmaceutical, and veterinary sectors (Salwan & Sharma, 2020). More than half of the naturally derived antibiotics currently available in the market originated from actinomycetes (Barka et al., 2016; Ochi, 2017). However, the chances of discovering new bioactive molecules from known actinomycetes have gradually reduced due to the saturation effect (Lee et al., 2014). Exploring unique natural settings such as mangrove and cave soils has resulted in the discovery of more than 220 non-*Streptomyces* or rare actinomycetes, with over a quarter producing 2500 bioactive metabolites (Ezeobiora et al., 2022; Jiang et al., 2016). Despite the potential, rediscovering known compounds or metabolites from actinomycetes remains a major concern (Tomm et al., 2019).

Although actinomycetes produce a wide array of natural metabolites with complex scaffolds and diverse therapeutic effects, a large portion of these molecules encoded in the actinomycete genomes remain unexplored (Covington et al., 2018). It is presumably because these genes are seldom expressed or expressed poorly, with the majority remaining phenotypically silent under conventional screening conditions (Abdelmohsen et al., 2015; Begani et al., 2018). A single *Streptomyces* strain is estimated to produce around 4 compounds but encodes 20–50 secondary metabolite pathways (Belknap et al., 2020; Caboche, 2014; Yagüe et al., 2022). Conversely, other actinomycete families, including *Corynebacteriales*, *Micromonosporaceae*, *Streptosporangineae*, as well as *Pseudonocardiales*, possess approximately 8.4, 13.3, 15.0, and 19.8 secondary metabolite biosynthetic gene clusters (BGCs) per genome and only a fraction of the compounds have been isolated using standard fermentation conditions (Doroghazi et al., 2014). Therefore, exploiting different practical means to induce these silent or cryptic BGCs is of major interest as it may lead to identifying novel scaffolds with targeted biological activities.

At present, various methods have been utilised to activate novel natural products from cryptic BGCs, including the one strain many compounds (OSMAC), chromatin remodelling,

high-throughput elicitor screening (HiTES), genome mining, physical/environmental stress (exposure to UV, changing temperature, and pH shock), co-cultivation with bacteria or fungi and incorporating chemical elicitors (rare earth elements, epigenetic modifiers, organic solvents, and nanoparticles) (Balagurunathan et al., 2020; Begani et al., 2018; Zong et al., 2022). The last approach is among the actively pursued methods as it involves a defined, single chemical agent that triggers a biological response and can easily be optimised to promote existing or new metabolites in actinomycetes (Akhter et al., 2018; Imai et al., 2015; Shentu et al., 2016). According to Narayani and Srivastava (2017), elicitors with the appropriate concentration will induce stress, thus resulting in the activation or inactivation of defence-related genes, transient phosphorylation or dephosphorylation of proteins, and upregulate or even downregulate important enzymes needed for the expression of specific secondary metabolite BGCs.

Growing evidence has revealed that antibiotics at subinhibitory concentrations can potentiate antibiotic production in different *Streptomyces* species (El-Hawary et al., 2023). For example, Imai et al. (2015) reported that a number of antibacterial compounds, including the well-known antibiotic actinorhodin, were induced in the methanolic extract of *S. lividans* 1326 when lincomycin was incorporated at subinhibitory concentration (1/12 or 1/3 of its MIC). The production of the corresponding antibiotic was also found to be dose-dependent, with 5 µg/mL being the ideal concentration. In a separate study by Zhang et al. (2015), cryptic gene clusters in *S. somaliensis* ZH66 were triggered and activated by an anticancer drug lead, fredericamycin A. It was accomplished by adding 300 µg/mL of rifampicin to the fermentation medium, and after 7 days of incubation, a considerable yield (679.5 ± 15.8 mg/L) of the bioactive compound was obtained. The high-dose toxicity, low-dose stimulatory effect is known as hormesis, where at optimum sub-lethal doses, antibiotics or other bioactive molecules can have pleiotropic effects on multiple unrelated bacterial gene expression (Davies et al., 2006; Okada & Seyedsayamdost, 2017). Here, we applied subinhibitory antibiotic concentration (streptomycin and erythromycin) to 30 soil actinomycete isolates. The secondary metabolite responses, as well as their antibacterial potential against four pathogens were assessed. The results were compared between stimulated and non-stimulated HPLC profiles to highlight the effect of antibiotic elicitors on the activation of cryptic secondary metabolites and their antibacterial potential.

MATERIALS AND METHODS

Bacterial Strains

The mangrove soil actinomycetes used in this study were previously obtained from Ariffin et al. (2017), while the cave soil actinomycetes were isolated from two cave soil samples (Gua Kelawar and Gua Wang Buluh) collected from Pulau Tuba Kedah, Malaysia in 2019.

For antibacterial screening, the test bacteria *Escherichia coli* ATCC 25922, *Salmonella enterica subsp. enterica* ser. Typhimurium ATCC 14028, *Staphylococcus aureus* ATCC 25923, and *Bacillus subtilis* ATCC 6633 were obtained from the American Type Culture Collection.

Revival of Actinomycete Isolates

Two selective growth media, tryptone yeast extract (ISP 1) and yeast malt extract medium (ISP 2), were prepared. For mangrove actinomycetes, 3% (final concentration) of sodium chloride (NaCl) was supplemented to replace seawater. All ingredients were dissolved in distilled water and adjusted to pH 7.0–7.2 prior to sterilisation. The actinomycetes glycerol stocks were then thawed, and 100 µL of bacterial culture was pipetted into a universal bottle containing 8 mL of ISP 1 (1.5 g yeast extract and 2.5 g tryptone) and ISP 2 (5.0 g malt extract, 2.0 g yeast extract, and 2.0 g glucose). Broths containing actinomycete isolates were incubated at 30°C for 14 days (170 rpm) and observed for growth. Pure actinomycete isolates were streaked and maintained on ISP 2 agar.

Determination of Elicitors' Minimum Inhibitory Concentration (MIC)

The elicitors' MIC values for each actinomycete isolate were pre-determined using the agar well diffusion method in accordance with the Clinical and Laboratory Standards Institute (CLSI, 2021) guidelines with slight modification. The isolates were cultured in ISP 2 broth and incubated at 30°C for 14 days (170 rpm). The bacterial suspension was adjusted to 0.5 McFarland standard before swabbing onto the minimal media (glucose 0.25 g, yeast extract 0.25 g, K₂HPO₄ 0.50 g, NaCl 0.25 g, MgSO₄·7H₂O 0.25 g, agar 15 g, pH 7.5–8.0). A 7 mm hole was punched aseptically with a cork borer, and 50 µL of the antibiotic elicitor, streptomycin, was introduced into the well with concentrations ranging from 0.25–2048 µg/mL. The agar plates were then incubated at 30°C for 14 days before the inhibition zones were measured in millimetres. 5 µg/mL of ciprofloxacin was used as the positive control, while 50 µL of sterile distilled water was the negative control. The concentration that inhibited actinomycetes growth completely was taken as the MIC value. All tests were carried out in triplicates, and similar procedures were applied to the erythromycin.

Fermentation of Actinomycete Isolates with and Without Elicitors

The revived actinomycete isolates were cultured into minimal media, and antibiotic elicitors (streptomycin and erythromycin) were added separately at a subinhibitory concentration ($\frac{1}{2}$ MIC value determined previously) to trigger cryptic secondary metabolites. For the seeding material, a pure colony of each actinomycete isolate was spread evenly onto ISP 2 agar using a sterile cotton swab and incubated at 30°C for 14 days. After incubation, 2 holes with a diameter of 7 mm were punched aseptically with a cork borer. The agar plugs

were then seeded into a 500 mL Erlenmeyer flask containing 250 mL of fermentation media and incubated at 30°C for 14 days (170 rpm). The above methods were repeated without the addition of elicitors. This served as a control for comparison purposes.

Extraction of Secondary Metabolites

After fermentation, each culture was filtered (Whatman No.1 filter paper), and the resulting cell-free filtrate was collected. Liquid-liquid extraction was carried out by mixing an equal volume of ethyl acetate 1:1 (v/v) with the filtrate and shaking vigorously for 2 hours. The organic layer was collected and separated from the aqueous layer using a separating funnel. This process was repeated three times, and the organic layer was concentrated using a rotary evaporator. All crude extracts were transferred into pre-weighed vials, air-dried, and weighed.

HPLC Profiling of Crude Extracts

Samples were prepared freshly by dissolving the crude extract in 70% acetonitrile (HPLC grade) to make a 1 mg/mL concentration. Similar procedures were also employed for both antibiotic elicitors. Each solution (1 mL) was filtered through a 0.22 µm PTFE filter before injecting into the HPLC system. An injection volume of 10 µL was used. HPLC analysis was performed using Dionex Ultimate 3000 chromatographic system (Thermo Scientific, Bremen, Germany) with rapid separation diode array detector and separated on a Phenomenex Luna C18 column (4.6 mm × 250 mm, 5 µm) with acetonitrile/water as the mobile phase, applying a gradient of 10-100% acetonitrile over 42 mins, using a flow rate of 0.8 mL/min (Sadiran, 2011). The column temperature was set at 30°C, and the secondary metabolite profiles were monitored at multiple wavelengths (210, 245, 270 and 366 nm). Differences in chemical profiles were then compared between the stimulated and non-stimulated actinomycete isolates based on the UV absorption peaks and retention time (t_r).

Antibacterial Activities of Crude Extracts

The antibacterial activities of the crude extracts were evaluated using the standard disc diffusion method following the CLSI (2021) guidelines. The test pathogens were cultured in Mueller Hinton broth and incubated for 16–24 hours at 37°C. The cultures were subsequently adjusted to an OD_{625nm} of 0.08-0.10 (equivalent to 0.5 McFarland standard) before swabbing onto Mueller Hinton agar (MHA). For this assay, ciprofloxacin (5 µg/disc) was used as the positive control, while 10% dimethyl sulphoxide (DMSO) was used as the negative control. A cell-free minimal media incorporated with streptomycin or erythromycin (256 µg/disc respectively) was also included as one of the controls to ensure that the activity observed is due to the crude extracts alone and not the elicitors used. All crude extracts were dissolved in 10% DMSO to produce a working concentration of 10

mg/mL. Sterile blank discs (6 mm) were impregnated with 50 μ L of extract, equal to a final concentration of 0.5 mg/disc. The saturated discs were then placed on the surface of the MHA plate containing the test bacteria and incubated at 37°C for 24 hours. The assay was conducted in triplicates. The zone of inhibition was measured to the nearest millimetre (mm).

Molecular Identification of the Hit Actinobacteria Isolates

Actinomycete isolates that displayed antibacterial activities were sent to the third party (Apical Scientific Sdn. Bhd., Malaysia) for DNA extraction, 16S rRNA gene amplification, PCR purification and sequencing. The DNA was extracted using the Presto™ Mini gDNA Bacteria Kit (Geneaid, GBB100). The 16S rRNA (1.5 kb) was amplified using universal primers (27F and 1492R). The identity of the isolates was determined using the Basic Local Alignment Search Tools (BLAST) and compared to the known species in the GenBank database using the National Centre for Biotechnology Information software (www.ncbi.nlm.nih.gov/).

RESULTS AND DISCUSSION

Effect of Antibiotic Elicitors on Secondary Metabolite Production

This work exposed 30 morphologically distinct actinomycete isolates recovered from different mangrove and cave soils around Malaysia to antibiotic elicitors, streptomycin and erythromycin separately. In order to determine the subinhibitory concentration needed during fermentation, the elicitors MIC towards each isolate was pre-determined. This was necessary to ensure that the concentration used was not lethal but enough to create environmental stress towards the selected actinomycete isolates. Based on the results gathered, most of the isolates tolerated streptomycin (MIC value ranging from 0.5–256 μ g/mL) compared to erythromycin (MIC value ranging from 8–2048 μ g/mL). Isolate CS3PT5 and PGS123 were the most resistant to erythromycin and streptomycin, respectively. After 14 days of fermentation, phenotypic differences such as colony size, colony pigmentation, and turbidity of the media were observed. In general, isolates exposed to elicitors showed delayed or slow growth initially, with smaller colonies but higher biomass, which resulted in a turbid fermentation media. The size difference is likely due to the actinomycetes' response to nutrient limitation and environmental stress (Maier & Pepper, 2015). Furthermore, the turbidity may be attributed to the inducing growth effect during the late growth phase when subinhibitory concentration was applied (Imai et al., 2015). Phenotypic changes were observed for both treated media compared to the control broth. As shown in Figure 1, media supplemented with erythromycin showed brownish pigment, while the streptomycin-treated media exhibited

white-pinkish pigmentation. Both broths supplemented with elicitors were also more turbid, suggesting environmental adaptation. A similar outcome was also observed for isolate CS3PT53 (Figure 2), where the media containing streptomycin showed light orange pigmentation. In contrast, the others were off-white (media with erythromycin) and leaning towards transparent broth (control media). Both media containing elicitors were likewise more turbid than the control media. Differences in colony sizes were also clearly observed. Such an outcome was also reported by Wang et al. (2017), where spectinomycin altered the morphology and pigmentation of *S. coelicolor* M145. Without this antibiotic, *S. coelicolor* M145 grows protruding hyphae and forms large pellets during fermentation. However, when spectinomycin was incorporated, pallet diameters were smaller, while the hyphae formation was barely visible.

In order to assess the effect of elicitors towards secondary metabolite production, all crude extracts were subjected to HPLC analysis, and the chromatograms were compared between stimulated and non-stimulated fermentation media. Due to the absence of chromophores in both elicitors, their chromatograms were not included for comparison. Observations were made in terms of the presence of new or additional peaks, enhanced or reduced peak intensities, loss of peaks, and no change. The different profile patterns gathered for each actinomycete isolate are summarised in Table 1. Based on the results tabulated, changes in the secondary metabolite profiles were observed for all the isolates (100%, 30/30) when elicitors were added to the fermentation media. Due to the complex secondary metabolism in actinomycetes, most of the isolates (66.7%, 20/30) exhibited a combination of patterns instead of a single change when streptomycin was incorporated, while for erythromycin, mixed patterns were seen in 43.3% of the isolates (13/30). Moreover, streptomycin elicited 'new' secondary metabolites in 14 isolates (46.7%), whereas such changes were only observed in 10 isolates (33.3%) when erythromycin was

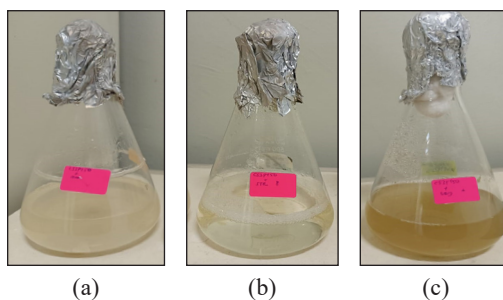


Figure 1. Isolate CS3PT50 after 14 days of fermentation: (a) control media (without elicitor); (b) media supplemented with streptomycin (8 µg/mL); and (c) media supplemented with erythromycin (4 µg/mL)

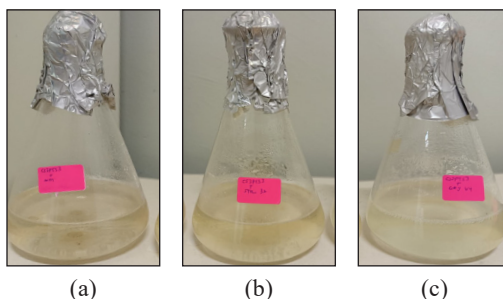


Figure 2. Isolate CS3PT53 after 14 days of fermentation: (a) control media (without elicitor); (b) media supplemented with streptomycin (32 µg/mL); and (c) media supplemented with erythromycin (64 µg/mL)

supplemented. It is also important to note that 17 isolates (56.7%) lose their original peaks compared to the control media profiles, suggesting that the elicitors likewise suppress the production of certain metabolites. The variation in patterns corroborated previous reports where the usage of ribosome-targeting antibiotics tends to produce different responses across the actinobacterial genera (Covington et al., 2018; Shentu et al., 2016). In summary, 40% (24/60) of the isolates activated ‘new’ secondary metabolites and 56.7% (34/60) enhanced the production of the original metabolites. The proportion of positive impacts (appearance of ‘new’ metabolites/ increase in metabolite production) is higher than the negative impacts (loss of original metabolites/ decrease in metabolite production), which are 61.7% (37/60) and 43.3% (26/60) respectively.

Table 1
The different pattern(s) in secondary metabolite profiles of the stimulated and non-stimulated media

Peak pattern(s)	Streptomycin	Erythromycin	Total
New	2/30	1/30	3/60
Enhance	4/30	9/30	13/60
New/ enhance	12/30	9/30	21/60
Reduce	3/30	6/30	9/60
Loss	2/30	3/30	5/60
Loss/ reduce	8/30	4/30	12/60
Change	30/30	30/30	60/60

Notes. The numbers represent the number of isolates

Among the 30 isolates exposed to the elicitors, two isolates (CS3PT50, CS3PT53) demonstrated a distinct inducing effect in the HPLC profiles where additional peaks were detected at 210 and 245 nm. The HPLC profiles of both isolates are shown in Figures 3 and 4, respectively. The metabolic profiles of isolate CS3PT50 at 245 nm (Figure 3) showed that more than 3 new peaks could be detected between retention time (t_R) 16.0 to 27.0 min when streptomycin was incorporated. Apart from 2 enhanced peaks (minute 27.0 and 36.0), a peak loss at 11.5 min can also be observed from the chromatograms. As for isolate CS3PT53, a new peak appeared at minute 13.5, while 2 peaks were enhanced (22.5 min and 35.5 min) in the presence of streptomycin. However, two important peaks (minute 8.0 and 9.0) disappeared when both antibiotic elicitors were added. The differences in the chemical profiles indicated that new cryptic secondary metabolites may be triggered when environmental stimuli were introduced. It is also worth noting that these ‘new’ metabolites may likewise be derivative(s) of the elicitors and could result from biotransformation. In addition, none of the antibiotic concentrations in this work was optimised during fermentation and, thus, should be carried out in the near future to increase the metabolite production of new peaks.

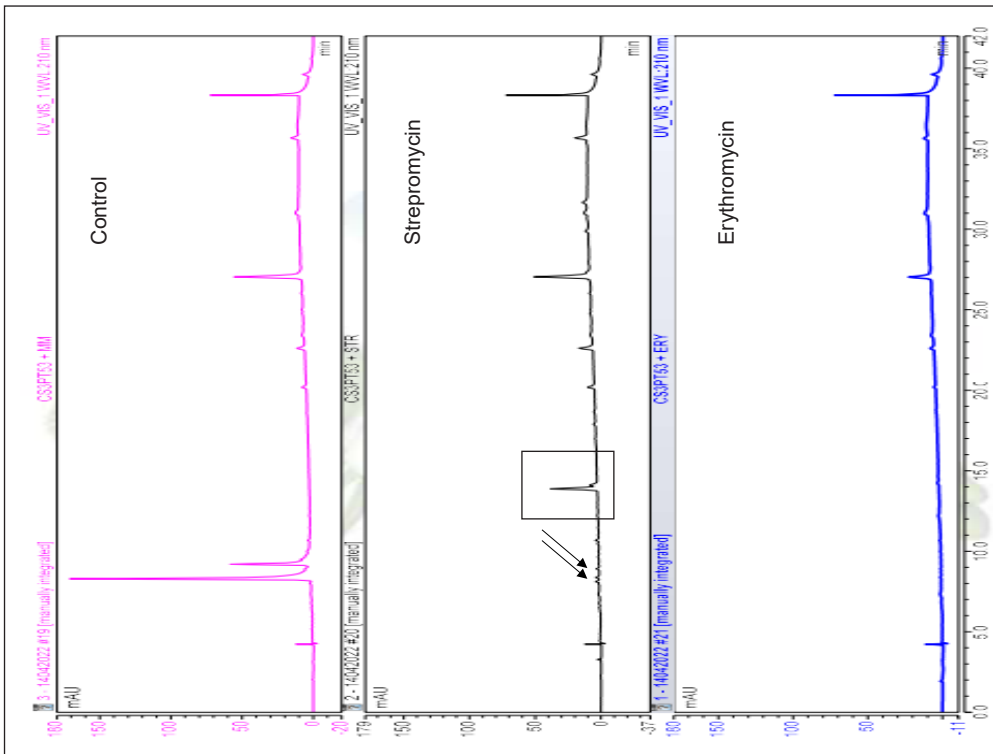


Figure 4. HPLC profiles of isolate CS3PT53 extracts at 210 nm

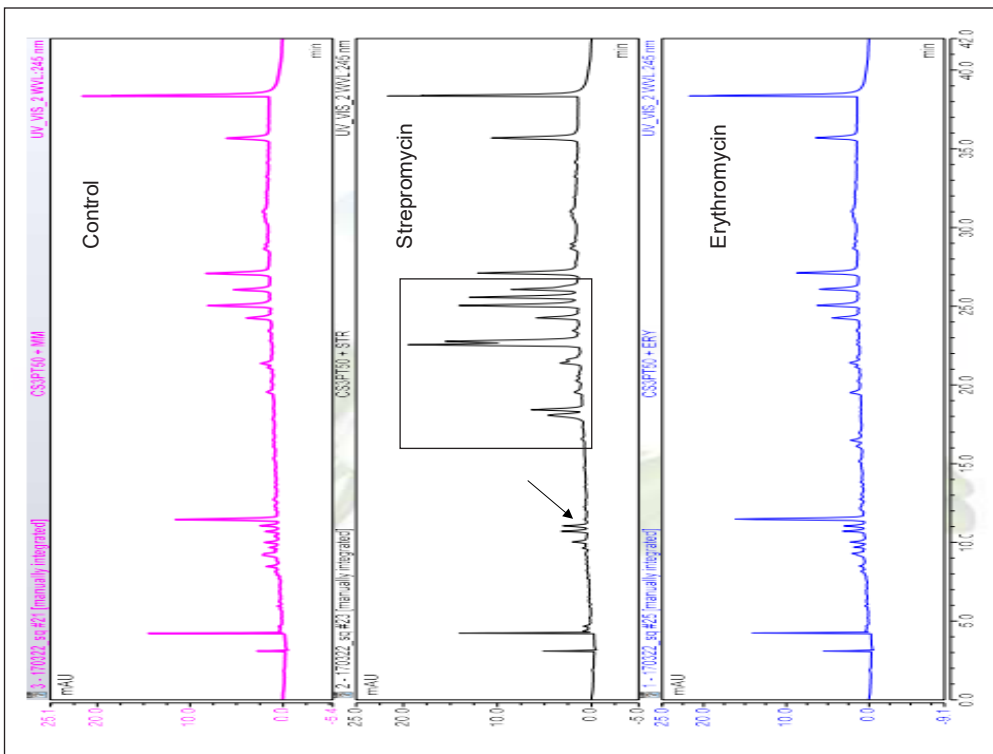


Figure 3. HPLC profiles of isolate CS3PT50 extracts at 245 nm

Antibacterial Activities of Extracts

Besides analysing the secondary metabolite profiles, the differences in antibacterial activity between stimulated and non-stimulated isolates were also investigated using the standard disc diffusion method. The inhibitory activities were further categorised according to their strength: strong for inhibition zone ≥ 20.0 mm, moderate for diameters ranging from 10.0–19.0 mm and weak for diameters < 10.0 mm (Raina et al., 2016). All erythromycin-stimulated crude extracts were excluded since the control extract (cell-free broth with erythromycin alone) inhibited the test bacteria. This was necessary to ensure that the inhibitory activities exerted were purely from the crude extracts, not the elicitors. Table 2 shows the mean diameter of inhibition zones each extract produces on the tested bacteria. Overall, 8 (26.7%) stimulated isolates showed antibacterial properties (6 new activities, 1

Table 2
Antibacterial activities of stimulated and non-stimulated crude extracts

Isolates	Zone of inhibition (mm)							
	Gram-positive				Gram-negative			
	<i>S. aureus</i> ATCC 25923		<i>B. subtilis</i> ATCC 6633		<i>E. coli</i> ATCC 25922		<i>S. Typhimurium</i> ATCC 14028	
NS	S	NS	S	NS	S	NS	S	
KMY9	-	23.3 ± 0.6***	-	-	-	-	x	x
PMS2B	-	-	x	x	-	11.0 ± 1.0**	x	x
PRS3FI	-	10.7 ± 0.6**	-	8.0 ± 1.0*	-	-	-	-
TBS127	-	10.0 ± 1.0**	x	x	-	-	x	x
PGS123	-	18.0 ± 1.0**	-	15.3 ± 0.6**	-	-	-	-
CS1PT57	7.3 ± 0.6*	-	10.0 ± 1.0**	-	-	-	-	-
CS3PT50	-	-	-	7.0 ± 1.0*	-	-	x	x
CS3PT53	19.3 ± 0.6**	-	x	x	-	-	11.0 ± 1.0**	8.3 ± 0.6*
CS3PT5	8.7 ± 0.6*	17.3 ± 0.6**	-	-	-	-	-	-
Positive control	31.3 ± 0.6		27.3 ± 0.6		33.0 ± 1.0		29.0 ± 1.0	
Negative control	-		-		-		-	

Notes. Values are expressed as mean \pm standard deviation of three replicates. NS = Non-stimulated isolate; S = Stimulated isolate; Positive control = Ciprofloxacin 5 μ g/disc; Negative control = 10% DMSO; x = not tested; - = no activity; *** Strong activity (≥ 20.0 mm); ** Moderate activity (10.0-19.0 mm); *Weak activity (< 10.0 mm)

improved, and 1 decreased in activities) against at least one test bacteria as compared to the non-stimulated isolates (3 isolates, 10.0%). As expected, most growth inhibitions were seen against Gram-positive as opposed to Gram-negative bacteria due to the differences in cell wall composition between both cells. Moreover, additional protection provided by the outer membrane offers intrinsic protection against external substances, thus increasing the resistance level of Gram-negative bacteria (Breijyeh et al., 2020).

There was a variation in the strength of activities exerted by the extracts, with the majority showing moderate inhibition (60.0%, 9/15). Among the active crude extracts, extract from stimulated KMY9 isolate exhibited the strongest antibacterial activity (23.3 ± 0.6 mm) against *S. aureus* ATCC 25923, while the weakest was CS3PT50 extract (7.0 ± 1.0 mm) against *B. subtilis* ATCC 6633. Four isolates were found to inhibit more than one test bacteria, including PRS3FI, PGS123, CS1PT57, and CS3PT53. Only isolate CS3PT5 showed more than a 2-fold increment (from 8.7 ± 0.6 mm to 17.3 ± 0.6 mm) in the inhibition zone against *S. aureus* ATCC 25923 when supplemented with streptomycin ($64 \mu\text{g/mL}$), which implied that the corresponding antibacterial compound produced may be enhanced upon antibiotic exposure. Moreover, the HPLC profiles correlate with the increase in growth inhibition as an enhanced peak was detected in the chromatogram (data not shown). This finding is in line with previous reports where the production of actinorhodin, toyocamycin, salinomycin, actinomycin D, tetramycin A, and other relevant antibiotics were significantly boosted using similar techniques (Imai et al., 2015; Shentu et al., 2016; Tanaka et al., 2017).

Apart from that, extract from CS3PT53 showed broad spectrum potential as it inhibited the growth of both *S. aureus* ATCC 25923 (zone inhibition of $19.3 \text{ mm} \pm 0.6$ mm) and *S. Typhimurium* ATCC 14028 (zone inhibition of $11.0 \text{ mm} \pm 1.0$ mm). However, the inhibition properties displayed were from non-stimulated extract instead of stimulated. A decrease in the inhibition zone was also observed against *S. Typhimurium* ATCC 14028. It might be attributed to the loss of 2 important peaks (shown by the arrows) or reduce in peak intensity at minute 27.0 in the streptomycin-induced chromatogram (Figure 4). In addition, a decrease and loss of activity were also observed in 2 isolates, CS3PT53 and CS1PT57, respectively. Although the HPLC profile of isolate CS3PT53 showed several new peaks when induced with streptomycin (Figure 3), this was not reflected in the antibacterial activities. Nevertheless, these possibly 'new' metabolites may possess other biological properties and should be tested further.

Molecular Identification of Hit Isolates

All actinomycete isolates displaying antibacterial activities against the test pathogens were sent to a third party (Apical Scientific Sdn. Bhd., Malaysia) for molecular identification. Most of the hit actinomycete isolates belonged to *Streptomyces* (55.6%), followed by

Nocardia (22.2%), *Nocardiosis*, and *Saccharomonospora* (11.1%, respectively). Detailed results are shown in Table 3.

Table 3
Molecular identification of active actinomycete isolates

No.	Isolates	Closest Cultivated Species	Identity (%)
1	KMY9	<i>Streptomyces</i> sp. JF917314.1	100
2	PMS2B	<i>Saccharomonospora</i> sp. JF806667.1	100
3	PRS3FI	<i>Nocardiosis alba</i> DSM 43377 NR_026340.1	100
4	TBS127	<i>Streptomyces variabilis</i> strain NRRL B-3984 NR_043840.1	99
5	PGS123	<i>Streptomyces carpaticus</i> strain NRRL B-16359. NR_043814.1	99
6	CS1PT57	<i>Streptomyces atrovirens</i> strain NRRL B-16357 NR_043508.1	99
7	CS3PT50	<i>Nocardia asteroides</i> strain NBRC 15531 NR_041856.1	99
8	CS3PT53	<i>Nocardia huaxiensis</i> strain WCH-YHL-001 NR_181411.1	99
9	CS3PT5	<i>Nocardia amamiensis</i> strain TT 00-78 NR_041531.1	99

Past studies have reported some identified hit isolates having other biological activities, including antioxidant, antibacterial, antifungal, and anti-biofilm. For example, Janardhan et al. (2014) reported that *N. alba* (PRS3FI) has shown good antioxidant properties. Separately, Quach et al. (2021) described the purification and structural elucidation of *S. variabilis*' metabolites (TBS127) and revealed that the plant-derived bioactive compounds (daidzein, genistein, and isoprunetin) displayed broad-spectrum inhibitory effects against methicillin-resistant *Staphylococcus epidermidis* ATCC 35984 and *S. Typhimurium* ATCC 14028 with MIC values ranging from 16 to 128 µg/mL. In addition, these compounds likewise exhibited significant growth inhibition ($IC_{50} < 46 \mu\text{M}$) against human lung carcinoma cell line A549. Meanwhile, the extract of *Streptomyces* sp. (similarity closest to *S. atrovirens* NRRL B-16357) isolated from the rhizosphere soil of India's wildlife sanctuary forest showed antimicrobial potential against a wide range of pathogenic bacteria as well as dermatophytes with MIC values $< 0.5 \mu\text{g/mL}$ (Mazumdar et al., 2023). Based on the literature search, no studies have attempted to elicit cryptic secondary metabolites using antibiotics from the present identified isolates.

CONCLUSION

Overall, this study demonstrated that incorporating antibiotic elicitor at subinhibitory concentration impacts actinomycetes' phenotypic, secondary metabolism, and antibacterial activities from unique environments. The effect can be positive, negative, or a combination. Despite the small percentage differences, metabolic changes were more significant in erythromycin-induced media than in streptomycin. In addition, greater antibacterial activities were found in extracts of stimulated as opposed to non-stimulated isolates with

higher inhibitory against Gram-positive than Gram-negative bacteria. The data suggests that antibiotic elicitors can potentially elicit new antibacterial metabolites in actinomycetes and can be exploited further for other biological activities. Further investigation is underway to optimise the production of bioactive compounds and identify the metabolite responsible for the biological activity.

ACKNOWLEDGEMENTS

This research was supported by the FRGS grant (FRGS/1/2019/STG05/UITM/02/03) from the Ministry of Higher Education. The authors are grateful for the facilities Atta-ur-Rahman Institute for Natural Product Discovery (AuRIns), UiTM Puncak Alam provided. The authors would also like to thank Mr. Muhammad Syafiq Razak for assisting in sampling limestone cave soil samples in Pulau Tuba, Kedah, Malaysia.

REFERENCES

- Abdelmohsen, U. R., Grkovic, T., Balasubramanian, S., Kamel, M. S., Quinn, R. J., & Hentschel, U. (2015). Elicitation of secondary metabolism in actinomycetes. *Biotechnology Advances*, 33(6), 798–811. <https://doi.org/10.1016/j.biotechadv.2015.06.003>
- Akhter, N., Liu, Y., Auckloo, B., Shi, Y., Wang, K., Chen, J., Wu, X., & Wu, B. (2018). Stress-driven discovery of new angucycline-type antibiotics from a marine *Streptomyces pratensis* NA-ZhouS1. *Marine Drugs*, 16(9), Article 331. <http://dx.doi.org/10.3390/md16090331>
- Ariffin, S., Abdullah, M. F., & Mohamad, S. A. S. (2017). Identification and antimicrobial properties of Malaysian Mangrove Actinomycetes. *International Journal on Advanced Science, Engineering and Information Technology*, 7(1), Article 71. <https://doi.org/10.18517/ijaseit.7.1.1113>
- Balagurunathan, R., Radhakrishnan, M., Shanmugasundaram, T., Gopikrishnan, V., & Jerrine, J. (2020). Bioassay-guided isolation and characterization of metabolites from Actinobacteria. In *Protocols in actinobacterial research* (pp. 147-163). Springer. https://doi.org/10.1007/978-1-0716-0728-2_8
- Barka, E. A., Vatsa, P., Sanchez, L., Gaveau-Vaillant, N., Jacquard, C., Klenk, H. P., Clément, C., Ouhdouch, Y., & van Wezel, G. P. (2016). Taxonomy, physiology, and natural products of actinobacteria. *Microbiology and Molecular Biology Reviews*, 80(1), 1–43. <https://doi.org/10.1128/membr.00019-15>
- Begani, J., Lakhani, J., & Harwani, D. (2018). Current strategies to induce secondary metabolites from microbial biosynthetic cryptic gene clusters. *Annals of Microbiology*, 68(7), 419–432. <https://doi.org/10.1007/s13213-018-1351-1>
- Belknap, K. C., Park, C. J., Barth, B. M., & Andam, C. P. (2020). Genome mining of biosynthetic and chemotherapeutic gene clusters in *Streptomyces* bacteria. *Scientific Reports*, 10(1), Article 2003. <https://doi.org/10.1038/s41598-020-58904-9>
- Breijyeh, Z., Jubeh, B., & Karaman, R. (2020). Resistance of gram-negative bacteria to current antibacterial agents and approaches to resolve it. *Molecules*, 25(6), Article 1340. <https://doi.org/10.3390/molecules25061340>

- Caboche, S. (2014). Bioinformatics bolster a Renaissance. *Nature Chemical Biology*, 10(10), 798–800. <https://doi.org/10.1038/nchembio.1634>
- CLSI. (2021). *M100 Performance Standards for Antimicrobial Susceptibility Testing* (31st ed.). Clinical and Laboratory Standards Institute. Wayne, Pennsylvania.
- Covington, B. C., Spraggins, J. M., Yniguez-Gutierrez, A. E., Hylton, Z. B., & Bachmann, B. O. (2018). Response of secondary metabolism of hypogean Actinobacterial genera to chemical and biological stimuli. *Applied and Environmental Microbiology*, 84(19), Article e01125-18. <https://doi.org/10.1128/AEM.01125-18>
- Davies, J., Spiegelman, G., & Yim, G. (2006). The world of subinhibitory antibiotic concentrations. *Current Opinion in Microbiology*, 9(5), 445-453. <https://doi.org/10.1016/j.mib.2006.08.006>
- Doroghazi, J. R., Albright, J. C., Goering, A. W., Ju, K. S., Haines, R. R., Tchalukov, K. A., Labeda, D. P., Kelleher, N. L., & Metcalf, W. W. (2014). A roadmap for natural product discovery based on large-scale genomics and metabolomics. *Nature Chemical Biology*, 10(11), 963–968. <https://doi.org/10.1038/nchembio.1659>
- El-Hawary, S. S., Hassan, M. H., Hudhud, A. O., Abdelmohsen, U. R., & Mohammed, R. (2023). Elicitation for activation of the actinomycete genome's cryptic secondary metabolite gene clusters. *RSC Advances*, 13(9), 5778-5795. <https://doi.org/10.1039/D2RA08222E>
- Ezeobiora, C. E., Igbokwe, N. H., Amin, D. H., Enwuru, N. V., Okpalanwa, C. F., & Mendie, U. E. (2022). Uncovering the biodiversity and biosynthetic potentials of rare actinomycetes. *Future Journal of Pharmaceutical Sciences*, 8(1), 1-9. <https://doi.org/10.1186/s43094-022-00410-y>
- Imai, Y., Sato, S., Tanaka, Y., Ochi, K., & Hosaka, T. (2015). Lincomycin at subinhibitory concentrations potentiates secondary metabolite production by *Streptomyces* spp. *Applied and Environmental Microbiology*, 81(11), 3869-3879. <https://doi.org/10.1128/AEM.04214-14>
- Janardhan, A., Kumar, A. P., Viswanath, B., Saigopal, D. V., & Narasimha, G. (2014). Production of bioactive compounds by actinomycetes and their antioxidant properties. *Biotechnology Research International*, 2014, Article 217030. <https://doi.org/10.1155/2014/217030>
- Jiang, Y., Li, Q., Chen, X., & Jiang, C. (2016). Isolation and cultivation methods of actinobacteria. In D. Dhanasekaran & Y. Jiang (Eds.), *Actinobacteria - Basics and Biotechnological Applications* (pp. 39-58). InTechOpen. <https://doi.org/10.5772/61457>
- Lee, L., Zainal, N., Azman, A., Eng, S., Goh, B., & Yin, W. (2014). Diversity and antimicrobial activities of actinobacteria isolated from tropical mangrove sediments in Malaysia. *The Scientific World Journal*, 2014, Article 698178. <https://doi.org/10.1155/2014/698178>
- Maier, R. M., & Pepper, I. L. (2015). Bacterial growth. In I. L. Pepper, C. P. Gerbal & T. J. Gentry (Eds.), *Environmental Microbiology* (3rd ed.; pp. 37–56). Academic Press.
- Mazumdar, R., Dutta, P. P., Saikia, J., Borah, J. C., & Thakur, D. (2023). *Streptomyces* sp. strain PBR11, a forest-derived soil *Actinomycetia* with antimicrobial potential. *Microbiology Spectrum*, 11(2), Article e03489-22. <https://doi.org/10.1128/spectrum.03489-22>
- Narayani, M., & Srivastava, S. (2017). Elicitation: A stimulation of stress in in vitro plant cell/tissue cultures for enhancement of secondary metabolite production. *Phytochemistry Reviews*, 16, 1227-1252. <https://doi.org/10.1007/s11101-017-9534-0>

- Ochi, K. (2017). Insights into microbial cryptic gene activation and strain improvement: Principle, application and technical aspects. *The Journal of Antibiotics*, 70(1), 25–40. <https://doi.org/10.1038/ja.2016.82>
- Okada, B. K., & Seyedsayamdost, M. R. (2017). Antibiotic dialogues: Induction of silent biosynthetic gene clusters by exogenous small molecules. *FEMS Microbiology Reviews*, 41(1), 19–33. <https://doi.org/10.1093/femsre/fuw035>
- Quach, N. T., Nguyen, Q. H., Vu, T. H. N., Le, T. T. H., Ta, T. T. T., Nguyen, T. D., Van Doan, T., Van Nguyen, T., Dang, T. T., Nguyen, X. C., Chu, H. H., & Phi, Q. T. (2021). Plant-derived bioactive compounds produced by *Streptomyces variabilis* LCP18 associated with *Litsea cubeba* (Lour.) Pers as potential target to combat human pathogenic bacteria and human cancer cell lines. *Brazilian Journal of Microbiology*, 52(3), 1215–1224. <https://doi.org/10.1007/s42770-021-00510-6>
- Sadiran, S. H. (2011). *Bioactive microbial metabolites from Malaysian rainforest soil fungi as a source of new drugs candidates*. [Master thesis]. UiTM Press. <https://ir.uitm.edu.my/id/eprint/65230/1/65230.pdf>
- Salwan, R., & Sharma, V. (2020). Molecular and biotechnological aspects of secondary metabolites in actinobacteria. *Microbiological Research*, 231, Article 126374. <https://doi.org/10.1016/j.micres.2019.126374>
- Shentu, X., Liu, N., Tang, G., Tanaka, Y., Ochi, K., Xu, J., & Yu, X. (2016). Improved antibiotic production and silent gene activation in *Streptomyces diastatochromogenes* by ribosome engineering. *The Journal of Antibiotics*, 69(5), 406–410. <https://doi.org/10.1038/ja.2015.123>
- Tanaka, Y., Kasahara, K., Hirose, Y., Morimoto, Y., Izawa, M., & Ochi, K. (2017). Enhancement of butanol production by sequential introduction of mutations conferring butanol tolerance and streptomycin resistance. *Journal of Bioscience and Bioengineering*, 124(4), 400–407. <https://doi.org/10.1016/j.jbiosc.2017.05.003>
- Tomm, H. A., Ucciferri, L., & Ross, A. C. (2019). Advances in microbial culturing conditions to activate silent biosynthetic gene clusters for novel metabolite production. *Journal of Industrial Microbiology and Biotechnology*, 46(9–10), 1381–1400. <https://doi.org/10.1007/s10295-019-02198-y>
- Wang, H., Zhao, G., & Ding, X. (2017). Morphology engineering of *Streptomyces coelicolor* M145 by sub-inhibitory concentrations of antibiotics. *Scientific reports*, 7(1), Article 13226. <https://doi.org/10.1038/s41598-017-13493-y>
- Yagüe, P., Willemsse, J., Xiao, X., Zhang, L., Manteca, A., & van Wezel, G. P. (2022). FtsZ phosphorylation pleiotropically affects Z-ladder formation, antibiotic production, and morphogenesis in *Streptomyces coelicolor*. *Antonie van Leeuwenhoek*, 116(1), 1–19. <https://doi.org/10.1007/s10482-022-01778-w>
- Zhang, Y., Huang, H., Xu, S., Wang, B., Ju, J., Tan, H., & Li, W. (2015). Activation and enhancement of fredericamycin A production in deepsea-derived *Streptomyces somaliensis* SCSIO ZH66 by using ribosome engineering and response surface methodology. *Microbial Cell Factories*, 14, 1–11. <https://doi.org/10.1186/s12934-015-0244-2>
- Zong, G., Fu, J., Zhang, P., Zhang, W., Xu, Y., Cao, G., & Zhang, R. (2022). Use of elicitors to enhance or activate the antibiotic production in *Streptomyces*. *Critical Reviews in Biotechnology*, 42(8), 1260–1283. <https://doi.org/10.1080/07388551.2021.1987856>

Review Article

Detection of Sedge Weeds Infestation in Wetland Rice Cultivation Using Hyperspectral Images and Artificial Intelligence: A Review

Muhamad Noor Hazwan Abd Manaf¹, Abdul Shukor Juraimi^{1*}, Mst. Motmainna¹, Nik Norasma Che'Ya², Ahmad Suhaizi Mat Su², Muhammad Huzaifah Mohd Roslim³, Anuar Ahmad⁴ and Nisfariza Mohd Noor⁵

¹Department of Crop Science, Faculty of Agriculture, Universiti Putra Malaysia, 43400 UPM, Serdang, Selangor, Malaysia

²Department of Agriculture Technology, Faculty of Agriculture, Universiti Putra Malaysia, 43400 UPM, Serdang, Selangor, Malaysia

³Department of Crop Science, Faculty of Agricultural and Forestry Sciences, Universiti Putra Malaysia Bintulu Sarawak Campus, 97008 Bintulu, Sarawak, Malaysia

⁴Department of Geoinformation, Faculty of Built Environment & Surveying, Universiti Teknologi Malaysia, 81310 Johor Bahru, Johor, Malaysia

⁵Department of Geography, Faculty of Arts and Social Sciences, University of Malaya, 50603 Kuala Lumpur, Malaysia

ABSTRACT

Sedge is one type of weed that can infest the rice field, as well as broadleaf and grasses. If sedges are not appropriately controlled, severe yield loss will occur due to increased competition with cultivated rice for light, space, nutrients, and water. Both sedges and grasses are monocots and have similar narrowed leaf characteristics, but most sedge stems have triangular prismatic shapes in cross sections, which differ them from grasses. Event sedges and grasses differ

in morphology, but differentiating them in rice fields is challenging due to the large rice field area and high green color similarity. In addition, climate change makes it more challenging as the distribution of sedge weed infestation is influenced by surrounding abiotic factors, which lead to changes in weed control management. With advanced drone technology, agriculture officers or scientists can save time and labor in distributing weed surveys in rice fields. Using hyperspectral sensors on drones can increase classification

ARTICLE INFO

Article history:

Received: 14 May 2023

Accepted: 02 November 2023

Published: 04 April 2024

DOI: <https://doi.org/10.47836/pjst.32.3.18>

E-mail addresses:

gs62094@student.upm.edu.my (Muhamad Noor Hazwan Abd Manaf)

ashukur@upm.edu.my (Abdul Shukor Juraimi)

motmainna@upm.edu.my (Mst. Motmainna)

niknorasma@upm.edu.my (Nik Norasma Che'Ya)

asuhaizi@upm.edu.my (Ahmad Suhaizi Mat Su)

muhammadhuzaifah@upm.edu.my (Muhammad Huzaifah Mohd Roslim)

anuarahmad@utm.my (Anuar Ahmad)

nish@um.edu.my (Nisfariza Mohd Noor)

* Corresponding author

accuracy and differentiation between weed species. The spectral signature of sedge weed species captured by the hyperspectral drone can generate weed maps in rice fields to give the sedge percentage distribution and location of sedge patch growth. Researchers can propose proper countermeasures to control the sedge weed problem with this information. This review summarizes the advances in our understanding of the hyperspectral reflectance of weedy sedges in rice fields. It also discusses how they interact with climate change and phenological stages to predict sedge invasions.

Keywords: Climate change, drone, internet of things (IoT), rice, smart farming, weed

INTRODUCTION

Rice is one of the world's most important food sources and Malaysia's third most important crop (Hakim et al., 2010). However, weed, a well-known rice pest, is causing significant crop loss in rice cultivation worldwide (Hakim et al., 2013). Moreover, the shift of abundance and dominance of sedges and other weeds, which are dynamic (Juraimi et al., 2013), make the invasion prediction for the coming season more challenging.

Several sedge weeds in rice fields and the most invasive species in Malaysia are *Fimbristylis miliacea*, *Cyperus iria*, *Cyperus difformis*, and *Scirpus grossus* (Hakim et al., 2013). Each weed species had its unique spectral signature captured by a hyperspectral camera (Norasma et al., 2020). However, the changing climate, including rainfall, daylight hours, temperature, relative humidity, and the duration of the drought season (Alam et al., 2014), may alter the levels of weed invasion and crop-weed competition, which is prone to benefit the weeds due to their better adaptation (Iqbal et al., 2020). These changes will also influence the spectral reading (Arias et al., 2021) and need to be considered when capturing the spectrum for sedge weed identification. Moreover, the phenological changes of a species will also result in different spectrum measurements as the biochemical biophysical traits occur when a sedge weed enters a new growth stage, for example, before and after the emission of floral tassel (Voss et al., 2021).

Smart farming utilizes Unmanned Aerial Vehicles (UAVs) and Internet of Things (IoT) paradigms to achieve sustainable agriculture. IoT technology will reduce the inherent climate impact with the combination of UAVs by enabling real-time reactions toward sedge infestations in rice fields (Islam et al., 2021). The weed infestation rate in rice fields can be determined by comparing spectral signature information with ground data, which can later be recorded in a smartphone app to help farmers combat weed problems (Norasma et al., 2020). Using a spectral signature enables faster detection of weeds in the field than the traditional method, which takes longer and requires more time to cover the entire rice field (Norasma et al., 2020). Hyperspectral remote sensing, or spectroscopy, can identify differences between species in agricultural and non-agricultural environments (Basinger et al., 2020).

With hundreds of spectral bands, hyperspectral simultaneously captures spectral and spatial information (Zhang et al., 2019). Numerous airborne hyperspectral scanning instruments have been developed by embedding the sensor in a UAV (Lillesand et al., 2015). UAVs, also known as drones, can provide high-quality images and are a more economical solution than human-crewed aircraft or satellite images (Radoglou-Grammatikis et al., 2020). In summary, a UAV is an uncrewed aircraft controlled remotely by an operator and can carry a variety of cameras, including hyperspectral cameras, to capture aerial photos. Insecticide and fertilizer prospecting and spraying, seed sowing, weed recognition, fertility testing, mapping, and crop forecasting are UAV applications in agriculture (Islam et al., 2021).

Forecasting sedge infestations based on the changing climate can create an early and real-time warning system for farmers to take suitable actions. However, there is insufficient information about the spectral information of sedges growing in rice fields. Predictive modeling using artificial intelligence (AI) technology with deep learning is also required to analyze spectral differences. Changes in sedge morphology at different phenological stages and climate conditions may result in variations in spectral reflectance. Therefore, hyperspectral information should also be considered in a few phenological phases of sedges under climate variation, including atmospheric temperature, relative humidity, flooding conditions, and soil salinity. This review aims to focus on the role of the hyperspectral sensor, which is a part of remote sensing (RS), in distinguishing weedy sedges in rice fields and discuss the potential of spectral reflectance responses in different climatic settings and phenological stages, which can potentially be used to create a forecasting system for sedge infestation in the rice cultivation industry.

WETLAND RICE CULTIVATION

Due to vast low and flat land availability, farmers hugely plant rice in Malaysia's northern and eastern sides, especially in Kedah and Kelantan (Norasma et al., 2020). In addition to low and flat land, wetland rice cultivation requires a steady and abundant water supply throughout its life cycle (Norasma et al., 2020; Simma et al., 2017). One study categorized rice land ecosystems into four types: irrigated, rainfed lowland, upland, and deep-water (Khush, 1997). With higher area coverage, irrigated rice is the primary technique farmers use and has higher production than other rice areas (Anwar et al., 2011; Juraimi et al., 2013). Approximately 57% of rice production in Peninsular Malaysia is obtained from ten granary areas with extensive irrigation and drainage facilities (Dilipkumar et al., 2020). However, fluctuations in rainfall patterns worldwide due to the changing climate have threatened water resources and rice productivity (Simma et al., 2017). Maintaining sustainable rice production is crucial because it supplies the primary food (Rahim et al., 2017). Rice production also contributes to farmers' social and economic aspects by providing jobs and opportunities (Rahim et al., 2017). A study also predicted a faster

increase in rice demand than in its production in most countries (Ismail & Abdullah, 2020). The Malaysian government imported rice from different countries to compensate for the shortage in domestic output supply (Dilipkumar et al., 2020). Moreover, a lack of weed management can reduce rice production (Norasma et al., 2020).

WEED PROBLEM

Weed problems have existed throughout history (Ismail & Abdullah, 2020; Juraimi et al., 2009). Weeds are unwanted plants that grow in the same area as the crops (Ahmad-Hamdani et al., 2021; Hasan, Hasan, Mokhtar et al., 2021; Motmainna et al., 2021a; Uddin et al., 2010). Weed infestation devastates crop production and overall yield (Hakim et al., 2014; Mondal et al., 2011). They interfere with the field activities of rice production systems during the crop-growing season. Besides, the existing practice uses uniform application of herbicides, resulting in high environmental degradation and low crop field productivity (Motmainna et al., 2021b; Motmainna et al., 2021c; Pantazi et al., 2016). In most situations, weeds take advantage of disturbed areas, allowing them to use the available resources effectively and grow abundantly (Ismail & Abdullah, 2020). They are very competitive with crops for all resources, such as nutrients, light, space, and water, negatively affecting crop production (Motmainna et al., 2021d; Galal & Shehata, 2015). In addition to the competition mentioned above, weeds can exert allelopathic effects on rice plants by reducing plant height and dry weight, which inhibit crop growth and development (Ismail & Siddique, 2012; Motmainna et al., 2021e).

Malaysia's average rice yield loss is between 10% and 35%, with grass, broad-leaved weed, and sedge yield losses of 41%, 28%, and 10%, respectively (Juraimi et al., 2013). Yield losses rely primarily on climate, weed species and density, rice varieties, growth rate, management practices, and rice ecosystems (Juraimi et al., 2013). Weed control is more critical in direct-seeded systems than transplanted systems because weeds can emerge simultaneously or before rice plants, leading to a severe competition problem (Begum et al., 2006; Galal & Shehata, 2015).

The weed flora population in rice fields usually consists of different types of grasses, sedges, and broadleaf weeds (Ismail & Abdullah, 2020). After grasses, sedges rank second in abundance among primary rice weeds (Yaduraju & Mishra, 2008). However, in the main season, sedges were the most common weeds, followed by broad-leaved weeds and grasses (Juraimi et al., 2010). During the early season, grasses are typically the most dominant, whereas sedges and broadleaf weeds dominate later (Yaduraju & Mishra, 2008)

SEDGES WEEDS INFESTATION

Many taxa in the Cyperaceae (sedges) family are highly aggressive weeds and are the main or even dominant components of many plant communities, especially in wetland

areas (Simpson et al., 2011). The Cyperaceae family is a monocotyledonous angiosperm containing 106 genera and 5387 species (Govaerts & Simpson, 2007). They are classified as Poales and have a superficial resemblance to the Poaceae (grasses) (Simpson et al., 2011). They have a global distribution and are absent from the Antarctic continent. They can be found at altitudes ranging from sea level to 5000 m in the Himalayas and various habitats, including high Arctic tundra, tropical woodland, and seasonally wet grasslands (Simpson et al., 2011).

Sedges are similar to grasses but have three leaves and typically have triangular stems that do not have nodes and internodes (Yaduraju & Mishra, 2008). Most sedges thrive in relatively wet habitats, such as rice fields (Ueno, 2001), and some are adapted to pH 4 and below (Gabriel et al., 1986). Similar to grasses and broad-leaved weeds, sedges drastically reduce the number of productive tillers due to weedy competition (Juraimi et al., 2010). Sedges are generally more competitive with underground components, such as rhizomes, tubers, or roots (Yaduraju & Mishra, 2008).

Fimbristylis miliacea, *Cyperus iria*, *Cyperus difformis*, and *Scirpus grossus* (Table 1) were the four most abundant sedges in 32 separate rice fields in the coastal zone of Sebarang Perak in West Malaysia (Hakim et al., 2013). Although *Cyperus rotundus* is not an aggressively infesting rice-planting area in Malaysia, it is one of Asia’s four most important sedge weeds (Issahaku et al., 2021). In the coastal rice-growing area of Kedah, *C. rotundus* was only 10 % in terms of frequency compared to *F. miliacea*, *C. iria*, *C. difformis*, and *S. grossus* with 67.50, 60.00, 60.00, and 52.50 %, respectively (Hakim et al., 2010). Figure 1 shows examples of pictures of sedge weeds in Asia that are inflorescent.

Table 1
 Details on the top four sedges infest Malaysia rice fields

Scientific name	Common name		Life cycle	Propagation	Chemical Control
	English	Malay			
<i>Fimbristylis miliacea</i> (L.) Vahl (C4)	Lesser fimbry	Rumput tahi kerbau	Annual/ Perennial	Seed	2,4-D, bensulfuron-methyl, ethoxysulfuron, pyrazosulfuron-ethyl
<i>Cyperus iria</i> L. (C4)	Grasshopper's cyperus	Para/Rusiga anak emas	Annual	Seed	2,4-D, bispyribac sodium, ethoxysulfuron, pyrazosulfuron-ethyl
<i>Cyperus difformis</i> L. (C3)	Small-flowered umbrella plant	Para	Annual	Seed	2,4-D, bensulfuron-methyl, cyclosulfamuron, ethoxysulfuron, pyrazosulfuron-ethyl
<i>Scirpus grossus</i> L. f. (C3)	Creater club-rush	Menderong	Perennial	Stolon, tuber, seed	2,4-D, bensulfuron-methyl, ethoxysulfuron

Source: Hakim et al., 2013; Bruhl & Wilson, 2007; Man et al., 2018

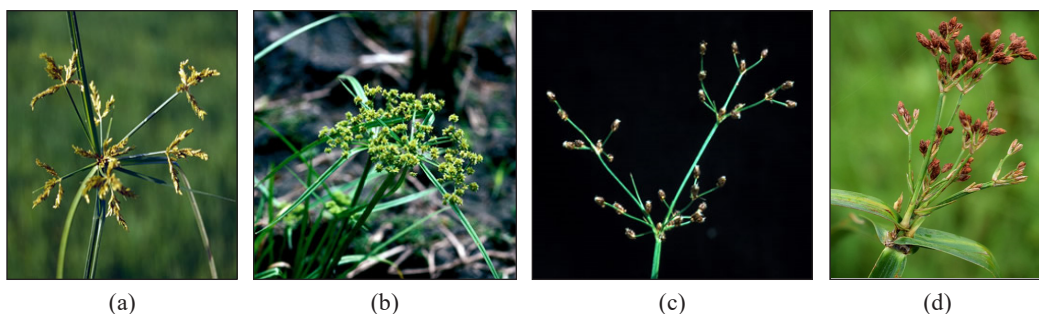


Figure 1. Pictures of the three most troublesome sedge rice weeds in Asia (Adapted from Caton et al., 2010): (a) *Cyperus iria* is a tufted weed with a dense flower ranging from yellowish-brown to greenish; (b) The umbellate and dense globose or ovoid inflorescence of *Cyperus difformis*; (c) *Fimbristylis miliacea* is a slender, tufted herb with a reddish-brown flower that is compound; and (d) *Scirpus grossus* is a rhizomatous perennial herb, with small spikelets flower that is often brown or greenish brown

The composition of the weed population in rice cultivation varies depending on a range of factors, including cultural practices (either transplanting or direct seeding), rice variety, location, water and soil management, methods of weed control, the current weed flora population, and climatic conditions (Ismail & Abdullah, 2020). For example, sedge and grass weeds are more dominant in transplanting than in broadleaved practices, but broadleaved weeds are the most prevalent in wet seedling practices (Aqilah et al., 2012). Weed populations are also distinct between conventional and organic rice farming systems (Kurniadie et al., 2019).

Integrated control techniques, including indirect and direct control methods, have been implemented to manage weed infestation in rice fields (Azmi et al., 2000). Clean and weed-free seeds, tilling, land preparation, water management, cultivar selection, and crop rotation are examples of indirect controls. Manual weeding and chemical applications are examples of direct controls. Flooding is the most prevalent method of weed control in irrigated rice fields, such as annual sedges, which suppresses young weed seedling germination and growth using standing water at a height of at least 5 cm above the ground at the early stage of planting (Rodenburg et al., 2011).

CHANGING CLIMATE ON RICE AND SEDGE WEEDS

Agriculture is highly reliant on climate (Alam et al., 2014). In addition to agronomics and genetics, climate change affects crop yield and productivity in the long run (Stuecker et al., 2018). This exogenous force has been shown to reduce the impact of genetics (Bell et al., 1995). According to Alam et al. (2014), variations in climatic conditions have significantly impacted crops in Malaysia. They also stated that human actions have caused most modern climate change. Climate change has various effects on agriculture, which vary by region, time, and crop type (Alam et al., 2014).

According to a study, the influence of climate on rice production varies significantly by region and is strongly seasonally modulated (Stuecker et al., 2018). Climate conditions, such as rainfall, daylight hours, temperature, relative humidity, and the duration of the drought season, have caused crop production to vary from season to season (Alam et al., 2014). A previous study found that variations in soil moisture significantly affect rice production (Stuecker et al., 2018). Although temperature variability is of little importance, they also suggested that temperatures might be regularly exceeded by the end of the century if warming continues unabated, limiting rice production.

As the climate changes, the levels of weed invasion and crop-weed competition are likely to be altered (Jinger et al., 2017). This alteration is prone to benefit weeds, as many have been resistant to climate change and have better adaptation (Iqbal et al., 2020). Although the number of C4 species was estimated to range from 27% to 34% of all Cyperaceae species, there is a high potential for C4 sedge weeds to spread and wreak havoc on agricultural systems, especially in temperate regions (Simpson et al., 2011). C4 species, including *F. milliacea* and *C. iria* (Issahaku et al., 2021), are anticipated to have more advantages under water stress, high temperatures, and high light intensity conditions (Simpson et al., 2011). These advantages result in better adaptation of C4 weeds to hot and drier climates (Rodenburg et al., 2011) over C3 plants, including rice (Jinger et al., 2017). In addition, *C. rotundus* is considered the world's worst weed, and it has the ability to expand its distribution significantly (Simpson et al., 2011).

While it is well-acknowledged that climate change affects long-term interactions between crops and weeds, the degree of this impact is unclear (Ramesh et al., 2017). Despite its widespread infestation, little climate change research on Cyperaceae has been conducted (Simpson et al., 2011). Seasonal forecasting will likely become more critical to provide the information needed to guide agricultural management and prevent the compounding effects of abiotic variability and stress (Stuecker et al., 2018).

Detecting weeds in the early season is a first and critical step; introducing precision farming methods can also effectively manage weed problems while minimizing operational costs and environmental pollution (Chlingaryan et al., 2018; Torres-Sánchez et al., 2015). Considering the diversity of weed problems, no single control method, whether cultural, manual, mechanical, or chemical, would be sufficient to provide season-long weed control in all situations. An integrated weed management system as part of an integrated crop management system would be a practical, economical, and eco-friendly approach to managing weedy rice sedges (Yaduraju & Mishra, 2008).

INTERNET OF THINGS (IOT)

The dynamic changes in weed infestation, including sedges caused by the changing climate in rice fields, will result in more challenging control methods by farmers. Researchers

and farmers can employ several strategies related to AI to monitor weedy pests regularly during and after rice production to prevent further damage (Bhoi et al., 2021). A real-time monitoring system that can precisely determine the severity of the current weed infestation can help farmers take appropriate and quick actions. Moreover, a prediction model to forecast weed infestation can create a warning system based on current and previous environmental factors.

Smart farming is a farming system in which AI and cutting-edge technologies are merged with traditional farming practices to improve agricultural products while reducing inputs (Glaroudis et al., 2020). IoT can create interconnections between different objects, such as smartphones, robots, sensors, and weather stations, through the Internet as the primary backbone of the communication channel (Agrawal & Das, 2011; Shahzadi et al., 2016). Using ubiquitous computing and unique identifiers (Agrawal & Das, 2011), IoT can connect humans and machines through a highly distributed network (Shahzadi et al., 2016).

IoT aims to make people's daily lives more sophisticated, flexible, and accessible to anything on the planet (Agrawal & Das, 2011). Novel and effective IoT-based methodologies have been developed to create weed-identification models (Dankhara et al., 2019). These IoT-based intelligent robots use pre-trained models to classify various plant-weed combinations depending on the season, environment, and crops. However, it requires a plant-weed classifier that can distinguish between plants and weeds by analyzing image data using computer vision techniques and labeling them in real time over IoT (Dankhara et al., 2019).

REMOTE SENSING

Remote sensing (RS) resembles the reading process in several ways. It refers to gathering data by utilizing information and communication technology (ICT) services from a distance. More precisely, RS is the science and art of obtaining information about an object, area, or phenomenon by analyzing the data collected by a device not in contact with the object, location, or event under inquiry (Lillesand et al., 2015). Image processing by satellites or UAVs is the most common RS technique (Radoglou-Grammatikis et al., 2020). Electromagnetic radiation is the main component of RS because measurements of reflected radiation from crops allow the collection of essential data on water stress, crop nutritional status, and other field variables (Radoglou-Grammatikis et al., 2020).

As the pressure on farmers to produce crops more effectively and advances in sensor technology, data management, storage, and processing power have increased, RS in agriculture has sparked renewed interest in the last 15 years (Basinger et al., 2020). Agriculture has been one of RS's most extensive application areas of RS since the 1930s (Lillesand et al., 2015). Crop production and biomass have been estimated using RS,

water stress, crop nutrient status, herbicide injury, plant diseases, insect damage, and weed detection and control (Basinger et al., 2020).

In weed management, RS usage can reduce the requirements for broadcast herbicide applications, reduce overall input costs, and limit the environmental implications of herbicide use, tillage, soil compaction, and off-target chemical movement (Basinger et al., 2020). It can differentiate between crops and weeds by analyzing image data using computer vision techniques while leaving crops untouched. However, this can be difficult, as many weed and crop species share similar biophysical plant properties (Basinger et al., 2020). Thus, obtaining unique spectral response patterns for each species is also recommended by obtaining multiple image acquisition dates during the growth cycle (Lillesand et al., 2015).

HYPERSPECTRAL IMAGING

Scientists have opted to utilize hyperspectral sensor technology to make the differences between crops and weeds more distinguishable. Unlike regular cameras, hyperspectral remote sensing captures solar radiation reflected off plant surfaces in narrow wavelength bands gathered between 350 and 2,500 nm, allowing for excellent spectral resolution (Basinger et al., 2020). Meanwhile, visible light (color photographs and human eyes) is limited to the RGB spectrum ranging from 300 to 700 nm, which lies in the red, green, and blue (RGB) spectra. With hundreds of spectral bands, hyperspectral simultaneously captures spectral and spatial data (Zhang et al., 2019).

Several models for hyperspectral sensors are regularly used in unmanned aerial vehicle (UAV) applications (Table 2). As each hyperspectral sensor can only detect a limited number of bands, the goal of the survey must be clearly defined to select the most appropriate sensor (Esposito et al., 2021). The spectral signatures of common green weeds and plants in the visible spectrum (RGB) were quite similar, and many of them overlapped, with a slight peak in green reflectance (Roslin et al., 2021). However, wavelengths outside the visible range, such as near-infrared (701–1,300 nm), shortwave-infrared I (1,301–1,900 nm), and shortwave-infrared II (1,901–2,500 nm), can help distinguish between species

Table 2
Hyperspectral sensors and their main characteristics

Camera model	Lens	Spectral range (µm)	Spectral bands (number and µm)	Weight (kg)
CUBERT	Snapshot + PAN	450–995	125 (8 µm)	0.5
Cornirg microHSI 410 SHARK	CCD/CMOS	400–1000	300 (2 µm)	0.7
Rikola Ltd. hyperspectral camera	CMOS	500–900	40 (10 µm)	0.6
Specim-AISA KESTREL16	Push-broom	600–1640	350 (3–8 µm)	2.5
Headwall Photonics Micro-hyperspec X-series NIR	InGaAs	900–1700	62 (12.9 µm)	1.1

Source: Esposito et al. (2021)

as the reflectance may separate from each other (Basinger et al., 2020). The quantity and radiometric range of bands must be carefully considered when dealing with hyperspectral applications (Esposito et al., 2021).

Although hyperspectral sensors have become more affordable recently, they are still significantly upfront compared with RGB and multispectral sensors (Esposito et al., 2021). Furthermore, they are heavier and larger than other sensors, making their assembly on UAV systems challenging and extremely payload intensive. Because hyperspectral imaging provides both spectral and image information, it has enormous potential for plant identification. However, determining which combination of input factors contributes the most to model accuracy requires a greater understanding of the hyperspectral images of crops and weeds (Su, 2020).

HYPERSPECTRAL REFLECTANCE ON DIFFERENT SPECIES, PHENOLOGICAL STAGES, AND CLIMATE

Although hyperspectral remote sensing has been successfully used to discriminate between crop and weed species in field settings, these studies have been limited to only a few crops and plant species (Basinger et al., 2020). Weeds, including sedges, have distinct spectral signatures that can be used as guides for detecting weeds in rice fields using RS (Norasma et al., 2020). Figure 2 shows an example of a different spectral band for the weeds. Spectral information can also be helpful for real-time decision-making, which can be presented on farmers' smartphones or even toward automation and robotic mechanisms to make a suitable response (Alam et al., 2014). Furthermore, the spectrum differences can be explained by combining field data on optical functional features with the canopy radiative transfer model (Punalekar et al., 2016).

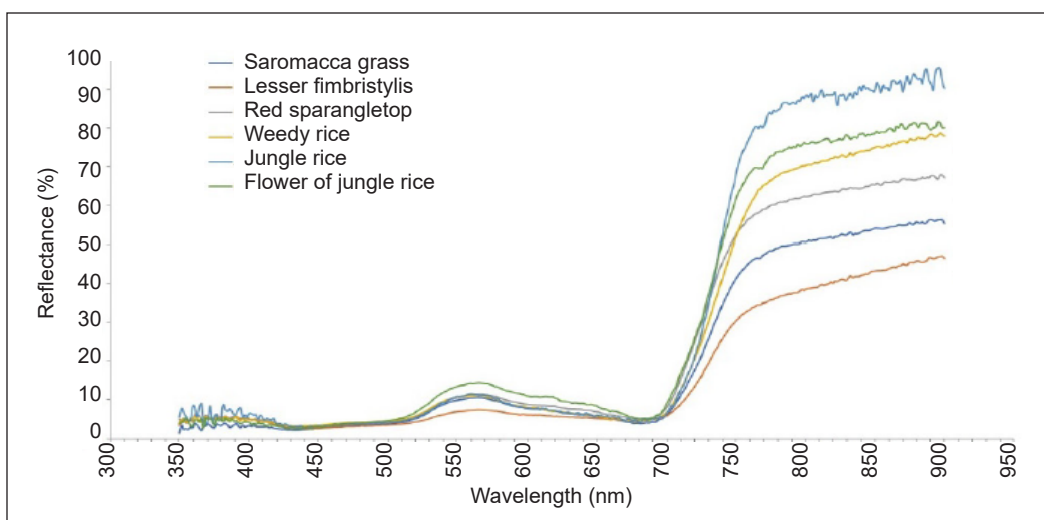


Figure 2. Graph overlays of spectral reflectance of rice weeds (Adapted from Roslin et al., 2021)

Vegetation undergoes several phenological stages during development. Plant physiology changes during these stages, leading to changes in biochemical, biophysical, and structural characteristics (Lausch et al., 2015). As crop traits change throughout the growing season, it is essential to use images taken at different times throughout the growing cycle for crop identification. Multiple image acquisition dates may be required to obtain distinct spectral response patterns for each plant species, including sedge weeds (Lillesand et al., 2015).

Phenological variations can alter species differentiation and can be exploited to improve weed detection accuracy using hyperspectral remote sensing data (Basinger et al., 2020). Combined with visible light and near-infrared reflectance, shortwave-infrared I and II wavelengths can differentiate across plant phenologies and should thus be investigated for future sensor technologies for species differentiation (Basinger et al., 2020). Moreover, the gravimetric water content of barley was found to be the most relevant characteristic for distinguishing between phenological macrostages (Lausch et al., 2015). Plant phenological development involves several biochemical and biophysical vegetation features in vegetation change, which can be captured in great detail using hyperspectral remote sensing technologies (Lausch et al., 2015).

The phenological stages of sedges can be divided into three phases by characterizing the sowing to emergence sub-periods (SOW–EME), emergence to the emission of the floral tassel (EME–EMI), and emission of the floral tassel to physiological maturity (EMI–MAT) (Voss et al., 2021). EME, EMI, and MAT were defined as the emergence of the first 50% of the total seedlings, the emission of the floral tassel (> 2 cm), and the physiological maturation of the seeds (brown color). After the first week of sedge planting, the thick waxy cuticular layer combined with a thick upper epidermis and uniformly distributed Kranz anatomy, which is prevalent in C4 plants, can result in brighter reflectance readings (Basinger et al., 2020).

Besides plant species and phenological stages, climate change can contribute to spectral reflectance differences. Even when a similar species enters the same phenological stages, a difference in the spectral band of two individual plants may occur because of different climate influences. Changes in biochemical–biophysical traits caused by weed or plant adaptation to climate change may influence spectral readings at a specific wavelength. Due to genetic variety and physiological plasticity (Varanasi et al., 2016), weeds respond quickly to resource changes. They can flourish in diverse ecosystems more than crops, which may create more distinguishable spectral differences.

Shifts in temperature trends, soil and water acidity, wind and water current patterns, seasonal duration changes, and other factors can all influence differences in spectrum responses (Arias et al., 2021). The use of hyperspectral remote sensing can estimate leaf chlorophyll content (SPAD) and leaf area index (LAI), which are influenced by changes in temperature and CO₂ (Xie et al., 2013). Although CO₂ significantly contributes to

climate change, a few Australian researchers have suggested that weed species respond differently when rainfall patterns change (Ramesh et al., 2017). Because of the changeable environment, which deals with various dynamic and complex aspects, requires an adequate record of spectral observations over multiple decades, if possible (Arias et al., 2021), to forecast the sedge invasion of rice fields.

AIRBORNE HYPERSPECTRAL

A hyperspectral camera can be embedded in a UAV, a flying robot with several configurations (Figure 3), and a standard tool in precision agriculture (Radoglou-Grammatikis et al., 2020). UAVs are frequently the first choice for fast and precise in-situ remote sensing or survey operations because of their affordability, user-friendliness, and versatility (Esposito et al., 2021). The UAV does not require a human pilot onboard and can be considered a flying IoT (Bhoi et al., 2021). In recent years, there has been a noticeable trend toward developing lightweight, portable hyperspectral equipment that can be deployed on UAVs and other tiny platforms (Lillesand et al., 2015).

UAVs can be grouped based on several technical characteristics, including aerodynamic features, autonomy level, size, weight, and power sources (Radoglou-Grammatikis et al., 2020). UAVs can be categorized into monitoring, spraying, and multiple applications. Data collected by UAV sensors can be spectral, spatial, or temporal. The ability to undertake monitoring and spraying missions can improve agriculture usage by maximizing the efficacy of pesticides and fertilizers, detecting potential pests and illnesses on time, and simplifying spraying procedures (Radoglou-Grammatikis et al., 2020).

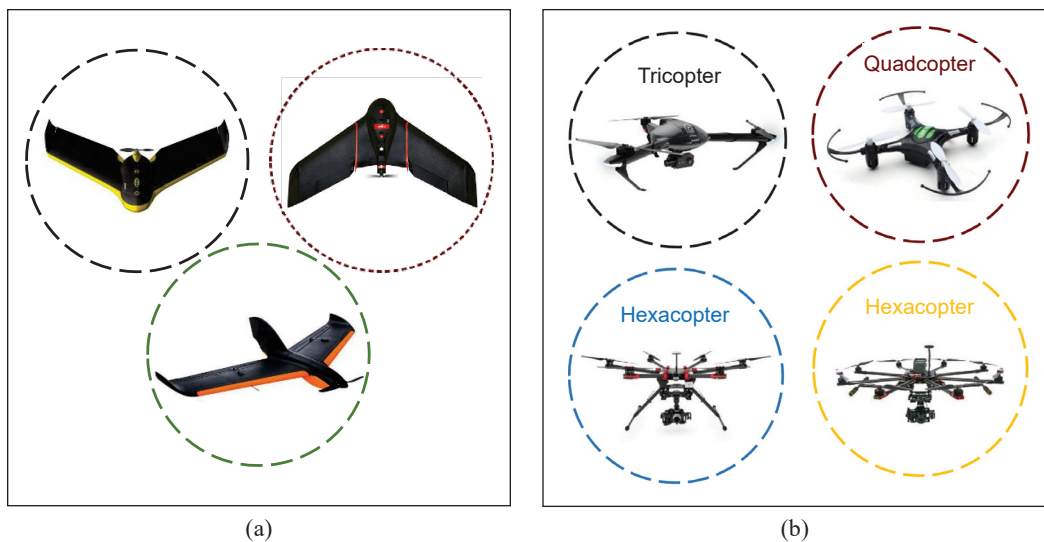


Figure 3. Several types of (a) fixed-wing and (b) rotary-wing UAVs (Adapted from Radoglou-Grammatikis et al., 2020)

CONCLUSION

This review summarizes the advance made in our understanding of the hyperspectral reflectance of the weedy sedge in rice fields. This review also discusses how they interact with climate change and phenological stages to forecast the sedge invasion. Sedge weed infestation in rice fields can cause severe yield loss if improperly handled. Climate change alters weed distribution in rice fields, affecting weed management as it depends on weed species' appearance and distribution. The spectral signature of sedges can be used for weed monitoring, and this method can save a lot of time and labor by utilizing RS technology and drones. The infrared region may display significant differences in the spectral reflectance of sedge weeds using hyperspectral sensors. AI technology with deep learning can analyze physiological and morphological changes for sedge outbreak detection. Forecasting and IoT real-time monitoring methods can be integrated with the decision support system, which stakeholders can use to take appropriate action. UAVs and hyperspectral sensors accurately identify weed species in cultivated rice fields and can improve weed management sustainability. The excellent capabilities of UAV technology can provide comprehensive analysis in the context of precision agriculture. Because of the importance of the phenological stage and climate change on sedge species classification using hyperspectral sensors, future studies should consider phenology and abiotic factors when investigating the spectral signature of sedge species in wetland rice fields.

ACKNOWLEDGEMENTS

The authors are grateful to the Research Project entitled "Pest and Disease Monitoring Using Artificial Intelligent for Risk Management of Rice Under Climate Change" under the Long-term Research Grant Scheme (LRGS), Ministry of Higher Education, Malaysia (LRGS/1/2019/UPM01/2/5; vote number: 5545002) also sincerely acknowledges the Universiti Putra Malaysia for providing facilities.

REFERENCES

- Agrawal, S., & Das, M. L. (2011, December 8-10). *Internet of things - A paradigm shift of future Internet applications*. [Paper presentation]. Nirma University International Conference on Engineering, Ahmedabad, India. <https://doi.org/10.1109/NUiConE.2011.6153246>
- Alam, M., Siwar, C., Talib, B., & Toriman, M. (2014). Impacts of climatic changes on paddy production in Malaysia: Micro study on IADA at North West Selangor. *Research Journal of Environmental and Earth Sciences*, 6(5), 251-258.
- Anwar, P., Juraimi, A. S., Puteh, A., Selamat, A., Man, A., & Hakim, A. (2011). Seeding method and rate influence on weed suppression in aerobic rice. *African Journal of Biotechnology*, 10(68), 15259-15271. <https://doi.org/10.5897/AJB11.060>

- Aqilah, A., Asyraf, M., & Azmi, M. (2012, November 22-24). *Weed survey in different cultural practice in Seberang Perai and Muda Rice Fields in Northern Malaysia*. [Paper presentation]. Proceedings of the 2nd Annual International Conference, Syiah Kuala University & The 8th IMT-GT Uninet Biosciences Conference, Aceh, Indonesia.
- Arias, F., Zambrano, M., Broce, K., Medina, C., Pacheco, H., & Nunez, Y. (2021). Hyperspectral imaging for rice cultivation: Applications, methods and challenges. *AIMS Agriculture and Food*, 6(1), 273-307. <https://doi.org/10.3934/agrfood.2021018>
- Azmi, M., Abdullah, M. Z., Mislamah, B., & Baki, B. B. (2000). *Management of Weedy Rice (Oryza sativa L.): The Malaysian Experience*. ReseachGate.
- Basinger, N. T., Jennings, K. M., Hestir, E. L., Monks, D. W., Jordan, D. L., & Everman, W. J. (2020). Phenology affects differentiation of crop and weed species using hyperspectral remote sensing. *Weed Technology*, 34(6), 897-908. <https://doi.org/10.1017/wet.2020.92>
- Begum, M., Juraimi, A. S., Amartalingam, R., Man, A., & Rastans, S. O. S. (2006). The effects of sowing depth and flooding on the emergence, survival, and growth of *Fimbristylis miliacea* (L.) Vahl. *Weed Biology and Management*, 6(3), 157-164. <https://doi.org/10.1111/j.1445-6664.2006.00209.x>
- Bell, M. A., Fischer, R. A., Byerlee, D., & Sayre, K. (1995). Genetic and agronomic contributions to yield gains: A case study for wheat. *Field Crops Research*, 44(2-3), 55-65. [https://doi.org/10.1016/0378-4290\(95\)00049-6](https://doi.org/10.1016/0378-4290(95)00049-6)
- Bhoi, S. K., Jena, K. K., Panda, S. K., Long, H. V., Kumar, R., Subbulakshmi, P., & Jebreen, H. B. (2021). An internet of things assisted unmanned aerial vehicle based artificial intelligence model for rice pest detection. *Microprocessors and Microsystems*, 80, Article 103607. <https://doi.org/10.1016/j.micpro.2020.103607>
- Bruhl, J. J., & Wilson, K. L. (2007). Towards a comprehensive survey of C3 and C4 photosynthetic pathways in Cyperaceae. *Aliso: A Journal of Systematic and Floristic Botany*, 23(1), 99-148. <https://doi.org/10.5642/aliso.20072301.11>
- Caton, B. P., Mortimer, M., Hill, J. E., Johnson, D. E. (2010). *A practical field guide to weeds of rice in Asia*. International Rice Research Institute. <https://ageconsearch.umn.edu/record/164472>
- Chlingaryan, A., Sukkarieh, S., & Whelan, B. (2018). Machine learning approaches for crop yield prediction and nitrogen status estimation in precision agriculture: A review. *Computers and Electronics in Agriculture*, 151, 61-69. <https://doi.org/10.1016/j.compag.2018.05.012>
- Dankhara, F., Patel, K., & Doshi, N. (2019). Analysis of robust weed detection techniques based on the internet of things (IoT). *Procedia Computer Science*, 160, 696-701. <https://doi.org/10.1016/j.procs.2019.11.025>
- Dilipkumar, M., Chuah, T. S., Goh, S. S., & Sahid, I. (2020). Weed management issues, challenges, and opportunities in Malaysia. *Crop Protection*, 134, Article 104347. <https://doi.org/10.1016/j.cropro.2017.08.027>
- Esposito, M., Crimaldi, M., Cirillo, V., Sarghini, F., & Maggio, A. (2021). Drone and sensor technology for sustainable weed management: A review. *Chemical and Biological Technologies in Agriculture*, 8(1), 1-11. <https://doi.org/10.1186/s40538-021-00217-8>

- Gabriel, B. P., Hamda, M., Thamrin, M., Budiman, A., Asikin, S., & Badaruddin, H. (1986, August 24-34). *Pest management of food crops in the tidal and monotonous swamps of South Kalimantan*. [Paper presentation]. Symposium on Lowland Development in Indonesia, Jakarta, Indonesia.
- Galal, T. M., & Shehata, H. S. (2015). Impact of nutrients and heavy metals capture by weeds on the growth and production of rice (*Oryza sativa* L.) irrigated with different water sources. *Ecological Indicators*, *54*, 108-115. <https://doi.org/10.1016/j.ecolind.2015.02.024>
- Glaroudis, D., Iossifides, A., & Chatzimisios, P. (2020). Survey, comparison and research challenges of IoT application protocols for smart farming. *Computer Networks*, *168*, Article 107037. <https://doi.org/10.1016/j.comnet.2019.107037>
- Govaerts, R., & Simpson, D. A. (2007). *World Checklist of Cyperaceae*. Kew Pub., Royal Botanic Gardens.
- Hakim, M. A., Juraimi, A. S., Hanafi, M. M., Ismail, M. R., & Selamat, A. (2013). A comparison of weed communities of coastal rice fields in Peninsular Malaysia. *Journal of Environmental Biology*, *34*(5), Article 847.
- Hakim, M. A., Juraimi, A. S., Hanafi, M. M., Ismail, M. R., Selamat, A., Rafii, M. Y., & Latif, M. A. (2014). Biochemical and anatomical changes and yield reduction in rice (*Oryza sativa* L.) under varied salinity regimes. *BioMed Research International*, *2014*, Article 208584. <https://doi.org/10.1155/2014/208584>
- Hakim, M. A., Juraimi, A. S., Ismail, M. R., Hanafi, M. M., & Selamat, A. (2010). Distribution of weed population in the costal rice growing area of Kedah in peninsular Malaysia. *Journal of Agronomy* *9*(1), 9-16. <https://doi.org/10.3923/ja.2010.9.16>
- Hasan, M., Ahmad-Hamdani, M. S., Rosli, A. M., & Hamdan, H. (2021). Bioherbicides: An eco-friendly tool for sustainable weed management. *Plants*, *10*(6), Article 1212. <https://doi.org/10.3390/plants10061212>
- Hasan, M., Mokhtar, A. S., Rosli, A. M., Hamdan, H., Motmainna, M., & Ahmad-Hamdani, M. S. (2021). Weed control efficacy and crop-weed selectivity of a new bioherbicide WeedLock. *Agronomy*, *11*(8), Article 1488. <https://doi.org/10.3390/agronomy11081488>
- Iqbal, M. A., Ali, S., Sabagh, A. E., Ahmad, Z., & Siddiqui, M. H. (2020). Changing climate and advances on weeds utilization as forage: Provisions, nutritional quality and implications. In H. El-Shafie (Ed.) *Invasive Species - Introduction Pathways, Economic Impact, and Possible Management Options* (pp. 1-13). IntechOpen. <https://doi.org/10.5772/intechopen.91386>
- Islam, N., Rashid, M. M., Pasandideh, F., Ray, B., Moore, S., & Kadel, R. (2021). A review of applications and communication technologies for internet of things (IoT) and unmanned aerial vehicle (UAV) based sustainable smart farming. *Sustainability*, *13*(4), Article 1821. <https://doi.org/10.3390/su13041821>
- Ismail, B. S., & Siddique, A. B. (2012). Allelopathic inhibition by *Fimbristylis miliacea* on the growth of the rice plants. *Advances in Environmental Biology*, *6*(8), 2423-2428.
- Ismail, S. N. F., & Abdullah, A. S. (2020). Recent developments of weed management in rice fields. *Reviews in Agricultural Science*, *8*, 343-353. https://doi.org/10.7831/ras.8.0_343
- Issahaku, A., Francis, K. O., & Richard, W. Y. (2021). Capabilities gained by rice farmers from JICA's training on sustainable rain-fed lowland rice production technology in Northern, Savanna and North-east. *ADRRJ Journal (Multidisciplinary)*, *30*(2 (7)), 33-52.

- Jinger, D., Kaur, R., Kaur, N., Rajanna, G. A., Kumari, K., & Dass, A. (2017). Weed dynamics under changing climate scenario: A Review. *International Journal of Current Microbiology and Applied Sciences*, 6(3), 2376-2388. <https://doi.org/10.20546/ijcmas.2017.603.272>
- Juraimi, A. S., Begum, M., Mohd. Yusof, M. N., & Man, A. (2010). Efficacy of herbicides on the control weeds and productivity of direct seeded rice under minimal water conditions. *Plant Protection Quarterly*, 25(1), 19-25.
- Juraimi, A. S., Najib, M. M., Begum, M., Anuar, A. R., Azmi, M., & Puteh, A. (2009). Critical period of weed competition in direct seeded rice under saturated and flooded conditions. *Pertanika Journal of Tropical Agricultural Science*, 32(2), 305-316.
- Juraimi, A. S., Uddin, M. K., Anwar, M. P., Mohamed, M. T. M., Ismail, M. R., & Man, A. (2013). Sustainable weed management in direct seeded rice culture: A review. *Australian Journal of Crop Science*, 7(7), 989-1002.
- Khush, G. S. (1997). Origin, dispersal, cultivation and variation of rice. *Plant Molecular Biology*, 35, 25-34. <https://doi.org/10.1023/A:1005810616885>
- Kurniadie, D., Irda, M., Umiyati, U., Widayat, D., & Nasahi, C. (2019). Weeds diversity of lowland rice (*Oryza sativa* L.) with different farming system in Purwakarta Regency Indonesia. *Journal of Agronomy*, 18(1), 21-26. <https://doi.org/10.3923/ja.2019.21.26>
- Lausch, A., Salbach, C., Schmidt, A., Doktor, D., Merbach, I., & Pause, M. (2015). Deriving phenology of barley with imaging hyperspectral remote sensing. *Ecological Modelling*, 295, 123-135. <https://doi.org/10.1016/j.ecolmodel.2014.10.001>
- Lillesand, T., Kiefer, R. W., & Chipman, J. (2015). *Remote Sensing and Image Interpretation*. John Wiley & Sons.
- Man, A., Mohammad Saad, M., Amzah, B., Masarudin, M. F., Jack, A., Misman, S. N., & Ramachandran, K. (2018). *Buku Poket Perosak, Penyakit dan Rumpai Padi di Malaysia [Pocket Book of Rice Pests, Diseases and Weeds in Malaysia]* (Cetakan Kelima). Institut Penyelidikan dan Kemajuan Pertanian Malaysia (MARDI).
- Mondal, M. M. A., Hakim, M. A., Juraimi, A. S., & Azad, M. A. K. (2011). Contribution of morpho-physiological attributes in determining the yield of mungbean. *African Journal of Biotechnology*, 10(60), 12897-12904. <https://doi.org/10.5897/AJB11.373>
- Motmainna, M., Juraimi, A. S., Uddin, M. K., Asib, N. B., Islam, A. K. M. M., & Hasan, M. (2021a). Allelopathic potential of Malaysian invasive weed species on Weedy rice (*Oryza sativa* f. *spontanea* Roshev). *Allelopathy Journal*, 53, 53-68. <https://doi.org/10.26651/allelo.j/2021-53-1-1327>
- Motmainna, M., Juraimi, A. S., Uddin, M. K., Asib, N. B., Islam, A. K. M. M., & Hasan, M. (2021b). Assessment of allelopathic compounds to develop new natural herbicides: A review. *Allelopathy Journal*, 52, 21-40. <https://doi.org/10.26651/allelo.j/2021-52-1-1305>
- Motmainna, M., Juraimi, A. S., Uddin, M. K., Asib, N. B., Islam, A. M., Ahmad-Hamdani, M. S., & Hasan, M. (2021c). Phytochemical constituents and allelopathic potential of *Parthenium hysterophorus* L. in comparison to commercial herbicides to control weeds. *Plants*, 10(7), Article 1445. <https://doi.org/10.3390/plants10071445>

- Motmainna, M., Juraimi, A. S., Uddin, M. K., Asib, N. B., Islam, A. K. M. M., Ahmad-Hamdani, M. S., Berahim, Z., & Hasan, M. (2021d). Physiological and Biochemical Responses of *Ageratum conyzoides*, *Oryza sativa* f. *spontanea* (Weedy Rice) and *Cyperus iria* to *Parthenium hysterophorus* Methanol Extract. *Plants*, *10*(6), Article 1205. <https://doi.org/10.3390/plants10061205>
- Motmainna, M., Juraimi, A. S., Uddin, M. K., Asib, N. B., Islam, A. K. M. M., & Hasan, M. (2021e). Bioherbicidal Properties of *Parthenium hysterophorus*, *Cleome rutidosperma* and *Borreria alata* Extracts on Selected Crop and Weed Species. *Agronomy*, *11*(4), Article 643. <https://doi.org/10.3390/agronomy11040643>
- Norasma, C. Y. N., Alahyadi, L. A. N., Fazilah, F. F. W., Roslan, S. N. A., & Tarmidi, Z. (2020). Identification spectral signature of weed species in rice using spectroradiometer handheld sensor. *IOP Conference Series: Earth and Environmental Science*, *540*, Article 012091. doi:10.1088/1755-1315/540/1/012091
- Pantazi, X. E., Moshou, D., & Bravo, C. (2016). Active learning system for weed species recognition based on hyperspectral sensing. *Biosystems Engineering*, *146*, 193-202. <https://doi.org/10.1016/j.biosystemseng.2016.01.014>
- Punalekar, S., Verhoef, A., Tatarenko, I. V., Van der Tol, C., Macdonald, D. M., Marchant, B., Gerard, F., White, K., & Gowing, D. (2016). Characterization of a highly biodiverse floodplain meadow using hyperspectral remote sensing within a plant functional trait framework. *Remote Sensing*, *8*(2), Article 112. <https://doi.org/10.3390/rs8020112>
- Radoglou-Grammatikis, P., Sarigiannidis, P., Lagkas, T., & Moscholios, I. (2020). A compilation of UAV applications for precision agriculture. *Computer Networks*, *172*, Article 107148. <https://doi.org/10.1016/j.comnet.2020.107148>
- Rahim, F. H. A., Hawari, N. N., & Abidin, N. Z. (2017). Supply and demand of rice in Malaysia: A system dynamics approach. *International Journal of Supply Chain Management*, *6*(4), 1-7.
- Ramesh, K., Matloob, A., Aslam, F., Florentine, S. K., & Chauhan, B. S. (2017). Weeds in a changing climate: Vulnerabilities, consequences, and implications for future weed management. *Frontiers in Plant Science*, *8*, Article 95. <https://doi.org/10.3389/fpls.2017.00095>
- Rodenburg, J., Meinke, H., & Johnson, D. E. (2011). Challenges for weed management in African rice systems in a changing climate. *The Journal of Agricultural Science*, *149*(4), 427-435. <https://doi.org/10.1017/S0021859611000207>
- Roslin, N. A., Che'Ya, N. N., Sulaiman, N., Alahyadi, L. A. N., & Ismail, M. R. (2021). Mobile application development for spectral signature of weed species in rice farming. *Pertanika Journal of Science & Technology*, *29*(4), 2241-2259. <https://doi.org/10.47836/pjst.29.4.01>
- Shahzadi, R., Ferzund, J., Tausif, M., & Suryani, M. A. (2016). Internet of things based expert system for smart agriculture. *International Journal of Advanced Computer Science and Applications*, *7*(9), 341-350.
- Simma, B., Polthanee, A., Goggi, A. S., Siri, B., Promkhambut, A., & Caragea, P. C. (2017). Wood vinegar seed priming improves yield and suppresses weeds in dryland direct-seeding rice under rainfed production. *Agronomy for Sustainable Development*, *37*, Article 56. <https://doi.org/10.1007/s13593-017-0466-2>

- Simpson, D. A., Yesson, C., Culham, A., Couch, C. A., & Muasya, A. M. (2011). Climate change and Cyperaceae. In T. R. Hodkinson, M. B. Jones, S. Waldren & J. A. N. Parnell (Eds.), *Climate Change, Ecology and Systematics* (pp. 439-456). Cambridge University Press.
- Stuecker, M. F., Tigchelaar, M., & Kantar, M. B. (2018). Climate variability impacts on rice production in the Philippines. *PLoS One*, *13*(8), Article e0201426. <https://doi.org/10.1371/journal.pone.0201426>
- Su, W. H. (2020). Advanced machine learning in point spectroscopy, RGB-and hyperspectral-imaging for automatic discriminations of crops and weeds: A review. *Smart Cities*, *3*(3), 767-792. <https://doi.org/10.3390/smartsities3030039>
- Torres-Sánchez, J., López-Granados, F., & Pena, J. M. (2015). An automatic object-based method for optimal thresholding in UAV images: Application for vegetation detection in herbaceous crops. *Computers and Electronics in Agriculture*, *114*, 43-52. <https://doi.org/10.1016/j.compag.2015.03.019>
- Uddin, M. K., Juraimi, A. S., Ismail, M. R., & Brosnan, J. T. (2010). Characterizing weed populations in different turfgrass sites throughout the Klang Valley of Western Peninsular Malaysia. *Weed Technology*, *24*(2), 173-181. <https://doi.org/10.1614/WT-09-046.1>
- Ueno, O. (2001). Environmental regulation of C3 and C4 differentiation in the amphibious sedge *Eleocharis vivipara*. *Plant Physiology*, *127*(4), 1524-1532. <https://doi.org/10.1104/pp.010704>
- Varanasi, A., Prasad, P. V., & Jugulam, M. (2016). Impact of climate change factors on weeds and herbicide efficacy. *Advances in Agronomy*, *135*, 107-146. <https://doi.org/10.1016/bs.agron.2015.09.002>
- Voss, H. M. G., Escobar, O. D. S., Trivisoli, V. S., Peripolli, M., Pivetta, M., Rubert, J., Nunes, E. A., & Dornelles, S. H. B. (2021). Phenology and thermal requirements of the species *Cyperus difformis* L. in southern Brazil. *Acta Scientiarum. Biological Sciences*, *43*, e47560-e47560. <https://doi.org/10.4025/actasciobiolsci.v43i1.47560>
- Xie, X., Li, Y. X., Li, R., Zhang, Y., Huo, Y., Bao, Y., & Shen, S. (2013). Hyperspectral characteristics and growth monitoring of rice (*Oryza sativa*) under asymmetric warming. *International Journal of Remote Sensing*, *34*(23), 8449-8462. <https://doi.org/10.1080/01431161.2013.843806>
- Yaduraju, N. T., & Mishra, J. S. (2008). Sedges in rice culture and their management. In Y. Singh, V. P. Singh, B. Chauhan, A. Orr, A. M. Mortimer, D. E. Johnson & B. Hardy (Eds.), *Direct Seeding of Rice and Weed Management in the Irrigated Rice-Wheat Cropping System of the Indo-Gangetic Plains* (pp. 191-203). Philippines International Rice Research Institute.
- Zhang, Y., Gao, J., Cen, H., Lu, Y., Yu, X., He, Y., & Pieters, J. G. (2019). Automated spectral feature extraction from hyperspectral images to differentiate weedy rice and barnyard grass from a rice crop. *Computers and Electronics in Agriculture*, *159*, 42-49. <https://doi.org/10.1016/j.compag.2019.02.018>

An Improved Ensemble Machine Learning Approach for Diabetes Diagnosis

Mohanad Mohammed Rashid¹, Omar Mahmood Yaseen², Rana Riyadh Saeed¹ and Maher Talal Alasaady^{3*}

¹Department of Radiology Techniques, Northern Technical University, Mosul 41001, Iraq

²Administrative and Financial Department, Ministry of Higher Education and Scientific Research, Baghdad 10001, Iraq

³Computer Systems Department, Northern Technical University, Mosul 41001, Iraq

ABSTRACT

Diabetes is recognized as one of the most detrimental diseases worldwide, characterized by elevated levels of blood glucose stemming from either insulin deficiency or decreased insulin efficacy. Early diagnosis of diabetes enables patients to initiate treatment promptly, thereby minimizing or eliminating the risk of severe complications. Although years of research in computational diagnosis have demonstrated that machine learning offers a robust methodology for predicting diabetes, existing models leave considerable room for improvement in terms of accuracy. This paper proposes an improved ensemble machine learning approach using multiple classifiers for diabetes diagnosis based on the Pima Indians Diabetes Dataset (PIDD). The proposed ensemble voting classifier amalgamates five machine learning algorithms: Decision Tree (DT), Logistic Regression (LR), K-Nearest Neighbor (KNN), Random Forests (RF), and XGBoost. We obtained the individual model accuracies and used the ensemble method to improve accuracy. The proposed approach uses a pre-processing stage of standardization and imputation and applies the Local Outlier Factor (LOF) to remove data anomalies. The model was evaluated using sensitivity, specificity, and accuracy criteria. With a reported accuracy of 81%, the proposed approach shows promise compared to prior classification techniques.

ARTICLE INFO

Article history:

Received: 15 August 2023

Accepted: 20 November 2023

Published: 04 April 2024

DOI: <https://doi.org/10.47836/pjst.32.3.19>

E-mail addresses:

mohanad.rashid@ntu.edu.iq (Mohanad Mohammed Rashid)
omar.yaseen1987777@gmail.com (Omar Mahmood Yaseen)
ranasaeed_1987@ntu.edu.iq (Rana Riyadh Saeed)
maher.alasaady@ntu.edu.iq (Maher Talal Alasaady)

* Corresponding author

Keywords: Diabetes diagnosis, ensemble learning, machine learning, PIDD, soft voting

INTRODUCTION

Diabetes is a chronic illness that affects millions of individuals worldwide and may lead to major health complications such as cardiovascular disease, stroke, and kidney failure (Chen et al., 2016). Patients with diabetes are divided into two distinct groups: Types 1 and 2. Patients with Type 1 diabetes are dependent on insulin for disease management. Patients with Type 2 diabetes do not require insulin to control the disease. According to research by the World Health Organization (WHO), more than ninety percent of people with this illness have Type 2 diabetes (WHO, 2014). Diabetes is associated with several negative effects, such as an increased chance of blindness, hypertension, kidney damage, and cardiovascular disease (Centers for Disease Control and Prevention, 2011). However, quick treatment may be started by people who get an early diagnosis of diabetes, lowering or even eliminating the possibility of negative outcomes.

Since diabetes has become one of the most common causes of severe illnesses, an expert system should be established and used to identify this condition. Machine Learning (ML) methods for developing autonomous diagnostic systems for various health disorders have been deemed beneficial (Saeed et al., 2022). Even though several ways have been presented to detect diabetes, the accuracy of different machine-learning algorithms is not exceptionally high (Barik et al., 2021). Previous efforts to enhance the predictive accuracy of these systems have frequently encountered challenges (Mirzajani & Salimi, 2018). In addition, the algorithms used to diagnose diabetes often come across data that is imprecise, missing, erroneous, or inconsistent (Swapna et al., 2018). The success of the model is dependent on the correctness of the diabetes data; thus, the researcher must offer precise data to the classifier to guarantee accurate illness prediction (Alasaady et al., 2022). Data pre-processing allows the construction of a highly accurate, robust classification model (Alasaady et al., 2019).

Ensemble learning is a method for ML in which many models are learned and integrated to enhance the system's overall performance and predictive ability (Khairan et al., 2023; Kunwar & Timalisina, 2021). Individual models, called base learners, are trained on separate subsets of data or with different techniques. Their outputs are merged using a predetermined way to give a final prediction. Ensemble learning may make ML models more accurate, stable, and generalizable. Voting, weighted averaging, and arithmetic mean are common strategies for mixing the outputs of the base learners (Kumari et al., 2021).

This research aims to detect diabetes using an ensemble approach to classify diabetes using a soft voting classifier. The techniques include Decision Tree (DT), Logistic Regression (LR), K-nearest neighbor (KNN), Random Forest (RF), and eXtreme Gradient Boosting (XGBoost). In addition, the Pima Indians Diabetes Dataset (PIDD) undergoes many preparatory procedures to improve classification accuracy. The assessment processes use measures for sensitivity, specificity, and accuracy.

LITERATURE REVIEW

This literature review explores previous research on diabetes diagnosis using machine-learning approaches, specifically focusing on an ensemble machine-learning approach based on the PIDD dataset.

Kavakiotis et al. (2017) conducted a systematic review of 104 studies. They identified decision trees, neural networks, and support vector machines as the most used ML algorithms in diabetes research. Ensemble methods, such as bagging and boosting, have also been applied to a diabetes diagnosis. Bagging combines multiple models to reduce variance and improve accuracy (Breiman, 1996). Conversely, boosting involves iteratively training weak models and integrating them into robust ones (Fernández-Delgado et al., 2014).

Qin (2022) presents a diabetes prediction model utilizing ensemble learning techniques. The model incorporates LR, KNN, DT, Gaussian Naïve Bayes (GNB), and Support Vector Machines (SVM). The initial four algorithms with low correlation are designed as fundamental learners, which are subsequently incorporated into a meta-learner SVM to establish an integrated learning model. The experiment was conducted on the PIDD. The level of accuracy achieved was 81%.

Atif et al. (2022) proposed a hard voting classifier-based ensemble learning approach. Both the Early-Stage Diabetes Risk Prediction Dataset and the PIDD dataset were put to the test. LR, DT, and SVM are the three ML techniques combined in the proposed ensemble hard voting classifier. The suggested ensemble technique achieves 81% accuracy on the PIDD diabetes dataset.

In Noor et al. (2021), various machine learning techniques were employed for the diagnosis of diabetes mellitus, including individual algorithms as well as ensemble approaches. Methods such as adaptive boosting via AdaboostM1, bagging, and hybrid classifiers that combine Random Forest with other base classifiers were investigated, along with the standalone Random Forest algorithm. The study selected an optimal diabetes classification model based on its accuracy and performance metrics. To improve the quality of the data inputted into the supervised learning models, data pre-processing methods such as Synthetic Minority Over-sampling Technique (SMOTE) were implemented to counteract data imbalance and eliminate missing values. The study concluded that the most effective diabetes classification model utilized a hybrid classifier combining Random Forest and Bayes Net, achieving an accuracy rate of 83%.

Kumari et al. (2021) employed an ensemble approach, which involved the combination of three ML algorithms: RF, LR, and Naïve Bayes (NB). The experimentation involved the utilization of two datasets: the PIDD dataset and the breast cancer dataset. A comparative analysis of the proposed methodology and conventional ML algorithms was conducted using both datasets. The ensemble approach that has been proposed demonstrates the highest level of accuracy, achieving a value of 79%, when applied to the PIDD dataset.

Kunwar and Timalina (2021) constructed an ensemble model for the classification of diabetes. The model incorporates various ML algorithms: LR, SVM, NB, and DT. The proposed ensemble method combines the base classifiers using the probability assigned to each classifier. It is done to determine the final result by calculating the statistical mode of the output. The empirical findings support that hybrid approaches exhibit greater implicitness than individual classifiers' isolated utilization. The level of accuracy achieved was 81%.

Agrawal et al. (2021) used an ensemble model by employing the voting classifier, which incorporated the RF, AdaBoost, and DT as contributing models. The PIDD dataset is utilized in the experiment. The ensemble models demonstrated superior accuracy compared to the individual models and reduced the occurrence of False Negatives. The level of accuracy achieved was 77%.

Singh and Singh (2020) propose developing a stacking-based evolutionary ensemble learning system to predict diabetes. The PIDD dataset is employed. In selecting a base learner, a multi-objective optimization algorithm is employed to effectively balance the objectives of maximizing classification accuracy and minimizing ensemble complexity to achieve this objective. The level of accuracy achieved was 83%.

Soni and Varma (2020) employed ensemble techniques and ML algorithms to predict diabetes, which includes GB, RF, DT, SVM, KNN, and LR. The results demonstrate that RF outperformed other ML methods in terms of accuracy. The precision was 79%.

Akyol and Şen (2018) used an ensemble method to diagnose diabetes. There are two main stages to this investigation. The feature selection or weighting approaches are examined in the first phase to determine the best qualities for this condition. The performance of the ensemble learning techniques AdaBoost, Gradient Boosted Trees (GBT), and RF are assessed in the following stage. According to test results, the Stability Selection method and AdaBoost learning algorithm's prediction accuracy is somewhat higher than that of other algorithms, which is 73%.

Li (2014) proposes a methodology that integrates three distinct classifiers, namely SVM, Artificial Neural Network (ANN), and NB, to diagnose diabetes. He has proposed a voting classifier technique called the weight-adjusted voting technique. The proposed methodology entails the modification of the weight assigned to each classifier, considering their performance and past track record in accurately predicting outcomes. After being implemented on the PIDD dataset, this method demonstrates a prediction accuracy of 77%.

In summary, the studies that have been identified suggest that individual ML and basic ensemble techniques may not attain satisfactory accuracy when diagnosing diabetes using the PIDD dataset. Hence, developing an enhanced ensemble machine learning methodology is imperative to augment the precision of diabetes diagnosis. Table 1 presents a comparative analysis of previous research endeavors, highlighting the respective levels of accuracy attained.

Table 1
Comparison of accuracies of related work

Author	Year	Method	Accuracy
Qin	2022	LR, KNN, DT, GNB, and SVM	81%
Atif et al.	2022	LR, DT, and SVM	81%
Kumari et al.	2021	RF, LR, and NB	79%
Noor et al.	2021	RF, LR, MLP, NB, AdaboostM1	83%
Kunwar and Timalisina	2021	LR, SVM, NB, and DT	81%
Agrawal et al.	2021	RF, AdaBoost, and DT	77%
Singh and Singh	2020	SVM, RF, and KNN	83%
Soni and Varma	2020	GB, RF, DT, SVM, KNN, and LR.	79%
Akyol & Şen	2018	AdaBoost, GBT, and RF	73%
Lin Li et al.	2014	SVM, ANN, and NB	77%

METHOD

This paper proposes an improved ensemble approach for predicting diabetes to get accurate classifications of patients with Type 2 diabetes based on PIDD. DT, LR, KNN, RF, and XGBoost algorithms have been ensemble. The model was tested using PIDD and implemented using Python 3.10.9. Standardization, imputation, and anomaly detection using the LOF technique are carried out at the pre-processing stage. Figure 1 illustrates the architecture and the activities carried out by each architectural component throughout the diagnosis of diabetes. The specifics of this diagram are as follows:

- The PIDD dataset has been used to analyze and test the proposed approach.
- The data pre-processing stage has been done to transform raw data into a format that can be understood. Standardization, imputation, and anomaly detection have been used in this stage.

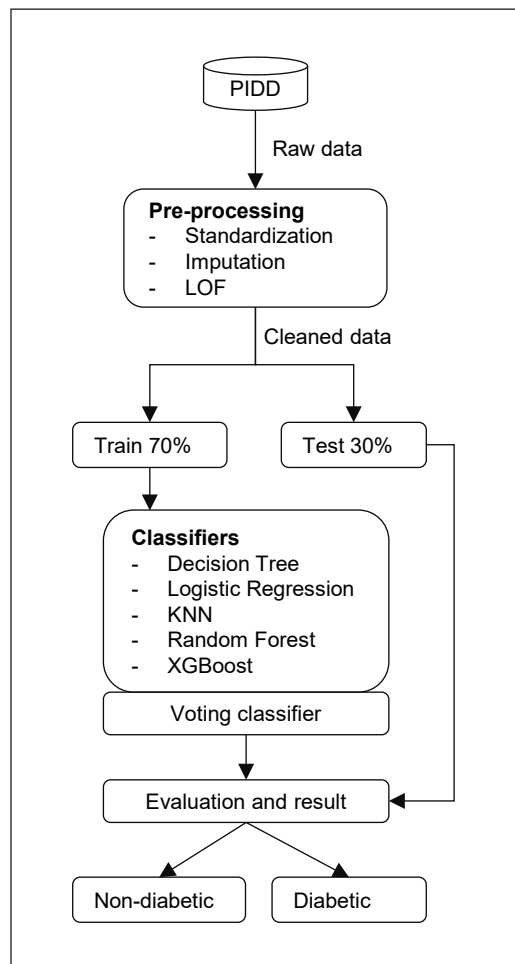


Figure 1. The main architecture

- The cleaned data has been split into train and test sets.
- Five machine learning models have been applied to the train set.
- Ensemble learning creates a hybrid model using the soft voting classifier. Finally, the trained algorithms and ensemble are applied to the test set and the evaluation.

PIDD Dataset

The dataset frequently employed for evaluating the effectiveness of diabetes diagnostic algorithms is the Pima Indians Diabetes Dataset (PIDD). The Pima Indians, a group of Native Americans who reside in the Arizona region of the USA, have the world’s highest prevalence of Type 2 diabetes. All the patients in this dataset are women over the age of 21. There was a total of 768 occurrences in the data set. The dataset is separated into two categories, diabetes and health, designated by 1 and 0, respectively. There are 268 examples in class 1, whereas there are 500 instances in class 0. Eight attributes are present: Number of pregnancies, Levels of plasma glucose, Heart rate (mm Hg), The triceps’ skinfold thickness (mm), The amount of serum insulin (mu U/ml), Body Mass Index, (BMI), Pre-degree function for diabetes, and Age. The features of PIDD are shown in Table 2. PIDD is frequently used to test new machine learning models, particularly in binary classification. The task at hand is to predict the onset of diabetes based on several medical predictor variables.

Although the dataset has several limitations regarding its representativeness for a diverse global population, it offers numerous benefits for academic applications. The dataset provides a straightforward way to evaluate the performance of algorithms due to its relatively clean and complete nature, making it suitable for academic and introductory applications (Ganesh & Sripriya, 2020). PIDD, originally collected to study the high prevalence of diabetes in the Pima Indian community in Arizona, USA, has some biases that we should mention. It is ethnically specific to Pima Indian women, excludes men, focuses on individuals over the age of 21, and is geographically restricted to Arizona. In healthcare, the data used to train models is one of the privacy concerns. Systems may collect data in a

Table 2
Pima Indians Diabetes Dataset

Attribute	Mean	SD	Min/max	Missing Value
Pregnant	3.8	3.4	1/17	0
Glucose	120.9	32	56/197	5
DBP	69.1	19.4	24/110	35
TSFT	20.5	16	7/52	227
INS	79.8	115.2	15/846	374
BMI	32	7.9	18.2/57.3	11
DPF	0.5	0.3	0.0850/2.3290	0
Age	33.2	11.8	21/81	0

way that violates privacy, such as scraping personal information or gathering information without consent. PIDD ethical consideration was mentioned in detail in (<https://www.kaggle.com/datasets/uciml/pima-indians-diabetes-database>).

Data Pre-processing

Preparing raw data for analysis by cleaning and converting it into a suitable format is known as data pre-processing (Han et al., 2022). It is an essential step in the data analysis pipeline as it can significantly impact the accuracy of the results obtained from data analysis. The pre-processing techniques for the proposed approach are standardization, imputation, and anomaly detection.

Standardization. Data standardization is essential to data preparation, which entails putting the data into a consistent and uniform format (Shanker et al., 1996). Standardization is especially crucial when dealing with data from many sources, which may employ different units of measurement, scales, and conventions (Berner & Judge, 2019). In data standardization, the data are rescaled with a mean of zero and a standard deviation of one. This procedure facilitates data comparison and analysis and increases the accuracy and dependability of the results received through data analysis. In our proposed approach, we utilized standard scalar as the standardization technique, as shown in Equation 1, where μ is the mean, and σ is the standard deviation.

$$z = \frac{x - \mu}{\sigma} \quad (1)$$

Imputation. Data imputation is a method used to replace missing data values in a dataset with estimated values based on existing data (Gelman & Hill, 2006). Imputation may be especially valuable in cases where missing data is prevalent since it permits the use of accurate data for analysis, which can increase the accuracy and dependability of the findings. There are numerous methods for data imputation, such as mean imputation, regression imputation, and multiple imputation (Buuren, 2012). Mean imputation entails substituting missing values with the mean of the existing data.

Local Outlier Factor. In data analysis, the Local Outlier Factor (LOF) is a kind of unsupervised technique used to find outliers (Breunig et al., 2000). The LOF method evaluates each data point's local density and compares it to the local densities of its neighbors. Potential outliers are points that have a substantially lower density than their neighbors. The relative density of a data point X with k neighbors is expressed by Equation 2, where \bar{N} = Average density of all data points in the neighborhood. The average distance between the k nearest data points and the X density have a proportional connection.

$$X = \frac{\text{Density of } X}{N} \quad (2)$$

Classification Models

In ensemble machine learning, the selection of models to combine is governed by several key criteria. Choosing base models that are diverse, competent, and ideally independent is crucial to ensure that the ensemble captures a wide range of features and characteristics of the data. The overarching objective is to form an ensemble that enhances generalization and robustness by effectively leveraging the strengths and mitigating the weaknesses of its constituent models (Caruana et al., 2004). The proposed approach has included several ML methods, including decision trees, logistic regression, KNN, random forests, and XGBoost classifiers. Combining the techniques above with a soft voting classifier increases accuracy.

Decision Tree. A supervised learning approach for classification and regression analysis is called a Decision Tree (DT) (Breiman et al., 2017). Each leaf node represents a class name or a numerical value, and each inside node reflects a choice based on a particular trait. The decision tree method is beneficial for studying complex relationships between variables and identifying the essential properties of a dataset (Breiman, 2001). Decision trees have been used in various sectors, including finance, health, and environmental science, as well as ensemble approaches like Random Forest and Boosting.

Logistic Regression. Logistic Regression (LR) is a common statistical model for binary classification issues with a categorical response variable (Hosmer et al., 2013). Based on one or more predictor variables, the logistic regression model evaluates the likelihood of a binary result. The model's output is a logistic function of the input variables, which maps the input space to the probability space of the binary development. Numerous fields extensively use logistic regression, including medical diagnosis, social sciences, and finance (Agresti, 2015).

K-Nearest Neighbors. In machine learning and data mining, K-Nearest Neighbors (KNN) is a well-known non-parametric classification and regression technique (Cover & Hart, 1967). The KNN algorithm determines a prediction based on the class or regression value of most of the k nearest neighbors of a particular test instance in the training dataset. KNN is a simple and versatile technique applicable to various applications, although it may be computationally costly for big datasets and high-dimensional feature spaces. KNN has been implemented in several domains, including bioinformatics, image processing, and recommendation systems (El Houbay et al., 2017).

Random Forest. Random Forest (RF) is a well-known ensemble machine learning technique that blends a variety of decision trees to boost prediction accuracy and model dependability (Breiman, 2001). It produces several trees and applies the bootstrap technique to each tree in the training data set. Every tree in the forest receives method input during classification, and each tree casts a unique vote for that class. The RF chooses the class with the most significant votes (Mansour & Schain, 2001). Various strategies can be employed to avoid overfitting in ensemble learning, including using RF, which generates random subsets of data and average predictions to negate individual model overfits.

XGBoost. XGBoost (eXtreme Gradient Boosting) is a gradient boosting method that has attracted much interest recently because of its excellent accuracy and scalability in extensive machine learning applications (Chen & Guestrin, 2016). With the help of a tree-based model, XGBoost is an improved version of gradient boosting that iteratively adds weak learners to the ensemble to reduce a particular loss function. The approach uses various regularization techniques to avoid overfitting and boost generalization performance, including shrinkage, subsampling, and pruning. XGBoost is used in many industries, including banking, natural language processing, and computer vision; XGBoost has won several machine-learning contests because of its outstanding performance (Ke et al., 2017).

Proposed Ensemble Voting Classifier

The ensemble is a strategy whose meta-algorithms integrate many machine learning approaches into a single optimal predictive model to reduce variance, bias or improve predictions. This strategy improves the prediction performance over a single model. Ensembling techniques include bagging, boosting, stacking, and voting (Prema et al., 2019). On the PIDD dataset, we have applied a voting-based ensembling technique. The vote-based ensembling approach mixes comparable or conceptually distinct machine learning classifiers for classification using majority or plurality voting. Utilize a voting mechanism to determine the best option among several alternatives. As a result, multiple classifiers can choose from a variety of options. There are two types of voting, hard and soft voting (Mahabub, 2019):

- **Hard Voting:** Hard voting is the most straightforward majority voting. Here, the results of all classifiers are treated equally. Votes are only computed using their median value. Each classifier C_j votes with the majority to select the class label Y , hard voting representation in Equation 3.

$$Y = \text{mode}\{C_1(x), C_2(x), \dots, C_m(x) \quad [i = 1, 2, \dots, m] \quad (3)$$

- Soft Voting:** Soft voting predicts the class using the classifier's projected probability (p.). Soft voting representation in Equation 4. Where W_j is the maximum load that the j^{th} classifier can handle.

$$Y = \operatorname{argmax}_i \sum_{j=1}^m W_j P_{ij} \quad (4)$$

The proposed model has ensembled decision trees, logistic regression, KNN, random forest, and XGBoost classifiers. A classifier based on soft voting has been employed. Using a voting aggregator and a soft voting strategy, each model generates its forecasts, and the majority vote results determine the final prediction. Figure 2 depicts the algorithm behind the suggested technique.

```

Procedure PreProcess (PIDD)
  PIDD.StandardScalar()
  PIDD.Imputation()
  PIDD.LOC()
  Return PIDD

Procedure Split_data(PIDD)
  Train_set, Test_set=split(PIDD, parameters)
  Return Train_set, Test_set
C1=Decision_tree(Train_set, Label, Test_set)
C2=Logistic_regression(Train_set, Lable, Test_set)
C3=KNN(Train_set, Label, Test_set)
C4=Randon_forest(Train_set, Lable, Test_set)
C5=XGBoost(Train_set, Label, Test_set)

Procedure Voting(C1, C2, C3, C4, C5,
voting=soft)
  Voting.fit(Train_set, Label)
  Voting.predict(Test_set)
    
```

Figure 2. The proposed approach algorithm

Evaluation

Model evaluation is an essential process that uses some metrics to evaluate the model's performance. The proposed ensemble approach for diabetes prediction has been tested in two experimental settings: (1) an assessment of the proposed approach's data preparation practices and (2) an evaluation of the effectiveness of machine learning classifiers. Sensitivity, specificity, and accuracy evaluate each situation's efficiency.

Sensitivity. The term sensitivity is used in biostatistics. It can distinguish between positive and negative patients in a test. This statistic represents the percentage of diabetic patients appropriately recognized as such. Equation 5 calculates sensitivity, where (TP) represents the true positives and (FN) the false negatives.

$$\text{Sensitivity} = \frac{TP}{(TP+FN)} \quad (5)$$

Specificity. Specificity is the process of differentiating between actual sturdy and general sturdy. It is the proportion of people classed as non-diabetic who do not have diabetes, the negative instances. It is the ratio of true negatives to the total number of true negatives and false positives (Equation 6).

$$\textit{Specificity} = \frac{TN}{(TN+FP)} \quad (6)$$

Accuracy. The test findings will likely be accurate when the correct sensitivity and specificity are combined in a single measure. The accuracy is calculated by dividing the number of correct predictions by the total number of predictions. Equation 7 is used to calculate accuracy.

$$\textit{Accuracy} = \frac{(TN + TP)}{(TN + TP + FN + FP)} \quad (7)$$

RESULTS AND DISCUSSION

The values in the dataset were first scaled, meaning that each value fits within a range (0 and 1). The StandardScalar method is used to standardize Equation 1. This modification helps offset the negative consequences of the prevalence of specific traits, especially undesired ones with more comprehensive value ranges. As numerous features have a value of zero, data imputation is then performed (for example, a blood pressure reading of 0 seems improbable, yet it is the lowest possible result).

As a direct consequence of this, incorrect information is provided. We may substitute these data with the median, as we cannot disregard these data. We have opted to impute since our dataset is small. The fact that pregnancy has a zero value rather than a missing value makes it an example of a feature that should not be imputed. Lastly, anomaly data is detected by utilizing the LOF technique (Equation 2).

The ensemble approach was implemented using Python 3.10.9. The PIDD dataset was used in the experiments. There are 768 rows and eight features in the dataset. The dataset was randomly split into two sets; the training set consists of 537 records (about 70% of the dataset), while the test set has 230 records (or 30 percent). The model is “trained” using the training data and then “tested” using the data to ensure accuracy and effectiveness.

The proposed approach employs five ML models: DT, LR, KNN, RF, and XGBoost. A comparison of traditional ML techniques for classifying diabetes as positive or negative has been conducted. It has been performed to compare and analyze the accuracy of conventional algorithms. Positive and negative classes comprise the PIDD dataset, which has been used for testing. Table 3 compares the outputs of several ML models using the PIDD dataset. Compared to previous machine learning methods. The proposed ensemble approach had the greatest accuracy, sensitivity, and specificity values of 64%, 74%, and 81%, respectively (Table 3). The results for the individual models in Table 3 also indicate the data quality after performing the pre-processing process.

It is clear from referring to Table 3 that none of these machine learning methods do very well on the dataset that has been presented since they both have an accuracy of less

than 80. Considering the performance of the suggested method reveals that it exceeds the other machine learning algorithms in terms of accuracy by an 81% margin. In contrast, in terms of sensitivity, it was equal to XGBoost and close to SVC by 64%, and in specificity, it also overcame the rest by 74%. Figure 3(a) shows the comparative analysis graph of the different algorithms on the PIDD datasets. The dataset had 49 false positives and false negatives, in addition to 141 genuine positives and 43 false positives. Consequently, the confusion matrix has helped us comprehend our forecasts better.

Figure 3(b) depicts the confusion matrix for diabetic patients, demonstrating whether the recommended ensemble approach made accurate or inaccurate predictions. The dataset had 141 true positives, 43 false positives, and 49 false positives and false negatives. Therefore, the confusion matrix has improved our understanding of our predictions.

In contrast to earlier research, our findings indicate enhanced accuracy, with a few exceptions. Notably, Nour’s study (Noor et al., 2021) employed specific data pre-processing techniques, including the Synthetic Minority Over-sampling Technique (SMOTE), to

Table 3
Comparison of accuracies with conventional machine learning algorithms

Classifier	Sensitivity	Specificity	Accuracy
Neural Network	54%	70%	78%
Logistic Regression	52%	70%	77%
XGBoost	64%	64%	77%
SVC	62%	64%	76%
KNN	52%	70%	77%
Decision Tree	56%	57%	72%
Random Forest	54%	70%	77%
Proposed Approach	64%	74%	81%

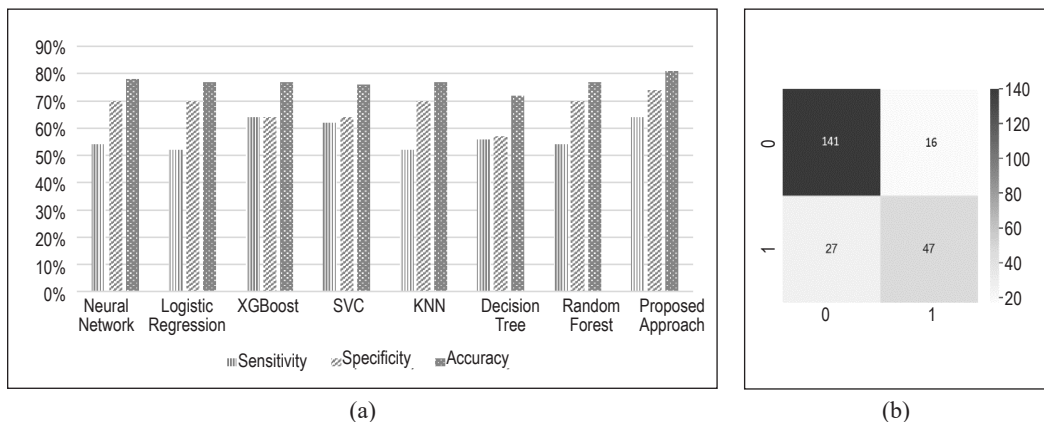


Figure 3. (a) Graphical comparison of accuracies; and (b) confusion matrix of diabetes patients

address data imbalance and remove missing data points. Given the limited data, we chose not to adopt these methods in our study. Eliminating data points could have constrained the model's learning capacity, potentially leading to overfitting.

The performance of the proposed ensemble method is attributed to several key factors. The diverse base algorithms collectively capture different data aspects, enhancing robustness and generalizability. The quality and relevance of the PIDD dataset, coupled with optimized hyperparameters, contribute to the model's accuracy. While the ensemble approach improves performance metrics like accuracy, specificity, and sensitivity, it balances computational efficiency without significant overfitting, although it may compromise interpretability.

CONCLUSION

This research aimed to develop a robust and precise algorithmic framework for predicting diabetes in patients. The study deployed an experimental design hinged on five prominent machine learning algorithms To realize this goal: Decision Trees, Logistic Regression, Random Forest, K-Nearest Neighbors (KNN), and Extreme Gradient Boosting (XGBoost). The Pima Indians Diabetes Dataset (PIDD) was utilized for the investigation and subjected to rigorous pre-processing procedures, including standardization, imputation of missing values, and anomaly detection via the Local Outlier Factor (LOF) methodology. These pre-processing techniques were pivotal in optimizing the dataset for machine learning applications, eliminating erroneous outcomes and enhancing the model's interpretability.

The ensemble approach, which employed soft voting classifiers, achieved an accuracy rate of 81%. While this level of accuracy is noteworthy and enriches the existing literature, there remains room for further improvement. Several directions for future research emerge from the findings and limitations of this study. These include the potential application of deep learning models to further improve prediction accuracy and the exploration of hyperparameter tuning techniques about the proposed model. Future research may also benefit from using real-world data sets for further validation. In subsequent phases, the model will be fine-tuned using empirical data. Should it exhibit robust performance across multiple evaluations, consideration may be given to its integration into clinical diagnostic procedures.

ACKNOWLEDGEMENT

The authors sincerely thank the administration leaders at Northern Technical University (NTU), Iraq. The authors would also like to thank all the professors who validated the data and results for their comments.

REFERENCES

- Agrawal, K., Bhargav, G., & Spandana, E. (2021). Diabetes diagnosis prediction using ensemble approach. In V. Nath & J. K. Mandal (Eds.), *Proceedings of the Fourth International Conference on Microelectronics, Computing and Communication Systems: Lecture Notes in Electrical Engineering, vol 673* (pp. 799–813). Springer. https://doi.org/10.1007/978-981-15-5546-6_66
- Agresti, A. (2015). *Foundations of linear and generalized linear models*. John Wiley & Sons
- Akyol, K., & Şen, B. (2018). Diabetes mellitus data classification by cascading of feature selection methods and ensemble learning algorithms. *International Journal of Modern Education & Computer Science, 10*(6), 10-16. <https://doi.org/10.5815/ijmecs.2018.06.02>
- Alasaady, M. T., Aris, T. N. M., Sharef, N. M., & Hamdan, H. (2022). A proposed approach for diabetes diagnosis using neuro-fuzzy technique. *Bulletin of Electrical Engineering and Informatics, 11*(6), 3590–3597. <https://doi.org/10.11591/eei.v11i6.4269>
- Alasaady, M. T., Saeed, M. G., & Faraj, K. H. (2019, February 13-14). *Evaluation and comparison framework for data modeling languages*. [Paper presentation]. 2nd International Conference on Electrical, Communication, Computer, Power and Control Engineering (ICECCPCE), Mosul, Iraq. <https://doi.org/10.1109/ICECCPCE46549.2019.203750>
- Atif, M., Anwer, F., & Talib, F. (2022). An ensemble learning approach for effective prediction of diabetes mellitus using hard voting classifier. *Indian Journal of Science and Technology, 15*(39), 1978–1986. <https://doi.org/10.17485/IJST/v15i39.1520>
- Barik, S., Mohanty, S., Mohanty, S., & Singh, D. (2021). Analysis of prediction accuracy of diabetes using classifier and hybrid machine learning techniques. In D. Mishra, R. Buyya, P. Mohapatra & S. Patnaik (Eds.), *Intelligent and Cloud Computing* (pp. 399–409). Springer. https://doi.org/10.1007/978-981-15-6202-0_41
- Berner, R., & Judge, K. (2019). *The Data Standardization Challenge* (Working Paper No. 438/2019). CIGI Press. https://papers.ssrn.com/sol3/papers.cfm?abstract_id=3323719
- Breiman, L. (1996). Bagging predictors. *Machine Learning, 24*, 123-140. <https://doi.org/10.1007/BF00058655>.
- Breiman, L. (2001). Random forests. *Machine Learning, 45*(1), 5–32. <https://doi.org/10.1023/A:1010933404324>
- Breiman, L., Friedman, J. H., Olshen, R. A., & Stone, C. J. (2017). *Classification and Regression Trees*. Routledge. <https://doi.org/10.1201/9781315139470>
- Breunig, M. M., Kriegel, H. P., Ng, R. T., & Sander, J. (2000, May 15-18). *LOF: Identifying density-based local outliers*. [Paper presentation] SIGMOD '00: Proceedings of the 2000 ACM SIGMOD International Conference on Management of Data, Texas, USA. <https://doi.org/10.1145/342009.335388>
- Buuren, S. V. (2012). *Flexible imputation of missing data*. CRC Press. <https://doi.org/10.1201/b11826>
- Caruana, R., Niculescu-Mizil, A., Crew, G., & Ksikes, A. (2004, July 4-8). *Ensemble selection from libraries of models*. [Paper presentation]. ICML '04: Proceedings of the Twenty-first International Conference on Machine Learning, New York, USA. <https://doi.org/10.1145/1015330.1015432>

- Centers for Disease Control and Prevention (2011). National diabetes fact sheet: National estimates and general information on diabetes and prediabetes in the United States. *Atlanta, GA: US Department of Health and Human Services, Centers for Disease Control and Prevention*, 201(1), 2568–2569.
- Chen, R., Ovbiagele, B., & Feng, W. (2016). Diabetes and stroke: Epidemiology, pathophysiology, pharmaceuticals and outcomes. *American Journal of the Medical Sciences*, 351(4), 380–386. <https://doi.org/10.1016/j.amjms.2016.01.011>
- Chen, T., & Guestrin, C. (2016, August 13-17). *XGBoost: A scalable tree boosting system*. [Paper presentation]. KDD '16: Proceedings of the 22nd ACM SIGKDD International Conference on Knowledge Discovery and Data Mining, California, USA. <https://doi.org/10.1145/2939672.2939785>
- Cover, T., & Hart, P. (1967). Nearest neighbor pattern classification. *IEEE Transactions on Information Theory*, 13(1), 21–27. <https://doi.org/10.1109/TIT.1967.1053964>
- El Houby, E. M. F., Yassin, N. I. R., & Omran, S. (2017). A hybrid approach from ant colony optimization and K-nearest neighbor for classifying datasets using selected features. *Informatica*, 41, 495–506.
- Fernández-Delgado, M., Cernadas, E., Barro, S., & Amorim, D. (2014). Do we need hundreds of classifiers to solve real-world classification problems? *The Journal of Machine Learning Research*, 15(1), 3133–3181.
- Ganesh, P. V. S., & Sripriya, P. (2020). A comparative review of prediction methods for pima indians diabetes dataset. In S. Smys, J. M. R. S. Tavares, V. E. Balas & A. M. Iliyasu (Eds.), *Computational Vision and Bio-Inspired Computing* (pp. 735–750). Springer. https://doi.org/10.1007/978-3-030-37218-7_83
- Gelman, A., & Hill, J. (2006). *Data Analysis using Regression and Multilevel/Hierarchical Models*. Cambridge University Press. <https://doi.org/10.1017/CBO9780511790942>
- Han, J., Pei, J., & Tong, H. (2022). *Data mining: Concepts and techniques*. Morgan Kaufmann.
- Hosmer, D. W., Lemeshow, S., & Sturdivant, R. X. (2013). *Applied logistic regression* (3rd ed.). Wiley. <https://doi.org/10.1002/9781118548387>
- Kavakiotis, I., Tsave, O., Salifoglou, A., Maglaveras, N., Vlahavas, I., & Chouvarda, I. (2017). Machine learning and data mining methods in diabetes research. *Computational and Structural Biotechnology Journal*, 15, 104–116. <https://doi.org/10.1016/j.csbj.2016.12.005>
- Ke, G., Meng, Q., Finley, T., Wang, T., Chen, W., Ma, W., Ye, Q., & Liu, T. Y. (2017). LightGBM: A highly efficient gradient boosting decision tree. In I. Guyon, U. Von Luxburg, S. Bengio, H. Wallach, R. Fergus, S. Vishwanathan & R. Garnett (Eds.), *Advances in Neural Information Processing Systems* (pp. 30). Curran Associates, Inc.
- Khairan, H. E., Zubaidi, S. L., Muhsen, Y. R., & Al-Ansari, N. (2023). Parameter optimisation-based hybrid reference evapotranspiration prediction models: A systematic review of current implementations and future research directions. *Atmosphere*, 14(1), Article 77. <https://doi.org/10.3390/atmos14010077>
- Kumari, S., Kumar, D., & Mittal, M. (2021). An ensemble approach for classification and prediction of diabetes mellitus using soft voting classifier. *International Journal of Cognitive Computing in Engineering*, 2, 40–46. <https://doi.org/10.1016/j.ijcce.2021.01.001>
- Kunwar, R., & Timalisina, A. K. (2021). An ensemble approach for the diagnosis of diabetes mellitus using multiple classifiers. *Proceedings of 9th IOE Graduate Conference*, 9, 202–207.

- Li, L. (2014, November 10-12). *Diagnosis of diabetes using a weight-adjusted voting approach*. [Paper presentation]. IEEE International Conference on Bioinformatics and Bioengineering, Florida, USA. <https://doi.org/10.1109/BIBE.2014.27>
- Mahabub, A. (2019). A robust voting approach for diabetes prediction using traditional machine learning techniques. *SN Applied Sciences*, 1(12), Article 1667. <https://doi.org/10.1007/s42452-019-1759-7>
- Mansour, Y., & Schain, M. (2001). Learning with maximum-entropy distributions. *Machine Learning*, 45(2), 123–145. <https://doi.org/10.1023/A:1010950718922>
- Mirzajani, S. S., & Salimi, S. (2018). Prediction and diagnosis of diabetes by using data mining techniques. *Avicenna Journal of Medical Biochemistry*, 6(1), 3–7. <https://doi.org/10.15171/ajmb.2018.02>
- Noor, N. A. B. S., Elamvazuthi, I., & Yahya, N. (2021, July 13-15). *Classification of diabetes mellitus using ensemble algorithms*. [Paper presentation]. 8th International Conference on Intelligent and Advanced Systems (ICIAS), Kuching, Sarawak. <https://doi.org/10.1109/ICIAS49414.2021.9642508>
- Prema, N. S., Varshith, V., & Yogeswar, J. (2019). Prediction of diabetes using ensemble techniques. *International Journal of Recent Technology and Engineering*, 7(6), 203-205.
- Qin, L. (2022, September 23-25). *A prediction model of diabetes based on ensemble learning*. [Paper presentation] AIPR '22: Proceedings of the 2022 5th International Conference on Artificial Intelligence and Pattern Recognition, Xiamen China. <https://doi.org/10.1145/3573942.3573949>
- Saeed, R. R., Yaseen, O. M., Rashid, M. M., & Ahmed, M. R. (2022, June 9-11). *Applications of machine learning in battling against novel COVID-19*. [Paper presentation]. International Congress on Human-Computer Interaction, Optimization and Robotic Applications (HORA), Ankara, Turkey. <https://doi.org/10.1109/HORA55278.2022.9799969>
- Shanker, M., Hu, M. Y., & Hung, M. S. (1996). Effect of data standardization on neural network training. *Omega*, 24(4), 385–397. [https://doi.org/10.1016/0305-0483\(96\)00010-2](https://doi.org/10.1016/0305-0483(96)00010-2)
- Singh, N., & Singh, P. (2020). Stacking-based multi-objective evolutionary ensemble framework for prediction of diabetes mellitus. *Biocybernetics and Biomedical Engineering*, 40(1), 1–22. <https://doi.org/10.1016/j.bbe.2019.10.001>
- Soni, M., & Varma, S. (2020). Diabetes prediction using machine learning techniques. *International Journal of Engineering Research & Technology*, 9(9), 921-925.
- Swapna, G., Soman, K. P., & Vinayakumar, R. (2018). Automated detection of diabetes using CNN and CNN-LSTM network and heart rate signals. *Procedia Computer Science*, 132, 1253–1262. <https://doi.org/10.1016/j.procs.2018.05.041>
- WHO. (2014). *World diabetes statistics*. World Health Organization. <http://www.who.int/diabetes/en/index.html>

Integrating Green Infrastructure Distribution and Green Corridor Mapping with Proposed Green Trail Area and Wildlife-Human Conflict Using Remote Sensing-GIS Approach

Syarifuddin Misbari*, Jacqueline Isabella Anak Gisen, Nur Arissa Farhanis Mohd Rosli, Amir Asyraf Mohd Fauzi and Aishah Abu Bakar

Faculty of Civil Engineering Technology, Universiti Malaysia Pahang Al-Sultan Abdullah, Lebuhr Persiaran Tun Khalil Yaakob, 26300 Gambang, Pahang, Malaysia

ABSTRACT

Most people now prefer to live in cities, and the urban population has grown significantly. The decrement of urban green corridors causes an essential need for livability in highly populated areas. The needs of population health and sustainable city development are put under prolonged stress by the shortage of publicly accessible green infrastructure and its placement in inappropriate areas. The inventory of green corridor areas and the distribution of significant infrastructure are not fully understood, thus encouraging conflicts between residents and wildlife and increasing flood risk in their vicinity. Optical satellite images were required to (1) develop a green corridor (GC) map, (2) investigate the green infrastructure (GI) demand with the existing land use, and (3) propose new green trails (GT) in the Kuantan district using a geospatial approach. NDVI and site suitability analysis were carried out on Landsat OLI and Sentinel-2 MSI images, which were integrated with GIS tools to achieve all the objectives. A GC map has been developed, and five new proposed areas for GI development have been identified. Based on the results, 5 proposed green trails (3 long GTs, 2 short GTs) with a total length of 79.3 km are scattered in the Kuantan district at the most suitable site, identified using a geospatial approach. This study supports SDG 15: Life on Land, where green corridors reinforce biological connectivity, provide conducive space for high-populated areas, and minimize the negative impact of urbanization on the designed areas of GC, GI and GT in the developing city of Kuantan.

ARTICLE INFO

Article history:

Received: 15 August 2023

Accepted: 26 October 2023

Published: 04 April 2024

DOI: <https://doi.org/10.47836/pjst.32.3.20>

E-mail addresses:

syarifuddinm@umpsa.edu.my (Syarifuddin Misbari)
isabella@umpsa.edu.my (Jacqueline Isabella Anak Gisen)
arssafrhns@gmail.com (Nur Arissa Farhanis Mohd Rosli)
aasyraf40@gmail.com (Amir Asyraf Mohd Fauzi)
aishahabubakar@umpsa.edu.my (Aishah Abu Bakar)

* Corresponding author

Keywords: Green corridor, satellite, sustainable city, urban

INTRODUCTION

The proportion of people living in cities increased from 62.0% in 2000 to 71.0% in 2010 (Department of Statistics Malaysia, 2011), aligning with national rapid growth. The four most urbanized cities in Malaysia are Kuala Lumpur and Putrajaya (100%), Selangor (91.4%) and Pulau Pinang (90.8%). In contrast, the three lowest urbanized states are Perlis (51.4%), Pahang (50.5%) and Kelantan (42.4%). With large-scale land clearance set for economic development and urbanization, fragmented green spaces are decreasing daily. Thus, a green initiative needs to be undertaken to create more sustainable living spaces for people. An increase in deforestation has occurred in Malaysia due to rapid urban development (Botezan et al., 2021; Danjaji & Ariffin, 2017). Shrinkage of green space has triggered slope failures, and many landslides jeopardize the stability of green infrastructure. Green trails should also be selected on non-steep surfaces where no or low landslide risk is infrequent (Zhan et al., 2022). The green corridors are critical for protecting pedestrians from dangerous pollution on open highways and increasing beneficial interactions between urban inhabitants and nature. Meanwhile, green infrastructure can be used with grey infrastructure measures to reduce stormwater runoff into streams and rivers and minimize infrastructure and property damage.

The objectives of this study are (1) to identify existing green infrastructure and green corridor distribution in the Kuantan district, (2) to analyze the spatio-temporal trends of Human-Wildlife conflict using spatial analysis in the Kuantan district, and (3) to propose remote sensing-Geographic Information Systems (GIS) approach for Green Trail in Kuantan district.

Developing cities trigger plenty of human-wildlife conflicts. Human-wildlife conflict (HWC) refers to adverse encounters between humans and wild animals that have ramifications for both humans and their resources, as well as wildlife and their ecosystems (Broekhuis et al., 2017). Meanwhile, deforestation reduced global forest areas lost to other uses such as agricultural croplands, urbanization, or mining (Al-Masri et al., 2019). Deforestation can lead to the direct loss of wildlife habitat and general habitat destruction. Creating a natural network for wildlife to migrate through cities and connecting green places has been demonstrated to promote biodiversity.

Remote sensing data was cost-efficient because satellite images resolved the cost and time-constraint issues in accomplishing field visits for various purposes, including crop estimation (Gallego et al., 2014). Satellites can capture images of large areas, allowing for comprehensive mapping of green corridors and critical habitat linkages for wildlife populations. It could be integrated with spatial analysis tools and techniques, such as GIS, to analyze and model the spatio-temporal trends of human-wildlife conflict. It can provide valuable insights into conflict patterns, drivers, and impacts and support evidence-based decision-making for conservation and management efforts.

This study supports one of the Sustainable Development Goals agenda, SDG15: Life on Land, which initiates minimizing the negative impact of urbanization on the designed area of GC, GI and GT in the developing city of Kuantan. Subsequently, there is a huge possibility of developing and creating an existing GT map and GT initiatives to achieve sustainability in Kuantan. Some parameters needed are accessibility distance, topology, slope and natural features.

METHODOLOGY

Study Area

This study focused on areas in Kuantan with high vegetative coverage, which aligned with the determination of this city to achieve status as a sustainable city according to the SDG. Kuantan is a Pahang state district that faces the South China Sea on the east coast of Peninsular Malaysia. The frequency of HWC, which occasionally increases each year, brings high motivation to conduct this study in Kuantan. Satellite images of Landsat OLI and Sentinel-2 with different spatial resolutions were used for this study to ensure the whole Kuantan district was covered. Moreover, elevation data from Shuttle Radar Topography Mission (SRTM) 1 Arc-second Global is used in conducting this study. Figure 1 illustrates the general workflow of the study.

Data Collection

This study gathers primary data, secondary data, including satellite images, and relevant supportive data for the comprehensive preparation required for this study. Primary data such as coordinates of land use type, green corridor, and existing GI from field visits has been gathered, along with other supportive information, including from newspapers, that is relevant to this topic. The field visit involved an area in Kuantan, Pahang, with various natural features and man-made infrastructures, an undulating topographical surface and a face-off of the South China Sea. Handheld GPS records the location of existing GI and different land use types in Kuantan. The drone system, including its sensor, panel board, and flight planning software, had been utilized to record the overall view and information of the Kuantan area, as well as the distribution of existing GI, land use type, green corridor area, and other relevant information that was used for result verification.

Besides that, the secondary data, which was used in this study is multispectral satellite images with a moderate spatial resolution (30 m) of the Landsat OLI and Sentinel-2 MSI, which has a 10 m spatial resolution that is important for mapping of GI and GT proposed locations in Kuantan, Pahang. Pre-processing of satellite data was performed using a licensed-authorized remote sensing-GIS processing system. Sentinel-2 and Landsat 8 could offer excellent accuracy and reliability for general use of monitoring and observation

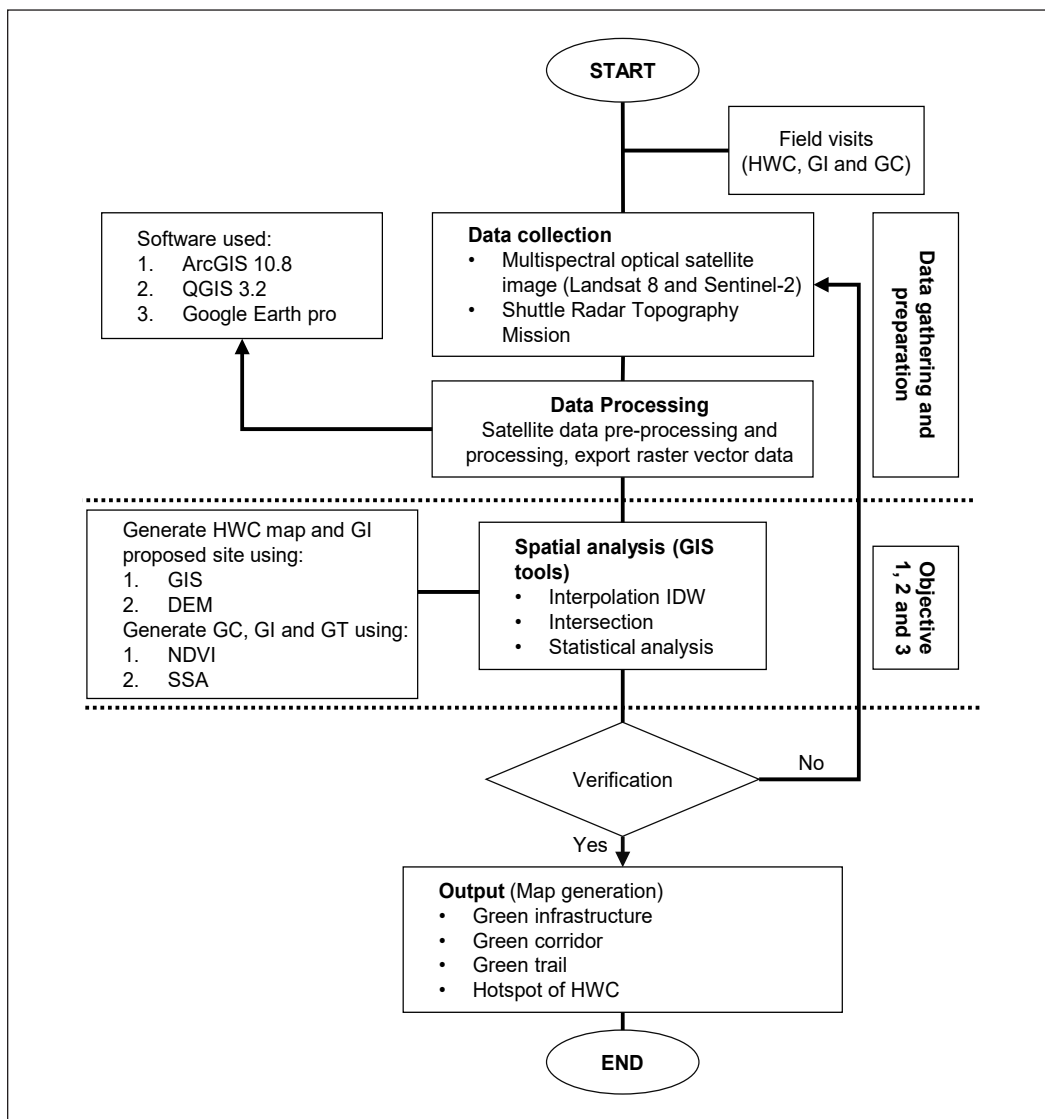


Figure 1. General workflow of the study

in the mapping process, especially for land use and green mapping in huge areas (Rasli & Kanniah, 2018). Sentinel-2 mainly gives specific specifications of the images as it accurately distinguishes different types of natural vegetation and crops in the mapping process (Espinosa & Schroder, 2019; Phelan et al., 2013).

Data Processing

Both primary and secondary data collected for this study were processed to fulfill the study's demands. Raster data format (grid form) of digital data, including optical remote

sensing satellite images and vector data format such as existing GI points, was processed using a geospatial processing system with the correct map projection suitable for Pahang state. The raster and vector data attribute was assessed using ArcGIS 10.8 and certain tasks on open-source software, namely Quantum GIS (QGIS) 3.2. Both programs are data interchangeable. Multispectral satellite images have been used to generate a Normalized Difference Vegetation Index (NDVI) map where red and near-infrared spectral bands are processed using the formulae $(\text{NIR Band} - \text{Red Band}) / (\text{NIR Band} + \text{Red Band})$. Before processing, the georeferencing of the images, stacking of band spectral bands, and loading of the spectral layer of bands into the software were performed to ensure its readiness in terms of conforming the coordinates of the satellite image with the real location on the earth's surface, which is very critical for result accuracy after further digital data processing.

Spatial Analysis

Subsequently, after data processing, spatial analysis was performed on the processed spatial data to achieve all the objectives. The characteristics of the acquired green corridor, NDVI, green trails, and their spatial interactions are investigated using spatial analysis. It is a very important task to assess the geographic suitability of specific locations for developing proposed GT based on existing GI and GC, considering the adjacent land use types, characteristics of places, and range of NDVI values, and detecting significant trends concealed within this study. The decision-making process is more convenient with the input information from spatial analysis.

This study performed spatial interpolation using the Inverse Distance Weighted (IDW) interpolation scheme provided in ArcGIS. A set of locational data on animal roadkill accidents, reports of wildlife disturbance from residents, and animal deaths observed during field visits in the Kuantan district was consolidated as the input for spatial analysis. The zoning area with very high, medium, and low HWC occurrences was automatically generated based on the input, which was then overlaid with NDVI, where high NDVI is typically closely related to a high rate of HWC. Besides that, the intersection of the produced map with other geographical features, such as land use type, and statistical analysis have also been performed to assist in interpreting the results obtained from the data processing.

Verification Process and Map Generation

The result verification phase began after conducting field visits and collecting the data using handheld GPS and drone systems (drone, sensor, panel board, and flight planning software). Those data were exported to a geospatial file format to align their compatibility with GIS processing systems. The transfer of data from multiple GIS devices is often

undertaken by converting the verification data, operated by a translational program in ArcGIS or Google Earth Pro, from the compact internal storage format to a new raster or vector data format with suitable map projection. This study used the geodetic coordinate reference system, GDM2000, with Well-Known ID (WKID) 3379 and ellipsoid of GRS 1980 as the spatial data projection. The verification process using field-based data is important to indicate the accuracy of the outputs from a satellite-based approach, including land use type GI, map, and HWC map. Data accuracy was checked, and a set of 85% (110 out of 150 points coordinate) of land use types and GI and 92% (18 out of 20 locations) of HWC area collected during the field visits were matched with processed results. The final and reliable existing GI-GC map, proposed GT-GI and HWC mapping were successfully generated using ArcGIS 10.8, QGIS 3.20, and Google Earth Pro software accomplished by all cartographic elements of a map.

RESULTS AND DISCUSSION

Existing GC and GI Map

The study is critical as green corridor mapping provides insightful inputs for the decision-makers of local agencies in projecting development plans for the city where human and man-made features and natural life share equal quality and comfort of livelihoods. This study also identified certain places to preserve and strategic areas for high conservation values. Instead of improving linear relationships between humans and animals, the focus should be reducing the frequency of conflict (Misbari et al., 2017). A green corridor is important to strengthen the ecological connection of the green spaces and reduce fragmentation patches in urban areas. According to Ashikin (2021), Pahang is the third largest Malaysian state, and Kuantan is the most developed city in the East Coast region.

This mapping was identified according to the NDVI and site suitability analysis in the spatial analysis process. The location with the highest vegetation index was selected as a green corridor. Based on Figure 2, the red area indicates the developed area, the blue area indicates the water body, the brown area indicates bare soil and the green area indicates the vegetative area. The green area is the most suitable location to build a green corridor, and the least suitable is the red area.

During the site visit, the coordinates of the existing green infrastructure in the Kuantan district were recorded using handheld GPS. Some of the types of green infrastructure are green streets, rain gardens, urban tree cover, permeable pavements, and recreational parks. After recording all green infrastructures in Kuantan, the coordinates were exported to Google Earth Pro to confirm and verify the data collected through the site visit. In total, over 300 green infrastructures of five different designs of GIs, shown in Figure 2, are mostly located in developed areas because of the low vegetation index. All proposed GI locations are free from slope failures where no or low potential of new landslides will occur.

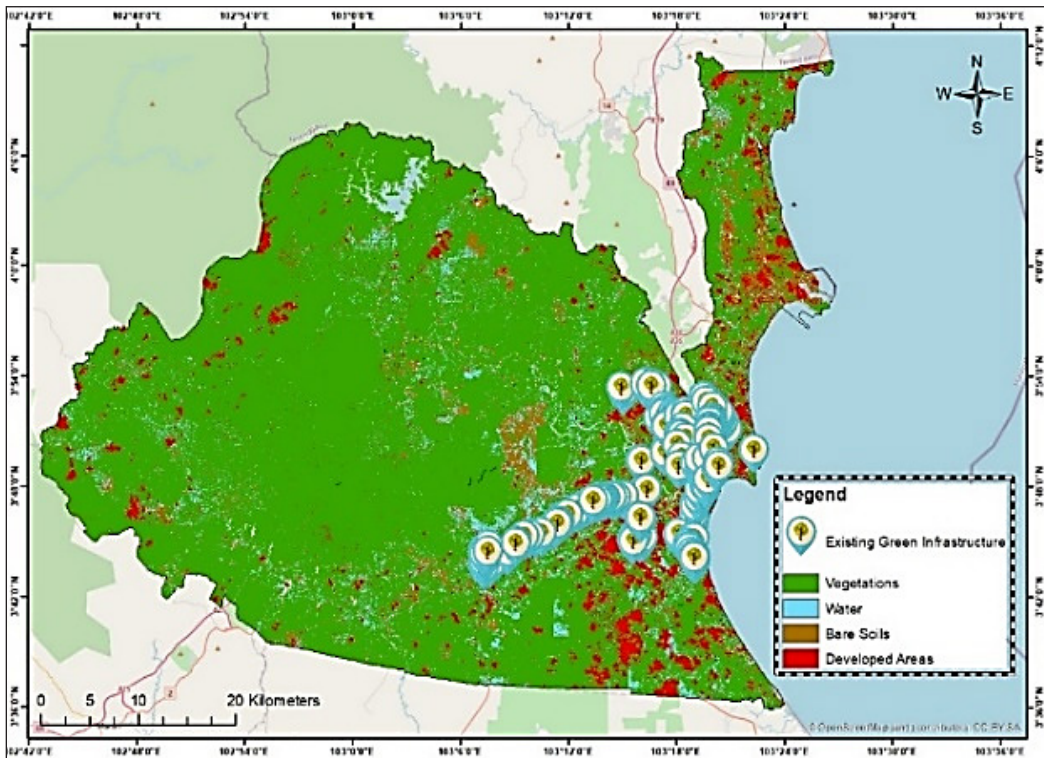


Figure 2. Existing green corridor and green infrastructure in Kuantan district

Proposed GT and GI Map

Site suitability analysis was conducted to generate green trails and proposed new green infrastructure mapping. In the site suitability analysis (SSA) process in ArcGIS for generating green trails, the road, river, slope, soil and NDVI were taken as the variables to obtain a suitable location for building the Green Trail in Kuantan. Most of the input data for SSA is from Kuantan Municipal Council, except slope and NDVI, which are generated from SRTM data and ground data collection. The SSA evaluates and grades places based on numerous weighted criteria to discover potential locations for GT and GI. SSA begins with defining the problem, determining the criteria for solving it, and creating the necessary input datasets.

Raster datasets, including the criteria of slope, river, and road in Kuantan, are used for the SSA. Inputs were ranked based on importance and priority using a common ratio such as 1/2, 1/4, 1/5, or 1/7 to compare the criteria. The author, who was familiar with Kuantan City, determined this rank. After that, the processing system, with the tool of the analytical hierarchy process, determined the weights for the criteria that have been used and combined them to get a score for each potential site. Finally, the scores determine the best feasible placements for the proposed GI. In this case, NDVI scored the highest (0.5381), while road data scored the lowest (0.1026). Thus, the green area is the most suitable for building a

green trail. Meanwhile, the red area is not suitable because it is heavily developed. Hence, there are 5 trails generated that can be built in Kuantan district.

As shown in Figure 3, the longest trail (Green Trail 1- green pale) is 41 km long; meanwhile, the shortest trail (Green Trail 5-pale blue) is 2 km long, and the total length of these 5 trails is 79.3 km. All these trails are prohibited from trespassing by any authority or any development. Thus, these trails are named as a reserved and conservation location for natural habitat flora and fauna. Similar to GI, all proposed GT locations have a low risk of landslides or flash flood events, which may cause casualties for the residents in Kuantan City (Sami et al., 2013).

Furthermore, in the SSA process for green infrastructure, the slope, soil and NDVI were taken as the variables to obtain a suitable location for building GI in Kuantan. The location near the waterfall and green trail is the most suitable location for GI because of the natural features, and the most suitable type of GI to build is recreational parks. The GI buildings are green streets, rain gardens, permeable pavements, and urban tree cover (Mustafa, 2011). Besides, after analyzing the existing GI map, we found that these types of green infrastructure are not well distributed in the Kuantan district. Hence, the proposed green infrastructure is needed to stabilize the distribution of green infrastructure and its type according to its suitability. Figure 3 also illustrates five new proposed sites for GI development.

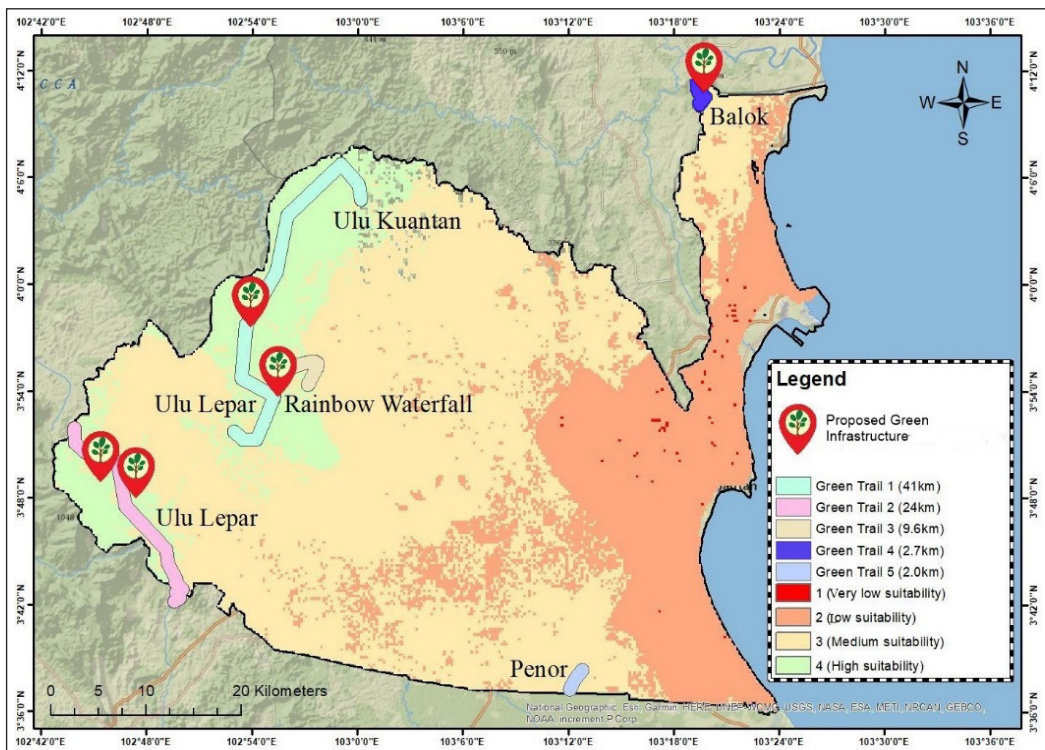


Figure 3. Proposed green trails and green infrastructure in Kuantan district

The proposed GI may benefit the residents' environment and quality of life. However, relevant stakeholders may take into consideration a few potential challenges in implementing the proposed green infrastructure in Kuantan. It may come from the maintenance of the proposed GI for the long term in terms of its operational cost and related tasks, including watering and pruning trees, integration of the proposed GI with existing urban infrastructure such as transportation systems and utilities, and selection of tree species. In addition, public perception may doubt the effectiveness of GI for urban hazards, including floods and heat, that cause low community engagement from residents. Therefore, a comprehensive solution involving collaboration among government agencies such as Kuantan Municipal Council and the Malaysian Public Works Department, community organizations, private stakeholders, and experts in urban planning and environmental research is required to address these challenges and ensure that the public well-accepts proposed and existing GI.

Human-wildlife Conflict Map

Figure 4 reveals hotspots of HWC in the Kuantan district and the types of animals involved in the casualties. The map shows a negative regression between the interpolated area of

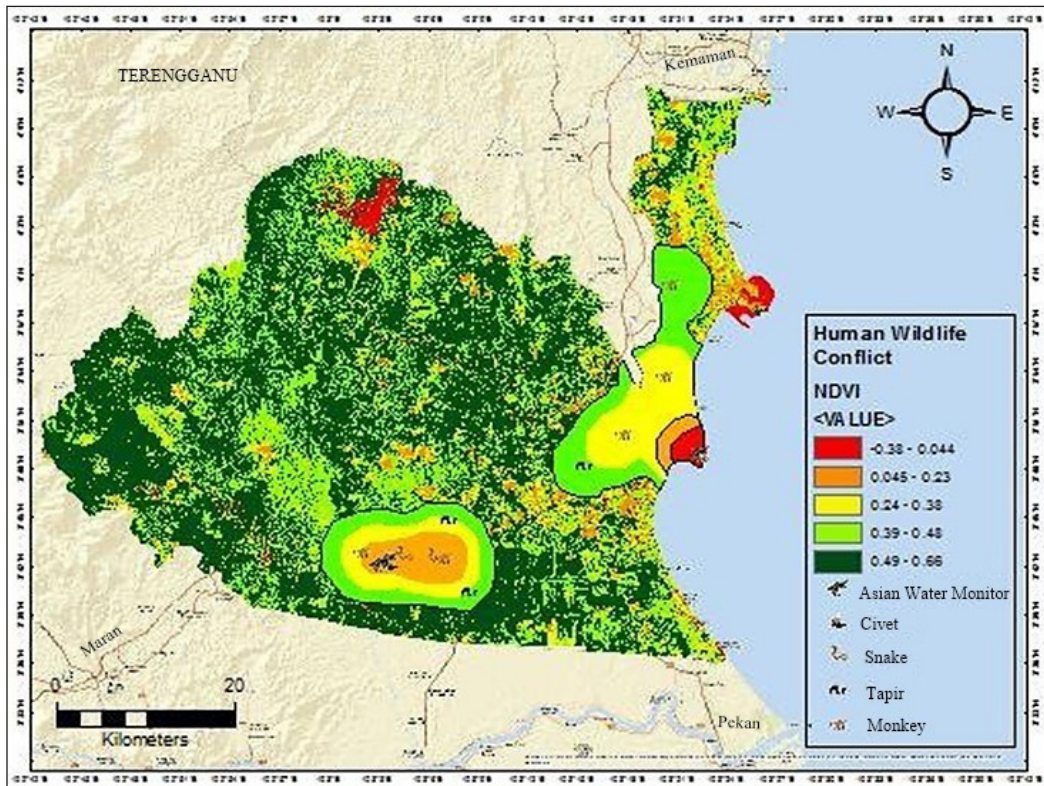


Figure 4. Human-wildlife conflict map in Kuantan district overlaid on NDVI layer

HWC and NDVI values, where HWC increased when the NDVI increased. It indicates low habitat density in low vegetation areas, which triggers conflicts between humans and wildlife. Besides that, the buffer zones were generated by using kernel density tools, and there are 5 categories of HWC hotspots, which consist of very high (red), high (orange), moderate (yellow), low (light green), and very low (dark green).

Furthermore, all recorded animals in the Kuantan district show different sizes, from medium to large mammals or reptiles, such as Asian water monitors, civets, snakes, tapirs, and monkeys. Indirectly, this result was recorded in 2021. Based on the results, the highest hotspot was recorded on the east side of Kuantan district, the Teluk Cempedak area.

CONCLUSION

This study was carried out to identify existing green infrastructure and green corridor distribution in the Kuantan district, analyze the spatiotemporal trends of HWC using spatial analysis, and implement a remote sensing-GIS approach for green trail mapping. Based on the findings, all objectives were achieved. The existing GI in Kuantan is concentrated in the urban area along the easy-accessed corridor. Thus, five locations of new GI are proposed to be built along the proposed GT. Based on the results, 5 proposed green trails (3 long GTs, 2 short GTs) with a total length of 79.3 km are scattered in the Kuantan district at the most suitable site, identified using the RS-GIS-based approach. As shown in Figure 3, two new GIs should be developed along the GT1, 2 new GIs along the GT2 and a new GI along the GT4. By improving GI and preserving the GT area, the rate of HWC could be reduced in the Kuantan district in the long term.

ACKNOWLEDGEMENTS

The authors would like to thank the Faculty of Civil Engineering Technology (FCET), Universiti Malaysia Pahang Al-Sultan Abdullah (UMPSA), Malaysia, for their great support and facilities in producing this publication in the *Pertanika Journal of Science and Technology*. The authors also express their gratitude to the Ministry of Higher Education for the grant [RDU210355: Satellite-Based Landslide Susceptibility Modelling in the Kuantan River Basin]. They greatly extend their appreciation to Irhamillah Khamsim from ESRI APAC and Huzari Mazelan from UMPSA for technical support on GIS software and drone observation at the field site, respectively.

REFERENCES

- Al-Masri, A., Ozden, O., & Kara, C. (2019). Green corridor development as an approach for environmental sustainability in Jordan. *European Journal of Sustainable Development*, 8(3), Article 418. <https://doi.org/10.14207/ejsd.2019.v8n3p418>

- Ashikin, A. N., Diana, M. I. N., Siwar, C., Alam, M. M., & Yassar, M. (2021). Community preparation and vulnerability indices for floods in Pahang state of Malaysia. *Land*, 10(2), Article 198. <https://doi.org/10.3390/land10020198>
- Botezan, C., Radovici, A., & Ajtai, I. (2021). The challenge of social vulnerability assessment in the context of land use changes for sustainable urban planning - Case studies: Developing cities in Romania. *Land*, 11(1), Article 17. <https://doi.org/10.3390/land11010017>
- Broekhuis, F., Cushman, S. A., & Elliot, N. B. (2017). Identification of human–carnivore conflict hotspots to prioritize mitigation efforts. *Ecology and Evolution*, 7(24), 10630–10639. <https://doi.org/10.1002/ece3.3565>
- Danjaji, A. S., & Ariffin, M. (2017). Green infrastructure policy for sustainable urban development. *International Journal of Environment and Sustainable Development*, 16(2), 112-127. <https://doi.org/10.1504/ijesd.2017.10004010>
- Department of Statistics Malaysia (2011). *Report on population distribution and basic demographic characteristic report 2010*. DOSM. https://v1.dosm.gov.my/v1/index.php?r=column/cthem&menu_id=L0pheU43NWJwRWVSZklWdzQ4TlhUUT09&bul_id=MDMxdHZjWtk1SjFzTzNkRXYzcVZjdz09
- Espinosa, A. S., & Schroder, C. (2019). Land use and land cover mapping in wetlands one step closer to the ground: Sentinel-2 versus Landsat 8. *Journal of Environmental Management*, 247, 484-498. <https://doi.org/10.1016/j.jenvman.2019.06.084>
- Gallego, F. J., Kussul, N., Skakun, S., Kravchenko, O., Shelestov, A., & Kussul, O. (2014). Efficiency assessment of using satellite data for crop area estimation in Ukraine. *International Journal of Applied Earth Observation and Geoinformation*, 29, 22-30. <https://doi.org/10.1016/j.jag.2013.12.013>
- Misbari, S., Hashim, M., Numata, S., & Hosaka, T. (2017, October 23-27). *Spatial analysis on relationship between wildlife-human conflicts in senai-desaru expressway (SDE)*. [Paper presentation]. 38th Asian Conference on Remote Sensing, New Delhi, India.
- Mustafa, M. (2011). The environmental quality Act 1974: A significant legal instrument for implementing environmental policy directives of Malaysia. *IJUM Law Journal*, 19(1), 1–34. <https://doi.org/10.31436/iiumlj.v19i1.1>
- Phelan, P., Otanicar, T., Taylor, R., & Tyagi, H. (2013). Trends and opportunities in direct-absorption solar thermal collectors. *Journal of Thermal Science and Engineering Applications*, 5(2), Article 021003. <https://doi.org/10.1115/1.4023930>
- Rasli, F. N., & Kanniah, K. D. (2018). Green corridors for liveable and walkable city: A case of Kuala Lumpur. *Chemical Engineering Transactions*, 63, 391–396. <https://doi.org/10.3303/CET1863066>
- Sami, K., Mohsen, B. A., Afef, K., & Fouad, Z. (2013). Hydrological modeling using gis for mapping flood zones and degree flood risk in Zeuss-Koutine Basin (South of Tunisia). *Journal of Environmental Protection*, 4(12), 1409–1422. <https://doi.org/10.4236/jep.2013.412161>
- Zhan, Z., Shi, W., Zhang, M., Liu, Z., Peng, L., Yu, Y., & Sun, Y. (2022). Landslide trail extraction using fire extinguishing model. *Remote Sensing*, 14(2), Article 308 <https://doi.org/10.3390/rs14020308>

Model-driven Approach to Improve Sago Drying with a Fluidized Bed Dryer

Nur Tantiyani Ali Othman* and Nurfadilah Izaty Senu

Department of Chemical and Process Engineering, Faculty of Engineering and Built Environment, Universiti Kebangsaan Malaysia, 43600, Bangi UKM, Selangor, Malaysia

ABSTRACT

This study presents a model-driven approach to enhance the efficiency of sago drying utilizing a two-dimensional fluidized bed dryer (FBD). ANSYS® DesignModeler™ 2020 R2 software was employed to simulate the drying profile, considering variations in sago bagasse particle diameter (ranging from 500 to 2000 μm), hot air temperature (ranging from 50 to 90°C), and inlet air velocity (ranging from 1.5 to 2.1 m/s). The simulation results provided valuable insights into the interplay between these critical drying parameters. The model enabled the prediction of moisture content profiles during the sago drying process under different conditions, thereby facilitating comprehension of the system's behavior. Using Design Expert® 7.00 (DX7), considering energy efficiency and product quality, an optimal set of conditions for sago drying was determined at 2000 μm , 90°C and 2.1 m/s. This approach not only streamlined the drying process but also significantly reduced energy consumption while ensuring consistent and high-quality sago. The findings of this research offer a practical and sustainable solution for sago producers, which, when applied, can contribute to improved product quality, reduced production costs, and enhanced food

security in the region. Furthermore, the model-driven approach and the integration of specialized software tools demonstrate the potential for broader applications in optimizing various drying processes in the food industry.

Keywords: Computational fluid dynamics, drying, fluidized bed dryer, respond surface methodology, sago waste

ARTICLE INFO

Article history:

Received: 21 August 2023

Accepted: 18 December 2023

Published: 04 April 2024

DOI: <https://doi.org/10.47836/pjst.32.3.21>

E-mail addresses:

tantiyani@ukm.edu.my (Nur Tantiyani Ali Othman)

chimchimmy1511@gmail.com (Nurfadilah Izaty Senu)

* Corresponding author

INTRODUCTION

Sago, a vital source of carbohydrates for many Southeast Asian communities, undergoes a protracted and inefficient drying process, significantly influencing its quality, shelf life, and economic viability. Southeast Asia produces nearly 60 million tons of sago starch annually (Wee et al., 2017). Malaysia is currently the world's largest sago producer, followed by Indonesia and Papua New Guinea, which account for around 94.6% of global sago production (Naim et al., 2016). The development of the agricultural industry has resulted in an increment in agricultural waste, which is largely cellulose-rich waste such as sago bagasse (Rashid et al., 2016). The increase in sago production yearly directly increases the amount of sago bagasse produced. Disposal of sago bagasse in rivers causes river pollution. Therefore, more studies on sago bagasse need to be conducted so that this sago bagasse has economic value and, thus, the environmental pollution that occurs due to the disposal of sago bagasse in the river can be minimized.

The primary purpose of this research is to revolutionize the sago drying process, making it more efficient, sustainable, and economically viable. As a staple food for many communities, sago plays a crucial role in food security, and its production impacts the livelihoods of numerous individuals. The traditional drying methods result in inconsistent product quality and entail significant energy consumption, making the production process economically challenging. This research is motivated by the need to address these pressing issues, enhance the quality of sago products, and make the sago industry more resilient.

Various methods have been carried out to convert sago bagasse into more valuable products, such as animal feed, through drying and fermentation. Sago bagasse needs to be dried before being used as animal feed as it is easily damaged due to its high moisture content. Drying is a highly energy-intensive operation used in industry, with an average of 12% of total energy consumption consumed in manufacturing (Sarker et al., 2015). Normally, an experiment conducted in the laboratory to develop this dryer model requires considerable time and effort and uses high costs (Malekjani & Jafari, 2018). Thus, this study applied the computational fluid dynamics (CFD) method to develop a dryer model, as this method is an effective way of overcoming these problems of high energy consumption. Besides, the CFD method can provide an excellent understanding of the transport phenomenon during the drying process and improve process control, leading to drying optimization and better quality of sago waste.

One of the common dryers, the fluidized bed dryer (FBD), has been widely used in drying final products or raw materials, such as agricultural produce, due to their advantages over other dryers, such as spray dryers and cabinet-type dryers. FBD has good mixing efficiency and a high heat and mass transfer rate between solids and gases (Zhang et al.,

2017). Moreover, FBD has a large contact surface area between solids and gases, produces high thermal inertia of solids, and can reduce drying time without damaging heat-sensitive materials (Rosli et al., 2020).

This innovative research combines FBD technology with traditional food production methods using a multidisciplinary approach. Insights into the complex drying process and the interaction of multiple variables can be obtained by employing ANSYS software for simulation. This innovative approach allows us to optimize the drying parameters to achieve a delicate balance between drying efficiency and preserving the nutritional and sensory qualities of sago. Furthermore, by employing the response surface methodology using Design Expert® 7.00 (DX7) software, the optimal conditions for sago drying can be determined, thereby streamlining the process and minimizing energy consumption.

Numerous researchers have applied the CFD method to dry their products in the FBD. For example, Arumuganathan et al. (2010) dried their mushroom in the FBD at the optimum temperature of 60°C, and Anthony and Shyamkumar (2016) dried sand particles in the FBD using ANSYS® software. Besides, Mortier et al. (2011) applied Eulerian-Eulerian two-fluid CFD models to analyze the behavior of dried wheat grain in the FBD. The study found that higher temperatures and inlet air velocities significantly impact the drying rate. This effect was observed in various industries such as oil palm fronds, millet pearl, coconut, wheat, grain, and sago bagasse industries (Assawarachan, 2013; Azmir et al., 2018; Li-Zhen et al., 2019; Maheswari, 2015; Othman et al., 2021; Puspasari et al., 2014).

Prior research has demonstrated the successful application of the CFD method in observing and analyzing the fluidizing rate within the FBD. This method offers the advantages of efficiency and cost-effectiveness. Thus, this research introduced a model-driven approach to improve sago drying using an FBD, employing ANSYS software to simulate the drying profile. In this study, various key drying parameters such as particle diameter of sago bagasse (ranging from 500 to 2000 µm), hot air temperature (varying from 50 to 90°C), and inlet air velocity (spanning from 1.5 to 2.1 m/s) were systematically utilized to optimize sago drying. The potential outcomes of this research hold promise for sago producers, the communities that rely on sago as a food source, and the broader food industry. The findings could reduce production costs, minimize post-harvest losses, and improve food security. Furthermore, utilizing the model-driven approach and specialized software tools provides opportunities for enhancing efficiency in different drying processes within the food industry, underscoring the potential for innovative and environmentally friendly solutions in food processing. This research aims to reconcile the disparity between traditional methods and technological advancements, promoting a more promising and environmentally friendly future for sago production.

METHODS

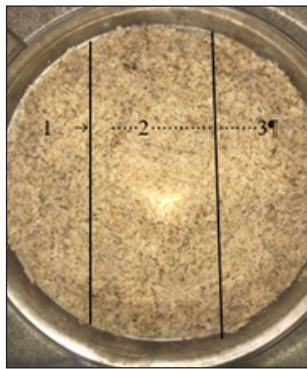
Development of Geometry and Mesh

In the drying process, a slurry of sago waste was dried using the FBD machine. Model Retsch TG 200 has a diameter of 220 mm and a height of 520 mm, including the filter bag, as shown in Figure 1(a), and Figure 1(b) shows the top view of a sample of particle sago that dried in the FBD. For this study, a 2D model of FBD is developed and designed using ANSYS® DesignModeler™ 2020 R2 software based on studies by Othman et al. (2021), as shown in Figure 2. Several assumptions were made, and equations were formulated to solve the simulation problem. Subsequently, the investigation ascertained the most favorable drying conditions by utilizing the response surface method (RSM).

The ANSYS® DesignModeler™ 2020 R2 software was used to develop a 2D model of an FBD based on the TG 200 FBD model. The height of the FBD model is 220 mm by 180 mm wide. The initial height of the sago waste bed in the dryer is 22.83 mm. Then, mesh development on the FBD model is accomplished using ANSYS® Meshing. The mesh size varies from 1-4 mm, with the shape of the resulting mesh being a hexahedral shape. A mesh dependency test was performed to obtain the most suitable mesh size. Figure 3 shows the 2D FBD model with 4 mm mesh.



(a)



(b)

Figure 1. (a) A model Retsch TG of FBD; and (b) a sample of dried sago from the top view

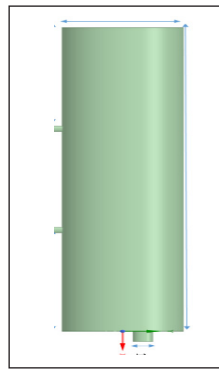


Figure 2. Two-dimensional model of the FBD

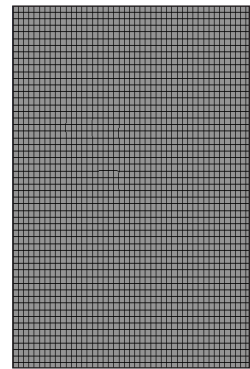


Figure 3. Schematic diagram of the 2D FBD model with 4 mm mesh

CFD Modelling

The CFD simulations have made some assumptions, assuming that no chemical reactions occur during the drying period. The gases and solids exhibit good miscibility. However, the slip condition was not established. The initial moisture content of sago waste was 40% based on its wet weight, while the final moisture content after the drying process was 10% based on its dried weight. In this study, the Eulerian-Eulerian model approach was used to

analyze the hydrodynamic and heat transfer properties in the FBD. The turbulence model was applied as there was a turbulent flow in the dryer, and the realized k-ε model was used due to minimal computational requirements. The transport and heat models were also utilized to account for the heat transfer between gases and solids. The air in this model represented the primary phase, the sago waste represented the secondary phase, and water vapor represented the tertiary phase. The SIMPLE algorithm was employed to achieve convergence. Table 1 details the settings set on the ANSYS® Fluent simulation code.

In the ANSYS® Fluent simulation, the creeping flow and turbulent modules were used to simulate fluid flow at very low Reynolds numbers where the inertia term in the Navier-Stokes equation can be ignored. The governing Equations 1 to 4 solved the fluid flow problem. Furthermore, the fluid mechanics in the FBD is a conservation of mass, momentum, and energy where \vec{v}_q is a velocity for q phase, p is pressure, \dot{m}_{pq} is a mass transfer from p phase to q phase, \dot{m}_{qp} is a mass transfer from q phase to p phase, h is a heat transfer coefficient, ρ is a density, q is a heat flux, ϵ is a volume fraction, Q is a heat

Table 1
ANSYS® Fluent setting

Input settings		Variables/ Parameters in ANSYS®	
General	Solver	Type	Pressure-based
		Velocity	Absolute
	Time	Transient	
Model	Multiphase (Eulerian)	Primary phase	Air
		Secondary phase	Sago waste
		Tertiary phase	Water vapor
		Particle size	2000 μm
		Phase interaction	Mass transfer Evaporation-condensation
		Viscous	k-epsilon
		Near-wall treatment	Scalable wall functions
		Turbulence Multiphase model	Dispersed
	Species	Species transport	H ₂ O vapor
Materials	Fluid	N ₂ , O ₂ , sago, H ₂ O (liquid), H ₂ O (vapor)	
	Mixture	Sago bagasse - sago, H ₂ O (liquid)	
Boundary conditions	Inlet (Air)	Momentum	Velocity magnitude (m/s) -2.1 Turbulence intensity- 5%
		Thermal	Temperature (°C) - 90
		Scheme	Phase coupled SIMPLE
Solution	Methods		
Initialization	Hybrid Initialization	Species settings	Sago bagasse H ₂ O (l) – 0.4
Calculation	Step time	35	
	Time step size	0.001 s	

transfer rate, v is a vector velocity, H is a latent heat and τ is a shear stress tensor (Othman et al., 2021).

Conservation of mass

$$\frac{\delta}{\delta t}(\alpha_q \rho_q) + \nabla \cdot (\alpha_q \rho_q \vec{v}_q) = \sum_{p=0}^n (\dot{m}_{pq} - \dot{m}_{qp}) + S_q \quad [1]$$

Conservation of momentum

$$\frac{\delta}{\delta t}(\varepsilon_s \rho_s) + \nabla \cdot (\varepsilon_s \rho_s v_s) = 0 \quad [2]$$

Conservation of energy

(i) For the gas phase

$$\frac{\delta}{\delta t}(\varepsilon_g \rho_g h_g) + \nabla \cdot (\varepsilon_g \rho_g v_g h_g) = -\varepsilon_g \frac{\delta p_g}{\delta t} + \tau_g^- : \nabla \vec{v}_g - \nabla \vec{q}_g + Q_{sg} + \dot{m} \Delta H_{vap} \quad [3]$$

(ii) For solid phase

$$\frac{\delta}{\delta t}(\varepsilon_s \rho_s h_s) + \nabla \cdot (\varepsilon_s \rho_s u_s h_s) = -\varepsilon_s \frac{\delta p_s}{\delta t} + \tau_s^- : \nabla \vec{u}_s - \nabla \vec{q}_s + Q_{gs} - \dot{m} \Delta H_{vap} \quad [4]$$

Analysis of Moisture Content

The moisture content analysis of sago waste at different variables was carried out once the 2D FBD model was successfully designed. A validated model was used to study the drying times for all variable conditions to achieve the desired final moisture content of 10% based on the average volume fraction of sago waste in FBD. At the beginning of the simulation, the volume fraction of sago waste in the FBD was set as 0.60. The simulation was carried out until the average value of the volume fraction of sago waste reached 0.42, equivalent to 10% moisture content.

Then, the effect of temperature on the moisture content of sago waste in FBD was studied. At the beginning of the simulation, the boundary conditions were changed to the temperature values of $T=50, 60, 70, 80,$ and 90°C , while the particle diameter and inlet air velocity were constant in $d_p=2000 \mu\text{m}$ and $v_i=2.1 \text{ m/s}$. Next, the effect of inlet air velocity on the moisture content of sago waste was studied at $v_i=1.5, 1.65, 1.8, 1.95,$ and 2.1 m/s while the sago diameter and air temperature were constant in $d_p=2000 \mu\text{m}$ and $T=90^\circ\text{C}$. At the beginning of the simulation, the velocity of the sago waste was set at 0 m/s to indicate that the bed remained at the initial position. Then, different size diameters of sago, $d_p=500, 1250,$ and $2000 \mu\text{m}$, were used to study their effects on drying. The boundary conditions were set at an air temperature of $T=90^\circ\text{C}$ and an inlet air velocity of $v_i=2.1 \text{ m/s}$. Based on these manipulated parameter conditions, the fractional contour of the volume of sago waste in the FBD was observed occasionally.

Mathematical Modelling of Drying Curves

The RSM method, a Design Expert® 7.00 (DX7) software, was used to optimize the sago drying process and parameter. The mixed design used was D-Optima, and the independent variables were the temperature, diameter of sago waste, and velocity of inlet air. The temperature was set up between 50 to 90°C, the range of particle diameter of sago waste was set to 500 to 2000 µm, and the inlet air velocity was between 1.5 to 2.1 m/s. Three code levels for each variable were defined as -1, 0, and +1, representing low, intermediate, and high levels, respectively. The details of the independent variables and levels used in the study are shown in Table 2, while Table 3 shows the central composite design and reaction results.

Table 2
Independent variables and levels used in the study

Independent variables	Unit	Symbol	Level		
			Low (-1)	Medium (0)	High (+1)
Temperature	°C	A	50	70	90
Inlet air velocity (m/s)	m/s	B	1.5	1.8	2.1
Sago bagasse diameter	µm	C	500	1500	2000

Table 3
Central composite design and response results

Run	Factor 1 A: Temperature (°C)	Factor 2 B: Air velocity (m/s)	Factor 3 C: Sago bagasse diameter (µm)	Response 1 Moisture content (%)	Response 2 Deff x 10 ⁻² (m ² /s)
1	50	1.5	500	25.02353	1.161982
2	90	1.5	500	20.84443	1.248123
3	50	2.1	500	13.22698	1.235517
4	90	2.1	500	10.33	1.259678
5	50	1.5	2000	22.4063	1.217133
6	90	1.5	2000	20.00562	1.304325
7	50	2.1	2000	14.7994	1.223436
8	90	2.1	2000	10.72495	1.305112
9	50	1.8	1250	19.75632	1.254163
10	90	1.8	1250	15.26491	1.303011
11	70	1.5	1250	22.09479	1.29986
12	70	2.1	1250	12.11061	1.299335
13	70	1.8	500	16.78013	1.225012
14	70	1.8	2000	19.63581	1.308527
15	70	1.8	1250	16.41505	1.299335
16	70	1.8	1250	16.41505	1.299335
17	70	1.8	1250	16.41505	1.299335
18	70	1.8	1250	16.41505	1.299335
19	70	1.8	1250	16.41505	1.299335
20	70	1.8	1250	16.41505	1.299335

Response Surface Analysis

The RSM is a statistical method that depends on variables, and each dependent parameter depends on a different input variable (control factor). Each variable has a mathematical relationship with the experimental parameter by a nonlinear polynomial equation with square terms, the interaction of two-factor terms, linear terms, and fixed terms as expressed in Equation 5 (Majdi et al., 2019), where “Res” indicates a reaction (moisture content and moisture diffusivity (D_{eff})), A, B, and C are codes for the values of temperature, inlet air velocity, and diameter of sago waste. The quality of the polynomial model is expressed using the coefficients of determination R^2 and R^2 -adjusted. Statistical significance was validated using accuracy factors and F tests.

$$Res = \alpha_0 + \alpha_1 A + \alpha_2 B + \alpha_3 C + \alpha_{11} A^2 + \alpha_{22} B^2 + \alpha_{33} C^2 + \alpha_{12} AB + \alpha_{13} AC + \alpha_{23} BC \quad [5]$$

RESULTS AND DISCUSSION

The study began with a meshing dependency test for the FBD model, followed by model validation by comparing the simulation results with the previous experimental study by Rosli et al. (2020). The 1.5 mm mesh size was selected as the suitable mesh to be used throughout this simulation due to its constant and stability of the test results. Once the 2D FBD model was developed, the final moisture content of the dried sago was determined at various conditions: temperature (50–90°C), inlet air velocity (1.5–2.1 m/s), and sago particle diameter (500–2000 μm). In summary, the simulation results demonstrated that increasing the air velocity and temperature at the inlet led to a higher drying rate. In addition, the diameter of sago waste solely influenced its moisture content when subjected to low drying temperatures. Subsequently, the RSM analysis was also carried out, and the optimum parameter values for drying sago were determined as $d_p=2000 \mu\text{m}$, $T=90^\circ\text{C}$, and $v_i=2.1 \text{ m. /s}$.

Effect of Temperature on Moisture Content

Figure 4 shows the fractional contours of the sago volume fraction in the FBD during drying time of 0–0.017 s at different temperature ranges: $T=50\text{--}90^\circ\text{C}$. Under fast step conditions, the simulation was conducted to observe contour patterns at five specific drying times ($t=0, 5, 10, 15,$ and 17 s) to determine the moisture content of sago waste in the FBD. The color bar represents the volume fraction of sago in the final sago waste after the drying process, where the red color indicates the highest sago fraction in the final sago waste with a value of 0.6, and the blue color indicates the lowest sago volume fraction.

The simulation results in Figure 4 show that at the beginning of the drying process, the partial area of the FBD is covered by the maximum fraction of sago waste, which is shown

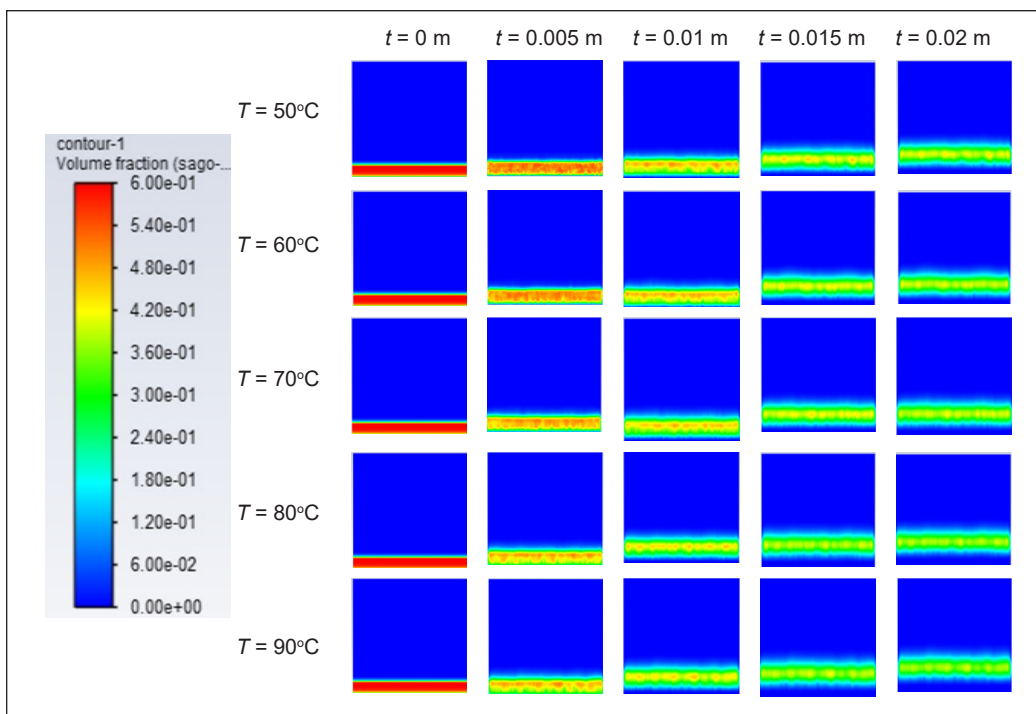


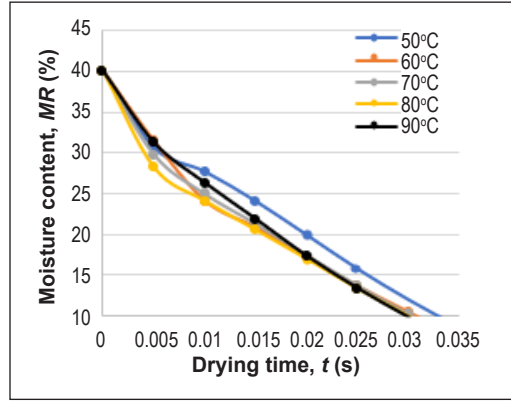
Figure 4. The contour of sago waste volume fraction at various temperatures: 50–90°C

by the red color at the bottom of the FBD area, because the sago waste is assumed to be already in the FBD with the height of the sago bed being 0.02283 m. The initial volume fraction of sago waste in the FBD is 0.6. However, as the evaporation process reduces the water content in the sago waste, the volume fraction of sago waste gradually decreases during the drying process. Furthermore, it indicates that the proportion of sago in the FBD is consistently diminishing. The FBD demonstrates the presence of fluidized sago waste, along with a hot air supply that enhances particle mobility and decreases the moisture content of the sago waste (Tamboli et al., 2018). Meanwhile, at the end of the drying process, $t=0.017$ s, the yellowish-green color contour shows that the volume of sago waste in the FBD is 0.45 and 0.42. It shows that the moisture content of sago waste has been reduced from 40% to around 10-15% after going through the drying process in this FBD model.

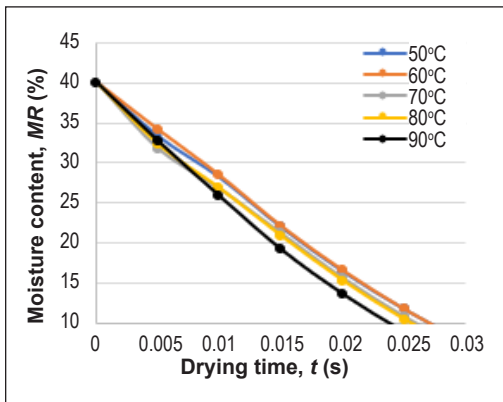
Based on Figure 4, the drying of sago waste at $T = 90^\circ\text{C}$ shows the smallest yellow spots on the volume contour of sago waste at the end of drying; $t = 0.017$ s. It indicates that the moisture content of sago waste is relatively lower at 90°C than at other drying temperatures. The moisture content values of sago waste obtained at the end of drying for the temperatures of $T=50^\circ\text{C}$, 60°C , 70°C , 80°C and 90°C are $\text{MC}_f=14.8\%$, 14.3% , 13.1% , 11% and 10.7% , respectively, indicating that the final moisture content of sago waste is relatively higher at lower drying air temperatures. In addition, to achieve the final moisture content of 10%, the drying time should be increased for the drying temperatures

of $T=50^{\circ}\text{C}$, 60°C , 70°C , and 80°C . It can be concluded that a high drying temperature is required to dry the sago waste quickly. Thus, a drying temperature of $T=90^{\circ}\text{C}$ is optimal for quickly drying the sago waste. In addition, a study has also proven that when the incoming air temperature increases, the drying time can be reduced (Antony & Shyamkumar, 2016). Thus, a drying temperature of $T=90^{\circ}\text{C}$ is the best and optimum temperature to dry sago.

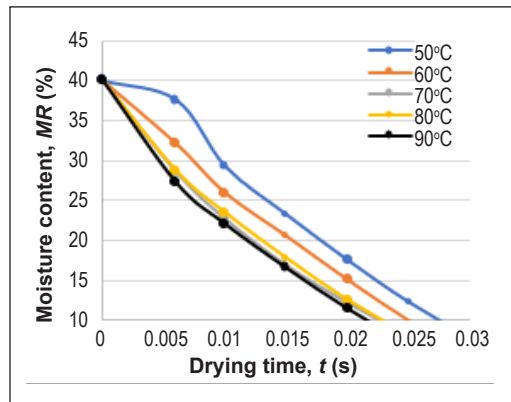
Figure 5 shows the effect of temperature on the final moisture content of sago waste and drying time at different inlet air velocities. The initial moisture content of sago waste before the drying simulation process is 40%. It is shown that as the drying temperature increases, the percentage of



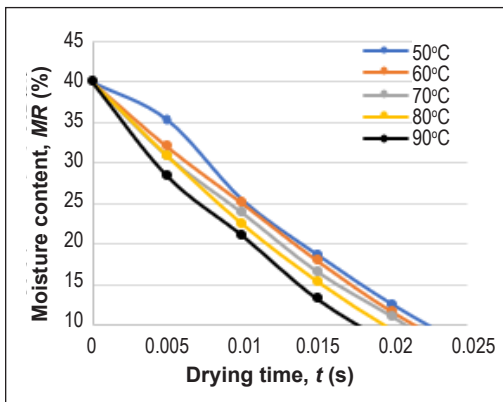
(a)



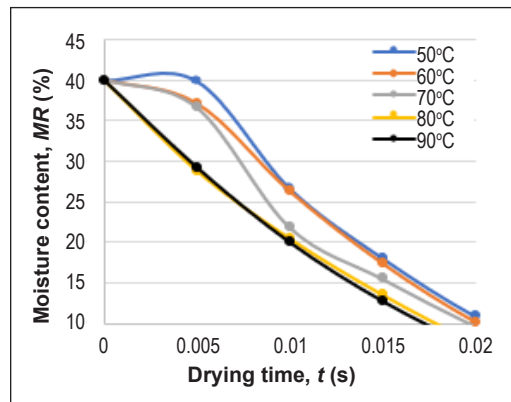
(b)



(c)



(d)



(e)

Figure 5. Moisture content against drying time at a diameter of $2000\ \mu\text{m}$ with different temperatures and air velocities: (a) $v_i=1.50\ \text{m/s}$; (b) $v_i=1.65\ \text{m/s}$; (c) $v_i=1.80\ \text{m/s}$; (d) $v_i=1.95\ \text{m/s}$; and (e) $v_i=2.10\ \text{m/s}$

final moisture content of sago waste decreases. In addition, as the drying time increases, the final moisture content of sago waste also decreases. The moisture content percentage of sago waste decreases rapidly at high and low temperatures. At $T=50^{\circ}\text{C}$, the percentage decrease in moisture content of sago waste is relatively slow. Figure 5(e) shows that at $T=90^{\circ}\text{C}$, a moisture content of 10% is reached within $t=0.017\text{s}$, while at $T=50^{\circ}\text{C}$, it takes a longer drying time of $t=0.021\text{s}$ to achieve a final moisture content of 10%. At a drying temperature of $T=80^{\circ}\text{C}$, the moisture content of sago waste reaches 10% within $t=0.018\text{s}$, followed by $T=70^{\circ}\text{C}$ and $T=60^{\circ}\text{C}$ with the drying time between $t=0.019\text{s}$ and $t=0.020\text{s}$, respectively. The simulation results show that the higher the drying temperature, the faster the moisture content of sago waste reaches 10% because the incoming air temperature is inversely proportional to the drying time and because the air temperature affects the permeation of moisture during the drying process (Gazor & Mohsenimanesh, 2010). At higher temperatures, the particles absorb more heat for water evaporation than at lower temperatures; thus, the evaporation rate increases (Luthra & Sadaka, 2020). The studies by Nasir et al. (2021) have also proven that sago waste dries faster at high temperatures than at low drying temperatures.

Effect of Air Velocity on Moisture Content

Simulations were performed repeatedly by manipulating five inlet air velocities at $v_i=1.50, 1.65, 1.80, 1.95$ and 2.10 m/s , while the temperature is kept constant at $T=90^{\circ}\text{C}$ with $d_p=2000\text{ }\mu\text{m}$ based on the minimum and maximum experiments data conducted by Rosli et al. (2020). Figure 6 shows the contours of the volume fraction of sago waste in the FBD at different inlet air velocities within the drying times of $t=0.017\text{ s}$. The contour patterns of the sago volume fraction are observed at $0\text{ s}, 0.005\text{ s}, 0.10\text{ s}, 0.015\text{ s},$ and 0.017 s . At the beginning of the simulation, $t=0\text{ s}$, the sago waste bed is maintained at a fixed position of 0.02283 m . As the drying process takes place within $t=0.005\text{ s}$, fluidization begins to occur, and the sago bed begins to act as a fluid when the incoming air interacts with the particle layer. This incoming air produces an attraction to overcome the force of gravity (Han, 2015). During this initial period, a rapid increase in bed height is observed until the bed reaches its maximum height. It occurs due to fluidization onset, which is called the fluidization minimum (Dechsiri, 2004). The particle concentration at the bottom area tends to rise uniformly. It indicates a uniform gas entry velocity according to the fluidized characteristics of the FBD (Shukrie et al., 2016).

At the end of the drying process at $t=0.017\text{ s}$, the yellowish-green color contour shows that the volume of sago waste in the FBD is between $0.42=0.48$. It shows that the moisture content of sago waste has been reduced from 40% to 10-20% after going through the drying process in this FBD model. The color contour bars show the fewest patches of yellow at $v_i=2.10\text{ m/s}$ air velocity, followed by $v_i=1.95, 1.80, 1.65,$ and 1.50 m/s . The FBD exhibits

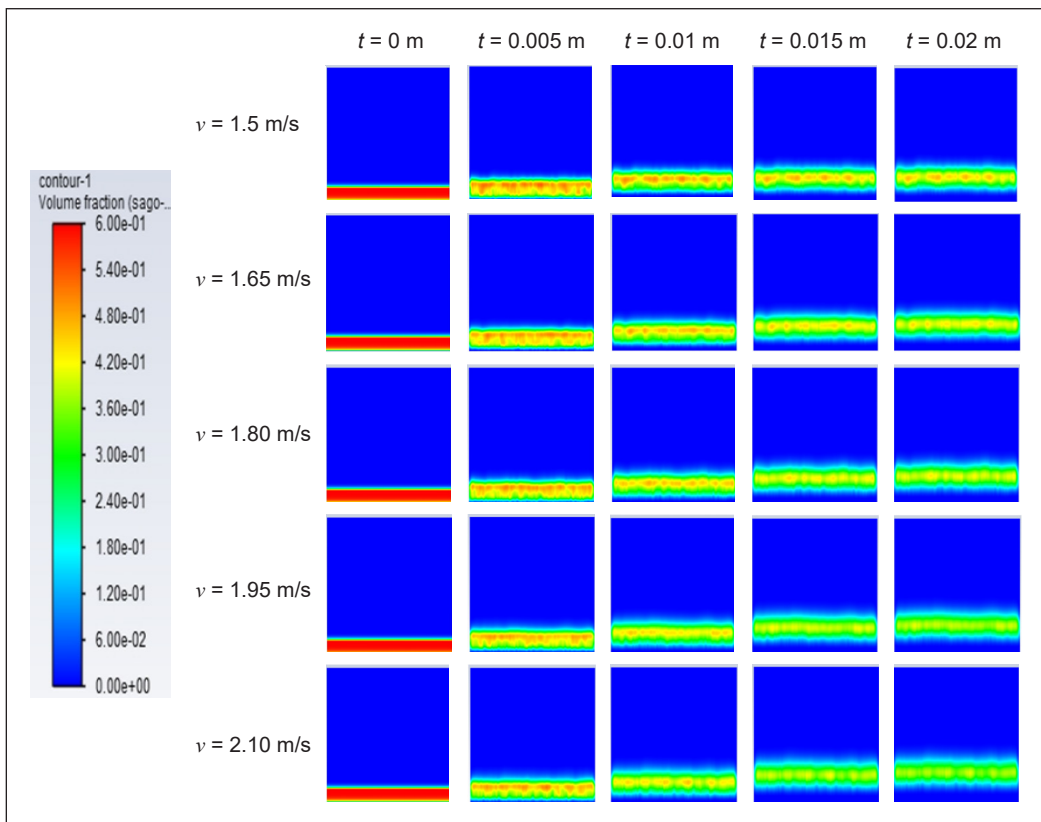


Figure 6. Contour of sago waste volume fraction at air velocity, $v_i=1.5\text{-}2.1$ m/s

a state of fluidized sago, facilitated by the introduction of hot air, effectively decreasing sago waste’s moisture level (Rosli et al., 2018). The velocity of the inlet air affects the sago waste’s drying process. At higher inlet air velocities, the volume of sago waste in the FBD decreases rapidly. It is supported by a study by Norhaida et al. (2020), which found that increased velocities led to reduced drying times.

Figure 7 shows the effect of inlet air velocity on the final moisture content of sago waste and drying time at different temperatures. It shows that the drying rate initially increases with the drying time before it decreases until the sago has dried to the desired final moisture content because free water is easier to evaporate at the beginning of drying and bound water that is difficult to rise to the surface of the material, so the rate of water evaporation decreases (Hasibuan et al., 2018). However, when the air velocity is increased, the drying rate increases, where the highest drying rate is at the inlet air velocity of $v_i=2.1$ m/s, which has the shortest drying time. It indicates that the drying rate is higher at higher air velocities due to higher heat and mass transfer between fluidized air and sago waste as air velocity increases (Halim et al., 2020). Also, this is evidenced by a previous where the highest drying rate occurred at a velocity of $v_i=2.1$ m/s, which resulted in the shortest drying time (Rosli et al., 2020).

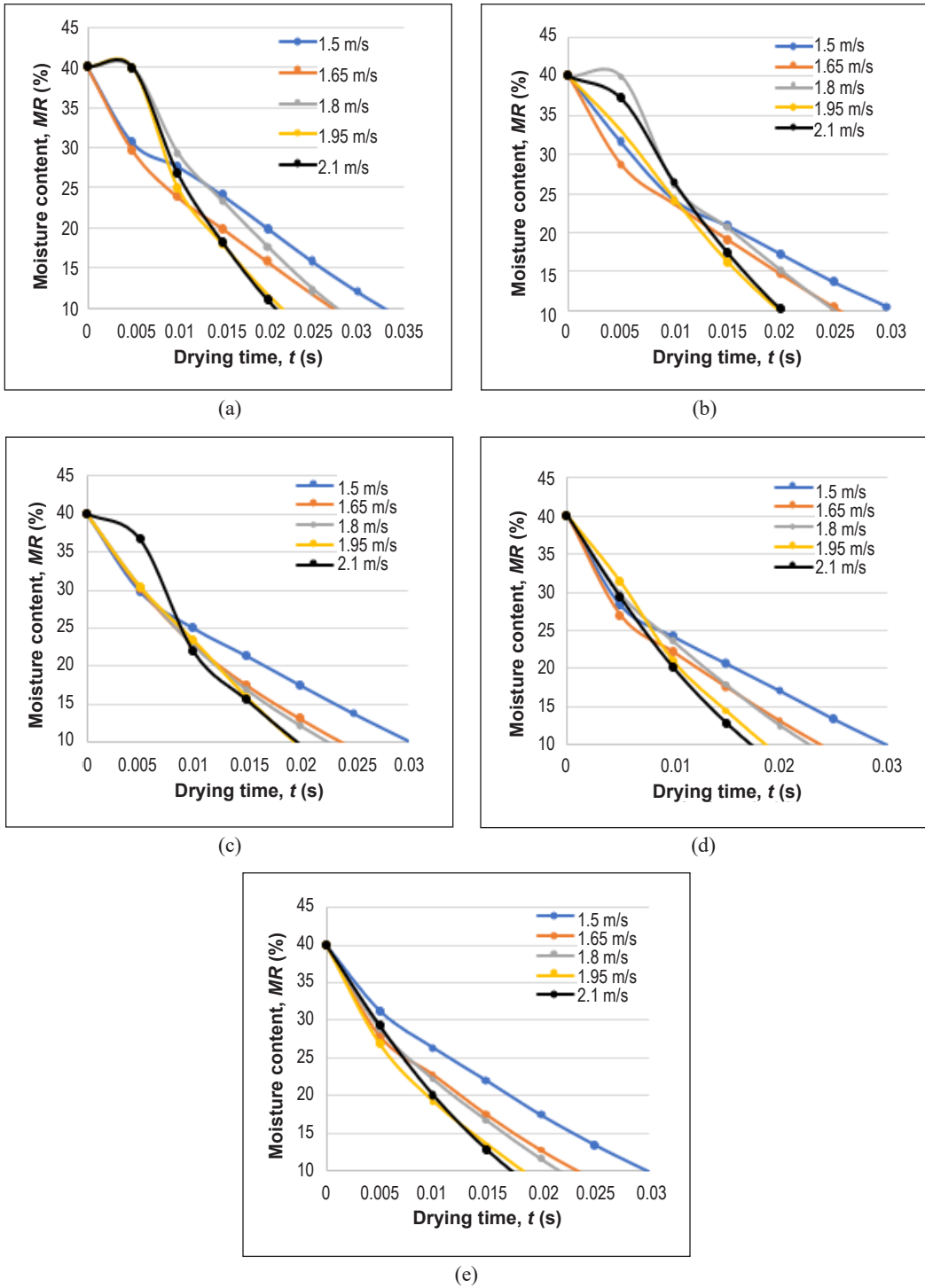
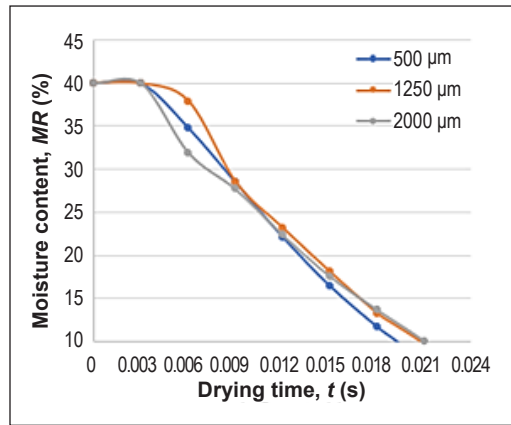


Figure 7. Moisture content against drying time at the diameter of 2000 μm with different air velocity temperatures and temperatures: (a) $T=50^\circ\text{C}$; (b) $T=60^\circ\text{C}$; (c) $T=70^\circ\text{C}$; (d) $T=80^\circ\text{C}$; and (e) $T=90^\circ\text{C}$

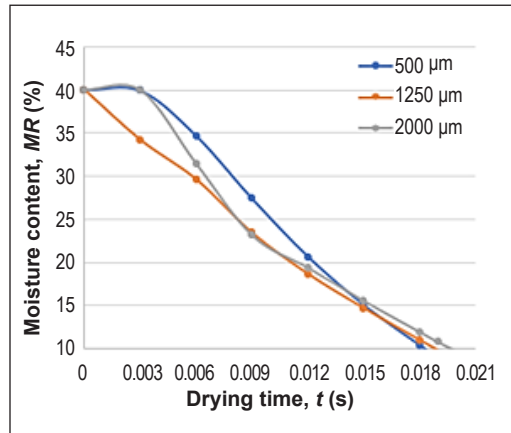
Effect of Diameter of Sago Bagasse on Moisture Content

Various ranges of particle diameters of sago waste $d_p=500, 1250, \text{ and } 2000 \mu\text{m}$ were studied to determine its effect on the final moisture content of 10%. Figure 8 shows the moisture content of sago waste against drying time at different sago waste diameters of $d_p=500, 1250, \text{ and } 2000 \mu\text{m}$ at $T=50^\circ\text{C}$ and $v_i=2.1 \text{ m/s}$. It shows that the moisture content directly decreases with increasing drying time. Besides, the sago waste diameter of $d_p=500 \mu\text{m}$ reaches a moisture content 10% faster than other sago diameters. At $T=50^\circ\text{C}$, the minimum drying times achieved for sago waste diameter of $d_p=500, 1250, \text{ and } 2000 \mu\text{m}$ are $t=0.019, 0.021, \text{ and } 0.021\text{s}$, respectively. The smaller particle fractions have a larger surface area, and thus, they can dry faster (Wang & Chen, 2000). In addition, the moisture transport distance within the particles decreases as the particle size decreases, and the time required to dry the particles increases with the particle size increase (Pusat et al., 2015).

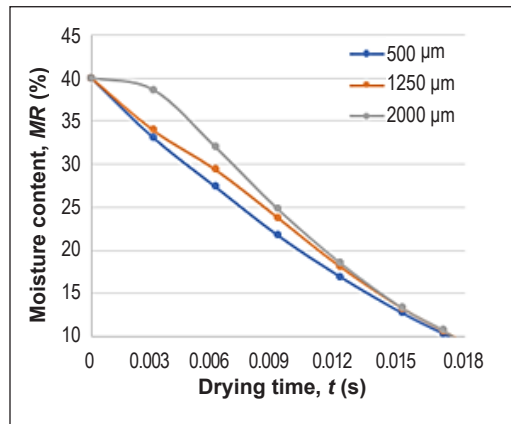
For $T=70^\circ\text{C}$, the minimum drying times achieved for sago waste diameter of $d_p=500, 1250, \text{ and } 2000 \mu\text{m}$ are $t=0.018, 0.019, \text{ and } 0.020\text{s}$, respectively. Meanwhile, At $T=90^\circ\text{C}$, the sago waste diameters of $d_p=500, 1250, \text{ and } 2000 \mu\text{m}$ reach a moisture content of 10.3%, 10.6%, and 10.7% at the time of drying of $t=0.017\text{s}$. The impact of sago particle diameter on the moisture content of sago waste is more pronounced at lower drying temperatures than at higher temperatures. The drying process is primarily influenced by the air



(a)



(b)



(c)

Figure 8. Moisture content against drying times at different diameters of sago at temperature: (a) 50°C; (b) 70°C; and (c) 90°C

temperature, and drying using FBD produces a uniform gas distribution (Okoronkwo et al., 2013; Silva et al., 2017). This results in the uniform drying of sago waste, which helps speed the drying process. The uniform drying in FBD and the air temperature are the primary factors significantly impacting the drying process. Consequently, the diameter of sago waste has a minimal effect on the drying process, particularly at high temperatures.

Analysis of Variance (ANOVA) and Estimated Regression of Each Response

Analysis of variance was performed to validate the accuracy of this FBD model and simulation result, where an average squared, degrees of freedom, sum squared, F-values, and P-values were used to check the model’s effectiveness. The variance of the data about the mean was estimated by determining the F-value. In addition, the P-value validates the model from a statistical point of view. According to the variance analysis, the parameter has more accuracy at higher F-values than one. Furthermore, P values less than 0.05 mean that the model is approved from a statistical point of view. Based on the result in Table 4, the F-value for this FBD model is 98.41, indicating that the model is important. A P-value of less than 0.05 indicates that the model term is important. Next, A-temperature and B-Air velocity are important model terms. At the same time, the C-diameter of sago waste is an insignificant model term because the P-value shows a value greater than 0.1. The R² and adjusted-R² values for these FBD models are 0.9486 and 0.9390, respectively. The predicted R² is 0.9108, which shows a reasonable agreement. These values for sufficient accuracy are used to measure the signal-to-noise ratio. Sufficient accuracy compares the range of forecast values at the design point with the average forecast error, where ratios with values greater than 4 are desirable. The ratio of 31.9996 indicates an adequate signal-to-noise ratio. Thus, it can be concluded that this FBD model can be used to navigate the design space.

Based on Table 4, the F-value model of 2416.19 indicates that the model is important. The values for sufficient accuracy are used to measure the signal-to-noise ratio. The R² and

Table 4
Analysis of variance for moisture content

Source	Sum of Squares	df	Mean Square	F-value	p-value
Model	279.19	3	93.06	98.41	< 0.0001
A-Temperature	33.76	1	33.76	35.69	< 0.0001
B-Air velocity	245.15	1	245.15	259.23	< 0.0001
C-Sago bagasse diameter	0.2880	1	0.2880	0.3045	0.5887
Residual	15.13	16	0.9457		
Lack of Fit	15.13	11	1.38		
Pure Error	0.0000	5	0.0000		
Cor Total	294.32	19			
R ²	0.9486		Adeq Precision: 31.9996		

adjusted-R² values for the models are 0.9995 and 0.9991, respectively. The predicted R² of 0.9964 is in reasonable agreement. Sufficient accuracy is determined by comparing the range of forecast values at the design point with the average forecast error. Using a ratio value higher than 4 is desirable. The ratio of 138.97 indicates an adequate signal-to-noise ratio. So, this FBD model can be used to navigate the design space. It can be concluded that the analysis of variance for the quadratic model in Table 5 shows that the values for temperature (A), sago waste diameter (C), sago waste diameter temperature (AC), and square sago waste diameter (C²) have p-values less than 0.05, that suggests all four terms are important.

Table 5
Analysis of variance for moisture diffusivity (D_{eff})

Source	Sum of Squares	df	Mean Square	F-value	p-value
Model	5.57	9	0.6192	2416.19	< 0.0001
A-Temperature	0.0123	1	0.0123	47.88	< 0.0001
B-Air velocity	0.0002	1	0.0002	0.7304	0.4128
C-Sago bagasse diameter	5.55	1	5.55	21643.92	< 0.0001
AB	0.0001	1	0.0001	0.5128	0.4903
AC	0.0059	1	0.0059	23.19	0.0007
BC	0.0001	1	0.0001	0.2336	0.6393
A ²	0.0018	1	0.0018	7.06	0.0240
B ²	0.0001	1	0.0001	0.3111	0.5893
C ²	0.0005	1	0.0005	1.78	0.2117
Residual	0.0026	10	0.0003		
Lack of Fit	0.0026	5	0.0005		
Pure Error	0.0000	5	0.0000		
Cor Total	5.58	19			
R ²	0.9995			Adeq Precision: 138.97	

Optimization Analysis

The results of optimizing sago waste drying in FBD are shown in Table 6. It shows the optimum values of temperature control factor, inlet air velocity, and sago waste diameter are at T=90°C, $v_i=2.1$ m/s, and $d_p=2000$ μm with the highest desirability value of 0.981. The predicted moisture content and D_{eff} values of sago waste are 10.439% and 2.016 m²/s, respectively. The detailed comparison between the RSM predicted analysis and the CFD simulation result is listed in Table 7. Based on the table, the errors between this CFD simulation results and RSM predictions are 0.03% and 0.04% for sago waste moisture content and D_{eff} values, respectively, indicating that the predictions generated by the RSM model are accurate.

Figure 9 shows the overall desirability for the combination of inlet temperature and air velocity by the response surface plot for the optimized sago waste diameter $d_p=2000$ μm.

Table 6
Results of optimization of the drying process in FBD

Temperature	Air velocity	Sago bagasse diameter	Moisture content	$D_{\text{eff}} \times 10^{-2}$	Desirability
90.000	2.100	2000.000	10.439	2.016	0.981
89.827	2.100	2000.000	10.455	2.016	0.980
90.000	2.100	1993.748	10.438	2.010	0.979
90.000	2.098	1999.999	10.480	2.016	0.979
89.533	2.100	1999.999	10.482	2.016	0.979
90.000	2.095	1999.999	10.529	2.016	0.977
90.000	2.100	1982.818	10.437	1.999	0.977
88.903	2.100	1999.998	10.540	2.016	0.977
90.000	2.100	1977.026	10.434	1.993	0.976
88.535	2.100	2000.000	10.574	2.015	0.975
90.000	2.091	2000.000	10.592	2.017	0.975
89.817	2.100	1970.962	10.450	1.987	0.974
88.067	2.100	1999.998	10.617	2.015	0.973
90.000	2.088	1998.705	10.636	2.015	0.972

Table 7
Comparison between the RSM predicted value and the CFD simulation result

	Temperature	Air velocity	Sago diameter	Moisture content	$D_{\text{eff}} \times 10^{-2}$
RSM prediction	90	2.1	2000	10.439	2.106
CFD simulation				10.72	2.014
Error(%)	-	-	-	0.03	0.04

This desirability surface plot shows that the control factor values $A=90^{\circ}\text{C}$ and $B=2.1\text{ m/s}$ are required to obtain desirability values $D=0.981$. Moreover, the surface plot shows that the air velocity and the air temperature play a role in the optimization process with the obtained desirability value of 0.981. It indicates that the RSM model is accurate and close to the ideal value because the reliability value lies between 0 and 1, and it represents the proximity of the response to its ideal value. If the reaction is in an unacceptable interval, its desirability value is 0, and if the reaction is in the ideal interval or reaches its ideal value, its desirability is 1.

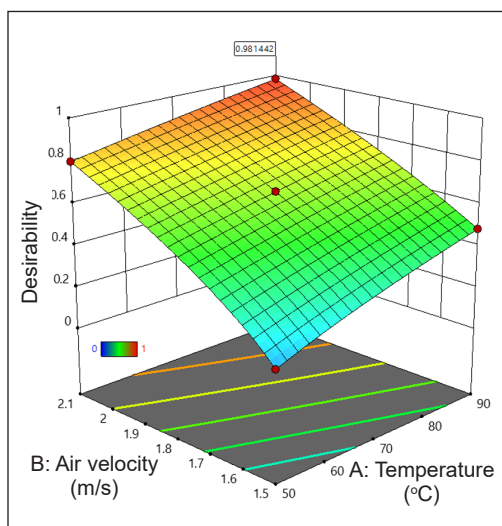


Figure 9. Desirability surface plot for sago bagasse diameter 2000 μm

1 (Rafik, 2016). Besides, a previous study obtained a tolerability value of $D=0.781$ with optimal conditions for the optimized reaction combination where the input temperature was at $T=90^{\circ}\text{C}$, and the input velocity was $v_i=5$ m/s, and the square geometry for cut drying Apple (Majdi et al., 2019).

Validation of CFD Model and RSM Optimization Parameters with Experimental Data

Comparing the present study’s findings with those of a previous study is essential to evaluate the progress and innovation achieved. In the case of drying efficiency, the present study applied the model-driven approach, which significantly improved drying efficiency, reducing the drying time required for sago bagasse. Besides, the systematic variation of parameters, including particle diameter, hot air temperature, and inlet air velocity, contributed to a more efficient moisture removal process. In the previous studies, it was challenging to provide a direct comparison in the absence of a wide range of drying parameters during the experimental process. However, this model-driven approach suggests potential improvements in drying efficiency over traditional methods. In the case of optimal conditions, this present study found that the optimal conditions for sago drying were obtained through the RSM. These conditions were tailored to maximize drying efficiency and product quality. Meanwhile, the details about optimal conditions in the previous study are unavailable for direct comparison. Thus, this present study compared the findings with the limitation of the experiment data conducted by Rosli et al. (2020), where the FBD model developed using CFD and optimized by the RSM approach was validated at $v_i=2.1$ m/s and $d_p=2000$ μm as shown in Figure 10. Figure 10(a) shows the results of experiments conducted by Rosli et al. (2020), and Figure 10(b) shows the CFD result obtained from this present study. Both results show a similar trend where the moisture content of sago waste decreases with a longer drying time but increases with a higher temperature.

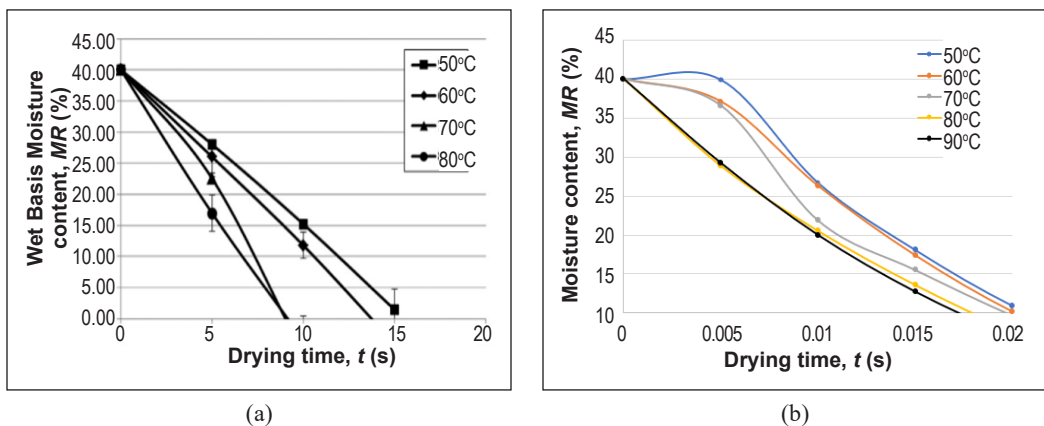


Figure 10. Moisture content against drying time of: (a) Previous studies; and (b) this CFD simulation

In addition, the current study hints at sustainability improvements through reduced energy consumption, which indirectly impacts environmental sustainability and the reduction of greenhouse gas emissions. However, the sustainability aspects in the previous study were not discussed. In summary, while the present study demonstrates the potential for significant advancements in sago drying efficiency and product quality through a model-driven approach, specific comparative data or findings from a previous study were not available for a direct, detailed comparison. However, the present study lays the groundwork for potential improvements and innovations in sago drying, which may have far-reaching implications for sago production, consumption, and the broader food industry. Future research could further build upon these findings and investigate the real-world implementation of the model-driven approach.

CONCLUSION

A two-dimensional model of an FBD for drying sago waste has been successfully constructed using ANSYS® DesignModeler™ 2020 R2 software. The mesh dependence test was carried out after the construction of the geometry, and the mesh size used was 1.5 mm. The simulations were performed until the moisture content was reduced to 10%. The CFD model was validated by comparing it with previous studies by Rosli et al. (2020). The analysis of the moisture content of sago waste was carried out at different inlet air velocities, inlet air temperatures, and diameters of sago waste at $v_i=1.5-2.1$ m/s with a diameter of $d_p=500-2000$ μm and $T=50-90^\circ\text{C}$. The simulation results showed that a drying temperature of $T=90^\circ\text{C}$ dried the sago waste faster than other temperatures. Sago waste was dried quickly at $v_i=2.10$ m/s as the hot air entering the drying chamber was at a higher air velocity. This condition increased the diffusion of hot air in the dryer, increasing the amount of water that can evaporate. In addition, the diameter of sago waste affects its moisture content at lower drying temperatures because uniform drying in FBD and air temperature factors significantly influence the drying process. Consequently, the diameter of sago waste has minimal effect on the drying process at high temperatures. Besides the RSM method, the Design Expert® 7.00 (DX7) software was used to optimize the sago waste drying process. It showed that the optimum drying process occurred at $T=90^\circ\text{C}$, $v_i=2.1$ m/s, and $d_p=2000$ μm . Since the obtained desirability value is 0.981, the RSM model is accurate and close to the ideal value.

ACKNOWLEDGEMENT

This research is fully supported by FRGS and GUP grants, FRGS/1/2020/TKO/UKM03/2 and GUP-2017-063. The authors fully acknowledge the Ministry of Higher Education (MOHE), Malaysia, and Universiti Kebangsaan Malaysia for the approved fund, which makes this important research viable and effective.

REFERENCES

- Antony, J., & Shyamkumar, M. B. (2016). Study on sand particles drying in a fluidized bed dryer using CFD. *International Journal of Engineering Studies*, 8(2), 129-145.
- Arumuganathan, T., Manikantan, M. R., Ramanathan, M., Rai, R. D., Indurani, C., & Karthiayani, A. (2017). Effect of diffusion channel storage on some physical properties of button mushroom (*Agaricus bisporus*) and shelf-life extension. *Proceedings of the National Academy of Sciences, India Section B: Biological Sciences*, 87(3), 705-718. <https://doi.org/10.1007/s40011-015-0628-4>
- Assawarachan, R. (2013). Drying kinetics of coconut residue in fluidized bed. *International Journal of Agriculture Innovations and Research*, 2(2), 263–266.
- Azmir, J., Hou, Q., & Yu, A. (2018). Discrete particle simulation of food grain drying in a fluidised bed. *Powder Technology*, 323, 238-249. <https://doi.org/10.1016/j.powtec.2017.10.019>
- Dechsiri, C. (2004). *Particle Transport in Fluidized Beds: Experiments and Stochastic Models*. [Unpublished Doctoral thesis]. University of Groningen.
- Gazor, H. R., & Mohsenimanesh, A. (2010). Modelling the drying kinetics of canola in fluidised bed dryer. *Czech Journal of Food Sciences*, 28(6), 531-537. <https://doi.org/10.17221/256/2009-CJFS>
- Halim, L. A., Basrawi, M. F., Faizal, S. N., Yudin, A. S. M., & Yusof, T. M. (2020). Effect of superficial air velocity on the fluidized bed drying performance of stingless bee pot-pollen. *IOP Conference Series: Materials Science and Engineering*, 863(1), Article 012041. <https://doi.org/10.1088/1757-899X/863/1/012041>
- Han, M. (2015). *Characterization of Fine Particle Fluidization*. [Doctoral dissertation]. The University of Western Ontario. <https://ir.lib.uwo.ca/etd/3073>
- Hasibuan, R., Pane, Y. M., & Hanief, S. (2018, August 30-31). *Effect of air velocity and thickness to drying rate and quality temulawak (Curcum xanthorrhiza roxb) using combination solar molecular sieve*. [Paper presentation]. The International Conference of Science, Technology, Engineering, Environmental and Ramification Researches-ICOSTEERR, Sumatera Utara, Indonesia. <https://doi.org/10.5220/0010103503890394>
- Li-Zhen, D., Arun, S.M., Qian, Z., Xu-Hai, Y., Jun, W., Zhi-An, Z., Zhen-Jiang, G., & Hong-Wei, X. (2019). Chemical and physical pretreatments of fruits and vegetables: Effects on drying characteristics and quality attributes – A comprehensive review. *Critical Reviews in Food Science and Nutrition*, 59(9), 1408-1432. <https://doi.org/10.1080/10408398.2017.1409192>
- Luthra, K., & Sadaka, S. S. (2020). Challenges and opportunities associated with drying rough rice in fluidized bed dryers: A review. *American Society of Agricultural and Biological Engineers*, 63(3), 583-595. <https://doi.org/10.13031/trans.13760>
- Maheswari, S. U. (2015). Drying of pearl millet using fluidised bed dryer: Experiments and modelling. *International Journal of ChemTech Research*, 8(1), 377-387.
- Majdi, H., Esfahani, J. A., & Mohebbi, M. (2019). Optimization of convective drying by response surface methodology. *Computers and Electronics in Agriculture*, 156, 574-584. <https://doi.org/10.1016/j.compag.2018.12.021>

- Malekjani, N., & Jafari, S. M. (2018). Simulation of food drying processes by computational fluid dynamics (CFD): Recent advances and approaches. *Trends in Food Science & Technology*, 78, 206-223. <https://doi.org/10.1016/j.tifs.2018.06.006>
- Mortier, S. T. F., De Beer, T., Gernaey, K. V., Remon, J. P., Vervaet, C., & Nopens, I. (2011). Mechanistic modelling of fluidized bed drying processes of wet porous granules: A review. *European Journal of Pharmaceutics and Biopharmaceutics*, 79(2), 205-225. <https://doi.org/10.1016/j.ejpb.2011.05.013>
- Naim, H. M., Yaakub, A. N., & Hamdan, D. A. A. (2016). Commercialization of sago through estate plantation scheme in Sarawak: The way forward. *International Journal of Agronomy*, 2016, Article 8319542. <https://doi.org/10.1155/2016/8319542>
- Nasir, A. M. A., Rosli, M. I., Takriff, M. S., Othman, N. T. A., & Ravichandar, V. (2021). Computational fluid dynamics simulation of fluidized bed dryer for sago pith waste drying process. *Jurnal Kejuruteraan*, 33(2), 239-248. [https://doi.org/10.17576/jkukm-2021-33\(2\)-09](https://doi.org/10.17576/jkukm-2021-33(2)-09)
- Norhaida, H. A. T., Ang, W. L., Kismurtono, M., & Siti, M. T. (2020). Effect of air temperature and velocity on the drying characteristics and product quality of *Clinacanthus nutans* in heat pump dryer. *IOP Conference Series: Earth and Environmental Science*, 462(1), Article 012052. <https://doi.org/10.1088/1755-1315/462/1/012052>
- Okoronkwo, C. A., Nwifo, O. C., Nwaigwe, K. N., Ogueke, N. V., & Anyanwu, E. E. (2013). Experimental evaluation of a fluidized bed dryer performance. *The International Journal of Engineering and Science*, 2(6), 45-53.
- Othman, N. T. A., & Ivan, A. H. (2021). Development of a fluidized bed dryer for drying of a sago bagasse. *Pertanika Journal of Science & Technology*, 29(3), 1831-1845 <https://doi.org/10.47836/pjst.29.3.13>
- Pusat, S., Akkoyunlu, M. T., Erdem, H. H., & Teke, I. (2015). Effects of bed height and particle size on drying of a Turkish lignite. *International Journal of Coal Preparation and Utilization*, 35(4), Article 150203135736008. <https://doi.org/10.1080/19392699.2015.1009051>
- Puspasari, I., Meor, Z., Wan Daud, D., & Tasirin, S. (2014). Characteristic drying curve of oil palm fibers. *International Journal on Advanced Science, Engineering and Information Technology*, 4(1), 20-24. <https://doi.org/10.18517/ijaseit.4.1.361>
- Rashid, M. R. M., Johari, M. A. M., & Ahmad, Z. A. (2016). Sago pith waste ash as a new alternative raw materials from agricultural waste. *Materials Science Forum*, 840, 389-393. <https://doi.org/10.4028/www.scientific.net/MSF.840.389>
- Rosli, M. I., Abdul Nasir, A. M., Takriff, M. S., & Lee, P. C. (2018). Simulation of a fluidized bed dryer for the drying of sago waste. *Energies*, 11(9), Article 2383. <https://doi.org/10.3390/en11092383>
- Rosli, M. I., Nasir, A. A., Takriff, M. S., & Ravichandar, V. (2020). Drying sago pith waste in a fluidized bed dryer. *Food and Bioproducts Processing*, 123, 335-344. <https://doi.org/10.1016/j.fbp.2020.07.005>
- Sarker, M. S. H., Ibrahim, M. N., Aziz, N. A., & Punan, M. S. (2015). Energy and exergy analysis of industrial fluidized bed drying of paddy. *Energy*, 84, 131-138. <https://doi.org/10.1016/j.energy.2015.02.064>
- Shukrie, A., Anuar, S., & Oumer, A. N. (2016). Air distributor designs for fluidized bed combustors: A review. *Engineering, Technology & Applied Science Research*, 6(3), 1029-1034. <https://doi.org/10.48084/etasr.688>

- Silva, B. G., Fileti, A. M. F., Foglio, M. A., Rosa, P. D. T. V., & Taranto, O. P. (2017). Effects of different drying conditions on key quality parameters of pink peppercorns (*Schinus terebinthifolius* Raddi). *Journal of Food Quality*, 2017, Article 3152797. <https://doi.org/10.1155/2017/3152797>
- Tamboli, T. G., & Bhong, M. G. (2018). Review on different drying methods: Applications & advancements. *International Journal on Theoretical and Applied Research in Mechanical Engineering*, 7(1), 33-40.
- Wang, A. H., & Chen, G. (2000). Heat and mass transfer in batch fluidized-bed drying of porous particles. *Chemical Engineering Science*, 55(10), 1857-1869. [https://doi.org/10.1016/S0009-2509\(99\)00446-7](https://doi.org/10.1016/S0009-2509(99)00446-7)
- Wee, O. Y., Ling, L. P., Bujang, K., & Fong, L. S. (2017). Physiochemical characteristic of sago (*Metroxylon sagu*) starch production wastewater effluents. *International Journal of Research in Advent Technology*, 5(9), 4-13.
- Zhang, W., Cheng, X., Hu, Y., & Yan, Y. (2017). Measurement of moisture content in a fluidized bed dryer using an electrostatic sensor array. *Powder Technology*, 325, 49-57. <https://doi.org/10.1016/j.powtec.2017.11.006>

Evaluation of Field Performance and Energy Consumption of a Medium-sized Combine Harvester for Harvesting Glutinous Rice in Malaysia

Nazmi Mat Nawi^{1,2,3*}, Bomoi Muhammad Isa^{1,4}, Samsuzana Abd Aziz^{1,3} and Mohamad Saufi Mohd Kassim^{1,3}

¹Department of Biological and Agricultural Engineering, Faculty of Engineering, Universiti Putra Malaysia, 43400 UPM, Serdang, Selangor, Malaysia

²Institute of Plantation Studies, Universiti Putra Malaysia, 43400 UPM, Serdang, Selangor, Malaysia

³SMART Farming Technology Research Centre, Faculty of Engineering, Universiti Putra Malaysia, 43400 UPM, Serdang, Selangor, Malaysia

⁴Scientific Equipment Development Institute, Minna 920001, Nigeria

ABSTRACT

A medium-sized combine harvester has been recently deployed to harvest newly introduced high-value glutinous rice in Malaysia. Thus, efficient utilisation of combine harvesters during harvest is essential to minimise operating costs and grain loss. This study evaluated a medium-sized combine harvester's performance and energy consumption for harvesting glutinous rice. The experiment was carried out on a one-hectare paddy field with three sub-plots using a central composite design (CCD). A time-motion study was conducted during the harvesting operation to determine the combine harvester's performance parameters, which included field operating speed (FS), field efficiency (FE), theoretical field capacity (TFC), effective field capacity (EFC), grain throughput capacity (GTC), fuel consumption (FC) and field machine index (MI). The energy expended during the operation, which included machinery energy (ME), fuel energy (FCE), human energy (HE), and total energy (TE) input, were also computed. The average FS, FE, TFC, EFC, FC, and MI values were 2.42 km/h, 59.78%, 0.56 ha/h, 0.33 ha/h, 14.89 l/ha, and 0.30, respectively. The mean values of ME, FCE, HE, and TE were 305.35, 711.69, 3.62, and 1020.66 MJ/ha, respectively. The combine harvester achieved an average grain throughput capacity (GTC) of 1796.91 kg/h, demonstrating its effectiveness in handling glutinous rice harvesting. The average time

ARTICLE INFO

Article history:

Received: 21 August 2023

Accepted: 20 November 2023

Published: 04 April 2024

DOI: <https://doi.org/10.47836/pjst.32.3.22>

E-mail addresses:

nazmimat@upm.edu.my (Nazmi Mat Nawi)

Mibomoi03@gmail.com (Bomoi Muhammaad Isa)

samsuzana@upm.edu.my (Samsuzana Abd Aziz)

saufi@upm.edu.my (Mohamad Saufi Mohd Kassim)

* Corresponding author

distribution for the harvesting operation, such as effective harvesting time, turning/reversing time, and unloading time, was 1.85 h/ha, 0.38 h/ha, and 1.05 h/ha, respectively. Based on the results, it is concluded that the medium-sized combine harvester is technically and economically suitable for harvesting glutinous rice.

Keywords: Combine harvester, energy utilisation, glutinous rice, performances, time distribution

INTRODUCTION

Glutinous rice (*Oryza sativa var. glutinosa*) is one of Southeast Asia's most popular rice cultivars, especially in Thailand and Malaysia. Glutinous rice is different from typical white rice because it contains negligible amounts of amylose and high amounts of amylopectin, making the cultivar gluten-free (Sattaka, 2019). Glutinous rice is always in high demand, especially during festivals (Sattaka et al., 2020). Previously, Malaysia imported glutinous rice from Thailand, accounting for approximately 15% of the total 891,000 metric tonnes of rice imported into the country (Zainal & Shamsudin, 2021). Recently, due to strong demand, Malaysia has started planting two important local glutinous rice cultivars known as Susu and Siding in Langkawi, with cultivation areas around 14.76 ha and 24.2 ha, respectively (Zainal & Shamsudin, 2021).

Harvesting is a critical process that can affect rice production's quantity, quality, and cost. The use of a combine harvester is an effective way to reduce production costs and enhance labour productivity (Alizadeh & Allameh, 2013). Using a combine harvester is one of the most advanced mechanised harvesting technologies in Malaysian paddy production, and about 100% of rice harvesting in this country has been fully mechanised (Pebrian & Ismail, 2018). Rice harvesting in Malaysia has traditionally been carried out using a large combine harvester. However, this type of combine is becoming obsolete due to the age and insufficient machine parts. Wagiman et al. (2019) reported that using large combine harvesters could also lead to soil damage and hardpan formation due to compaction, especially when the soil is too wet during harvest. Recently, a medium-sized combine harvester has been introduced into the rice field as a cost-effective alternative to a large combine harvester. Therefore, optimising the working performance of the new medium-sized combine harvester is very important to maximise crop yield during harvesting while minimising operating costs at the optimal time and moisture level.

The field speed of the combine harvester is an important contributing factor to the harvest operation's efficiency. According to Hunt and Wilson (2016), the most critical aspect in optimising the performance of a combine harvester is field speed. Additionally, Jawalekar and Shelare (2020) stated that the machine's forward speed is the primary element affecting the combine harvester's performance. Mokhtor et al. (2020) reported that farmers' satisfaction with automated rice harvesting in Malaysian paddy fields was

significantly affected by the field speed of the combine harvester. As a result, the field speed of the combine harvester is a major concern during mechanical harvesting. Thus, optimising the field speed and other factors such as cutting height, concave clearance, drum speed, fan speed and crop moisture content during harvest will minimise harvesting costs and reduce grain loss.

In addition, energy consumption and its efficiency are also important factors to be considered in managing agricultural machinery (Canakci et al., 2005). Efficiently utilising energy may improve rice production, profitability, sustainability, and industry competitiveness (Singh et al., 2004). Farmers who are able to identify and measure various energy sources involved in grain harvesting operations may be able to increase energy efficiency, thereby decreasing production costs (Masroon et al., 2020a).

In Malaysia, medium-sized combine harvesters have gained popularity in recent years for harvesting white rice. The machine has also been employed to harvest glutinous rice. However, despite the distinct differences in mechanical and physical properties, culinary uses, and cultural significance between glutinous and normal white rice, no research has been undertaken to quantify the field performance and energy consumption of a medium-sized combine harvester utilised for harvesting glutinous rice in a field. Therefore, this study aims to determine a medium-sized combine harvester's field performance and energy consumption when harvesting glutinous rice. The specific goals were to measure the theoretical field capacity, effective field capacity, field efficiency, the distribution of human, fuel, and machine energy, and time distribution during harvesting.

MATERIALS AND METHODS

Study Location

This research was conducted in a glutinous rice field in Ayer Hangat (06°25'14.7"N, 99°48'23.00"E), Langkawi Island, Malaysia. The weather data recorded during the operation included ambient temperature (33°C), humidity (83%), wind speed (5km/h) and atmospheric pressure (1008 Pa). These weather data were obtained using a real-time digital weather detection instrument (AcuRite 02077 colour weather station forecaster). The experiment was carried out on a one-hectare paddy field using a central composite design (CCD). The experimental plot was designed to have three plots; each plot accommodated ten random runs of the experiment for 30 runs throughout the experiment.

Rice Variety

The variety of glutinous rice planted by the farmers was Pulut Siding. In Malaysia, Pulut Siding variety is the most improved local variety which most farmers use. The rice was sown in November 2021 and harvested in March 2022. It reached maturity at 116 days

after germination. The average crop’s height at harvest was 0.85 m. During harvest, the rice had an average moisture content and yield of 19.50% and 5870 kg/ha, respectively.

Medium-size Combine Harvester

A medium-sized combine harvester (FM World Star; model WS 7.0 Plus) with a 2.3-meter cutting width and rated power of 108 hp at 2600 rpm was utilised in this study (Figure 1). This type of combine harvester is Malaysia’s most recent model employed for paddy harvesting. The specifications of the combine harvester are presented in Table 1.



Figure 1. Typical medium-sized combine harvester for harvesting glutinous rice

Table 1
 Technical specification of the medium-sized combine harvester

Parameters	Specifications
Model	WS 7.0 Plus++ (4G33-TC)
Overall Dimension (mm)	5150 × 2620 × 3030
Weight (kg)	3400
Power (kW/hp)	80.53/108
Rotational speed (rpm)	2600
Fuel tank capacity (lit)	130
Track type	Rubber track
Cutting width (m)	2.36
Feeding capacity (kg/s)	6
Threshing type	Axial flow, beater bar
Threshing cylinder (mm)	620 × 2010
Fan type	Centrifugal fan
Grain tank capacity (m ³)	1.7
Unloading discharge (kg/s)	1.68

Measurement of Parameters for Field Performance and Energy Consumption

Measurement of Harvesting Time. A stopwatch was used to record the time the combine harvester took to perform an individual task in each run during the harvesting experiment, including harvesting, turning, reversing, unloading the grain, refuelling, or adjusting the machine. The total field time represents when the combine harvester engine was turned on, run, and turned off once the job was completed (Olt et al., 2019). The data was used to compute the field performances, which included the forward speed (FS), effective field capacity (EFC), field efficiency (FE), and field machine index (FMI).

Determination of the Forward Speed. The range of the forward speeds reported in the previous studies and the rated engine speed of the medium-sized combine harvester used in this study were considered in determining the optimum forward speed. The field forward speed (FS) of the combine harvester was determined by measuring the distance travelled by the machine divided by the time taken to travel. It was determined from Equation 1 by Mokhtor et al. (2020).

$$FS = \frac{D}{t} \quad [1]$$

Where FS represent the field speed of the machine (km/h), D is the distance travelled by the machine during the operation (km), and t is the time taken to cover the distance travelled (h).

Determination of the Theoretical Field Capacity. The theoretical field capacity (TFC) is the product of the field speed and the effective working width of the machine. It was obtained from Equation 2, reported by ASABE (2011).

$$TFC = \frac{W \times S}{10} \quad [2]$$

Where TFC represents the theoretical field capacity of the machine (ha/h), W is the width of the machine (m), and S is the speed of the machine (km/h).

Determination of the Effective Field Capacity. The effective field capacity (EFC) is the ability of the machine to harvest the crop under the actual field conditions (Masroon et al., 2020a). The EFC was determined as the area harvested by the machine divided by the total working time in the field (Elsoragaby et al., 2019). It was obtained using Equation 3.

$$EFC = \frac{A}{T} \quad [3]$$

Where EFC represents the effective field capacity of the machine (ha/h), A is the area of the harvested plot (ha), and T is the total working time taken to harvest the plot (h).

Determination of the Field Efficiency. Field efficiency (FE) is the ratio between the combine harvester's productivity under actual working conditions and the theoretical maximum possible productivity (Elsoragaby et al., 2019). It describes how efficiently the time was spent to conduct the operation by the machine. It was determined by Equation 4, reported by ASABE (2011).

$$FE = \frac{EFC}{TFC} \quad [4]$$

Determination of the Fuel Consumption. The fuel consumption (FC) was recorded using a measuring cylinder of known volume by refilling the fuel tank to its full capacity after each run of harvesting tasks (ASABE, 2011).

Determination Of the Grain Throughput Capacity. The grain throughput capacity (GTC) of the combine harvester is a performance metric representing the amount of grain the machine can harvest and process over a specific area or time. It is measured in tons or kilograms per unit of area or time. The GTC of the combine harvester (kg/ha) was obtained using Equation 5, reported by Amponsah et al. (2017).

$$GTC = \frac{10 \times \text{total weight of grain (g)}}{\text{Area covered in 30 m run (m}^2\text{)}} \quad [5]$$

Equation 5 can be re-arranged to reflect an actual field operation, as shown in Equation 6.

$$GTC \text{ (kg/h)} = GTC \text{ (kg/ha)} \times \text{Effective rate of harvesting (ha/h)} \quad [6]$$

Determination of Energy Expenditure for Harvesting Operation

Energy expenditure during harvesting operation is a very important factor in evaluating the performance of the combine harvester. Understanding energy expenditure may help reduce energy loss and operation costs as much as possible, particularly during harvesting. The energy sources used during harvesting include machine, fuel, and human energy.

Machine Energy. Machine energy (ME) is an indirect energy assumed to be embodied in equipment during manufacturing (Elsoragaby et al., 2019). To measure the machinery energy, the machine's total useful life and EFC were considered (Muazu et al., 2014). The machine's weight was included by equally distributing it over the total economic life. It was determined using Equation 7 by Masroon et al. (2020a)

$$ME = \frac{C_f \times W}{EFC \times L} \quad [7]$$

Where ME is the machinery energy (MJ/ha), Cf is the energy conversion coefficient for the combine harvester, W is the weight of the combine harvester (kg), EFC is the effective field capacity (ha/h), and L is the economic life of the combine harvester (h). The machinery energy conversion factor used for the combine harvester was 87.63 MJ/kg (Masroon et al., 2020a).

Fuel Energy. Fuel energy (FCE) per unit area is a function of the fuel type and the amount of fuel the machinery consumes to power an engine when harvesting. FCE was calculated using Equation 8 (Masroon et al., 2020a).

$$FCE = \frac{F_{con} \times F_c}{A} \quad [8]$$

Where FCE is the fuel energy (MJ/ha), Fcon is the quantity of fuel consumed (lit), Fc is the fuel energy conversion coefficient (MJ/lit), and A is the farm area covered (ha). The fuel energy conversion factor used for the combine harvester was 47.80 MJ/kg (Masroon et al., 2020a).

Human Energy. Human energy (HE) expenditure during the harvesting operation was evaluated based on the number of farm workers engaged in the harvesting operation per unit area and the time spent in performing the operation multiplied by an energy conversion coefficient. It was obtained from Equation 9 by Masroon et al. (2020a).

$$HE = \frac{n \times H \times I_c}{A} \quad [9]$$

Where HE is the human energy (MJ/ha), n is the number of workers engaged in the operation, H is the duration of the operation (h), Ic is the energy conversion coefficient for human labour, and A is the farm area covered (ha). The human energy conversion factor used for the harvesting operation was 1.96 MJ/kg (Masroon et al., 2020a).

Total Energy Input. The total energy input (TEI) for the harvesting operation per hectare was calculated as the sum of all energy sources. It was calculated using Equation 10 (Elsoragaby et al., 2019).

$$TEI = ME + FCE + HE \quad [10]$$

Mechanization Index. The percentage of machine energy expresses the mechanisation index (MI) to the sum of human, fuel, and machine energies. It was computed using Equation 11 by Elsoragaby et al. (2019).

$$MI = \frac{ME}{ME + FCE + HE} \quad [11]$$

Where MI is the mechanisation index, ME is the machinery energy (MJ/ha), FCE is the fuel consumption energy (MJ/ha), and HE is the human energy (MJ/ha).

Statistical Analysis

The study results were statistically evaluated using Design Expert Software (version 13.0.5.0) as a Central Composite Design with three experimental blocks, each comprising 10 replications. A one-way analysis of variance (ANOVA) was performed using the statistical analysis software (SAS) using the general linear model (GLM) method, and the mean results were compared for P-value with 95% confidence and a 5% significant level (0.05).

RESULTS AND DISCUSSION

Table 2 presents the results of the medium-sized combine harvester's performance in a glutinous rice field. The results show insignificant differences for each parameter at a 5% significance level ($P \leq 0.05$) between the harvesting plots. In addition, no mechanical or technical problems were observed during the machine's operation.

Field Speed and Theoretical Field Capacity

From Table 2, the average mean of FS and TFC of the medium-sized combine harvester was 2.42 km/h and 0.56 ha/h, respectively. Plot 3 had a higher FS value of 2.47 km/h than Plots 2 and 1, which have FS values of 2.38 km/h and 2.40 km/h, respectively, indicating that Plot 3 had 3.8 and 2.9% higher TFC than Plots 2 and 1, respectively. The result of FS in this study is lower than the results reported by Elsoragaby et al. (2019) and Masroon et al. (2020b) but higher than the result reported by Amponsah et al. (2017). It also agrees with the results reported by Masroon et al. (2020a), who also reported a moderate FS of 2.55 km/h and stated that when harvesting with a medium-sized combine harvester, a

Table 2
Performance of the medium-sized combine harvester during harvesting operation

Field Performance	Plot 1 (Mean ± SD)	Plot 2 (Mean ± SD)	Plot 3 (Mean ± SD)	Average (Mean ± SD)	P-Value
FS (km/h)	2.40±0.41	2.38±0.39	2.47±0.43	2.42±0.40	0.84
TFC (ha/h)	0.55±0.09	0.57±0.09	0.57±0.10	0.56±0.09	0.84
EFC (ha/h)	0.33±0.04	0.33±0.04	0.33±0.04	0.33±0.04	0.96
FE (%)	60.05±2.44	60.30±2.57	58.97±3.90	59.77±2.99	0.59
FC (l/ha)	15.61±2.00	14.78±1.63	14.28±1.41	14.89±1.68	0.69
GTC (kg/h)	1799.94±30.25	1798.88±35.40	1791.90±40.35	1796.91±35.33	0.75

Note. P-values for experimental parameters at a confidence level of 95% (n = 10). There were no significant differences in experimental parameters at 0.05

lower field speed should be used to avoid overloading the feeding rate thus reduce grain losses. Hamid et al. (2018) reported that a medium-sized combine harvester operated at a higher FS of 4.3 km/h would lead to a lower yield, while a lower FS of 2.25 km/h led to a higher yield. Inappropriate FS has the potential to reduce grain yield due to unpredictable losses. These results might be due to the high moisture level in the field at the time of the experiment because of the rainfall a few hours before harvest, which might have influenced the performance of the combine harvester. The optimum field speed was evaluated based on the quantity of grain harvester and fuel consumed by the combine harvester, with minimum grain loss.

Effective Field Capacity and Field Efficiency

The average mean of EFC and FE for the medium-sized combine harvester in glutinous rice fields were 0.33 ha/h and 59.77%, respectively (Table 2). Plot 2 had an average FE value of 60.30%, higher than Plots 1 and 3, which have average FE values of 60.05 and 58.97%, respectively. It indicates that the FE difference between the three experimental plots is insignificant. The EFC and FE values in this study are greater than those obtained by Masroon et al. (2020a) and Masroon et al. (2020b) but less than those obtained by Elsoragaby et al. (2019). It demonstrated that the medium-sized combine harvester investigated in this study was adequate to perform appropriately during the harvesting of glutinous rice. The operating distance covered by the machine during the operation was one of the elements that affected the efficiency of the harvesting performance. This study had a total working distance of 30 meters, which was longer than the distances reported in the previous studies with lower working distances (Amponsah et al., 2017; Elsoragaby et al., 2019; Masroon et al., 2020a, 2020b). The efficiency results obtained in this study may also be attributed to disparities in the settings of the operational parameters of the combine harvester and the swath covered by the machine. Such differences can lead to changes in the percentage of field efficiency, either by increasing or decreasing non-productive time.

Fuel Consumption

The average mean of FC for the medium-sized combine harvester employed in a glutinous rice field was 14.89 l/ha (Table 2). Plot 1 had a higher FC value of 15.61 l/ha than Plots 2 and 3, which have FC values of 14.78 l/ha and 14.28 l/ha, respectively, indicating that Plot 1 had 5.32% and 8.52% higher FC than Plots 2 and 3. Elsoragaby et al. (2019) and Masroon et al. (2020a) obtained 18.46 l/ha and 37.25 l/ha for fuel consumption, respectively, which are 60% and 19.34% higher than what was obtained in this study. It demonstrates that the performance of the medium-sized combine harvester on glutinous rice is adequate and cost-effective.

Grain Throughput Capacity

The average grain throughput of the combine harvester obtained in this study was 1796.91 kg/h at an effective machine operation of 0.33 ha/h (Table 2). The results show an insignificant difference between the plots, indicating that the performance of the combine harvester was consistent among the three plots. The average speed at which the combine harvester operated was relatively effective. The current operational setting of the combine harvester has allowed the machine to achieve a higher grain yield while maintaining grain quality and minimum losses. Therefore, farmers and operators need to consider the optimum setting of the combine harvester, crop conditions, and operator proficiency to maximise the grain throughput capacity.

Time Distribution for Harvesting Operation

Field time distribution is an essential performance parameter for analysing the combine harvester's effective time in the field. The field time distribution for harvesting glutinous rice includes the effective harvesting time, turning/reverse time, and unloading time, as presented in Table 3. The result shows insignificant differences at the 5% significance level ($P \leq 0.05$) between harvesting operations for each plot.

Effective Harvesting Time. Table 3 shows that the average effective harvesting time in glutinous rice fields utilising the medium-sized combine harvester was 1.85 h/ha. Plot 2 had a higher harvesting time value of 1.89 h/ha than Plots 1 and 3, which have harvesting time values of 1.86 h/ha and 1.81 h/ha, respectively. However, the difference in time between the three plots is negligible. The effective harvesting time is accounted for 56.40% of glutinous rice fields' total combine harvester operation time. Masroon et al. (2020a) and Masroon et al. (2020b) reported that the harvesting time of 2.14 h/ha and 2.68 h/ha, respectively, which are 13.55 and 30.97% greater than the harvesting time recorded in this study. In another study, Elsoragaby et al. (2019) obtained 1.36 h/ha, 26.50% less than the time recorded in this study. The differences in harvesting time

Table 3
Field time distribution for the harvesting operation

Operation	Plot 1 (Mean \pm SD)	Plot 2 (Mean \pm SD)	Plot 3 (Mean \pm SD)	Average (Mean \pm SD)	P-Value
Effective harvest (h/ha)	1.86 \pm 0.10	1.89 \pm 0.11	1.81 \pm 0.13	1.85 \pm 0.11	0.86
Turning-reverse (h/ha)	0.41 \pm 0.008	0.37 \pm 0.001	0.37 \pm 0.002	0.38 \pm 0.004	0.25
Unloading (h/ha)	1.04 \pm 0.004	1.04 \pm 0.002	1.05 \pm 0.001	1.05 \pm 0.002	0.76
Total (h/ha)	3.31 \pm 0.63	3.30 \pm 0.66	3.23 \pm 0.63	3.28 \pm 0.64	0.96

Note. P-values for experimental parameters at a confidence level of 95% ($n = 10$). There were no significant differences in experimental parameters at 0.05

between the combine harvesters were due to machinery specifications, terrain conditions, and the types and varieties of grain crops.

Turning/Reversing Time. The average mean for turning and reversal time in glutinous rice fields using the medium-sized combine harvester was 0.38 h/ha (Table 3). Plot 1 had a higher turning/reversing time of 0.41 h/ha than Plots 2 and 3, both of which had 0.37 h/ha—from the experiment, the time taken for turning/reversing of the machine accounted for 11.59% of the total harvesting operation time. By comparing the results obtained in this study with those of the existing studies, Masroon et al. (2020b) reported a turning/reversing time of 0.50 h/ha, equivalent to 12.53% of the total harvesting operation time, which is greater than the result of this study. In contrast, Elsoragaby et al. (2019) and Masroon et al. (2020a) reported 0.26 h/ha and 0.17 h/ha, respectively, equivalent to 5.98% and 8.95% of the total harvesting operation time, which is lower than the result obtained in this study. However, this study's result is reasonable compared to the results of the previous studies.

Unloading Time. According to Table 3, the average unloading time of glutinous rice utilising the medium-sized combine harvester was 1.05 h/ha, equivalent to 32.01% of the total harvesting operation time. When the findings of this study were compared to earlier findings, Elsoragaby et al. (2019) found that grain unloading accounted for 18.95% (0.36 h/ha) of total field time. Masroon et al. (2020) also reported that unloading the grain consumed 28.41% (1.24 h/ha) of the total field time. Masroon et al. (2020b) revealed that the time spent unloading grain utilising Kubota (KDS) and WordStar (WS) mid-size combine harvesters was 1.25 and 1.21 h/ha, respectively. Unloading time varies depending on the type of combine harvester, crop, and standard management practice. Inadequate or inconsistent farm machinery standard management practices during field operation reduce the total field time (Masroon et al., 2020b). The result of this study is higher than that reported by Elsoragaby et al. (2019) but lower than that reported by Masroon et al. (2020a) and Masroon et al. (2020b). It shows that the standard management procedures demonstrated in this study are appropriate and consistent.

Energy Inputs for Harvesting Glutinous Rice

Energy consumption is one of the most critical elements that must be monitored and analysed during field operation. Energy losses should be avoided to reduce operating costs, particularly during harvesting. Table 4 shows the energy consumption from three sources while harvesting glutinous rice with the medium-sized combine harvester. The results demonstrate insignificant variations across the three harvested plots.

Table 4
The energy input of harvesting operation for glutinous rice

Energy Input	Plot 1 (Mean ± SD)	Plot 2 (Mean ± SD)	Plot 3 (Mean ± SD)	Average (Mean ± SD)	P-Value
ME (MJ/ha)	305.83±40.96	307.45±39.92	302±44.05	305.34±41.64	0.97
FCE (MJ/ha)	746.1	706	682.36	713.68	-
HE (MJ/ha)	3.64±0.65	3.67±0.60	3.54±0.71	3.62±0.65	0.9
TE (MJ/ha)	1055.57±41.59	1017.73±40.50	988.68±44.73	1020.66±42.27	0.006
MI	0.29	0.3	0.31	0.3	-

Note. P-values for experimental parameters at a confidence level of 95% (n = 10). There were no significant differences in experimental parameters at 0.05

Machinery Energy. Table 4 shows that the average mean of machinery energy (ME) input for harvesting glutinous rice using the medium-sized combine harvester was 305.34 MJ/ha, equal to 29.73% of the total energy consumed during the harvesting operation. This study's findings are consistent with the 303.53 MJ/ha machinery energy input reported by Muazu et al. (2014). Elsoragaby et al. (2019) reported the machinery energy of 275.65 MJ/ha for harvesting wetland rice with a medium-size combine harvester, equivalent to 26.14% of the total energy input during the harvesting operation. Masroon et al. (2020a) also reported that 24.77% of machinery energy of the total energy utilised in the harvesting operation. This study indicates a higher machinery energy input than the previous studies due to differences in EFC, field and crop conditions, and operator expertise. Masroon et al. (2020a) revealed that harvesting operations with lower EFC values use more machinery energy than those with higher EFC values.

Fuel Energy. The average fuel energy (FCE) consumed for harvesting glutinous rice using the medium-sized combine harvester was 713.68 MJ/ha, as presented in Table 4. The energy consumed equals 69.92% of the total energy utilised during harvesting. Masroon et al. (2020a) recorded fuel energy consumption of 1780.70 MJ/ha for harvesting wetland rice with a medium size combine harvester. The value obtained was equivalent to 74.93% of the total energy input during the harvesting operation. According to a study by Amponsah et al. (2017), the fuel energy consumption was 882.39 MJ/ha, equivalent to 76.07% of the total energy input during the harvesting operation. Muazu et al. (2014) also reported that 853.54 MJ/ha of fuel energy, equivalent to 73.59% of the total energy utilised in harvesting wetland paddy. In this study, the fuel energy used by the medium-sized combine harvester is less than that obtained in the previous studies. It reveals that the fuel energy used is reasonable and economical.

Human Energy. The average value of human energy (HE) used in harvesting glutinous rice fields is 3.62 MJ/ha, equivalent to 0.35% of the total energy consumed during harvesting.

The percentage of human energy used in this study is consistent with the findings of (Masroon et al., 2020a). Elsoragaby et al. (2019) reported 0.23% human energy of total energy input during harvesting, similar to the amount obtained by Muazu et al. (2014). This study consumed more energy than previous studies due to a smaller harvested area and increased labour time per harvested area because of the lower EFC.

Total Energy. The average total energy (TE) consumed to harvest glutinous rice with the medium-sized combine harvester was 1020.66 MJ/ha. Muazu et al. (2014) and Elsoragaby et al. (2019) reported a total energy input of 1159.77 MJ/ha and 1160 MJ/ha for harvesting wetland paddy with medium-size combine harvesters, which is 12% greater than the energy expended in this study. Compared to other crop types, Masroon et al. (2020a) recorded a total energy input of 2376.96 MJ/ha for harvesting grain corn with a medium-sized combine harvester. The result yields an energy input that is 132.88 % greater than the energy utilised in this experiment. This study demonstrates a lower energy requirement for the harvesting operation, which is very desirable for harvesting contractors.

CONCLUSION

This study evaluated the field performance of the medium-sized combine harvester in harvesting glutinous rice. From the experiment, the average values of FS, FE, TFC, EFC, FC, and FMI were found to be 2.42 km/h, 59.78%, 0.56 ha/h, 0.33 ha/h, 14.89 l/ha, and 0.29, respectively. The average grain throughput capacity of the combine harvester was 1796.91 kg/h at an effective machine operation of 0.33 ha/h. The average time distribution for the harvesting operation, such as effective harvesting time, turning/reversing time, and unloading time, were 1.85 h/ha, 0.38 h/ha, and 1.05 h/ha, respectively. The mean values of ME, FCE, HE, and TE were 305.35 MJ/ha, 711.69 MJ/ha, 3.62 MJ/ha, and 1020.66 MJ/ha, respectively. Based on the findings of this study, the medium-sized combine harvester performed very well in the paddy field, as reflected by the field efficiency, grain throughput capacity, harvesting time, and energy consumption during harvesting. As a result, it can be concluded that the combine harvester is technically suitable for use in glutinous rice fields.

ACKNOWLEDGMENT

This research was supported by the Ministry of Higher Education of Malaysia under the Trans-disciplinary Research Grant Scheme (TRGS/1/2020/UPM/7).

REFERENCES

Alizadeh, M. R., & Allameh, A. (2013). Evaluating rice losses in various harvesting practices. *International Research Journal of Applied and Basic Sciences*, 4(4), 894–901.

- Amponsah, S. K., Addo, A., Moreira, J., & Ndindeng, S. A. (2017). Performance evaluation and field characterization of the sifang mini rice combine harvester. *Applied Engineering in Agriculture*, 33(4), 479–489. <https://doi.org/10.13031/aea.11876> 479
- ASABE. (2011). *Agricultural machinery management data* (ASAE D497.7). American Society of Agricultural and Biological Engineers. http://www.abe-research.illinois.edu/Faculty/grift/TSM262_2017/Standards/ASAE_D497_7.pdf
- Canakci, M., Topakci, M., Akinci, I., & Ozmerzi, A. (2005). Energy use pattern of some field crops and vegetable production: Case study for Antalya Region, Turkey. *Energy Conversion and Management*, 46(4), 655–666. <https://doi.org/10.1016/j.enconman.2004.04.008>
- Elsoragaby, S., Yahya, A., Mahadi, M. R., Nawi, N. M., & Mairghany, M. (2019). Comparative field performances between conventional combine and mid-size combine in wetland rice cultivation. *Heliyon*, 5(4), Article e01427. <https://doi.org/10.1016/j.heliyon.2019.e01427>
- Hamid, M. A., Rohazrin, A. R., Chan, C. S., Yahya, S., Shanmugavelu, S., Aris, A., & Saleh, B. (2018, April 17-19). *Preliminary study of the performance of imported grain corn combine harvester machines*. [Paper presentation]. Proceedings of the National Conference on Agricultural and Food Mechanization (NCAFM), Sarawak, Malaysia.
- Hunt, D., & Wilson, D. (2016). *Farm power and machinery management*. Waveland Press
- Jawalekar, S. B., & Shelare, S. D. (2020). Development and performance analysis of low-cost combined harvester for rabi crops. *Agricultural Engineering International: CIGR Journal*, 22(1), 197–201.
- Masroon, M. H., Nawi, N. M., Yahya, A., Shukery, M. F. M., & Amin, M. E. S. (2020a). Performance of mid-size combine harvester of grain corn on the field efficiency and energy consumption at the northern Johor of Malaysia. *Pertanika Journal of Science and Technology*, 28(4), 1277–1296. <https://doi.org/10.47836/pjst.28.4.08>
- Masroon, M. H., Nawi, N. M., Yahya, A., Shukery, M. F. M., & Amin, M. E. S. (2020b). Comparison of field performances between two typical mini combine harvesters in grain corn production. *Journal of Agricultural and Food Engineering*, 1(3), Article 0022. <https://doi.org/10.37865/jafe.2020.0022>
- Mokhtor, S. A., Pebrian, D. E., & Johari, N. A. A. (2020). Actual field speed of rice combine harvester and its influence on grain loss in Malaysian paddy field. *Journal of the Saudi Society of Agricultural Sciences*, 19(6), 422–425. <https://doi.org/10.1016/j.jssas.2020.07.002>
- Muazu, A., Yahya, A., Ishak, W. I. W., & Khairunniza-Bejo, S. (2014). Machinery utilization and production cost of wetland, direct seeding paddy cultivation in Malaysia. *Agriculture and Agricultural Science Procedia*, 2, 361–369. <https://doi.org/10.1016/j.aaspro.2014.11.050>
- Olt, J., Küüt, K., Ilves, R., & Küüt, A. (2019). Assessment of the harvesting costs of different combine harvester fleets. *Research in Agricultural Engineering*, 65(1), 25–32. <https://doi.org/10.17221/98/2017-RAE>
- Pebrian, D. E., & Ismail, M. I. (2018). The characteristics of the repair and maintenance costs distribution of rice combine harvester in Malaysian paddy fields. *Agricultural Engineering International: CIGR Journal*, 20(4), 132–138.

- Sattaka, P. (2019). Potential development of glutinous rice community towards new agricultural culture tourism in upper northeastern Thailand. *Journal of the International Society for Southeast Asian Agricultural Sciences*, 25(1), 92–103.
- Sattaka, P., Muengpak, S., Xuan, H. P., & Mueangkhrot, T. (2020). Comparison of glutinous rice production systems for sustainable development in Sakon Nakhon Province. *Journal of the International Society for Southeast Asian Agricultural Sciences*, 26(1), 54–62.
- Singh, R. K. P., Sinha, D. K., & Singh, L. N. (2004). Impact of modern agriculture technology on rice production in Bihar. *Agricultural Economics Research Review*, 17, 59–67. <https://doi.org/10.22004/ag.econ.265889>
- Wagiman, N. A., Nawati, N. M., Yahya, A., Su, A. S. M., & Nasir, R. M. (2019). Field performance comparison of the combine harvesters utilized for rice harvesting in Malaysia. *Food Research*, 3(2), 177–181. [https://doi.org/10.26656/fr.2017.3\(2\).136](https://doi.org/10.26656/fr.2017.3(2).136)
- Zainal, N., & Shamsudin, R. (2021). Physical properties of different local glutinous rice cultivar (susu and siding) and commercial Thai cultivar (susu). *Advances in Agricultural and Food Research Journal*, 2(1), Article a0000178. <https://doi.org/10.36877/aafjr.a0000178>.

Effect of Maturity Stages on Physical Properties of Cocoa (*Theobroma cacao* L.) Pods

Babatunde Oluwamayokun Soyoye¹, Nazmi Mat Nawawi^{2,3*}, Mohamad Ariffin Zulkifli², Guangnan Chen⁴, Nurfadzilah Madian^{2,5}, Ahmad Faiz Mokhtar², Siti Nooradzah Adam² and Dimas Firmanda Al Riza⁶

¹Agricultural and Environmental Engineering Department, School of Engineering and Engineering Technology, Federal University of Technology, Akure, Nigeria

²Institute of Plantation Studies, Universiti Putra Malaysia 43400 Serdang, Selangor Malaysia

³Department of Biological and Agricultural Engineering, Universiti Putra Malaysia, 43400 UPM Serdang, Selangor, Malaysia

⁴School of Agriculture and Environmental Science, University of Southern Queensland, Toowoomba, QLD 4350, Australia

⁵Division of Cocoa Upstream Technology, Cocoa Research and Development Centre, Malaysian Cocoa Board, Jalan Jengka 23. P. O. Box 34, 28000, Temerloh, Pahang, Malaysia

⁶Biosystems Engineering Department, Faculty of Agricultural Technology, Universitas Brawijaya, Jalan Veteran, Malang 65145, Indonesia

ABSTRACT

Cocoa is one of the main plantation crops in Malaysia. Significant efforts have been made to modernise the industry using mechanisation and automation technologies. Thus, determination of the physical properties of cocoa pods at different maturity stages is paramount for an appropriate design and development of a post-harvest machinery system for pod breaking, sorting and grading. This study investigated the effect of five different maturity stages (unripe, under-ripe, ripe, very-ripe and over-ripe) on the physical properties of cocoa pods. A total of 80 cocoa pods (Clone PBC140) were used as samples, where 16 pods represented each maturity stage. For the unripe stage, the largest mean dimensional values were 172.45, 89.3 and 111.18 mm for the pods' length, diameter and geometric mean diameter, respectively.

The highest mean values of 0.66 and 0.54 for the over-ripe stage were recorded for sphericity and aspect ratio, respectively. The geometric mean diameter, weight and

ARTICLE INFO

Article history:

Received: 25 October 2023

Accepted: 18 December 2023

Published: 04 April 2024

DOI: <https://doi.org/10.47836/pjst.32.3.23>

E-mail addresses:

bosoyoye@futa.edu.ng (Babatunde Oluwamayokun Soyoye)

nazmimat@upm.edu.my (Nazmi Mat Nawawi)

ariffin@myinvent.com.my (Mohamad Ariffin Zulkifli)

Guangnan.Chen@usq.edu.au (Guangnan Chen)

nurfadzilah@koko.gov.my (Nurfadzilah Madian)

faiz_mokhtar@upm.edu.my (Ahmad Faiz Mokhtar)

snadzah@upm.edu.my (Siti Nooradzah Adam)

dimasfirmanda@ub.ac.id (Dimas Firmanda Al Riza)

* Corresponding author

firmness were found to be inversely proportional to the maturity stages. The advanced maturity stages experience greater colour intensity, as reflected in the chroma (C^*) and higher L^* , a^* and b^* values. This study has found that the colour and texture of the cocoa pods change throughout their maturity. In conclusion, the results reported in this study can be used as a reference for designing and developing a machinery system for post-harvest fruit processing.

Keywords: Cocoa fruits, colour intensity, dimensional analysis, firmness, maturity stages

INTRODUCTION

Cocoa (*Theobroma cacao* L.) is one of the most prominent and lucrative plantation crops commonly grown in tropical regions worldwide. In the last decade, world cocoa production has reached 4.48 million tonnes annually, valued at USD98.38 billion, with a steady production increment of 3% annually (Beg et al., 2017). Cocoa is a perennial tropical crop that continuously produces pods throughout the year to fulfil tremendous demand for cocoa-based products, especially chocolates. Cocoa beans are the main cocoa product used to produce chocolate and its derivatives, including cosmetics, foods and pharmaceutical products (Subroto et al., 2023). In addition, it was revealed that cocoa, rich in flavonoids, has also been used in the medical industry due to its ability to reduce high blood pressure and increase the suppleness of blood vessels (Avendaño-Arrazate et al., 2018).

Typically, a cocoa pod is an ovoid indehiscent fruit 15–30 cm long and 8–10 cm wide, available in various shapes such as oblate, spherical, elliptical and oblong (Ramji et al., 2018). The skin surface of a cocoa pod can be smooth or rough during its immature state with green and red colours, depending on its genotype (Avendaño-Arrazate et al., 2018). Generally, unripe cocoa pods have green or reddish-purple skin, which changes to yellowish or reddish-orange when they mature (Motamayor et al., 2013). The colour of cocoa pods is one of the indicators of their maturity level, and farm workers widely use it to decide when to harvest the crop. Harvesting is an initial field operation which could influence the quality level of cocoa beans during post-harvest processing (Apriyanto, 2016). Ideally, only fully ripe pods should be harvested for optimum yield and quality of cocoa beans (Rojas et al., 2020). However, since the maturity level of cocoa during harvesting is subjectively determined by visual inspection, it is difficult to ensure that all the harvested cocoa pods are at optimum maturity levels. Sometimes, slightly overripe and underripe cocoa pods are also harvested.

After harvesting, cocoa pods will be sent to a processing centre for post-harvest processing. Post-harvest processing of cocoa pods includes sorting, breaking, splitting, fermenting, drying, and storage (Forte et al., 2023). Post-harvest handling is a crucial step to be considered because it can greatly affect the yield of cocoa beans (Subroto et al., 2023). Unfortunately, in most countries, labourers still carry out post-harvest processing manually.

Post-harvest processing of cocoa should be modernised to cope with the growing demand using mechanisation and automation technologies, which could reduce the drudgery to workers, thus increasing the efficiency of the process (Arulmari et al., 2021). In specific terms, mechanisation technology is needed to replace labourers, especially during the post-harvest processing of matured cocoa pods, which involves handling, sorting, cleaning, grading, pod breaking and drying.

The physical properties of cocoa pods during harvest should be quantified to develop specific machinery for processing equipment. Among the typical physical properties of the pods to be measured are size, volume, mass, density, friction angle, angle of repose, curvature, sphericity, colour, and firmness (Arulmari et al., 2021). Various types of cleaning, grading, separation, and conveying equipment were designed and constructed based on the physical properties of the targeted crops (Sandoval et al., 2019). Thus, this study was carried out to investigate the effect of different maturity stages of cocoa pods on their physical properties. The findings of this study will provide useful data for the design and development of various cocoa processing machines.

MATERIALS AND METHODS

Materials Acquisition and Preparation

Cocoa pod samples from clone PBC140 were carefully selected for experimentation. The clone was chosen because it has a fine and unique flavour as well as good agronomic traits (Haya et al., 2021). A total of 80 cocoa pods, with 16 pods for each maturity stage [unripe (*UR*), under-ripe (*DR*), ripe (*RP*), very-ripe (*VR*) and over-ripe (*OR*)] were acquired from the Cocoa Research and Development Centre, Malaysian Cocoa Board (MCB), Jengka, Pahang, Malaysia. The fruits were carefully chosen to guarantee they were free from being infested by pests and diseases, and their size and weight were remarkably uniform. Subsequently, the maturity stages of the harvested cocoa pods were determined and classified by a senior research officer from the Centre based on the characteristics as presented in Table 1. Before the commencement of the experiment, the fruits were cleaned with a soft brush, labelled and numbered to assist the identification process. The dimensional parameters such as the length, diameter and weight were taken and recorded immediately after harvesting on the farm. Then, the fruits were immediately transported to a laboratory at the Institute of Plantation Studies, Universiti Putra Malaysia, for laboratory analysis. All the laboratory experiments were concluded within 24 hours after harvesting.

Table 1
Characteristics of the cocoa pods at different maturity stages

Maturity Stage	Characteristic
Unripe (UR)	Fully green
Under-ripe (DR)	More green than yellow
Ripe (RP)	Mix of green and yellow
Very-ripe (VR)	More yellow than green
Over-ripe (OR)	Fully yellow

Determination of Physical Properties

The physical properties of each cocoa pod sample, such as length, L and diameter, D , were measured using digital vernier callipers (Mitutoyo Corporation, Kawasaki, Kanagawa, Japan. Model 500-196-20). In contrast, the weight was measured using an electronic balance (A&D GF-10K, precision weighing balance, USA, sensitivity: ± 0.03 g). The diameter was measured in the middle of the pod, perpendicular to its length. The geometric mean diameter (GMD), sphericity (S), aspect ratio (R_a) and surface area (S_a) were determined using Equations 1 to 4.

$$\text{Geometric mean diameter (GMD)} = \sqrt[3]{(L \times D^2)} \quad [1]$$

$$\text{Sphericity (S)} = \frac{GMD}{L} \quad [2]$$

$$\text{Aspect ratio (R}_a\text{)} = \frac{L}{D} \quad [3]$$

$$\text{Surface area (S}_a\text{)} = \pi(GMD) \quad [4]$$

Where L is the length while D is the diameter of the pod (m), respectively.

Colour Measurement

The colour of the cocoa pod samples was measured using a colorimeter (CR-400, Minolta Corp, Osaka, Japan) with a measuring head of 8 mm in diameter and calibrated with standard white tiles. Before the measurement, the colorimeter was calibrated to values $Y = 85.40$, $X = 0.3184$ and $y = 0.3356$ as recommended in the manual at room temperature. The colour readings of the cocoa pods were measured from six different portions of each fruit. The mean of these measurements was determined, and the colour description of the fruits was described as the CIE values where lightness (L^*) was represented from 0 (black) to 100 (white), redness (a^*) was represented by red to green components of the colour, where +ve a^* (positive) is more to red values and -ve a^* (negative) is more to green values, yellowness (b^*) was represented by yellow to blue components of the colour, where +ve b^* (positive) more to yellow values and -ve b^* (negative) more to blue values, chroma (C^*) was represented by saturation or vividness of the colour, and hue (h°) was the actual colour which varies continuously from 0° to 360° . A h° of 0° or 360° corresponds to red, 90° to yellow, 180° to green, and 270° to blue (Ly et al., 2020). After taking the first three readings, the last three were taken after 180° rotation of the samples, giving six readings for each cocoa pod sample.

Moisture Content Measurement

Moisture content was determined using an air oven method according to the Association of Official Analytical Chemists (AOAC) standard (Rojas et al., 2020). Each of the cocoa

pod samples was weighed using an electronic balance (Mettler Toledo Model- JS1203C, Columbia. sensitivity: ± 0.0002 g) and placed in a petri dish inside a recirculating oven (Memmert GMBH, Model-30-1060, Germany). The samples were dried for 24 h in the oven at 70°C, and the dry weight was recorded. The sample was dried and weighed again every 3 h until a constant weight was obtained. The moisture content was determined based on a wet-weight basis method (MC%, w.b.) using Equation 5.

$$\text{Moisture content (\%)}w.b. = \frac{W_2 - W_3}{W_2 - W_1} \quad [5]$$

Where W_1 is the weight of the petri dish, W_2 is the weight of the petri dish with the sample before drying, and W_3 is the weight of the petri dish with the sample after drying.

Firmness Determination

The firmness of the cocoa pod samples was measured using an Instron Universal Testing Machine fitted with a 6.0 mm diameter plunger tip and 5 kg load cell (GY-1, G-tech Ltd., China). Figure 1 illustrates the intact cocoa pod which was placed on the plate before the Instron probe was allowed to punch the fruit to 5 mm depth at a crosshead speed of 20 mm min^{-1} into each punch, following the same speed applied by Wang et al. (2019). The firmness readings were recorded in Newton (N) using Instron Merlin Software version M12- 13664-EN. These measurements were made at three points per fruit to represent the pods' upper, middle and lower portions.

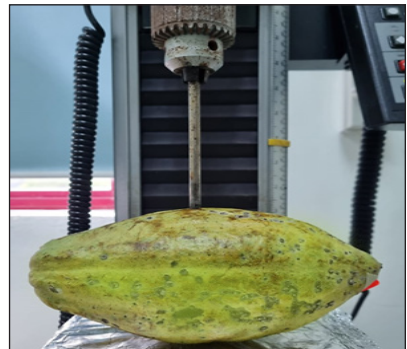


Figure 1. Firmness test using Instron Universal Testing Machine

Statistical Analysis

A one-way analysis of variance (ANOVA) complemented with Turkey (honestly significant difference) HSD Post Doc tests were used to establish the significant effect of maturity stages on the properties of the cocoa pods. All the data analyses were done using Statistical Package for Social Sciences (SPSS) software (Version 25.0, SPSS Inc. Chicago, USA).

RESULTS AND DISCUSSION

Dimensional Characterisation

The dimensional results reveal the differences in the physical morphologies of the fruits at different maturity stages, as presented in Table 2. The size of the cocoa pods was determined based on their length and diameter. The length and diameter of the pods ranged from 152 to 198 mm and 81 to 99 mm, respectively, for the UR category; 151 to 195 mm and 80 to 99

mm, respectively, for *DR* maturity stage; 145 to 181 mm and 77 to 93 mm respectively for *RP* category; 142 to 181 mm and 77 to 93 mm respectively for *VR* category and 136 to 194 mm and 74 to 99 mm respectively for *OR* maturity stages. The largest mean dimensional values of 172.45 mm, 89.30 mm and 111.18 mm were recorded for the length, diameter and geometric mean diameter of the cocoa pods for *the UR* maturity stage, respectively. The least 159.45 mm, 85.15 mm and 104.92 mm were recorded for the *OR* maturity stage. In contrast, the least values of 159.45 mm, 85.15 mm and 104.92 mm for the same categorical order were recorded for the *OR* maturity stage, respectively. This finding shows that the dimensional values decreased as the maturity level increased.

There is no significant difference in the diameter of the cocoa pods for all maturity stages. In addition, at the maturity stages of *DR*, *RP* and *VR*, the length exhibits no significant difference in the mean values. However, the maturity stages of *UR* and *OR* show significant differences in the pods' length and geometric mean diameters ($P>0.05$). The findings align with the published study by Bojacá et al. (2019), who reported that a decrease in the dimensional parameters of the fruits was a sign that fruit growth does not occur during the ripening process. In addition, Doaré et al. (2020) reported that fruit development depended on climatic factors such as temperature and genetic variation in the fruiting cycle. The results of ANOVA reveal that the effect of maturity stages on the geometric mean diameter of the cocoa pods was significantly different ($P<0.05$). The geometric mean diameter of the cocoa pods decreased as the maturity stage increased from *UR* to *OR* category.

Table 2
Dimensional properties of the cocoa pod samples

Property	Variation	Maturity Stage				
		<i>UR</i>	<i>DR</i>	<i>RP</i>	<i>VR</i>	<i>OR</i>
Length (mm)	Min	152.00	151.00	145.00	142.00	136.00
	Max	198.00	195.00	200.00	181.00	194.00
	Mean	172.45 ^b	168.15 ^{ab}	171.00 ^{ab}	164.95 ^{ab}	159.45 ^a
	SD	11.91	12.13	15.12	11.88	16.05
Diameter (mm)	Min	81.00	80.00	79.00	77.00	74.00
	Max	99.00	99.00	95.00	93.00	99.00
	Mean	89.30 ^a	87.05 ^a	87.60 ^a	86.70 ^a	85.15 ^a
	SD	4.85	5.36	4.07	5.16	6.08
Geometric mean diameter (mm)	Min	100.78	99.69	96.73	94.43	91.46
	Max	122.63	121.28	121.35	115.28	123.89
	Mean	111.18 ^b	108.38 ^{ab}	109.43 ^{ab}	107.40 ^{ab}	104.92 ^a
	SD	6.09	6.50	6.04	6.39	8.14

Note. ^{a-b} Equal letters in a column mean that there are no significant differences based on the Tukey-HSD test ($P>0.05$)

In the same trend, the highest mean values of 0.66 and 0.54 were recorded for sphericity and aspect ratio for the *OR* maturity stage, respectively (Table 3). In contrast, the lowest mean value of 329.61 mm² was obtained for the surface area of the *OR* maturity stage, and the highest surface area of 349.27 mm² was recorded for the *UR* maturity stage. At all maturity stages, no significant difference was recorded for sphericity and aspect ratio. However, there was a significant difference in surface area between *UR* and *OR* maturity stages ($P > 0.05$).

Table 3
Sphericity, aspect ratio and surface area of the cocoa pod samples

Parameters	Variation	Maturity Stage				
		<i>UR</i>	<i>DR</i>	<i>RP</i>	<i>VR</i>	<i>OR</i>
Sphericity	Mean	0.65 ^a	0.65 ^a	0.64 ^a	0.65 ^a	0.66 ^a
	SD	0.02	0.02	0.03	0.02	0.02
Aspect ratio	Mean	0.52 ^a	0.52 ^a	0.51 ^a	0.53 ^a	0.54 ^a
	SD	0.03	0.03	0.04	0.03	0.03
Surface area (mm ²)	Mean	349.27 ^b	340.48 ^{ab}	343.78 ^{ab}	337.42 ^{ab}	329.61 ^a
	SD	19.12	20.43	18.99	20.08	25.59

Note. ^{a-b} Equal letters in a column mean that there are no significant differences based on the Tukey-HSD test ($P > 0.05$)

Firmness

The summary of the firmness level of the cocoa pods at different maturity stages is presented in Table 4. It is evident from the Table that the firmness level decreased as the maturity stages increased from *UR* to *OR* categories. It shows that firmness is inversely proportional to the maturity stages. The mean maximum value of 148.30 N was recorded for the firmness of *UR* pods, while the mean minimum value of 130.44 N was recorded for the firmness of *OR* pods. The results agree with the report by Rojas et al. (2020), which also showed a significant decrease in fruit firmness as the maturity state of cocoa pods increased. Yapo et al. (2013) reported that the decrease in firmness in relation to maturity stages may be related

Table 4
Descriptive analysis of the firmness values for different maturity stages

Maturity Stage	Max (N)	Min (N)	Mean (N)	SD
<i>UR</i>	198.86	107.82	148.30 ^b	23.50
<i>DR</i>	199.64	107.32	145.79 ^b	22.61
<i>RP</i>	199.48	89.47	142.38 ^{ab}	28.39
<i>VR</i>	200.03	75.66	138.03 ^{ab}	26.49
<i>OR</i>	188.52	73.16	130.44 ^a	24.83

Note. ^{a-b} Equal letters in a column mean that there are no significant differences based on the Tukey-HSD test ($P > 0.05$)

to the bark's high fibre and pectin contents, which can degrade to ethylene-independent components and affect the fruit texture. In addition, Torres et al. (2015) also stated that the decrease in firmness with respect to maturity is more pronounced in climacteric fruits like bananas and papaya.

Moisture Content and Weight

The results of the moisture content and weight of cocoa fruits at different maturity stages are presented in Table 5. The moisture content does not significantly differ from one another within the group and at different maturity stages ($P>0.05$). In contrast, a significant difference occurred between the weight of cocoa fruit between *UR* and *OR* maturity stages ($P>0.05$). Loss of weight and moisture content were observed as the maturity stage increased. The early increase in moisture content of the cocoa fruit may be attributed to the fact that the maturity stages of *UR* to *DR* might be termed a developmental stage where moisture is required for metabolic reactions.

Table 5
The effect of maturity stages on moisture content and weight

Maturity Stage	Moisture Content (%)		Weight (g)	
	Mean	SD	Mean	SD
<i>UR</i>	85.84 ^a	1.84	643.91 ^a	95.89
<i>DR</i>	86.50 ^a	0.91	586.74 ^{ab}	94.69
<i>RP</i>	86.48 ^a	1.02	576.89 ^{abc}	104.44
<i>VR</i>	85.44 ^a	1.15	523.51 ^{bc}	88.14
<i>OR</i>	83.78 ^b	1.51	494.07 ^c	113.43

Note. ^{a-c} Equal letters in a column mean no significant differences based on the Tukey-HSD test ($P>0.05$).

Consequently, as the maturity stage of *RP* was attained, the moisture content began to decrease due to fruit shrinkage. The fruit had completed its developmental stage, attained maturity, and was ready to be harvested. Rojas et al. (2020) reported that the moisture content of cocoa pods showed a significant decrease in values as the maturity level increased. In addition, Lopez and Dimick (1995) recommended that the over-ripe pods should not be utilised because they tend to be dry, and their beans have the potential to germinate inside the pods and are susceptible to a fungal disease.

Colour Measurement

The colour parameters of the cocoa pod samples at different maturity levels are presented in Table 6. The samples from the *OR* maturity stage have higher values for L^* (58.90), followed by the *VR* maturity stage (58.84) and the least L^* values were obtained at the *UR* maturity stage (51.66). It is evident from Table 6 that the maturity stages and L^* values

exhibit direct proportionality (L^* increased as the maturity stage increased). The result aligns with the report by Lockman et al. (2019), who reported that the L^* increased from 53.87 to 59.71 as the maturity level increased. The same trend was also observed for the values of b^* and the chrome C^* and there were significant differences in all maturity stages for the colour index of b^* and C^* ($P>0.05$). Rojas et al. (2020) also reported that the cocoa pods exhibited a significant increase in a^* , b^* and C^* as their ripeness increased. The authors also reported that the L^* increased as the ripeness increased, showing that the brightness of the bark increased as the maturity stages increased.

Table 6
Colour parameters of the cocoa pods at different maturity stages

Maturity Level	Variation	Colour Parameters				
		L^*	a^*	b^*	C^*	h°
UR	Mean	51.66 ^a	-6.96 ^a	18.15 ^a	19.48 ^a	-68.99 ^a
	SD	4.56	1.31	1.65	1.67	3.78
DR	Mean	53.05 ^a	-7.23 ^a	20.98 ^b	22.28 ^b	-68.69 ^a
	SD	4.18	1.65	3.89	3.72	16.89
RP	Mean	56.48 ^b	-6.42 ^a	27.58 ^c	28.44 ^c	-74.34 ^a
	SD	4.11	2.07	5.48	5.23	17.36
VR	Mean	58.84 ^c	-4.06 ^b	33.75 ^d	34.19 ^d	-67.67 ^a
	SD	3.78	3.43	4.38	4.13	46.63
OR	Mean	58.90 ^c	4.63 ^c	40.53 ^c	41.17 ^c	39.36 ^b
	SD	3.99	6.14	5.25	5.85	72.95

Note. ^{a-c} Equal letters in a column mean that there are no significant differences based on the Tukey-HSD test ($P>0.05$)

The UR, DR, RP, and VR maturity stages have negative (-ve) values of a^* , which shows the presence of green pigments in the samples, while positive (+ve) a^* values were recorded for the OR maturity stage. The results justified the visual classification of the cocoa fruits when the pod is fully yellow and fully matured (OR maturity stage). For hue (h°), the OR maturity stage was the only sample with positive (+ve) values ($\tan \theta = +ve$). The h° value of 39.36^o was recorded for the OR maturity stage, and this falls in the first quadrant, making the samples showcase yellow pigments to complement the a^* results. There is no significant difference in the hue angle or colour index of all the maturity stages except in the OR maturity stage with a mean value of 39.36 ^ohue ($P>0.05$).

CONCLUSION

This study has quantified the physical properties of the cocoa pods (clone PBC140) at different maturity stages. This study investigates considerable physical differences between the maturity stages (UR, DR, RP, VR and OR). The cocoa pods in early maturity stages

have the largest length, polar diameter, weight and firmness values. The moisture content peaked between the *DR* and *RP* maturity stages and decreased as maturity progressed. The advanced maturity stages experienced greater colour intensity, as reflected in the chroma (C^*) and higher L^* , a^* and b^* values. The results showed that all the parameters considered in this study exhibit different patterns during the maturation process of the cocoa pods. It is also evident that the colour and texture of the fruits change throughout their maturity. In conclusion, the data presented in this study can be used as a reference for designing and developing a mechanisation system for the cocoa industry.

ACKNOWLEDGEMENTS

The Tertiary Education Trust Fund (TETFund) Nigeria through the Federal University of Technology, Akure (FUTA) is appreciated for the fund released towards the execution of this Postdoctoral Research work at the Institute of Plantation Studies (IKP), Universiti Putra Malaysia (UPM).

REFERENCES

- Apriyanto, M. (2016). Changes in chemical properties of dried cocoa (*Theobroma cacao* L.) beans during fermentation. *International Journal of Fermented Foods*, 5(1), 11-16. <https://doi.org/10.5958/2321-712X.2016.00002.8>
- Arulmari, R., Yadav, A. P., & Visvanathan, R. (2021). Effect of pod size on physical properties of cocoa pods (*Theobroma cacao* L.) with reference to farm level mechanization of cocoa processing. *Agricultural Engineering Today*, 45(2), 13-19. <https://doi.org/10.52151/aet2021452.1534>
- Avendaño-Arrazate, C. H. Bolaños, M., & Mendoza-López, A. (2018). The cocoa (*Theobroma cacao* L.) native in Mexico. *Biodiversity International Journal*, 2(6), 535-536. <https://doi.org/10.15406/bij.2018.02.00109>
- Beg, M. S., Ahmad, S., Jan, K., & Bashir, K. (2017). Status, supply chain, and processing of cocoa-A review. *Trends of Food Science and Technology*, 66, 108-116. <https://doi.org/10.1016/j.tifs.2017.06.007>
- Bojacá, A. F. C., Muñoz, C. C. G., Salamanca, A. M. C., Rojas, G. H. C., & Tarazona-Díaz, M. P. (2019). Study of the physical and chemical changes during the maturation of three cocoa clones, EET8, CCN51 and ICS60. *Journal of the Science of Food and Agriculture*, 99(13), 5910-5917. <https://doi.org/10.1002/jsfa.9882>
- Doaré, F., Ribeyre, F., & Cilas, C. (2020). Genetic and environmental links between traits of cocoa beans and pods clarify the phenotyping processes to be implemented. *Scientific Reports*, 10(1), Article 9888. <https://doi.org/10.1038/s41598-020-66969-9>
- Forte, M. Currò, S. de-Walle, D. V., Dewettinck, K., Mirisola, M., Fasolato, L., & Carletti, P. (2023). Quality evaluation of fair-trade cocoa beans from different origins using portable near-infrared spectroscopy (NIRS). *Foods*, 12(1), Article 4. <https://doi.org/10.3390/foods12010004>
- Ly, B. C. K., Dyer, E. B., Feig, J. L., Chien, A. L., & Del Bino, S. (2020). Research techniques made simple: cutaneous colorimetry: A reliable technique for objective skin colour measurement. *Journal of Investigative Dermatology*, 140(1), 3-12. <https://doi.org/10.1016/j.jid.2019.11.003>

- Lockman, N. A., Hashim, N. & Onwude, D. I. (2019). Laser-based imaging for cocoa pods maturity detection. *Food and Bioprocess Technology*, 12, 1928-1937. <https://doi.org/10.1007/s11947-019-02350-7>
- Lopez, A. & Dimick, P. (1995). Cocoa fermentation. *Biotechnology*, 9, 561-577.
- Motamayor, J. C., Mockaitis, K., Schmutz, J., Haiminen, N., Iii, D. L., Cornejo, O., Findly, S. D., Zheng, P., Utro, F., Royaert, S., Sasaki, C., Jenkins, J., Podicheti, R., Zhao, M., Scheffler, B. E., Stack, J. C., Feltus, F. A., Mustiga, G. M., Amores, F., ... & Kuhn, D. N. (2013). The genome sequence of the most widely cultivated cacao type and its use to identify candidate genes regulating pod colour. *Genome Biology*, 14(6), 53-67. <https://doi.org/10.1186/gb-2013-14-6-r53>
- Ramji, K. S. H., Kumar, P. S., Yogeshkumar, T., & Bharathkumar, M. (2018). Design and development of semi-automatic cocoa pod splitting machine. *International Journal for Scientific Research and Development*, 6(1), 2321-0613.
- Rojas, K. E., García, M. C., Ceron, I. X., Ortiz, R. E., & Tarazona, M. P. (2020). Identification of potential maturity indicators for harvesting cacao. *Heliyon*, 6(2), Article e03416. <https://doi.org/10.1016/j.heliyon.2020.e03416>
- Sandoval, A. J., Barreiro, J. A., De Sousa, A., Valera, D., & Müller, A. J. (2019). Determination of the physical properties of fermented and dried Venezuelan Trinitario cocoa beans (*Theobroma cacao* L.). *Revista Técnica de la Facultad de Ingeniería, Universidad del Zulia*, 42(2), 50-56.
- Subroto, E., Djali, M., Indiarito, R., Lembong, E., & Baiti, N. (2023). Microbiological activity affects post-harvest quality of cocoa (*Theobroma cacao* L.) beans. *Horticulturae*, 9(7), Article 805. <https://doi.org/10.3390/horticulturae9070805>.
- Torres, R., Montes, E., Perez, O., & Andrade, R. (2015). Influence of colour and maturity stages on the texture of tropical fruits (Mango, Papaya and Plantain). *Information Technological*, 26, 47-52.
- Wang, D., Yu, Y., Ai, X., Pan, H., Zhang, H., & Dong, L. (2019). Polylactide/ poly (butylene adipate-co-terephthalate)/rare earth complexes as biodegradable light conversion agricultural films. *Polymer for Advance Technology*, 30(1), 203-211. <https://doi.org/10.1002/pat.4459>
- Yapo, B. M., Besson, V., Koukala, B. B., & Koffi, K. L. (2013). Adding value to cacao pod husks as a potential antioxidant-dietary fiber source. *American Journal of Food and Nutrition*, 1(3), 38-46. <https://doi.org/10.12691/ajfn-1-3-4>

C-Slot Circular Polarized Antenna for Hybrid Energy Harvesting and Wireless Sensing

Irfan Mujahidin¹, Sidiq Syamsul Hidayat^{1*}, Muhamad Cahyo Ardi Prabowo² and Akio Kitagawa³

¹Department of Telecommunication Engineering, Faculty of Electrical Engineering, Semarang State Polytechnic, Semarang 50275, Indonesia

²Department of Electronic Engineering, Faculty of Electrical Engineering, Semarang State Polytechnic, Semarang 50275, Indonesia

³Department of Electrical Engineering and Computer Science, Kanazawa University, Ishikawa 9201192, Japan

ABSTRACT

This paper presents a new hybrid energy harvesting on electromagnetic solar for wireless energy harvesting of ambient from sensors of low-power devices. The axial ratio (AR) requirements produce Left-Hand Circular Polarization (LHCP) and Right-Hand Circular Polarization (RHCP) and simultaneously produce a 90-degree phase difference during energy harvesting, adopting a new design in designing a dual-feed broadband circular polarized (CP) antenna. To get the frequency band 2.3–2.4 GHz, we propose a C-Slot antenna with a circular patch dual feed. To estimate the diversity of the phase and magnitude output of the feed configuration under AR value, we used a 50 Ohm feed network output of the characteristic analysis for a dual feed CP antenna. An Axial ratio frequency range of less than 3 dB is achieved using polarization analysis with different branch channel couplers. To produce a DC output voltage, a high-frequency rectifier circuit embedded with a thin-film solar cell on the antenna is then connected to two T-junction power divider rectifiers, resulting in a high-efficiency design. A complete system-level analysis will include multiple signal classification methods of powered ambient RF energy using a wireless energy harvesting array that proposes a compact structure and demonstrates

optimal configuration. Reliable operation in typical indoor environments indicates a self-contained sensor Node. Therefore, it has significant implications for powering small electronics and wireless sensor applications independently of the IoT Network or real implementation telecommunications industry.

Keywords: CP antenna, hybrid energy harvesting, wireless sensing

ARTICLE INFO

Article history:

Received: 16 August 2023

Accepted: 02 November 2023

Published: 04 April 2024

DOI: <https://doi.org/10.47836/pjst.32.3.24>

E-mail addresses:

irfan.mujahidin@polines.ac.id (Irfan Mujahidin)

sidiqsh@polines.ac.id (Sidiq Syamsul Hidayat)

m.cahyoardi.p@polines.ac.id (Muhamad Cahyo Ardi Prabowo)

kitagawa@is.t.kanazawa-u.ac.jp (Akio Kitagawa)

*Corresponding author

INTRODUCTION

Hybrid electromagnetic solar energy harvesting (HES-ER) has become a promising solution to next-generation power of wireless communication, such as sensor nodes in wireless sensor networks and self-supporting Internet of Things (IoT) devices that recognize the latest research developments with energy harvesting techniques of radio frequency combining thin-film solar cells (Kim et al., 2019; Reynaud et al., 2017; Yuwono et al., 2015;). The HES-ER technique utilizes ambient and solar power to enable wireless devices to harvest solar and electromagnetic energy from RF signals (Pal et al., 2021). Ambient HES-ER is a green renewable energy solution that has attracted many researchers despite the great challenge of low incident power for the simultaneous and integrated design of HES-ER.

So, to increase the demanding requirements of the power ambient on the rectenna HES-ER system, research has been carried out for useful options regarding reliability and sustainability (Bahhar et al., 2020b; Wagih et al., 2021). The previous research has antennas with linear polarization, which are incapable of accommodating various polarizations caused by fading compared to CP antennas. Additionally, the antenna structure arrangement in the previous research did not mutually support the RF and solar energy harvesters, which are not situated in the same layer and have antenna impedance that needs to be matched (Mujahidin & Kitagawa, 2021a; Mujahidin & Kitagawa, 2021b).

This paper presents a hybrid electromagnetic solar energy harvesting design for ambient over a 2.3–2.4 GHz frequency band. It proposed a resonance structure-based matching stub. Circular polarization (CP) HES-ER strategically uses three layers of semiconductors to make up the antenna to achieve an axial ratio below 3 dB, a radiation pattern directional with many beams, and a relatively high gain (Hernowo et al., 2022; Hidayat et al., 2008). The integrated CP Antenna is exceptionally low-profile and compact, outperforming the existent HES-ER using a much more complex configuration. Furthermore, the applied array rectenna can be comfortably integrated into any embedded circuit board-based sensor device with mutually supporting performance layers in a single circuit board layer (Bahhar et al., 2020a; Bougas et al., 2021). More importantly, the simple design's overall circuit structure indicates that an antenna's impedance is tuned directly to serve a conjugate match with the impedance rectifier input in the expected working frequency under different input power and impedance matches between circuits (Mujahidin et al., 2020; Prasetya & Mujahidin, 2020).

MATERIALS AND METHODS

C-Slot CP Antenna HES-ER Sensor Circuit Design

The block diagram illustration of the C-Slot CP Antenna HES-ER Sensor Integrated Circuit

consists of a single circular antenna element with two output feeds connected linearly and directly to the sensor circuit and an energy harvester with an output impedance of 50 ohms (Figure 1). The configuration feed element uses a T-junction signal divider so that the CP antenna produced four outputs with the ability to harvest energy and produce phases with a 90-degree difference as a passive sensor element.

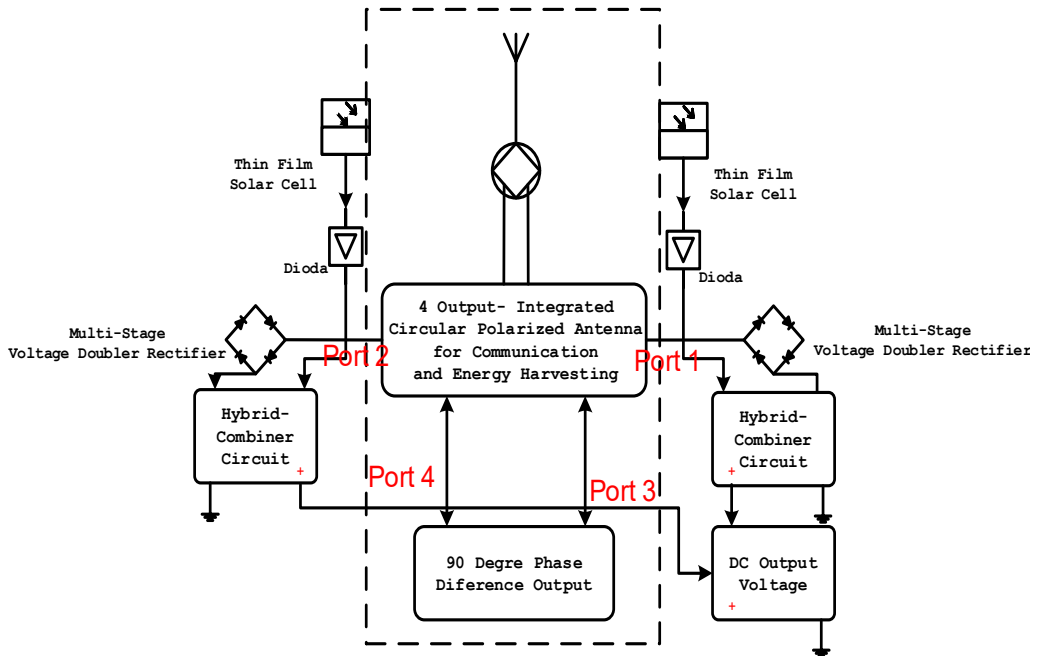


Figure 1. Block diagram of the circuit structure

The design of each component of the block considers the sustainability of the circuit with a model of one source of electromagnetic energy and two sources of solar energy. In the block diagram, the two solar sources take the position separately to show that the solar harvesting system still exists as a design with the antenna, but on the implementation of solar cells attached and integrated with the circuit C slot CP antenna (Bulu et al., 2006; Martinez et al., 2020). The connection between blocks can connect two models, the integrated circuit sensor and the SMA connector, on the energy harvesting system with a configured impedance matching.

C-Slot CP Antenna

Design C Slot CP Antenna consists of two-line feeds that connect based on the optimization of the antenna with a circular patch to produce an AR of less than 3 dB to produce circular polarization. The circular patch configuration optimizes by shifting the position of the via as a feed connector around the disk side surface based on the propagation model calculations

on the antenna radiating element (Bai et al., 2020; Liu et al., 2018; Prasetya & Mujahidin, 2020). This optimization has the consequence of a continuous propagation change process on the disk surface so that symmetrically, the two probes can generate LHCP on the left and RHCP on the right. Add a C-slot antenna design to increase the sensitivity to circular polarization waves and optimize the antenna's working frequency. In our design, the receiving antenna's C slot and the asymmetric coupler circuits print on a single layer of partially grounded phenolic white paper substrate ($\epsilon_r = 4.2$, $\tan\delta = 0.0027$). The complete C-Slot CP Antenna-Integrated Asymmetric Coupler design is shown in Figure 2.

Optimizing the antenna's shape and ground dimensions in designing working frequency as antenna performance is a mathematical approach to shift the resonance frequency to patch and slot dimension changes. The mathematical approach of the C slot is one of the

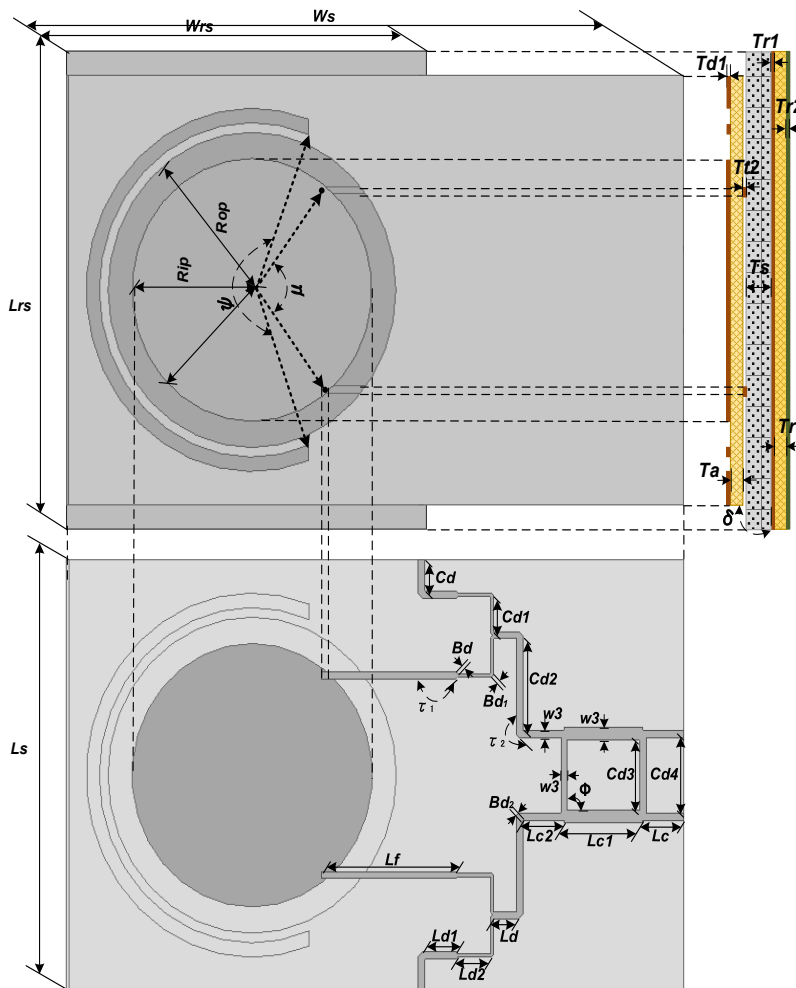


Figure 2. The structure design of C-slot CP antenna-integrated asymmetric coupler block diagram of the circuit structure

most crucial performance optimizations to improve accuracy and resonant frequency shift. The classification is based on the width of the slot dimensions and $C_{St} = C_{so} - C_{si}$ to determine the distance between the inner and outer radius to the main patch with the slot position on the ground antenna. The slot dimension change accuracy is 0.0001 m with a tolerance value of 5%.

Harvesting Circuit

The circuit harvesting configuration design optimizes by maximizing the available output power of the energy harvester by modeling the appropriate impedance at each transmission circuit. Therefore, the chosen design is a circuit voltage doubler proven effective in collecting RF and solar energy. So, as performance optimizes harvesters using a voltage multiplier, it is necessary to understand the stress multiplier process—the match of impedance between the harvester and the load. The harvesting part employing a stress multiplier applies the operation to the stress multiplier design with a freestanding inductive harvester based on the analysis design (Jones et al., 2018; Chen et al., 2022). It drives a monitoring sensor of wireless conditions using energy to extract from the magnetic field of ambient power frequency in an RF environment. The approximation of harvester calculation to the inductance L_{At} in step doubler with the resistance R_{At} in Figure 3 using the coil impedance. Analysis at the operating frequency F , where $\omega = 2\pi f$ expresses the impedance in Figure 3.

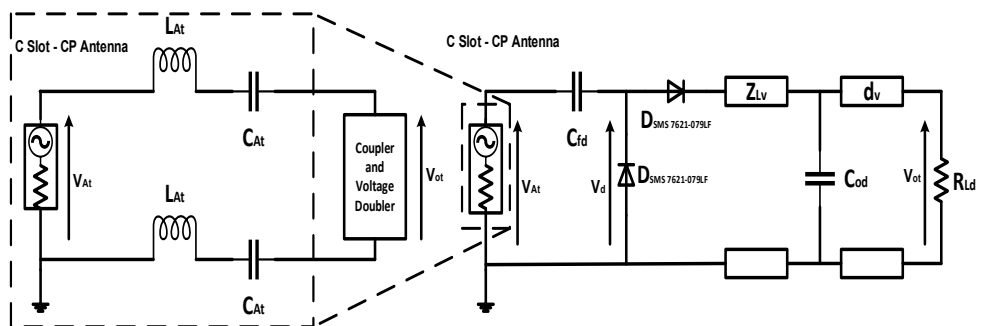


Figure 3. Harvester impedance of circuit configuration

This analysis applies to harvester designs using multipliers at the operating frequency in imaginary and real terms of components representing harvester impedance. An antenna is a source of AC voltage in ambient space, where at $V_{At} = V_{in} \sin(\omega t - \theta)$, in cycle with the impedance of coil impedance following Equation 1.

$$R_{At} + j\omega L_s \tag{1}$$

V_{in} is the voltage of the open circuit that will turn up across the coil when positioned in the same magnetic domain; it is the frequency dominant in the magnetic domain through

which the antenna collects the energy and the phase shift between the harmonic base and the magnetic domain of the SMS 7750 Schottky diode. The series circuit with the antenna, Capacitor C_{At} has two roles: (1) it compensates for the self-inductance of the antenna, and (2) it is also in the multiplier circuit, which is the first capacitor. The C_{cp} is a connection of capacitor at the multiplier output to provide energy storage for the density of low magnetic periods flux while also serving as a capacitor of smoothing for the multiplier (Mitani et al., 2017; Mustafizur Rahman et al., 2020; Sonalitha et al., 2020).

The diode for the multiplier is the SMS 7750 Schottky diode, functioning as a low conduction loss. The harvester in Figure 4 provides power to the resistive load R_{Ld} , while the leak resistor R represents the leakage through $D1, D2, C_{cp}$, and parallel to R_{Ld} . It will also be the capacitance of the diode load, but this has an insignificant impact on the circuit's action as per the frequency specifications of the diodes, which is involved in most energy-harvesting multistage applications with the whole multistage circuit.

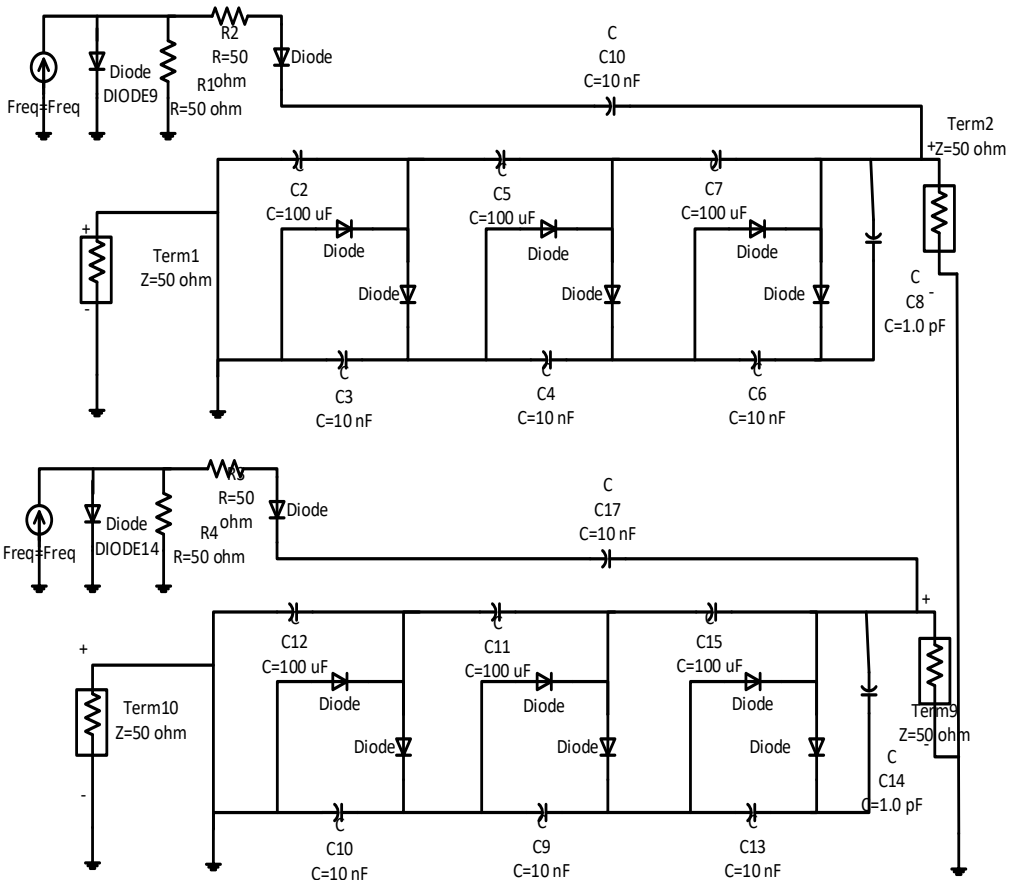


Figure 4. Harvesting multistage circuit configuration

The energy harvester in this work uses a 3-stage voltage doubler by accumulating in parallel with the coaxial connection with the solar cell integration (Figure 4). A single frequency dominates the design frequency in the circuit according to the antenna as a source with an AC harvesting source. Furthermore, in multistage operation, the AC surge harvester applied to a machine is dominated by a single band, although this band can often diverge with time. The output of the sine wave of the harvester goes to the voltage multiplier input. During the half-cycle negative, D1 establishes, so the voltage builds up on C_{At} .

During the half-cycle positive, the D2 charge transfers from C_{At} to C_{fd} . The circuit shows that both diodes cannot conduct simultaneously and will continue to increase to the next stage. The capacitor values are selected with values of $100\mu\text{f}$ and 10pf , so the charge time constant is much more extended than the input sine wave period (Bhattacharjee et al., 2018). Therefore, based on the analysis of the circuit construction method, determining the value of each component is based on the analysis in Figure 3, and then optimization is performed in the research to obtain the values of components that yield the highest power output (Mujahidin & Kitagawa, 2023).

To confirm the impedance output for the multiplier and the harvester, we analyze the circuit for an equilibrium state, where the power that will produce the harvester is equal to the power delivered to the RLd. With a magnetic flux density, the forward conduction loss in the SMS 7750 Schottky is a few W, in diversity to the loss between 10 W and a few mW. The diode conduction loss is therefore neglected in the analysis because it has a minimal value and is within the tolerance of the transmission voltage.

RESULTS AND DISCUSSIONS

C-Slot CP Antenna

A polarizing dual-feed C-Slot CP antenna with a configuration and a photo of the antenna fabrication is in Figure 5. The implementation of the optimized antenna configuration is in caption 1. The antenna size is $37.8\text{ mm} \times 40.4\text{ mm} \times 1.6\text{ mm}$. A feedline microstrip characteristic impedance of 50 excites the antenna. Four branches propagate RF-AC waves as sensors and harvest energy divided with the feedline. The four branches have the same width as the microstrip feedline with a T-junction configuration.

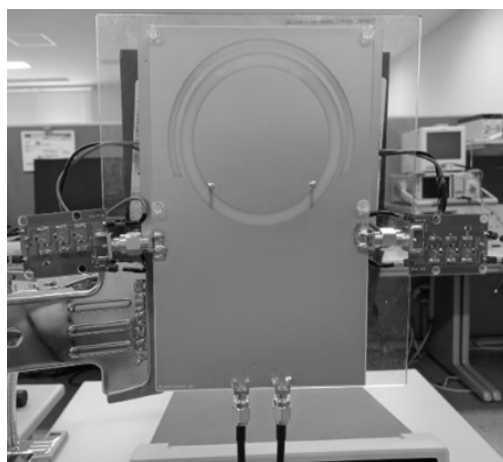


Figure 5. Fabrication of C-Slot CP antenna

The previous design report shows the impact of circular patch and C-slot parameters on characteristic impedance bandwidth. So, in this brevity, communication only discusses shorted vias and their effects on impedance matching and radiation characteristics. The antenna configuration was measured using Rhode and Schwarz ZVL Network Analyzer 9 KHz–13.6 GHz. The first is the characteristic impedance bandwidth of a dual-feed circular patch antenna and a C-slot with a via-hole connection in Figure 6. Bandwidth yields about 230 MHz (11%), about 2.4 GHz focus working frequency with a 2.35 GHz to 2.45 GHz frequency range.

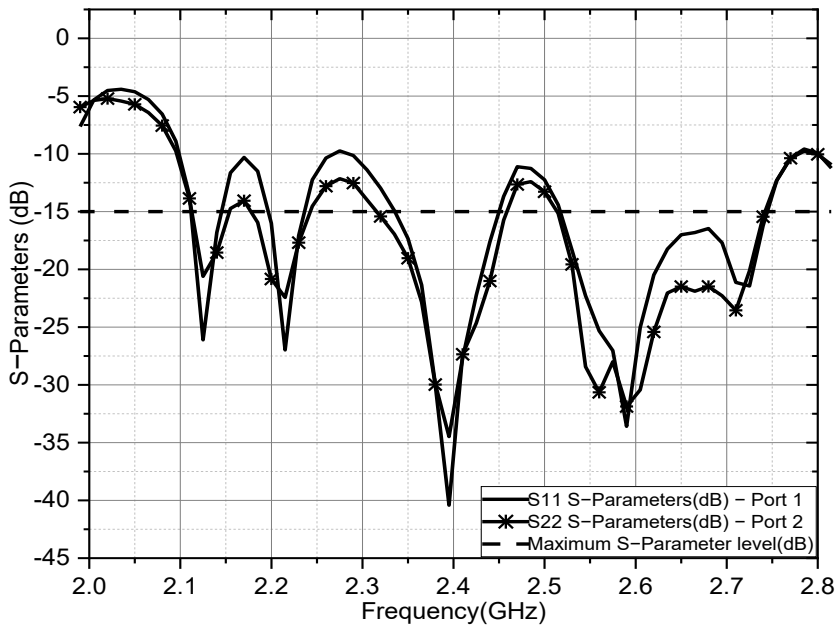


Figure 6. S parameter of C-slot CP antenna

The antenna element in the implementation has a symmetrical configuration to get a microstrip antenna with CP operation. Each fed and via hole position in this work is placed symmetrically to provide the wave propagation impulse needed to produce an axial ratio with a vertical and horizontal linear ratio below 3 dB. The proposed antenna’s gain and axial ratio on antenna parameter results at the resonant frequency of 2.3–2.4 GHz in Figure 6. With an effective bandwidth of 24%, in Figure 7, the antenna exhibits complete coverage at the frequency range with AR < 3 and a gain power level of 5.23 dB in the coverage field (Yuwono & Mujahidin, 2019; Zhang et al., 2022). The dual-feed configuration of a double C slot was developed to meet the requirements for impedance bandwidth, circular polarization features, 3 dB beamwidth with the dual feed technique, and antenna material with a low-cost profile.

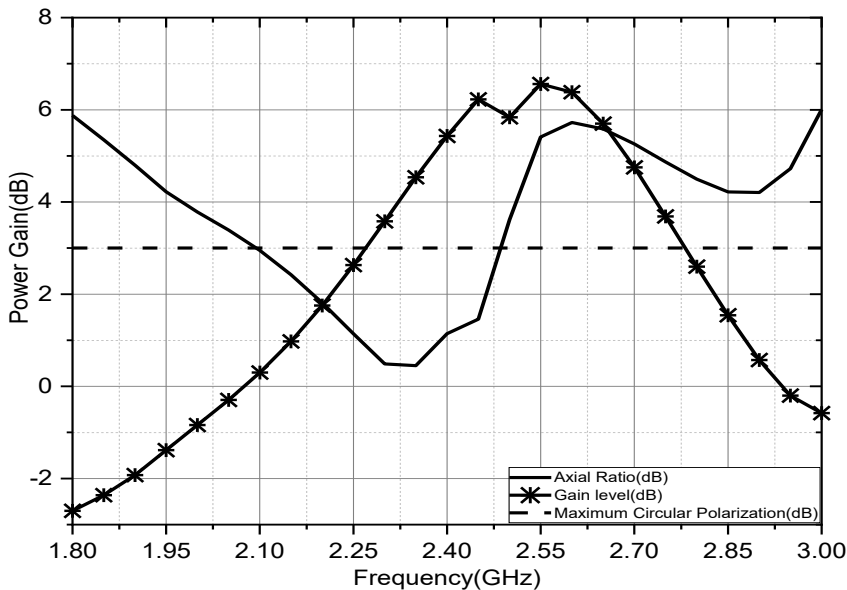


Figure 7. Gain level-axial Ratio of C-Slot CP antenna

Stage Energy Harvester on Hybrid Electromagnetic Solar and Wireless Sensor

The test field produces periodic transmission of electromagnetic waves with different power levels with the same frequency, namely 2.4 GHz, so that the test configuration can represent the ambient propagation empirically with these variables. The spectrum levels are 9.57 dBm, 0.27 dBm, -8.4 dBm, -16.8 dBm, and -31.32 dBm. After setting up the spectrum level configuration, the thin-film solar cell test on the energy harvesting circuit needs to be measured as a simultaneous integration of two energy sources. Still, the solar cell test setup needs to be measured independently first to identify the process of generating solar energy on the circuit with a high level of illumination as the main variable to describe the ability of the voltage to stream in the circuit (O'Conchubhair et al., 2017; Yan et al., 2021). Figure 8 represents the light lumination value on thin-film solar cells' exposure to the output and electromagnetic integration.

Figure 8 shows a stable voltage increase with increasing luminance for solar energy generation. Then, it is essential to measure RF energy independently. RF energy radiates and transmits isotropically evenly in the area according to the test variable with maximum effectiveness of the propagation power level of 30 dBm in the test field. The energy harvesting circuit uses a configuration with a constant resistance value, so the main focus of testing is high power.

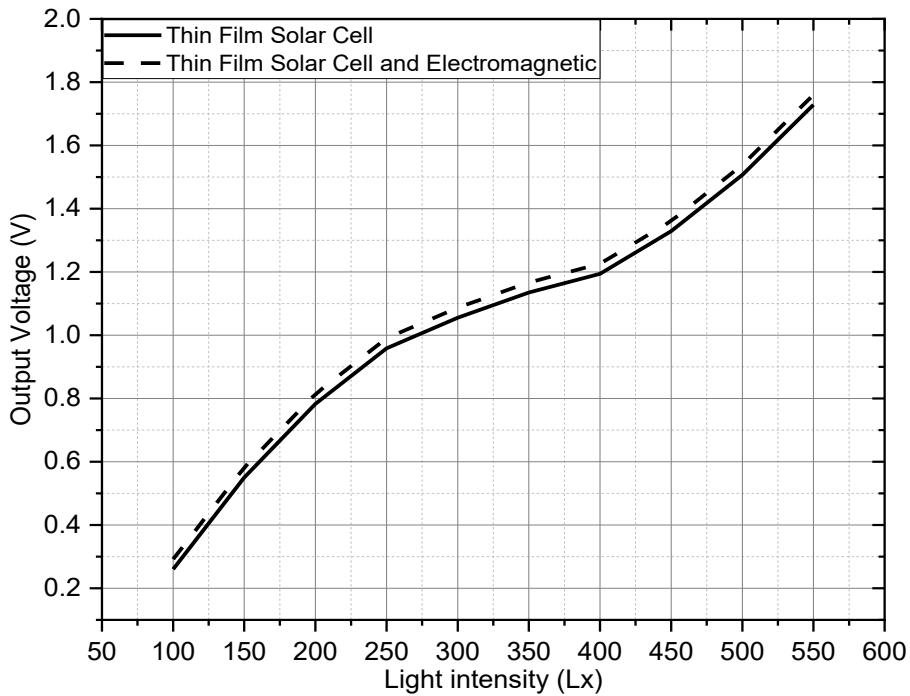


Figure 8. The light lamination value on thin-film solar cells' exposure to the output and electromagnetic integration.

CONCLUSION

This study's compact C-slot CP antenna focuses on the structure and configuration of the new energy harvesting using hybrid electromagnetic solar in the wireless energy harvesting of ambient from low-power device sensors. The system configuration has a C-slot antenna with a circular patch dual-feed frequency band of 2.3–2.4 GHz. C-slot CP Antenna has a wideband circular polarized (CP) dual-feed adopted for axial ratio (AR) requirements, producing LHCP and RHCP and a 90-degree phase difference simultaneously during energy harvesting. The approximation function determines the variance of the output phase and magnitude of the feed configuration under the needed AR by examining the 50 Ohm feed configuration output characteristics for a dual feed CP antenna. The analysis shows that several branch channel couplers can individually attain an AR bandwidth of less than 3 dB, with a directional radiation pattern and a high gain value above 5 dBm, with an integrated reflector system optimization.

Furthermore, a high-frequency rectifier circuit embedded with a thin-film solar cell on the antenna then connects two rectifiers that divide the power T-junction to design an output voltage of high-efficiency DC. In the measurement and analysis of the configuration structure, the maximum voltage value is 1.76 V at the integrated source in the hybrid

solar electromagnetic harvesting configuration. With a compact energy harvesting and wireless sensor structure, to make a significant improvement to the wireless sensor system with a complete communication system-level analysis in an electromagnetic propagation environment using the multiple signal classification method of powered ambient RF energy, the independent sensor node demonstrates reliable operation in an indoor environment.

Therefore, it has significant implications for powering small electronics and wireless sensor applications independently of the IoT network or real-world telecommunications industry, so this prototype model is very efficient in energy harvesting using hybrid electromagnetic solar and wireless sensing processes. From this work, future research can be proposed in the form of increasing the power that can be produced by re-optimizing the voltage doubler circuit. In this research scheme, it is also necessary to carry out a more in-depth analysis regarding propagation analysis in communication networks apart from its function as energy harvesting.

ACKNOWLEDGEMENTS

The authors acknowledge the financial, technical, and research support provided by the Graduate School of Natural Science and Technology, Kanazawa University, Japan and the Department of Telecommunication Engineering, Faculty of Electrical Engineering, Semarang State Polytechnic, Indonesia which made completing this work possible.

REFERENCES

- Bahhar, C., Baccouche, C., & Sakli, H. (2020a). A novel 5G rectenna for IoT applications. In *2020 20th International Conference on Sciences and Techniques of Automatic Control and Computer Engineering (STA)* (pp. 287–290). IEEE. <https://doi.org/10.1109/STA50679.2020.9329349>
- Bahhar, C., Baccouche, C., & Sakli, H. (2020b). Optical RECTENNA for energy harvesting and RF transmission in connected vehicles. In *2020 17th International Multi-Conference on Systems, Signals and Devices (SSD)* (pp. 262–266). IEEE. <https://doi.org/10.1109/SSD49366.2020.9364243>
- Bai, B., Zhang, Z., Li, X., Sun, C., & Liu, Y. (2020). Integration of microstrip slot array antenna with dye-sensitized solar cells. *Sensors* 2020, 20(21), 6257. <https://doi.org/10.3390/S20216257>
- Bhattacharjee, A., Saha, S., Elangovan, D., & Arunkumar, G. (2018). Naturally clamped, isolated, high-gain DC–DC converter with voltage doubler for battery charging of EVs and PHEVs. In A. Garg, A. K. Bhoi, P. Sanjeevikumar & K. K. Kamani (Eds.) *Advances in Power Systems and Energy Management. Lecture Notes in Electrical Engineering* (pp. 439–450). Springer. https://doi.org/10.1007/978-981-10-4394-9_44
- Bougas, I. D., Papadopoulou, M. S., Boursianis, A. D., Kokkinidis, K., & Goudos, S. K. (2021). State-of-the-Art Techniques in RF Energy Harvesting Circuits. *Telecom*, 2(4), 369–389. MDPI. <https://doi.org/10.3390/TELECOM2040022>
- Bulu, I., Caglayan, H., & Ozbay, E. (2006). Designing materials with desired electromagnetic properties. *Microwave and Optical Technology Letters*, 48(12), 2611–2615. <https://doi.org/10.1002/mop.21988>

- Chen, Q., Li, Z., Wang, W., Huang, Z., Liang, X., & Wu, X. (2022). A broadband dual-polarized solar cell phased array antenna. *IEEE Transactions on Antennas and Propagation*, 70(1), 353–364. <https://doi.org/10.1109/TAP.2021.3098520>
- Hernowo, R., Suharjono, A., Supriyo, B., Mukhlisin, M., Hidayat, S. S., Wardihani, E. D., & K.K, S. B. (2022). Power consumption optimization for flood monitoring system using NB-IoT. In *2022 5th International Seminar on Research of Information Technology and Intelligent Systems (ISRITI)*, (pp. 58-63). IEEE. <https://doi.org/10.1109/ISRITI56927.2022.10052891>
- Hidayat, S. S., Kim, B. K., & Ohba, K. (2008). Learning affordance for semantic robots using ontology approach. In *2008 IEEE/RSJ International Conference on Intelligent Robots and Systems*, (pp. 2630–2636). IEEE. <https://doi.org/10.1109/IROS.2008.4651193>
- Jones, T. R., Grey, J. P., & Daneshmand, M. (2018). Solar panel integrated circular polarized aperture-coupled patch antenna for cubesat applications. *IEEE Antennas and Wireless Propagation Letters*, 17(10), 1895–1899. <https://doi.org/10.1109/LAWP.2018.2869321>
- Kim, S., Tentzeris, M. M., & Georgiadis, A. (2019). Hybrid printed energy harvesting technology for self-sustainable autonomous sensor application. *Sensors*, 19(3), 728. <https://doi.org/10.3390/s19030728>
- Liu, S., Hou, Y., Xie, W., Schlücker, S., Yan, F., & Lei, D. Y. (2018). Quantitative determination of contribution by enhanced local electric field, antenna-amplified light scattering, and surface energy transfer to the performance of plasmonic organic solar cells. *Small*, 14(30), 1800870. <https://doi.org/10.1002/SMLL.201800870>
- Martinez, V. S., Jimenez, F. M., Baladron, I. P., Bautista, I. M., Ingelmo, J. V., Idoigabeitia, I. G., Besada, J. L., Iraguen, B. G., Gonzalez, J. M. F., & Mascarello, M. (2020). Steerable high-gain dual-reflector antenna at X-band for solar orbiter. *IEEE Transactions on Antennas and Propagation*, 68(8), 5784–5795. <https://doi.org/10.1109/TAP.2020.2980333>
- Mitani, T., Kawashima, S., & Nishimura, T. (2017). Analysis of voltage doubler behavior of 2.45-GHz voltage doubler-type rectenna. *IEEE Transactions on Microwave Theory and Techniques*, 65(4), 1051–1057. <https://doi.org/10.1109/TMTT.2017.2668413>
- Mujahidin, I., & Kitagawa, A. (2021a). CP antenna with 2×4 hybrid coupler for wireless sensing and hybrid RF solar energy harvesting. *Sensors*, 21(22), 7721. <https://doi.org/10.3390/S21227721>
- Mujahidin, I., & Kitagawa, A. (2021b). The novel CPW 2.4 GHz antenna with parallel hybrid electromagnetic solar for IoT energy harvesting and wireless sensors. *International Journal of Advanced Computer Science and Applications*, 12(8), 393–400. <https://doi.org/10.14569/IJACSA.2021.0120845>
- Mujahidin, I., & Kitagawa, A. (2023). Ring slot CP antenna for the hybrid electromagnetic solar energy harvesting and IoT application. *TELKOMNIKA (Telecommunication Computing Electronics and Control)*, 21(2), 290–301. <https://doi.org/10.12928/TELKOMNIKA.V21I2.24739>
- Mujahidin, I., Prasetya, D. A., Nachrowie, Sena, S. A., & Arinda, P. S. (2020). Performance tuning of spade card antenna using mean average loss of backpropagation neural network. *International Journal of Advanced Computer Science and Applications*, 11(2), 639–642. <https://doi.org/10.14569/ijacsa.2020.0110280>

- Mustafizur Rahman, M., Krishno Sarkar, A., & Chandra Paul, L. (2020). A voltage dependent meander line dipole antenna with improve read range as a passive RFID tag. In H. S. Saini, R. K. Singh, M. Tariq Beg & J. S. Shambi (Eds.) *Innovations in Electronics and Communication Engineering. Lecture Notes in Networks and Systems* (Vol. 107, pp. 123–138). Springer. https://doi.org/10.1007/978-981-15-3172-9_14
- O'Conchubhair, O., McEvoy, P., & Ammann, M. J. (2017). Dye-sensitized solar cell antenna. *IEEE Antennas and Wireless Propagation Letters*, *16*, 352–355. <https://doi.org/10.1109/LAWP.2016.2576687>
- Pal, P., Krishnamoorthy, P. A., Rukmani, D. K., Joseph Antony, S., Ocheme, S., Subramanian, U., Elavarasan, R. M., Das, N., & Hasanien, H. M. (2021). Optimal dispatch strategy of virtual power plant for day-ahead market framework. *Applied Sciences*, *11*(9), 3814. <https://doi.org/10.3390/APP11093814>
- Prasetya, D. A., & Mujahidin, I. (2020). 2.4 GHz double loop antenna with hybrid branch-line 90-degree coupler for widespread wireless sensor. In *10th Electrical Power, Electronics, Communications, Controls and Informatics Seminar* (pp. 298–302). IEEE. <https://doi.org/10.1109/EECCIS49483.2020.9263477>
- Reynaud, C., Duché, D., Palanchoke, U., Dang, F. X., Patrone, L., Le Rouzo, J., Gourgon, C., Charaï, A., Alfonso, C., Lebouin, C., Escoubas, L., & Simon, J. J. (2017). Harvesting light energy with optical rectennas. *Advanced Materials - TechConnect Briefs 2017*, *2*(2017), 45–48.
- Sonalitha, E., Zubair, A., Molyo, P. D., Asriningtias, S. R., Nurdewanto, B., Prambanan, B. R., & Mujahidin, I. (2020). Combined text mining: Fuzzy clustering for opinion mining on the traditional culture arts work. *International Journal of Advanced Computer Science and Applications*, *11*(8), 294–299. <https://doi.org/10.14569/IJACSA.2020.0110838>
- Wagih, M., Weddell, A. S., & Beeby, S. (2021). Powering e-textiles using a single thread radio frequency energy harvesting rectenna. *Proceedings*, *68*(1), 16. <https://doi.org/10.3390/PROCEEDINGS2021068016>
- Yan, N., Ji, C., Luo, Y., & Ma, K. (2021). A high gain solar cell aperture-coupled patch antenna based on substrate-integrated suspended line platform for 5G application. *Microwave and Optical Technology Letters*, *63*(11), 2876–2881. <https://doi.org/10.1002/MOP.33006>
- Yuwono, R., & Mujahidin, I. (2019). Rectifier using UWB microstrip antenna as electromagnetic energy harvester for GSM, CCTV and Wi-Fi transmitter. *Journal of Communications*, *14*(11), 1098–1103. <https://doi.org/10.12720/JCM.14.11.1098-1103>
- Yuwono, R., Mujahidin, I., Mustofa, A., & Aisah. (2015). Rectifier using UFO microstrip antenna as electromagnetic energy harvester. *Advanced Science Letters*, *21*(11), 3439–3443. <https://doi.org/10.1166/asl.2015.6574>
- Zhang, W., Liu, T., Yang, G., Jiang, C., Hu, Y., Zhu, X., Lan, T., & Zhao, Z. (2022). The application of beamforming technology in ionospheric oblique incidence sounding with Wuhan Multi-Channel Ionospheric Sounding System (WMISS). *IEEE Geoscience and Remote Sensing Letters*, *19*, 1–5. <https://doi.org/10.1109/LGRS.2021.3095910>

Modeling of Light Lifting Robotic Arm

Norfarahana Adibah Raffie¹, Noor Hafizah Amer^{1,2*}, Syed Mohd Fairuz Syed Mohd Dardin¹, Khisbullah Hudha¹ and Saiddi Ali Firdaus Mohamed Ishak¹

¹Department of Mechanical Engineering, Faculty of Engineering, National Defense University of Malaysia, Sg. Besi Army Camp, 57000 Kuala Lumpur, Malaysia

²Centre of Defense Research and Technology, National Defense University of Malaysia, Sg. Besi Army Camp, 57000, Kuala Lumpur, Malaysia

ABSTRACT

Robotic arms are often chosen as the primary manipulator for teleoperated robots specializing in executing tasks that require high skills from humans. The optimization of robotic arm design has been studied extensively using various types of optimization algorithms. However, studies validating and optimizing robotic arms with a high degree of freedom (DOF) using co-simulation techniques are scarce. This study presents the validation and modeling of a five-DOF robotic arm by observing the torques produced by each robotic arm joint using the co-simulation method between Solidworks and Simscape Multibody. The system is modeled in a Solidworks environment with full freedom and overall configurations. The model is then exported to Simscape Multibody for modeling processes. Several validation processes were conducted to validate the Simscape Multibody by comparing torques produced from the three-DOF robotic arm in Simscape with three DOF dynamic equations. Further validation was conducted using coordinate geometry of the end effector position in Solidworks, Simscape, and mathematical geometry models. The proposed co-simulation model agrees with the mathematical model with an average error of 7.6%. This study will likely provide a new approach to the co-simulation technique for systems with a high degree of freedom.

Keywords: Design optimization, lagrange equation, Simscape Multibody, Simulink, Solidworks

ARTICLE INFO

Article history:

Received: 16 August 2023

Accepted: 21 November 2023

Published: 04 April 2024

DOI: <https://doi.org/10.47836/pjst.32.3.25>

E-mail addresses:

farahanaraffie@gmail.com (Norfarahana Adibah Raffie)

noorhafizah@upnm.edu.my (Noor Hafizah Amer)

syedfairuz@upnm.edu.my (Syed Mohd Fairuz Syed Mohd Dardin)

k.hudha@upnm.edu.my (Khisbullah Hudha)

saiddi@upnm.edu.my (Saiddi Ali Firdaus Mohamed Ishak)

*Corresponding author

INTRODUCTION

It is well known that assessing in a hazardous environment poses a huge challenge to humans. The chance of an accident has become the main motivation for continuously studying robotics as a human assistant. In carrying out a task, some robots may be equipped with controllable arms that could reach a distance range with moveable

claws to grip any desired object. Programmed robotic arms that can be operated remotely are among various industries' most common human replacements. A wide range of robotic arms can be observed in the manufacturing and production industries, where programmable robotic arms perform tasks such as drilling, machining, and assembling. Apart from the industrial field, robotic arms are also used for tasks in hazardous environments to manage safety risks to human personnel. Examples of the utilization of a robotic arm in a hazardous environment can be observed in Pioneer, a teleoperated robot used to explore the Chernobyl power plant in the 1986 disaster, and LOUIE 1, which was deployed at Three Mile Island in 1979 (Tsitsimpelis et al., 2019). Pioneer has a robotic arm that collects the radioactive material remaining from the blast. Meanwhile, LOUIE 1 was assigned as a surveying robot.

The efficiency of the robotic arm lies in how well it is being designed. Therefore, many studies have focused on the design optimization of the robotic arm by first developing an analytical and simulation model of the system. It is usually beneficial to be used in the preliminary design stages to finalize the dimensions and concept designs. It will save time and cost to develop the final product. An industrial robotic arm was developed using the ANSYS Shape Optimization analysis (Bugday & Karali, 2019). The study used a model developed in ANSYS to optimize and analyze mechanical properties for each shape selection of the arm. In addition, a modification was proposed to modify the robotic arm kinematics from an originally non-redundant manipulator by adding virtual joints, making the robotic arm kinematically redundant, and introducing free motion of the mechanism (Maarroof et al., 2022). This mechanical redundancy allows researchers to visualize the robot configuration and optimize specific structural configuration variations.

Another research study has been conducted by Santosh et al. (2022) to develop a small-scale robotic arm using Creo Parametric software and Ansys Workbench. The paper focused on optimizing the design by observing the effect of changing the materials in the Ansys Workbench Finite Element Method under different loading conditions applied in the analysis. This similar process in robotic arm development could also be observed from a study by Ali et al. (2023) that used Solidworks to design the robotic arm for lightweight lifting and export it to Ansys Workbench to analyze the robotic arm. It was found that Finite Element Method (FEM) in the Ansys Workbench could provide feasible data in developing the robot arm for both studies. Yang and Hein (2023) suggested a training program that used machine learning to predict the weight of the objects lifted by the robot arm by observing the torques produced by the robot. The study promotes the ability of machine learning to grasp a larger variety of data as a tool in developing and optimizing robotic arms. However, the proposed method will depend on the data for one particular system. Another system will have to be developed with perhaps a different machine learning technique as proposed.

There are a few other recent studies on modeling robotic arms for further optimization (Seth et al., 2022; Seki et al., 2021). Among these, most designs were generic with two

to three degrees of freedom (DOF). More DOFs will pose different challenges and constraints on the modeling process. Those studies that consider more DOFs considered methods that will apply only to the specific design. By combining finite element analysis and dynamic analysis in MATLAB/Simulink, more complicated problems can be solved. Several researchers have explored the co-simulation approach between the FEA software and MATLAB/Simulink to allow more dynamic analyses. Among these, no proposal on the robotic arms modeling with more than three DOFs using co-simulation between FEA and MATLAB/Simulink software has been proposed.

In addressing this gap, this paper outlines the proposal to model and validate the design of a five-DOF robotic arm using the co-simulation technique between Solidworks and Simscape module in MATLAB/Simulink. This co-simulation will consider the more complicated DOFs as well as an easier transition to be used for other systems. This paper will discuss a co-simulation approach to model the considered system, which can be beneficial for numerical optimization works and applicable to various systems. It includes the derivation of three and five DOFs robotic arm Lagrangian mathematical model to verify the proposed co-simulation method, followed by the verification process to validate the proposed approach.

METHODS

Design of Robotic Arm

A robotic arm with five DOFs has been designed in a previous study (Raffie et al., 2021) based on the product design specification required. Five concept designs of the robotic arm have been generated and evaluated to select the finalized robotic arm for the light lifting task. The robotic arm will have one twisting joint, three rotating joints, and one prismatic joint. Four stepper motors will actuate these joints for rotational motion, and a brushless

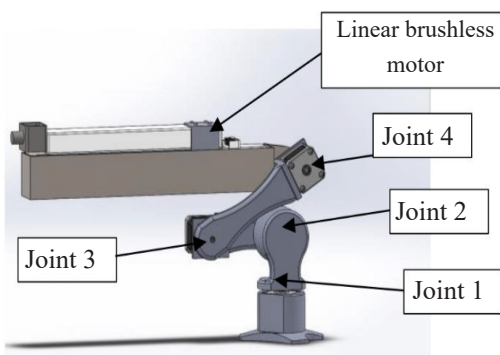


Figure 1. The finalized design of the five-DOF robotic arm

linear motor will act as an actuator for linear motion for the fifth link. The finalized design of the robotic arm considered in this study is shown in Figure 1.

Development of Mathematical Model

Development of the Three-DOF Model.

The Lagrange equation is an alternative to the Newton-Euler equation often used to describe the motion of systems with many DOFs and is more advantageous when the systems have more derivable forces

obtained from potential energy (Lee, 2006). The Lagrange equation is one of the most powerful tools in deriving equations of motion for a complicated system (Stutts, 2017). Equation 1 is using this approach.

$$\frac{d}{dt} \frac{\partial L}{\partial \dot{q}_i} - \frac{\partial L}{\partial q_i} = Q_i, \quad i = 1, \dots, n \quad [1]$$

Where q_i is the generalized coordinate, \dot{q}_i is the generalized velocity, and Q_i is the generalized external force in the system. Here, L is the Lagrangian term, which consists of the total kinetic energy within K and total potential energy, P , within the moving system, described in Equation 2.

$$L = K - P \quad [2]$$

In deriving the Lagrange equation for the three-DOF robotic arm shown in Figure 2, the generalized coordinate for the system can be derived as shown in Equations 3 and 4.

$$x_i = L_i \cos \theta_i \quad [3]$$

$$y_i = L_i \sin \theta_i \quad [4]$$

Here, x_i and y_i are the displacements in the x -axis and y -axis. L_i is the length of each robotic arm link, and θ_i is the angle of the link from the x -axis. From the geometry expression, kinetic and potential energy can be obtained. Hence, the Lagrangian as in Equation 5.

$$L = \sum \frac{1}{2} m V_i^2 + \sum \frac{1}{2} I \dot{\theta}_i^2 + \sum mgy_i \quad [5]$$

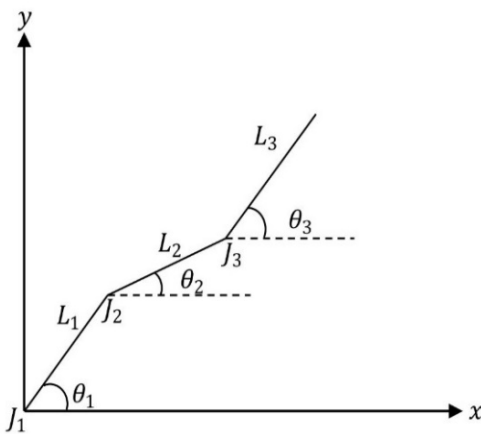


Figure 2. Three-DOF robotic arm free body diagram

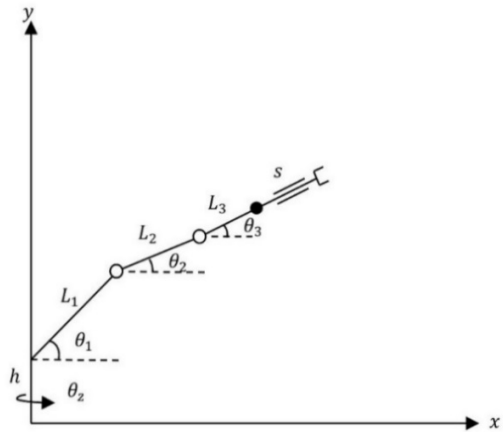


Figure 3. Five-DOF diagram

Since there are three generalized coordinates for the robotic arm, the Lagrange equation can be expressed as Equations 6, 7, and 8.

$$\frac{d}{dt} \frac{\partial L}{\partial \dot{\theta}_1} - \frac{\partial L}{\partial \theta_1} = T_1 \tag{6}$$

$$\frac{d}{dt} \frac{\partial L}{\partial \dot{\theta}_2} - \frac{\partial L}{\partial \theta_2} = T_2 \tag{7}$$

$$\frac{d}{dt} \frac{\partial L}{\partial \dot{\theta}_3} - \frac{\partial L}{\partial \theta_3} = T_3 \tag{8}$$

The final form of the governed equations for the three-DOF robotic arm can be obtained as in Equations 9, 10 and 11.

$$T_1 = L_1(M_1g\cos(\theta_1) + M_2g\cos(\theta_1) + M_3g\cos(\theta_1) + L_2M_2\dot{\theta}_2\dot{\theta}_1\sin(\theta_1 - \theta_2) + L_2M_3\dot{\theta}_2\dot{\theta}_1\sin(\theta_1 - \theta_2) + L_3M_3\dot{\theta}_3\dot{\theta}_1\sin(\theta_1 - \theta_3)) \tag{9}$$

$$T_2 = L_2M_2g\cos(\theta_2) + L_2M_3g\cos(\theta_2) - L_1L_2M_2\dot{\theta}_1\dot{\theta}_2(\sin(\theta_1 - \theta_2)) - L_1L_2M_3\dot{\theta}_1\dot{\theta}_2(\sin(\theta_1 - \theta_2)) + L_2L_3M_3\dot{\theta}_2\dot{\theta}_3(\sin(\theta_2 - \theta_3)) = 0 \tag{10}$$

$$T_3 = L_3M_3g\cos\theta_3 - L_1L_3M_3\dot{\theta}_3\dot{\theta}_1\sin(\theta_1 - \theta_3) - L_2L_3M_3\dot{\theta}_3\dot{\theta}_2\sin(\theta_2 - \theta_3) = 0 \tag{11}$$

Development of the Five-DOF Model. A similar derivation method was used to generate a mathematical model for the five-DOF of the proposed robotic arm using the Lagrange equation. The derivation of torque equations using the Lagrangian was conducted based on the free-body diagram of the five DOFs shown in Figure 3. Here, the same coordinates are used as in Equations 3 and 4. The final form of the derived equations can be observed from Equations 17, 18, 19, 20 and 21. There would be an addition to the velocity equation for the fifth link as the distance of the link can vary depending on the controller’s desire due to its translational motion. The derivation for kinetic energy for the fifth link is complicated due to the sliding distance that is not constant. Hence, the displacement notation and velocity in *the x* and *y* axes can be observed from the following Equations: 12, 13, 14, 15, and 16.

$$x_5 = s \cos \theta_3 \tag{12}$$

$$y_5 = s \sin \theta_3 \tag{13}$$

$$\dot{x}_5 = \dot{s} \cos \theta_3 - s\dot{\theta}_3 \sin \theta_3 \tag{14}$$

$$\dot{y}_5 = \dot{s} \sin \theta_3 + s\dot{\theta}_3 \cos \theta_3 \tag{15}$$

$$\text{Therefore, } K_5 = \frac{1}{2} m_5 (\dot{s}^2 + s^2 \dot{\theta}_3^2) \tag{16}$$

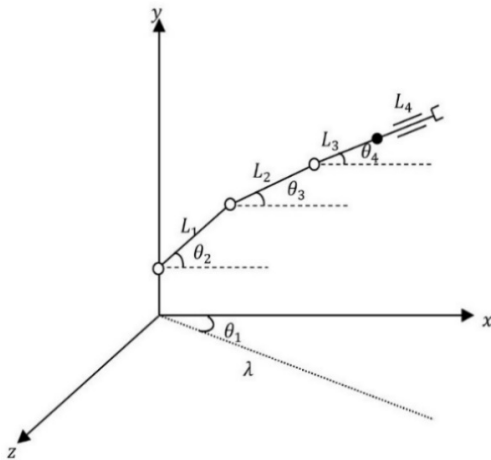


Figure 4. Free body diagram of the five-DOF robotic arm for coordinate geometry model

The generalized coordinates for all five DOFs of the Lagrange equation can be expressed as follows: Equations 17, 18, 19, 20, and 21.

$$\frac{d}{dt} \frac{\partial L}{\partial \dot{\theta}_1} - \frac{\partial L}{\partial \theta_1} = T_1 \quad [17]$$

$$\frac{d}{dt} \frac{\partial L}{\partial \dot{\theta}_2} - \frac{\partial L}{\partial \theta_2} = T_2 \quad [18]$$

$$\frac{d}{dt} \frac{\partial L}{\partial \dot{\theta}_3} - \frac{\partial L}{\partial \theta_3} = T_3 \quad [19]$$

$$\frac{d}{dt} \frac{\partial L}{\partial \dot{\theta}_4} - \frac{\partial L}{\partial \theta_4} = T_4 \quad [20]$$

$$\frac{d}{dt} \frac{\partial L}{\partial \dot{s}} - \frac{\partial L}{\partial s} = F_s \quad [21]$$

Development of the Geometric Model. The simulation model will also be validated using a geometric model that describes the coordinate of the end effector upon rotational input in each joint. The geometric model of the five-DOF robotic arm can be derived as Equations 22, 23, 24 and 25 using the same notation in Figure 3.

$$Y_{eff} = h + L_1 \sin \theta_2 + L_2 \sin \theta_3 + (L_3 + L_4) \sin \theta_4 \quad [22]$$

$$\lambda = L_1 \cos \theta_2 + L_2 \cos \theta_3 + (L_3 + L_4) \cos \theta_4 \quad [23]$$

$$X_{eff} = \lambda \cos \theta_1 \quad [24]$$

$$Z_{eff} = \lambda \sin \theta_1 \quad [25]$$

Where Y_{eff} , X_{eff} and Z_{eff} are the coordinates of the end effector at each axis x , y , and z , respectively. The coordinates of the end effector were observed from equations with three different robot arm trajectories, where the free-body diagram for the five-DOF robot arm could be observed in Figure 4.

Development of the Simscape Model

The 3D model of the robotic arm was then imported into the MATLAB Simscape Multibody environment. Simscape Multibody features that can convert rigid subassemblies in Solidworks into a rigid body in Multibody became the greatest advantage in minimizing the time consumption for the user in modeling CAD in Simulink. In this study, both robotic arms with three DOFs (based on Ramish et al., 2016) and five DOFs (based on the finalized design in Figure 1) were developed in Solidworks before being converted into the

Simscape multibody model. The co-simulation was carried out in the SOLIDWORKS 2020 and MATLAB Simulink version R2021b using solver ode45 and 0.01s step size settings. Further investigations on the effect of software versions and simulation settings yield indifferent results, meaning the proposed approach can be carried out on different versions.

RESULTS AND ANALYSIS

Validation of the Simscape Multibody Simulation Method

Stage 1 Validation of the Three-DOF. A previous study by Ramish et al. (2016), which outlined the validation process for a three-DOF robotic arm, was taken as a reference for the validation process. Based on the paper, the same motion input was supplied to each link of the proposed robotic arm. Using MATLAB/Simulink and Simscape Multibody, all modeling was simulated with the acceleration and trajectory inputs (Figure 5) within the duration of 1 second. The simulation showed a comparison of joint torques between the mathematical model from the previous study and the Simulink Multibody model (Figure 6). The percentage of error of the results was calculated to analyze the difference between the measured value from the Simulink Multibody and previous data. The purpose of finding the percentage of error, obtainable using Equations 26 and 27, is to observe the closeness of the measured torque from the multibody with the torque in the previous study. The calculated percentage of errors can be observed in Table 1.

$$\text{Percentage of error} = \frac{|T_{\text{multibody}} - T_{\text{previous}}|}{T_{\text{max}}} \times 100\% \tag{26}$$

$$RMS = \sqrt{\frac{(x_1^2 + x_2^2 \dots + x_n^2)}{N}} \tag{27}$$

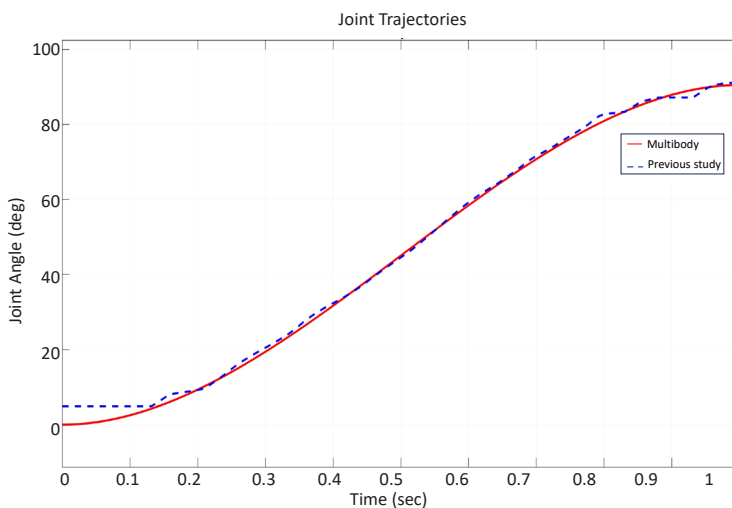


Figure 5. Trajectory input for each joint

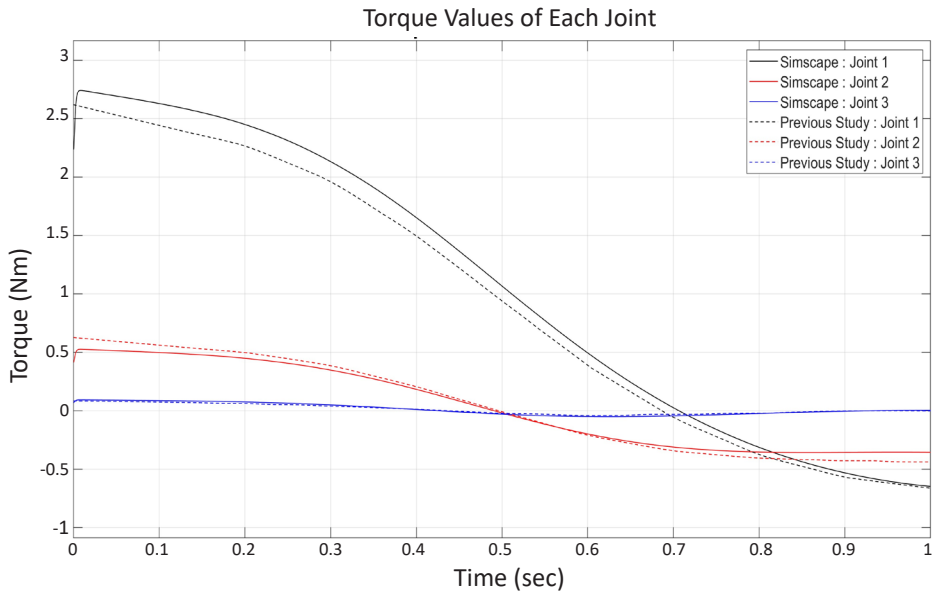


Figure 6. Torques produced by the Lagrange equation and Simscape Multibody

Stage 2 Validation of the Five-DOF. In this stage, the Simscape model of the proposed five-DOF robotic arm will be verified against the Lagrange mathematical equation with five systems based on the robotic arm in Figure 1. The trajectory inputs of the validation were generated using the cubic polynomial trajectory planning method (Guan et al., 2005). The cubic trajectory for the robotic arm can be observed in Equations 28, 29 and 30, where $q(t)$, $q'(t)$ and $q''(t)$ are the joint variables for the joint angle, angular velocity, and angular acceleration of the joint, which vary with time, t .

$$q(t) = a_0 + a_1t + a_2t^2 + a_3t^3 \quad [28]$$

$$q'(t) = a_1 + 2a_2t + 3a_3t^2 \quad [29]$$

$$q''(t) = 2a_2 + 6a_3t \quad [30]$$

The joint trajectory is shown in Figure 7, where the joint angles were set from 0° at the initial position and 50° at the final position within 5 seconds, while the fifth link was actuated to be fully extended within the same time set. These settings are based on the product design specification for the robotic arm to ensure efficient response (arm should be fully extended within 5 seconds) and workspace limitation (extended arm should not block LIDAR and remain within designated dimensions). The generated torques from the Simulink Multibody model were then observed and compared with the torque values produced from the mathematical model (Figure 8). The percentage errors between them were calculated and tabulated in Table 1 and Table 2, which shows a decent comparison between the two methods. The average error for the five DOFs model validation can be determined from values in Table 2, which is 7.6%. It shows that the variation between the

proposed Simscape model and the mathematical model is well within the acceptable limit of experimental accuracy (10%). The large error for Joint 1 (32.16 %) can be attributed to its ability to withstand more mass than the other joints, as shown in Figure 1. It will give rise to more resistance to motion between joints in the actual system that were not fully captured in the mathematical equations.

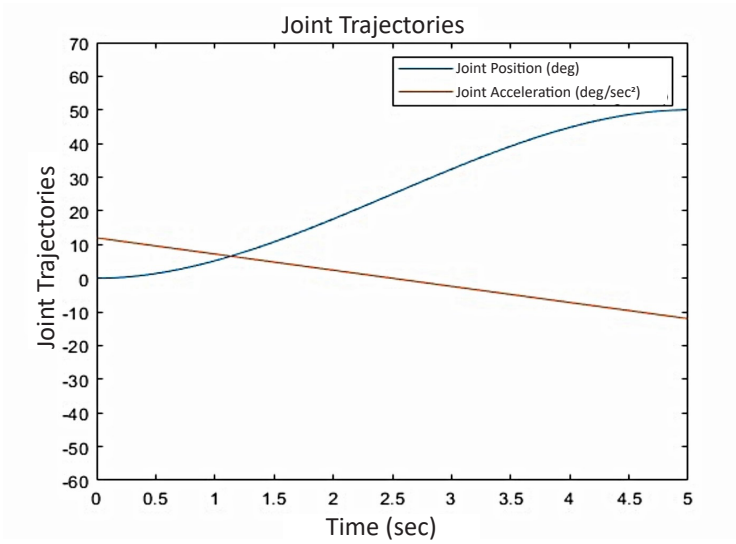


Figure 7. Trajectories of the five-DOF robotic arm

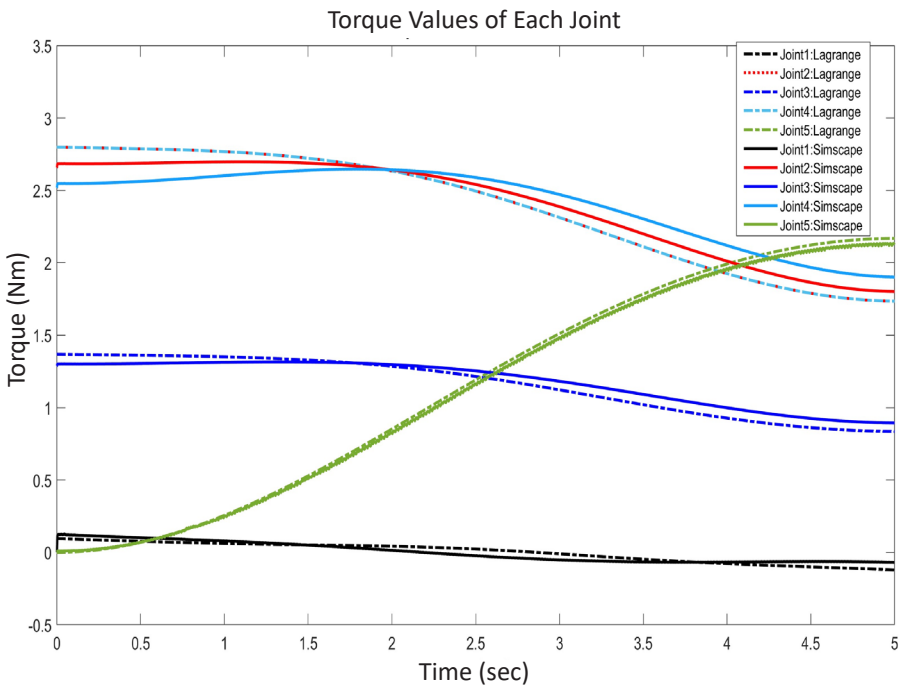


Figure 8. Torques produced from each joint in the proposed robotic arm

Table 1
Percentage error of each joint for the three-DOF

Percentage of Error (%)	
Joint 1	32.16
Joint 2	15.14
Joint 3	9.22

Table 3
The angle of each joint for different positions

	Position 1	Position 2	Position 3
Joint 1	0	0	45
Joint 2	0	45	45
Joint 3	0	45	45
Joint 4	0	45	45

Table 2
RMS error (RMSE) for five-DOF system

RMS Percentage Error (%)	
Joint 1	24
Joint 2	3
Joint 3	4
Joint 4	6
Joint 5	1
AVERAGE	7.6

Table 4
Coordinate end effector (in meters) for different positions

	Position 1	Position 2	Position 3
Simscape model	[0.67,0.16, 0.03]	[0.30,0.71, 0.03]	[0.19,0.71, 0.25]
Geometric model	[0.66,0.16, 0]	[0.35, 0.73, 0]	[0.18, 0.73, 0.30]

Stage 3 Validation of Coordinate Geometric.

The Simscape simulation model is further validated using a geometric model of the derived robotic arm. This step acts as another validation layer to verify the model against theoretical values before further simulation. This time, the position of the robotic arm's end effector will be verified. Three different cases were shown, which indicate different orientations of the arm: Position 1 (initial arm position with all joints at 0°), Position 2, and Position 3 (extended arm with all joints at maximum angle). The subsequent joint angle for each orientation and position is shown in Table 3. The end coordinate will be recorded from the Simscape and mathematical geometric models. Table 4 presents the obtained coordinates. Each set of values corresponds to the X, Y, and Z coordinates of the arm's end effector from the system origin.

DISCUSSION

Validation results for the three-DOF robotic arm in Figures 5 and 6 proved that the robotic arm model developed in the Simscape Multibody (by converting the CAD design of the robotic arm in Solidworks into the MATLAB Simscape Multibody) could produce a similar torque response compared to the experimental torque values from a previous study. By deriving a Lagrangian model based on the previous method, the five-DOF validation showed that the torque responses from the mathematical and Simscape models have a similar trend throughout the simulation. Some slight differences can be observed for joints two, three, and four in the five-DOFs system validation, which can be attributed to the various interactions and friction not modeled by the Lagrangian mathematical model. The

validation and percentage errors in Table 2 show that the Simscape model could produce a torque value close to the torques from the mathematical model for the five-DOF robotic arms, with an average of 7.6% deviations in all joints.

Further validation using the geometric model in Table 4 shows that the Simscape model managed to predict the end effector positions well within 0.05 m of X , Y , and Z coordinates. The difference can be attributed to the exclusion of friction and interaction effects in the mathematical model. Despite the errors in Joint 1, all the other joints were recorded as acceptable, which fulfills the main focus of this study, which is to model the end effector located at the rod on Joints 4 and 5. In addition, a very significantly lower error on Joint 5 (1%), which only has translational motion, shows that the error is small on the most important location of interest. In conclusion, the proposed co-simulation method between Simscape and Solidworks has been developed and validated using multiple verification methods. The overall difference between the simulated and theoretical responses is well within satisfactory range. This study will move into applying the proposed model to optimize the design of robotic arms in the future.

ACKNOWLEDGMENTS

This research has received support and funding from the Malaysian Ministry of Higher Education through the Fundamental Research Grant Scheme (FRGS/1/2021/TK02/UPNM/02/2) and Universiti Pertahanan Nasional Malaysia (UPNM) under the internal grant of UPNM/2019/CHEMDEF/ST/6.

REFERENCES

- Ali, Z., Sheikh, M. F., Al Rashid, A., Arif, Z. U., Khalid, M. Y., Umer, R., & Koç, M. (2023). Design and development of a low-cost 5-DOF robotic arm for lightweight material handling and sorting applications: A case study for small manufacturing industries of Pakistan. *Results in Engineering*, *19*, 101315. <https://doi.org/10.1016/j.rineng.2023.101315>
- Bugday, M., & Karali, M. (2019). Design optimization of industrial robot arm to minimize redundant weight. *Engineering Science and Technology, an International Journal*, *22*(1), 346–352. <https://doi.org/10.1016/j.jestch.2018.11.009>
- Guan, Y., Yokoi, K., Stasse, O., & Kheddar, A. (2005). On robotic trajectory planning using polynomial interpolations. In *2005 IEEE International Conference on Robotics and Biomimetics - ROBIO* (pp. 111-116). IEEE. <https://doi.org/10.1109/ROBIO.2005.246411>
- Lee, W. H. (2006). Lagrangian method. *Computer Simulation of Shaped Charge Problems*, 5-30. https://doi.org/10.1142/9789812707130_0002
- Maarroof, O. W., Dede, M. İ. C., & Aydin, L. (2022). A robot arm design optimization method by using a kinematic redundancy resolution technique. *Robotics*, *11*(1). <https://doi.org/10.3390/robotics11010001>
- Raffie, N. A., Amer, N. H., Dardin, S. M. F. S. M., Hudha, K., & Ishak, S. A. F. M. (2021). Preliminary concept modelling, evaluation and selection of robotic arm for light lifting application. In *2021 7th International*

- Conference on Mechanical Engineering and Automation Science (ICMEAS)* (pp. 178-183). IEEE. <https://doi.org/10.1109/ICMEAS54189.2021.00043>
- Ramish, Hussain, S. B., & Kanwal, F. (2016). Design of a 3 DoF robotic arm. In *2016 Sixth International Conference on Innovative Computing Technology (INTECH)* (pp. 145-149). IEEE. <https://doi.org/10.1109/INTECH.2016.7845007>
- Santosh, L. P. S., Mishra, N., Mahanta, S. S. A., Dharmarajan, V., Varma, S. K., & Shoor, S. (2022). Design and analysis of a robotic arm under different loading conditions using FEA simulation. *Materials Today: Proceedings*, *50*, 759–765. <https://doi.org/10.1016/j.matpr.2021.05.457>
- Seki, H., Nakayama, S., Uenishi, K., Tsuji, T., Hikizu, M., Makino, Y., & Kanda, Y. (2021). Development of assistive robotic arm for power line maintenance. *Precision Engineering*, *67*, 69-76. <https://doi.org/10.1016/j.precisioneng.2020.09.006>
- Seth, A., Kuruvilla, J. K., Sharma, S., Duttagupta, J., & Jaiswal, A. (2022). Design and simulation of 6-DOF cylindrical robotic manipulator using finite element analysis. *Materials Today: Proceedings*, *62*, 1521-1525. <https://doi.org/10.1016/j.matpr.2022.02.365>
- Stutts, D. S. (2017). *Analytical Dynamics: Lagrange's Equation and its Application – A Brief Introduction*. Missouri University of Science and Technology.
- Tsitsimpelis, I., Taylor, C. J., Lennox, B., & Joyce, M. J. (2019). A review of ground-based robotic systems for the characterization of nuclear environments. *Progress in Nuclear Energy*, *111*, 109-124. <https://doi.org/10.1016/j.pnucene.2018.10.023>
- Yang, F., & Hein, J. E. (2023). Training a robotic arm to estimate the weight of a suspended object. *Device*, *1*(1). <https://doi.org/10.1016/j.device.2023.100011>

REFEREES FOR THE PERTANIKA JOURNAL OF SCIENCE & TECHNOLOGY

Vol. 32 (3) Apr. 2024

The Editorial Board of the Pertanika Journal of Science and Technology wishes to thank the following:

Ahmad Hairul Basori
(KAU, Kingdom of Saudi Arabia)

Fateen Nabilla Rasli
(UKM, Malaysia)

M. Veera Krishna
(Royalaseema University, India)

Ahmad Jahanbakhshi
(UMA, Iran)

Gholamhosein Sodeifian
(University of Kashan, Iran)

Marsyita Hanafi
(UPM, Malaysia)

Ahmet Celik
(Ataturk University, Turkey)

Guangneng Dong
(XJTU, China)

Md Asaduzzaman
(NSW DPI, Australia)

Anchittha Rujeerapaiboon
(Chulalongkorn University, Thailand)

Hesam Kamyab
(MJIIT, Malaysia)

Mona Riza Mohd Esa
(UTM, Malaysia)

Anjan N Padmasali
(MIT, India)

Hu Kunhong
(HFUU, China)

Monalisa Ghosh
(IITKGP, India)

Aulia Saputra Azhar
(TMU, Japan)

Intan Sari Areni
(UNHAS, Indonesia)

Muhammad Fairuz Abdul Jalal
(UNITEN, Malaysia)

Chan Weng Howe
(UTM, Malaysia)

Ishak Aris
(UPM, Malaysia)

Muhammad Harussani
Moklis
(TITECH, Japan)

Che Zulzikrami Azner Abidin
(UniMAP, Malaysia)

Jianxun Ding
(CIAC, China)

Muhammad Idzdihar Idris
(UTeM, Malaysia)

Chukwu Ogbonnaya
(FUTMinna, Nigeria)

Joewono Prasetijo
(UTHM, Malaysia)

Muhammad Mukhlisin
(Polines, Indonesia)

Darius El Pebrian
(UiTM, Malaysia)

Jyotir Moy Chatterjee
(GEU, India)

Muhammad Naquiddin
Mohd Warid
(UTM, Malaysia)

Deepankar Kumar Ashish
(MAU, India)

Kamal Berahmand
(QUT, Australia)

Naoyuki Takesue
(TMU, Japan)

Dusan Gordic
(University of Kragujevac, Serbia)

Lee Foo Wei
(UTAR, Malaysia)

Noor Azlinda Ahmad
(UTM, Malaysia)

Erzam Marlisah
(UPM, Malaysia)

Lim Soh Fong
(UNIMAS, Malaysia)

Noor Azline Mohd Nasir
(UPM, Malaysia)

Fanhui Meng
(TYUT, China)

Lindah Roziani Jamru
(UMS, Malaysia)

Nor Hamizah Miswan
(UKM, Malaysia)

Sri Atmaja P. Rosyidi
(UMY, Indonesia)

Vali Rasooli Sharabiani
(UMA, Iran)

Noramalina Abdullah
(USM, Malaysia)

Suhad Hadi Mohammed
(UoK, Iraq)

Weihong Chin
(TMU, Japan)

Nur Azam Abdullah
(IIUM, Malaysia)

Sunny Goh Eng Giap
(UMT, Malaysia)

Yahui Guo
(CCNU, China)

Prasanna Rani K. N.
(IICT, India)

Surender Singh Samant
(GEU, India)

Yusuke Yamauchi
(University of Queensland, Australia)

Purabi Mazumdar
(UM, Malaysia)

Suzaimah Ramli
(UPNM, Malaysia)

Zdzislaw Kaliniewicz
(UWM, Poland)

Ratna Ika Putri
(POLINEMA, Indonesia)

Takenori Obo
(TMU, Japan)

Zhongqi He
(USDA, USA)

Sanjeeb Kumar Mandal
(CBIT, India)

Tee Tuan Poy
(UPM, Malaysia)

CBIT – Chaitanya Bharathi Institute of Technology
CIAC – Changchun Institute of Applied Chemistry
FUTMinna – Federal University of Technology Minna
GEU – Graphic Era University
HFUU – Hefei University
IICT – Indian Institute of Chemical Technology
IITKGP – Indian Institute of Technology Kharagpur
KAU – King Abdulaziz University
MAU – Maharaja Agrasen University
MIT – Manipal Institute of Technology
MJIIT – Malaysia-Japan International Institute of Technology
NSW DPI – New South Wales Department of Primary Industries
POLINEMA – Politeknik Negeri Malang
Polines – Politeknik Negeri Semarang
QUT – Queensland University of Technology
TITECH – Tokyo Institute of Technology
TMU – Tokyo Metropolitan University
TYUT – Taiyuan University of Technology
UITM – Universiti Teknologi MARA

UKM – Universiti Kebangsaan Malaysia
UM – Universiti Malaya
UMA – University of Mohaghegh Ardabili
UMS – Universiti Malaysia Sabah
UMT – Universiti Malaysia Terengganu
UMY – Universitas Muhammadiyah Yogyakarta
UNHAS – Hasanuddin University
UNIMAP – Universiti Malaysia Perlis
UNIMAS – Universiti Malaysia Sarawak
UNITEN – Universiti Tenaga Malaysia
UoK – University of Kerbala
UPM – Universiti Putra Malaysia
USDA – United States Department of Agriculture
USM – Universiti Sains Malaysia
UTAR – Universiti Tunku Abdul Rahman
UTeM – Universiti Teknikal Malaysia Melaka
UTHM – Universiti Tun Hussein Onn Malaysia
UTM – Universiti Teknologi Malaysia
XJTU – Xi'an Jiaotong University

While every effort has been made to include a complete list of referees for the period stated above, however if any name(s) have been omitted unintentionally or spelt incorrectly, please notify the Chief Executive Editor, *Pertanika* Journals at executive_editor.pertanika@upm.edu.my

Any inclusion or exclusion of name(s) on this page does not commit the *Pertanika* Editorial Office, nor the UPM Press or the university to provide any liability for whatsoever reason.

Effect of Maturity Stages on Physical Properties of Cocoa (*Theobroma cacao* L.) Pods 1401

Babatunde Oluwamayokun Soyoye, Nazmi Mat Nawi, Mohamad Ariffin Zulkifli, Guangnan Chen, Nurfadzilah Madian, Ahmad Faiz Mokhtar, Siti Nooradzah Adam and Dimas Firmanda Al Riza

Selected papers from the 5th International Conference on Innovation in Science and Technology

Guest Editors: Eri Sato-Shimokawara, Muslihah Wook and Kurnianingsih

C-Slot Circular Polarized Antenna for Hybrid Energy Harvesting and Wireless Sensing 1413

Irfan Mujahidin, Sidiq Syamsul Hidayat, Muhamad Cahyo Ardi Prabowo and Akio Kitagawa

Modeling of Light Lifting Robotic Arm 1427

Norfarahana Adibah Raffie, Noor Hafizah Amer, Syed Mohd Fairuz Syed Mohd Dardin, Khisbullah Hudha and Saiddi Ali Firdaus Mohamed Ishak

- Optimisation of the Distribution System Reliability with Shielding and Grounding Design Under Various Soil Resistivities 1263
Jia-Wen Tang, Chin-Leong Wooi, Wen-Shan Tan, Hadi Nabipour Afrouzi, Hana Abdull Halim and Syahrin Nizam Md Arshad@Hashim
- Identifying Communities with Modularity Metric Using Louvain and Leiden Algorithms 1285
Siti Haryanti Hairol Anuar, Zuraida Abal Abas, Norhazwani Md Yunos, Mohd Fariduddin Mukhtar, Tedy Setiadi and Abdul Samad Shibghatullah
- Elicitation of Cryptic Secondary Metabolites and Antibacterial Activities from Mangrove and Cave Soil Actinomycetes 1301
Intan Azzween Natasha Ahmad Razi, Nurunajah Ab Ghani, Siti Hajar Sadiran, Suhaidi Ariffin, Sharifah Aminah Syed Mohamad and Anis Low Muhammad Low
- Review Article*
- Detection of Sedge Weeds Infestation in Wetland Rice Cultivation Using Hyperspectral Images and Artificial Intelligence: A Review 1317
Muhamad Noor Hazwan Abd Manaf, Abdul Shukor Juraimi, Mst. Motmainna, Nik Norasma Che'Ya, Ahmad Suhaizi Mat Su, Muhammad Huzaifah Mohd Roslim, Anuar Ahmad and Nisfariza Mohd Noor
- An Improved Ensemble Machine Learning Approach for Diabetes Diagnosis 1335
Mohanad Mohammed Rashid, Omar Mahmood Yaseen, Rana Riyadh Saeed and Maher Talal Alasaady
- Integrating Green Infrastructure Distribution and Green Corridor Mapping with Proposed Green Trail Area and Wildlife-Human Conflict Using Remote Sensing-GIS Approach 1351
Syarifuddin Misbari, Jacqueline Isabella Anak Gisen, Nur Arissa Farhanis Mohd Rosli, Amir Asyraf Mohd Fauzi and Aishah Abu Bakar
- Model-driven Approach to Improve Sago Drying with a Fluidized Bed Dryer 1363
Nur Tantiyani Ali Othman and Nurfadilah Izaty Senu
- Evaluation of Field Performance and Energy Consumption of a Medium-sized Combine Harvester for Harvesting Glutinous Rice in Malaysia 1385
Nazmi Mat Nawati, Bomo Muhammad Isa, Samsuzana Abd Aziz and Mohamad Saufi Mohd Kassim

An Accident Prediction Model Based on ARIMA in Kuala Lumpur, Malaysia, Using Time Series of Actual Accidents and Related Data <i>Boon Chong Choo, Musab Abdul Razak, Mohd Zahirasri Mohd Tohir, Dayang Radiah Awang Biak and Syafie Syam</i>	1103
Effects of NaOH Concentration and Plate Surface Texture on the Performance of the HHO Generator <i>Asmawi Marullah Ridwan, Muhd Ridzuan Mansor, Noreffendy Tamaldin, Fahamsyah Hamdan Latief and Viktor Vekky Ronald Repi</i>	1123
Effect of Bimetallic Co-Cu/Dolomite Catalyst on Glycerol Conversion to 1,2-Propanediol <i>Norsahida Azri, Ramli Irmawati, Usman Idris Nda-Umar, Mohd Izham Saiman, Yun Hin Taufiq-Yap and Ghassan Abdulkareem-Alsultan</i>	1141
Evaluation of Microalgae <i>Chlorella vulgaris</i> and <i>Tetradesmus bernardii</i> for Cultivation and Nutrient Removal in Palm Oil Mill Effluent <i>Mohammad Navid Wais, Shahrizim Zulkifly, Mohd Hafiz Ibrahim, Afiqah Mohamed and Zana Ruhaizat Zana Rudin</i>	1161
Study of LED Retrofit Lamps in HSPV Luminaires Based on Photometric Method for Road Lighting <i>Mohd Hanif Jamaludin, Wan Zakiah Wan Ismail, Elina Mohd Husini and Nor Ain Mohd Bahrar</i>	1187
Application of Membrane-less Microbial Fuel Cell in Reducing Human Hazards from Dewatered Sludge <i>Fatin Nur Izzati Mohd Fadzil, Chen Sep Ngee, Mohammed Zharif Asyrani Mohammed Alias, Muhammad Adib Fadhlullah Muhammad Lukman, Amira Suriaty Yaakop, Muaz Mohd Zaini Makhtar and Ana Masara Ahmad Mokhtar</i>	1203
<i>Review Article</i> Weed Management Using UAV and Remote Sensing in Malaysia Paddy Field: A Review <i>Zaid Ramli, Abdul Shukor Juraimi, Mst. Motmainna, Nik Norasma Che'Ya, Muhammad Huzairah Mohd Roslim, Nisfariza Mohd Noor and Anuar Ahmad</i>	1219
SPICE Modeling and Performance Analysis of Enhancement- Mode GaN HEMTs for Augmented Hard-Switching Energy Conversion Efficiency <i>Xinzhong Liu, Suhaidi Shafie, Mohd Amran Mohd Radzi, Norhafiz Azis, Nurbahirah Norddin, Ismail Lawal, Normaziah Zulkifli and Abdul Hafiz Abdul Karim</i>	1243

Pertanika Journal of Science & Technology

Vol. 32 (3) Apr. 2024

Content

- Foreword i
Mohd Sapuan Salit
- Review Article*
A Review of Non-wood Lignocellulose Waste Material Reinforced Concrete for Light-weight Construction Applications 979
Hossam Saleh Salem Saeed, Agusril Syamsir, Mohd Supian Abu Bakar, Muhammad Imran Najeeb, Abdulrahman Alhayek, Zarina Itam, Muhammad Rizal Muhammad Asyraf and Mohd Radzi Ali
- Development of Small-scale Integrated Hydroponics—Animal Waste Bioreactor (AWB) for Romaine Lettuce (*Lactuca sativa* L. var. longifolia) Production 1003
Elman Cantero Torres, Theody Bernardo Sayco, Marvin Mateo Cinense, Jonathan Viernes Fabula, Wendy Mateo and Carolyn Grace Galo Somera
- Anti-friction and Wear Resistance Performance of Palm Olein Grease with Molybdenum Disulfide Additive 1023
Nadiyah Aqilahwati Abdullah, Nurul Farhana Mohd Yusof and Zaidi Mohd Ripin
- Review Article*
Supercritical Carbon Dioxide Extraction of Citronella Oil Review: Process Optimization, Product Quality, and Applications 1043
Nicky Rahmana Putra, Ahmad Hazim Abdul Aziz, Dwila Nur Rizkiyah, Mohd Azizi Che Yunus, Ratna Surya Alwi, Reny Tri Anggraini, Siti Khodijah, Irianto Irianto and Lailatul Qomariyah
- An Empirical Evaluation of Adapting Hybrid Parameters for CNN-based Sentiment Analysis 1071
Mohammed Maree, Mujahed Eleyat and Shatha Rabayah
- Mathematical Modelling of Scission Electrospun Polystyrene Fibre by Ultrasonication Scission 1087
Cheryl Rinai Raja, Marini Sawawi, Shirley Johnathan Tanjong and Nurliyana Truna



Pertanika Editorial Office, Journal Division,
Putra Science Park,
1st Floor, IDEA Tower II,
UPM-MTDC Center,
Universiti Putra Malaysia,
43400 UPM Serdang,
Selangor Darul Ehsan
Malaysia

<http://www.pertanika.upm.edu.my>
Email: executive_editor.pertanika@upm.edu.my
Tel. No.: +603- 9769 1622

PENERBIT
UPM
UNIVERSITI PUTRA MALAYSIA
PRESS

<http://www.penerbit.upm.edu.my>
Email: penerbit@upm.edu.my
Tel. No.: +603- 9769 8851

